NEW YORK CITY DEPARTMENT OF ENVIRONMENTAL PROTECTION
BUREAU OF WATER SUPPLY

Multi-Tiered Water Quality Modeling Program
Annual Status Report

This status report describes work completed by NYCDEP's Multi-Tiered Water Quality Modeling Program during October 2012 – December 2013.

March 31, 2014

Prepared in accordance with Section 5.2 of the July 2007 United States Environmental Protection Agency Filtration Avoidance Determination

Prepared by: Donald Pierson, WWQSR, Water Quality Modeling
Elliot Schneiderman, WWQSR, Water Quality Modeling
Mark Zion, WWQSR, Water Quality Modeling
David Lounsbury, WWQSR, Water Quality Modeling
Donald Kent, WWQSR, Water Quality Modeling
Soni Pradhanang, City University of New York, Institute for Sustainable Cities
Rajith Mukundan, City University of New York, Institute for Sustainable Cities
Yongtai Huang, City University of New York, Institute for Sustainable Cities
Nihar Samal, City University of New York, Institute for Sustainable Cities
Antoine Randolph, City University of New York, Institute for Sustainable Cities
Allan Frei, City University of New York, Institute for Sustainable Cities

Table of Contents

1. Introduction

This status report describes work completed for DEP's Multi-Tiered Water Quality Modeling Program during October 2012 – December 2013. The report presents progress on activities discussed in Section 2.4.2 of the New York City's Long-Term Watershed Program (DEP, 2006a). The following activities are reported herein:

- Application of DEP's reservoir, watershed and system models to inform operational decisions during the reporting period (Section 2);

- Model applications and projects related to climate change analyses including a summary of the findings of Phase I of the Climate Change Integrated Modeling Project (CCIMP), an analysis of the seasonal changes in phytoplankton under climate change, a study of climate change effects on reservoir thermal properties, a study of climate change effects on streamflow hydrologic indicators and description of the WRF 4262 and WRF 4305 projects on vulnerability assessment and risk management tools (Section 3);

- Studies related to model development including: an application of SWAT for sediment loading; a study of THMs using an empirical model; a description of the hydro-ecological modeling project; a description of SWAT model upgrades current being developed; a description of recent improvement to the CEQUAL-W2 turbidity models; application of a lake ice model; and a study of 1D reservoir model uncertainty. (Section 4);

- Data analyses that support model development and the understanding of watershed processes including: a description of USGS monitoring of sediment and turbidity in Esopus Creek watershed; a study of phosphorus loading hysteresis; and a study of recent trends in precipitation and snowfall. (Section 5);

- Model data acquisition, development and organization (Section 6);

- Collaboration of the Water Quality Modeling Section with other projects and organizations including cooperative arrangements, contracts and proposals. (Section 7); and

- Summary of scientific journal papers and presentations at scientific conferences that the Water Quality Modeling Section has given over the last year (Section 8).

2. Use of Models for Support of Operational Decisions

In total, the Water Quality Modeling Section performed eight separate turbidity modeling analyses for Kensico, Ashokan and/or Schoharie Reservoirs during the October 2012- December 2013 reporting period. Turbidity model simulations to support operational decisions during the reporting period were necessitated by elevated Catskill System turbidity due initially to a large streamflow event in Esopus Creek during September 2012. In addition, during the fall of 2012 a series of smaller events continued to impact the Catskill System. A rain and snowmelt driven event in March 2013 also resulted in slightly increased turbidity in the system, further requiring application of turbidity modeling runs. As the turbidity generated by these events affected the Catskill and Delaware Systems, these model simulations were used to better guide the operations of the system to ensure the delivery of high quality water without the use of alum. In addition to these model simulations, the Water Quality Modeling Section continued to support development of the Operations Support Tool (OST) through collaboration with DEP's Operations Support Section and the OST contractors.

Simulation Descriptions

Two types of model simulations were used for operational support during the reporting period: (1) Kensico Reservoir sensitivity simulations and (2) Operation Support Tool (OST) (DEP 2011) applications. For both types of simulations, a "position analysis" strategy was used. The initial conditions of the reservoir water quality and storage are used as the starting point for the model simulations. Then the models are run for a forecast period which ranges from 1 to 6 months into the future, depending on the simulation goals. For the forecast period, inputs of streamflow, meteorology and/or inflow water temperature are based on the historical record (1948-2004 for OST runs and 1987-2004 for Kensico model runs). Each forecast trace is therefore driven using historical data occurring over the forecast period. Each year of data becomes a separate realization (or trace) of the simulated model outcomes. The complete set of position analysis traces, can then be used to develop a statistical probability of future simulated reservoir storage levels and effluent turbidity.

For the Kensico Reservoir sensitivity simulations LinkRes and its component 2D reservoir model CEQUAL W2 (DEP 2004, Cole and Buchak 1995) were used to simulate turbidity values within the reservoir and aqueduct withdraws. The initial conditions of reservoir water quality and temperature are set to most recently measured values based on a combination of limnological survey data and in-lake automated buoy measurements. For the forecast period, input aqueduct flows and turbidity are set at fixed values associated with the range of the sensitivity analyses, while inputs of meteorology and aqueduct water temperature are based on each year in the historical record. This allows for sensitivity analysis of the Kensico effluent based on a series of fixed aqueduct turbidity and flow influent conditions with the year-to-year variability in the traces representing the potential variability in forecast weather conditions. The results can then be used to better understand the implications of given influent flow rates and turbidity on future Kensico Reservoir effluent turbidity.

For OST simulations the forecast reservoir input streamflows and turbidity are based on the historical record and are conditioned to recent history. These flows and corresponding turbidity loads are input to the OASIS model, which predicts reservoir storage, water quality and aqueduct flows based on a set of operating rules. In these cases, each trace represents a simulated outcome incorporating both climatic and flow variability of the forecast period. To help guide operations, the model is run using different sets of operating rules, and the resulting ranges of future reservoir storage and water quality, are compared for simulations using varying operating strategies

Figure 2.1 shows the Esopus Creek streamflow and turbidity and the Catskill Aqueduct turbidity in the Ashokan effluent for the reporting period along with the dates of water quality modeling analyses performed to aid in operational decisions. Table 2.1 details the modeling analyses performed during the period. A storm event in mid-September 2012 caused elevated turbidity in the Ashokan West Basin and in Neversink Reservoir. Since the West Basin was already drawn down, the East Basin was not severely impacted by the event. After more storm events in the fall the higher turbidity from the West Basin began to impact the East Basin of Ashokan. In response to these fall events OST runs were conducted to understand (a) the potential timing and magnitude of movement of water and turbidity from the West Basin to the East Basin, (b) the extent to which the use of the Ashokan Release Channel (ARC) would change the this timing and magnitude of turbidity movement from West to East; (c) the effects of ARC use on potential Catskill Aqueduct flow reductions due to turbidity, and (d) the temporary loss of the Neversink diversion on reservoir storage. In addition, during the fall of 2012, three Kensico Reservoir sensitivity simulations were performed to help determine optimal Catskill Aqueduct flows that would maintain water quality standards at Kensico effluents while avoiding alum use.

In January 2013, OST was used to understand the possible timing and magnitude of the expected peak turbidity in Ashokan Reservoir due to upcoming spring runoff events. This was of particular importance as more Catskill water would be needed during the spring due to a drawdown of Rondout Reservoir. After a rain and snowmelt event in mid-March a Kensico Reservoir sensitivity simulation was run to continue to ensure that Kensico effluents would meet turbidity standards. Finally, in April 2013, OST was used once more to ascertain the water quality benefits versus the storage draw down trade-offs of using the ARC to reduce the impact of West Basin to East Basin movement of water and turbidity in Ashokan Reservoir.

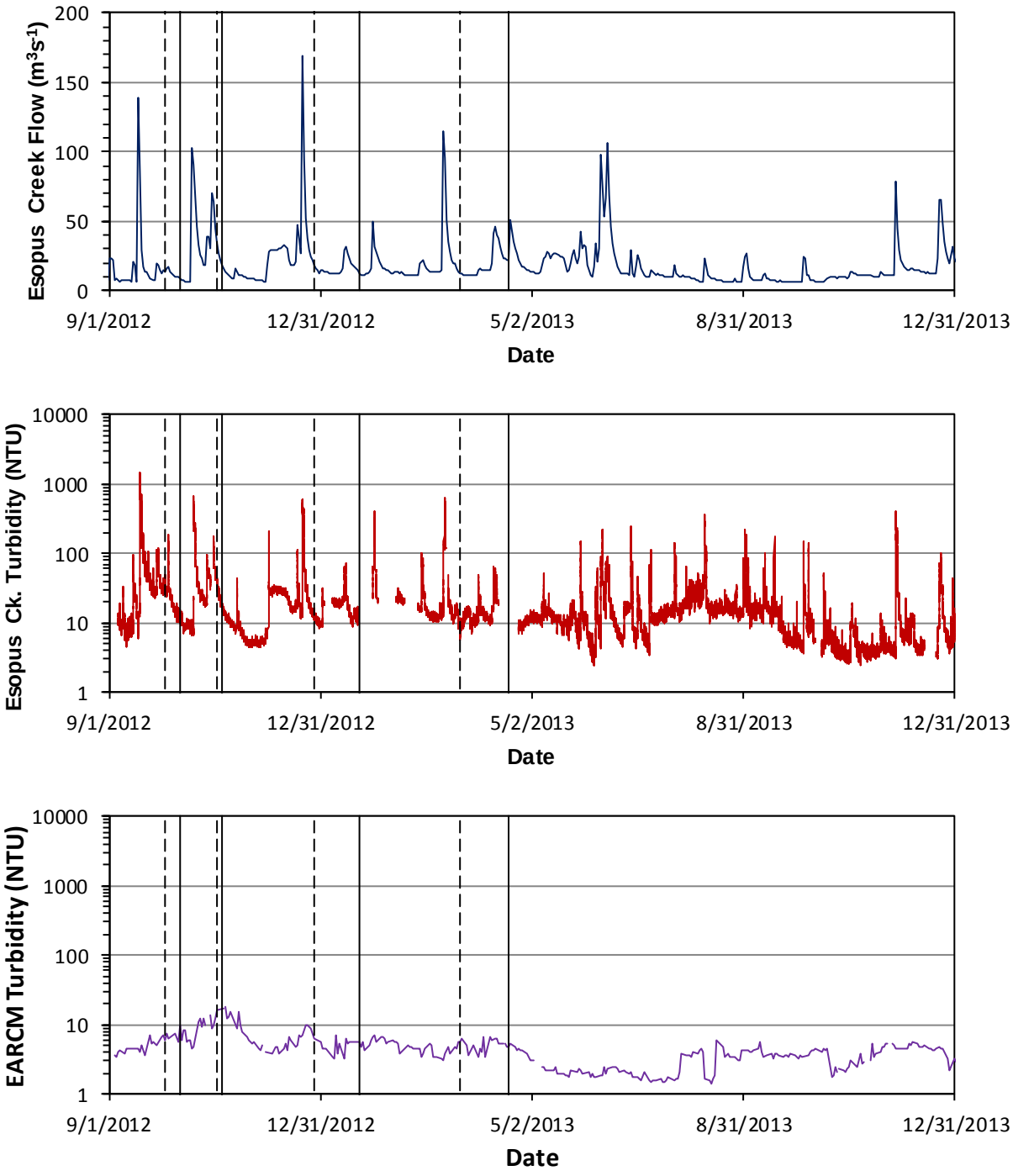

Figure 2.1. Time series of (a) flow at Esopus Creek at Coldbrook (USGS gage# 01362500); (b) turbidity as measure by automated sampling at station E16I along the Esopus Creek and (c) turbidity at keypoint site EARCM at the Catskill Aqueduct effluent from Ashokan Reservoir. The vertical lines show dates of water quality modeling runs to support operation decisions including OST runs (solid lines) and Kensico sensitivity runs (dashed lines).

Table 2.1. List of modeling analyses performed during the reporting period including descriptions of each analysis.

Turbidity Modeling Runs October 2012-December 2013			
Date	**Background**	**Modeling Description**	**Results**
10/03/2012	A turbidity event on September 18, 2012 produced a large input of turbidity into the Ashokan West Basin (Figure 2.1). The event did not fill the West Basin, but created a plume of 200-300 NTU water just above the thermocline with values of >30 NTU at other depths. Since West Basin was not filled, the East Basin was only impacted to the extent that the dividing weir was required to stay partially open. East Basin turbidity near the gate house was about 7-9 NTU near the surface with a plume of about 25 NTU at the thermocline and greater turbidity near the bottom.	Kensico reservoir sensitivity simulations were run to provide guidance for the turbidity that could be tolerated as input to Kensico Reservoir from the Catskill Aqueduct given the current turbidity and possible future turbidity increases as the flow through the dividing weir continued to affect the East Basin turbidity. The tested Catskill inflow rates were 200, 275, 350 and 400 MGD aqueduct turbidity of 8, 10, 12 and 15 NTU.	Results gave an indication that effluent turbidities would stay below about 2.5 NTU with input flow and turbidity combination s of 350 MGD at 8 NTU; 200 MGD at 10 NTU; and less than 200 MGD at 12 NTU.

Turbidity Modeling Runs October 2012-December 2013 (cont'd)			
Date	**Background**	**Modeling Description**	**Results**
10/12/2012	The turbidity event on September 18, 2012 continued to impact the Ashokan and Neversink Reservoirs. In Ashokan, there continued to be a plume of 100-200 NTU water near the thermocline with values of >30 NTU at other depths. East Basin was still not severely impacted as West Basin was not yet filled. East Basin turbidity near the gate house was about 5-10 NTU near the surface with a plume of about 20-30 NTU at the thermocline. Neversink Reservoir was also impacted by the event and was offline at the time with the diversion expected to remain offline for at least the remainder of the month.	These OST simulations were performed to provide an estimate of (a) the period of time that it would take Ashokan Reservoir West Basin turbidity to reach the East Basin, (b) the extent to which the use of the ARC would change the timing and magnitude of turbidity movement from West to East; (c) the effects of ARC use on potentially necessary Catskill Aqueduct flow reductions due to turbidity, and (d) the effects of the temporary loss of the Neversink diversion on reservoir storage. As part of the run, there were a number of operating rules related to the Ashokan dividing weir gate, the ARC and the Schoharie diversion that were updated to better simulate anticipated operations.	Greater use of release channel resulted in a delay and/or a reduction in the movement of turbid water from West Basin to East Basin, and therefore, reduced the potential magnitude of elevated turbidity in the East Basin, especially under the effects of medium sized storms. The modeling also indicated that greater use of the ARC did not reduce the number of traces that required alum use, since these simulation traces all were all associated with extremely large streamflow events that overwhelmed the system. Reduction of Catskill Aqueduct flow could be used to reduce Kensico Reservoir turbidity inputs such that alum treatment might be avoided, however, this might result in some drawdown of West Branch and Kensico Reservoirs. Greater use of the ARC provided some reduction in the number of traces that would result in drawdown of West Branch and Kensico Reservoirs.
11/02/2012	A number of events during fall 2012 moved elevated turbidity from the West Basin to the East Basin of Ashokan. East Basin turbidity near the gate house was above 15 NTU and the reservoir was isothermal. Stop shutters were in place to limit Catskill Aqueduct flow to Kensico. Kensico Reservoir turbidity generally ranged from 0.7-1.5 NTU with higher turbidity of 2.4-2.8 NTU at site 5 near the Catskill influent.	Kensico Reservoir sensitivity simulations were run to provide guidance for the turbidity that could be tolerated as input to Kensico Reservoir from the Catskill Aqueduct given the current turbidity and possible future turbidity increases as the flow over the dividing weir continues to affect the East Basin turbidity. The tested Catskill inflow rates were 50, 150 and 250 MGD with aqueduct turbidity of 15, 20, and 25 NTU.	Results suggested that effluent turbidities would stay below about 2.5 NTU with input flow and turbidity combination s of 150 MGD at 15 NTU and 50 MGD at 20 NTU.

Turbidity Modeling Runs October 2012-December 2013 (cont'd)

Date	Background	Modeling Description	Results
11/05/2012	Ashokan West was continuing to spill over the dividing weir. The Ashokan West automated buoys indicated turbidity of 25-35 NTU with a plume of higher turbidity at the lower portion of the profile. East Basin turbidity near the gate house was above 15 NTU and the reservoir was isothermal as indicated by the Ashokan East automated buoy. Stop shutters were in place to limit Catskill Aqueduct flow to Kensico.	The OST was used to investigate the potential effects of the usage of the ARC on East Basin turbidity and future reservoir storage. These simulations were set up in a manner similar to that used on Oct. 12. Two alternatives were explored: using the ARC with and without operational releases as defined by the DEC interim release channel protocol. In both alternatives the conservation and discharge mitigation releases were used. In addition a number of operating rules pertaining to the Ashokan Dividing Weir Gate, the ARC and the Schoharie Diversion were updated to better simulate anticipated operations.	The modeling indicated that use of operational releases for the ARC decreased the predicted East Basin turbidity for cases when the turbidity was below about 15 NTU. For cases of greater turbidity operational use of the ARC had little effect. Without use operational releases for the ARC the need for discharge mitigation releases was predicted to increase later in the winter. Reduction of Catskill Aqueduct flow could be used to reduce Kensico Reservoir turbidity inputs such that alum treatment might be avoided, however, this might result in some drawdown of West Branch and Kensico Reservoirs. Use of ARC provided reduction in the number of traces resulting in significant drawdown of West Branch Reservoir. Operational use of ARC reduced the probability of refill for WOH Catskill System reservoirs and had no effect on refill of Delaware System reservoirs.

Turbidity Modeling Runs October 2012-December 2013 (cont'd)

Date	Background	Modeling Description	Results
12/28/2012	An early winter storm event moved slightly elevated turbidity from the West Basin to the East Basin of Ashokan. East Basin turbidity near the gate house ranged from 11-14 NTU and the reservoir was isothermal at <4^{o}C as indicated by the Ashokan East automated buoy. Stop shutters were being installed to limit Catskill Aqueduct flow to Kensico. Based on limno survey of Dec. 26, Kensico Reservoir turbidity generally ranged from 1.3-1.7 NTU with higher turbidity of 6.8-7.0 NTU at site 5 near the Catskill influent.	Kensico Reservoir sensitivity simulations were run to provide guidance for turbidity that could be tolerated as inputs to Kensico Reservoir from the Catskill Aqueduct given the current and possible future East Basin turbidity. The tested Catskill inflow rates are 50, 150 and 250 MGD with aqueduct turbidity of 8, 10, and 15 NTU.	Results gave an indication that effluent turbidities would stay below about 2.5 NTU with input flow and turbidity combination s of 250 MGD at 10 NTU and 150 MGD at 15 NTU
01/23/2013	Events from the fall continued to have an impact on the turbidity in the Ashokan Reservoir with turbidity in the East Basin Aqueduct withdrawal of 5-7 NTU and West Basin turbidity near the dividing weir of 10-11 NTU. At the beginning of February it was planned to lower the storage elevation of the Rondout Reservoir by about 10 feet to accommodate a construction project. After this drawdown a greater reliance on Catskill System water would be needed so that Delaware system water could refill Rondout Reservoir to normal seasonal levels.	OST was used to evaluate the range of potential turbidity levels in the Ashokan Reservoir Catskill Aqueduct effluent during the period from late February through the spring when greater use of Catskill water would be necessary to allow Rondout Reservoir to refill to normal storage levels...	The model results indicated that the peak of the median simulated turbidity for the Ashokan East would occur near mid-April with ~60% of the traces exceeding 5 NTU and ~25% of the traces exceed 8.3 NTU. Generally there was lower probability of elevated turbidity at mid-March as compared to mid-April.

Turbidity Modeling Runs October 2012-December 2013 (cont'd)			
Date	**Background**	**Modeling Description**	**Results**
03/22/2013	Catskill Aqueduct turbidity increased to about 6-7 NTU due to a spring snowmelt/rain event (Figure 2.1). Snowpack in the Esopus watershed was about normal for mid-late March and spring events were expected to begin to impact the watershed in the upcoming weeks. Kensico Reservoir turbidity generally ranged from 1.3-1.7 NTU with somewhat higher turbidity >3 NTU near the Catskill influent.	Kensico Reservoir sensitivity simulations were run to provide guidance for aqueduct flow rates into Kensico Reservoir for given current and possible future East Basin turbidity. The tested Catskill inflow rates are 300, 400 and 500 MGD with aqueduct turbidity of 6, 8, and 10 NTU.	Results gave an indication that Kensico effluent turbidities would stay below about 2.5 NTU with input flow and turbidity combination s of 400 MGD at 6 NTU and 300 MGD at 8 NTU and less than 300 MGD at 10 NTU
4/19/2013	Turbidity in Ashokan Reservoir continued to be elevated slightly with West Basin turbidity ranging from 10-12 NTU and East Basin Turbidity ranging from 2.5-6.5 NTU. Both basins were just beginning to thermally stratify. The West Basin was near capacity and was expected to spill into the East Basin following any significant runoff event.	OST was used to investigate the potential effects of implementing operational releases via the ARC on turbidity in the Ashokan Reservoir Catskill Aqueduct effluent and on reservoir storage levels during the upcoming spring through mid-summer period.	Operational releases from the ARC only slightly decreased the predicted East Basin turbidity through mid-summer. Alum treatment was not indicated in any of the simulations (with or without operational releases) Operational use of ARC slightly reduced the probability of refill for WOH Catskill System reservoirs and had virtually no effect on the predicted refill of Delaware System reservoirs

3. Modeling Applications of Climate Change Impacts

3.1. Completion of Phase I of the Climate Change Integrated Modeling Project

The Climate Change Integrated Modeling Project (CCIMP) is led by the water quality modeling group and has the goal to evaluate the effects of future climate change on the quantity and quality of water in the NYC water supply. The project is an element of DEP's Climate Change Action Plan released in 2008. The CCIMP is designed to address three issues of concern to NYC: (1) overall quantity of water in the entire water supply; (2) turbidity in the Catskill System of reservoirs, including Kensico; and (3) eutrophication in Delaware System reservoirs. In the first phase of the project an initial estimate of climate change impacts was made using available GCM data sets and DEP's suite of watershed, reservoir and system operation models. Phase I focuses on water quantity in the West of Hudson (WOH) System, turbidity in the Schoharie Reservoir and eutrophication in the Cannonsville Reservoir.

During 2013 the first phase of the CCIMP was brought to a close with the holding of a review workshop in September and the subsequent publication and distribution of a report detailing our Phase I activities and expert panel review. (The report is available online at DEP website: http://www.nyc.gov/html/dep/html/about_dep/climate_resiliency.shtml)

Some of the general findings of Phase I of the CCIMP were:

- The timing of the spring snowmelt was predicted to shift from a distinct peak in late March and April to a more consistent distribution throughout the winter and autumn. This shift is a function of increased temperatures, which will cause less precipitation to fall as snow and faster melting of the snowpack that does develop. The consequent shift in streamflow drives many of the findings obtained from applications of the water system and reservoir water quality models.

- Greater winter streamflow will cause the WOH reservoirs to fill earlier in the year, and for spill from the reservoirs to increase during the winter. The increased winter spill will come at the cost of lost storage in the spring snowpack.

- For the WOH System, drought seems to be less prevalent, because the GCM simulations used in the study predict increased precipitation throughout the year, which compensates for lost snow storage and increased evapotranspiration due to higher temperatures.

- The shifting seasonal pattern in streamflow will similarly affect the turbidity loads into Schoharie Reservoir, which in turn will impact the Schoharie withdrawals, resulting in increased turbidity in the autumn and winter and decreased turbidity in the spring.

- The nutrient loads to Cannonsville Reservoir will also exhibit shifts similar to the streamflow shifts noted above. However, despite increased nutrient loads during the winter and autumn, the response of the phytoplankton will be small, presumably due to unfavorable growth conditions at this time of the year. The thermal structure of the reservoir will be impacted by the higher temperatures of the future climate, with thermal stratification beginning earlier in the spring and lasting longer into the autumn.

Phase II of the CCIMP is now underway. The general goals are the same but in this phase of the project we will be making use of a more extensive set of GCM data and improved downscaling methods to develop a wider variety of future climate scenarios. We will also be making use of additional models and subject all models to increased testing and scrutiny in respect to their climate change predictions.

Initial results of the Phase II of the CCIMP are presented in this report. Section 4.3 describes our work to develop an initial application of the RHESSys hydro-ecological model that we hope will be of value for estimating the effects of climate change on water supply forested lands. Section 4.4 describes work to improve the SWAT watershed model to better represent the hydrology in the West of Hudson watershed area, particularly Cannonsville watershed. If successful, these improvements should allow for more realistic future simulation of hydrology and biogeochemistry using SWAT. Section 3.4 examines the effects of simulated future changes in hydrology on indices of stream biotic habitat. In terms of reservoir limnology Section 3.3 evaluates the effects of future climate conditions on reservoir thermal structure, and Section 3.2 further evaluates how such changes can affect the phytoplankton community.

3.2. Seasonal Effects of Climate Change on Cannonsville Reservoir Phytoplankton

Introduction

Cannonsville Reservoir has in the past been affected by phytoplankton blooms that exceeded 40 mg m^{-3} of chlorophyll and included cyanobacterial species (Effler and Bader 1998). The eutrophic state of Cannonsville Reservoir was linked to excessive nutrients, and beginning in the early 1990s, a variety of FAD mandated programs were implemented to reduce point and non-point source nutrient loading. To evaluate the effects of these programs, the water quality modeling group developed a system of linked watershed and reservoir models that are currently used to evaluate the effects of changing land use, watershed management, and climate change on Cannonsville Reservoir (Figure 3.1).

When considering the potential impacts of climate change on Cannonsville Reservoir trophic status there are two potential drivers of change in phytoplankton community biomass and composition: 1) changes in the amount and seasonality of nutrient loading to the reservoir; and 2) changes to the reservoir thermal and mixing regime. Previously, it has been the first factor, nutrient loading that has received the greatest attention. DEP has simulated long term variations in nutrient loading under different levels of watershed management and changing land use, and demonstrated that FAD program-driven reductions in nutrient loading have led to reduced reservoir chlorophyll concentrations (DEP 2006b). The second factor while not directly examined in the FAD evaluation is implicitly recognized by the use of an evaluation method (Owens et al. 1998) which examines the long-term shift in the frequency distribution of reservoir water quality data. One important source of the year to year variability captured by the frequency distributions is inter-annual variations in stratification and mixing.

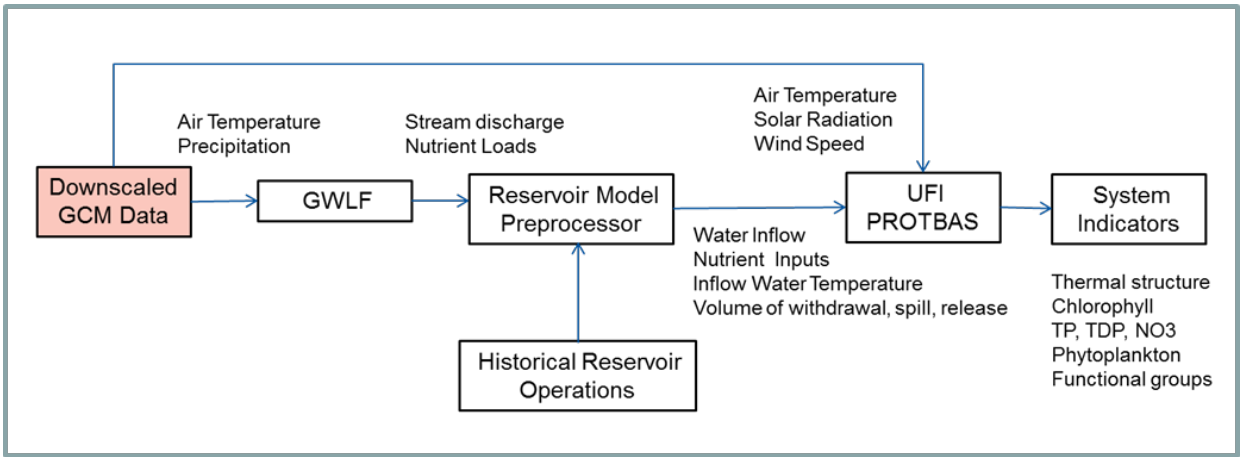

Figure 3.1. Diagram of linked watershed and reservoir models used by the DEP modeling group to evaluate Cannonsville Reservoir trophic status. The configuration shown here is used to evaluate the effects of climate change. The same system driven by historical meteorological data instead of the downscaled GCM data can be used to evaluate changes in land use and watershed management.

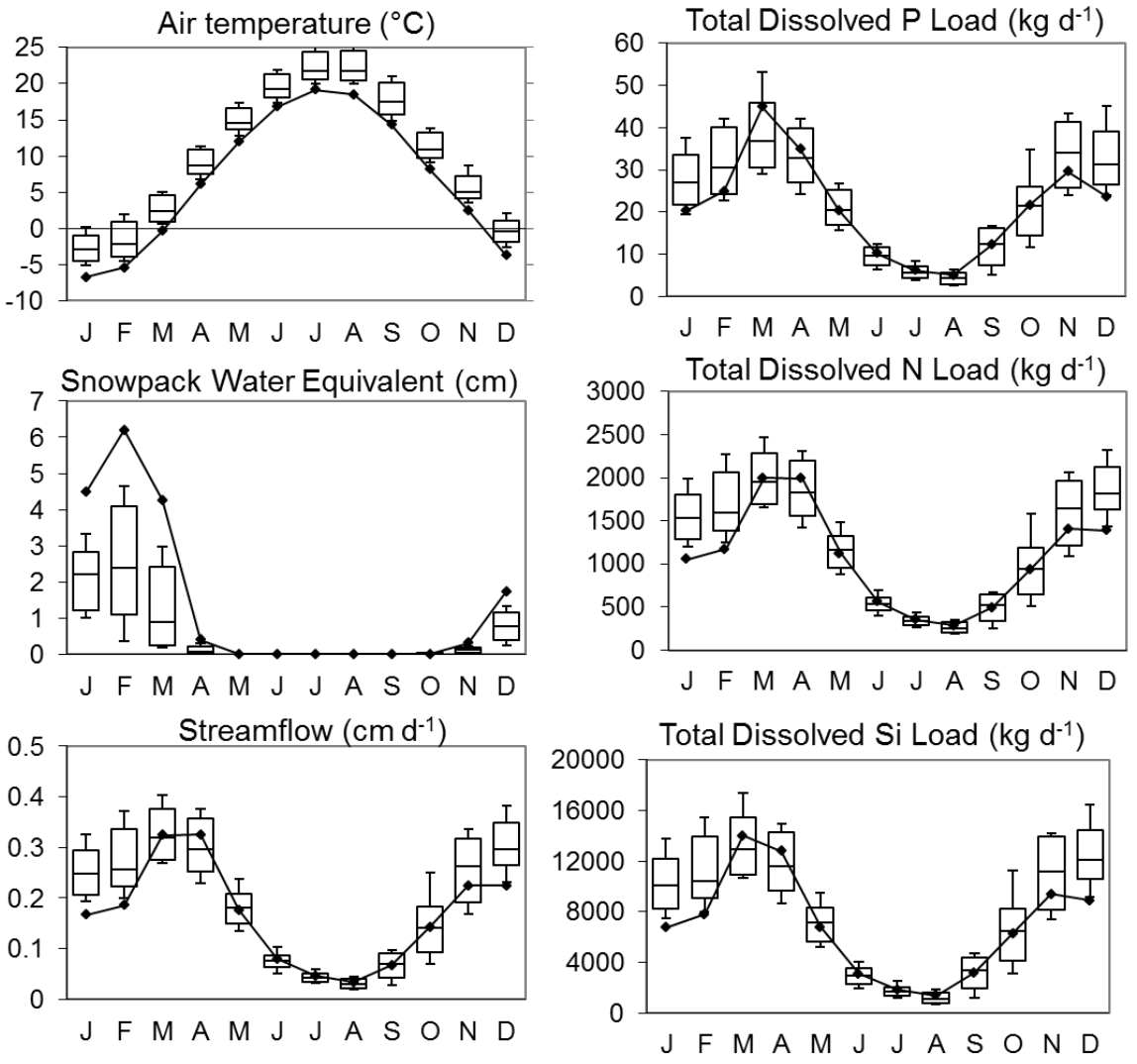

Figure 3.2. Seasonal patterns in mean monthly air temperature driving the GWLF watershed model, and GWLF simulated mean monthly snowpack water equivalent, stream discharge, and nutrient loads. Effects of future climate change can be seen by comparing the historical mean patterns plotted as a line with the range of mean monthly values associated with future scenarios and shown as box plots. In months where the boxplots do not intersect with the line all future scenarios were different from the historical conditions.

Future changes in watershed hydrology and nutrient loading simulated by the GWLF model are shown in Figure 3.2 The solid line shows the pattern of mean monthly historical data, while the bar plots show the range in the monthly means obtained from simulations driven by 36 different GCM/emission scenarios. More information on the climate scenarios is available from (Pierson et al. 2013)

As a result of higher winter air temperatures we simulate reduced snow water storage, and increased winter snow melt. This combined with increased winter and fall precipitation (not shown) leads to a distinct change in the seasonality of the streamflow and nutrient loads entering Cannonsville Reservoir. For example, the median annual loading of total dissolved P increases by about 6 %, while there are much greater changes in the seasonality of the nutrient inputs with an approximately 15-33% increase in the median November-February loading as a consequence of the changing seasonality of streamflow.

Changes in reservoir thermal structure as a result of future changes in the climate inputs to the reservoir model are discussed in detail in Section 3.3 of this report. In summary, it can be stated that under future climate scenarios the reservoir will become thermally stratified earlier in the year and become de-stratified later in the year. Epilimnetic water temperatures will be warmer, and the vertical temperature gradient will become greater leading to more stable thermal stratification. These changes are most strongly related to future changes in air temperature and its effect on reservoir thermal structure. Since air temperature is a climate parameter that is consistently projected to increase in the future simulations (Figure 3.2), our confidence in these projected changes in reservoir thermal structure is high.

The coupled modeling system (Figure 3.1) simulates the combined effects of increased nutrient loading, a shift in the seasonality of nutrient loading, increased reservoir water temperature and longer lasting and more stable thermal stratification. To separate these effects, two additional sets of model simulations were run. These (Figure 3.3) were done by manipulating the climate data sets that are inputs to the watershed and reservoir models so that one model was driven by a contemporary historical data set, while the other model was driven by a future climate scenario derived from the same historical data set (Anandhi et al. 2011). Using this scheme, illustrated by Figure 3.3A , we are able to simulate the watershed effects of climate change on the timing and magnitude of nutrient loading to the reservoir, while keeping the hydrothermal regime of the reservoir as that which would occur under a contemporary climate. Conversely, in (Figure 3.3B), we isolate the effects of changing hydrothermal conditions by using future climate data to drive the reservoir model, while the watershed model is driven with historical data.

The simulations of the combined watershed and hydrothermal effects of climate change on reservoir chlorophyll concentration, using the data coupling shown in Figure 3.1 are shown in Figure 3.4A, while the simulations that isolate watershed and hydrothermal effects using the data coupling shown in Figure 3.3 are shown in Figures 3.4B and C. When examining the total effect of climate change on both watershed and reservoir hydrothermal processes (Figure 3.4A), it is clear that in most months there is a modest (10-15%) increase in reservoir chlorophyll concentration

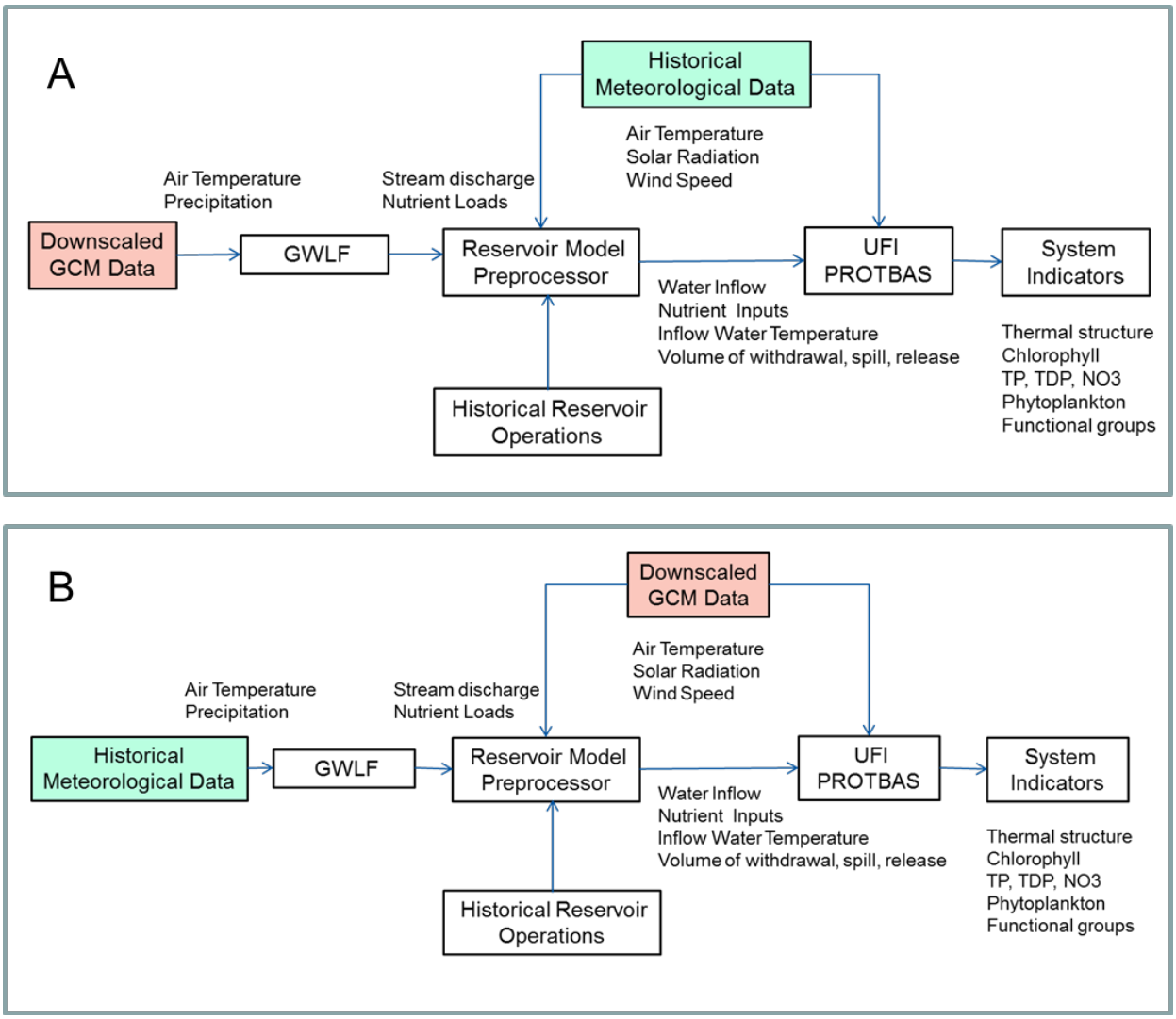

Figure 3.3. Schematic of the coupling of models and data sets used to simulate the effects of climate change on A) watershed processes only and B) reservoir hydrothermal processes only. In A) downscaled GCM scenarios are used to influence only the watershed model and consequently the inputs of water and nutrient to the reservoir. In B the downscaled GCM scenarios are used only to as input to the reservoir model and the model that simulates inflow stream temperature. The future climate scenarios therefore, only affect reservoir thermal structure and mixing.

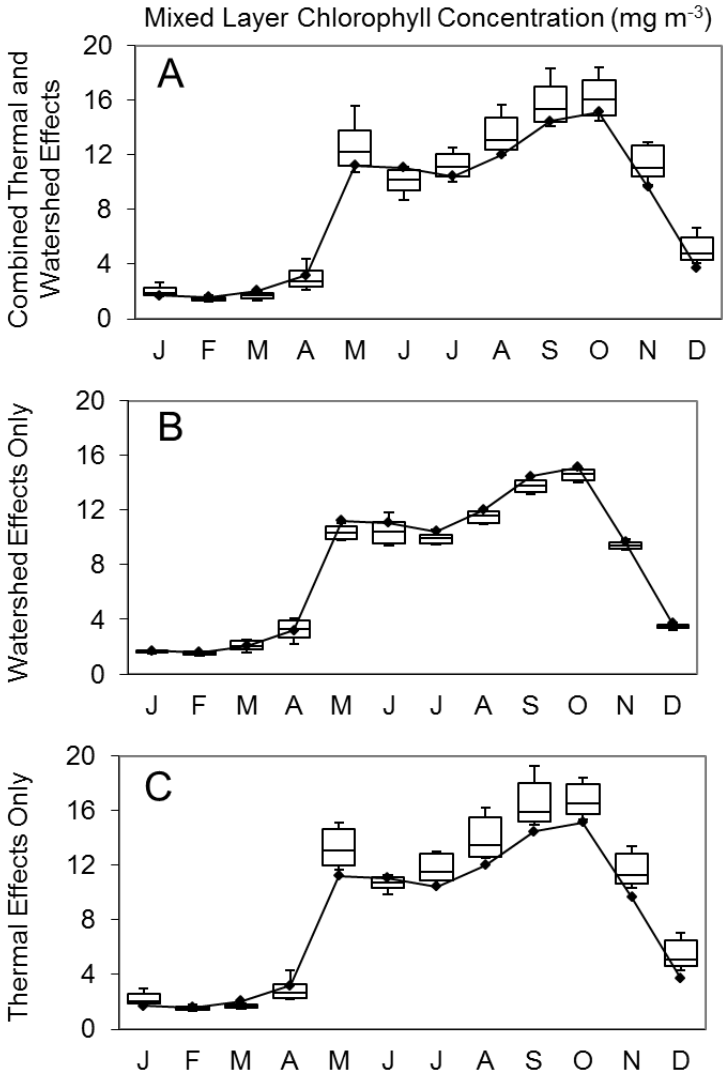

Figure 3.4. Average seasonal patterns of reservoir monthly mean mixed layer chlorophyll concentration. Solid line shows the results with the model driven by historical conditions, box plots show the range from future scenarios The box plots in A show the range in future conditions when both watershed and hydrothermal effects are allowed to impact the phytoplankton, while B and C show the separate effects of watershed and hydrothermal effects.

Table 3.1**.** The eight indicator species used to define the major phytoplankton functional groups used in the UFI-PROTBAS model. In addition to these properties the growth rates are related to morphological characteristics of the species – namely the typical longest dimension of the cell or colony and the surface area to volume ratio.

Indicator species	**Special property**	**Floating/Sinking Rate**	**Functional group name in this study**
Aulacoseira	Need silica, sinks fast	Sink 0.4-1.0 m/d depending on light exposure	Diatom
Stephanodiscus	Need silica, Grazed	Sink 0.1 m/day	Diatom
Aphanizomenon	Nitrogen fixer, actively moves	Sink 0.3-Float 0.1 m/d depending on light exposure	Cyanobacteria
Anabaena	Nitrogen fixer, actively moves	Sink 0.3-Float 0.1 m/d depending on light exposure	Cyanobacteria
Microcystis	Actively moves	Sink 0.5-Float 3.0 m/d depending on light exposure and water temperature	Cyanobacteria
Rhodomonas	Grazed, actively moves	Sink 0.5 – Swim Upward 0.1 m/d depending on light exposure	Flagellate
Cryptomonas	Grazed, actively moves	Sink 1.0 – Swim Upward 1.0 m/d depending on light exposure and nutrient levels	Flagellate
Ceratium	Actively moves	Sink 5.0 – Swim Upward 1.0 m/d depending on light exposure and nutrient levels	Flagellate

More striking are the results of the simulations that attempt to separate the effects of the future changes in reservoir loading from future changes in reservoir thermal structure and mixing. These suggest that despite an overall increase in future levels of nutrient loading (Figure 3.2), these effects on their own (Figure 3.4B) have virtually no effect on the seasonal patterns of chlorophyll concentration, and in fact actually lead to a slight decrease in chlorophyll concentration during thermally stratified conditions in May- October. The reason for this was discussed by Pierson et al. (2013) – shifts in the seasonality of nutrient loading (Figure 3.2) results in greater amounts of nutrient loading in the late fall to winter when conditions are not favorable to phytoplankton growth. It was further hypothesized that in the time between nutrient input and favorable growth conditions, nutrient bioavailability could decrease, and nutrients could be lost from the reservoir in spills and releases. This effect is illustrated by the results of Figure 3.4B.

Simulations which allowed future climate conditions to affect only reservoir thermal structure (Figure 3.4C), show that it is largely these effects that account for future increases in reservoir chlorophyll concentration. Hydrothermal effects enhance phytoplankton growth due to a positive effect of the warmer water temperatures on the simulated rate of growth, as well as stratification's effect on phytoplankton light exposure (Huisman et al. 2004). This is an important result that does not invalidate global relationships between nutrient loading and phytoplankton biomass as measured by chlorophyll (Vollenweider 1968). Rather, it does illustrate that the interaction between nutrient loading and variability in the physical environment moderates nutrient impacts on phytoplankton biomass. In fact, both the negative effects associated with changes in the seasonality of hydrology and nutrient loading (Figure 3.4B) and

the positive effects associated with changes in thermal structure (Figure 3.4C) are illustrated by these simulations.

The UFI-PROTBAS model simulates the biomass of 8 functional phytoplankton groups (Table 3.1) which have different growth characteristics and successional strategies (Reynolds et al. 2001, DEP 2008a). The seasonal variations in total biomass show in Figure 3.4 are obtained by summing the biomass of all groups. In Figure 3.5 the seasonal variations in the biomass of diatoms and cyanobacteria, the two major groups dominating the phytoplankton biomass, are plotted as in the previous figure. Again, there is a striking difference in the climate effects influencing watershed vs. hydrothermal processes, with the hydrothermal effects having the largest potential influence on future levels of phytoplankton biomass.

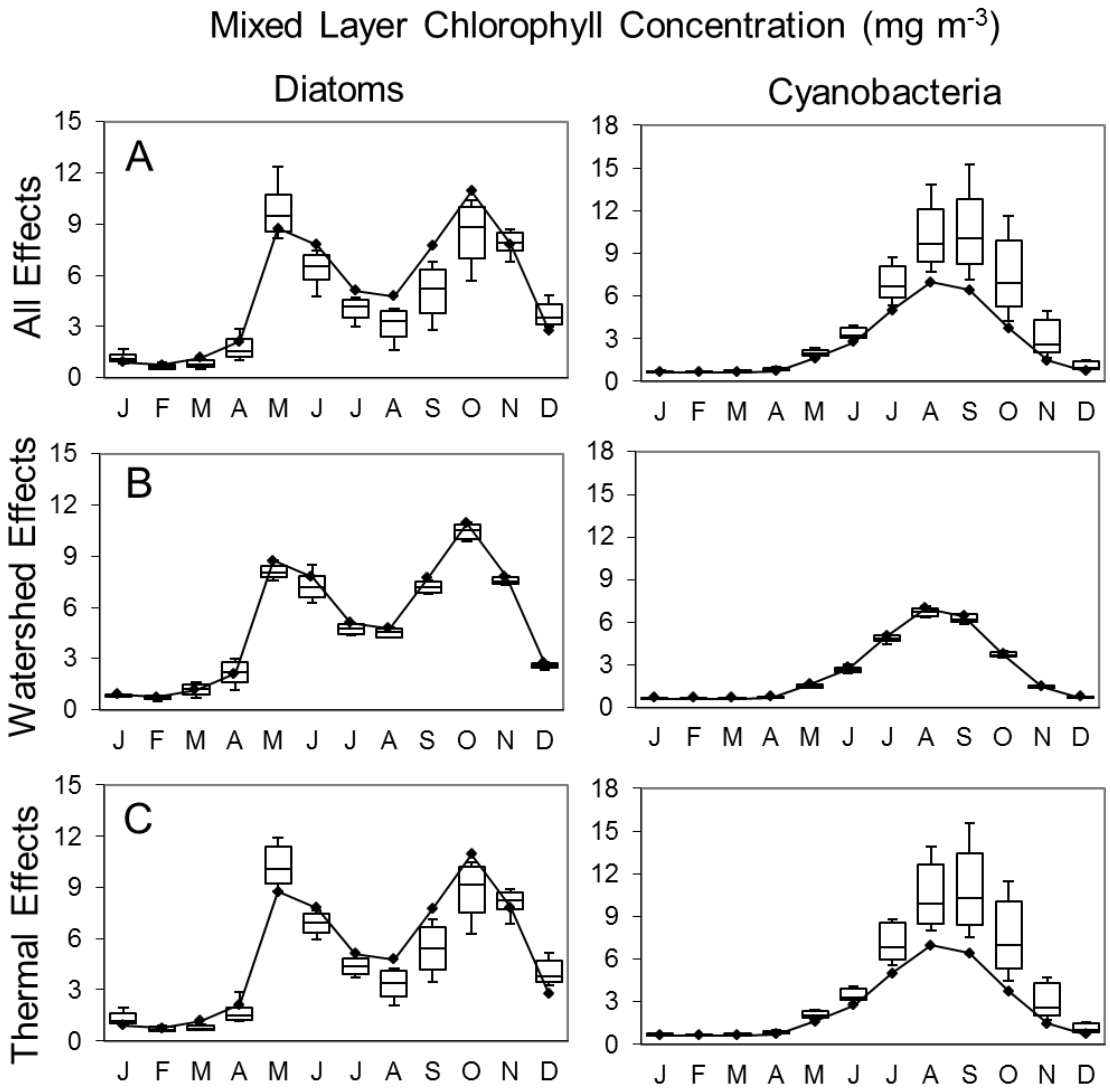

Figure 3.5. Average seasonal patterns of reservoir monthly mean mixed layer chlorophyll concentration associated with the two dominant phytoplankton functional groups. Panel C shows the importance of changes in reservoir stratification and mixing on the responses of diatoms and cyanobacteria. This may cause a shift in their relative abundance.

Figure 3.5 also shows an additional result: The increased phytoplankton chlorophyll under future conditions is simulated to come as a consequence of a successional change which favors the growth of cyanobacteria, at the expense of diatoms. This simulated change is consistent with the physiology and ecology of these phytoplankton functional groups. The diatoms (Table 3.1) generally have no upward motility, a relatively high sinking rate and grow well at lower light intensity. They tend to dominate under conditions of energetic mixing that keeps them in suspension, even when this mixing results in reduced light exposure. Cyanobacteria are expected to dominate future climate conditions and warmer water temperatures (Paerl and Huisman 2008, Paul 2008, Paerl and Huisman 2009, Kosten et al. 2012) since their maximum rate of growth generally occurs at higher temperatures than other phytoplankton groups (Reynolds 2006) although there are some contradictory studies (Lürling et al. 2013). Furthermore, cyanobacteria are positively buoyant, allowing them to remain suspended in the euphotic zone during the more persistent stratification simulated to occur under future conditions. Some of the large colonial cyanobacteria simulated here can exhibit relatively rapid rates of upward vertical movement. This can also be of competitive advantage in a stable, seasonally-stratified epilimnion that nevertheless experiences intermittent vertical mixing i.e. diurnal cycles of weak stratification in the upper mixed layer (Imberger 1985). Under such conditions, buoyant cyanobacteria can migrate to the upper water column during periods of intermittent stratification, and gain a competitive advantage from greater light exposure (Reynolds and Walsby 1975, Huisman et al. 2004, Jöhnk et al. 2008).

The consequences of future climate conditions on cyanobacterial growth and succession is a topic that is receiving intense scrutiny in limnological literature (Carey et al. 2012, Reichwaldt and Ghadouani 2012, Rigosi et al. 2014). The simulations here suggest that future climate conditions, while leading to moderate increases in total phytoplankton biomass, can result in up to a doubling in the biomass of cyanobacteria. This could be a concern for the future water quality of Cannonsville Reservoir given cyanobacteria can lead to taste and odor problems and also in some cases produce cyanotoxins (El-Shehawy et al. 2012). However, with a new steady-state set by major nutrient reductions as a result of the watershed protection programs, the changes in cyanobacteria due to thermal changes will still likely be lower than levels observed in the past.

It is however, important to remember that these are simulations and as such are highly dependent on a multitude of assumptions embedded in the coupled models and climate scenarios used here, especially so in regards to the phytoplankton growth characteristics (Reynolds et al. 2001) as parameterized by the UFI-PROTBAS model. The results here are an indication of what could occur, but are not absolute predictions. The most important consequence of these simulations is to heighten awareness of the possibility that future climate change could possibly lead to impacts on the drinking water quality as a result of increased cyanobacteria levels, and that it is the changes in thermal stratification that will the major factor leading to this potential impact. Such a concern for water resources in general has already been raised in the literature (Paerl and Huisman 2008, 2009). For DEP this highlights the importance of continuing to examine the validity of our modeling assumptions, and to also heighten awareness of the possible future increases in cyanobacteria, so that monitoring and management strategies are in place to mitigate these blooms if they do in fact become more frequent.

3.3. Sensitivity Analysis on Reservoir Water Temperature under Future Climate Change Scenarios Using Hydrologic and Hydrothermal Models

Introduction

Water temperature in lakes and reservoirs is the major driving force that governs all biogeochemical changes and has considerable influence on water quality and ecosystem dynamics (Stefan et al. 1998). Variations in local weather affect water temperature, patterns of thermal stratification and mixing in lakes. Thermal stratification represents the vertical temperature structure of the water column and consists of: epilimnion (a surface mixed layer of approximated uniform temperature maintained by wind induced turbulence); the hypolimnion (a bottom mixed layer of also approximately uniform temperature maintained by the turbulence generated by bottom shear); and the metalimnion (an intermediate depth between possessing large vertical temperature and density gradients between the higher temperature epilimnion and the generally lower temperature hypolimnion). The thermocline, within the metalimnion, represents the depth of the greatest rate of temperature decrease. The development of the thermal stratification limits the vertical transport of nutrients and gas vertically through the water column. Thermal stratification strongly influences the kinetics at the sediment-water interface (Condie and Webster, 2001; Lorke et al. 2003), and it also influences algal growth rates (Peeters et al. 2002; Joehnk et al. 2008). Thus the timing and duration of seasonal patterns of thermal stratification is an important influence to freshwater systems supplying drinking water. Sensitivity of thermal structure to observed changes in meteorological factors (surface air temperature, wind speed and ice cover) has been studied on Lake Superior by Austin and Allen (2011) They found that observed trends in air temperature and ice cover led to higher summer water temperatures, while trends of increased wind speed led to a reduction in summer surface water temperature. Surface water temperatures are strongly affected by meteorological forcing, such as air temperature and dew point temperature (Hondzo and Stefan, 1992). Variation in air temperature is also responsible for onset and loss of ice along with ice cover formation in small lakes (Livingstone and Adrian 2009), while the wind speed induces turbulence at the water surface layers and may form surface mixed layer. The increase in wind speed controls the surface heat exchange at the air-water interface and it is found to be the dominant variable in the destruction of the thermocline (Henderson-Sellers, 1977).

Projected scenarios of water availability and water quality under future climate conditions will be affected by changes in lake and reservoir thermal structure. Changing climatic conditions affecting local meteorological forcing will alter both thermal structure and vertical transport by mixing (Samal et al., 2012), which in turn will affect the limnological attributes of lakes and reservoirs (Austin and Colman 2007; 2008). Thermal structure is accurately simulated with mathematical models driven by readily available meteorological data (Ahsan and Blumberg, 1999; Samal et al. 2009). Modeling has been widely used to evaluate the thermal responses of lakes of varying size, in watersheds of different topography and geographical location to climate, making it possible to detect gradual as well as abrupt shifts in their thermal characteristics (Peeters et al. 2002; Sahoo et al. 2011; Rao et al. 2012; Fang et al. 2009; Komastu et al. 2007, Samal et al. 2009; 2012). Observed meteorological forcing commonly used in lake water temperature modeling are air and dew point temperature, solar radiation or cloud cover and wind speed.

The ability of lake and reservoir hydrothermal models to simulate water temperature and thermal structure under future as opposed to present climate conditions is of paramount importance and necessitates evaluation of the sensitivity of model output to projected future variations in meteorological parameters. Sensitivity analysis (SA) may be used as a tool to evaluate variations of model outputs that occur as a consequence of different sources of variation in model components such as parameters, sub-models and forcing data (Saltelli et al., 2000; 2008). SA may be used to identify the governing parameters and processes subjected to certain drivers or even to improve the mathematical formulations in the model. Sensitivity analysis of model parameters can be carried out by adjusting them within acceptable ranges and observing the corresponding response in the output variables. Likewise, the sensitivity analysis of forcing functions needed to drive the model can be made by changing them with certain factors/percentages and observing the response of output variables and their possible implications on the system.

Even though the potential impact of climate change on lakes and reservoirs will be strongly influenced by changes in thermal stratification and mixing, systematic investigations of the effects of climate change on reservoir hydrodynamics are not common (Stefan et al. 1998; Fang and Stefan, 2009; Samal et al. 2013). This paper is centered on the analysis of model sensitivity and climate scenario sensitivity. The sensitivity of a reservoir hydrothermal model to realistic variations in atmospheric forcing is evaluated by changing individual meteorological drivers by fixed factors/percentages and evaluating model output. To further test the sensitivity of model output to variations in individual meteorological drivers as they occur in the A2 climate scenarios, individual A2 scenarios drivers are substituted into the historical meteorological data set used to drive the reservoir model under baseline conditions. Stratification characteristics, such as onset, loss, and duration of stratification are estimated under varied atmospheric forcing and A2 scenario characteristics and compared to the baseline conditions. By identifying the dominant physical processes affecting the reservoir water temperature, these results can provide guidance for others simulating the effects of climate change on lake and reservoir hydrodynamics.

Methodology

Study area: Cannonsville Reservoir

Cannonsville Reservoir is a dimictic, mesotrophic reservoir, one of the four located at the western edge of Delaware County, New York about 190 km northwest of New York City. The reservoir has a contributing watershed area of 1178 km^2 (Figure 3.6) consisting largely of forested land use with some dairy agriculture and a few small hamlets. The reservoir supplies 325,000 $m^3 day^{-1}$ or roughly 7.1% of the total average daily consumption, to 9 million people in New York City and other New York State localities. The detailed descriptions of the reservoir's morphometry, hydrology and operation have been published elsewhere (Samal et al. 2012; Owens et al. 1998). The climate in this region is strongly influenced by elevation with mean annual air temperature ranging from -1.17 ^oC to 18.85 ^oC and mean annual precipitation about 1100 mm, of which approximately one-third falls as snow (Pradhanang et al. 2011). Regular water quality monitoring of this reservoir is conducted by DEP.

Vertical variation in water quality constituents associated with eutrophication has been simulated using a coupled hydrothermal model (Owens, 1998a) and eutrophication model (Doerr et al. 1998). Previous studies on the thermal structure in Cannonsville Reservoir indicate that vertical transport of heat to the lower waters of the reservoir in summer is largely associated with advection caused by release of water at the base of the dam and is less sensitive to vertical diffusion (Owens, 1998a).

The reservoir experiences stratification during summer and winter (inverse thermal stratification under the ice), with turnover occurring in fall and spring. Previous studies indicate that the substantial year to year to differences in the stratification regime of the reservoir are influenced by interannual differences in reservoir operation (Effler and Bader, 1998). Based on measured temperature data collected over a period of 8 years (1988-1995), Owens (1998b), estimated that the duration of stratification ranges from 164 to 221 days and the range of August hypolimnetic temperature is 8.3 to 13.9 ^{o}C. Gelda et al. (1998) have documented the application and testing of a two-dimensional simulation model (CE-Qual-W2(t)) to Cannonsville Reservoir and evaluated the accurate simulation of all important features of the stratification regime of the reservoir for the 1988-1994 interval, a period in which wide interannual differences were related to variations in meteorology and operations.

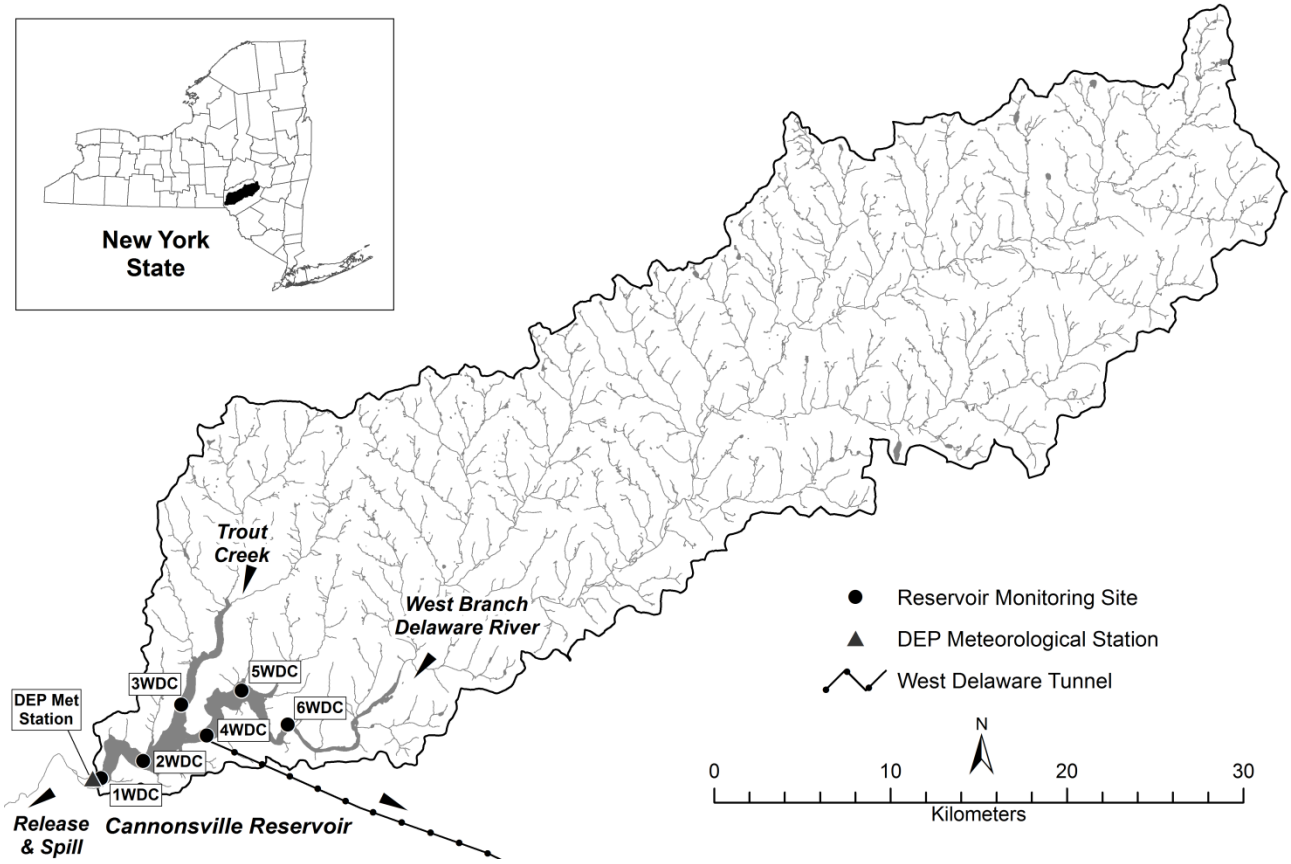

Figure 3.6. Location of Cannonsville Reservoir and its watershed area

Hydro-meteorological data

Daily historical meteorological data for Cannonsville Reservoir were obtained from meteorological station located at the reservoir dam (Figure 3.6) since 1995. Prior to 1995, meteorological data were collected at a National Weather Service (NWS) station located at Binghamton, NY - approximately 64 km northwest of the reservoir. The one-dimensional reservoir model used in the present study is driven by daily air temperature, dew point temperature (approximated as minimum daily temperature), solar radiation and/or cloud cover and wind speed. Daily inflows of the major tributaries entering the reservoir are measured by the United States Geological Survey (USGS), while daily outflows, and water surface elevation for the reservoir are measured by the DEP. These water balance components are also inputs to the model. The major inflow to the reservoir is the West Branch Delaware River (WBDR) which contributes 80% of the total inflow; 5% and 15% of the total are contributed by Trout Creek and other ungauged tributary inflows respectively. USGS stream gages measure flow at the WBDR and Trout Creek inflows. Outflows from the reservoir are spillway, dam-release and drinking water withdrawal, which on average represent approximately 40%, 32% and 28% of the total outflow (Owens et al. 1998a). The daily inflow temperatures were estimated based on air temperature measured near the mouth of tributaries using a simple empirical model that was incorporated into a data preprocessing program (Figure 3.7).

Daily tributary temperature is estimated as:

$$W_t = \max(0 , W_{t-1} + S*(A_{t-1} - W_{t-1})) \qquad (3.1)$$

where W_t is the predicted water temperature on day t; W_{t-1} is the predicted water temperature on day t-1; A_{t-1} is the average air temperature on day t-1 (average air temp is calculated by (T_{min} + T_{max})/2); T_{min} is the minimum daily air temperature; T_{max} is the maximum daily air temperature; and S is the slope of change (two constants for either rising (0.412444) or falling (0.078582) water temperature). The rising temperature constant is used when $A_{t-1} > W_{t-1}$ and the falling temperature constant is used when $W_{t-1} > A_{t-1}$. W_t is set such that it does not go below 0^oC and assuming the first day stream water temperature to be zero.

General Circulation Model and Climate Change Scenarios

Increasing concentrations of atmospheric CO_2 and other greenhouse gases lead to the possibility of future climatic warming, the extent of which has been projected using General Circulations Models (GCMs). This study uses the output from three GCMs: the Canadian Center for Climate Modeling and Analysis (CGCM3); the European Center Hamburg Model (ECHAM); and the Goddard Institute of Space Studies (GISS).

Future scenarios of mean daily air temperature, wind speed, and solar radiation have been previously derived (Samal et al. 2012) using three emission scenarios (A1B, A2 & B1) for the 2081-2100 future periods. GCM simulated values were used to produce monthly change factors. Here, change factors were calculated from the differences between simulations of baseline (1981-2000) and future (2081-2100) time periods associated with the three GCMs and the A2 emission scenarios. The A2 emission scenario, representing the highest expected future

greenhouse gas emissions, was used with the 2081-2100 time period in order to produce scenarios of the greatest possible climate change... Single monthly change factors were developed, by pooling all of the data in a scenario for any given month and then calculating a scenario monthly mean. For air temperature, additive monthly change factors were calculated as the difference between the monthly means of a given future scenario and the baseline scenario. For all other meteorological variables (precipitation, solar radiation and wind speed) monthly multiplicative change factors were calculated as the ratio of the mean monthly future to mean monthly baseline values. These change factors were then used to adjust a 39 year record of meteorological observations, that was based on local measurements made at the reservoir (for the reservoir model), and another set of measurements that were representative of the entire reservoir watershed as a whole (for the watershed model). Additive change factors associated with a future scenario were added to the daily temperature data in the month corresponding to the change factor. In the case of multiplicative factors, the daily data were multiplied by the change factor associated with a given month. The detailed method of producing the future climate change data is described elsewhere (Anandhi et al. 2011).

Description of the coupling of hydrothermal and hydrologic model

A deterministic one dimensional lake hydrothermal model (Owens, 1998b; UFI, 2001) was used to simulate lake thermal conditions under historical and future climate conditions. The model was calibrated with long-term observed temperature data (1986-2004) measured by DEP. The calibration results and calibrated parameter values are discussed in detail elsewhere (Samal et al. 2012).

The hydrothermal model is driven by daily meteorological forcing, and daily hydrological parameters (inflow, outflow and water surface elevation). For future climate simulations the hydrologic inflows are simulated using the Generalized Watershed Loading Function-Variable Source Area (GWLF-VSA) watershed model (Schneiderman et al. 2007. The driving meteorological data needed for the watershed model are daily precipitation and air temperature. GWLF-VSA has been successfully calibrated for the West Branch Delaware River basin by Schneiderman et al. (2007) and generates daily average streamflow and nutrient loads, which are in turn, the inputs to the hydrothermal model. The coupling of the hydrothermal and hydrological model driven by the historical and future meteorological forcing is depicted in Figure 3.7. When simulating future climate scenarios using the coupled reservoir watershed model a simple reservoir model pre-processing program was developed which calculated reservoir spill in response to future inflows, adjusted reservoir withdrawal in order to prevent unrealistic drawdown in response to future low flow periods, and adjusted tributary inflow temperatures in response to future increases in air temperature.

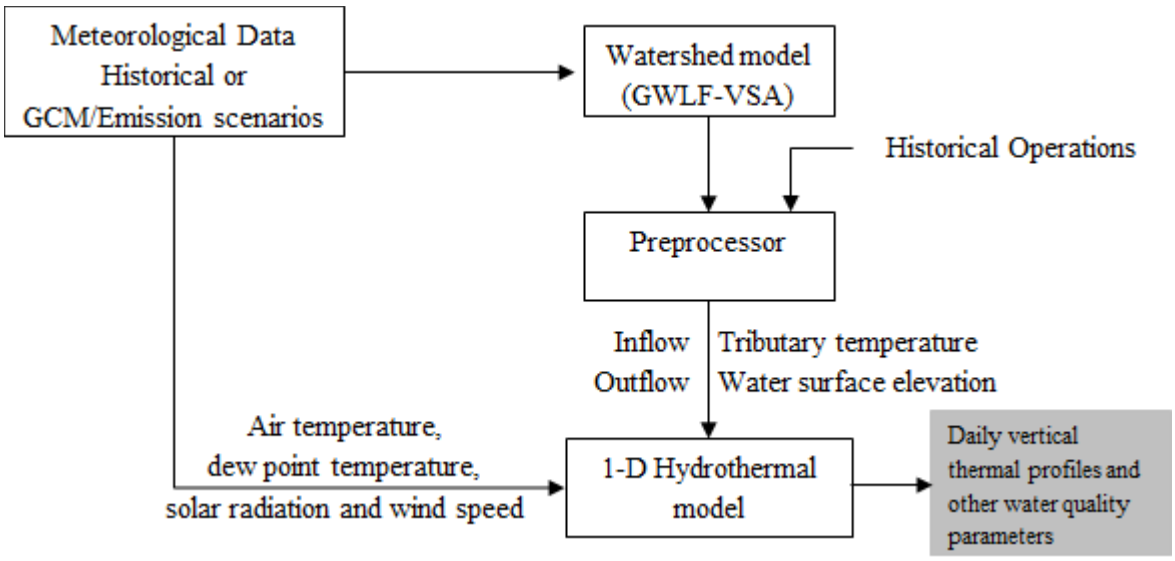

Figure 3.7. Coupling of hydrothermal and hydrological model run with climate data

Strategies for forcing sensitivity and scenario sensitivity analysis in the 1-D model

Model simulations were used to evaluate future changes in reservoir thermal structure that could occur in the 2081-2100 time periods under A2 emissions. Simulations were made that included the simulated effects of changes in meteorological conditions directly acting on the reservoir, and the indirect effects of climate change on watershed processes that effect the volume and timing of reservoir inflows and the temperature of the inflowing waters. Direct reservoir effects and watershed effects were examined both together and separately (Table 3.2). Future changes in meteorology can affect the hydrothermal model inputs in two ways. The changes in meteorology can have a direct effect on the forcing applied at the reservoir surface-atmosphere boundary (e.g., air temperature at the water surface, wind speed, incoming solar radiation), or the changes in meteorology can have an indirect effect by changing the hydrology of the contributing watershed (e.g., inflow quantity and timing, input water temperature). To further understand the model sensitivity to changes in meteorological forcing directly on the reservoir versus the changes in watershed hydrology, three scenarios were developed: (1) using all input both direct meteorology and the watershed hydrology based on the future climate scenarios discussed above, (2) using the direct meteorology as developed from the GCMs in combination with the baseline hydrologic inputs and (3) using the baseline direct meteorology combined with the hydrology as predicted under the future climate scenarios.

To understand the effects of each individual direct meteorologic input on reservoir thermal structure, two additional sets of sensitivity analyses were performed. The first examined the effects of each individual meteorological variable in influencing reservoir thermal structure under A2 scenario conditions. For these simulations all but one meteorological variable used by the reservoir and watershed models (Table 3.2) were taken from the time series of historical baseline conditions while the remaining variable was drawn from the A2 scenario averaged over the three GCM (CGCM3, ECHAM and GISS) scenarios. The results of this first sensitivity illustrate the effects of A2 level variation in meteorology, but do not show the absolute sensitivity of the reservoir hydrothermal model to variation in the different meteorological

variables, since these changed by differing degrees under the A2 conditions. To gain a better understanding of the absolute sensitivity of the hydrothermal model, a second set of sensitivity analyses were run (Table 3.2 and Figure 3.8) using uniform changes to the entire time series of historical input data. In these scenarios each meteorologic input was changed individually by a constant additive amount or percentage: the air temperature was shifted by -6, -4, -2, 2, 4, and 6 ^{o}C; the dew point temperature was shifted by -6, -4, -2, 2, 4, and 6; the wind speed was shifted by -6, -4, -2, 2, 4, and 6%; and the solar radiation was shifted by -6, -4, -2, 2, 4, and 6%. .When estimating the sensitivity of the reservoir model to changes in air temperature or dew point temperature the coupling between air temperature and dew point temperature was considered (Table 3.2).

The onset, loss and duration of stratification is defined here as occurring when the difference in surface temperature (Ts) at 1m and the temperature at 1m above bottom $\geq$ 5 ^{o}C., The duration of seasonal stratification is defined as the longest period between the beginning of stratification and the loss of stratification is defined by the 5 ^{o}C temperature difference.

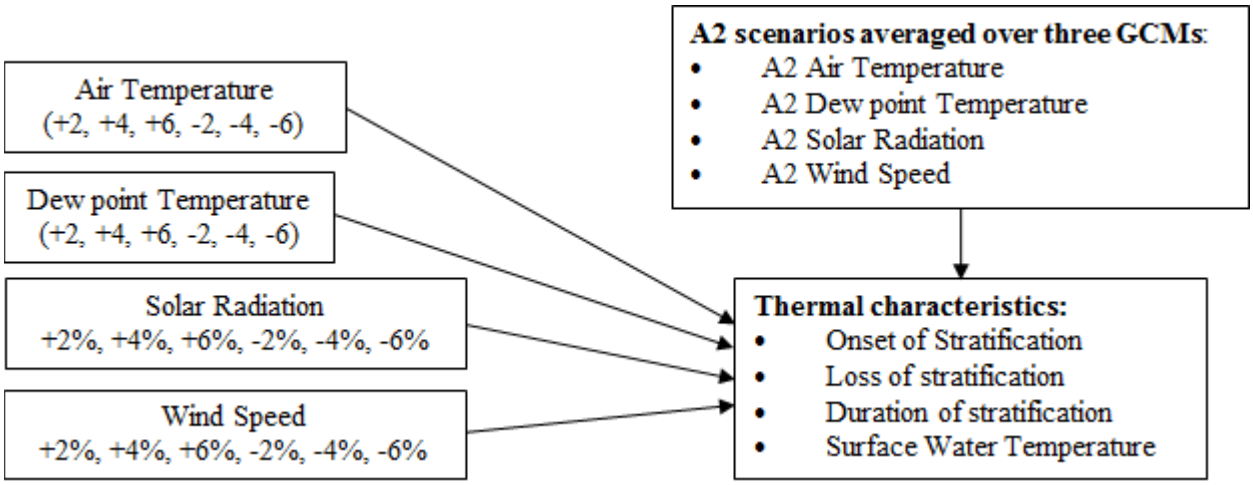

Figure 3.8. Schematic summary of the effect of changes in meteorological forcing on water temperature

Table 3.2. Sensitivity analysis using the 1-D hydrothermal model and detailed description of model run

Table 1a.Watershed model and Reservoir model using baseline and A2 Scenarios meteorological forcing		
Watershed model meteorological data	**Reservoir model meteorological data**	**Remarks**
A2 Scenarios	A2 Scenarios	Effects of climate change on watershed and reservoir processes
Baseline	A2 Scenarios	Effects of climate change on Reservoir meteorology while watershed inflows and tributary temperatures are unchanged
A2 Scenarios	Baseline	Effects of climate change on watershed inflows and tributary temperatures. Meteorological forcing to the reservoir is not changed.
Table 1b. Single future meteorology runs		
Changes in individual meteorological parameters		**Scenario sensitivity analysis**
Baseline: solar radiation, wind speed; A2 tributary temperature ($A2T_{Trb}$), New dew point temperature estimated using baseline relative humidity and A2 saturation vapor pressure	A2 air temperature (A2AT)	A2 emission scenario is chosen since atmospheric CO_2 concentrations reach 850 ppm the maximum in the year 2100 (Girod et al. 2009). Only A2 specific meteorological parameter is changed in each run while others are baseline
Baseline: air temperature solar radiation, wind speed; tributary temperature (T_{Trb}), New dew point temperature estimated using A2 relative humidity and baseline saturation vapor pressure	A2 dew point temperature	
Baseline: air temperature, relative humidity, wind speed, tributary temperature (T_{Trb})	A2 solar radiation (A2SR)	
Baseline: air temperature, relative humidity, solar radiation, tributary temperature (T_{Trb})	A2 wind speed (A2WS)	
Table 1c. Meteorologic fixed change sensitivities		**Meteorologic sensitivity analysis**
Baseline: solar radiation, wind speed; new tributary temperature (T_{Trb}) and new dew point temperature	air temperature	Increased/decreased by +2, +4, +6, -2, -4, -6 ^{o}C
Baseline: air temperature, solar radiation, wind speed; new tributary temperature (T_{Trb}) and new dew point temperature	dew point temperature	
Baseline: air temperature, dew point temperature, wind speed; new tributary temperature (T_{Trb})	solar radiation	Increased/decreased by +2%, +4%, +6%, -2%, -4%, -6%
Baseline: air temperature, dew point temperature, solar radiation; new tributary temperature (T_{Trb})	wind speed	

Results and discussion

The annual average air temperature, simulated water temperature, dew point temperature and solar radiation all show a slight increasing trend while wind speed shows a slight decreasing trend (Figure 3.9). The slopes of these trends while suggestive of ongoing climate change were not significantly different from zero. We therefore assumed that the 39 year record approximated a stationary baseline climate.

Model Verification - simulations under present conditions in Cannonsville Reservoir

Historical baseline simulations of water temperature closely match water temperature profiles measured in the reservoir (Figure 3.10). Simulated and measured water temperature profiles beginning with well mixed spring conditions and continuing through the fall turnover are presented in Figure 3.10. These figures demonstrate the model's ability to reproduce the entire vertical profile of the measured water temperature. In general, the model captures both the seasonal and vertical distributions observed in the data. Usually, the onset of stratification begins from mid-April and in early May, permanent stratification occurs between June through September and breaks down in October. The model was able to reproduce all these events successfully.

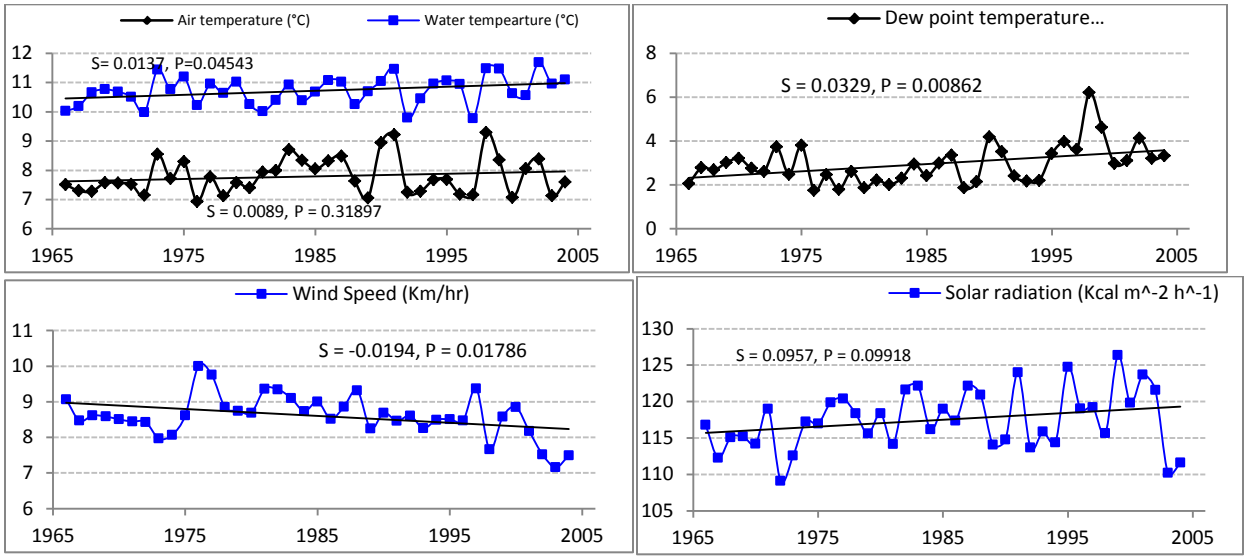

Figure 3.9. Variations of annual average air and water temperature, dew point temperature, mean solar radiation and wind speed for Cannonsville Reservoir (over 39 years)

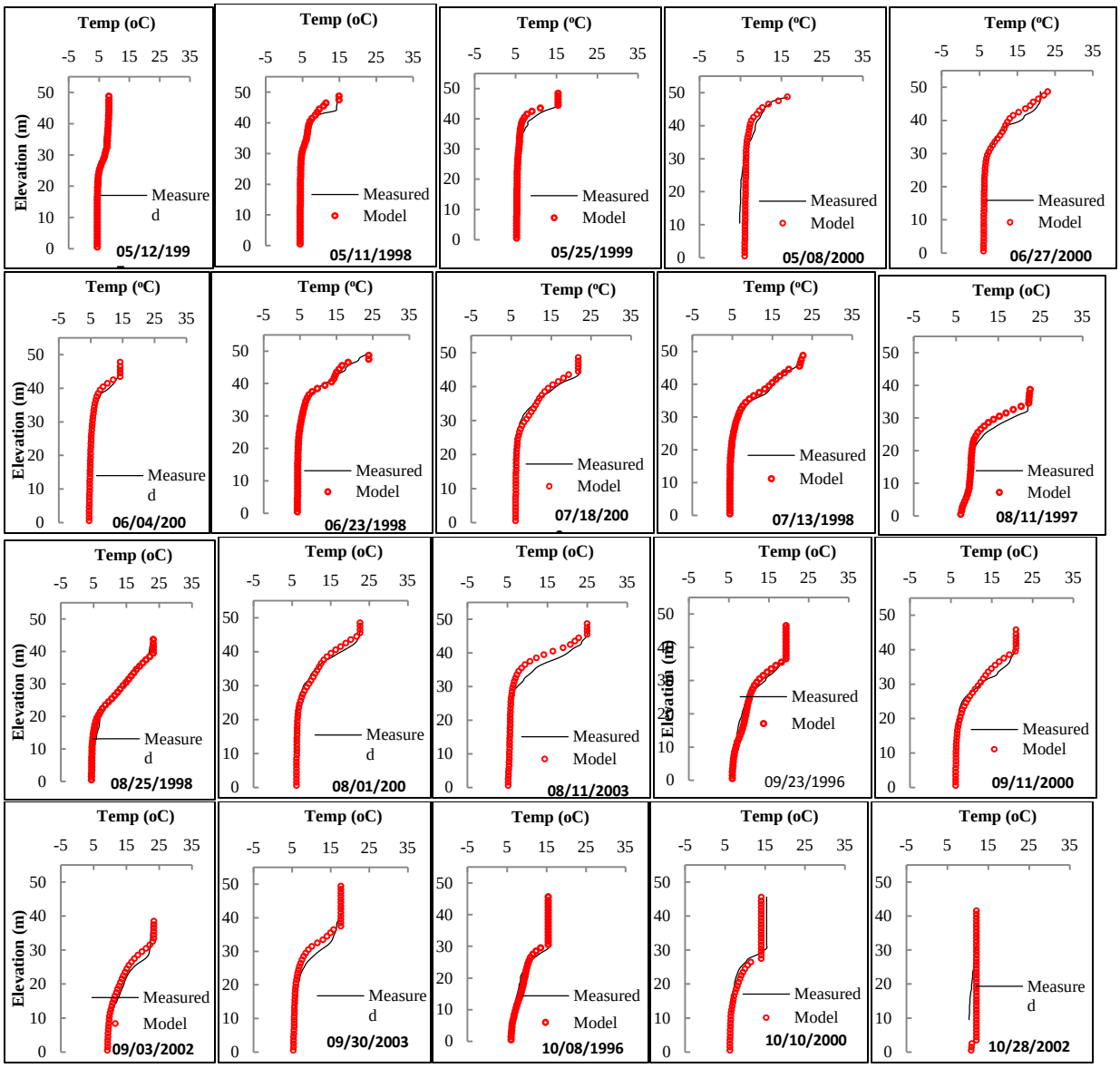

Figure 3.10. Model comparison results for temperature profile during summer stratification months. Solid lines represent measured temperatures profiles and the open circles represent model-computed temperature profiles

Relationship between monthly air temperature and simulated water temperature in Cannonsville Reservoir

Monthly mean air temperature and the simulated water temperature were compared on a monthly basis during the stratification period (April to October), and regression equations are derived (Figure 3.11).

The mean monthly surface water temperature of the reservoir was shown to be directly related to changes in air temperature. However, distinct differences were observed in the relationships between temperature of air and surface water on monthly basis, differentiating a warming phase (April, May, June and July) having rising slope range from 0.6 to 0.9 and a cooling phase (August, September, October), in which the slope in the regression lines range from 0.4 to 0.8. April represents a transition from winter to the warming phase as shown by the negative (low) intercept. The lower slopes (May-October) indicate that there is a smaller year to year variation in the water temperature than in the air temperature both during warming and cooling phase. This smaller water temperature variation reflects the higher specific heat and consequent greater heat capacity of the water. It may be possible that the greater scatter in October with small R^2 (0.3) is associated with the final breakdown in thermal stratification.

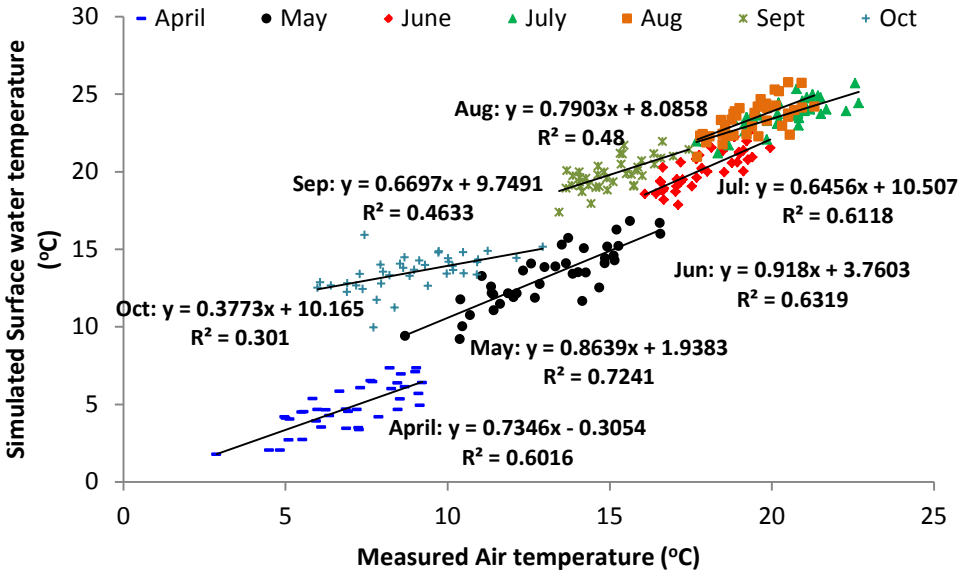

Figure 3.11. The relation between the monthly means of air and simulated water temperature in Cannonsville Reservoir (based on 1966-2004 baseline period)

Comparison of vertical temperature distribution under baseline and A2 emission scenario (2081-2100)

Isopleths of the vertical variation of simulated water temperature are presented in Figure 3.12 for historical baseline conditions and for future A2 scenario conditions, where both watershed and reservoir models were driven by the A2 scenarios (Figure 3.7). The isopleths are constructed using daily average water temperature profiles associated with the 39 years baseline period and the combined mean daily profiles derived from the three A2 scenarios. The figures show the overall seasonal variation of water temperature and comparison of the two figures show the predicted increase in future mixed layer depth and surface temperatures in the A2 scenario in comparison to baseline. Overall the A2 emission scenario is simulated to have warming water temperatures, a longer stratification period, greater vertical temperature gradients and more stable thermal stratification.

Statistics describing stratification characteristics, such as onset, loss and duration of stratification and the surface and bottom temperature in baseline and A2 scenario are listed in Table 3.3. It is estimated that on average for the future A2 scenarios, the onset of stratification will begin 19 days earlier; loss will occur 4 days later with duration of stratification will increase by 23 days. The surface water temperature will on average increase by + 1.8 ^{o}C and the bottom water temperature will increase by 0.8 ^{o}C.

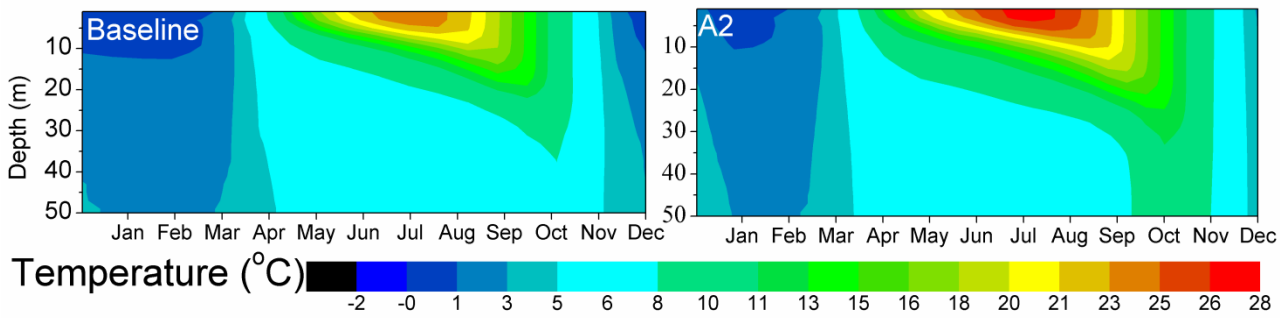

Figure 3.12. Mean annual isopleths of simulated temperature under baseline and A2 emission scenario. Profiles from which these were calculated are the mean daily profiles of all baseline scenario years and the combined means of all A2 scenarios (CGCM3, ECHAM & GISS)

Table 3.3. Thermal characteristics under baseline and A2 scenario (Surface Water Temperature, T_s = temp at 1m; Bottom Water Temperature, T_b = temp at 1 m above bottom) Days are Julian day (1-365) of the year. All values are means calculated over all the years from a given scenario.

	Stratification under baseline (in days)				
	Onset (day)	**Loss (day)**	**Duration (days)**	**Ts (^{o}C)**	**Tb (^{o}C)**
Average	129.64	295	165.35	19.93	5.31
Range	111-148	267-325	139-204	18.28-21.54	2.14-8.53
	Stratification under A2 (in days)				
	Onset (day)	**Loss (day)**	**Duration (days)**	**Ts (^{o}C)**	**Tb (^{o}C)**
Average	110.89	298.79	187.89	21.7	6.09
Range	95-132	275-330	160-221	20.20-23.43	4.21-9.50

A2 Scenario sensitivity run

The annual average increase in air temperature (+4 ^{o}C) and dew point temperature (+2 ^{o}C), as well as the percent increase in wind speed (+2%) and solar radiation (+0.25%) in A2 emission scenario in comparison to baseline conditions are presented in Figure 3.13 and Table 3.4.

In order to evaluate the relative sensitivity of water temperature and thermal stratification to the changes in the different meteorological drivers that occur in the A2 future scenario, a set of sensitivity simulations was run which used the baseline meteorological data for all but one meteorological variable which was instead drawn from the A2 scenario time series. When the coupled model system was driven using these hybrid data it is possible to see the relative effects of A2 level changes in a single meteorological variable.

The onset loss and duration of stratification during the 39 years of the baseline simulations and the sensitivity simulations which used single A2 meteorological variables with the remaining variables being baseline are shown in Figure 3.14.

Table 3.4. Variation in meteorological data under baseline and A2 scenario

	Tair (^oC)	Tdp (^oC)	mSR (Kcal m^{-2} h^{-1})	Wind Speed (km/hr)
Baseline				
Average	7.79	2.95	8.61	117.51
Range	(9.29-6.93)	(6.20-1.75)	(10.00-7.16)	(126.36-109.10)
A2 Scenarios				
Average	11.86	4.95	8.78	117.80
Range	(13.35-11.00)	(6.92-3.62)	(10.23-7.29)	(126.40-109.39)

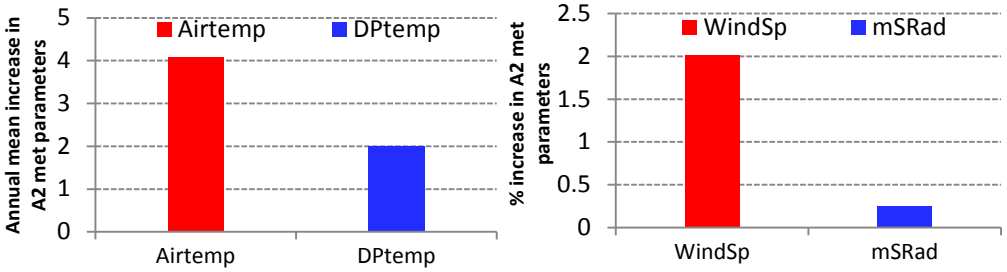

Figure 3.13. Increase in mean annual values of meteorological data compared from the baseline run and the combined A2 scenario data set. Differences in air temperature and dew point temperature are absolute and in degrees C. Differences in wind speed and solar radiation are expressed as a percent change from the baseline.

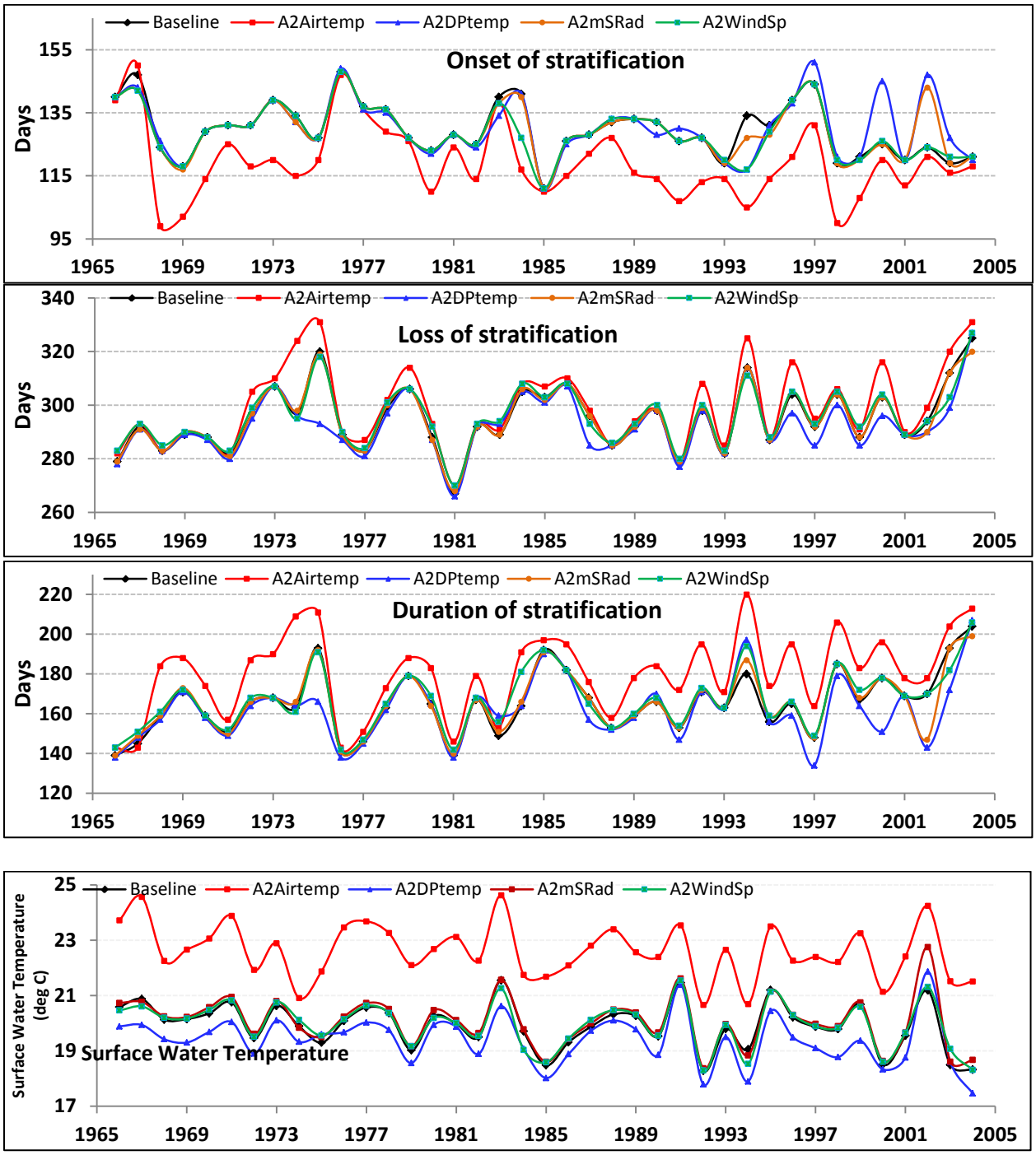

Figure 3.14. Inter-annual variation in the onset loss and duration of thermal stratification for baseline conditions, and for hybrid data sets of baseline conditions and a single meteorological driver from the A2 scenario.

From the results in Figure 3.14, it is clear that the onset of stratification is most sensitive to air temperature in comparison to the other A2 meteorological drivers. In fact variations in the other sensitivity runs were very similar to the baseline run, showing that simulated changes in the onset of thermal stratification were largely the result of A2 level changes in air temperature. There are a few interesting occasions (1997, 1999, 2002) where A2 level changes in dew point temperature also led to variations in the onset of thermal stratification, and these are currently under investigation.

Usually, the loss of stratification is also found to be sensitive to A2 level changes in air temperature, although to a lesser extent than was the case for the onset of stratification. This is the result of the onset of stratification being most strongly influenced by the conductive warming by significantly warmer air temperatures (Figure 3.13), while the loss of stratification is more strongly related to cooling and convective mixing that are closely linked to the seasonal cycle of air temperature, and not as strongly linked to changes in the absolute magnitude of the surface air temperature. As a result of changes in the onset of stratification and to a lesser extent the loss of stratification, the duration of stratification is longer throughout the simulation period except the year 1976, which was storm affected. The results shown in Figure 3.13 clearly show the sensitivity of stratification and water temperature to A2 level changes in air temperature, followed by dew point temperature. Changes in wind speed and solar radiation simulated to occur in our A2 scenarios had only minimal impact on reservoir thermal structure.

Simulations with the 2081-2100 A2 scenarios clearly indicate that there will be important changes in reservoir thermal structure, and that these changes are largely the result of the air temperature increases expected under these future conditions. However, it is also clear that in the future scenarios it is air temperature which shows the greatest and most consistent increase (Figure 3.13). As a consequence, the changes simulated in Figures 3.12 and 3.14 can be related to the greater climate sensitivity of air temperature and also possibly to a greater model sensitivity to changes in air temperature. To better separate the effects of model sensitivity from climate change sensitivity a second set of model sensitivity analyses was run where each meteorological driver was varied over a series of fixed steps.

Model sensitivity run (changing meteorological forcing) under baseline conditions

The hydrothermal model was run with uniform changes in meteorological forcing, i.e. +2, +4, +6, -2, -4 and -6 ^{o}C for air temperature, and dew point temperature, and with +2%, +4%, +6%, -2%, -4% and -6% changes in mean solar radiation and wind speed. The thermal characteristics of each run are analyzed and are presented in Table 3.5. Changes in the onset, loss and duration of stratification in response to changes in each of the four meteorological forcing are shown in Figure 3.15. The results show that model sensitivity for simulating changes in stratification is most sensitive to changes in air temperature.

For a rise in air temperature of +2, +4 and +6 ^{o}C, the onset of stratification begins 5, 9 and 18 days earlier and the loss of stratification occurs 1, 3 and 5 days later resulting in a longer duration of stratification in comparison to the baseline. With a decrease of air temperature, the onset of stratification occurs 5, 10 and 18 days later while the loss of stratification occurs 4, 8 and 12 days earlier resulting in a shorter duration of stratification.

The stability of the water column also changes markedly with changing air temperature, becoming more stable with increased air temperature and less stable with decreased air temperatures. This change is caused by a more rapid and greater response in epilimnion temperatures compared to the hypolimnion temperatures, so that increased air temperature increases the vertical temperature gradient and water column stability. A similar change in dew point temperature results in no significant change in onset, loss and duration of stratification. This implies the effects of dew point on the evaporative latent heat flux are much less than the conductive heating associated with air temperature increases.

When the solar radiation and wind speed are increased or decreased by 2%, 4% and 6%; there is only a marginal change in onset of stratification (1-2 days earlier for maximum changes in solar radiation and 1-2 days later for maximum changes wind speed). There is no change in the loss of stratification with the same changes in solar radiation while there is 1-2 days earlier occurrence of loss of stratification with increase in wind speed. With decrease in wind speed, the loss of stratification occurs 1-3 days later. Thus, wind speed has a measureable effect on the onset and loss of stratification. Such effects in reality could be greater since actual changes in wind are unlikely to occur as a fixed percentage as in this sensitivity test. Rather, wind changes could be more episodic with larger but temporally shorter increases having more significant effects on the timing of stratification

Table 3.5. Thermal characteristics resulting from a change in each meteorological forcing. Positive values for onset and loss signify the number of day later in the year for the event, values for the duration signify the change in the number of days of stratified conditions.

Air Temperature					**Dew Point Temperature**				
Change	**onset**	**loss**	**duration**	**Ts**	**Change**	**onset**	**loss**	**duration**	**Ts**
2	-5	+1	+5	1.51	2	0	+1	+2	-0.06
4	-9	+3	+12	2.89	4	+1	+1	+1	-0.01
6	-18	+5	+22	4.08	6	+1	+1	+1	0.00
-2	+5	-4	-10	-1.24	-2	+1	+1	+1	-0.06
-4	+10	-8	-18	-2.65	-4	+1	+1	+1	-0.09
-6	+18	-12	-29	-3.92	-6	+1	0	0	-0.08
Solar Radiation					**Wind Speed**				
Change	**onset**	**loss**	**duration**	**Ts**	**Change**	**onset**	**loss**	**duration**	**Ts**
2%	-1	0	+1	0.09	2%	+1	-1	-1	-0.04
4%	-2	0	+2	0.13	4%	+1	-2	-3	-0.06
6%	-1	0	+2	0.26	6%	+2	-2	-4	-0.11
-2%	0	0	0	-0.12	-2%	0	+1	+1	0.00
-4%	+1	0	-1	-0.14	-4%	0	+2	+2	0.07
-6%	+1	-1	-2	-0.22	-6%	-1	+3	+4	0.09

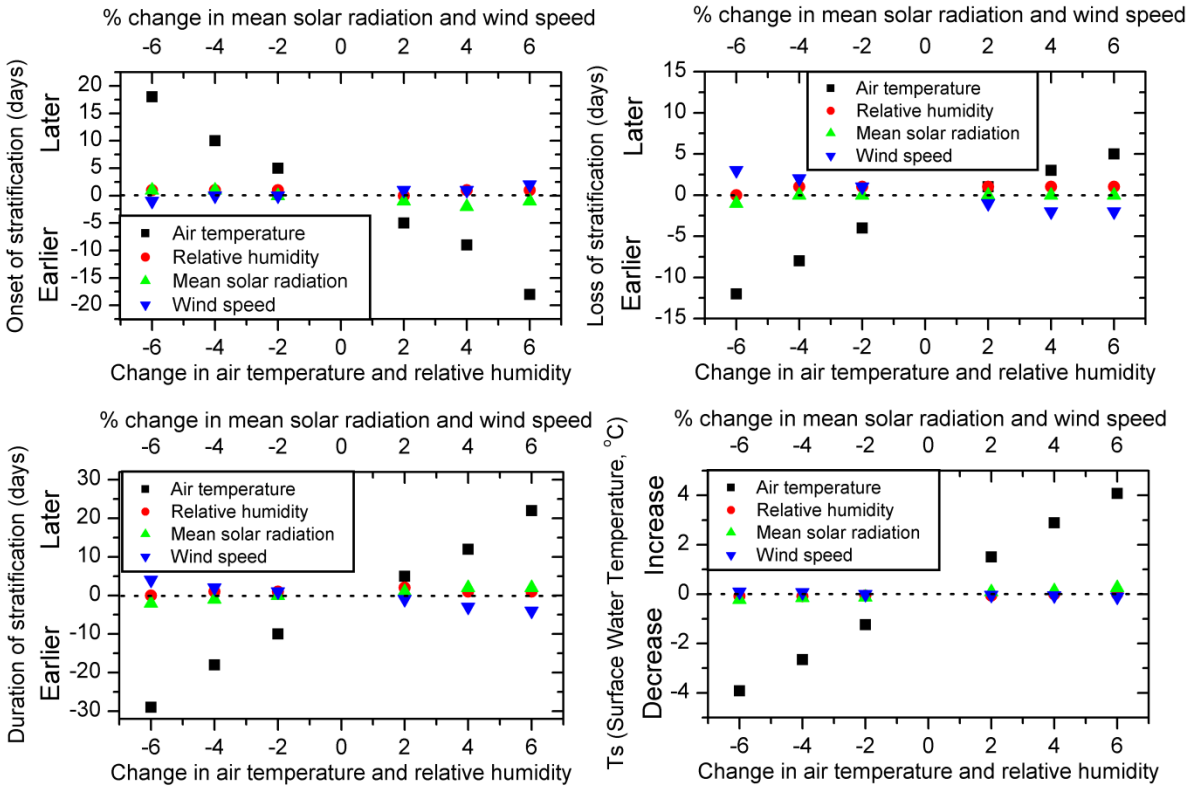

Figure 3.15. Comparison of Stratification Characteristics for various runs under changes in meteorological forcing

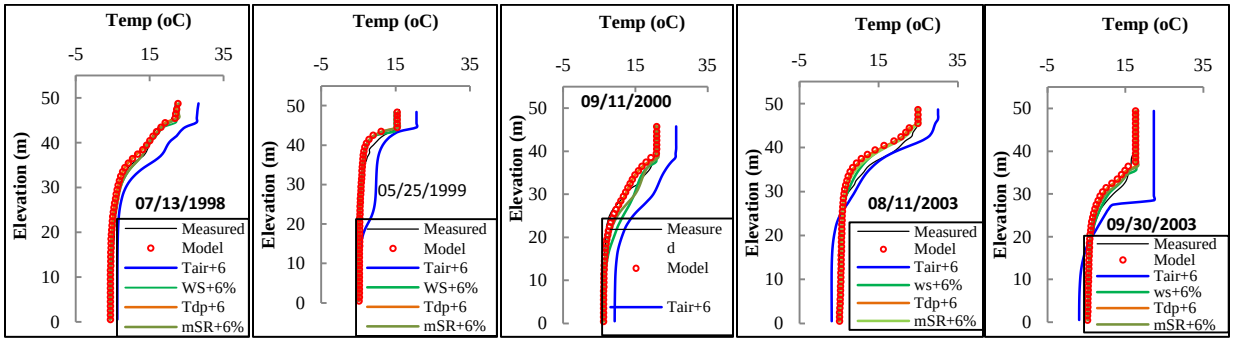

Figure 3.16. Selected vertical temperature profiles with under baseline conditions and from the sensitivity runs that increased air temperature and dew point temperature by +6 ^{o}C and wind speed and solar radiation by +6%

Response of water temperature profiles to the changes in meteorological variables

Several examples of vertical temperature profiles are selected at times when there was a measured well established thermocline (Figure 3.16). These show changes in the vertical variation of water temperature with respect to the changes in air temperature and wind speed. It was observed from these vertical temperature profiles that with the rise in air temperature, the water temperature is fairly uniform within the depths of the upper mixed layer (epilimnion), showing that the induced warming is distributed vertically by convective mixing. It may be concluded that the model is very sensitivity to changes in air temperature in comparison to other meteorological forcing. As was the case with Figures 3.14 and 3.15 the simulated temperature profiles in Figure 3.16 are insensitive to changes in any of the meteorological parameters other than air temperature.

Conclusions

The coupled hydrologic and hydrothermal models used in the present study are capable of reproducing the physical processes affecting the thermal structure of the Cannonsville reservoir system. In general, the onset of stratification begins from mid-April and by early May, a permanent stratification becomes established, which stays until mid-October). It is estimated that under the future A2 emission scenario in the 2081-2100 time period, the onset of stratification will begin 19 days earlier, loss will occur 4 days later with duration of stratification 23 days more. The surface water temperature will increase by 1.8 ^{o}C and the bottom water temperature will increase by 0.8 ^{o}C.

By selectively examining the effects of different meteorological parameters in the A2 emission scenario, it was concluded that the onset of stratification is most sensitive to air temperature in comparison to other meteorological drivers of the reservoir hydrothermal model. A separate sensitivity analysis that systematically varied each of the meteorological drivers over a similar range of variation confirmed that the simulated timing of thermal stratification was most sensitive to changes in air temperature.

The sensitivity of future simulations of reservoir thermal stratification to changes in air temperature is therefore, related to two different sensitivities: 1) Climate sensitivity of air temperature. It is changes in air temperature embodied in the GCM data which are predicted with the greatest certainty, and which show the greatest change relative to other reservoir model meteorological drivers. 2) Model sensitivity to changes in air temperature. Sensitivity analyses which varied each meteorological driver by a similar amount also show that simulations of thermal stratification are most strongly influenced by variations in air temperature, and the model is therefore most sensitive to this meteorological driver...

The timing and pattern of thermal stratification, is of fundamental importance in regulating the ecology and biogeochemistry of lakes and reservoirs. Based on our results it appears predictions of changing thermal stratification can be made with a high level of certainty that is similar to that now attributed to future scenarios of air temperature.

3.4. Streamflow Responses to Climate Change: Analysis of Hydrologic Indicators

Introduction

Streamflow and its components reflect the combined impact of climate change because of the spatially integrated hydrologic response that they provide. Small perturbations in precipitation frequency and/or quantity can impact mean annual streamflow (Risbey and Entekhabi, 1996). An examination of historical data and results of model simulations in the northeastern US have shown an increasing trend in precipitation and streamflow during the last fifty years (Burns et al., 2007; Zion et al., 2011). Changes in precipitation and even temporal shifts in the water balance may bring changes in hydrologic regimes and affect stream habitat, ecosystem diversity, and water resource management. The characteristics related to the amount and variability of discharge are considered to be the most fundamental variables defining the stream ecosystem (Bunn and Arthington, 2002; Poff and Ward, 1990) and the alteration of flow regimes is identified as a potentially serious threat to the ecological sustainability of rivers (Richter et al., 1996). Ecologists have consistently identified flow magnitude, duration, frequency, timing, and rate of change (Poff and Ward, 1990; Poff et al., 1997) as the most influential responses to consider in ecological studies. The goals of this study are:

1. To examine how changes in precipitation and air temperature translate into changes in streamflow responses in the Cannonsville Reservoir Watershed (CRW) using a physically based semi-distributed SWAT-WB model (Easton et al., 2010; White et al., 2011).

2. To analyze baseline and future streamflow scenarios using the Indicators of Hydrologic Alterations (IHA) tool (Richter et al., 1996) to gain an overall indication of the extent of hydrological change from reference conditions.

The potential effect of climate change on streamflow was assessed using scenarios derived from a suite of nine Global Climate Model (GCMs) that represent a range of future (2081-2100) climate conditions (Table 3.6) for A1B scenario (representing rapid economic growth with balanced emphasis on all energy sources) (IPCC, 2007). Climate scenarios were downscaled using change factor methodology described in (Anandhi et al., 2011).

Methods

Hydrologic Assessment

The general approach for hydrologic assessment consisted of defining a series of 33 hydrologic attributes that characterize intra-annual variability in streamflow conditions and then analyzing these variations as a foundation to compare baseline streamflow versus the impact of climate change on streamflow. The hydrologic attributes are based upon five characteristics of hydrologic regimes, known as Indicators of Hydrologic Alterations (IHA). Details on IHA tool can be obtained from IHA Manual (Richter et al., 1996). A summary of the parameters, and their characteristics, used in the IHA is provided in Table 3.6. The IHA analysis statistically characterizes inter-annual variation in flow regimes and, because the methodology uses median daily streamflow, it is suitable for detecting the hydrological characteristics relevant to sustaining

Table 3.6. Indicators of Hydrologic Assessment (Richter et al., 1996)

IHA group	Hydrologic parameters	Ecosystem Influences
Magnitude of monthly water conditions	Median value for each calendar year (12 parameters)	Availability of habitat for aquatic organisms Availability of soil moisture for plants Availability of water Reliability of water supplies for wildlife Effects of water temperature and dissolved oxygen
Magnitude and duration of annual extreme water conditions(median daily flow)	Annual 1-day minima Annual 3-day minima Annual 7-day minima Annual 30-day minima Annual 90-day minima Annual 1-day maxima Annual 1-day maxima Annual 1-day maxima Annual 1-day maxima Annual 1-day maxima Number of zero flow days 7-day minima/median for year	Balance of competitive and stress tolerant organisms Creation of sites for plant colonization Structure of river channel morphology and physical habitat conditions Soil moisture stress in plants Dehydration of wildlife Duration of stressful conditions Distribution of plant communities
Timing of annual extreme of high and low pulses	Julian date of each annual 1-day maxima Julian date of each annual 1-day minima	Predictability and avoidability of stress for organisms Spawning cues for migratory fish
Frequency and duration of high and low pulses	Number of low pulses within each year Median duration of low pulses each year Number of high pulses within each year Median duration of high pulses each year	Frequency and magnitude of soil moisture stress for plants Availability of floodplain habitat for aquatic organisms Effects of bedload transport and channel sediment distribution, and duration of substrate disturbance
Rate and frequency of water condition changes	Medians of all positive difference between consecutive daily values Medians of all negative difference between consecutive daily values Number of hydrologic reversals	Drought stress on plants Desiccation stress on low-mobility stream-edge organisms

Table 3.7. Global Climate Models (GCMs) used in this study

GCM ID*	Acronym used
CGCM3.1(T47)	CC4
CGCM3.1 (T63)	CC6
CSIRO-MK 3.0	CS0
GISS-AOM	GAO
GFDL-CM 2.0	GF0
IPSL-CM4	IPS
MIROC3.2 (HIRES)	MIH
ECHAM5/MPI-OM	MPI
MRI-CGCM 2.3.2	MRI

aquatic ecosystems. Seventeen of the 33 IHA parameters (Groups 2, 3 and 4 in Table 3.6) focus on the magnitude, duration, timing and frequency of extreme events, whereas the other 16 parameters (Groups 1 and 5 in Table 3.6) are measures of the median of the magnitude of flows or the rate of change of water conditions.

The steps used in hydrologic assessment are as follows:

1. The streamflow time series for baseline simulation (1964-2008) and nine climate change scenarios were defined. During the data set up, baseline simulation was treated as pre-impact scenario and each climate change scenario as post-impact scenarios.

2. The values for the ecologically relevant 33 parameters (Table 3.6) for each year in each time series were calculated.

3. Inter-annual statistics such as measures of central tendency and dispersion were calculated for each time series for 33 parameters.

4. The median and coefficient of variations for each parameter was then compared between simulated streamflow and streamflow as a result of climate change.

Changes in daily streamflow metrics were analyzed to identify changes in dynamics of streamflow in the CRW between the baseline simulation period and the various climate change scenarios (Table 3.7). When examining the hydrologic effects of climate change scenarios, the change in the hydrologic responses were calculated relative to the results from the calibrated baseline simulation, rather than the historic observations.

Results and Discussion

We used the median as an estimate of central tendency and the variance as an estimate of dispersion. For each 33 hydrologic parameters the differences between the baseline and climate change ensemble scenario was expressed as both a magnitude of difference and a deviation percentage (Table 3.8).

Magnitude of the monthly median of daily flows

The hydrologic assessment showed an increase in median monthly streamflow for winter months. The highest increase in median daily flow was observed for during January (379%). Such a large increase in winter flow can affect not only habitat suitable for winter flora and fauna, but can increase stream bank erosion and mass flux of pollutants. The streamflow decreased from April through September. The reduced flow during April and summer months can have adverse impacts on fish habitats and spawning. A study specific to the Catskill Mountain region of NYS (Burns et al., 2007) reported that there was a notable shift in peak snowmelt from early April at the beginning of the historic record to late March by the end of the record, and an increase in runoff from June to October. Annual mean streamflow increased for all the climate change scenarios. (Gan, 1998), in a study of the Canadian Prairies, found that over

Table 3.8. Results of indicators of hydrologic alteration analysis for stream at Walton, NY

	Medians			Dispersion		
	Baseline Condition (1964-2008)	Ensemble scenario (2081-2100)	Deviation[b]/ Magnitude%	Baseline Condition (1964-2008)	Ensemble scenario (2081-2100)	Deviation/ Magnitude%
Parameter Group #1: Monthly magnitude (streamflow[a])						
January	4.07	19.5	15.4/ 379	2.10	1.02	-1.08/ -51.4
February	4.99	22.2	17.2/ 344	2.44	0.81	-1.63/ -66.9
March	25.5	31.6	6.10/ 23.9	0.98	0.47	-0.51/ -52.0
April	40.8	24.7	-16.1/ -39.5	0.40	0.52	0.12/ 29.2
May	19.9	12.9	-7.03/ -35.3	0.47	0.67	0.20/ 41.5
June	9.69	8.06	-1.63/ -16.8	0.81	1.01	0.20/ 24.6
July	7.00	6.58	-0.42/ -6.0	0.84	0.83	-0.01/ -1.20
August	4.71	4.44	-0.27/ -5.8	0.68	0.65	-0.03/ -5.00
September	4.61	4.11	-0.50/ -10.9	0.88	0.91	0.02/ 2.80
October	7.12	7.59	0.47/ 6.6	1.63	1.74	0.11/ 6.80
November	12.5	20.2	7.68/ 61.2	0.99	0.98	-0.02/ -1.50
December	8.73	19.2	10.5/ 120	0.82	0.82	0.00/ -0.20
Group averages [c]			**68.4%**			**-6.11%**
Parameter Group #2: Magnitude and duration of annual extremes (streamflow[a])						
1-day minimum	0.21	0.50	0.29/ 140	2.81	1.38	-1.43/ -50.8
3-day minimum	0.27	0.65	0.38/ 144	2.55	1.27	-1.28/ -50.4
7-day minimum	0.47	1.04	0.58/ 124	2.16	0.89	-1.27/ -58.9
30-day minimum	2.44	2.73	0.29/ 12.0	0.95	0.70	-0.24/ -25.5
90-day minimum	5.20	5.11	-0.09/ -1.80	0.46	0.49	0.03/ 6.0
1-day maximum	130.0	137.4	7.40/ 5.70	0.59	0.57	-0.10/ -2.30
3-day maximum	98.3	105	6.57/ 6.70	0.54	0.49	-0.05/ -9.30
7-day maximum	80.2	82.4	2.17/ 2.70	0.54	0.39	-0.15/ -28.0
30-day maximum	51.7	53.5	1.80/ 3.50	0.49	0.37	-0.12/ -24.0
90-day maximum	36.5	35.3	-1.14/ -3.10	0.30	0.35	0.50/ 17.0
Base flow index	0.02	0.07	0.05/ 222	2.41	0.80	-1.61/ -66.7
Group averages [c]			**54.6%**			**-24.4%**
Parameter Group #3: Timing of annual extremes						
Date of minimum	50.0	253.5	202.5/ 397	0.14	0.11	-0.03/ -23.6
Date of maximum	84.0	79.8	-4.22/ -5.0	0.14	0.19	0.04/ 29.2
Group averages [c]			**196%**			**2.80%**
Parameter Group #4: Frequency and duration of high and low pulses						
Low pulse count	11.0	9.11	-1.89/ -17.20	0.55	0.56	0.02/ 3.30
Low pulse duration	5.00	4.67	-0.33/ -6.70	0.60	0.68	0.08/ 13.9
High pulse count	12.0	14.2	2.22/ 18.50	0.42	0.44	0.027/ 5.1
High pulse	4.00	3.94	-0.66/ -1.40	0.50	0.58	0.08/ 16.9
Group averages [c]			**-1.70%**			**9.80%**
Parameter Group #5: Rate and frequency of change in conditions						
Rise rate	2.16	2.33	0.17/ 8.1	0.61	0.42	-0.19/ -31.5
Fall rate	-1.12	-1.37	-0.25/ 22.5	-0.28	-0.35	-0.07/ 24.3
Number of	116	126.2	10.22/ 8.8	0.15	0.11	-0.04/ -24.5
Group averages [c]			**13.1%**			**10.6%**

[a]Daily median streamflow in $m^3 \cdot sec^{-1}$.

[b]The deviation represent the Indicators of Hydrologic Alternations.

[c]Group averages are computed as the mean of all deviations within the group.

the last 40-50 years many stream and river gauging stations observed an increase in streamflow during March, attributed to earlier snowmelt, followed by reduced flow in May and June. Lower summer flows can lead to increase in water temperatures and reduced dissolved oxygen. Lower flows also indicate a reduced wetted perimeter, which would decrease habitat availability and impact lateral exchanges between the riparian zone and the stream.

Magnitude and duration of extreme annual conditions

The percent change values are less for the annual maximum daily streamflow compared to the annual minimum and median daily streamflow for non-winter months, similar to the observations made by (McCabe and Wolock, 2002) for the conterminous United States. Our study indicates that streamflow will become much more extreme with increases in both consecutive 7-day low flow (124% increase from baseline) and in 7-day high flow (3.5% increase from baseline) under future climate scenarios. The magnitude of increase however is higher for annual daily minimum flow. A study in Monroe County, NY (Coon, 2005) assessing trends from 1965 to 2005 noted an increase in temperature, precipitation, and 7-day low-flows in rural streams, consistent with trends observed elsewhere in the U.S. Because the amount of water available in a river system defines the suitability of a habitat to aquatic organisms, flow alteration, especially at low flows, may create unfavorable conditions for native species (Poff et al., 1997).

Timing of the annual extreme conditions

The timing of the maximum 1-day flow shifted back from March 25 to March 19 (by approximately 6-days), while there was a forward shift in the timing of minimum flow as it shifted from early February to late October. This degree of shift would likely adversely affect the fall spawners such as brook trout due to reduced habitat availability resulting from extended low flow conditions. A shift in the timing of peak flow can alter the retention time of organic matter (Mulholland et al., 1997), disrupt the recruitment of riparian species that rely on appropriately-timed high flows to disperse seeds on the flood plain (Auble et al., 1994; Rood et al., 1995), and impact the survival of certain fish species whose larval emergence is timed to avoid high spring flows (Hauer et al., 1997).

Frequency, Rate and frequency of change in conditions

The pulsing behavior of the stream at the USGS gauge in Walton NY shows a reduced (17.2%) number of low pulse events but an increase of 18.5% in high pulse events compared to the baseline scenario. Changes in flow pulses will lead to changes in channel geometry depending on the channel substrate. Increase in high flow pulses also lead to shift towards weedy invertebrate species and loss of species with poor re-colonization ability. Our results showed an increase in both rise and fall rate of the hydrograph (e.g., steeper rising and receding limbs) resulting in increase in number of reversals.

Table 3.8 shows the temporal variability in streamflow for baseline and climate change scenarios. The variability has been reduced for the summer monthly median flows, the 90-day minimum and maximum flow, the timing of annual highs, the frequency and duration of low

pulses, and the duration of high pulses. Temporal variance increased for April through June and during fall months, specifically the 90-days minimum and maximum, timing of annual extremes and hydrograph rise rate. These results of IHA analysis for Walton, NY reflect the effect that climate change may have on stream flow conditions. This higher variability in rise and fall rate of hydrograph may affect aquatic invertebrates inhabiting the littoral zone along the river's edge (Richter et al., 1996; Richter et al., 2003).

Conclusions

This study used the SWAT-WB model to simulate streamflow and evaluate effects of climate change on streamflow, and flow regime, including metrics calculated using the IHA tool. These indicators are important for understanding how river flow dynamics will impact the health of the aquatic environment as well as water supply and other infrastructure. Based on the future climate scenarios used in this study, the indicator analysis showed that watershed water yield is expected to increase at an annual scale. Winter and spring streamflow will increase but summers will be drier in future. Lower flows indicate a reduced wetted perimeter, which would decrease habitat availability and impact lateral exchanges between the riparian zone and the stream. The magnitude and duration of annual extremes are also expected to increase due to climate change. Baseflow index increase, i.e., decrease in baseflow may result due to the change in projected climate effecting soil moisture and soil water storage. The timing of annual extremes will be shifted for maximum flow by approximately 6 days backward and minimum flow from early winter to late October. Such shifts can impact the survival of certain fish species whose larval emergence is timed to avoid high spring flows. Both the rise and fall rates of the hydrograph will increase indicating the increase in flashiness. Changes in land surface hydrology due to changing climate, such as changes in the discharge of large rivers, have potentially far reaching implications both for human populations and for regional-scale physical and ecological processes.

3.5. WRF Project 4262 - Vulnerability Assessment and Risk Management Tools for Climate Change: Assessing Potential Impacts and Identifying Adaptation Options

The WRF Project 4262 – Vulnerability Assessment and Risk Management Tools for Climate Change – was completed in 2013 and the final report entitled "A Framework for Assessing Climate Change Vulnerability and Defining Robust Risk Management Strategies for Water Utilities" was published by the Water Research Foundation. Project collaborators included researchers from Stockholm Environment Institute, Rand Corporation, Hydrologics, Hazen and Sawyer, NYC DEP, and National Center for Atmospheric Research (NCAR). The project focused on the use of a quantitative, iterative analytical framework called Robust Decision Making (RDM) to assess climate vulnerability for water supply systems. Guidelines for application of RDM were provided by means of examples in two pilot studies – Colorado Springs Utilities and the New York City Water Supply. RDM was demonstrated to be an efficient tool for testing the sensitivity of water supply systems to climate change, and may prove useful in future studies of the effects of climate change on the NYC Water Supply.

3.6. WRF Project 4306 – Dynamic Reservoir Operations: Managing for Climate Variability and Change

The WRF Project 4306 – Dynamic Reservoir Operations: Managing for Climate Variability and Change – was completed in 2013 and the final report was published by the Water Research Foundation. The project focused on the use of Dynamic Reservoir Operations (DRO) in improving system reliability, resilience and performance under challenging climate conditions. DRO are operating rules that change based on the present state of the system, such as storage levels, current inflow, and/or forecasted conditions. The project included a literature review; creation of a DRO development guide with step-by-step guidelines for developing effective rules; and case studies that included the Washington D.C. Metropolitan Area, New York City, and the City of Calgary. The NYC case study focused on the use of dynamic hydrologic forecast-based rules. An assessment of the incremental effect of increasingly sophisticated forecasting techniques on performance measures under historical and climate-adjusted hydrology showed a substantial benefit of the use of forecasts. The DRO guide and case studies provide valuable guidance for application of DRO in future studies of the effects of climate change on the NYC Water Supply.

4. Model Development and Applications

4.1. Simulating Spatial Sediment Loading in the Esopus Creek Watershed

Introduction

In the United States sediment is one of the leading pollutants impacting water quality in over 100,000 miles of assessed streams and rivers (USEPA, 2009). Sediment source assessment is thus not only important to our understanding of sediment dynamics in fluvial systems but is increasingly becoming an important management tool. The New York City (NYC) water supply is currently the largest unfiltered water supply in the world and supplies over 1 billion gallons (~3.78×10^6 m^3) of water per day to more than 9 million residents of NYC and upstate communities. While water quality is usually pristine, high magnitude runoff events can cause significant increases in stream and reservoir turbidity, which at times limit the use of this unfiltered drinking water supply (Effler et al., 1998; Gelda et al., 2009). This is particularly true for the Upper Esopus Creek (UEC) that drains into the Ashokan Reservoir (Figure 4.1) (Mukundan et al., 2013a). Previous modeling analysis of sediment sources in the UEC watershed indicated that the majority of suspended sediment in the UEC originated from stream channels (NYCDEP, 2008). And while there is a general consensus on the dominant source of suspended sediment in the UEC watershed, the spatial distribution of suspended sediment sources as well as the relative contribution by stream channels, uplands, and point sources is not well documented.

An approach for estimating sediment at the watershed scale is application of the Soil and Water Assessment Tool (SWAT) model (Gassman et al., 2007; Arnold et al., 2012). While calibrated models are cost effective tools to quantify sediment loading, lack of data for model parameterization remains a problem. (Moriasi et al., 2011a). This is particularly true for the application of SWAT model in the UEC watershed where sub-watersheds behave heterogeneously in respect to sediment transport rates. Recently, the NYC Department of Environmental Protection (NYCDEP) and the U.S. Geological Survey (USGS) developed and completed a monitoring project to collect detailed spatial and temporal turbidity and suspended sediment data in the UEC and its tributaries (McHale and Siemion, in press Section 5.1). One of the objectives of this three year (October 1, 2009 to September 30, 2012) project was to generate field data that can support water quality modeling analysis. In this study we use information generated from this monitoring project to guide a spatially distributed model parameterization and modeling analysis. The specific objectives of this study are:

- To use short-term monitoring data from multiple sites across the study watershed for model parameterization and develop a predictive model for long-term simulation of sediment transport.

- To simulate spatial variations in sediment entrainment within the Upper Esopus Creek watershed and its tributaries and predict sediment concentrations at the watershed outlet.

- To quantify sediment yield at the watershed outlet.

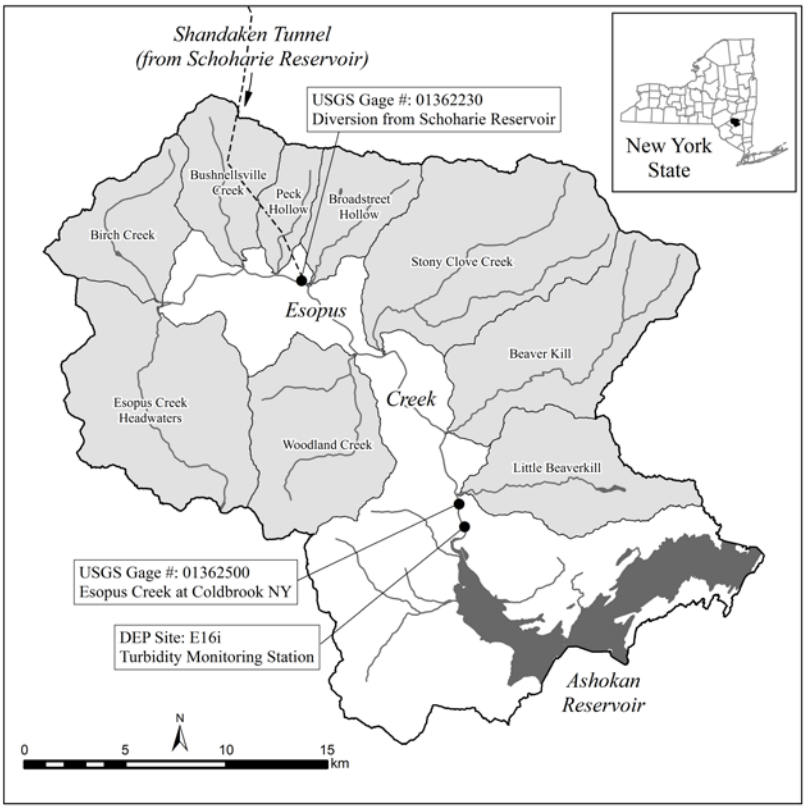

Figure 4.1. Location of the Upper Esopus Creek Watershed (UECW) and tributary sub-basins

Materials and Methods

Description of study area and water quality monitoring

The Upper Esopus Creek watershed drains 493 km^2 and is dominated by forests which occupy more than 90% of the watershed area. The elevation of the watershed ranges from about 194 m near the watershed outlet at Coldbrook to 1275 m at the headwaters. An automated turbidity monitoring system was installed on the main stem of the watershed near the confluence of the creek and the Ashokan reservoir. Water was pumped into a riverside hut where measurements of turbidity were made using a YSI water quality sonde. A strong relation (not shown) between turbidity and TSS permitted the use of turbidity data from the field sonde to be used as a surrogate for TSS in our modeling analysis. While the above data were used for model calibration at the watershed outlet, sub-basin level parameterization of the model for simulating sediment entrainment used the information generated by the monitoring project discussed in the Section 5.1 (McHale and Siemion, in press).

Model description and set up

The SWAT model estimates water, nutrient, and sediment loading from a watershed. In SWAT, sediment is generated by landscape and stream channel erosion and routed through the stream which is explicitly characterized as a network of connected reaches.

The UEC watershed was delineated from a 10-m resolution Digital Elevation Model (DEM) into 89 SWAT sub-basins using the automatic delineation tool in the ArcSWAT2012 interface. This ensured that the stream reaches within each major sub-basin were sufficiently small in length for channel parameterization and to simulate reach scale variability in channel processes. A land use map from 2001 with 39 classes derived from Landsat Enhanced Thematic Mapper Plus (ETM+) satellite imagery and ancillary data was used for land use information. For soil information, the SSURGO soils database was used. Daily precipitation and air temperature data were obtained from cooperator stations recognized by the National Climate Data Center (NCDC). All other regional weather parameters were simulated by the model using a weather generator encoded within SWAT. The contribution of water and sediment by the Shandaken Tunnel diversion from the nearby Schoharie Reservoir (point source) was input from a measured daily time series of flow and turbidity at the sub-basin where the tunnel entered the Esopus Creek.

Model parameterization, calibration and validation

A three step approach was used for model parameterization and calibration for spatially distributed sediment entrainment and transport simulation. A combination of automatic and manual calibration approach was used in this study.

In the first step, the model was calibrated for streamflow using measured values from the USGS gauge (#01362500) at Coldbrook. The calibration parameters related to processes involved in streamflow generation, including partitioning precipitation into infiltration and runoff, baseflow recession, and the rates of snowpack development and depletion, were adjusted using the ParaSol method in the SWAT-CUP automatic calibration tool (Abbaspour, 2008). The calibrated hydrology model was used to derive estimates of landscape erosion using default MUSLE parameters. We expect the model to perform adequately well with default parameters as there is very little disturbance for causing significant landscape erosion in this predominantly forested watershed.

In the second step channel parameters were adjusted one major sub-basin at a time to simulate sediment entrainment from the channel reaches. With land use being uniform across the watershed, a constant value for the channel cover [CH_COV] parameter was used. The channel erodibility parameter [CH_EROD] was adjusted so that the proportion of sediment contributed by each major sub-basin to the total sediment load at the entire watershed outlet matched estimates from the monitoring project described above (McHale and Siemion, in press). For major sub-basins channel erodibility was adjusted for the outlet reaches to represent the cumulative rates of channel erosion that resulted in sediment yields ranging between 2% and 37% of the total. The main stem of the watershed was parameterized to produce about 25% of the total yield as estimated by the monitoring project. The SWAT check program (White et al., 2012) was used in this step to determine the simulated contribution of stream channels to the overall sediment yield at the watershed outlet using the one sub-basin at a time parameterization approach described above. In the final step three parameters related to channel transport capacity ([SP_CON], [SP_EXP], and [PRF]) were optimized using SWAT-CUP. Model predicted TSS concentrations were calibrated against TSS estimated from high frequency turbidity measurements.

The period from June 2003 to December 2006 was considered as the calibration period for both streamflow and sediment concentration. The calibrated model was validated for streamflow and sediment concentration during the period from October 2008 to September 2010. The validated model was continuously simulated for the period from 1997 to 2010 (14 yr. with a 2 yr. model warm up period) under a wide range of hydrologic conditions observed during this period.

Results and Discussion

Model simulation of flow and sediment

The calibrated model made reasonable predictions of streamflow (Figure 4.2) and sediment concentrations (Figure 4.3) at the watershed outlet. The relative contribution of suspended sediment from the three sources in the UECW based on long-term simulation of the calibrated model was: stream channel processes – 85%; surface/upland erosion – 11%; and point source – 4%. This finding on the contribution of stream channels as the major source of suspended sediment in the UECW is consistent with previous estimates (NYCDEP, 2008) and field observations.

Sediment yield at the Esopus Creek watershed outlet and tributaries

Sediment yield (t km^{-2} yr^{-1}) from sub-basins (tributaries) and main stem of the Esopus Creek watershed based on a 12 year simulation (1999-2010) of the calibrated model are presented in Figure 4.4. The simulated average annual sediment yield at the watershed outlet at Coldbrook is about 80 t km^{-2} yr^{-1}. In comparison all tributaries except Stony Clove had much lower average annual sediment yields ranging between 12 t km^{-2} yr^{-1} to 57 t km^{-2} yr^{-1}. At 161 t km^{-2} yr^{-1} the Stony Clove sub-basin had an area normalized average annual sediment yield value that was twice that as at the watershed outlet.

The contribution of Stony Clove was estimated as 37% of the total sediment load; Woodland Creek (7%) contributed the next highest, followed by Beaverkill (5%). All other tributaries contributed less than 2% of the total sediment load at the outlet. In terms of a sediment load, this study, along with data collected by USGS (Section 5.1), indicate that Stony Clove is a critical watershed for sediment reduction efforts. Two major stream restoration projects were completed in this tributary in 2012-2013; they included channel realignment, regrading and bank stabilization. This study shows that short-term detailed water quality monitoring programs complemented with watershed modeling efforts can help to quantify the sub-basin sources of suspended sediment and help to inform management options.

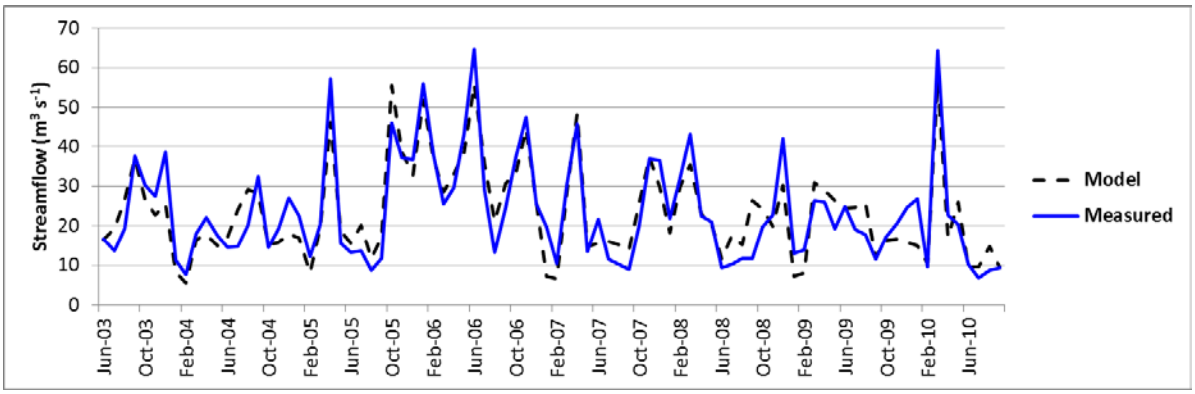

Figure 4.2. Comparison of measured and SWAT simulated average monthly streamflow at the Esopus Creek watershed outlet at Coldbrook

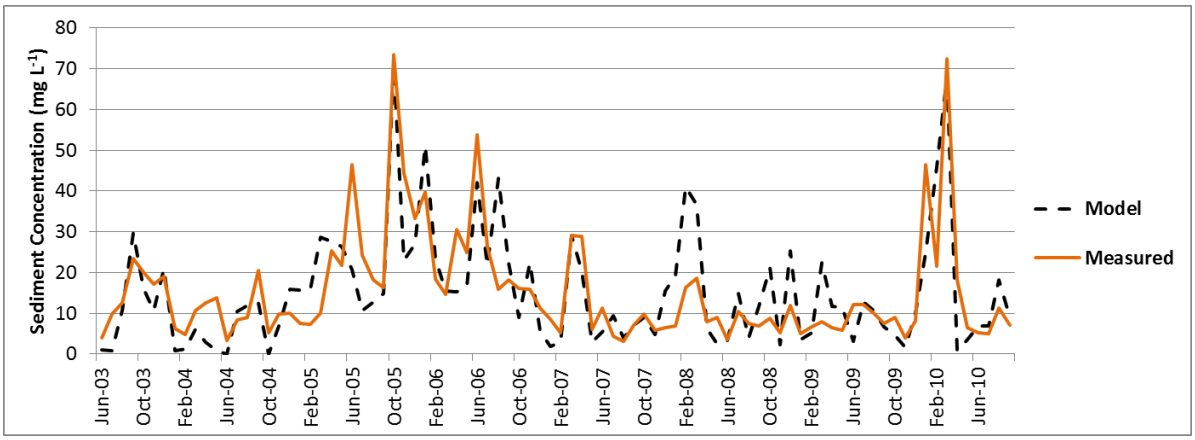

Figure 4.3. Comparison of measured and SWAT simulated average monthly stream sediment concentration at the Esopus Creek watershed outlet at Coldbrook

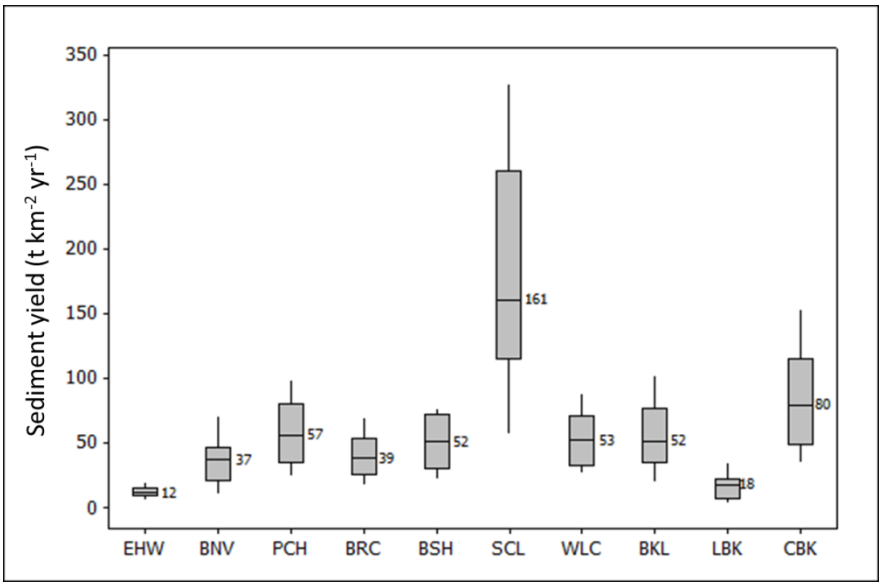

Figure 4.4. Simulated average annual suspended sediment yields from major sub-basins and outlet of the Esopus Creek at Coldbrook. (EHW - Esopus headwaters; BNV – Bushnellsville; PCH - Peck Hollow; BRC – Birch Creek; BSH – Broadstreet Hollow; SCL – Stony Clove; WLC – Woodland Creek; BKL – Beaverkill; LBK – Little Beaverkill; CBK – Coldbrook)

4.2. Trihalomethanes in the New York City Water Supply - Empirical Modeling and Tropical Storm Effects

Introduction

Chlorine is commonly used to achieve disinfection in most water supply systems in North America (USEPA, 2006; Health Canada, 2006), and can combine with organic carbon to produce a number of disinfection byproducts (DBPs) including trihalomethanes (THMs) and haloacetic acids (HAAs); some of which are probable carcinogenic compounds (Sadiq and Rodriguez, 2004; USEPA, 2006; Chowdhury et al., 2009). Regulatory agencies around the world have imposed regulations to meet certain levels for specific DBPs in drinking water. The USEPA has set a MCL of 80 μg/L for total trihalomethanes (TTHMs) and 60 μg/L for the sum of 5 haloacetic acids (HAA5) as site-specific running annual averages (USEPA, 2006).

A number of factors are involved in the formation of DBPs that can potentially cause operational challenges for a drinking water supply. These factors include disinfectant reaction time with natural organic matter (NOM) (Rathburn, 1996; Rodriguez and Serodes, 2001), pH (Nokes et al., 1999; Liang and Singer, 2003; Chowdhury and Champagne, 2008), temperature (Ozekin, 1994), types and amounts of NOMs (Tyrovola and Diamadopoulos, 2005), chlorine dose (Sadiq and Rodriguez, 2004), and the presence of bromide ions (Hong et al., 2007). A number of predictive models have been developed which consider at least some of these factors (Sadiq and Rodriguez 2004, Chowdhury et al. 2009). Predictive models developed both empirically using operational and water quality parameters or based on kinetics of DBP formation can be a useful complement to field monitoring. Typically DBP concentrations in drinking water are measured in the laboratory using gas chromatography (GC) analysis that can be both time consuming as well as expensive. Predictive models can provide quick and reasonable estimates of DBPs to help managers decide how to best optimize water supply operations (Westerhoff et al., 2000). Moreover, predictive models can be used to determine the relative importance of water quality and operational parameters influencing DBP formation for a particular region.

The objective of this study was to develop an empirical predictive model of total trihalomethanes (TTHMs) for the New York City (NYC) water supply. The 600 billion gallon water supply is currently the largest unfiltered water supply in the US, operating under a renewable Filtration Avoidance Determination (FAD) granted by the New York State Department of Health and the US Environmental Protection Agency. In October and November 2011, following Hurricane Irene and tropical storm Lee, TTHM levels in the water supply often exceeded the 80 μg/L MCL. A recent study by Van Dreason (2012) investigated the factors associated with the TTHM increase including quantity of NOM, water temperature, water age, chlorine dose and pH. In this study we develop a predictive model of TTHMs and quantify the relative importance of these factors that are specific to the NYC water supply system. Models that can reasonably estimate TTHM levels can also be used for evaluating strategies to minimize its formation and for simulating future scenarios of varying water quality and operational variables reflecting changes in land use, climatic conditions and water demand.

Materials and Methods

Empirical model development

Water quality data based on monthly analysis of water samples from 24 locations from within the NYC water supply distribution system, obtained from the New York City Department of Environmental Protection (NYCDEP) were used in this analysis. This dataset includes 866 measured values for TTHMs and other measured water quality parameters that include pH, total organic carbon (TOC), and water temperature, collected between January 2009 and April 2012. All analyses used Standard Methods (pH – 4500H B; Temperature – 2550B; THMs – EPA method 524.2; TOC – 5310B) as seen in APHA (1995). Chowdhury and Champagne (2008) recommended the use of one parameter related to NOM along with chlorine dose, pH, temperature and reaction time for future modeling of THMs. Empirical models for predicting DBPs in drinking water supplies are found in the literature (Sadiq and Rodriguez, 2004; Hong et al., 2007; Chowdhury et al., 2009) in the general form:

$$Y = 10^{b0}.{X_1}^{b1}.{X_2}^{b2}.\ldots{X_n}^{bn} \qquad (4.1)$$

where *Y* is the concentration of DBP in drinking water supply on any given day, X_1, X_2,… X_n are predictor variables, and *b0, b1, b2….bn* are the regression coefficients. Empirical models of TTHMs were developed using a multiple regression procedure with SAS software version 9.3 (SAS Institute Inc, 2012). The TTHM level (μg/L) for any given day was used as the response variable and water quality parameters; pH (pH), water temperature (Temp, °C), and total organic carbon (TOC, mg/L) were used as predictor variables. In the absence of water age (reaction time) at the time of sampling, modeled estimates of the average water age (Time, hours) for each site was used. Water age estimates ranged from 26-95 hours for the 24 sites used in our study (NYCDEP, 2010). Chlorine dose and bromide levels may also contribute to TTHM formation but chlorine dose data were not available to test in our model. The only detected brominated DBP was bromodichloromethane with a 3 year average concentration of 4.0 μg/L and range of 1.6-6.1 μg/L. Since brominated DBPs are relatively low in the NYC system they were not considered in our model. Model predictions relative to the measured values were evaluated using coefficient of determination (R^2), root mean square error (RMSE) and mean absolute error (MAE). Model performance was validated independently using quarterly data for TTHMs and predictor variables (96 measured values) collected from April 2012 to March 2013 from the same 24 sites. To quantify the contribution of each independent variable to the model predictions, sensitivity analysis was performed using the 5th and 95th percentile data points (representing boundary conditions of water quality range for which the model is expected to be accurate) for each variable as inputs in the empirical model keeping other predictors as measured. For water temperature only values above 10°C were used as THMs are usually formed above this temperature (Van Dreason, 2012).

Results and Discussion

Empirical model and relative importance of predictor variables

The empirical model (Equation 4.2) made reasonable estimates of TTHM levels in the NYC water supply distribution system. The model evaluation statistics showed good agreement between measured and predicted values with an overall R^2 of 0.75 (Figure 4.5) during both calibration and validation periods. The average RMSE and MAE values were 7.89 and 6.16 respectively for the calibration period and 6.72 and 5.5 respectively for the validation period. Although the overall model performance was acceptable we noticed that the model consistently over predicted the measured values by 13% during the validation period (Figure 4.5b).

$$TTHMs = 0.0072\, pH^{2.60}\, Temp^{0.396}\, Time^{0.475}\, TOC^{1.397} \qquad (4.2)$$

About 25-50% increase in THMs formation is estimated per 10°C increase in water temperature (Chowdhury and Champagne, 2008) and in general TTHMs in the NYC water supply system peak during the warmest summer months. However, higher water demands in the summer, resulting in shorter reaction time within the distribution system may offset the effect of temperature to a certain extent. Sites receiving sodium hypochlorite have higher pH which tends to favor TTHM formation. Because water from all upstate reservoirs typically flows through Kensico Reservoir and is well mixed before entering the distribution system, TOC concentrations are generally uniform throughout the distribution system at any given time.

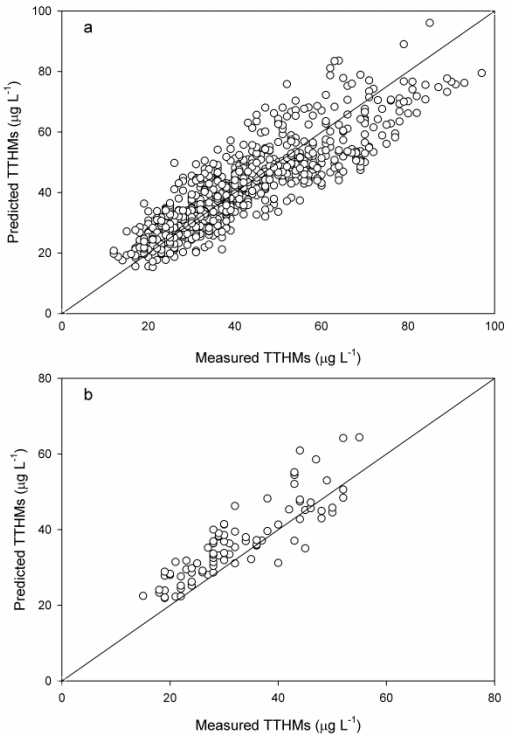

Figure 4.5. Predicted versus measured TTHM concentrations (a) Calibration (b) Validation

Table 4.1. Predicted range in TTHM levels (μg/L) based on sensitivity analysis. Values in parenthesis are predictor values used.

Predictor	5th percentile	Average	95th percentile
pH	38 (7.12)	41 (7.31)	45 (7.57)
Temp*	41 (11.1)	49 (16.7)	54 (21.7)
TOC	33 (1.38)	41 (1.62)	53 (1.94)
Water age	31 (26)	42 (49)	50 (70)

*For water temperature only values above 10°C were used in the analysis

Relative importance of predictor variables (natural and management related) estimated using sensitivity analysis were in the following order: TOC, water age (reaction time)>water temperature>pH. Model predictions based on the 5th and 95th percentile values of TOC indicated that TTHM levels changed by 20 μg/L (Table 4.1). Similar predictions for average water age (reaction time), water temperature and pH resulted in TTHM changes of 19 μg/L, 13 μg/L, and 7 μg/L respectively. Although TTHM changes associated with TOC and water age were similar, it is possible that the importance of water age would increase if it were known at the time of sample collection rather than as an estimated average. Nonetheless, our finding on the relative importance of predictor variables is generally consistent with observations made by Wert et al. (2012) in a water supply distribution system in Las Vegas, Nevada.

TTHM levels in the aftermath of Hurricane Irene and Tropical Storm Lee

During 2011, Hurricane Irene (August 26-29) and Tropical Storm Lee (September 5-8) resulted in total rainfall ranging from 38cm to 50cm in the NYC water supply watersheds located in the Catskill Mountain region. In one major stream, Esopus Creek, about 43% of the average annual DOC flux was transported by Hurricane Irene alone in a span of 5 days (Yoon and Raymond, 2012). The TTHM levels in the water supply distribution system increased post Irene and Lee with 45% (17/38) of the samples recording values higher than the maximum contaminant level (MCL) of 80 μg/L in October and November 2011. However, since compliance during this period was based on a system-wide running quarterly average, the water supply was able to maintain compliance throughout 2011. We found that samples which exceeded the MCL in October and November of 2011 were mostly from 10 monitoring sites, eight of which were in Manhattan, one each in Queens and Staten Island. In Table 4.2 we compare the difference in TTHM levels and associated water quality parameters between 2011 and the previous two years during the same months (October and November) for the 10 sites where MCLs were exceeded in 2011 in the aftermath of the tropical storms.

Following these extreme events usage of WOH reservoirs was greatly reduced due to elevated levels of fecal coliform, turbidity and TOC (Klug et al., 2012). To compensate for the loss of WOH water, usage of less storm impacted EOH reservoirs, West Branch and Boyd Corners, was correspondingly increased. Because the TOC concentration of West Branch and Boyd Corners is typically higher than the WOH reservoirs (more wetlands and algal contributions) the TOC increase observed in distribution was not only due to the storm related TOC loading to WOH reservoirs but also to the necessary reliance on relatively high TOC water from West Branch and Boyd Corners. Compared to October and November of 2009 and 2010, there was a 0.51 mg/L

increase in median TOC during October and November of 2011 at the 10 sites discussed above. The TOC increase translates to about a 24 μg/L increase in TTHMs based on our empirical model. Increases of 0.14 pH units (38% increase in H+ ion concentration) and in water temperature (1.4 °C) were also observed in October and November 2011. Our model predicts that TTHM would increase about 4.0 μg/L for the pH change and about 3.0 μg/L for the increase in water temperature. The sum of these effects, 31 μg/L, is very close to the observed TTHM increase of 35 μg/L post tropical storms Irene and Lee. Inclusion of chlorine dose (not available for this analysis) may have resulted in even better agreement. Even without chlorine dose such close agreement provides a level of confidence in our model results. Water age (i.e. reaction time) was similar during post- and pre-storm periods (S. Freud, *Personal Communication*), and therefore, was not considered a factor responsible for increased TTHM formation.

Discussion

The empirical model explains the relative importance of predictor water quality variables. Management scenarios can be simulated for each site or region using the empirical model (e.g., effect of choosing low TOC source water on TTHM levels). Natural organic matter levels as measured by TOC vary between and within the NYC water supply reservoirs (SWRC, 2008). The importance of TOC as a predictor variable highlights the need to improve our understanding of the sources, fate, and transport of TOC in the NYC Water Supply system. In some circumstances TTHM levels may potentially be reduced by altering reservoir operations (i.e., withdrawal patterns) as discussed in Weiss et al. (2013). Advanced warning capabilities could be enhanced by using automated water quality sensors, such as those recommended by the USEPA (e.g., Panguluri et al., 2009) to provide the inputs to our model. Advanced warning of TTHM levels may allow utilities to make adjustments in the treatment process to avoid violations and to reduce costs.

Further improvement in model predictions may be obtained by using site specific and real time estimates of water age using methods described in Wert et al. (2012). The empirical model presented in this study clearly demonstrates its utility in a water supply system for understanding formative factors of TTHM and their relative importance. This has implications for developing management scenarios and real-time estimation of TTHMs in water supply systems under changing land use, climatic conditions and water demand.

Table 4.2. Comparison of median TTHM levels and water quality parameters between 2011 and 2009-2010 periods. These values are for October and November from 10 sites where TTHM levels exceeded the regulatory limit in 2011

Year	TTHM (μg/L)	TOC (mg/L)	pH	TEMP (°C)
2011	85	2.03	7.48	18.3
2009-2010	50	1.52	7.34	16.9
Difference	+35 (+70%)	+0.51(+33%)	+0.14 (+38%)	+1.4 (+8%)

4.3 Hydro-Ecological Modeling Project

One of the great challenges in assessing the potential consequences of global climate change is to understand and quantify fine scale vegetation response, such as the response of an individual forest stand on an individual hillslope. This is true because even after the complicated process of downscaling global climate change model (GCM) predictions to local scale has been accomplished, the equally daunting task of interpreting potential interactions between topography, vegetation and climate still remains. Complex ecological problems such as this are often advantageously approached through modeling, where numerous scenarios and permutations can be assessed across varying spatial and temporal scales. To this end, implementation of a hydro-ecological forest model (RHESSys) has been undertaken by NYC DEP Modeling Group using Biscuit Brook (in the headwaters of the Neversink Basin, Catskill Mountains, New York, USA) as a test basin.

RHESSys (Tague and Band 2004; RHESSys homepage: http://fiesta.bren.ucsb.edu/~rhessys/) is a spatially distributed hydro-ecological model that simulates integrated water, carbon and nutrient dynamics over spatial scales ranging from a small catchment (a few square hectares, e.g., the combined area of a few football fields) to regional scale extents (i.e., multiple square kilometers). RHESSys models landscapes by using a DEM (digital elevation model) to delineate progressively nested basins (catchments), hillslopes (land areas draining into either side of, or the headwater of a stream segment), zones (micro-climatic zones), patches (portions of hillslopes having relatively uniform slope, aspect and soil characteristics) and strata (the vegetation types and vertical layers modeled within each Patch). RHESSys does not model individual plants, but rather the carbon content of various sinks that represent physiological vegetation compartments, where carbon content serves as a proxy for biomass accumulation (e.g., leaf carbon, stem carbon, coarse root carbon, fine root carbon etc.). Likewise, RHESSys does not model individual tree canopies but rather uses a dual "Big-leaf" paradigm in which one leaf represents the shaded rate of photosynthesis and the other represents the unshaded rate of photosynthesis, and the result is mathematically scaled-up to forest canopy scale based on leaf area index (LAI), mean canopy height, sun angle, and day of the year.

Carbon assimilation rates are controlled based on the Jarvis model (Jarvis and Davies 1998) of stomatal conductance, in which stomatal conductance stress multipliers are used (e.g., soil water status, ambient air temperature, vapor pressure deficit, PAR radiation absorption, etc.) to decrease the maximum rate of stomatal conductance, which in turn limits CO_2 uptake and reduces gross photosynthesis (GPSN). Carbon assimilation is also limited by plant available mineralized soil nitrogen (i.e., the nitrogen available after microbial uptake requirements have been met) and/or by the amount of nitrogen available from retranslocation within the Stratum. The effects of growth limitation by other micro-nutrients (e.g., phosphorus, calcium) and by soil pH are not modeled at present. Vegetation is modeled as individual species (e.g., Sugar Maple, Red Maple, White Pine, etc.) or as vegetation biomes (e.g., deciduous broad-leaf, evergreen needle-leaf, grassland, etc.). Soils are modeled based on data from the NCSS (National Cooperative Soil Survey, http://websoilsurvey.sc.egov.usda.gov/App/HomePage.htm) categorical descriptions of soil types and the accompanying data concerning texture, porosity, saturated hydraulic conductivity and other related soil characteristics.

RHESSys is particularly well-suited to the water management needs of NYC DEP for several reasons. First, because of the flexibility of RHESSys to model both small catchments (e.g., Biscuit Brook) and large basins (e.g., Neversink). Second, because the model can be customized for a particular site using NYC DEP data such as high resolution LiDAR data (i.e., laser-based remote sensing data, which permits highly detailed landscape delineations, Figure 4.6) and forest inventory data, which permits the model to be parameterized with spatial patterns of vegetation that are consistent with actual vegetation patterns on the landscape. Third, because fine-scale outputs from RHESSys (e.g., DOC, DON, litter loading, stream discharge, etc.) can be used as inputs to inform larger scale models such as those used to assess and manage NYC watersheds and reservoirs. And finally, because the model is process-based, spatially distributed, and utilizes a three-dimensional landscape representation, the complex west of Hudson terrain can be incorporated into modeling results (for example, RHESSys considers topographic shadowing, slope, and aspect as these factors interact to affect radiation loading, which in turn generates differential rates of snow melt across the landscape).

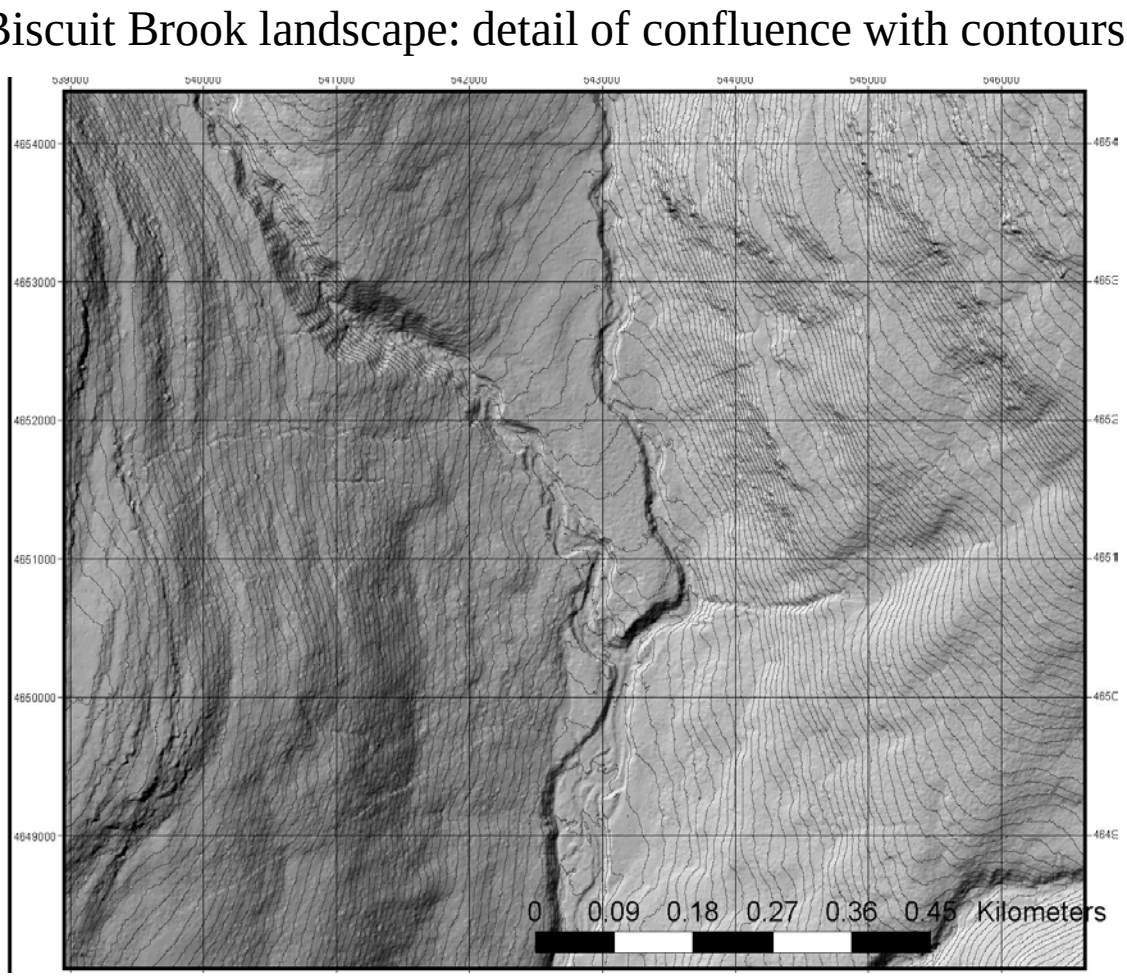

Figure 4.6. Detail of Biscuit Brook topography

At present, RHESSys version 5.18r2 (January 2014) has been implemented for Biscuit Brook. Model calibration (utilizing USGS stream discharge data from Frost Valley) is presently underway. Two different hydrological modes of RHESSys will be tested: Topmodel (Beven and Kirkby 1979), which is a statistically based quasi-distributed approach utilizing a GIS-derived wetness index to re-distribute hillslope moisture as a function of landscape steepness and specific catchment area (i.e., the total area draining through a particular landscape pixel); and explicit routing which is based on DHSVM (Distributed Hydrology Soil and Vegetation Model, Wigmosta et al 1994) which calculates the actual surface and sub-surface movement of water between individual RHESSys landscape Patches. Topmodel has the advantage of being less computationally expensive. However, under certain circumstances, the underlying assumptions of the approach can limit its applicability. General speaking, these limitations would rarely be applicable to NYC DEP watersheds, and therefore both Topmodel and DHSVM modes of RHESSys will be used.

The calibration process involves adjusting parameter values for soil moisture infiltration rate, decrease/increase in infiltration rate with soil depth, rate of movement of water from soil water to ground water and rate of movement of water from ground water to stream base flow. Figure 4.7 provides an example of preliminary Biscuit Brook calibration results against USGS stream discharge data (Frost Valley) from the period January 1999 through June 1999 using the Topmodel approach. Figure 4.8 illustrates the period July 1999 through December 1999. The modeled vegetation cover was equally divided in the simulation across four common West of Hudson tree species (red maple, sugar maple, American beech and red oak). Generally speaking, in the first half of the year underestimations of peak streamflow occurred more often, typically at points in the year suggesting that snow-melt and/or snowpack depth was being underestimated (e.g., late January 1999). In the second half of the year, peak flow events were generally overestimated (e.g., September 19th). This overestimation could result from any number of factors, including incorrect infiltration rates, incorrect soil types and/or spatial distributions and incorrect vegetation types and/or spatial distributions. Through feedback from DEP staff who have expert knowledge of conditions in the field, it might be possible to determine which potential causes of peak flow overestimation are most likely.

As an additional part of the calibration process, the sensitivity of the model is also assessed, in particular, its sensitivity to modeled vegetation type. In Figure 4.9, a comparison of modeled stream discharge for red maple, sugar maple, beech and red oak mono-crop simulations is illustrated. Modeled red oak and beech simulations have higher peak flow than do modeled red maple and sugar maple simulations. This is due to modeled differences in LAI across species, Figure 4.10 (note: these results are from a different simulation year from Figures 4.7 and 4.8) and modeled differences in interception capacity (both, canopy and litter). Also, differential sensitivity to environmental stress across species is an important factor that influences evapo-transpiration rates, resulting in differences in water budgets across species (Figure 4.11).

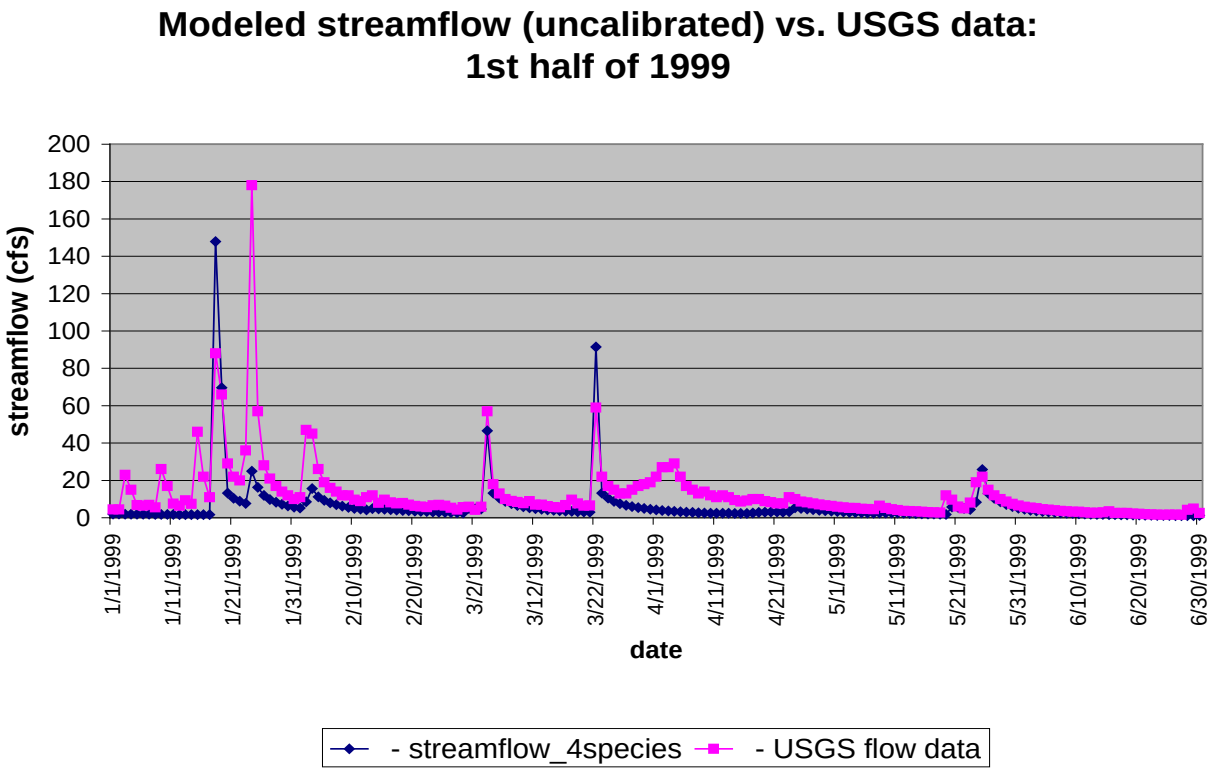

Figure 4.7. Modeled streamflow results against USGS stream discharge for Biscuit Brook from the period January 1999 through June 1999

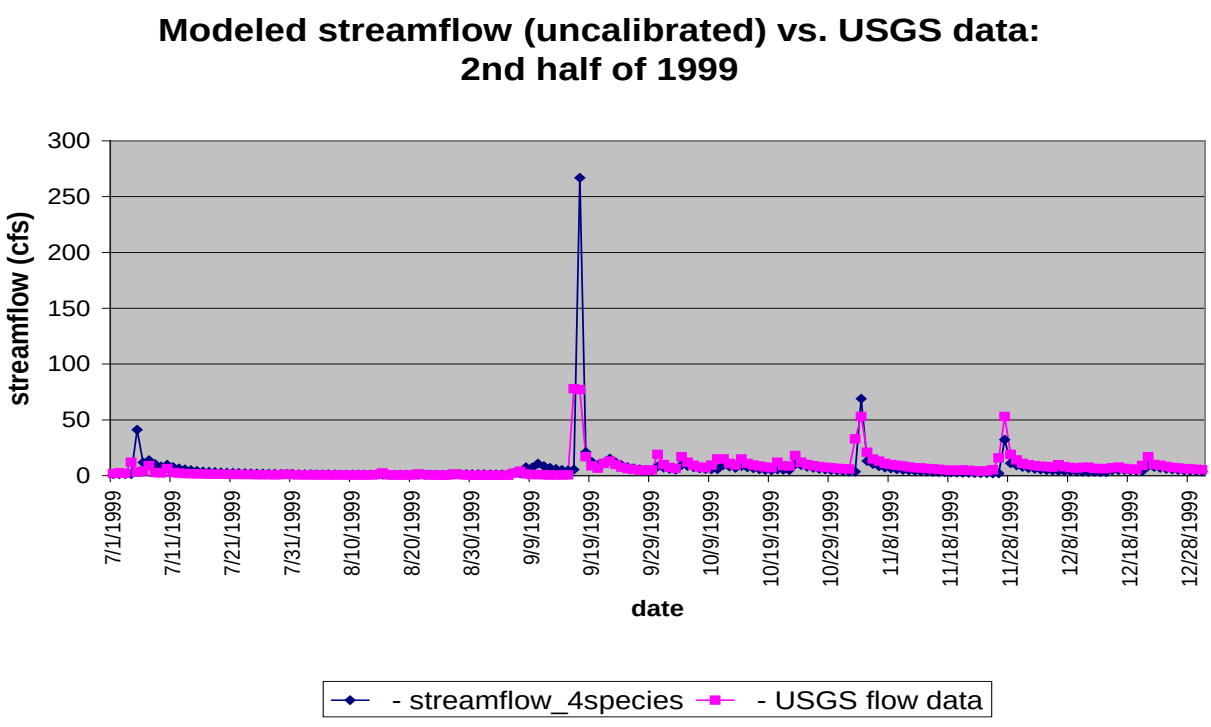

Figure 4.8. Modeled streamflow results against USGS stream discharge for Biscuit Brook from the period July 1999 through December 1999

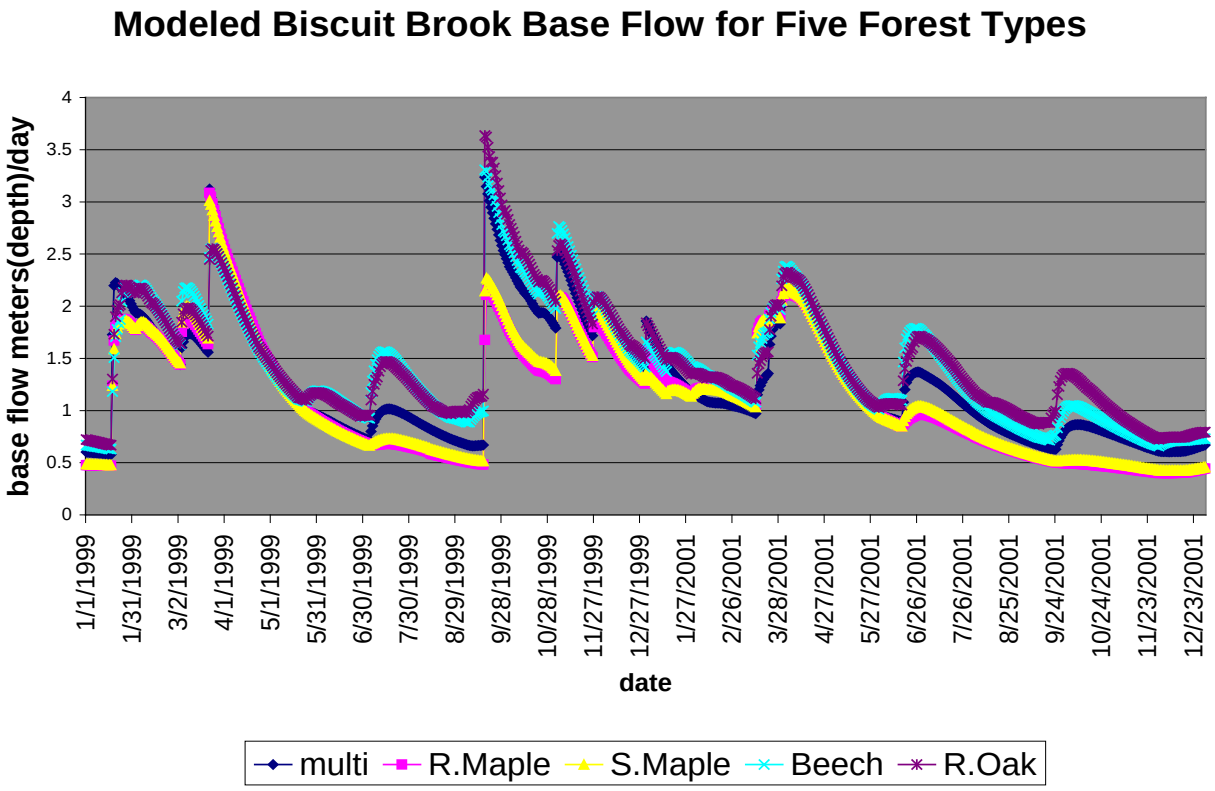

Figure 4.9. Modeled baseflow for different forest types.

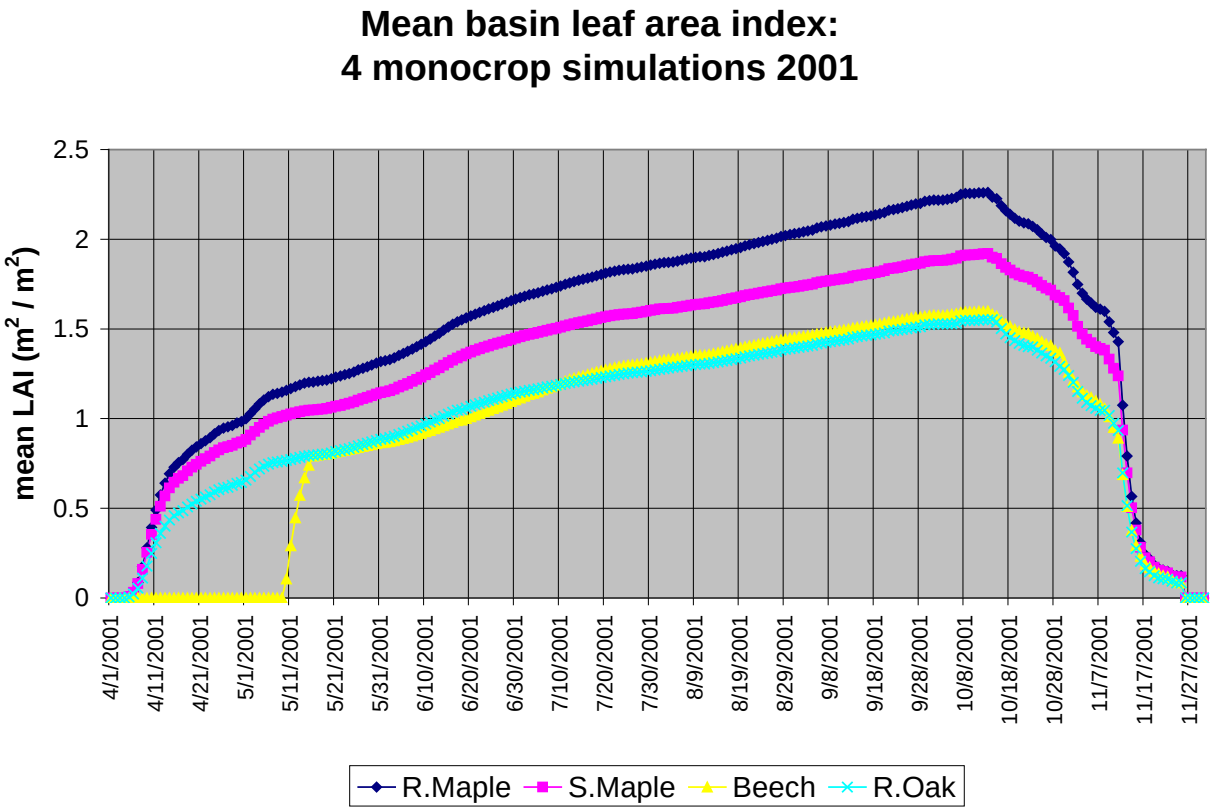

Figure 4.10. Mean basin leaf area index for different monocrop types.

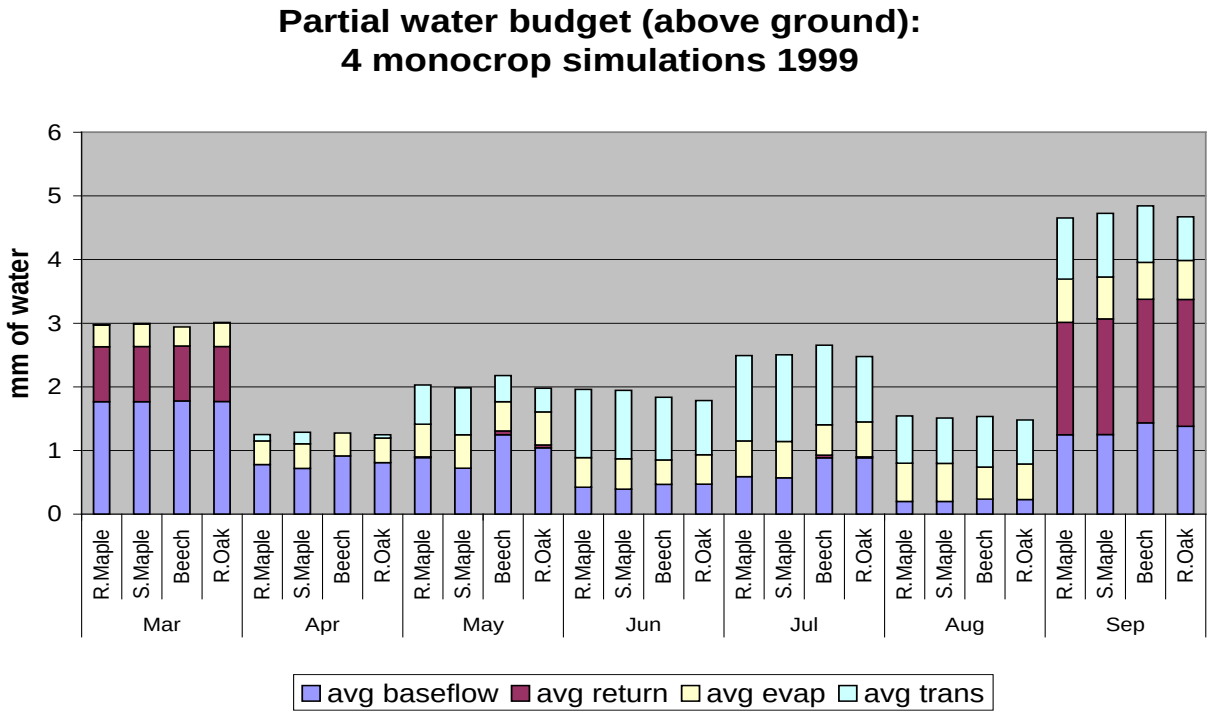

Figure 4.11. Modeled water balance for different monocrop types.

4.4 SWAT Watershed Model Development

A version of the USDA SWAT model for use in NYC watershed studies is under development. The following describes the rationale and methods of SWAT model development. Model development continues along with model testing which will be reported on in future reporting.

Introduction

In temperate climate hilly landscapes a perched aquifer forming above a relatively impervious soil layer plays a major role in hillslope hydrology, transmitting subsurface flow laterally through the hillslope, controlling soil saturation as the perched water table approaches the surface, providing water for plant use, and influencing biogeochemical transformations related to saturated conditions in soils. Two different approaches have been used for simulating a perched aquifer and hillslope hydrology in watershed models (Wigmosta et al 1994). In the explicit modeling approach (as in DHSVM, Wigmosta et al 1994, and CSMR, Frankenberger et al 1999) the catchment is discretized into a contiguous grid, water is explicitly routed from cell to cell based on topography, and a water balance is performed at each time step to determine stored water and the height of the perched water table for each cell location. In the statistical-dynamical (SD) approach (as in TOPMODEL, Sivapalan et al 1997; VIC , Wood et al 1992; PDM, Moore 2007; and the XINANJIANG model, Zhao and Liu 1995) the mean height of the perched water table is modeled as a time-varying dynamic process while the shape of the water table (i.e. the spatial distribution of depth to water table) within the hillslope is modeled by a statistical relationship. The explicit approach can account for fine temporal and spatial scale variability but is computationally expensive with high input data requirements and has typically been used for small watersheds and highly detailed applications, although advances in computing power makes applications to larger catchments possible. The SD approach is more computationally efficient and less demanding in data requirements.

Representation of hillslope hydrology in the official USDA SWAT model has evolved. In early versions of SWAT an isolated perched aquifer could be simulated for a specific HRU by specifying an impervious layer at depth *dep_imp*, but there was no lateral connectivity between HRUs to transmit water through the hillslope. Du et al (2005) in the modified SWAT version SWAT-M utilized the impervious layer set at the bottom of the soil profile to generate a perched aquifer which supplies tile flow when the perched water table is located above the tile drain; this tile drainage algorithm was incorporated into a later official version of SWAT. Moriasi et al (2009, 2011b) and Vazquez-Amabile and Engel (2005) also set the impervious layer at the bottom of the soil profile and calculated shallow water table depth by tracking daily change in soil profile water storage and translating unoccupied drainable volume into water table depth based on soil physical properties as in DRAINMOD. In the 2012 version of SWAT lateral connectivity and explicit landscape unit routing was added along with two catchment discretization schemes: grid cells or hillslope catena. SWAT2012 routing with grid cells is a fully-distributed explicit approach with similar computational and data requirement limitations to other explicit models. The catena discretization routes water downslope through hillslope elements defined by landscape position (ridge, slope, valley) rather than cell to cell which improves computational efficiency; but defining meaningful catena-based landscape units for large heterogeneous catchments may be problematic.

Parallel to the development of explicit routing in SWAT have been efforts to apply an SD approach. Easton et al (2008) used a topographic index to define HRUs by probability of saturation and curve numbers related to saturation excess runoff in an alternative SWAT application methodology (SWAT-VSA) designed for simulating variable source areas. White et al (2011) in SWAT-WB used a statistical distribution of soil water storage capacity and applied a water balance in place of the curve number method to calculate runoff as water in excess of local soil water capacity. Both SWAT-VSA and SWAT-WB were found to capture the spatial distribution of saturation excess runoff, but in both models the underlying mechanism of a perched water table that rises to the surface creating saturated conditions and saturation-excess runoff is not incorporated in the model.

Application of the SD approach in hillslope hydrology models is varied. In TOPMODEL a topographic index (TI) that represents the relative probability of soil saturation based on topography is calculated for each cell in a catchment. The statistical distribution of storage capacity (Figure 4.12a) is a function of the TI that defines a constant offset from the average water table depth for each cell, and this distribution is assumed to express an equilibrium water table shape. Thus, in TOPMODEL the water table as a whole moves up and down as the average depth of water in the perched aquifer changes, while the shape of the water table remains constant over time (Figure 4.13). VIC, XINANJIANG and PDM models use a pareto distribution (Figure 4.12b) of moisture storage capacity to derive the saturated fraction of the catchment without simulating the specific spatial locations of saturated areas. SWAT-WB uses a statistical soil moisture distribution based on the USDA Curve Number equation interpreted as a saturation excess runoff process (Figure 4.12c, Steenhuis et al 1995). The soil moisture distribution is spatially referenced to specific catchment locations by associating the moisture distribution with the TI.

Here we present a generalized SD approach that incorporates a dynamic perched aquifer and its implications for runoff generation, plant growth, evapotranspiration, and soil biogeochemistry in SWAT. Any of the above-mentioned soil moisture capacity distribution functions can be used to define the shape of the perched water table, or an empirically-defined distribution based on water table depth measurements in a catchment can be specified. If the TOPMODEL moisture capacity distribution function is used the resulting SWAT model is essentially an implementation of TOPMODEL. The TI is used to define wetness classes of increasing probability of soil saturation, and the TI-based wetness classes are referenced to the moisture capacity distribution function as in SWAT-WB. A perched aquifer is explicitly added to the model. For any given precipitation or snowmelt event infiltration-excess surface runoff is first calculated by Green-amp method; then saturation-excess surface runoff by HRU is calculated as water inputs in excess of available soil moisture storage capacity. Soil percolation and lateral flow calculations are adjusted to accommodate the explicit perched aquifer as the source of lateral flow. Tile drainage and plant water use are calculated based on the location of the perched water table relative to the rootzone and tile drains. Nitrate calculations are adjusted to account for effects of the perched aquifer.

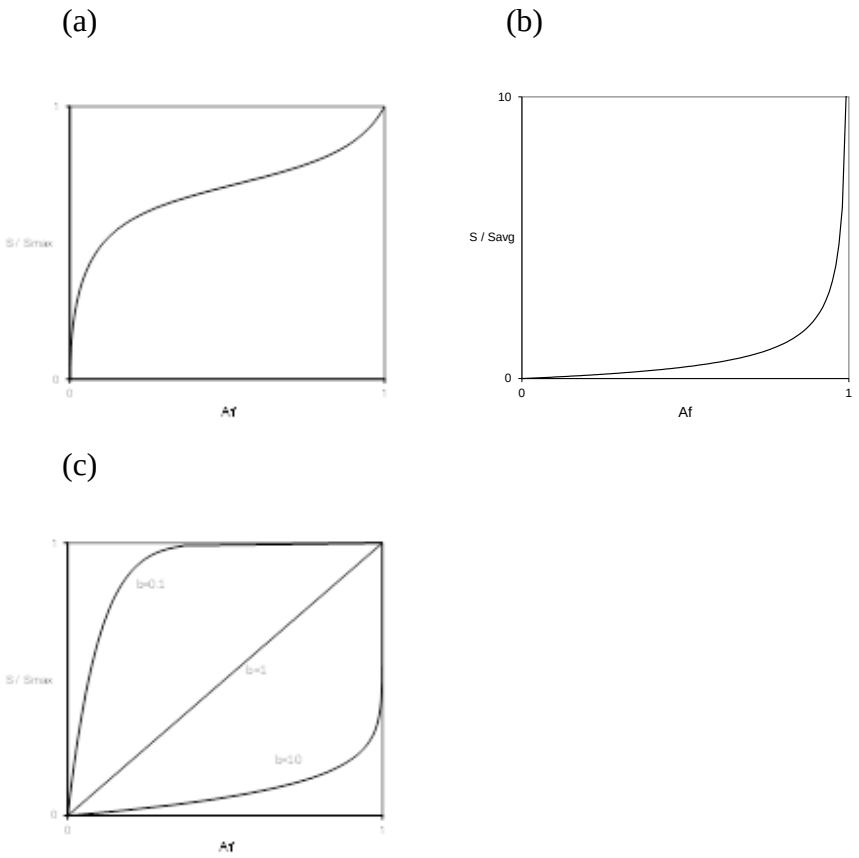

Figure. 4.12: Moisture Storage Capacity distribution functions commonly used in saturation-excess runoff models. Af (x-axis) is fraction of area of watershed with normalized storage capacity less than or equal to corresponding y-axis value. a) based on TOPMODEL topographic index. b) Pareto distributions with b=0.1, 1, and 10. c) based on USDA Curve number equation.

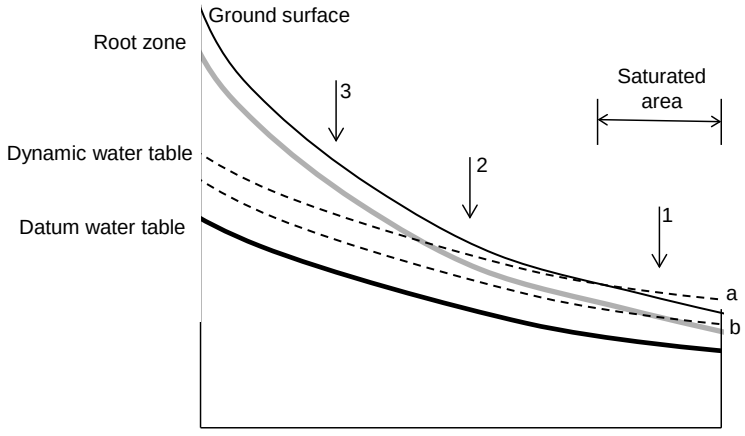

Figure 4.13. Idealized hillslope profile with datum water table that defines shape of dynamic equilibrium water table. Water table at depth (a) saturates location 1, intersects the root zone at location 2, and is below the root zone at location 3. As perched aquifer depletes, water table drops to depth (b).

Methods

HRUs defined by Wetness Class

SWAT is a spatially-distributed model which discretizes the watershed into HRUs (Hydrologic Response Units) spatially-defined by land use, soils, and slope. For the SDH model the watershed is further discretized into wetness classes ordered by soil water storage capacity. In our application we define these classes from a raster map of the scaled topographic index (Ti_scaled) from the TOPMODEL distribution of storage capacity (Sivapalan et al 1997)

$$Ti\_scaled = lmax - \ln(a/\tan b) \quad (4.3)$$

where a is contributing area of grid cell i, tanb is slope of i, lmax is maximum ln(a/tanb) in the watershed. Raster map grid cells are aggregated into 10 wetness classes representing successive slices of the cumulative distribution of scaled Ti values, following Easton et al (2008, SWAT-VSA) and White et al (2011, SWAT-WB). The wetness classes 01 to 10 are ordered by increasing soil water capacity. Each wetness class is defined in this ordering by the fraction of the watershed area (Af) with less water storage capacity (the lower Af boundary of the wetness class) and the fraction of the watershed with higher storage capacity (the upper Af boundary of the wetness class).

The wetness class map is combined with the soils map, essentially redefining the soils component of the traditional SWAT discretization to include a wetness class assignment for each HRU in the final discretization. The wetness class and soils maps can be combined in several ways: 1) Use the wetness maps to spatially-define soil type; derive the dominant soil type within each wetness map unit; rename the wetness map units ETIxx_DominantSoilType where xx is the wetness class 01 thru 10; for each renamed map unit add a record to SWAT usersoils database with map unit name and DominantSoilType soil properties; use ARCSWAT soil definition and HRU creation tool; 2) same as 1 but rather than using dominant soil type properties, derive weighted average soil properties within each wetness map unit; 3)Intersect the 2 maps to get all combinations of wetness class and soil type; rename each resultant combination ETIxx_SoilType where xx is wetness class 01-10; for each wetness class/soil type combination add a record to SWAT usersoils database with ETIxx_SoilType name and SoilType soil properties; use ARCSWAT soil definition and HRU creation tool. This option allows multiple soil types in same wetness class. With this option it may be useful to lump similar soil types prior to combining the 2 maps to minimize the number of resultant HRUs.

Maximum Soil Water Storage Capacities

Each wetness class is initially assigned an effective depth coefficient (*edc*) based on a statistical distribution of storage capacities across the catchment. An input flag (*pareto_flg*) determines whether the set of *edc* values are calculated in the model ((*pareto_flg* =1) or input in the BASINS.bsn parameter file. The model calculation of *edc* values is based on the pareto distribution:

$$Ci = Cmax*(1-(1-Af)^{(1/b)}) \quad (4.4)$$

where Cmax is the maximum storage capacity in the basin, Af is the fraction of the basin where storage capacity is less than Ci, and b is a shape parameter. For any wetness class, the maximum storage capacity (edc) is the areally integrated Ci between the upper Af boundary (x) and lower Af boundary(y) of the wetness class:

edc(pareto distribution) =
cmax *b/(b+1)*((1-y)^((b+1)/b) -(1-x)^((b+1)/b)/(y-x) +cmax (4.5)

Alternative soil water distributions may be developed and input as *edc* parameter values to the model. The TOPMODEL topographic index (Eqn. 4.3) associated with the defined wetness classes may serve as a soil water storage distribution, whereby the mean *Ti_scaled* value for each wetness class is input as an unadjusted *edc*.

An alternative storage capacity distribution function based on the SCS Runoff Curve Number equation (Steenhuis et al 1995, Schneiderman et al 2007) is:

Ci = Cavg (sqrt(1/(1-As))-1) (4.6)

where Cavg is the is the spatially-averaged storage capacity for the basin when runoff begins. For any wetness class, the storage capacity is the areally integrated Ci between the upper and lower Af bounds of the wetness class:

edc(Curve Number Distribution) =
2*Cavg*(sqrt(1-x)-sqrt(1-y)) / (y-x) –Cavg (4.7)

Also, If adequate soil moisture data under datum conditions exist they may be used to develop an empirical distribution of storage capacity.

edc values input as parameters or calculated by Pareto Distribution are adjusted in the model as follows. First a calibratable scaling factor *(edc_factor*) is applied.

edc = edc_factor edc* (4.8)

This factor is not applied (i.e. *edc_factor*=1) if *edc* are calculated in the model, since the Pareto distribution function includes parameters that control both shape and mean depth of the moisture distribution. Note that edc_factor corresponds to the scaling factor in the TOPMODEL moisture distribution function that accounts for the decrease in hydrologic conductivity with depth (Sivapalan et al 1997).

The *edc* distribution corresponds to a datum watershed state when discharge from the perched aquifer (i.e. return flow or lateral flow) is zero (Sivapalan et al 1997). The datum condition is further adjusted by adding mean datum perched aquifer depth (*perchst_datum*) to all *edc*

edc=edc + perchst_datum (4.9)

In the absence of perched aquifer data it is suggested that *perchst_datum* be set to the mean Root Zone Depth of the wettest wetness class, so the perched aquifer empties to the bottom of the root zone of the wettest class (Figure 4.13). *Perchst_datum* is adjustable because the average depth of the perched aquifer has important implications for the responsiveness of the aquifer to nitrate fluxes – a larger perched aquifer is slower to respond to nitrate fluxes.

Perched aquifer

A perched aquifer is added to the SWAT model. The perched aquifer is defined by HRU, and localized (vertical) fluxes – inputs from infiltration in excess of soil field capacity, losses from plant water use when the perched aquifer intersects the rootzone, and tile drainage – are calculated for each HRU at each time step.

perchst(j) = perchsti(j) + rchrg_pa(j) – qtile(j) –et_perch(j) – latq(j) (4.10)

where perchst(j) (mm H_2O) is the amount of water stored in the perched aquifer for the jth HRU, perchsti is the amount of water stored in the perched aquifer at the beginning of the time step (calc. in varinit.f) rchrg_pa (mm H_2O) is recharge to the perched aquifer (added to perchst in percmain.f), qtile (mm H_2O) is tile flow (taken from perchst in percmain.f), et_perch (mm H_2O) is plant water use taken from the perched aquifer (taken from perchst in swu.f), and latq (mm H_2O) is lateral flow (taken from perchst in gwmod.f)).
At the end of the time-step subbasin-average perched aquifer storage (*sub_perchst(sb)*) is calculated as the weighted average of perched aquifer content of individual HRUs (perchst(j).

sub_perchst = SUM over j HRUs (perchst(j) * hru_dafr(j)) (4.11)

where hru_dafr(j) is the fraction of the watershed area in the jth HRU.

At the beginning of the next time-step the previous subbasin-average perched aquifer storage is assigned to the perched aquifer storage of all HRUs, which effectively redistributes (implicitly routes) water in the perched aquifer from aquifer recharge zones characterized by high rchrg_pa, low et_perch, and low lat_q to aquifer discharge zones (low rchrg_pa, high et_perch, high lat_q).

perchsti(j) = sub_perchst (4.12)

Available Soil Water Storage Capacity and Lateral Flow

Available storage capacity is represented by a series of paired buckets (Figure 4.14a,b), following the variable bucket model (VBM) approach to TOPMODEL of Sivapalan et al 1997. Each pair of buckets constitutes the maximum soil water storage capacity apportioned between drainable and non-drainable storage for an HRU. This distinction of two functionally-distinct soil moisture storage components follows parallel model approaches to water transport in porous material (Brutsaert 2005, pp. 283). Non-drainable maximum storage capacity is the field capacity of the soil profile (*sol_sumfc(j)).* The available non-drainable storage capacity (*unsat_deficit(j))*

is the difference between the maximum storage capacity and the non-drainable soil water content of the soil profile (*sol_sw(j))* for the j^{th} HRU:

$$unsat\_deficit(j) = \max(0, sol\_sumfc(j) - sol\_sw(j)) \quad (4.13)$$

The available drainable storage capacity (*eff_sat_deficit(j))* for the j^{th} HRU is the adjusted drainable maximum capacity (*edc(j))* reduced by the subbasin-average water content of the perched aquifer (*sub_perchst(sb)*) that occupies the drainable storage:

$$eff\_sat\_deficit(j) = edc(j) - sub\_perchst(j) \quad (4.14)$$

This SD formulation of available storage capacity, like in TOPMODEL, effectuates implicit lateral redistribution of the perched aquifer among HRUs to maintain the pre-defined relative distribution of storage capacities while the water table as a whole moves up and down over time with average perched aquifer water content.

The total available storage capacity (*sol_availst)* is the sum of these two:

$$sol\_availst = unsat\_deficit + \max(0,eff\_sat\_deficit) \quad (4.15)$$

When the water table rises so high that the perched aquifer depth exceeds the capacity of the drainable bucket (Eqn. 4.15), the resultant negative saturation deficit (*eff_sat_deficit)* is translated into return flow or lateral flow (*latq*):

$$latq = lat\_ttime * \max(0,-eff\_sat\_deficit) \quad (4.16)$$

where *lat_ttime* as in original SWAT is the exponential of lateral flow travel time (days). *Latq* is subsequently removed from the perched aquifer (Eqn. 4.10), but the negative deficit and lateral flow may persist as the implicit redistribution of perched aquifer water (Eqn. 4.12) continues until the perched aquifer drains sufficiently to re-establish a positive deficit. During this period the soil is saturated so both saturation excess runoff and return flow may co-occur in the HRU.

Infiltration Excess Runoff

For any given precipitation or snowmelt event infiltration is first calculated by Green-Ampt method. Several modifications were made to the Green-Ampt algorithm in SWAT to accommodate the co-occurrence of the two runoff-generating mechanisms (infiltration vs. saturation excess). The SWAT Green-Ampt algorithm includes adjusts the hydraulic conductivity of the top soil layer as a function of the USDA Curve Number. The Curve Number hydraulic conductivity adjustment was calibrated so that the Green-Ampt model would give compatible results to the Curve Number runoff equation. This adjustment was eliminated in the SDH model. Curve number runoff is total surface runoff including both infiltration and saturation excess runoff in unknown proportions, so the Green-Ampt algorithm adjusted by Curve number would simulate total runoff. The intention of the SDH model is to use Green-Ampt strictly for infiltration-excess runoff only, as saturation-excess runoff is explicitly

simulated separately. The curve number adjustment was replaced with an empirical hydraulic conductivity adjustment factor (*hcfactor*) and a frozen soil factor (*fsfactor*)

$$adj\_hc = \max(0., sol\_k * hcfactor) \quad (4.17)$$

$$If(sol\_tmp(2,j) < 0.)\ adj\_hc = adj\_hc * fsfactor \quad (4.18)$$

where adj_hc is adjusted hydraulic conductivity, sol_k is unadjusted hydraulic conductivity, and sol_tmp(2,j) is soil temperature of soil layer 2.

The static depressional storage term in SWAT (SSTMAXD) was activated in the Green-Ampt equations so that infiltration-excess water put in depressional storage is held and can infiltrate in subsequent time steps. In addition, the Green-Ampt algorithm was modified to include the case where ponding occurs during a time step as in WEP and other implementations of Green-Ampt.

Saturation Excess Runoff

Surface runoff in the SD model is simulated, as in SWAT-WB (ref), by a local water balance in place of the standard curve number approach in SWAT. Saturation-excess runoff is generated when the net daily water input to the ground surface from rain and snowmelt minus canopy interception (*precipday(j)*), minus infiltration-excess runoff (surfq_inf), exceeds the available soil moisture storage capacity (*sol_availst(j))* of the soil for the j^{th} HRU*:*

$$Surfq\_sat(j) = \max(0, precipday(j) - surfq\_inf(j) - sol\_availst(j)) \quad (4.19)$$

Infiltration (*inflpcp(j))* is the remainder that doesn't run off:

$$Inflpcp(j) = precipday(j) - surfq\_sat(j) \quad (4.20)$$

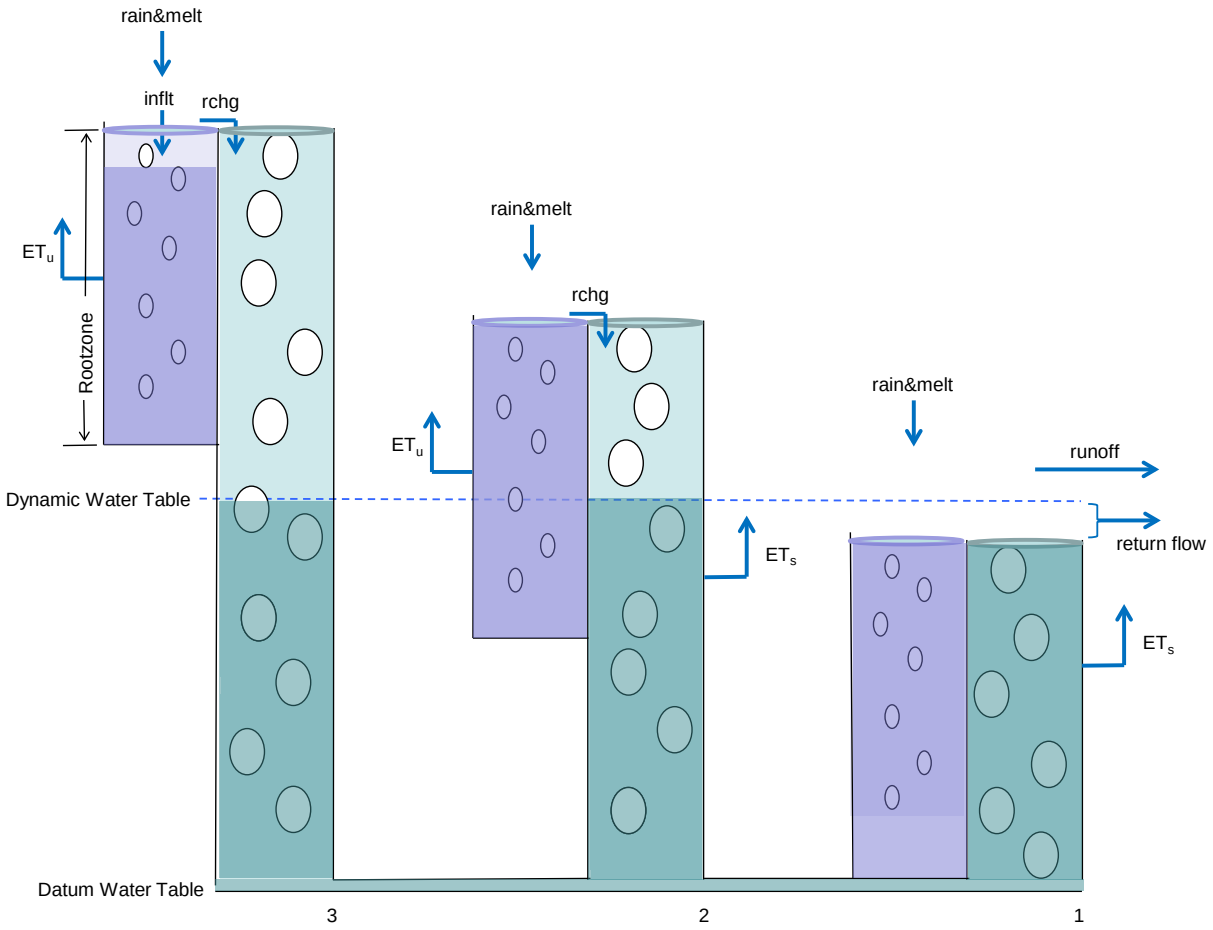

Figure 4.14a. Variable parallel bucket model depicting hydrologic storages and fluxes at 3 locations. At each location infiltrating water is first applied to the non-drainable (small pores) bucket. Infiltration in excess of soil profile field capacity recharges the perched aquifer represented by the drainable(large pores) bucket. When both parallel buckets are filled the location is saturated, excess rain and snowmelt becomes saturation excess runoff, and return flow (lateral flow) from the perched aquifer occurs. ET occurs from the non-drainable bucket but may also occur from the drainable bucket when the water table is high enough to intersect the rootzone. The drainable buckets are laterally-connected, increasing together by the aggregate recharge from all locations and decrease by aggregate losses to return flow. Three locations depicted correspond to figure 4.12 with water table at depth a: high water table, wetter soils at field capacity, location 1 saturated.

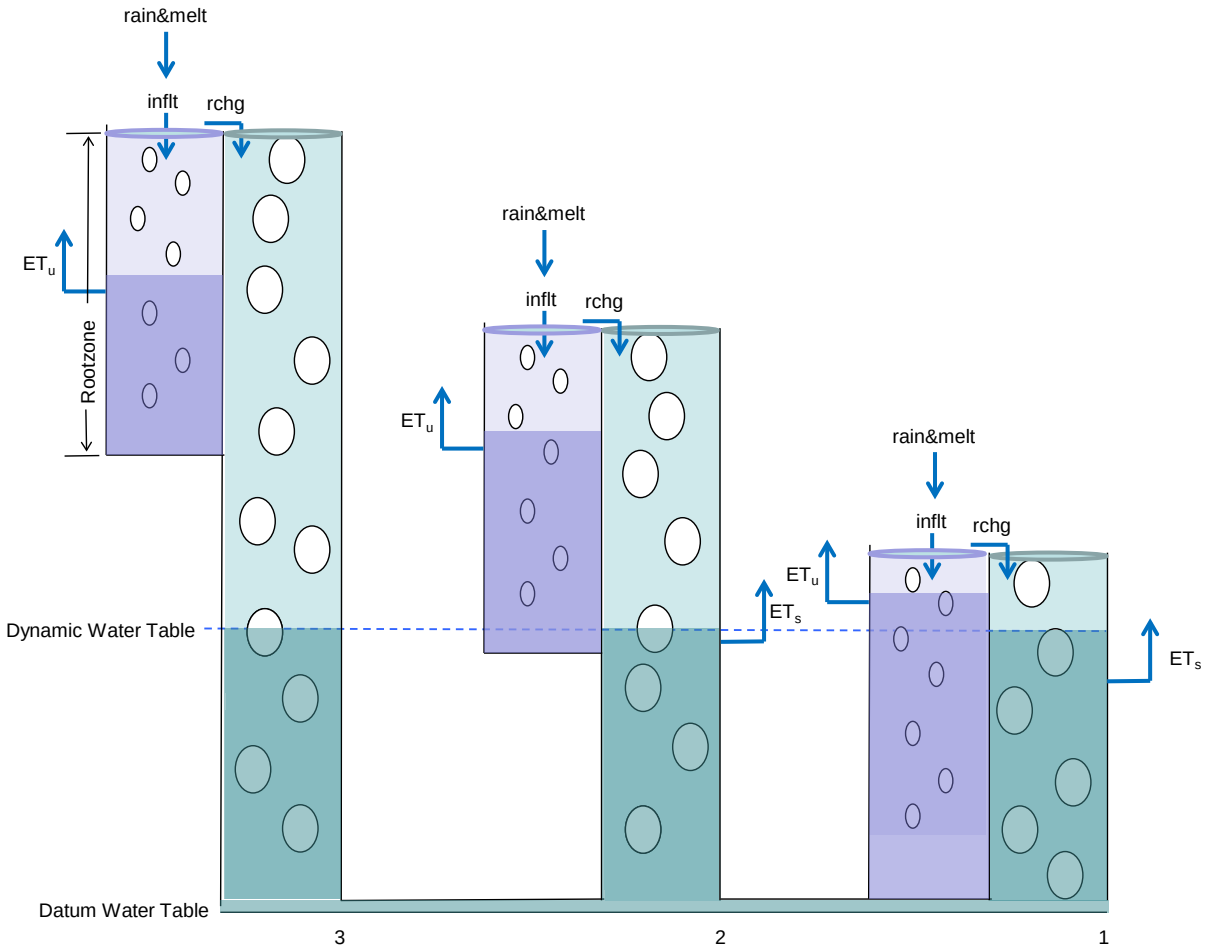

Figure 4.14b. Three locations depicted correspond to figure 4.13 with water table at depth b: summer, lower water table, soils below field capacity, water table near surface at location 1 and near bottom of rootzone at location 2.

Soil Percolation

The soil percolation and lateral flow routines in SWAT are modified for the SD model. For each soil layer in SWAT starting with the top layer, water input from above is added to the water already stored in the soil layer, and excess water above field capacity percolates to the next layer at a rate limited either by hydraulic conductivity of the layer or by an impervious layer imposed within or below the soil profile at a prescribed depth. These restrictions on percolation rate permit soil layers to build up soil water in excess of field capacity, and lateral flow is generated from this excess water. We eliminate the percolation rate restrictions that allow soil water build-up above field capacity and the related lateral flow extractions. The resultant percolation algorithm simulates only changes in non-drainable soil water storage, and the key variable in SWAT for the amount of water stored in a soil layer (sol_st(lyr)) has field capacity as its maximum and is effectively redefined as the amount of non-drainable stored water (except for nitrate and other nutrient algorithms as described later). Build up of soil water in excess of field

capacity is accounted for by the perched aquifer, which also acts as the source of lateral flow. This is not to say that local percolation rates do not influence perched water table development, but rather that the effect of an impeding layer on perched water table development for an HRU is accounted for in the assignment of soil water storage capacity (edc) rather than in the percolation routine.

In the revised percolation scheme all water in excess of field capacity moves successively downward so that percolation from the bottom soil layer (sepbtm) represents the total amount of soil water in the profile that exceeds field capacity. sepbtm is then primarily transferred to the perched aquifer (rchrg_pa), but a fraction (1-rchrg_paf) of the excess drainable soil water is allowed to leak thru the implied confining layer that creates the perched aquifer and recharge the groundwater aquifer (rchrg to shallst) that supplies long-term baseflow. rchrg_paf is a basin-wide parameter input in basins.bsn file.

$$rechg\_pa = sepbtm * rchrg\_paf \quad (4.21)$$

$$rechg = (1. - gw\_delaye) * (sepbtm * (1 - rchrg\_paf)) + gw\_delaye * rchrg(t-1) \quad (4.22)$$

Note that recharge to the groundwater aquifer (rchrg) has a vadose zone delay as in original SWAT, while transfer of excess drainable water to the perched aquifer is immediate.

Depth to Water Table

Vertical depth to the perched water table in relation to the rootzone and to tile drain depth is used to determine the availability of perched aquifer water for plant use and tile drainage. Depth to water table (*wt_depth)* is calculated by converting the saturation deficit to a depth of soil from the surface, by dividing by the effective porosity (*effpor*) of the soil:

$$wt\_depth = eff\_sat\_deficit / effpor \quad (4.23)$$

$$effpor = (sol\_ul - sol\_fc) * effporfactor \quad (4.24)$$

where *sol_ul* is the amount of water held in the soil at saturation, *sol_fc* is the amount of water held in the soil at field capacity, and *effporfactor* is the fraction of effective porosity that can hold water under saturated conditions. Since effpor varies for different soil layers, the water table depth calculation is repeated iteratively from the top soil layer down until the entire effective saturation deficit is translated to a depth of soil from the surface to the water table.

Tile Drainage

Tile drainage is calculated, as in original SWAT, by estimating the amount of drainable water above the tile drain (sw_excess_drain), based on wt_depth in relation to tile drain depth (ddrain). Drainable water above the tile drain is calculated starting with the top soil layer and working downward by adding up sw_excess_drain from all layers above ddrain and within or below wt_depth:

sw_excess_drain = sw_excess_drain +
max(0.,min(solzbot(lyr),ddrain)-max(solztop(lyr),wt_depth)) / effpor (4.25)

where solzbot is the depth from surface to bottom of soil layer and solztop is depth to top of soil layer. Tile drainage (qtile) is then calculated by transferring sw_excess_drain to the tile drain based on the time-to-drain-soil-to-field-capacity (tdrain) parameter, as in original SWAT:

qtile = sw_excess_drain * (1. - Exp(-24. / tdrain)) (4.26)

Plant Water Use

SWAT estimates plant water use by distributing potential plant evaporation through the root zone and calculating actual plant water use based on soil water availability. This scheme is preserved, except drainable water in the perched aquifer is made available to plants when the perched water table intersects the rootzone. Plant water use is calculated by layer. If the layer is above the perched water table, plants use only non-drainable soil water, and the SWAT equations (including uptake adjustment when stored non-drainable water in layer is low) hold unaltered. If the layer is completely below the perched water table and saturated, potential plant evaporation is extracted from the perched aquifer. If the perched water table is within a soil layer, the layer is temporarily split at wt_depth: potential plant evaporation in the unsaturated sub-layer above wt_depth is treated as a layer above the water table, and the saturated sub-layer below wt_depth is treated as a layer below the water table. The SWAT variable revapday, defined originally as the amount of water moving from the shallow aquifer into the soil profile or being taken up by plant roots in the shallow aquifer, is redefined as the amount of water taken up by plant roots in the perched aquifer and set equal to the calculated drainable plant water use.

Nitrate

Two important interrelated effects of a perched water table for nitrate (NO3) and other nutrients are a) the local effect of saturated conditions on soil biogeochemistry, and b) the spatial averaging effect of the laterally mixed perched aquifer. We approach the interplay of these two processes by alternately mixing the perched aquifer with non-drainable soil water NO_3 at the local HRU scale, and then separating the aquifer from the soil water NO_3 to perform spatially averaging of the perched aquifer NO_3 at the sub-basin scale.

Perched aquifer NO_3 content is tracked by HRU (perchstn) and by soil layer (perchstn_lyr). Local fluxes (including biogeochemical transformations, leaching, transfers between non-drainable and drainable soil water, and losses to lateral flow and tile flow) are calculated for each HRU. At the end of the time step the sub-basin average perched aquifer NO_3 content (*sub_perchstn)* is calculated by summing up HRUs, and the sub-basin average perched aquifer concentration (sub_perchstn_conc) is calculated for use in the next time step:

sub_perchstn = SUM over j HRUs perchstn(j) * hru_dafr(j) (4.27)

sub_perchstn_conc = sub_perchstn / sub_perchst (4.28)

At the start of each time step, the NO_3 content associated with the drainage water content of each soil layer (perchstn_lyr) is derive by applying the sub-basin average perched aquifer NO_3 concentration to the drainable water content of the soil layer.

perchstn_lyr(lyr) = sub_perchstn_conc * sol_satst(lyr) (4.29)

where sol_satst is the drainable water content of the soil layer, calculated from the fraction of effective porosity for the soil layer that is filled with water (sol_satf) based on the location of the perched water table.

sol_satst(lyr) = sol_satf(lyr) * effpor(lyr) (4.30)

sol_satf(lyr) =
max(0.,min(1.,(solzbot(lyr) - wtdepth(lyr)) / (solzbot(lyr - solztop(lyr))) (4.31)

SWAT performs biogeochemical soil transformations in a series of algorithms starting with the grow subroutine (called in Plantmod.f) through the nlch subroutine in which NO_3 leaching occurs. These algorithms account for the effects of saturated conditions (soil water content exceeding field capacity) within a soil layer. The parallel bucket approach maintains drainable and non-drainable soil water as two distinct storages. To make proper use of the soil N transformation algorithms in SWAT the parallel storages of both water and NO_3 are combined (in Plantmod.f) for the series of subroutines between grow and nlch.

sol_st(lyr) = sol_st(lyr) + sol_satst(lyr) (4.32)

sol_no3(lyr) = sol_no3(lyr) + perchstn_lyr(lyr) (4.33)

where sol_no3 is the NO_3 content of the soil layer.

After the biogeochemical soil transformations are performed, NO_3 leaching occurs (in nlch.f) unmodified for soil layers above the perched water table. If the perched water table is above or within the soil layer, further leaching stops. Leached NO_3 from the layer above is added to the saturated or partially saturated layer. Soil water is then partitioned back into non-drainable (sol_st) and drainable (sol_satst) components by layer, and NO_3 is partitioned back into non-drainable (sol_no3) and drainable (perchstn_lyr) components by layer. This repartitioning effectuates the transfer of NO_3 between the local non-drainable soil water in the HRU and the perched aquifer.

sol_st(lyr) = sol_st(lyr) - sol_satst(lyr) (4.34)

sol_no3(lyr) =
sol_no3(lyr) * sol_st(lyr) / (sol_st(lyr) + sol_satst(lyr)) (4.35)

perchstn_lyr(lyr) =
sol_no3(lyr) * sol_satst(lyr) / (sol_st(lyr) + sol_satst(lyr)) (4.36)

The total NO_3 content of drainable water in the HRU is calculated as the sum of NO_3 in saturated or partially saturated layers (perchstn_lyr) within the soil profile and the NO_3 content of drainable water below the soil profile (perchstn_below), calculated by applying sub-basin average perched aquifer NO_3 concentration to the portion of the perched aquifer below the soil in the HRU.

perchstn(j) = sum over layers:perchstn_lyr + perchstn_below (4.37)

perchstn_below =
(perchsti(j) – sum over layers:sol_satst)* sub_perchstn_conc(sb) (4.38)

NO_3 leaches from the bottom layer of the soil (percn) by the unmodified SWAT leaching algorithm if the perched water table is below the soil profile. Leaching NO_3 recharges aquifer storages, partitioned between the perched (rchrg_pan) and shallow aquifers (rchrg_n) similarly to the partitioning of H_2O aquifer recharge (Eq. 4.21,4.22):

*rechg_pan = percn * rchrg_paf* (4.39)

rechg_n = ((1. – gw_delaye) * (*percn *(1 – rchrg_paf*))
+ gw_delaye *rchrg_n(t-1) (4.40)

perchstn = perchstn + rchrg_pan (4.41)

shallst_n = shallst_n + rchrg_n (4.42)

The shallow aquifer contribution of NO_3 to the stream (no3gw) is calculated by unmodified SWAT. The perched aquifer contributes NO_3 to the stream by tile flow (tileno3) and lateral flow (latno3), with both calculated similarly as no3gw is calculated for NO_3 in groundwater: NO_3 concentration in the perched aquifer (perchstn_conc) is applied to the respective flows, and the losses are subtracted from the perched aquifer storage:

perchstn_conc = perchstn / perchst (4.43)

latno3 = perchstn_conc * latq (4.44)

tileno3 = perchstn_conc * qtile (4.45)

perchstn = perchstn - latno3 – tileno3 (4.46)

Finally, the half-life of NO_3 (hlife_ngw) as applied to the shallow aquifer is also applied to the perched aquifer:

perchstn = perchstn * Exp (-.693 / hlife_ngw) (4.47)

Note Eqs. 4.27 – 4.47 are solved for each HRU. Subsequently at the end of the time step perched aquifer NO_3 is summed up over all HRUs (Eq. 4.27,4.28).

Model Input parameters

The Basins.bsn parameter input file is modified, with 13 additional basin-wide parameters added (Table 4.3). The USGS Curve Number parameter *CN2* which controls surface runoff generation in original SWAT is not used. The partitioning of water inputs to the ground into surface runoff, lateral flow, and baseflow are primarily controlled by a) Green-Ampt infiltration-excess runoff parameters *hcfactor*, *fsfactor*, and *sstmaxd* and b) 3 saturation-excess runoff parameters - *rchrg_paf* and either the soil water storage distribution shape parameters *pareto_b* and *pareto_cmax* (if *pareto_flg*=1) or *edc(weti*) and *edc_factor* (if *pareto_flg*=0). *rchrg_paf* partitions soil percolation to the perched and shallow aquifers. If *rchrg_paf* is 1 (default), all soil percolation in excess of field capacity is transferred to the perched aquifer, and lateral flow alone constitutes the baseflow of a traditional 2-way baseflow separation (runoff and baseflow). Use of *rchrg_paf* <1 allows a 3-way baseflow separation (runoff, lateral flow, baseflow). The shape of the soil water storage distribution along with the areal definition of wetness classes (*weti*) determines the areal extent of the saturated area and thus the amount of saturation-excess surface runoff vs. return flow from the perched aquifer. The saturation-excess runoff parameters may be calibrated against streamflow source partitioning data, soil moisture data, and/or results of baseflow separation techniques applied to streamflow data.

Partitioning of water inputs also controls the depth to water table and thus the amount of perched aquifer water available for plant use evapotranspiration. *effporfactor* adjusts the effective porosity (available drainable pore space) in the water table depth calculation (Eqs. 4.17,4.18). *effporfactor* can be used as a calibration parameter that controls the translation of available soil moisture storage capacity to water table depth. Wigmosta and Lettenmeier (1999) suggest that the assumption of an equilibrium water table in TOPMODEL and here may result in too shallow simulated water table depths particularly at the lower (wetter) parts of a hillslope where the perched aquifer may intersect the root zone. *effporfactor* may be adjusted to compensate for this and can be calibrated if soil moisture data is available. GW_REVAP and REVAPMIN, which control the amount of water taken up by plant roots in the shallow aquifer in original SWAT, are not used because plant water use is controlled by the perched aquifer in the new model.

Additional new parameters *perchst_datum* and *perchstn_init* (the depth of the perched aquifer when discharge from the perched aquifer is zero and the initial nitrate concentration in the perched aquifer respectively) control the volume and nitrate content of the perched aquifer and thus the responsiveness of the aquifer to nitrate fluxes. *ppt_factor* adjusts for bias in measured precipitation inputs. Iveno is a flag for producing alternative output format.

Tables 4.3, 4.4, and 4.5 summarize additional parameters and variables that were added to original SWAT2012 model and the subroutines where changes were made.

Table 4.3. Parameters added to SWAT

NAME	UNITS	DEFINITION	USED IN…
Parameters: HRU			
hcfactor(mhru)	none	Adjustment factor for hydraulic conductivity in Green Ampt equation	readbsn.f, readhru.f surq_greenampt.f
weti(mrhu)	none	Wetness index class (1-10) assigned to each HRU. Read from .sol, embedded in soil series name	readsol.f, hydro_init.f
Parameters: Basin			
edc(weti)	mm H20	Effective Depth Coefficient: Soil water deficit when perched aquifer is empty and soil is at field capacity. Defined at wetness class level. Input or calculated by pareto distribution.	readbsn.f, hydroinit.f
edc_factor	none	Calibration factor adjusts all edc values	readbsn.f, satdef.f, wtdepth.f
Fsfactor	none	Frozen Soil adjustment factor for hydraulic conductivity in Green Ampt	readbsn.f, surq_greenampt.f
pareto_b	none	b parameter in pareto distribution of edc	readbsn.f, hydroinit.f
pareto_cmax	m H20	Cmax parameter in pareto distribution of edc. Max storage capacity of basin	readbsn.f, hydroinit.f
pareto_flg	none	Flag; if flag=0, input edc(j); if flag=1, calculate edc(j) by pareto distribution	readbsn.f, hydroinit.f
perchst_datum	mm H20	Mean depth of perched aquifer for datum condition – i.e. when most wet weti(1) has zero saturation deficit	readbsn.f, hydroinit.f
perchstn_init	mg N/kg	Initial nitrate concentration of perched aquifer	readbsn.f, hydroinit.f
effporfactor	none	Fraction of effective porosity that can hold water under saturated conditions. Adjusts effective porosity.	readbsn.f, readsol.f, wtdepth.f, percmain.f
Iveno	none	Flag; if flag=1, use alternate format and output variables in output files (.bsn,.sub,hru,.rch); .std output also to output.bsn	readfile.f,header.f, headout.f, hruday.f, subday.f, rchday.f, bsnday.f, writed.f
ppt_factor	none	Multiplicative factor adjusts measured precipitation inputs	readbsn.f, pmeas.f
rechg_paf	none	Fraction of root zone percolation that recharges the perched aquifer	readbsn.f, percmain.f, gwmod.f, gw_no3.f
Sstmaxd	mm H20	Static depressional storage used in Green-Ampt algorithm	readbsn.f, surq_greenampt.f

Table 4.4: Variables added to SWAT

NAME	UNITS	DEFINITION	USED IN…
Variables: HRU			
Canmxl	mm H20	Maximum canopy storage at current day's leaf area (previously local variable changed to global variable)	canopyint.f
edc(mhru)	mm H20	edc(weti) parameter values assigned to each HRU.	readbsn.f, hydroinit.f, satdef.f, wtdepth.f,
Deprstor	mm H20	Depressional storage in Green-Ampt infiltration excess runoff calculations	surq_greenampt.f
eff_sat_deficit(mhru)	mm H20	amount of water that would have to be added to soil (when at field capacity) before a saturation excess runoff response begins	satdef.f, wtdepth.f,
et_perch(mhru)	mm H20	Plant water use taken from perched aquifer	swu.f, gwmod.f
maxwtdep(mhru)	mm	Maximum (datum) perched water table depth	readsol.f, wtdepth.f, swu.f
perchst(mhru)	mm H20	Depth of water in perched aquifer	Varinit.f, percmain.f, swu.f, gwmod.f, gw_no3.f, virtual.f
perchsti(mhru)	mm H20	Depth of water in perched aquifer at beginning of time step	varinit.f, satdef.f, nlch.f, gw_no3.f
perchstn(mhru)	kg N/ha	Amount of nitrate in perched aquifer	nlch.f, gw_no3.f, virtual.f
qday_inf(mhru)	mm H20 /day	Infiltration-excess surface runoff loading to main channel on day in hru	surfst_h2o.f
qday_sat(mhru)	mm H20 /day	Saturation-excess surface runoff loading to main channel on day in hru	surfst_h2o.f
qday_urb(mhru)	mm H20 /day	Urban surface runoff loading to main channel on day in hru	surfst_h2o.f
rchrg_pa(mhru)	mm H20	Amount of water recharging perched aquifer	percmain.f, gwmod.f
rchrg_pan(mhru)	kg N/ha	Amount of nitrate percolating from soil profile	gw_no3.f
sol_availst(mhru)	mm H20	Available soil moisture storage capacity.	satdef.f, surq_waterbalance.f,
surfq_inf(mhru)	mm H20 /day	Infiltration-excess surface runoff generated on day in hru	surface.f, surfst_h20.f, surq_greenampt.f, surq_waterbalance.f, virtual.f
surfq_sat(mhru)	mm H20 /day	Saturation-excess surface runoff generated on day in hru	surface.f, surfst_h20.f, surq_greenampt.f, surq_waterbalance.f, virtual.f
surfq_urb(mhru)	mm H20 /day	Urban surface runoff generated on day in hru	surface.f, surfst_h20.f, surq_greenampt.f, surq_waterbalance.f, virtual.f
unsat_deficit(mhru)	mm H20	amount of water that can be added to the available non-drainable pore space in the soil	satdef.f
wt_depth(mhru)	mm	depth to water table vertically downward from soil surface	wtdepth,f, percmain.f, swu.f

Table 4.4 (cont'd). Variables added to SWAT

NAME	UNITS	DEFINITION	USED IN…
Variables: HRU/Soil Layer			
sol_satf(mlyr,mhru)	none	fraction of drainable pore space in the soil layer that is saturated	wtdepth.f
sol_satst(mlyr,mhru)	mm H20	amount of drainable pore space in the soil layer that is saturated	plantmod.f, wtdepth.f, nlch.f
sol_st_i	mm H20	water in soil layer at start of timestep	varinit.f
wuse_drn	mm H20	Water uptake by plants taken from perched aquifer, by soil layer	swu.f
wuse_nondrn	mm H20	Water uptake by plants taken from non-drainable soil water, by soil layer	swu.f
Variables: Subbasin			
sub_perchst(msub)	mm H20	sub-basin average perched aquifer storage	virtual.f
sub_perchst2(msub)	mm H20	Sub_perchst(sb), used to reset perchst for all hru's to the subbasin average at start of next time step	varinit.f, virtual.f
sub_perchstn(msub)	kg N/ha	sub-basin average perched aquifer nitrate	virtual.f
sub_perchstn_conc(msub)	kgN/mm	sub-basin average perched aquifer nitrate concentration	virtual.f, plantmod.f, nlch.f
sub_qd_inf(msub)	mm H20 /day	Infiltration-excess surface runoff that reaches main channel	virtual.f
sub_qd_sat(msub)	mm H20 /day	Saturation-excess surface runoff that reaches main channel	virtual.f
sub_qd_urb(msub)	mm H20 /day	Urban surface runoff that reaches main channel	virtual.f
sub_surfq_inf(msub)	mm H20 /day	Infiltration-excess surface runoff generated on day in subbasin	virtual.f
sub_surfq_sat(msub)	mm H20 /day	Saturation-excess surface runoff generated on day in subbasin	virtual.f
sib_surfq_urb(msub)	mm H20 /day	Urban surface runoff generated on day in subbasin	virtual.f
sub_swe(msub)	mm H20	Snowpack snow water equivalent in subbasin	virtual.f
Variables: Basin			
Latqcntrbf	None	Contributing area fraction for lateral flow	Percmain.f
Surqcntrbf	None	Contributing area fraction for saturation-excess runoff	Surq_waterbalance.f

Table 4.5: Modified or New Subroutines in Sourcecode. Typecodes: A=algorithm, B=Bug fix, D=define variable, I = input, O = output, (N) = New subroutine. Output (O) subroutines are optional.

SUBROUTINE	DESCRIPTION	TYPECODE
allocate_parms	allocate new arrays	D
Bsnday	write daily standard output to output.bsn file if IVENO==1	O
Canopyint	canmxl changed from local to a global variable for output	O
Crackflow	Only calculate hrly crackflow for ievent(3)	A
Etact	fix bug in orig for esmax when canopyint is active	B
gw_no3	NO3 aquifer loading from recharge is partitioned to perched vs. shallow aquifers; calc. NO_3 in lateral flow and tile flow from perched aquifer is calculate; update perched aquifer nitrate storage; NO_3 losses from perched aquifer calc. like shallow aquifer nloss	A
Gwmod	fraction ((1-rchrg_paf) of sepbtm goes to shallow aquifer; Update perched aquifer; revapday redefined as et from perched aquifer (et_perch)	A
Header	revised header cols for output.hru and .sub for revised hruday and subday output vars	O
Headout	revised format output.hru and .sub; tab-delimited, add exceltime	O
Hruday	Alternative .hru file output if IVENO==1	O
Hydroinit	Calculate edc values by Pareto distribution for wetness classes; assign edc values to hrus	A
Modparm	declare new variables	D
Nlch	revise NO_3 leaching when perched aquifer within rootzone	A
ovr_sed	fix bug: only calc hrly overland flow for ievent=3	B
Percmain	revise percolation loop; calc rchrg_pa and add to perchst; Calc. latq from the perched aquifer; revise calc for tileq	A
Percmicro	lateral flow turned off here; sepday=sw_excess for all non-septic hrus	A
plantmod	Combine sol_st + sol_satst, sol_no3 + perchstn_lyr) in soil layers that are intersected by perched aquifer, so that nutrient routines between nup.f and nlch.f take perched aquifer into account	A
Pmeas	apply PPT_FACTOR	A
Rchday	Alternative .rch file output if IVENO==1	O

Table 4.5 (cont'd). Modified or New Subroutines in Sourcecode. Typecodes: A=algorithm, B=Bug fix, D=define variable, I = input, O = output, (N) = New subroutine. Output (O) subroutines are optional.

SUBROUTINE	DESCRIPTION	TYPECODE
Readbsn	input new vars: PPT_FACTOR,RCHRG_PAF,EDC_FACTOR, EFFPORFACTOR,PARETO_B,PARETO_CMAX,PARETO_FLG, FSFACTOR,ETI,PERCHST_DATUM, PERCHSTN_INIT. Input as basinwide varS: ALPHA_BF,DELAY, LAT_TTIME,CANMX,HCFACTOR	I
readfile	open output.bsn file; read iveno from file.cio	I
Readgw	ALPHA_BF,DELAY read in from basins.bsn; if basinwide var=0, readgw.f	I
readhru	LAT_TTIME,CANMX input from .bsn; if basinwide var=0, readhru.f. HCFACTOR input from .bsn; if hru var>0, readhrn.f	I
readmgt	ddrain_hru, tdrain_hru,gdrain_hru	I
routres	Only call reshr when ievent(3)	A
Satdef	(NEW) Calc. saturation deficit; call wtdepth	A(N)
sim_initday	initialize new vars	D
Snom	fix bug in orig code - allow snowmelt when tavband<sftmp	B
std2	Write hru info to hrutable.txt fro postprocessing	O
Subday	Alternative .sub file output if IVENO==1	O
substor	latq and latno3 not calc here now	A
sumv	Calculate additional watershed summation variables	O
Surface	call satdef.f before calling volq.f; combine saturation-excess and infiltration-excess runoff	A
surfst_h20	Calculate net surface runoff components: _inf,_sat,_urb	A
surq_greenampt	Calculate surfq_inf, surfq_urb; revise effective conductivity	A
surq_waterbalance	(NEW) calc. surfq_sat: runoff as precipday in excess of saturation deficit	A(N)
Swu	revise wuse calc; et from soil vs from perched aquifer	A
Varinit	initialize new vars; assign sub_perchst(t-1) to all perchst(t)	D
Virtual	Calc. sub_perchst(sb): sub-basin average perched aquifer storage; Calc. sub_perchst2(sb) = sub_perchst(sb), used to reset perchst for all hru's to the subbasin average at beginning of next time step; Do same for sub_perchstn: sub-basin average perched aquifer NO3	A
Volq	call surq_greenampt and surq_waterbalance	A
Writed	call bsnday if iveno==1	O
wtdepth	(NEW) calc. wtdepth, maxwtdep, and sol_satst	A(N)
zeroini	initialize new variables	D

4.5 CEQUAL-W2 Reservoir Turbidity Model Development Projects

During the reporting period, DEP contracted with Upstate Freshwater Institute to perform a number of studies, develop improvements, and expand the capabilities to the CEQUAL-W2 models that are used by the Operations Support Tool (OST). UFI has developed a water quality component for the CEQUAL-W2 model to simulate turbidity transport in the NYC reservoir system. Many of these projects were undertaken as part of Operations Support Tool (OST) development. These projects are briefly discussed in this section.

Development of Rondout W2 Turbidity Model

UFI was contracted to develop an application of the CEQUAL-W2 model for Rondout Reservoir to allow DEP to better simulate turbidity in the Delaware System. Under normal condition the Delaware System reservoirs are not impacted by turbidity issues. However when extremely large storm events occur in the Delaware watersheds, elevated turbidity may occur. This was the case for Rondout Reservoir during Tropical Storm Irene and more recently for Neversink Reservoir during an event in September 2012. As the Rondout Reservoir turbidity is especially important when Catskill water is turbid, a better understanding and predictive capability for the Rondout is a useful addition to DEP's modeling capabilities. DEP contracted with UFI to perform this work and the summary below is based on the final project report (UFI, 2013a; Gelda et al, 2013)

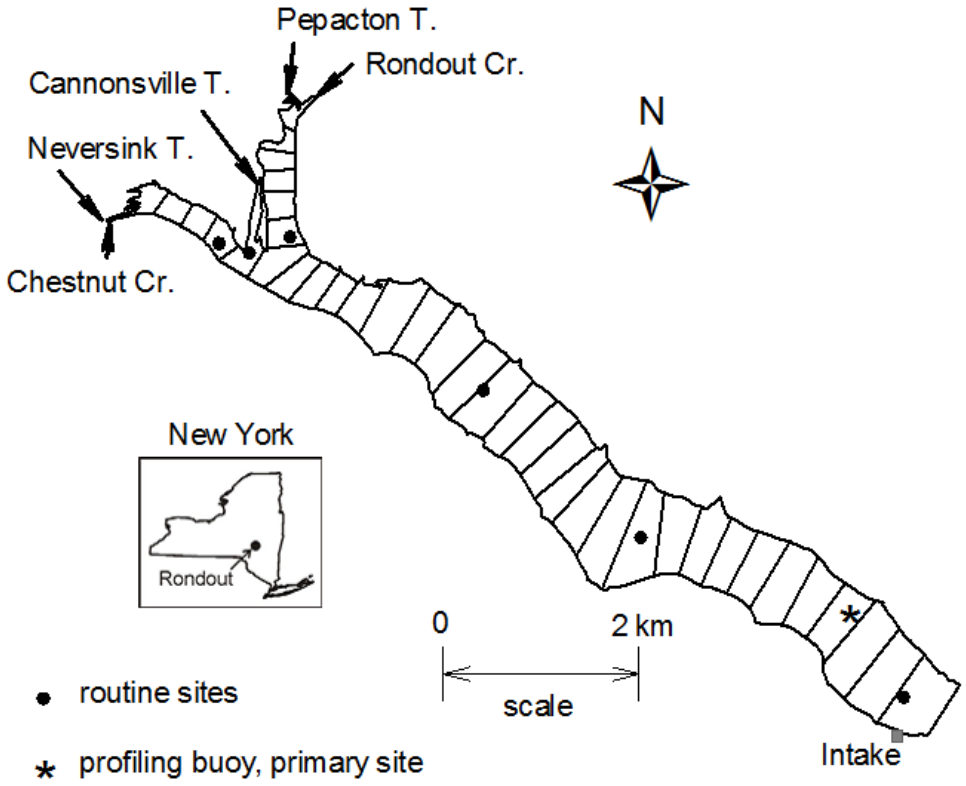

Figure 4.15. Map showing setup of Rondout Reservoir CEQUAL-W2 model showing reservoir segmentation and major inflow and outlet locations

The Rondout Reservoir CEQUAL-W2 model segmentation is illustrated in Figure 4.15. Inputs to the model include stream inputs of flow, water temperature and turbidity from the two major stream inputs, Rondout Creek and Chestnut Creek, and the three influent aqueducts from Neversink, Pepacton (East Delaware Tunnel) and Cannonsville (West Delaware Tunnel). In addition the model requires input meteorologic data including air temperature, dew point temperature, wind speed, wind direction and solar radiation.

Meteorologic data were obtained from the DEP meteorologic stations available on or near Merriman Dam. In addition, as part of model testing, data collected on an automated sampling buoy in the reservoir were used. For longer term periods, relationships between these measurements taken near the lake surface were compared to both DEP meteorologic stations located near or on Merriman Dam and to the regional weather service site at Binghamton airport. Correction factors were developed based on these comparisons so either the DEP meteorologic station or the Binghamton station data could be corrected to best match the conditions at the reservoir.

For application within the OST, methods for developing long term historical inputs and shorter term inputs based on streamflow forecasts were necessary. For stream temperature, monthly empirical regression relationships based on air temperature and flow were developed. For input stream turbidity, an empirical relationship between Rondout Creek flow and turbidity was developed using automated monitoring data available from 17 storm events from 2010-2012. (Figure 4.16a)) A similar turbidity-flow relationship was used for the Chestnut Creek input with parameters calibrated based on DEP's long term fixed frequency monitoring conduct at that site (Figure 4.16(b)).

(a) (b)

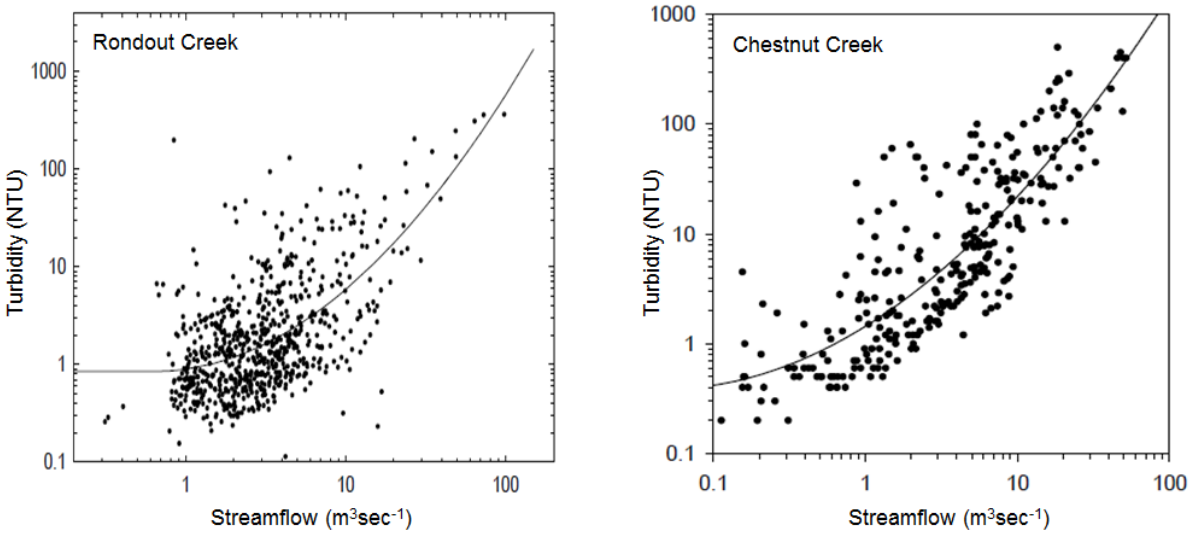

Figure 4.16. Regression relationships for turbidity versus flow for (a) Rondout Creek and (b) Chestnut Creek inputs to Rondout Reservoir CEQUAL-W2 model (UFI 2013a).

In addition to stream inputs, temperature and turbidity inputs from the Cannonsville, Pepacton and Neversink aqueduct inputs to the reservoir were estimated for the period prior to 1987 when measurements of aqueduct temperature and turbidity were readily available. To better understand the variability of these values, monthly distributions of the temperature and turbidity from each aqueduct input were developed. Based on these distributions, the median value is used at the default aqueduct input was recommended for periods prior to 1987.

Particle-size distribution (PSD) along with the particle composition information, as obtained from SAX/IPA analysis, was used to compute light scattering coefficient as a function of particle size. Turbidity causing particles are broken into three classes based on the relationship of light scattering to particle size. Results of the particle size analyses conducted on the water samples from the intake locations in Cannonsville, Neversink, and Pepacton reservoirs, and at the Rondout Creek input are shown in Table 4.6. The three fractions in Rondout Creek were 20%, 65%, and 15% for the size class I, II, and III, respectively. These fractions are very similar to those obtained for Esopus Creek for flow less than 40 $m^3 s^{-1}$.

For the Rondout Reservoir, particle coagulation can play an important role. This process was added to the turbidity model, allowing a fraction of the smallest two particle size classes to be transferred to the largest size class. This conversion is controlled by a calibrated rate constant for each size class. In addition the rate constant is reduced as turbidity decreases, which is consistent with the effects of reduced collision frequencies for lower particle concentrations.

To account for the configuration of the Rondout Reservoir outlet, the model code was modified to separately calculate the turbidity from each level of the outlet and from the spillway. The results of these outputs are then combined so that the aqueduct turbidity and the turbidity released downstream (release plus spill) are calculated so these values can be consistently compared with sampled data.

Table 4.6. Contributions (%) to the total turbidity from the three size classes of particles for various sources of water. (UFI, 2013a)

Size Class (Size)	Cannonsville (West Delaware Tunnel)	Neversink (Neversink Tunnel)	Pepacton (East Delaware Tunnel)	Rondout Creek
Class I (1 μm)	15%	65%	45%	20%
Class II (3 μm)	50%	35%	45%	65%
Class III (10 μm)	35%	0%	10%	15%

Fall 2012 Event Application

A large storm event on September 18-19, 2012 caused a plume of higher than normal turbidity in Rondout Reservoir. The turbidity in the reservoir did not significantly impact the withdrawal water quality. However, spatial variations in reservoir turbidity were great enough to provide an opportunity to test the CEQUAL-W2 turbidity model using short term hindcasting simulations. . Two hindcasting model runs were performed:

Simulation Aug 7 (prior to event) through Oct 11, 2012
Simulation Sept. 25 (after event) through Oct 11, 2012

These two simulations allow for (1) testing of the prediction of reservoir turbidity due to the storm event and (2) testing the model's performance for the timing of the post-event turbidity reduction within the reservoir.

The model drivers included Rondout Creek flow, Chestnut Creek flow, Cannonsville, Neversink, and Pepacton Tunnels inflows, aqueduct withdrawal, reservoir and release and spill, water surface elevation, intake level (i.e., withdrawal elevation); and temperature and turbidity data from keypoints water quality monitoring sites, stream survey sites, field survey sites, and limnological survey sites. Meteorological data were obtained from the DEP's onsite meteorological station.

For the longer Aug. 7 – Oct 11 simulation period, the model showed excellent results for the outlet temperature (Figure 4.17). Similarly good results were also obtained when looking at reservoir temperature profile data (not shown here). For outlet turbidity, however, the model overestimated the intensity of the turbidity plume (Figure 4.17). This over-estimation was mainly due to uncertainty in the turbidity input to the reservoir, especially for the Chestnut Creek inflow and, to a lesser extent, the Rondout Creek input.

The shorter simulation period (Sep. 25 – Oct 11), the model was initialized with gridded survey data (YSI turbidity probe) collected by UFI shortly after the storm event impacted the reservoir. The gridded survey included measuring turbidity profiles at 15 longitudinal locations of the reservoir. The gridded survey allowed for a good measure of both the longitudinal and vertical variability of turbidity throughout the reservoir. When the model simulations of withdrawal turbidity are compared with observations with the model successfully simulated the small rise in turbidity experienced at the Rondout withdrawal in addition to effectively predicting the observed trend and the general magnitude of withdrawal temperature and turbidity for the duration of the simulation (Figure 4.18).

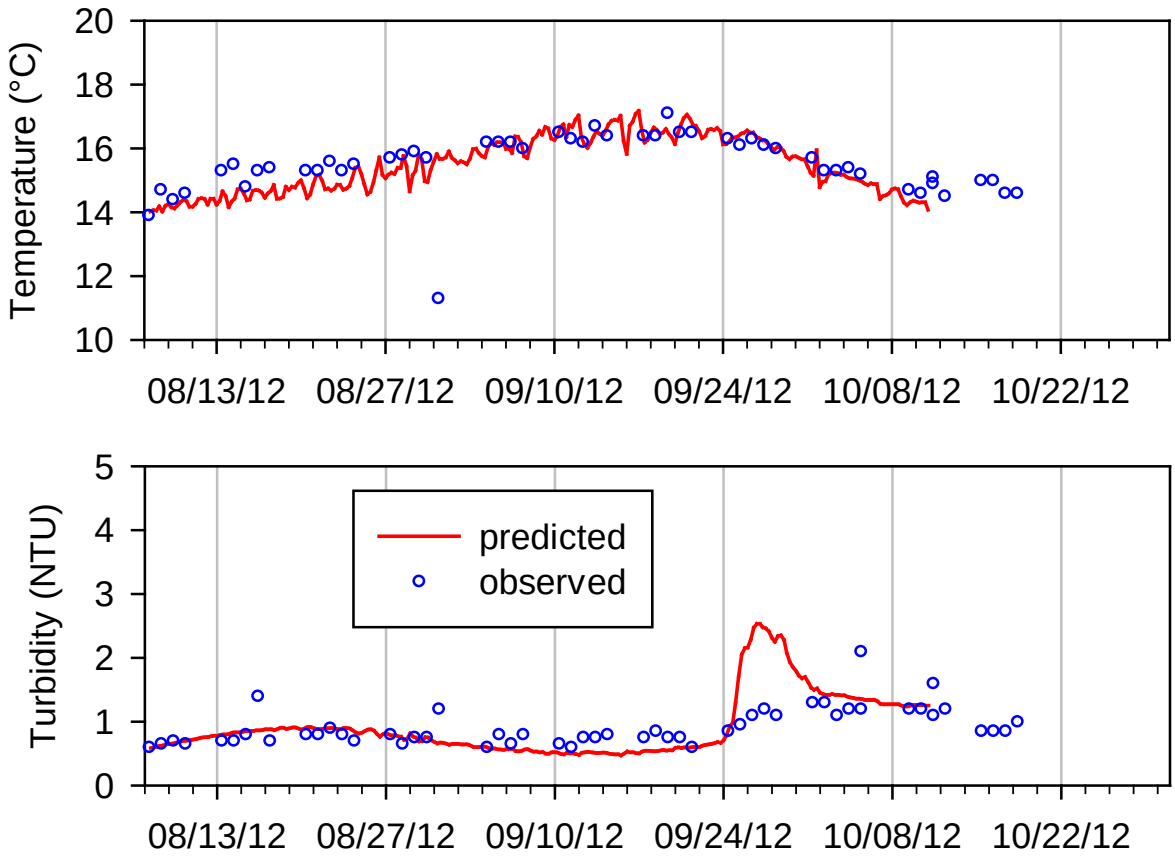

Figure 4.17. Results of withdrawal temperature and turbidity for the hindcasting CEQUAL-W2 Rondout Reservoir model for Aug 7- Oct. 11, 2012. Blue dots show observed values; red lines show model prediction. (Gelda et al, 2013)

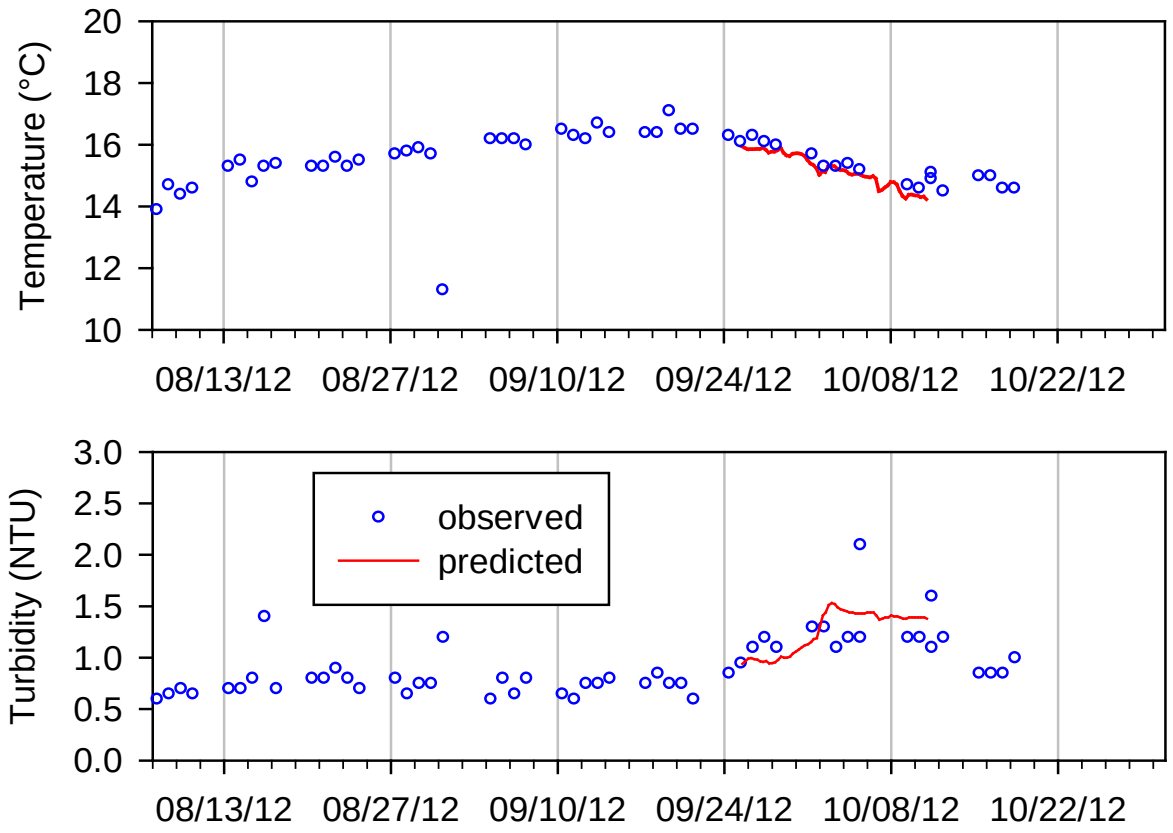

Figure 4.18. Results of withdrawal temperature and turbidity for the hindcasting CEQUAL-W2 Rondout Reservoir model for Sept. 25- Oct. 11, 2012. Blue dots show observed values; red lines show model prediction. (Gelda et al, 2013)

Upgrade W2 Models to Version 3.7

During the reporting period, the latest upgraded version 3.7 of the CEQUAL-W2 model for the Catskill System reservoirs was implemented within the OST. The implementation has dramatically reduced the run time for these models and should shorten the time it takes for modeling analyses that support operational decisions based on water quality. DEP contracted with UFI to perform this work and the summary below is based on the final project reports (UFI, 2013b; Hazen and Sawyer, 2012)

One of the major changes between the original and upgraded models is that the segmentation for Ashokan East and Kensico models was changed (Figures 4.19 and 4.20). The new model setups have a reduced number of segments, thus allowing for less calculations and faster runtime. Tests show that, the new segmentation does not greatly affect the results of the model output for turbidity (Figures 4.21 and 4.22).

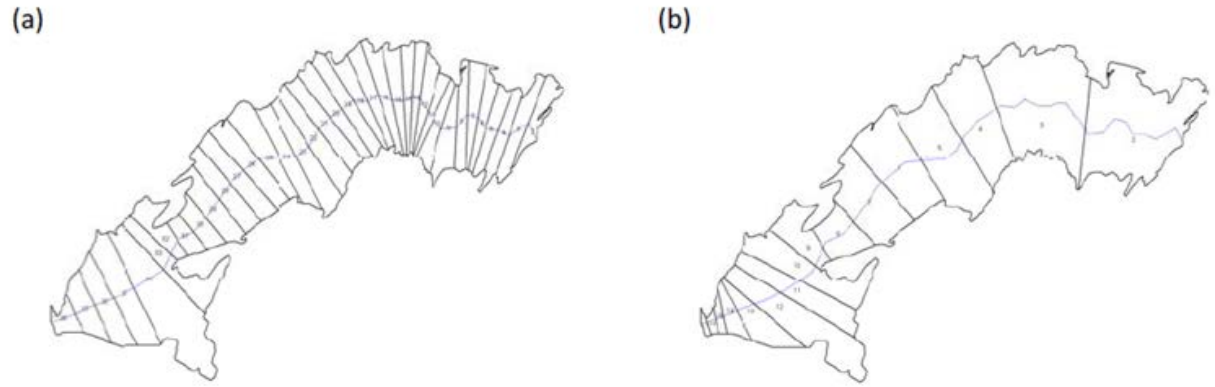

Figure 4.19. (a) Original Ashokan East Basin model grid and (b) modified Ashokan East Basin model grid. (Hazen and Sawyer, 2012)

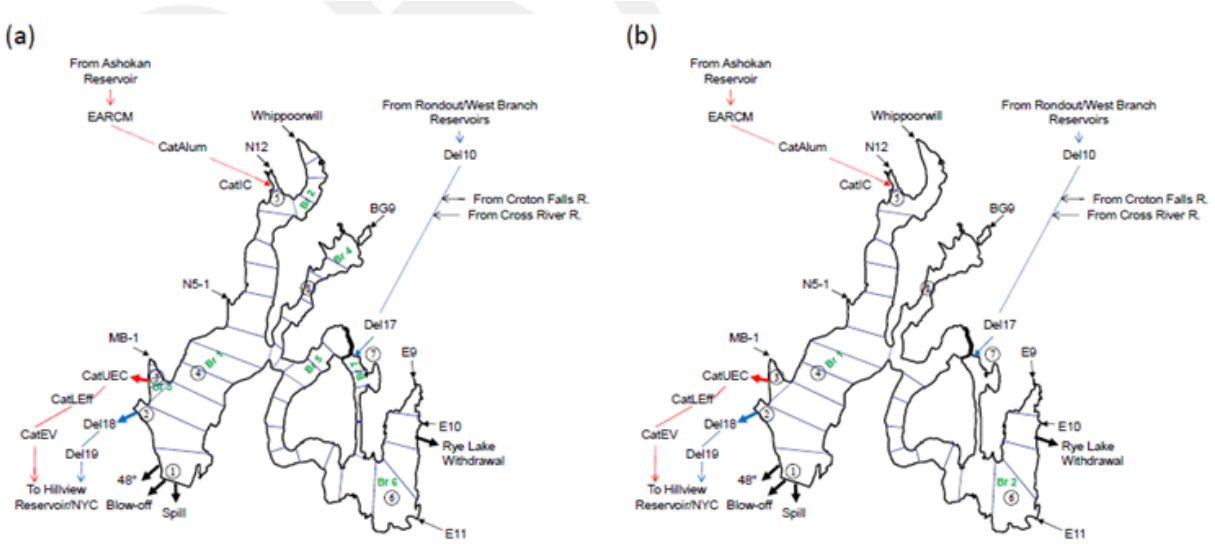

Figure 4.20. (a) Original Kensico Reservoir model grid and (b) modified Kensico Reservoir model grid. (Hazen and Sawyer, 2012)

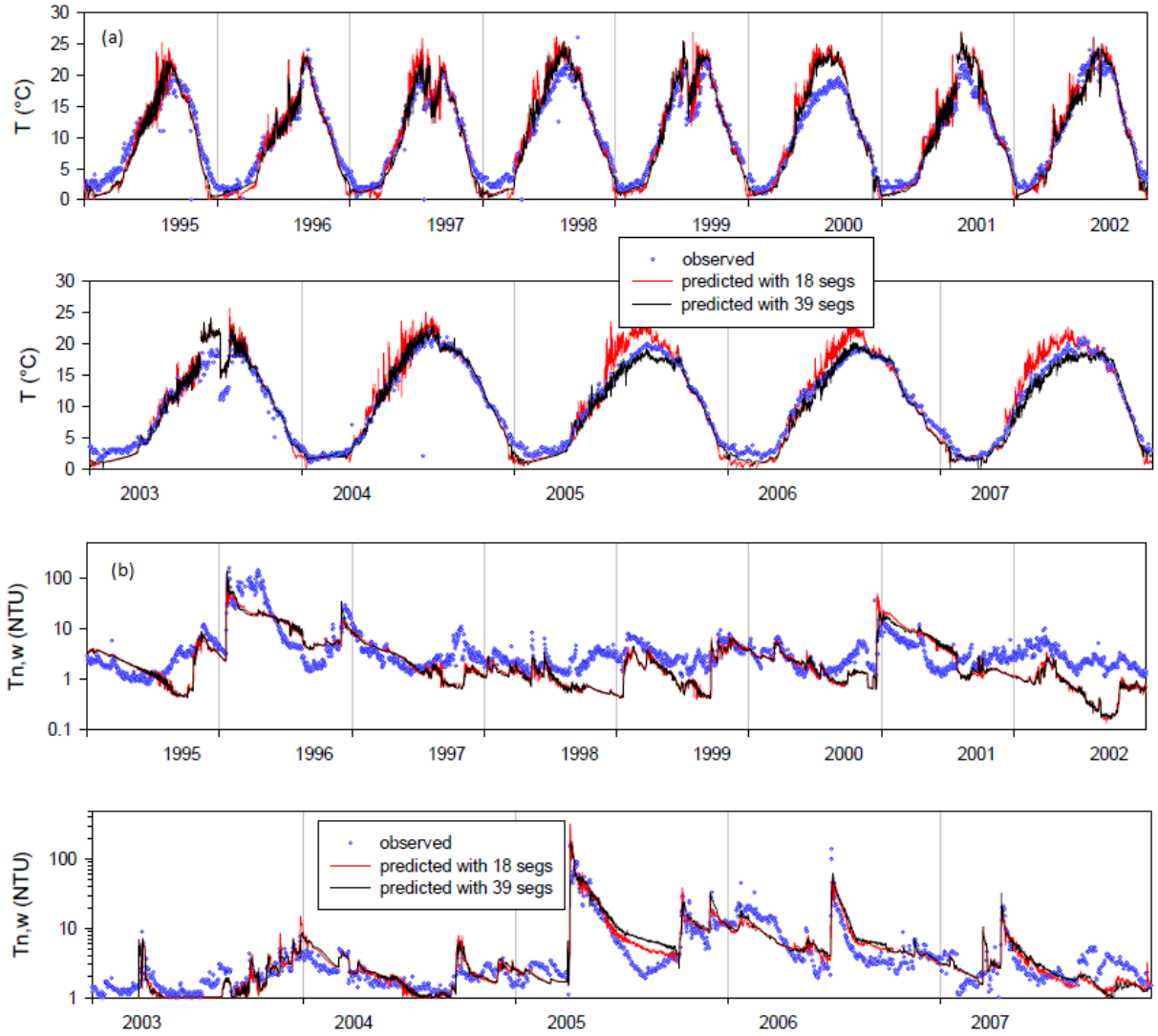

Figure 4.21. Time-series plot of (a) diversion temperature and (b) diversion turbidity from Ashokan Reservoir for the observed record from 1995-2008. Blue dots show observations, black line shows results with original grid (39 segments); red line shows results with modified grid (18 segments). (Hazen and Sawyer, 2012)

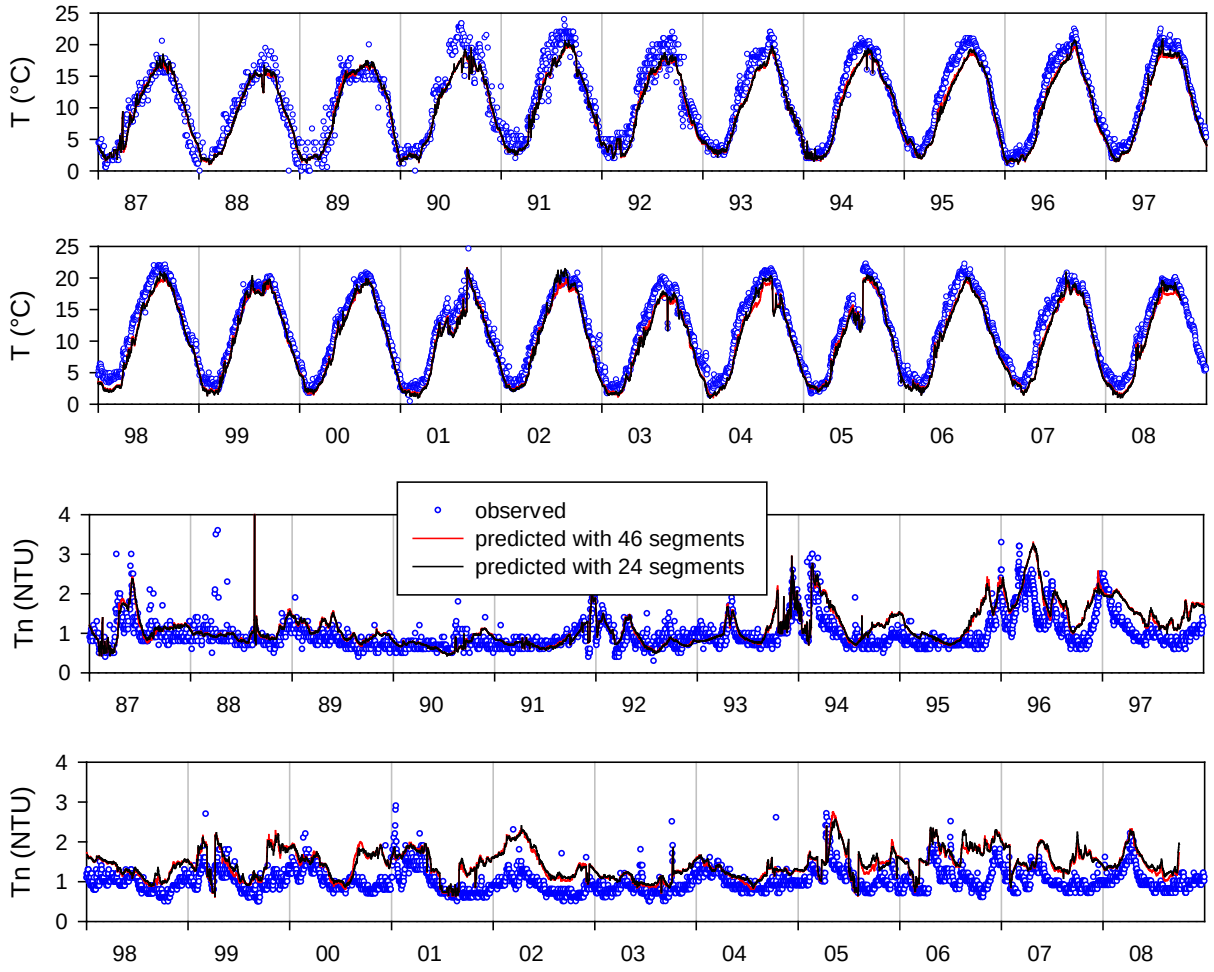

Figure 4.22. Time-series plot of Kensico Reservoir DEL18 effluent (a) temperature and (b) turbidity from Kensico Reservoir for the observed record from 1987-2008. Blue dots show observations, red line shows results with original grid (46 segments); black line shows results with modified grid (24 segments). (Hazen and Sawyer, 2012)

The upgraded models also include a new algorithm to account for the density effects of extremely high turbidity (UFI, 2013b). As an example, during extreme events of December 2010 and August 2011, at peak flows the turbidity in Esopus Creek were estimated to greatly exceed 2000 NTU, which are levels considered high enough to affect water density. Soon after these storms, inverted temperature profiles were observed in the reservoir (Figure 4.23). In the December 4, 2010 profile, warmer water was found near the bottom and in the August 30, 2011 profile colder water was found at mid-depths with warmer waters above and below. Both of these examples lead to unstable conditions if only temperature is used to calculate density. The density correction is applied based on the turbidity, with higher turbidity adding more to the density (UFI 2013b). Figure 4.24 shows the effects of TSS concentration on density with the equivalent densities for the December 2010 and August 2011 events shown.

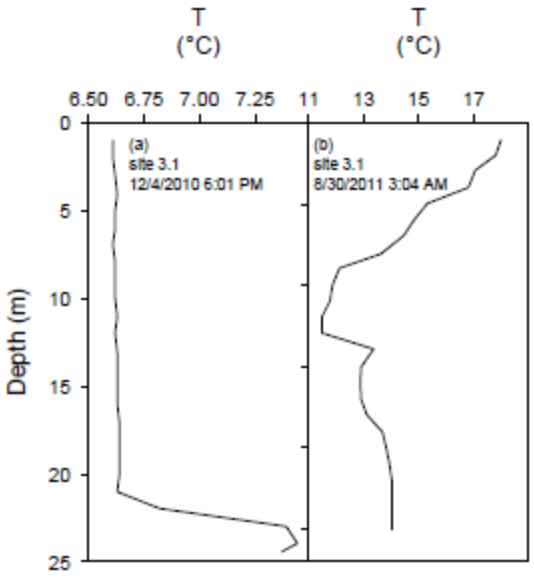

Figure 4.23. Examples of "inverted" temperature profiles observed in West Basin of Ashokan Reservoir: (a) December 4, 2010 and (b) August 30, 2011. (UFI 2013b)

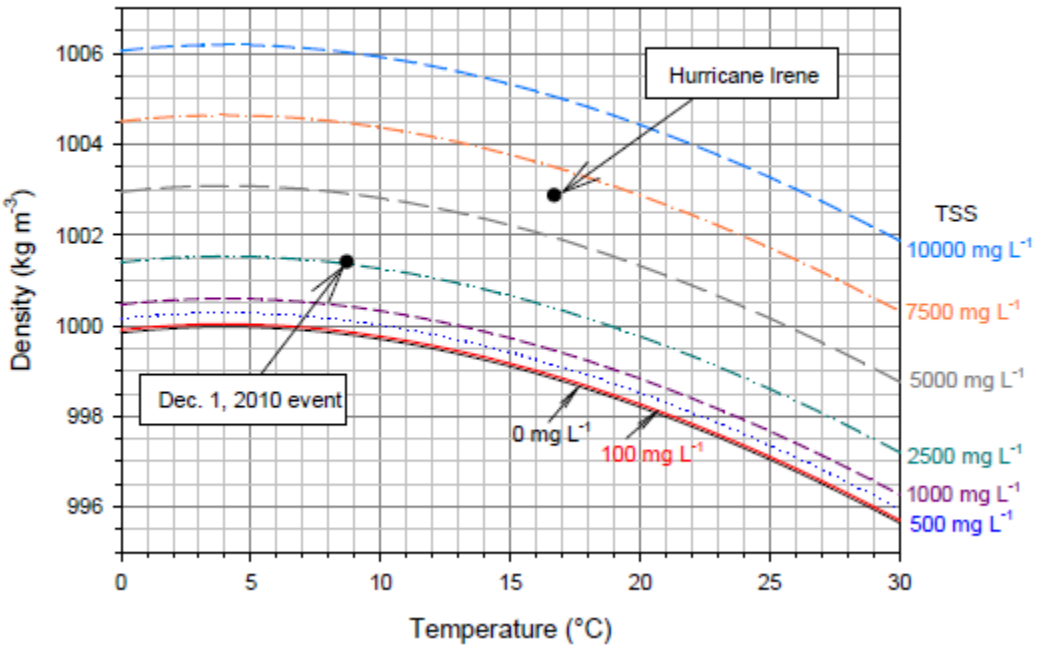

Figure 4.24. Effect of solids (turbidity) on density with corresponding values for the peak Esopus Creek inflow turbidity during Hurricane Irene (August 2011) and the December 2010 event. (UFI 2013b)

Ashokan Outlet Correction

In the East Basin of Ashokan Reservoir, inflow from the West Basin enters the same W2 model segment from which the withdrawal from the East Basin occurs. There is evidence from observations of the reservoir and from model applications that the inflow to the East Basin, may not always mix completely throughout this model segment before exiting the reservoir through the withdrawal structure, as assumed by the 2D model. This pattern of inflow to the East Basin has been described as "short-circuiting". (UFI, 2013c)

An approach was developed by UFI to correct for the short circuiting in the W2 model application as part of the OST. The method involves applying a more detailed 3D model near the gate house for selected events. Then the 3D model and W2 model results are compared to obtain an empirical post-processing correction for the W2 model. This approach accepts the 3D simulations as most accurate, based on its more complete representation of transport in both the lateral and longitudinal dimensions. The 3D model simulations provide a basis to adjust the 2D simulations to accommodate the effects of lateral short circuiting.

UFI had previously developed and applied a three-dimensional (3D) model, the Environmental Fluid Dynamics (EFDC) model, to the East Basin of Ashokan Reservoir as part of the CAT-211 project. The 3D model uses a much more detailed segmentation of the reservoir basin, allowing spatial variations in water motion, temperature, and turbidity in all 3 coordinate directions, and over shore length scales, to be simulated.

In the above discussion of short-circuiting, it was assumed that a portion of the inflow to the East Basin, via either the weir or gate, may be transported "directly" to the intake structure (Q_{ISC} in Figure 4.25). In this schematic the withdrawal turbidity (Tn_w) is the weighted value of the short circuited and the East Basin contributions to the outlet:

$$Q_W \, Tn_W = Q_{ISC} \, Tn_{IN} + (Q_W - Q_{ISC}) \, Tn_3 \qquad (4.48)$$

Where Q_W is the withdrawal flow rate, Tn_{IN} is the turbidity of water moving across dividing weir from the West Basin to the East Basin and Tn_3 is the turbidity in segment three as predicted by the W2 model, and Q_{ISC} is the unknown short circuited flow. For ten events, the withdrawal turbidity (Tn_w) was predicted with the 3D model. Using the 3D model result for Tn_w and the W2 model results for the value of Tn_3 and Tn_{IN} in Eq. 4.48, a value of Q_{ISC} was calculated for each event. These values of Q_{ISC} were then used in a regression analysis to understand which environmental and operational variables were most predictive of Q_{ISC}. These independent variables included: (1) East Basin withdrawal flow Q_W; (2) inflow from the West Basin to the East Basin (sum of weir and gate flow); north-south component of wind speed; (4) top-to-bottom temperature difference in East Basin water column; (5) temperature difference between East Basin inflow and East Basin surface waters; and (6) water surface elevation in the East Basin above the top of the diversion wall.

The only independent variable with any reasonable correlation with Q_{ISC} was found to be the withdrawal flow Q_W. As a result, the following regression equation was used for forecast predictions of short circuited flow:

$$Q_{ISC} = 0.773\ Q_W - 0.283 \qquad (4.49)$$

This is the correction that has now been implemented within the OST to better predict Ashokan withdrawal turbidity.

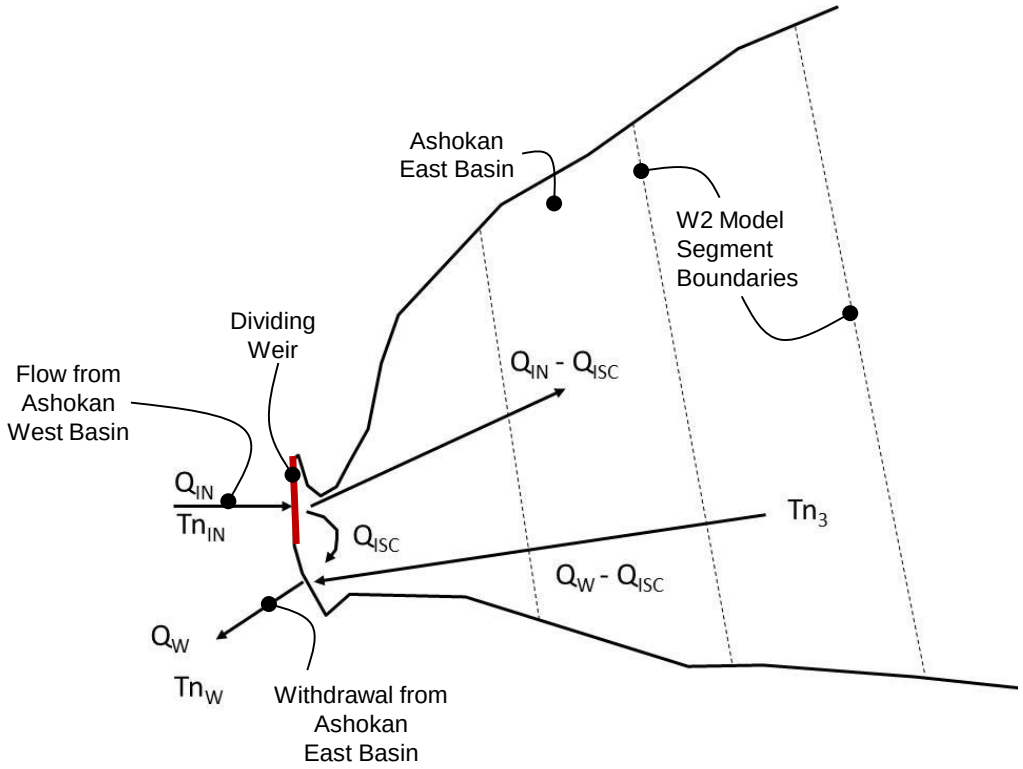

Figure 4.25. Schematic of short circuiting flow directly from Ashokan West Basin input (via dividing weir) to gate house withdrawal from Ashokan East Basin. (UFI, 2013c)

4.6 Modeling Long-Term Trends in Ice Seasons of New York City Drinking Water Reservoirs

Introduction

The presence of a seasonal freshwater-ice cover controls most interactions between the atmosphere and the underlying aquatic systems. Reductions in lake-ice cover under future climate will produce changes in temperature and light levels, water circulation patterns and aquatic UV radiation exposure, all of which are important to biological productivity and diversity. Of particular concern are variations and changes in light field and nutrient availability under ice and in the periods of deep mixing proceeding and following ice cover development and loss. In general, the life cycles of most aquatic organisms are affected by the timing and duration of ice cover, and future changes in these will result in a complex response affecting many aspects of the aquatic ecosystem. It is also interesting to determine the relationship between the timing of ice loss, the onset of thermal stratification, and how this timing will influence the thermal structure in the summer. Long-term simulations of ice conditions/duration are needed to understand the mechanics through which ice cover mediates the effects of climate on lake thermal structure and mixing, and how changing ice cover may ultimately influence phytoplankton succession and trophic status of a lake.

A second water quality issue affected by reservoir ice cover is the winter time turbidity inputs occurring during extreme winter events. Accurate simulation of the onset, loss, and duration of ice cover, in the water supply reservoirs is important since it can modify the transport of turbidity. Ice in these reservoirs affects distribution of water temperature (and density), which in turn can result in the movement of turbidity as plume under the ice, thereby influencing the rate of transport and distribution of turbidity in the reservoir. The presence of ice also influences settling velocity of turbidity-causing particles, and water column stability (Samal et al. 2013).

The simulation of the vertical distribution of temperature and other water quality parameters in lakes and reservoirs has been recognized as an important tool for conservation, restoration and management of natural resources. Many one or two-dimensional models have been developed to fill this role with varying degree of success in different tropical and temperate lakes and reservoirs (Orlob 1983, Patterson and Hamblin 1988). In temperate climates the formation and ablation of a winter ice cover and its interaction with underwater dynamics must be incorporated into the simulation problem. Several one dimensional (1-D) model approaches which simulate the unsteady heat transfer through a two-component (ice and snow) cover have been developed and applied for the study of ice phenology (Wang et al. 2010, Jeffries et al. 2005, Fang et al. 1996, Semmler et al. 2012, Walsh et al. 1998, Brown and Duguay, 2012). The predictive capability of these models that integrate water temperature, snow cover, and solution of the heat balance equations across the ice column is dependent on the accurate estimation of lake snow cover, which can be challenging due to the lack of measurements needed to provide data for model calibration and verification and the high spatial variability of lake snow cover data.

In the present study, a simple ice model (Ashton, 1986, 2011) that predicts the onset, loss and duration of ice cover is developed and applied to New York City drinking water reservoirs. The model is driven by daily or hourly air temperature and wind speed as these are the most

important factors influencing ice breakup and formation (Pierson et al. 2011). Using more than 19 years of observed ice-on and off data for Ashokan and Rondout Reservoirs, the one dimensional ice model driven by air temperature and wind is applied to estimate the ice-on and off dates along with ice thickness. Even though this simple model does not make detailed calculations of the ice cover energy budget, ice-on and off dates for these two reservoirs are well reproduced

The long-term observed ice phenology of these reservoirs can provide a powerful, integrative description of wintertime and springtime climatic conditions for the region. Work is ongoing to include simple snow cover estimates derived from precipitation and temperature data and expand simulations to a wider set of lakes, which will allow more in-depth model inter-comparison.

Materials and Methods

Study area

The present investigation is carried out using data from Ashokan Reservoir and Rondout Reservoir (Figure 4.26)

Simple Ice Model (SIM) description: Ice modelling algorithms

The ice algorithm used in the Simple Ice Model developed by Klaus D. Jöhnk, CSIRO, Australia, is the sub model of the LAKEoneD lake stratification model (Jöhnk et al. 2001 and Samal et al. 2009). This is based on the solution of the 1-D heat conduction equation under steady state conditions in the ice (Ashton, 1980, 1983, 2011). In this simple model, a snow layer on the ice is not included and the modeled ice cover is not influenced by the underlying water temperature. Therefore, the model does not take into account the under-ice melting and freezing due to changes in water temperature. Despite these simplifications, the model is a good approximation for shallow lakes, where water temperature is closely related to air temperature. Deeper lakes need more time to cool down and will show a bias which can be corrected by comparing the lag between water and air temperatures, as long as there are some measurements available. In practice this is handled by changing the number of frost days (days below a threshold temperature) necessary to freeze the lake in the model parameter set (Yao et al 2014).

ASHOKAN RESERVOIR KENSICO RESERVOIR

Figure 4.26. Ice cover investigations in New York City Drinking Water Reservoirs

The model is driven by daily or hourly time series of air temperature and wind speed (as a modifier for ice break-up). No explicit snow or precipitation data is needed. The output of the model gives the timing of ice formation & ice loss and ice thickness. In the model, the meteorological parameter, temperature of frost days which contributes to freezing, is usually set to -1°C, the wind speed threshold (1 m/s) at which an ice layer of certain ice thickness (0.02 m) will break up again can be used for calibration. The ice growth and melting is varied by the internal ice parameters, such as density of ice, latent heat, freezing and melting coefficients and the thermal conductivity. The latter is included here as a parameter to reflect a possible parameterization of a snow cover by varying the conductivity between that for ice and snow. The calibration parameters of frost days and the heat transfer coefficients for freezing and melting are used in this simulation study. In SIM, the ice albedo is considered to be 0.5

Parameters used in the ice model:

Meteorology:

13	Temperature of frost day	- TempFrostDay	-1 – -3 °C
14	Number of frost days	- MinFrostDay	2 – 4 d
15	Wind speed threshold for	- WindBreakUp	1 m/s
16	Ice thickness to break up	- WindMinIce	0.02 m

Ice parameter:

21	Density of ice [kg/m^3]	- RhoIce	916.0
25	Latent heat of fusion [J/kg]	- L	334000
26	Heat transfer freezing [W/(m2 K)]	- Qf	10 – 20
27	melting [W/(m2 K)]	- Qm	10 – 20
28	Thermal conductivity [W /(m K)]	- Tcond	2.24*

Highlighted: calibration parameters
* can be lowered to include effects of snow cover

Results and Discussion

In the present investigation, the dates of ice on and ice off are visually observed by the wildlife research group and the police aviation group in the New York City Department of Environmental Protection. Observations are not specifically made for the purposes of ice observation, but coincide with other routine monitoring activities. The frequency of sampling is approximately weekly to twice monthly.

The simulated time of ice formation and ice break-up (as shown in Figures 4.27 and 4.28) is often close to the observed dates of ice on and ice off, although ice break-up is predicted with a greater degree of certainty Most predictions are within two weeks of the corresponding observations, which is acceptable given that the observational sampling frequency is not high. Furthermore, the model does not show a bias in under or over predicting the formation and break-up dates.

Measurement of ice thickness in these two reservoirs is not made and thus not available for comparison with model prediction. The ice thickness predicted by this model has however been tested and compared by Yao et al (2014) for Harp lake in Canada, who found that this simple model often performed better than more complex models, probably because it captured the major factors – air temperature and wind speed, and reflected their controls on ice phenology in an effective way (Yao et al 2014).

Conclusions

Even though this simple model does not make detailed calculations of the ice cover energy budget, it performed reasonably well when simulations were compared to observations of timing of onset, loss, and duration of ice cover, for multiple winter seasons for Ashokan and Rondout Reservoirs. Interannual variations in ice cover duration are evident for both of the reservoirs. Ice formation begins in early January and the thickness of ice ranges from < 0.1 m to ~ 0.4 m in both reservoirs. Based on the model results, maximum ice thickness simulated in Ashokan Reservoir (~ 0.2-0.3 m) was significantly more than in Rondout Reservoir (~0.1 m – 0.2 m). The simple model tested here shows promise in allowing lake ice phenology to be simulated using readily available input data.

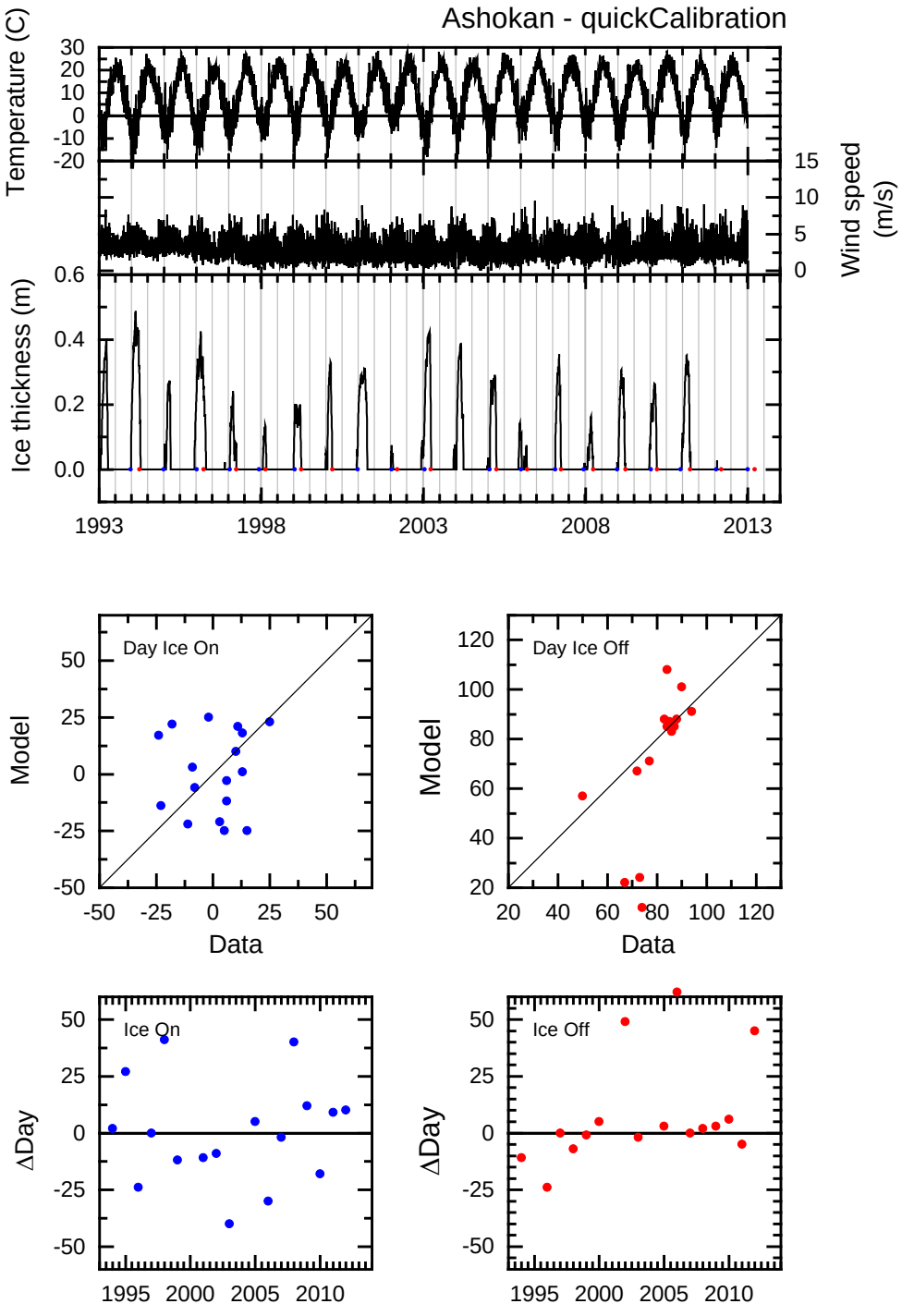

Figure 4.27. Meteorological forcing driving the ice model (top panel) and model simulating ice on and ice off and the difference in days between observed ice data and model for Ashokan Reservoir

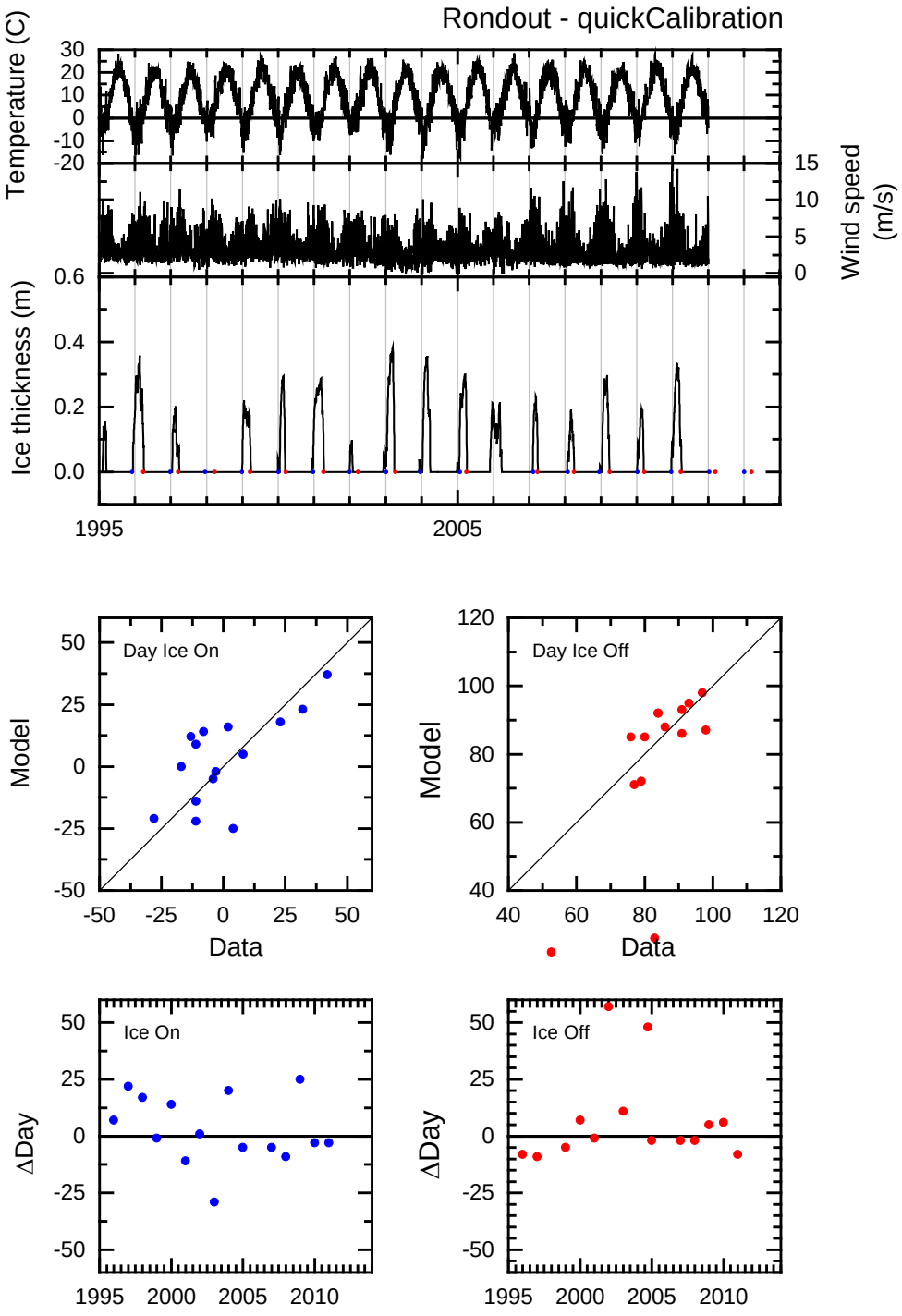

Figure 4.28. Meteorological forcing driving the ice model (top panel) and model simulating ice on and ice off and the difference in days between observed ice data and model for Rondout Reservoir

4.7 Uncertainty Assessment in Water Quality Modeling

Introduction

Water quality models are important tools for predicting the transport and fate of contaminants in receiving waters such as reservoirs and lakes and can be very helpful in water resource management. Despite the physical basis of these models, model parameters often cannot be reliably estimated *a priori* and require calibration to fit measured data, which may bring uncertainty into the models. In addition, error in model inputs (such as the inflow and loadings predicted using watershed models or estimated using measured data) may be significant. The error may result in high uncertainty in model predictions. In general, there are three principal sources contributing to modeling uncertainty: imperfection in model structure, uncertainty in model parameters, and error associated with input data and the measurement data for model calibration (Omlin et al., 2001; Lindenschmidt et al., 2007; Rueda, et al. 2007; Elsawwaf et al., 2010; Janse et al. 2010; Rigosi and Rueda, 2012). Uncertainty analysis in water quality modeling can provide information for model improvement and quantify the level of reliability of model results.

The objective of this study was to assess the uncertainty that arises from parameter uncertainty and error in model inputs (forcing data) in the modeling of Pepacton Reservoir using a one-dimensional hydrothermal and water quality model (V3.5B) developed by UFI (2001).

Table 4.7. Sensitive model parameters and their ranges and calibrated values

No	Name	Definition	Range	Calibrated value
1	aC2CHL	Ratio of carbon (C) to chlorophyll (Chl) (µgC/µgChl)	40–100	51.3
2	aC2P	Ratio of carbon to phosphorus (P) (µgC/µgP)	80–150	80.8
3	Betaw	Surface adsorption fraction	0.3–0.7	0.34
4	Emisi	Ice emissivity	0.9–0.99	0.98
5	Eta	Wind mixing	1–1.5	1.01
6	Fardl	Fraction algal respiration as dissolved labile	0.5–1	0.74
7	Htcwi	Ice transfer	0.01–0.1	0.054
8	Kc	Chlorophyll multiplier (L/µgChl/m)	0–0.05	0.031
9	kldoc	Oxidation of labile dissolved organic carbon (DOC) (1/d)	0.01–0.015	0.012
10	kldop	Decay of labile dissolved organic phosphorus (DOP) (1/d)	0.01–0.1	0.099
11	phir	Respiration multiplier	0.01–0.15	0.11
12	PPvel	Settling organic particulate phosphorus (m/d)	0.264–1.496	1.48
13	Rz	Exponent	0.2–0.6	0.38
14	Sod	Sediment oxygen demand ($g/m^2/d$)	0.32–0.48	0.38
15	trncon	Evaporation multiplier	0.001–0.005	0.0047
16	Turb	Atmospheric turbidity	2–3	2.96

Table 4.8. Inputs and their variation ranges

No	Inputs	Variation ranges
1	Air temperature	-1.5–1.5℃
2	Dewpoint temperature	-1.5–1.5℃
3	Wind speed	-5–5%
4	Solar radiation	-5–5%
5	Dissolved phosphorus	-15–15%
6	Dissolved nitrogen	-15–15%
7	Dissolved organic carbon	-15–15%
8	TSS load	-15–15%
9	Inflow	-10–10%
10	Stream temperature	-1.5–1.5℃

Methodology

In this study, a general and flexible method based on generalized likelihood uncertainty estimation (GLUE) was used. Sixteen sensitive model parameters were taken as uncertain parameters and the model inputs including meteorological data, hydrological and loading data which were provided as time series (daily data) in the model were taken as uncertain inputs (see Tables 4.7 and 4.8). The Latin hypercube sampling (LHS) technique, described by McKay et al. (1979) and used widely in other studies such as Rueda, et al. (2007) and Rigosi and Rueda (2012), was adopted to generate 13500 sets of parameter values and input data.

Results and Discussion

Posterior likelihood of parameters and inputs

The shape of the distributions of parameter values indicates the degree of uncertainty of the parameter estimates. Sharp and narrow distributions are associated with well identifiable parameters, while flat uniform distributions indicate higher parameter uncertainty. The probability distributions of parameters are classified into five categories according to their shapes. The probability distributions of five parameters including kldop (decay of labile dissolved organic phosphorus), phir (respiration multiplier), trncon (evaporation multiplier), htcwi (ice transfer), and aC2CHL (ratio of carbon to chlorophyll) were plotted in Figure 4.29 as examples to provide visual impressions of the distributions. The main results of distributions of parameters are as follows: (1) Four parameters including kldoc (oxidation of labile dissolved organic carbon), kldop (decay of labile dissolved organic phosphorus), PPvel (settling organic particulate phosphorus), and rz (exponent) follow negatively skewed triangular distributions (Figure 4.29(a)). The values of these parameters tend to cluster toward their upper bounds. The results imply that if the upper bounds of the parameters are raised, better results (the simulations match the measurement data better) may be obtained by model calibration. On the other hand, it is important to make sure the upper bounds of these parameters are appropriate in model calibration because low simulation error can be achieved if these parameters are assigned higher values. If the upper bounds are wrong, incorrect results may be obtained. (2) Three parameters including eta (wind mixing), fardl (fraction algal respiration as dissolved labile), and phir (respiration multiplier) follow positively skewed triangular distributions (Figure 4.29(b)). The

results mean that if the lower bounds of the parameters are lowered, better results may be obtained by model calibration. Appropriate lower bounds for these parameters are the basis for good calibration results. (3) Two parameters including betaw (surface adsorption fraction) and trncon (evaporation multiplier) follow skewed normal distributions (Figure (c)). These parameters tend to have middle values of their ranges and they are well defined. (4) Six parameters including aC2P (ratio of carbon to phosphorus), emisi (ice emissivity), htcwi (ice transfer), kc (chlorophyll multiplier), sod (sediment oxygen demand), and turb (atmospheric turbidity) follow uniform distributions (Figure 4.29(d)). Their values distribute evenly within their ranges. These parameters are of high uncertainty. (5) One parameter, aC2CHL (ratio of carbon to chlorophyll), follows a righted-angled trapezoid distribution (Figure 4.29(e)). The results mean that if the lower bounds of the parameters are lowered, better results may be obtained by model calibration. It is very important to check the lower bound of this parameter in model calibration.

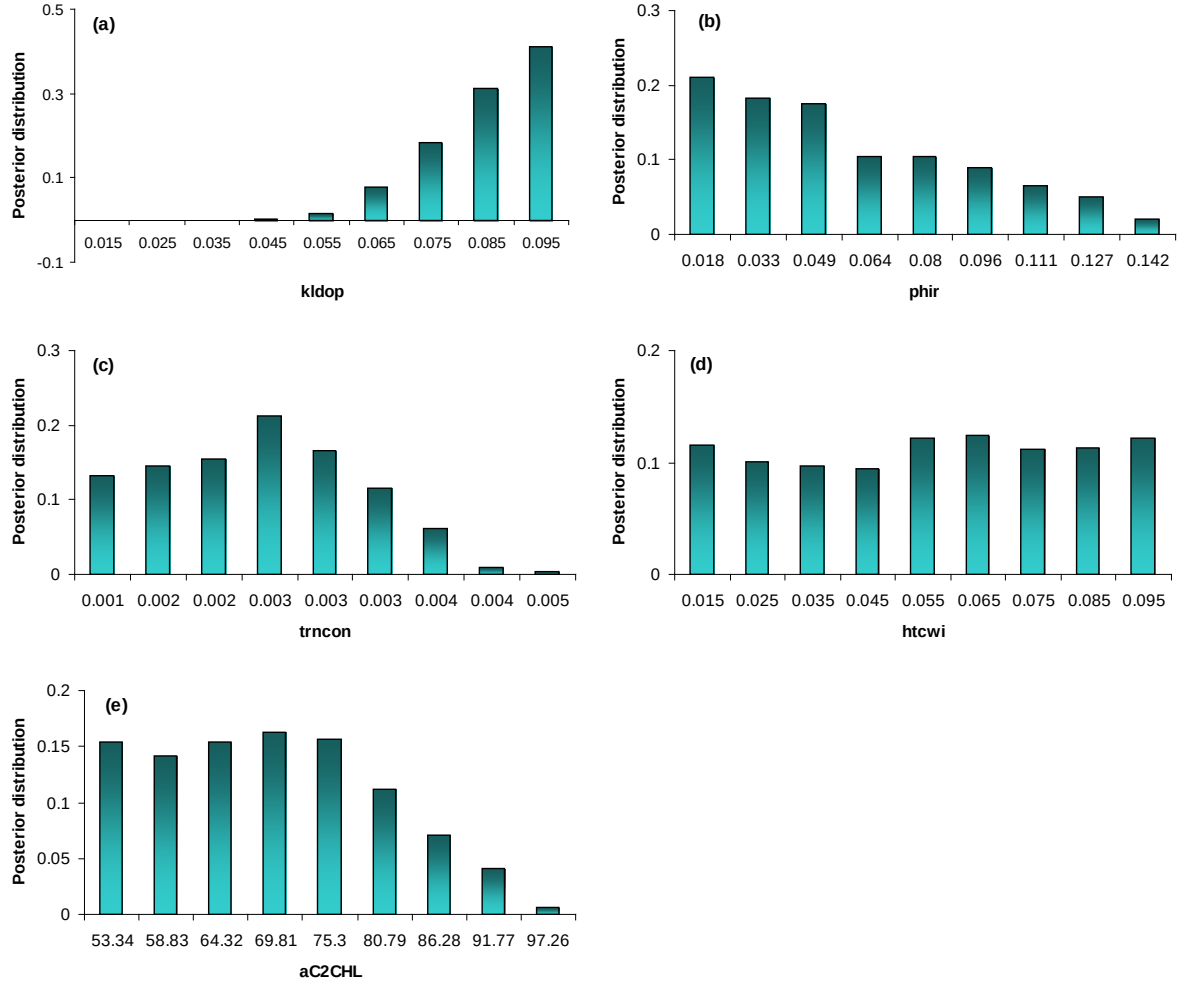

Figure 4.29. Example histograms of posterior probability distributions of parameters including kldop (decay of labile dissolved organic phosphorus), phir (respiration multiplier), trncon (evaporation multiplier), htcwi (ice transfer), and aC2CHL (ratio of carbon to chlorophyll): (a) negatively skewed triangular distribution, (b) positively skewed triangular distribution, (c) normal distribution, (d) uniform distribution, and (e) right-angled trapezoid distribution.

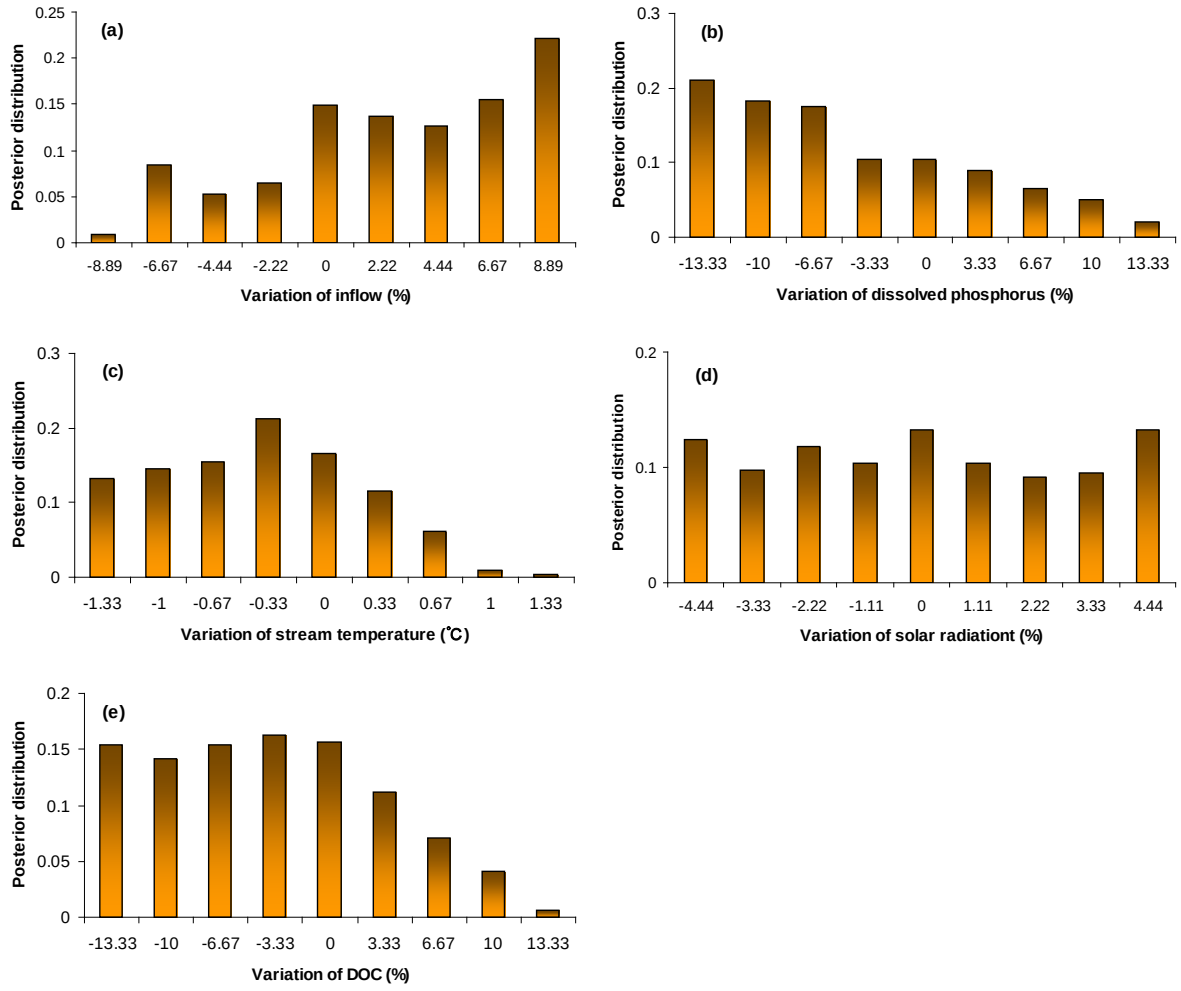

Figure 4.30. Example histograms of posterior probability distributions for increments of inputs: (a) negatively skewed triangular distribution, (b) positively skewed triangular distribution, (c) normal distribution, (d) uniform distribution, and (e) right-angled trapezoid distribution.

Understanding the distribution of inputs can help improve the model. The probability distribution for each set of input time series data was plotted and it is found that most inputs follow non-Gaussian distributions. The probability distributions of five of them were plotted in Figure 4.30. In these bar charts in Figure 4.30, abscissas show the discrete variations of daily air temperatures (zero value represents the daily air temperatures were not varied), while ordinates (y-axes) show the (normalized) posterior probability. The main results are as follows: (1) Three series of inputs (air temperature, dew-point temperature, and inflow) follow negatively skewed triangular distributions (Figure 4.30(a)), implying that their current input data may have been under-estimated and increasing these inputs may lead to better modeling results. (2) Two series of inputs (wind speed and dissolved phosphorus) follow positively skewed triangular distributions (Figure 4.30(b)), implying that their current input data may have been over-estimated. (3) One time series data (stream temperature) follows a skewed normal distribution (Figure 4.30(c)). They are well-estimated. (4) Two time series data (solar radiation and dissolved nitrogen) follow uniform distributions (Figure 4.30(d)). Their uncertainties are high. (5) Two time series data including dissolved organic carbon and total suspended solid (TSS) loads follow righted-angled trapezoid distribution (Figure 4.30(e)). They may have been over-estimated.

Prediction intervals

The uncertainty of model results can be stated by giving a range (or a band) of values. Wider bands mean higher uncertainty in the estimation of the modeling output and thus lower confidence in the model results; vice versa, smaller bands containing the observations are indicators of reliable modeling results (Freni and Mannina, 2012). Figure 4.31 presents the daily simulated and measured temperatures of the epilimnion and the hypolimnion, along with 90% prediction intervals. As shown by the narrow prediction intervals, the simulation uncertainty is low. Low uncertainty can also be observed for DO concentrations of the epilimnion in Figure 4.32(a). Unfortunately, the simulation uncertainty is high for DO concentrations of the hypolimnion, and the TP and CHLA of the epilimnion and the hypolimnion, especially at low and high concentrations as shown in Figures 4.32(b), 4.33 and 4.34. The results are consistent with the results of other studies such as Rigosi and Rueda (2012).

The number of observations included in the uncertainty intervals is one of the main issues in evaluating GLUE results, since it is important that the GLUE bounds are able to account for all or most of the output variability (Blasone et al. 2008). As shown in Figures 4.31-4.34, most measurements are included in the prediction intervals for the TEMP, CHLA and TP of the epilimnion, and the TP of the hypolimnion (89.5, 74.1, 89.5 and 80.4%, respectively). However, the percentages of the measurements included in the prediction intervals are low for the DO of the epilimnion, and the TEMP, DO and CHLA of the hypolimnion (47.1, 48.4, 56.0, 50.0%, respectively). The results show that the uncertainty in model structure, or the error in measurement data is significant, or the parameter ranges are too narrow.

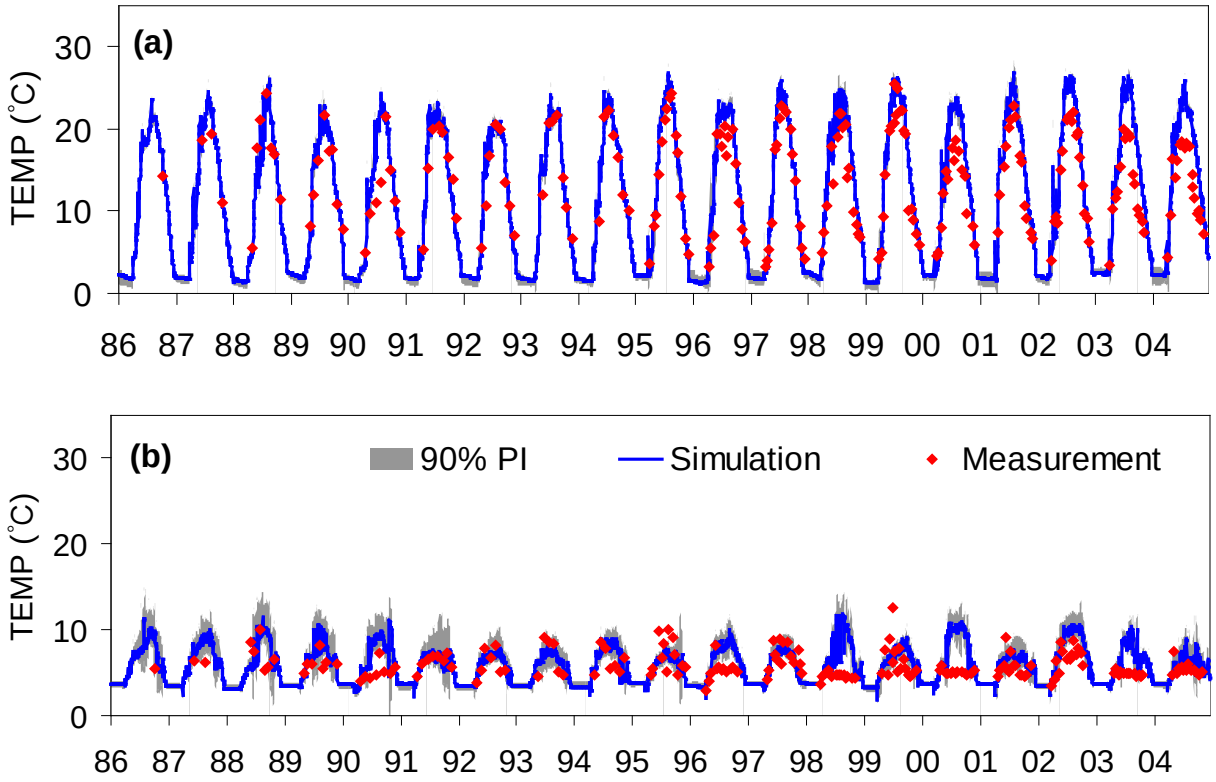

Figure 4.31. Daily simulated and measured temperatures, along with 90% prediction intervals (90%PI) of (a) the epilimnion and (b) the hypolimnion.

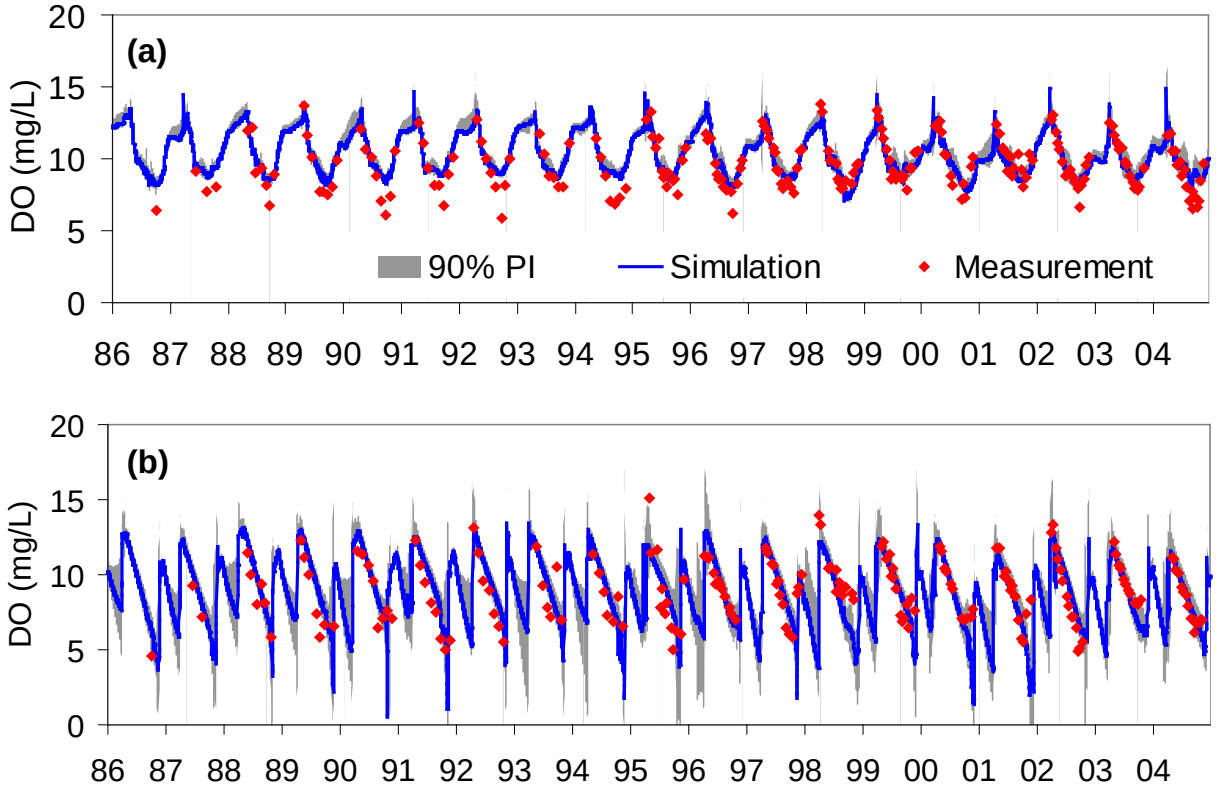

Figure 4.32. Simulated and measured dissolved oxygen, along with 90% prediction intervals (90% PI) of (a) the epilimnion and (b) the hypolimnion.

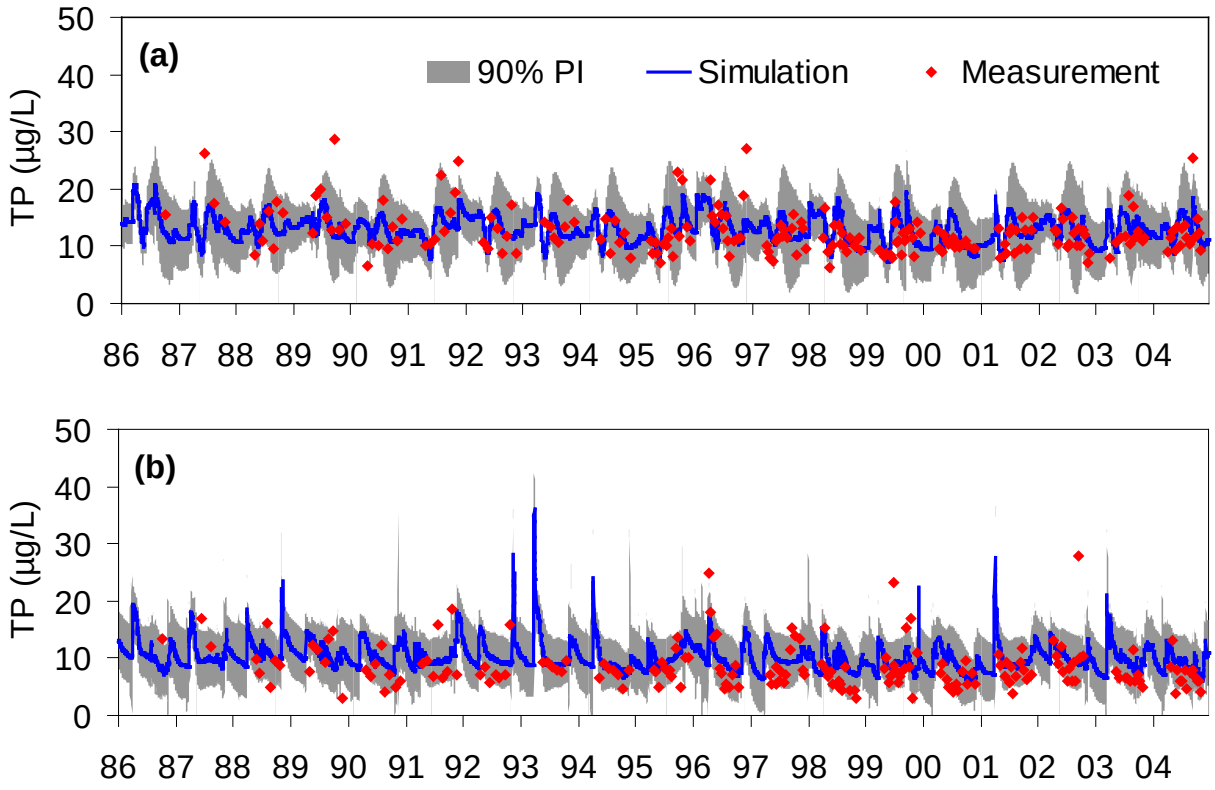

Figure 4.33. Daily simulated and measured total phosphorus, along with 90% prediction intervals (90%PI) of (a) the epilimnion and (b) the hypolimnion.

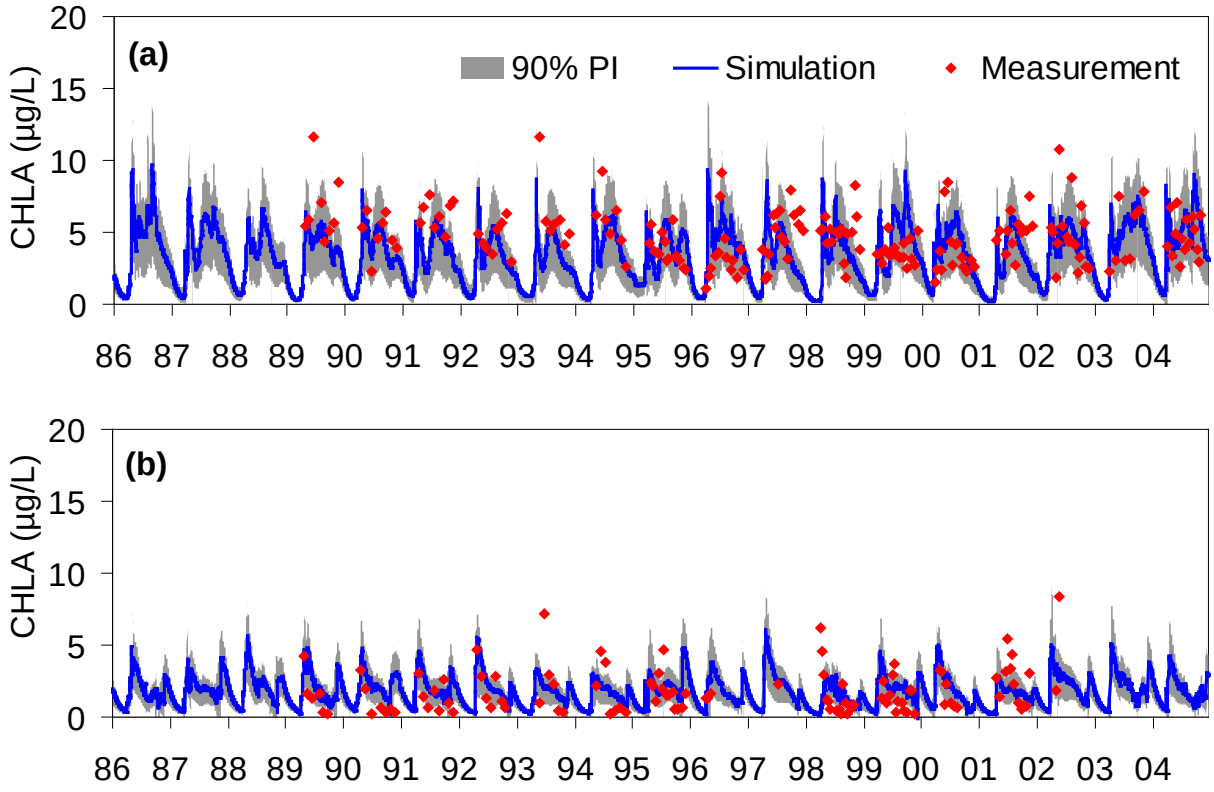

Figure 4.34. Daily simulated and measured chlorophyll *a*, along with 90% prediction intervals (90%PI) of (a) the epilimnion and (b) the hypolimnion.

Summary and Conclusions

In this work, a general and flexible method based on generalized likelihood uncertainty estimation (GLUE) is applied to the estimation of the uncertainty in reservoir water quality modeling that arises from parameter uncertainty and errors in model inputs. A one-dimensional hydrothermal and water quality model of Pepacton Reservoir was used to demonstrate the method. Main conclusions are as follows:

- The GLUE method proves to be a valid tool to obtain well-defined posterior distributions of parameters and inputs. The application results show that almost all parameters and inputs have wide posterior distributions, indicating the parameters and inputs are of high uncertainty. The posterior probability distributions of parameters and inputs can be classified into five categories according to the shapes of their distributions. The classification can be helpful for model calibration.

- The GLUE method helps us to understand the simulation uncertainty (i.e., prediction intervals) for multiple variables. As shown by the narrow prediction intervals, the simulation uncertainty is low for simulated temperatures. Low uncertainty can also be observed for dissolved oxygen concentrations of the epilimnion. Unfortunately, the simulation uncertainty of total phosphorus and chlorophyll *a* of the epilimnion and hypolimnion, and the dissolved oxygen of the hypolimnion is high, especially at peak concentrations.

- The application results show that most measurements are included in the prediction intervals for the temperature, chlorophyll *a* and total phosphorus of the epilimnion, and the total phosphorus of the hypolimnion. However, the percentages of the measurements included in the prediction intervals are low for the dissolved oxygen of the epilimnion, and the temperatures, dissolved oxygen and chlorophyll *a* of the hypolimnion. The model needs to be improved by, for example, reducing the uncertainty in model structure.

5. Data Analysis to Support Modeling

5.1. Turbidity and Suspended Sediment Monitoring in the Upper Esopus Creek Watershed

Introduction

Suspended sediment concentration (SSC) and turbidity are primary water quality concerns in New York City's (NYC) water supply system (FAD, 2007). Turbidity can make water appear cloudy or muddy; it is caused by the presence of suspended and dissolved matter, such as clay, silt, fine organic matter, plankton and other microscopic organisms, organic acids, and dyes (ASTM International, 2003). Turbidity measurements are a quantification of the optical properties of a liquid that causes light rays to be scattered and absorbed rather than transmitted through a water sample (ASTM International, 2003). The U.S. Geological Survey quantifies turbidity levels as nephelometric turbidity units (NTUs) for instruments that use white light (a broadband light source) or as formazin nephelometric units (FNUs) for instruments that use a monochrome light source (Anderson, 2005). The Environmental Protection Agency limits turbidity to 5 NTUs in unfiltered water entering a water supply system such as that of NYC. Turbidity was identified as a source of water-quality impairment in the management plan for the NYC watershed because it is aesthetically unpleasing, reduces the effectiveness of drinking water disinfection, and may indicate the presence of bacteria and viruses. During large storms high turbidity levels can also limit the use of portions of the drinking water supply system.

The Catskill portion of the Catskill/Delaware water supply system is the primary source of turbidity in the NYC Water Supply System (CCE, 2007). Through watershed geomorphic assessments and watershed modeling, the NYC-DEP, in cooperation with the New York State Museum and the State University of New York at New Paltz, have identified streambank and streambed erosion of fine sediments from glacial lake deposits as the primary source of suspended sediment and turbidity in the Catskill water supply watershed (CCE, 2007). As a result, reduction of stream sediment and turbidity has been the focus of stream stabilization projects within the watershed. The NYC-DEP and the U.S. Geological Survey (USGS) developed a monitoring strategy to elucidate the spatial and temporal variability of suspended sediment and turbidity in the upper Esopus Creek watershed. These monitoring data will also be used to support the water-quality modeling efforts that require more detailed spatial and temporal turbidity and suspended sediment data. This report summarizes the results of SSC and turbidity monitoring within the upper Esopus Creek watershed (Figure 5.1), the main tributary to the Ashokan Reservoir, for the period October 1, 2009 through September 30, 2012. Turbidity and SSC were measured at 6 monitoring stations within the upper Esopus Creek watershed as part this project. Stations were chosen to coincide with existing USGS stream gaging stations to take advantage of existing infrastructure and streamflow data. This work was conducted for DEP by the U.S. Geological Survey (USGS) and here we present a concise summary of the provisional project report. The final USGS open file report will provide more extensive information on the project (McHale and Siemion, In Press)

The specific objectives of the project were to:

1. Examine temporal and spatial patterns in turbidity and suspended sediment in the upper Esopus Creek watershed.
2. Quantify SSC and turbidity at each of 6 monitoring stations in the upper Esopus Creek and estimate suspended sediment loads at each station.
3. Evaluate the relations between SSC and turbidity and construct sediment and turbidity rating curves at the six USGS stream gaging stations within the upper Esopus Creek watershed.

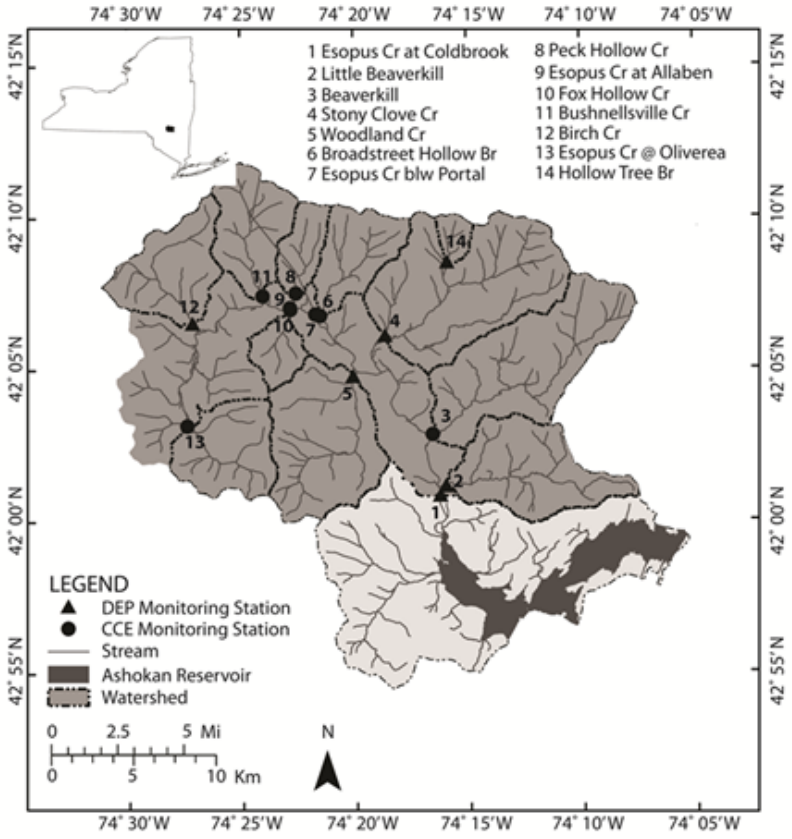

Figure 5.1. The Upper Esopus Creek watershed showing the locations of 14 monitoring stations. Monitoring stations included in the current study (DEP) are shown as triangles; monitoring stations used in a previous NYSDEC/CCE study (CCE) are shown as circles.

Field Methods

All field data collection was conducted according to standard USGS protocols (Wilde and others, 1999). Stream suspended sediment and turbidity grab samples were collected monthly throughout the study from a well-mixed area of the stream (identified through flow measurements) at each sampling station. Storm samples were collected with automated samplers triggered to sample in response to changes in stream stage. Grab samples, automated samples, and turbidity measurements from in-situ probes were all collected in as close proximity as was possible at each station to minimize differences caused by sampling location. The goal was to capture samples throughout the range of flow conditions and during every season at each site throughout the study period. Field quality assurance and quality control were assessed through approximately quarterly collection of triplicate samples and equal width - depth integrated samples. Turbidity was monitored at a 15-minute interval using in-situ turbidity probes at 10 of the stations. Two types of turbidimeters were used (1) the Forest Technology Systems DTS-12 probe and (2) the HACH Environmental Surface Scatter 7 Turbidimeter (SS7). The DTS-12 probe is a true in-situ probe that is deployed in-stream, it uses a sidescatter optical nephelometer with an infrared laser light source and a specified range of 0 to 1,600 nephelometric units (NTU) and a resolution of 0.01 NTU. The DTS-12 is specified to be accurate to within ±2 percent in the range of 0-399 NTU and ±4 percent in the range 400 to 1,600 NTU. The SS7 is a flow-through system mounted on the wall of a gage house and water is pumped into it from the stream. EccentricPumps SLP Mini10 peristaltic pumps delivered water to the SS7 at a rate of 2 L/min. The SS7 uses a photocell positioned at a 90 degree angle to the broad spectrum light source with a specified range of 0 to 9999 NTU and a resolution of 0.01 NTU below 100 NTU and 0.1 NTU above 100 NTU. The SS7 is specified with an accuracy of ±5 percent from 0 to 1999 NTU and ±10 percent from 2000 to 9999 NTU. Both types of probes were calibrated and checked monthly using Formazin standard solutions. Measurements from the DTS-12 probes are reported as Formazin Nephelometric Units (FNU). Measurements from the SS7 are reported as Nephelometric Turbidity Units (NTU). The calibration was checked and probes were cleaned every month for both types of in-situ turbidimeters. Cleaning and fouling data corrections were applied to the turbidity data according to standard methods (Wagner, 2006).

Laboratory Methods

All water-quality samples were transported to the USGS Soils and Low Ionic Strength Water Quality Laboratory in Troy, N.Y. where turbidity was determined using a Hach Model 2100AN turbidimeter. Suspended sediment concentration was analyzed at the USGS Sediment Laboratory in Louisville, Kentucky using the ASTM [D3977-97(2002)] standard test methods for determining sediment concentration in water samples (Guy, 1969).

Results and Discussion

Suspended Sediment and Turbidity Loading from Tributaries

One of the objectives of this study was to quantify SSC and turbidity levels, and suspended sediment loads at each of 6 gaging stations in the upper Esopus Creek for a period of three years.

Although flow conditions were quite different between water years 2010 and 2011, the contributions of suspended sediment from the various tributaries relative to the total remained remarkably similar (Figure 5.2). Stony Clove Creek contributed by far the largest amount of the total annual suspended sediment load at the Cold Brook station: 37 percent of in water year 2010, 30 percent in 2011 and 57 percent in 2012. Indeed, Stony Clove Creek accounted for a higher percentage of the load calculated for Coldbrook outlet during 2010 and 2011than all of the other tributaries combined. The large increase in the percent of load accounted for by Stony Clove Creek during the 2012 water year was probably caused by the channel disturbance associated with stream bank stabilization work that followed Hurricane Irene. There were several times throughout 2012 when high concentrations of turbidity were measured by the in-situ probes that were not accompanied by increases in stream discharge. The Woodland Valley tributary also accounted for a substantial percentage of the load at Coldbrook, 7 percent in 2010, 14 percent in 2011, and 9 percent in 2012. Comparing suspended sediment loads from watersheds of different size can be misleading because the largest watersheds typically produce the largest sediment loads. Figure 5.2 shows loads as tons per hectare, in other words the loads have been divided by watershed area (in hectares) to normalize for watershed area. Viewed in this way, Stony Clove Creek produces more sediment per hectare than any other tributary and indeed more than the entire upper Esopus Creek watershed. The contribution from Woodland Valley is also consistently high although not nearly as high as Stony Clove. The per hectare load from the different tributaries varies substantially from year to year: the Stony Clove Creek watershed appears to be a chronic source of suspended sediment and turbidity to the Esopus Creek; it produces the largest amounts of suspended sediment regardless of the hydrologic conditions whereas the rest of the tributaries do not rank in consistent order in terms of largest to smallest contributors of suspended sediment from year to year.

Relation between SSC and turbidity, and streamflow-SSC/turbidity rating curves

Data from the six stations monitored as part of the present study were used for developing relations between SSC and turbidity, and rating curves that relate streamflow to SSC and turbidity because these were the stations with the best quality discharge data (Table 5.1). Three types of data were used to examine the relations between SSC and turbidity; suspended sediment concentrations and turbidity values from discrete sampling (grab samples and samples collected with automatic samplers) that were both analyzed in the laboratory and turbidity values from in-situ turbidity probes. The relations between discharge, SSC, and turbidity were also investigated for each station. The relation between discharge and SSC was strongest at the Coldbrook station at the outlet of the upper Esopus Creek watershed and weakest at Hollow Tree Brook (Table 5.1). This pattern was consistent with results from regression analyses of discharge and laboratory turbidity (Table 5.1). The two stations with the lowest SSC and turbidity levels, Little Beaver Kill and Hollow Tree Brook had the weakest relations to discharge. The two watersheds did not produce high SSC and turbidity and therefore the concentrations did not increase as strongly with increasing discharge compared to the other stations. In general the stations with the highest concentrations had the strongest relations between discharge and suspended sediment or turbidity; however this was not true for Stony Clove Creek which had the highest volume weighted mean concentrations of any of the watersheds in the study. This inconsistency may be caused by several stream bank failures along the length of the stream that can produce high concentrations through the range in flow conditions in the watershed. Therefore, although SSC

and turbidity are consistently high at the station, those concentrations are not strongly related to discharge (Table 5.1). Regression results between discharge, SSC, and laboratory turbidity at Birch Creek and Woodland Creek were similar to those calculated for Stony Clove Creek with r^2 values ranging from 0.57 to 0.75 (Table 5.1).

Relations between SSC and turbidity are of particular interest because of the potential to use turbidity and SSC as a surrogate for one another. First, relations between SSC and turbidity from samples analyzed in the laboratory were examined (Table 5.1). The relations were stronger than those calculated for discharge and SSC at all of the stations except Coldbrook. Nonetheless, Coldbrook still had the strongest relation between SSC and turbidity of any of the stations. Regression results showed a strong relation between laboratory turbidity and SSC at all of the stations with r^2 values ranging from 0.72 at Stony Clove Creek to 0.82 at Cold Brook. Hollow Tree Brook, the station with the lowest SSC and turbidity values, was an exception. The relation between SSC and turbidity was also strong when data from all of the stations were considered together with SSC and laboratory turbidity data log-transformed (Figure 5.3).

Information generated from this study will be useful for modeling of suspended sediment concentrations in the Esopus Creek.

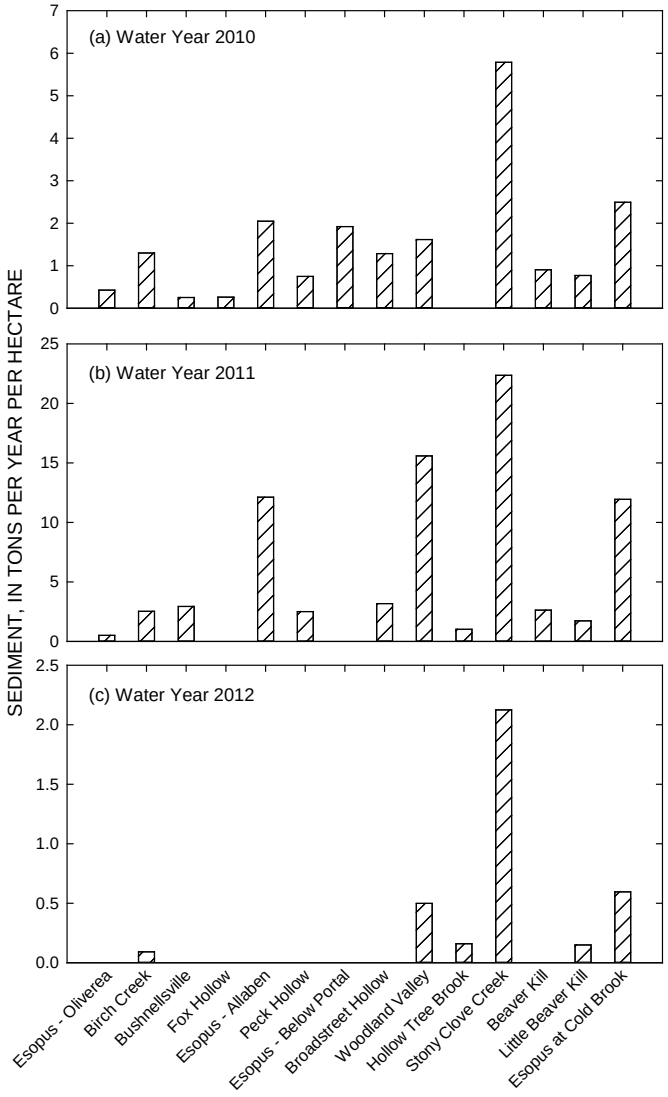

Figure 5.2. Suspended sediment loads per unit area (ha) for water years (a) 2010, (b) 2011, and (c) 2012 at 14 sites throughout the upper Esopus Creek watershed. In water year 2012 only six sites were sampled: Birch Creek, Woodland Valley, Hollow Tree Brook, Stony Clove Creek, and Esopus at Coldbrook. Note the change in scale between years. See Figure 5.1 for station locations. Note that in 2010 and 2011 monitoring included sites that were part of another collaborative project described in Figure 5.1.

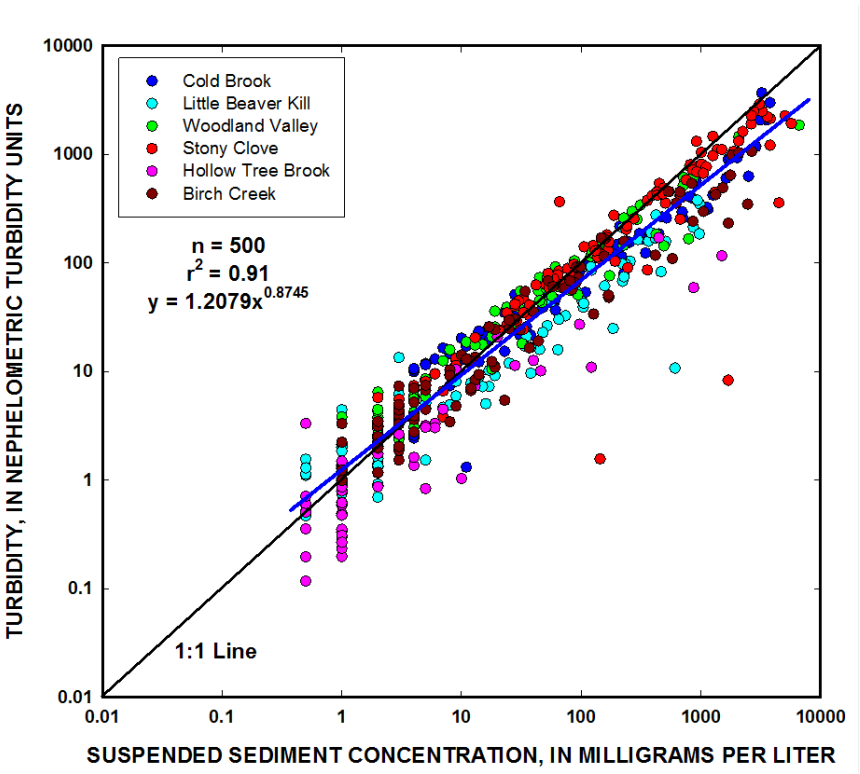

Figure 5.3. The relation between suspended sediment concentration and turbidity measured in the laboratory with a Hach 2100AN instrument for data collected from water years 2010-2012 at the six long-term USGS stream gaging stations in the upper Esopus Creek watershed. See Figure 5.1 for station locations.

Table 5.1. Results of regression analyses between discharge (Q) and suspended sediment concentration (SSC), laboratory turbidity (LabTurb), and in-situ turbidity (Turb15) at six stations in the upper Esopus Creek watershed. See Figure 5.1 for locations.

Station: Esopus Creek at Cold Brook (Hach Surface Scatter 7)

Independent	Dependent	r^2	p	n	Equation
Q	SSC	0.91	<0.001	102	$SSC = 0.09 \times Q - 37.9$
Q	LabTurb	0.83	<0.001	105	$LabTurb = 0.06 \times Q - 67.2$
Q	Turb15	0.61	<0.001	39,360	$Turb15 = 0.05 \times Q - 3.21$
LabTurb	SSC	0.82	<0.001	92	$SSC = 1.36 \times LabTurb + 116.9$
Turb15	LabTurb	0.96	<0.001	30	$LabTurb = 1.14 \times Turb15 - 7.8$
Turb15	SSC	0.86	<0.001	31	$SSC = 2.02 \times Turb15 - 26.3$

Station: Little Beaver Kill at Beechford (DTS-12)

Independent	Dependent	r^2	p	n	Equation
Q	SSC	0.56	<0.001	103	$SSC = 0.42 \times Q - 8.0$
Q	LabTurb	0.45	<0.001	98	$LabTurb = 0.15 \times Q + 0.37$
Q	Turb15	0.37	<0.001	52,685	$Turb15 = 0.08 \times Q - 0.91$
LabTurb	SSC	0.77	<0.001	92	$SSC = 2.54 \times LabTurb + 6.2$
Turb15	LabTurb	0.40	<0.001	56	$LabTurb = 0.38 \times Turb15 + 19.3$
Turb15	SSC	0.32	<0.001	59	$SSC = 0.97 \times Turb15 + 46.2$

Station: Stony Clove Creek at Chichester – DTS-12

Independent	Dependent	r^2	P	n	Equation
Q	SSC	0.64	<0.001	118	$SSC = 0.53 \times Q + 228.6$
Q	LabTurb	0.60	<0.001	103	$LabTurb = 0.37 \times Q + 182.8$
Q	Turb15	0.29	<0.001	24,955	$Turb15 = 0.16 \times Q + 85.6$
LabTurb	SSC	0.72	<0.001	100	$SSC = 1.4 \times LabTurb + 45.1$
Turb15	LabTurb	0.79	<0.001	32	$LabTurb = 1.5 \times Turb15 - 15.4$
Turb15	SSC	0.66	<0.001	39	$SSC = 2.2 \times Turb15 - 120.7$

Station: Stony Clove Creek at Chichester – Hach Surface Scatter 7

Q	Turb15	0.25	<0.001	32,544	$Turb15 = 0.27 \times Q + 69.6$
Turb15	LabTurb	0.74	<0.001	33	$LabTurb = 1.93 \times Turb15 - 42.2$
Turb15	SSC	0.52	<0.001	39	$SSC = 3.2 \times Turb15 - 98.6$

Station: Hollow Tree Brook– DTS-12

Independent	Dependent	r^2	P	n	Equation
Q	SSC	0.50	<0.001	60	$SSC = 2.3 \times Q - 29.6$
Q	LabTurb	0.61	<0.001	53	$LabTurb = 0.31 \times Q - 3.2$
Q	Turb15	0.02	<0.001	23,986	$Turb15 = 0.37 \times Q + 3.0$
LabTurb	SSC	0.58	<0.001	51	$SSC = 6.4 \times LabTurb + 0.72$
Turb15	LabTurb	0.96	<0.001	16	$LabTurb = 0.64 \times Turb15 + 0.84$
Turb15	SSC	0.63	<0.001	16	$SSC = 2.8 \times Turb15 + 15.6$

Q = discharge, in cubic feet per second; SSC = suspended sediment concentration, in milligrams per liter; LabTurb = laboratory turbidity (Hach 2100AN); Turb15 = in-situ turbidity from either DTS-12 or Hach Surface Scatter 7 in-situ probes. Turbidity units are Nephelometric Turbidity Units for laboratory turbidity and Hach Surface Scatter 7 and Formazin Nephelometric Units for DTS-12.

Table 5.1 (cont'd). Results of regression analyses between discharge (Q) and suspended sediment concentration (SSC), laboratory turbidity (LabTurb), and in-situ turbidity (Turb15) at six stations in the upper Esopus Creek watershed. See Figure 5.1 for locations.

Independent	Dependent	r^2	P	n	Equation
Station: Woodland Creek at Phonecia– DTS-12					
Q	SSC	0.68	<0.001	86	$SSC = 0.38 \times Q + 27.8$
Q	LabTurb	0.57	<0.001	81	$LabTurb = 0.31 \times Q + 35.8$
Q	Turb15	0.30	<0.001	22,345	$Turb15 = 0.26 \times Q + 2.8$
LabTurb	SSC	0.79	<0.001	79	$SSC = 2.4 \times LabTurb - 100.6$
Turb15	LabTurb	0.98	<0.001	17	$LabTurb = 0.90 \times Turb15 + 1.92$
Turb15	SSC	0.65	<0.001	17	$SSC = 1.2 \times Turb15 + 15.9$
Station: Birch Creek - DT-12 and Hach Surface Scatter 7 data were combined for Turb15 values for regressions with LabTurb and SSC due to low sample numbers					
Independent	Dependent	r^2	P	n	Equation
Q	SSC	0.75	<0.001	104	$SSC = 2.74 \times Q - 91.0$
Q	LabTurb	0.65	<0.001	91	$LabTurb = 0.95 \times Q - 12.2$
LabTurb	SSC	0.79	<0.001	85	$SSC = 2.3 \times LabTurb + 9.6$
Turb15	LabTurb	0.99	<0.001	11	$LabTurb = 0.68 \times Turb15 + 0.40$
Turb15	SSC	0.99	<0.001	12	$SSC = 1.0 \times Turb15 - 4.4$
DTS-12 only					
Q	Turb15	0.62	<0.001	11,223	$Turb15 = 1.65 \times Q - 5.2$
Hach Surface Scatter 7 only					
Q	Turb15	0.29	<0.001	6,920	$Turb15 = 0.40 \times Q - 2.4$

Q = discharge, in cubic feet per second; SSC = suspended sediment concentration, in milligrams per liter; LabTurb = laboratory turbidity (Hach 2100AN); Turb15 = in-situ turbidity from either DTS-12 or Hach Surface Scatter 7 in-situ probes. Turbidity units are Nephelometric Turbidity Units for laboratory turbidity and Hach Surface Scatter 7 and Formazin Nephelometric Units for DTS-12.

5.2. Behavior of Dissolved and Total Phosphorus in Relation to Stream Discharge: The Form of Hysteresis During Storm Events

Introduction

Nutrient pollution in surface and groundwater is of major concern in the many streams of the US and worldwide. Routine measurement of nutrient concentrations is important in determining the nutrient status of a river. However, monitoring alone does not provide enough information on the sources of these nutrients. Many studies have used export coefficients to estimate total diffuse pollutants at the watershed scale (Endreny & Wood 2007; Hanrahan et al. 2001; Johnes 1996; May et al. 2001). Since these studies are specific to certain areas, the export coefficients reported are not applicable universally. Water quality modeling is also often used to identify source areas of nutrient and sediments (Easton et al. 2008; Easton et al. 2009; Reckhow et al. 1980; Schneiderman et al. 2002; Sharpley et al. 2002; Sharpley et al. 2006; Vadas et al. 2008). Another approach that is widely used in sediment studies is the analysis of hysteresis behavior of pollutants during storm and non-storm events (Andrea et al. 2006; Bowes et al. 2005; Evans & Davies 1998; House & Warwick 1998; Minella et al. 2011; Siwek et al. 2012; Stutter et al. 2008). Hysteresis describes a constituent concentration curve that is offset from its corresponding hydrograph, nutrient sediment delivery, and source areas. Variations of concentrations of pollutants in streams during events often result in a hysteresis effect, with difference concentrations during the rising and falling limbs of the hydrograph (Bowes et al. 2005). The shape and length of the particular hydrograph limbs vary for events, land use and watersheds. Based on single event analysis, Williams (1989) identified five possible forms of concentration and discharge (hereafter denoted as c-q) curves (Table 5.2).

This study illustrates and analyzes c–q hysteresis of TDP and TP in West Branch Delaware River (WBDR) located in Beerston, NY from 1999-2003 (5 year period, 90 events). TDP and TP typically increased in concentration at high discharges due to the mobilization of reactive nutrients stored in agricultural, forest and riparian top soils during rains (Fiebig et al. 1990; McGlynn & McDonnell 2003; Sickman et al. 2003). However, discharge explains only a small fraction of the temporal variability in nutrient concentrations in this river (Bernal et al. 2002). In addition, bio-geochemical catchment scale models have so far been unable to capture satisfactorily this variability in nutrient response Bernal et al. 2004).

The first objective of this study was to examine whether the variability of the hysteresis forms of TDP and TP, could be clustered following a general scheme. The second objective was to explore the influence on main features of TDP and TP hysteresis, in the WBDR, of storm hydrology and antecedent hydrological conditions. General features of TDP-q and TP-q hysteresis were described using two simple descriptors that summarized their changes in concentration, trends, rotational patterns and hysteresis areas. The latter , i.e., hysteresis patterns indicate the hydrological mixing of water flow components during storm events (Evans & Davies 1998; Hooper 2003) and investigates influence of phosphorus hysteresis during storm events and relationship to antecedent hydrologic conditions to understand nutrient flushing and dilution processes.

Table 5.2. Classes and criteria of c-q relations (Adapted from Williams, 1989)

Class	Relations	c/q criteria	Reference
I	Single-valued line	$(c/q)_r \cong (c/q)_f$	Wood (1977)
	A. Straight Line	A. Slopes of two subsections of the overall relation are equal	
	B. Curve, slope of which increases with increasing values of q	B. Slopes of two subsections of the overall relation are unequal - steeper for larger values of q	-
	C. Curve slope of which decreases with increasing values of q	C. Slopes of two subsections of the overall relation are unequal – flatter for larger values of q	
II	Clockwise loop	$(c/q)_r < (c/q)_f$ for all values of q	Paustian and Beschta (1979)
III	Counterclockwise loop	$(c/q)_r > (c/q)_f$ for all values of q	Axelsson (1967)
IV	Single line plus a loop	$(c/q)_r \cong (c/q)_f$ for one range of q values $(c/q)_r >< (c/q)_f$ for other range of q values	-
V	Figure eight	$(c/q)_r > (c/q)_f$ for one range of q values $(c/q)_r < (c/q)_f$ for other range of q values	Arnborg et al (1967)

$(c/q)_r$ = (c/q) on hydrographs's rising limb; $(c/q)_f$ = (c/q) on hydrograph's falling limb, paired to a particular (c/q).

Methods

Data Analysis

The described biogeochemical parameters include:

(a) A parameter describing the relative changes in concentration during the storm event (dC%), using the following formula:

$$dC = (Cp-Cb)Cmax*100 \quad (5.1)$$

where Cb is the concentration at base flow, Cp is the concentration during peak flow, Cmax is the highest observed concentration during the storm event. dC can range from -100 to +100. Negative dC indicates the effect of concentration dilution during storm events, whereas the positive dC indicates the positive trend for c-q hysteresis and also the effect of solute flushing.

(b) A parameter that integrates information about the area and rotational pattern of the c-q hysteresis loop (dR%) using the formula:

$$dR = R*Ac*100 \quad (5.2)$$

where R describes the rotational pattern of the loop. Three possible values for this loop are +1 for clockwise rotation, -1 for anticlockwise rotation, and 0 for loops with unclear rotation. Ac describes the area of the *c-q* loop. This area is estimated using the trapezoidal method after

standardizing the *c-q* values to a unity scale. The variability of the concentration and discharge hysteresis descriptors for different pollutants were explored in the unity plane of dR vs. dC. In the plane, four regions can be identified (Figure 5.4).

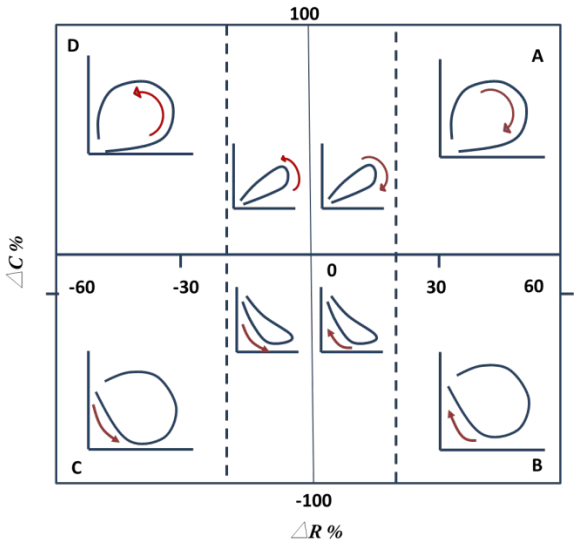

Figure 5.4. Schematic representation of the unity plane △R vs. △C. In this plane, four regions can be identified. In region A (△C>0, △R>0), are located the c–q hysteresis with clockwise rotational pattern and with a general positive trend (i.e. solute flushing during the discharge rising limb). Region B (△C<0, △R>0) describes c–q hysteresis with a clockwise rotational pattern but with a general negative trend (i.e. solute dilution during the recession discharge limb). Region C (△C<0, △R<0) describes the c–q hysteresis with a counterclockwise rotational pattern and with a general negative trend (i.e. solute dilution during the discharge rising limb). Region D (△C>0, △R<0) describes c–q hysteresis with a counterclockwise rotational pattern but with a general positive trend (i.e. solute flushing during the recession discharge limb).

Hydrological parameters characterize the hydrograph formation for particular storm events. These parameters include:

(a) The magnitude of the storm event relative to the baseflow

$$dQ_T = (Q_P - Q_B)/Q_B \quad (5.3)$$

where Q_P is the peak streamflow during the storm event (m^3s^{-1}),and Q_B is the baseflow (m^3s^{-1}) ;

(b) The slope of the initial phase of the hydrograph recession limb denoted by *k*.;

(c) The maximum discharge during the previous storm event denoted by dQ_{t-1} (m^3s^{-1});

(d) The time since the last storm denoted by t (days);

(e) The total amount of precipitation during the storm event, P (mm);

(f) The precipitation amount during the last storm event, P_{t-1}.(mm); and

(g) The ratio between the length of the rising limb and the falling limb of the storm hydrograph denoted by Q_r:Q_f.. The Q_r:Q_f values greater than 1 indicate a slower increase in runoff during the storm event and also a steeper decrease in the falling limb of the storm hydrograph.

Statistical Analysis

The pollutant concentrations versus discharge relationships of all events were plotted in a semi-logarithmic plot in which discharge had been log-transformed (Newbold et al. 1997). Regression fitting was considered significant at $p < 0.05$.

Results and Discussions

The response of storm episodes differ widely for total dissolved phosphorus and total phosphorus. On our study sites, phosphorus concentrations typically increased during events suggesting that these patterns are driven by similar hydrochemical mechanisms (Bowes et al. 2005; Stutter et al. 2008; Verstraeten & Poesen 2002). Overall, the temporal patterns of the phosphorus concentrations were similar in the study site, however hysteresis behavior was not consistent resulting in random patterns... The flood event sometime may consist of multiple peaks creating situation of a non-unique concentration for a given stream discharge resulting in many relationships with no distinct shape, i.e., infinite loop. In the classic mixing model with two input components (baseflow and stormflow), a *c-q* hysteresis of a conservative tracer with a small hysteresis area or/and unclear rotational pattern indicate the near co-occurrence of the hydrological input components generating the storm water in the stream. The TDP increased for most of the storm events and therefore data points of TDP-q hysteresis were located exclusively in the region of A and B of the unity plane of dR vs. dC (Figure 5.4). The rotational pattern of TDP-q hysteresis ranged from clockwise ($dR > 0$) pattern to counter-clockwise ($dR < 0$) , with

many located on the zero plane (dR=0) where no distinct patterns could be discerned (Figure 5.5a). On the other hand, the rotational pattern of TP-q exhibited clockwise (dR >0) pattern, with many located on the zero plane where no distinct patterns could be discerned. Very few storm events showed counter-clockwise hysteresis pattern for TP (Figure 5.5b). The dispersion of TDP-q was markedly larger than that of TP-q hysteresis although there is no evidence of TDP dilution (i.e., dC <0) and hence no significant regression fitting could be obtained.

The differences in storm event intensity can have substantial effect on the nutrient flushing. However, even with a large number of storm events studied, there was no clear response patterns to storm magnitude for both TDP and TP (Figure 5.6a,b). Out study indicates that there is a remarkable variability in TDP and TP-q hysteresis forms and rotational patterns, both among the storm events and between the nutrients. The humid climate of the study region is characterized by a marked within and between year variability, with a summer dry period which has strong effect on both the hydrology and biogeochemistry streams. Uncertainty associated with TDP and TP-q hysteresis and rotational patterns in our study prevented us from reaching to a general hydrological and biogeochemical explanation for temporal dynamics in the study site during storms events. This contrasts with the typically consistent clockwise for other nutrients such as DOC and NO_3-q hysteresis observed in Alpine catchments in response to snowmelt (Carey 2003; Hornberger et al. 1994), or in steep and wet small catchments (McGlynn & McDonnell 2003). The randomness of rotational patterns of and hysteresis form may be better understood through further analysis of seasonal behavior of TDP and TP-q behaviors.

Conclusions

A complete understanding of the variability in solute concentrations during storm events is dependent on stream watershed biogeochemical interactions and of pollutants origin in stream waters. Relationship between discharge and solute concentration during storm events often exhibit cyclic trajectories. This study illustrated and analyzed c-q hysteresis at WBDR from 1999-2003 (5 yr period, 90 events). TDP typically increased in concentration at high discharges due to the mobilization of reactive solutes stored in agricultural top soil during rains. The characteristics of storm hydrograph, particularly the relative duration of the rising limb, and the magnitude of antecedent storm events may be useful parameters in describing changes in concentration of TDP and TP in the WBDR site. Discharges alone did not adequately explain the temporal variability in solute concentration.

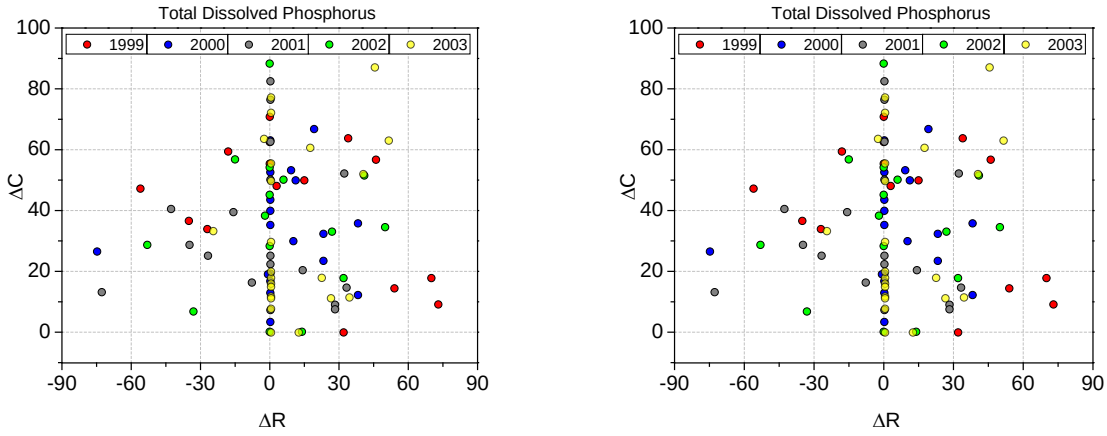

Figure 5.5. Representation of the c–q hysteresis characteristics of (a) TDP and (b) TP in the unity plane △R vs. △C.

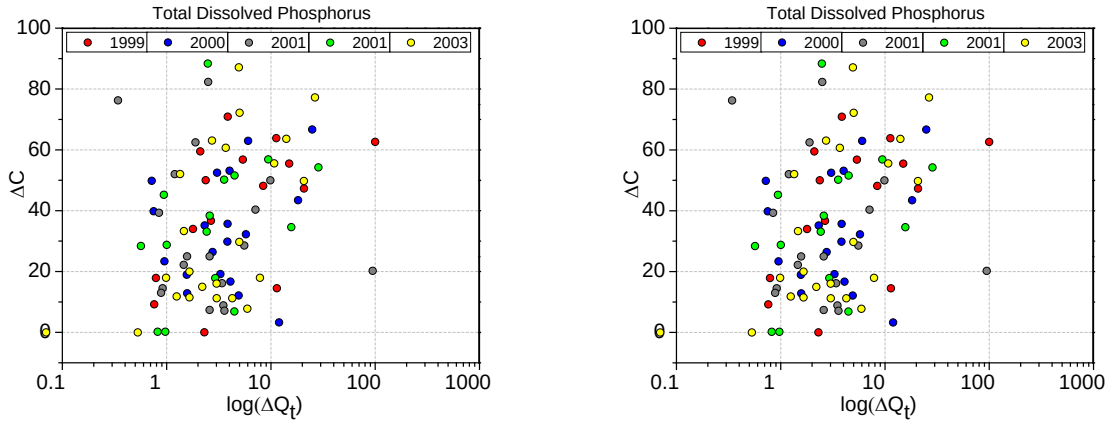

Figure 5.6. Relationships between storm discharge increase (△Qt) and the relative nutrients concentration changes (△C) observed in the study sites for the nutrients (a) TDP and (b) TP concentrations.

5.3. Precipitation and Snowfall Trends in NYC Watersheds and Northeastern US

Introduction

The Northeastern United States (US), located between 38^{o}N and 48^{o}N and 82^{o}W and 66^{o}W, has recently experienced noticeable winter warming that has led to numerous changes in the region's ecosystems, hydrology, and economy. Changes in regional hydrology include earlier peak spring river flow (Hodgkins et al. 2003), earlier river (Hodgkins & Dudley 2006) and lake ice-out (Hodgkins et al. 2002), and decreases in river ice thickness (Huntington et al. 2003). Recent warming of surface air temperatures across New England has been well documented (Trombulak & Wolfson 2004). Warmer spring temperatures are linked to significant reductions in mid-latitude northern hemisphere snow cover extent (SCE) from 1966 to 2005 during the months of March and April, as identified from satellite-based data (Lemke et al. 2007). Analysis of snow to total precipitation (S/P) ratios in northern New England over the period 1949–2000 indicates that most of the 0.30 to 0.23 decrease in S/P ratio has occurred since 1975 (Huntington et al. 2004). Snow cover duration in the NE-US was found to be strongly correlated with temperature during that time period. Changes in snow cover can be an important indicator of climate change at the regional scale because of its strong influence on the surface radiation balance and its resulting impact on surface air temperatures (Lemke et al. 2007).

Detailed analysis of winter climate trends is essential to understanding the cause of recent winter warming, and to evaluate the potential impacts on the northeastern United States. In this study, we analyze winter climate trends in snowfall, temperature, and snow cover data over the period 1965–2005. Because snowfall and the number of snow-covered days (SCD) in March often exceed December snowfall and snow-covered days in this region, winter trends include the months of December, January, February and March.

Data and Methods

Data Source

For this study, the northeastern United States includes Connecticut, Maine, Massachusetts, New Hampshire, New Jersey, New York, Pennsylvania, Rhode Island, and Vermont (Figure 5.7). In order to accommodate for maximum station density, daily snowfall, snow depth, and mean temperature data are compiled from the United States Historical Climate Network (USHCN) for the period of 1940 to 2010. The USHCN dataset consists of high-quality daily data set compiled by the National Climatic Data Center (NCDC), and is available for download at the Carbon Dioxide Information and Analysis Center (http:// cdiac.ornl.gov/ftp/ndp070/) (Easterling 2002; Williams et al. 2006). We used precipitation, temperature (minimum, maximum temperature and average temperature), snowfall, snow depth data from 65 USHCN stations in Northeastern United States (Figure 5.7) where continuous daily records were available to calculate annual or winter-spring (here defined as November through March) composite records (Easterling 2002; Karl et al. 1999; Williams et al. 2006). We also conducted winter spring center of volume analysis for streamflow data from 50 USGS stream gages across the Northeastern United States (Figure 5.7).

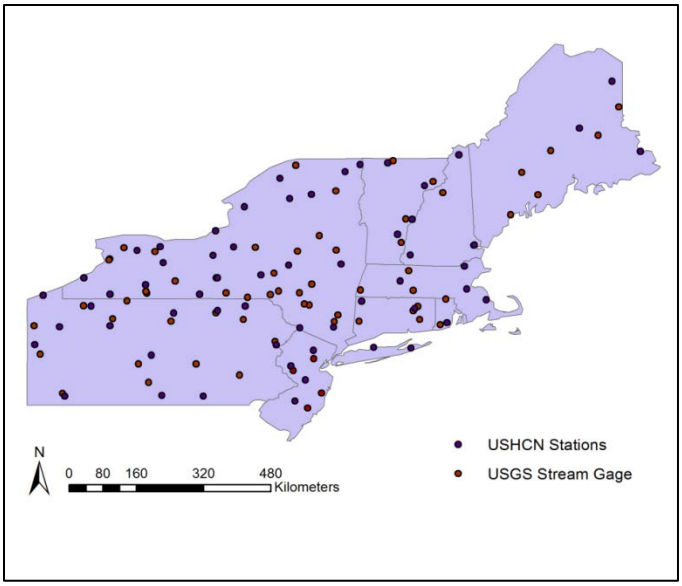

Figure 5.7. USGS gages and USHCN sites within Northeastern United States

Data Analysis

For each station, seasonal (November of one year through March of the following year) and monthly time series are computed for the following climate variables: (1) total snow water equivalent (SWE), (2) winter-spring precipitation total, (3) ratio of SWE to precipitation for the period of winter-spring, (4) minimum temperature, (5) maximum temperature, (6) mean temperature, and (7) winter-spring center of volume (WSCV) for 50 USGS stream gage data. The WSCV is defined as the Julian date (sequential day of year) on which 50% of the total runoff volume that occurs over the period January 1st through May 31st has passed the stream gage. This variable has been shown to be sensitive to late winter/early spring air temperature (Dudley and Hodgkins, 2002, Hodgkins et al., 2003).

Trend Analysis and Sen's Slope

In the study, we used trend analysis by using non-parametric Mann-Kendall test and Sen's slope estimator. Sen's method proceeds by calculating the slope as a change in measurement per change in time. This is a statistical method which is being used for studying the spatial variation and temporal trends of hydro-climatic data series. The significance of trends is evaluated by computing p-values for Pearson's correlation of the time series, for which the assumption of normality was satisfied by inspecting residuals. Station trends with $p < 0.10$ for all 70-year trends were considered statistically significant.

Results and Discussions

Time Series Analysis

Out of 55 USHCN sites, 49 sites in the Northeastern United States showed a decrease in the SWE to precipitation (PCP) ratio. However, this decrease in SWE:PCP was significant for only 21 sites. We analyzed S/P ratio for trends in individual months to determine which months had the strongest trends. For the 55 sites, March and January had significant decreasing trends in SWE to PCP ratio. The trend was pronounced for March compared to January. When averaged across the Northeastern US, the SWE:PCP ratio showed a significant decrease from 1940 to 2010 (Figure 5.8a). Similar observations were made for the SWE estimate (Figure 5.8b). This suggests that the annual and winter trends are driven in large part by changes in SWE: PCP during the winter season when temperatures are more frequently near freezing. Most of the coastal or near-coastal sites showed no significant trends in winter-spring SWE to PCP ratio. Comparisons with other recent studies showing hydrologic responses to climate variability indicated some consistent geographic patterns in responses within New England. Northern New England had the most consistent trends in annual S/P ratio and also had the most consistently significant trends in earlier (by 1 to 2 weeks during the 20th century) high spring flows (Hodgkins et al. 2003). These northern regions that had the largest trends towards decreasing S/P ratio and earlier high spring flows have substantially greater snow accumulation, thus warming would have a greater impact on snowmelt- (and rain on snow-) driven runoff than in more southerly regions (Pradhanang et al. 2013).

Decreasing S/P ratio could be explained by snowfall decreases that were proportionately larger than decreases in rainfall, by constant snowfall and increasing rainfall, or increases in both, but larger increases in rainfall than snowfall. We tested for temporal trends in total annual and total winter precipitation, and we tested for trends in total snow water equivalent to determine which could best explain the observed trends in S/P ratio. Analysis of precipitation data for the Northeast shows that, over the period of 1940-2010, the mean annual precipitation was 103.6 mm, calculated by taking an area weighted mean of the climate divisions represented in the region. The regional average annual precipitation for the 55 stations across the Northeast has an overall increasing trend of 105 mm from 1940 – 2010 (Figure 5.10). Figure 5.10 shows the trend of annual precipitation across the Northeastern US. The trend for the average precipitation during winter-spring period for the Northeast is also positive.

Total annual SWE and winter SWE for the period 1940 through 2010 showed a significant increase during November and decrease in March, but exhibited weak but insignificant decreasing trends during December, January and February. Significant trends towards decreasing snowfall is the dominant factor in explaining the significant decrease in SWE to PCP ratio. In this northern region, the weak trend towards increasing precipitation also contributes to the observed trends in decreasing SWE to PCP ratio. Winter temperatures have increased substantially in the northeastern United States, with the most warming occurring in the months of January and February for minimum, average, and maximum temperatures. Our study showed an increasing trend of winter-spring average temperature trends for the Northeastern United states (Figure 5.11). It has been suggested that climate warming may result in increased precipitation, temperature and increased snowfall in many northern temperate latitude areas (McCarthy et al.

2001). Out study showed similar results for increase in temperature and increase in snowfall for certain areas up in the northern region.

Conclusions

Winter temperatures have increased substantially in the northeastern United States, with the most warming occurring in the months of January and February for minimum, average, and maximum temperatures. Statistically significant decreasing trends in monthly snowfall were identified in January and March records, although all other months showed slight decrease in trends. These documented changes in wintertime climate have and will continue to have an impact on the region's natural ecosystems and hydrology.

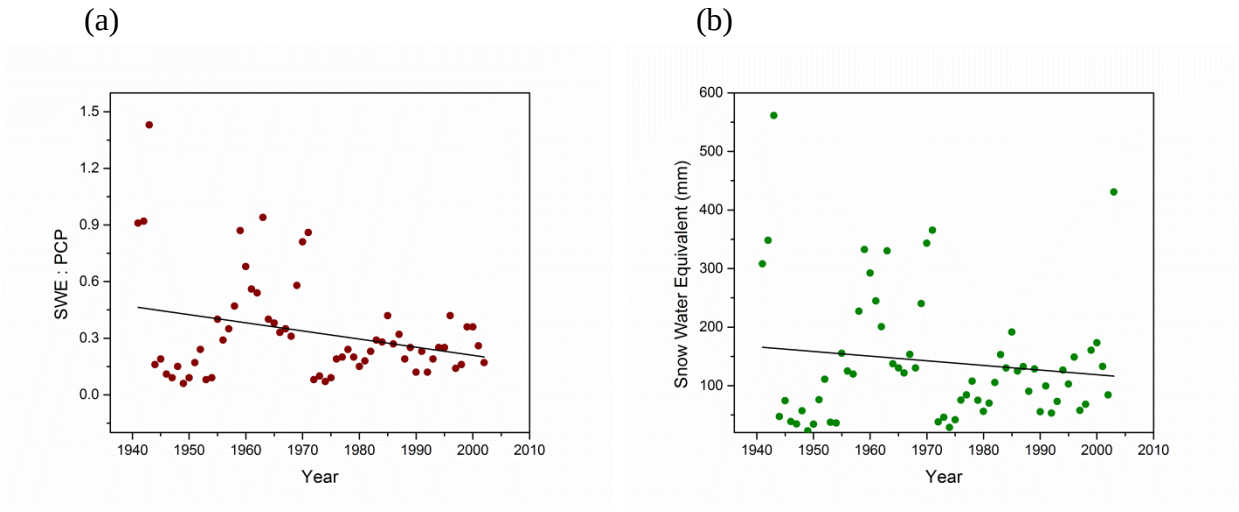

Figure 5.8. a), Trend of Snow Water Equivalent (SWE) to Winter-Spring precipitation (mm) ratio and b), Snow Water Equivalent (SWE) (mm) trends for USHCN sites within Northeastern United States

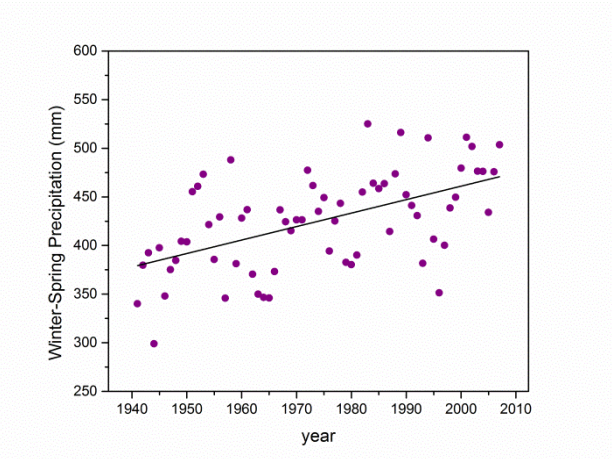

Figure 5.9. Winter-Spring total precipitation (mm) trends for USHCN sites within Northeastern United States

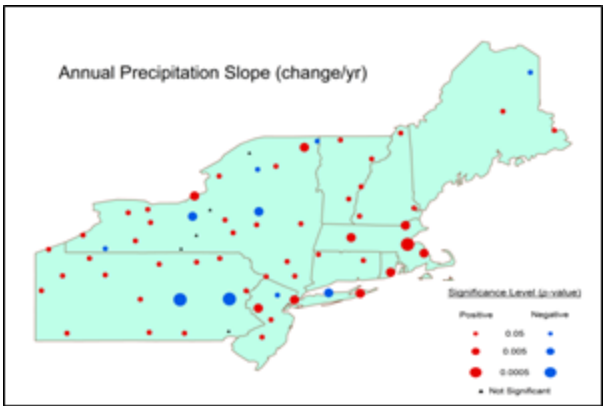

Figure 5.10. Slope change in annual total precipitation for USHCN sites within Northeastern United States

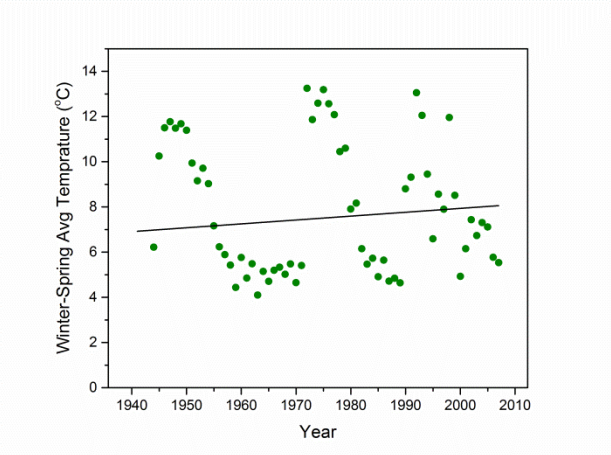

Figure 5.11. Winter-Spring average temperature trends for USHCN sites within Northeastern United States

6. Model Data Acquisition and Organization

6.1. GIS Data Development for Modeling

Water Quality Monitoring Sites

Additional locations were added throughout the reporting period to the ArcSDE point feature class of DEP water quality monitoring sites. The dataset is comprised of stream, reservoir, keypoint, waste water treatment plant, and other DEP water quality monitoring sites included in the Laboratory Information Management System (LIMS).

Stream Power

Rasters of flow direction and flow accumulation were created for each WOH reservoir basin from the newly-acquired 1-meter DEM in order to expand work on using ArcGIS ModelBuilder to derive values of stream power as a function of stream gradient and stream discharge, for tributaries throughout the watershed. This work may more accurately identify stream reaches of potentially increased erosion that merit field investigation.

Miscellaneous

Additional data development efforts and mapping support were provided throughout the reporting period to various members of the DEP Water Quality Modeling Section, the Division of Watershed Water Quality Science and Research, and the Water Quality Directorate. A majority of this support was related to preparation of DEP reports, peer-reviewed publications, conference posters, and conference presentations. Such events included the annual Watershed Science Technical Conference, the Eastern Snow Conference, and the annual meeting of the American Geophysical Union, among others.

6.2. Ongoing Modeling/GIS Projects

Bathymetric Survey of NYC Water Supply Reservoirs

An Intergovernmental Agreement with USGS to provide bathymetric surveys of the six West of Hudson reservoirs, last surveyed in the mid- to late-1990s, was approved in August 2013. Survey work was completed for Ashokan West and approximately one-half of Rondout during the fall fieldwork season. Work on the remaining reservoirs will be undertaken in 2014 and early 2015. Final products are to include a TIN surface model of reservoir bottom, 2-foot elevation (depth) contours, and an updated elevation-area-capacity table for each reservoir. Undertaking the work as an Investigative Study, USGS will prepare a final report, available online, in which a map sheet for each water body describes the survey methodology, includes at least a portion of the updated capacity tables, and graphically presents reservoir bottom surface and contour data.

Watershed Atlas

Work continued towards completion of a New York City Watershed Atlas with incorporation of the newly-acquired 2009 Land Cover / Land Use data and updated basin/sub-basin boundaries delineated from the new 1-meter DEM.

6.3. Time Series Data Development

An inventory of the necessary raw time series data for watershed and reservoir model input and calibration is presented in Tables 6.1 and 6.2, respectively. The time series data includes meteorology, streamflow, water quality, and point source loads for watershed models. For reservoir models the data includes meteorology, streamflow, stream, reservoir and key point water quality and reservoir operations. Data sets are updated as new data become available. Lag times between the current date and the dataset end dates are the result of QA/QC processes at the data source and/or procurement timelines driving the acquisition of any purchased data.

For this reporting period, the Northeast Regional Climate Center (NRCC) Meteorology, NYCDEP Stream and Limnology Water Quality, and NYCDEP Key Point through calendar year have either become available via online sources and/or have been added to the inventory.

The NYSDEC Water Quality data has provided the Modeling Group with a robust dataset from baseline and storm event sampling of the West Branch of the Delaware River at Beerston from 1992 to the 2010. NYCDEP has taken over the collection and analysis of samples from this site and, as such, the data from this site are now included in the NYCDEP Water Quality dataset. Historically the NYSDEC has collected the samples and calculated the nutrient loads. That role has transitioned over to the NYCDEP which is currently calculating the nutrient loads from WY 2010 to WY2013.

The NRCC Meteorological Data is now also available via the NRCC's Applied Climate Information System (ACIS). ACIS is a data access system developed by the NRCC to assist in the dissemination of data. In addition to access to updated data from the NRCC cooperative stations the ACIS will provide access to gridded meteorological data sets.

Table 6.1. Inventory of data used for watershed modeling.

Data Type	Data Source	Data Description	Dates*	Modeling Needs
Meteorology	Northeast Regional Climate Center	Daily Precipitation and Max/Min Temperature	Pre 1960-2012	Model Input
Wastewater Treatment Plants	DEP	Monthly WWTP Nutrient Loads	1990-2009	Model Input
Streamflow	USGS	Daily and Instantaneous Streamflow	Period of record available online via USGS	Hydrology Module Calibration / Nutrient and Sediment Loads
Water Quality	DEP	Routine and Storm Stream Monitoring	Period of record avail. via LIMS	Nutrient and Sediment Loads for Water Quality Calibration
	NYSDEC**	Stream Monitoring at West Branch Delaware River	1992-2010 w/ recent years avail. via LIMS	Nutrient and Sediment Loads for Water Quality Calibration

*Dates represent total span for all data sets combined. Individual station records vary.
**Now part of the DEP Water Quality dataset.

Table 6.2. Inventory of data used for reservoir modeling.

Data Type	Data Source	Data Description	Dates*	Modeling Needs
Meteorology	DEP	Air Temp., Relative Humidity, Solar Radiation., PAR, Wind Speed, Wind Direction, and Precipitation	1994-June, 2010	Model Input
Key Point and Reservoir Operations	DEP	Tunnel Water Quality, Flow and Temp.; Reservoir Storage, Spill, Withdrawal, and Elevation	Period of record avail. via LIMS	Model Input
Streamflow	USGS	Daily and Instantaneous Streamflow	Period of record available online via USGS	Model Input
Stream Hydrology	DEP	Stream Water Quality, Flow and Temperature	Period of record avail. via LIMS	Model Input
Limnology	DEP	Reservoir Water Quality, and Temperature Profiles	Period of record avail. via LIMS	Model Input

*Dates represent total span for all data sets combined. Individual station records vary.
.

7. Modeling Program Collaboration

7.1. Participation in Ongoing External Research Projects

In the last year, the Water Quality Modeling Section has participated in several projects related to the Section's ongoing work on testing and improving models simulating watershed hydrology and water quality, reservoir water quality and reservoir system operations. A number of projects also supported Water Quality Modeling Section evaluation of climate change as outlined in DEP's Climate Change Integrated Monitoring Project (CCIMP).

Water Research Foundation Project 4262 - Vulnerability Assessment and Risk Management Tools for Climate Change: Assessing Potential Impacts and Identifying Adaptation Options
Collaborators: Hazen and Sawyer, National Center for Atmospheric Research, Hydrologics, Stockholm Institute, Rand Corporation.

The main focus of the CCIMP is to identify potential climate change impacts on the water supply using the structured quantitative framework of water quality models. Project 4262 complements the CCIMP by going one step further. Once climate change impacts have been identified this project seeks to develop risk management approaches that will help managers prioritize risks and decide on a course of action. This project focused on climate change impacts related to turbidity and water availability, and made use of climate and streamflow scenarios developed as part of the CCIMP. Through an iterative modeling process, using the DEP OASIS and CE Qual W2 models, water supply vulnerability was examined in relationship to uncertainties~~,~~ in future climate, stream turbidity relationships, and water supply demand. The project confirmed that under present conditions dynamic system operations remain an effective turbidity control measure. The project also showed that system vulnerability is sensitive to changes in future water supply demand and the erosional processes controlling the turbidity inputs to the reservoirs (as captured in present models by turbidity vs. flow relationships). This project ended in April 2013. A more detailed description of our contribution is given in Section 3.5 of this report.

Water Research Foundation Project 4306 – Analysis of Reservoir operations under Climate Change
Collaborators: Hazen and Sawyer, National Center for Atmospheric Research, Hydrologics.

WRF project 4306 evaluated the possibilities of adapting and modifying reservoir operation policy to mitigate the impacts of climate change on water supply quantity and quality. This project tested methodologies needed to systematically evaluate and update operational policies in response to a changing climate, by working with 6 water utilities as test cases. For NYC the project is closely related to WRF project 4262, and the same Water Quality Modeling Section future climate and stream flow scenarios used in project 4262 were also used here. The main difference between these projects is that 4306 focused more on the possibility of improving outcomes through better reservoir operation rules that make use of inflow forecasts (dynamic rules) whereas 4262 focused on identifying uncertainty in the modeling assumptions that would lead to unacceptable levels of system vulnerability. This project reached similar conclusions as

4262 regarding the resiliency of the NYC water supply to a range of hydrologic conditions and confirmed that uncertainty in water demand and stream turbidity response affected levels of resilience. Incorporation of inflow forecasts into dynamic reservoir operating rules (as is being done by the OST) was shown to improve water supply operation. This project ended in April 2013. A more detailed description of our contribution is given in Section 3.6 of this report.

Water Utility Climate Alliance (WUCA) Piloting Utility Modeling Applications (PUMA)

WUCA is a group of ten of the nation's largest water utilities, whose mission is to improve research on the effects of climate change on drinking water supplies, and to help water suppliers to develop strategies to cope with the potential impact of climate change (http://www.wucaonline.org). The purpose of the PUMA project is: 1) to identify climate modeling tools and techniques that are appropriate for analysis of climate change impacts on water supplies; 2) develop guidelines for the use of climate data and model simulation data including methodologies for describing uncertainty; 3) to suggest how these data can be used to support water planning and decision making; 4) to build and enhance collaboration between water utilities and NOAA Regional Integrated Sciences and Assessment (RISA) centers; and 5) to identify future research investments that would serve the water utility community. The Water Quality Modeling Section has participated in the WUCA/PUMA project by attending the project kickoff meeting in December 2010, and by participating in regular phone conferences and planning meetings since then. The NYC water supply and the work undertaken as part of the CCIMP will be highlighted as a case study in a white paper that will be a product of the PUMA project. The NYC water supply provides a unique case study since climate change impacts expected for the Northeastern United States are more water quality related as opposed to the water quantity concerns that are more prevalent in the Western United States. Furthermore, financial support for the CCIMP (as part of FAD funding) is unusually generous allowing DEP to have one of the most extensive climate change research programs of any of the WUCA utilities. DEP is the only utility using post-doctoral support scientists to carry out much of its climate change research in house, whereas other utilities have instead to rely more extensively on contracts with outside consultants to evaluate climate change impacts. Information for the case study is being collected through a series of interviews and surveys developed by Status Consulting for WUCA. DEP was one of the first utilities to participate in the survey and during 2013 we were re-surveyed to follow our progress in the CCIMP.

NASA Earth Science Division, Applied Sciences Program. Application of evapotranspiration and soil moisture remote sensing products to enhance hydrological modeling for decision support in the New York City water supply.
Collaborator: CUNY CREST

This project is being led by the City University of New York (CUNY) Remote Sensing of the Earth Science and Technology (CREST) Center. The DEP Water Quality Modeling Section supported a research proposal developed by CUNY CREST that has been funded by NASA. The purpose of the project is to evaluate shortwave, thermal, and microwave remote sensing products that could provide DEP with independent and spatially variable estimates of soil moisture and

evapotranspiration. These remote sensing products will be used to test, calibrate and verify watershed hydrology models in the WOH region under present climate conditions.

Presently watershed model calibration and testing must be based on comparison with measured discharge and nutrient loads at the outlets of large watersheds in the WOH region, since these are the only data available for calibration purposes. While models can successfully simulate watershed scale outputs, there are multiple models processes that influence these outputs. The accuracy of model representations of such processes as evapotranspiration or soil water storage cannot at present be independently verified. Consequently even though watershed outputs are simulated with good accuracy, the simulated watershed processes can be in error since differing contributions from differing processes result in similar outputs. Correctly representing soil moisture and evapotranspiration in our watersheds models will be critical for simulating future changes in watershed hydrology, especially during summer periods when low flows and drought conditions could occur.

The project has been underway for approximately eighteen months. The DEP Water Quality Modeling Section has supplied a version of the GWLF-VSA watershed hydrology and water quality model used by DEP to CUNY CREST, and provided support in setting up and running the model. Initial comparisons between model output and the remote sensing products are encouraging. During 2013 the water quality modeling group has worked with CUNY CREST to develop improvements to the GWLF model and the model calibration that will allow it to better simulate the patterns of evapotranspiration that are measured using satellite remote sensing. A publication regarding this work is in preparation. During 2014 we intend to submit a second proposal that will provide support for an evaluation of the possibilities of using time series of satellite derived data as direct inputs to our watershed hydrology models.

NASA SMAP Early Adopter Project
Collaborator: CUNY CREST

The Soil Moisture Active Passive (SMAP) satellite is being developed by NASA and is scheduled for launch during November of 2014. The SMAP satellite mission focuses on measurements valuable to water resources using a combination of passive and active microwave sensors. Products include estimates of soil moisture and soil freezing which will be made at greater accuracy and at higher spatial and temporal resolution than with the current generation earth observing satellites. SMAP soil moisture data will therefore be of use to DEP for the reasons described in the CUNY CREST project immediately above, but will be of greater accuracy and improved resolution. Changes in the timing and extent of soil freezing is an expected effect of climate change in the WOH water supply watersheds, and changes in soil freezing have documented effects on watershed hydrology and biogeochemistry. Monitoring soil freezing will therefore be of importance for monitoring the impacts of climate change, and for providing data to develop and test simulation models that include processes affecting soil freezing. During 2012, CUNY CREST and DEP were chosen to be early adaptors of SMAP data products. During 2013, CUNY CREST, has evaluated the synthetic sensor products, and has become familiar with the expected satellite file format and grid resolution prior to the satellite launch. As early adopters, we expect to begin testing the SMAP data products in late 2014 or

early 2015. This work is clearly complementary to the project above and ensures that DEP will be able to rapidly make use of the SMAP data products as soon as they become available.

7.2. Modeling Program Contract Management

During 2013 the Water Quality Modeling Section managed three external contracts that support our work. These contracts provide data that are used for testing, calibrating and verifying models, and provide support for the development and testing of models used by the modeling section. In the case of the contract with the research foundation of the City University of New York (CUNY-RF), support for model and data development is provided by post-doctoral scientists who work with the Water Quality Modeling section on a day to day basis. These contacts are described below.

Contractor: Upstate Freshwater Institute.
Contract Title: Short-term Variations in Temperature and Turbidity at Shandaken Tunnel Intake: Internal Wave Activity in Schoharie Reservoir

During the summer of 2013 periodic variations in the turbidity and temperature of water discharged to the Esopus Creek from Schoharie reservoir were recorded. These variations were occurring on approximately a diurnal time scale and could be as large as 50-100 NTU. Neither variations in reservoir operations nor the timing of storm events could provide a good explanation for the observed short-term variations in turbidity. Given the short term and highly periodic nature of the variations in turbidity, DEP hypothesized that they could be related to internal seiche movement in the reservoir, which was apparently resulting in turbidity rich water being withdrawn from the reservoir to the Shandaken tunnel. The purpose of this project was to further evaluate the validity of this hypothesis through data analysis and the use DEPs reservoir turbidity transport model for Schoharie reservoir. The report was completed in early 2014, and confirmed that the internal seiche was responsible for the observed fluctuations in water temperature. Spectral analysis of the fluctuations in water temperature identified periods of fluctuation related to the periodicity of north-south winds. Model simulation accurately reproduced the variations in water temperature, as a result of internal seiche movement. The model was unable to simulate the periodic variations in turbidity;, presumably due to the fact the sediment resuspension related to seiche induced turbulence is not included in the model.

Contractor: United States Geological Survey.
Contract Title: Turbidity and Suspended Sediment Monitoring in the Upper Esopus Creek Watershed, Ulster County, NY

This contract involved involves retrofitting the five existing USGS flow gauges in the Esopus Creek watershed to automatically monitor turbidity at high (15 min) frequency. These five stations provide a high frequency record of flow and turbidity that will allow the water quality modeling group to evaluate temporal and spatial variations in turbidity sources and transport within the Esopus creek watershed; develop improved turbidity vs. discharge rating relationships; and collect high quality data that can be used to develop and test watershed sediment erosion and transport models. This project ended in 2013.

Three years of data were collected at all sites monitored by this project and have been analyzed, The data have been used for model testing at the sub-basin scale in the Esopus creek watershed, and to evaluate the spatial and temporal variability in the turbidity vs. discharge, Total Suspended Solids concentration (TSS) vs discharge and the turbidity vs. TSS relationships. The final project report uses these data to evaluate the spatial variability of turbidity loading to the Ashokan reservoir. As in previous studies this study confirms that the Stony Clove sub-basin is consistently the greatest source of turbidity to the Ashokan reservoir. The turbidity loads from the remaining sub-basins, varied in importance from year to year as a consequence of differences in the sub-basin hydrologic conditions.

Contractor: Research Foundation City University of New York.
Contract Title: Scientific Modeling Support

This contract provides CUNY with the funding needed to hire seven post-doctoral research associates (post-docs) who are jointly advised by CUNY faculty, external faculty advisors, and DEP scientists. The post docs are stationed in Kingston, New York working with the Water Quality Modeling Section on a day-to-day basis. The positions are for an initial two year period, with the possibility of an additional two year extension. This project was originally scheduled to end in 2013, but has been extended in time to ensure that all of the hired post docs have a chance to use their full four year term of employment. The contract is now scheduled to end in August of 2014.

The contract post-doc positions are for

- Climate Data Analysis
- Reservoir system modeling
- Reservoir turbidity modeling
- Reservoir eutrophication modeling
- Watershed nutrient modeling
- Watershed sediment erosion and transport modeling
- Forest ecosystem modeling

This contract has been very successful leading to improved model applications, new and improved data sets including future climate scenarios used by the CCIMP and the development and test of new applications. To date 17 peer reviewed publications related to water quality modeling group work and the CCIMP have been authored by the CUNY post-docs. The sections of this report describing model applications, model development and data analysis benefited from the work of our post-doctoral scientists. Furthermore, many of the conference presentations made in the last year (Section 8.2) were the result of work by the post-doctoral scientists. One post-doctoral scientist has moved to full time employment with DEP.

7.3. Support of Applications for External Research Funding

All of the collaborative projects described above result from the Water Quality Modeling Section collaborating with universities and research institutes to prepare and submit grant applications to different research funding organizations. During 2013 the Water Quality Modeling Section has supported one additional grant application.

Use of NASA satellite data to improve model simulations of snow extent and snow water equivalent in the NYC Water Supply System
Principle Investigators: Allan Frei, CUNY Hunter College, and Dorothy K. Hall, NASA / Goddard Space Flight Center (GSFC)
Funding Agency: NASA

Snow makes up about 15% of the annual precipitation entering the New York City West of Hudson (WOH) water supply region. Although not a major proportion of the annual precipitation, snow plays and important role in defining reservoir operating policies, and changes in snow accumulation, melt and winter stream flow is one of the major expected effects of climate change on the WOH watersheds.

The main objective of this study will be to develop a methodology to utilize a variety of remote~~ly~~ sensing products, in combination with *in situ* observations and modeling results, to provide the most accurate possible estimate of snow cover in the WOH New York City watershed region. The project will focus on two primary snow cover parameters that are key to the management of the water supply. First, the spatial distribution of snow cover across the basin and second, the Snow Water Equivalent (SWE, the mass of water in the snowpack) of the watershed If successful, the data obtained will be used to better refine estimates of watershed snow accumulation and to test and improve modeling algorithms that simulate snow accumulation and melt.

8. Modeling Program Scientific Papers and Presentations

8.1. Published Work

Below is a listing of journal articles in which Water Quality Modeling Section members have been authors during the previous year. Copies of the articles are included in Appendix A of this report.

Anandhi, A., M. S. Zion, P. H. Gowda, D. C. Pierson, D. Lounsbury, and A. Frei. 2013. Past and future changes in frost day indices in Catskill Mountain region of New York. *Hydrological Processes* **27**(21):3094-3104.

Gelda, R. K., S. W. Effler, A. R. Prestigiacomo, F. Peng, A. J. P. Effler, B. A. Wagner, M. Perkins, D. M. O'Donnell, S. M. O'Donnell, and D. C. Pierson. 2013. Characterizations and modeling of turbidity in a water supply reservoir following an extreme runoff event. *Inland Waters* **3**:377-390

Matonse, A., and A. Frei. 2013. A seasonal shift in the frequency of extreme hydrological events in southern New York State. *Journal of Climate* **26:** 9577-9593.

Mukundan, R., D. C. Pierson, E. M. Schneiderman, D. M. O'Donnell, S. M. Pradhanang, M. S. Zion, and A. H. Matonse. 2013. Factors affecting storm event turbidity in a New York City water supply stream. *Catena* **107**:80-88.

Mukundan, R., N. R. Samal, D. C. Pierson, M. S. Zion, and E. M. Schneiderman. 2013. Turbidity in a New York City Water Supply Stream: Sensitivity to Projected Changes in Winter Streamflow. *Hydrologic Processes* **27**:3014-3023.

Mukundan, R., S. Pradhanang, E. Schneiderman, D.C. Pierson, A. Anandhi, M. Zion, A. Matonse, D. Lounsbury, and T. Steenhuis. 2013. Suspended Sediment Source Areas and Future Climate Impact on Soil Erosion and Sediment Yield in a New York City Water Supply Watershed, USA. *Geomorphology* 183:110-119.

Pierson, D. C., N. Samal, E. Owens, E. M. Schneiderman, and M. S. Zion. 2013. Changes in the Timing of Snowmelt, and the Seasonality of Nutrient Loading: Can Models Simulate the Impacts on Freshwater Trophic Status? *Hydrologic Processes* **27**:3083-3093.

Pradhanang, S. M., R. Mukundan, E. M. Schneiderman, M. Zion, A. Anandhi, D. C. Pierson, A. Frei, Z. M. Easton, D. Fuka, and T. S. Steenhuis. 2013. Streamflow responses to climate change: Analysis of hydrologic indicators in a New York City Water Supply watershed. *Journal of American Water Resource Association* **49:** 1308-1326

Pradhanang, S. M., E. M. Schneiderman, A. Frei, M. S. Zion, T. S. Steenhuis, and D. C. Pierson. 2013. Rain-On-Snow Events in New York. *Hydrologic Processes* **27**:3035-3049.

Samal, N. R., R. Mukundan, D. C. Pierson, R. K. Gelda, E. M. Schneiderman, M. S. Zion, and A. H. Matonse. 2013. Turbidity in a New York City Water Supply Reservoir: Sensitivity to Anticipated Future Changes in Winter Turbidity Loading. *Hydrologic Processes* **27**:3061-3074.

Schneiderman, E. M., A. H. Matonse, D. G. Lounsbury, S. M. Pradhanang, R. Mukundan, M. S. Zion, and D. C. Pierson. 2013. Comparison of Spatially-Distributed Snowpack Models for New York City Watersheds. *Hydrologic Processes* **27**:3050-3060.

Tilahun, S., R. Mukundan, B. Demisse, T. Engda, C. Guzman, B. Tarakegn, Z. Easton, A. Collick, A. Zegeye, and E. Schneiderman. 2013. A Saturation Excess Erosion Model. *Transactions of the American Society of Agricultural and Biological Engineers (ASABE)* 56:681-695.

8.2. Conference Presentations

During this reporting period members of the Water Quality Modeling Section have made presentations regarding our modeling activities at a number of scientific meetings. Below the presentations and associated abstracts are listed for each of the meetings.

American Geophysical Union Fall Meeting. December 2012. San Francisco, CA.

Samal, N. R., D. C. Pierson, E. Schneiderman, Y. Huang, E. M. Owens, and M. S. Zion. (2012). ***Sensitivity analysis on reservoir water temperature under future climate change scenarios using a hydrologic and hydrothermal model.***

Abstract:

Future simulations of reservoir water temperature based on three Global Circulation Models (CGCM3, ECHAM & GISS), and each of three emission scenarios (A1B, A2 and B1) for the 2081-2100 future period were developed using a lumped watershed model (Generalized Watershed Loading Functions-Variable Source model or GWLF-VSA) coupled to an one dimensional reservoir hydrothermal model. Global Circulation Model (GCM) simulated values of mean daily air temperature, wind speed, and solar radiation were used to produce change factors that were applied to a 39 year record of local meteorological data to produce future climate scenarios. Water temperature in two deep, drinking water reservoirs of the New York City Water Supply System (NYCWSS) was simulated considering the meteorological and watershed effects under present day climate data (baseline conditions) and future simulations (change factor adjusted baseline conditions). Stratification characteristics and hydrodynamic indices over this long period of simulation under future scenarios were examined. Model sensitivity analysis identified the dominant physical processes affecting the reservoir water temperature. These results can provide guidance for others simulating the effects of climate change on lake and reservoir hydrodynamics.

Pradhanang, S. M., E. Schneiderman, D. Pierson, and M. Zion. (2012). ***Climate Change Impacts on Stream Temperature in Catskill Mountain watersheds.***

Abstract:

Stream water temperature is an important physical attribute that has a direct impact on the organisms living in the water. A simple stream temperature model based on air temperature is developed and calibrated to a data-set from the streams of the Catskill Mountain region. Stream temperature – air temperature regression models can be used to characterize stream temperature in current conditions and to make estimates of the sensitivity of stream temperature to future increases in air temperature predicted by global climate models. Future climate scenarios are produced from General Circulation Models (GCMs) for the region under different emission scenarios. These are applied to the model as input data based on air temperature output from the GCM. The purpose of this study is to quantify potential climate change impacts on stream water temperature for the New York City water supply watersheds, and to assess possible impacts to aquatic ecosystems. Because water temperature is a critical component of in-stream nutrient processing, fish habitat, and plant productivity, changes in water temperature may affect aquatic ecosystem health.

American Geophysical Union Fall Meeting. December 2012. San Francisco, CA (cont'd)

Huang, Y. 2012. ***Multi-objective calibration of a reservoir model: aggregation and non-dominated sorting approaches.***

Abstract:

Numerical reservoir models can be helpful tools for water resource management. These models are generally calibrated against historical measurement data made in reservoirs. In this study, two methods are proposed for the multi-objective calibration of such models: aggregation and non-dominated sorting methods. Both methods use a hybrid genetic algorithm as an optimization engine and are different in fitness assignment. In the aggregation method, a weighted sum of scaled simulation errors is designed as an overall objective function to measure the fitness of solutions (i.e. parameter values). The contribution of this study to the aggregation method is the correlation analysis and its implication to the choice of weight factors. In the non-dominated sorting method, a novel method based on non-dominated sorting and the method of minimal distance is used to calculate the dummy fitness of solutions. The proposed methods are illustrated using a water quality model that was set up to simulate the water quality of Pepacton Reservoir, which is located to the north of New York City and is used for water supply of city. The study also compares the aggregation and the non-dominated sorting methods. The purpose of this comparison is not to evaluate the pros and cons between the two methods but to determine whether the parameter values, objective function values (simulation errors) and simulated results obtained are significantly different with each other. The final results (objective function values) from the two methods are good compromise between all objective functions, and none of these results are the worst for any objective function. The calibrated model provides an overall good performance and the simulated results with the calibrated parameter values match the observed data better than the un-calibrated parameters, which supports and justifies the use of multi-objective calibration. The results achieved in this study can be very useful for the calibration of water quality models of rivers and lakes. They can also be helpful for the calibration of other models, such as hydrological models.

Wang, L., R. Mukundan, M. Zion, and D. Pierson. 2012. ***Beyond Rating Curves: Time Series Models for in-Stream Turbidity Prediction.***

Abstract:

The New York City Department of Environmental Protection (DEP) manages and operates New York City's water supply, which is comprised of 19 reservoirs and supplies over 1 billion gallons of water per day to more than 9 million customers. DEP's "West of Hudson" reservoirs located in the Catskill Mountains are unfiltered per a filtration avoidance determination granted by the EPA. While water quality is usually pristine, high volume storm events occasionally cause the reservoirs to become highly turbid. A logical strategy for turbidity control is to temporarily remove the turbid reservoirs from service. While effective in limiting delivery of turbid water and reducing the need for in-reservoir alum flocculation, this strategy runs the risk of negatively impacting water supply reliability. Thus, it is advantageous for DEP to understand how long a particular turbidity event will affect their system. In order to understand the duration, intensity and total load of a turbidity event, predictions of future in-stream turbidity values are important. Traditionally, turbidity predictions have been carried out by applying streamflow observations/forecasts to a flow-turbidity rating curve. However, predictions from rating curves are often inaccurate due to inter and intra event variability in flow-turbidity relations. Fortunately, predictions can be improved by applying an autoregressive moving average (ARMA) time series model on top of a traditional rating curve.

Since 2003, DEP and the Upstate Freshwater Institute have compiled a relatively consistent set of 15-minute turbidity observations at various locations on Esopus Creek above Ashokan Reservoir. Using daily averages of this data and streamflow observations at nearby USGS gauges, flow-turbidity rating curves were developed via linear regression. Time series analysis revealed that the regression residuals may be represented using an ARMA(1,2) process. Based on this information, flow-turbidity regressions with ARMA(1,2) errors were fit to the observations. Preliminary model validation exercises at a 30-day forecast horizon show that the ARMA error models generally improve the predictive skill of the linear regression rating curves. Skill seems to vary based on the ambient hydrologic conditions at the issue of the forecast. For example, ARMA error model forecasts issued before a high flow/turbidity event do not show significant improvements over the rating curve approach. However, ARMA error model forecasts issued during the "falling limb" of the hydrograph are significantly more accurate than rating curves for both single day and accumulated event predictions.

In order to assist in reservoir operations decisions associated with turbidity events and general water supply reliability, DEP has initiated design of an Operations Support Tool (OST). OST integrates a reservoir operations model with 2D hydrodynamic water quality models and a database compiling near-real-time data sources and hydrologic forecasts. Currently, OST uses conventional flow-turbidity rating curves and hydrologic forecasts for predictive turbidity inputs. Given the improvements in predictive skill over traditional rating curves, the ARMA error models are currently being evaluated as an addition to DEP's Operations Support Tool.

70th Eastern Snow Conference. June 2013. Huntsville, ON

Samal, N. R., D. C. Pierson, H. Yao, K. D. Jöhnk, M. S. Zion, and L. Bruce. 2013. ***Preliminary simulations of ice formation and ice loss on some selected Lakes and Reservoirs in Northeastern North America.: Comparison of a simple and complex model.***

Abstract:

Long-term records of observed ice data from lakes and reservoirs are related to the variability of local climate and also provide robust indications of climate change. In the present investigation, ice phenology (timing of ice formation, loss and ice duration) is simulated for some selected lakes and reservoirs in Northeastern North America using a simple empirical model driven by daily measurements of air temperature and wind speed, and a complex deterministic water quality model which requires more detailed daily meteorological forcing and hydrological inputs. The more complex model includes simulation of lake snow cover and its effect on lake ice phenology. The results of both models are compared to historical measurement of the onset and loss of lake ice and we find that ice-on and off days are well reproduced by both models, even though the simple model does not make detailed calculations of the ice cover energy budget or the effects of snow on ice growth. Further, the relationship between the timing of ice off, and its relationship to the onset of thermal stratification and summer thermal structure is investigated. These initial comparisons are the first steps in a larger project to simulate the lake ice phenology in a large number of lakes spanning geographically extensive area under the umbrella of the Global Lake Ecological Observatory Network (GLEON).

Pradhanang, S. M., A. Frei, M. S. Zion, E. M. Schneiderman, and D. C. Pierson. 2013. ***Precipitation and Snowfall Trends in the Northeastern United States.***

Abstract:

Snowpack water storage and melt is an important component of annual runoff, recharge, and an important source to water supplies. The accumulation and melt of snow greatly affects water management in the northern United States. The water resources of the northeastern United States depend on snowpack water storage, but are also affected by interannual variations in the magnitude of snow accumulation and the partitioning of winter precipitation between snow and rain. Many studies have reported an ongoing shift towards earlier runoff in recent decades, which has been attributed to more precipitation falling as rain instead of snow and earlier snowmelt. In this study, we analyze the trends of precipitation and snowfall in the Northeastern United States using United States Historical Climate Network data product. The main goal of this study is to document a trend toward smaller ratios of winter-total snowfall water equivalent to winter-total precipitation.

Yao, H., N. Samal, J. Rusak, D. Pierson, and A. James. 2013. ***Impacts of climate and ice variability on water quality of lakes in Ontario and New York, using simulation models.***

Abstract:

Lakes and reservoirs respond to climatic and environmental forcing via changes to the hydrodynamic and biogeochemical processes that regulate their water quality and ecology. The interactions among climate, land use, water quality and ecology are both the subject of research and the basis of management. Enhanced simulation and prediction of these interactions are desirable. In our study, we applied a one-dimensional water quality model (General Lake Model – Framework for Aquatic Biogeochemical Models, or GLM-FABM) in two natural head-water lakes in central Ontario and a reservoir in New York City, in order to simulate, at a daily time-scale, the status of physical, chemical and biological variables over more than a century (1978-2100), and analyzed the impacts of climate and ice variability on water quality.

The three different water bodies compared were Harp Lake representing a dimictic stratified system; Heney Lake representing a polymictic mixed system; and Cannonsville Reservoir as a mesotrophic artificial system. These lakes span a variety of important gradients and allow us to compare various biogeochemical responses of lakes to environmental stressors. Hydro-meteorological and chemical inputs for the years 1978-2012 are from observed datasets, and inputs for 2013-2100 are provided by a regional climate model. These inputs will also be used to run SWAT catchment model for future scenarios. Changes in water temperature and ice cover are simulated by the GLM-FABM model, and changes in dissolved oxygen, nitrogen, phosphorus, chlorophyll and other indices are predicted. Interactions among these indices and the differences in response between lakes and reservoirs will be analyzed and discussed.

8th Annual NOAA-CREST Symposium, June 2013, New York, NY

Pradhanang, S. M., R. Mukundan, E. M. Schneiderman, M. S. Zion2, A. Anandhi, D. C. Pierson, A. Frei, Z. M. Easton, D. Fuka, and T. S. Steenhuis. 2013. ***How do hydrologic indicators respond to climate change?***

Abstract:

Recent works have indicated that climate change in the northeastern United States is already being observed in the form of shorter winters, higher annual average air temperature, and more frequent extreme heat and precipitation events. These changes could have profound effects on aquatic ecosystems, and the implications of such changes are less understood. The objective of this study is to examine how future changes in precipitation and temperature translate into changes in streamflow using a physically based semi-distributed model, and subsequently how changes in streamflow could potentially impact stream ecology. Streamflow parameters were examined in a New York City water supply watershed for changes from model simulated baseline conditions to future climate scenarios (2081-2100) for ecologically relevant factors of streamflow using the Indicators of Hydrologic Alterations tool. Results indicate that earlier snowmelt and reduced snowpack advance the timing and increase the magnitude of discharge in the winter and early spring (Nov-Mar) and greatly decrease monthly streamflow later in the spring in April. Both the rise and fall rates of the hydrograph will increase resulting in increased flashiness and flow reversals primarily due to increased pulses during winter seasons. These shifts in timing of peak flows, changes in seasonal flow regimes, and changes in the magnitudes of low flow can all influence aquatic organisms and have the potential to impact stream ecology.

Watershed Science and Technical Conference. September 2013. West Point, NY.

Matonse, A., A. Frei, D. Lounsbury, and D. C. Pierson. 2013. ***Hydrological Impact of Hurricane Irene and Tropical Storm Lee in Historical Context: Is the Frequency and Magnitude of Extreme Hydrological Events Changing in Southern New York State?***

Abstract:

Hurricane Irene and Tropical Storm Lee caused unprecedented flooding and significant material damage across the Catskill Mountains and Hudson River Valley in southern NYS. We analyze (i) these events in historical context; and (ii) trends in frequency and magnitude of extreme events across the region. Despite a spatially heterogeneous impact, each event was among the most extreme on record, and the frequency of extreme hydrologic events has been increasing during the last two decades.

Samal, N. R., D. C. Pierson, K. D. Jöhnk, and M. S. Zion. 2013. ***Ice Cover in New York City Drinking Water Reservoirs: Modeling Simulations and Observations.***

Abstract:

The timing of ice formation and loss in lakes and reservoirs will modulate the impact of regional weather conditions on lake thermal structure and mixing, since heat and momentum transfer into the water column are greatly reduced by the presence of ice cover. Changes in the duration and timing of ice cover are well documented effects of climate change that are expected to continue into the future. In the present study, a simple model that predicts the onset, loss and duration of ice cover is applied to New York City drinking water reservoirs, as well as nearby lakes with long ice cover records. The model is driven by daily or hourly air temperature and wind speed as these are the most important factors influencing ice breakup and formation.

The simple model was tested by comparing simulated ice cover to 8 years of observed ice-on and off data for Ashokan and Rondout reservoirs. Further, these 8 years of observed data are compared to 163 years Otsego lake ice phenology. The long-term observed ice phenology of Otsego Lake, when translated to hindcast the Ashokan reservoir's ice conditions, can provide a powerful, integrative description of long-term wintertime and springtime climatic conditions for the region. Long-term simulations of ice conditions/duration are essential to understand the mechanics through which ice cover mediates the effects of climate on lake thermal structure and mixing, and how changing ice cover may ultimately influence phytoplankton succession and trophic status of lakes and reservoirs.

Watershed Science and Technical Conference. September 2013. West Point, NY (cont'd).

Randolph, A. L., L. E. Band, C. L. Tague, and E. M. Schneiderman. 2013. ***An enhanced hydro-ecological model (RHESSys) to explore climate change interactions between precipitation patterns, topography and forests in a New York City water supply watershed.***

Abstract:

Current theory suggests that climate change may manifest itself in the form of changes in the temporal sequencing of storm events and changes in the characteristics of storm events (e.g., storm depth, inter-storm period, rainfall intensity, etc.). As a consequence, the partitioning of rainfall between interception, throughfall, runoff, infiltration, evaporative loss and stream discharge will change. Collectively, these changes in the surface water budget can be expected to have differential impacts on forested watersheds because of differential sensitivity to water stress across tree species and due to interactions between landscape, vegetation and climate.

The hydro-ecological model RHESSys operates at regional or local scales and can explicitly model the spatio-temporal variability in precipitation (i.e., storm sequence) associated with particular weather patterns, thus capturing the full range of natural variability associated with storms and storm sequence. Vegetation modeling in the presently described enhanced version of RHESSys also considers forest structure and composition and models the processes that define interactions between landscape, vegetation and climate. Additionally, topographic effects (e.g., shadowing) and topology (e.g., the effect of landscape structure on redistribution of water) are modeled at a scale fine enough to capture (potential) species-specific impacts of climate change on watershed dynamics.

This presentation provides an overview of the above described enhancements to RHESSys. The enhancements are designed to expand the model's ability to downscale and investigate the potential effects of global climate change scenarios on individual catchments and hillslopes. In particular, this version of RHESSys emphasizes modeling changes in forest structure, composition and spatial distribution and changes in surface water budget. We present initial results of RHESSys simulations of the Biscuit Brook watershed, which is part of drainage to the Neversink reservoir.

Watershed Science and Technical Conference. September 2013. West Point, NY (cont'd).

Zion, M. S. D. C. Pierson, E. M. Schneiderman, and A. Matonse. 2013. ***An Evaluation of Water Quality Modeling used to Inform Operational Decisions for the NYC Water Supply.***

Abstract:

Turbidity is a primary factor that potentially limits use of Catskill System portion of the New York City Water Supply. During the elevated turbidity events daily decisions are carefully taken to optimize system operations for turbidity control, while ensuring adequate water storage levels within the entire water system. To support these decisions, a combination of watershed, reservoir water quality and water system simulation models are used to evaluate alternative operational scenarios within a probabilistic framework. These simulation models form the basis for the Operational Support Tool (OST) currently under development by DEP.

The OST model predictions are based on future forecasts of meteorology, streamflows, and operations to better understand the implications of a given operating strategy on future water quality. Uncertainty in future forecasts is estimated using a range of possible futures scenarios that are judged to be representative of present conditions, but based on past history. A retrospective analysis of water quality data collected during the model forecast period measures the response that actually occurred during the model forecast period, and gives an indication of the accuracy of the model results. This presentation compares the model forecasts to the data collected during the forecast period to better understand and evaluate the use of the modeling system in minimizing the impacts of turbidity within the water supply system.

American Water Resources Association (AWRA) Annual Conference. November 2013. Portland, OR.

Zion, M. S., D. C. Pierson, N. R. Samal, R. Mukundan, D. G. Smith, E. M. Schneiderman, and A. H. Matonse. 2013. ***An Evaluation of Potential Effects of Climate Change on water quality in the New York City Water Supply.***

Abstract:

New York City Department of Environmental Protection (DEP) is using an integrated modeling system to simulate the effects of potential future climate change on the quantity and quality of the New York City (NYC) Water Supply. One concern is turbidity within certain reservoirs of the system. Large streamflow events usually occurring from late-summer through spring can cause naturally occurring fine clay particles to enter the reservoir. The events can be caused by snowmelt, rain-on-snow, large extra-tropical rain events, or tropical cyclones. Understanding the potential impacts of climate change on these loading events and on the fate and transport of the turbidity-causing clay particles in the reservoir is critical to ensuring high quality water of the water system in the future.

Quantitative assessment of the effect of climate change on water resources and water supply systems has followed two basic methods. The first approach, sometimes referred to as "top-down", utilizes future scenarios of meteorological data associated with climate projections as input to hydrologic, water quality, and water system models to simulate the potential impact of future climate on water resource systems. The other approach, sometimes described as "bottom-up", investigates the sensitivity of a water system, generally through the use of models, to changes in climate. This sensitivity analysis can be used to identify the most important climate factors that may present a risk to system performance. Then these risks are placed into the context of potential climate change for the local area of concern.

Current quantitative predictions of climate change can be more useful for understanding the implications for some types of events, while for other event types, predictions are less certain. For example, a outcome predicted for the New York City water supply is a future shift in the timing of spring snow melt to earlier in the season. This is largely driven by increases in air temperature. Since temperature changes are reasonably predicted in climate model projections, this process may be well defined using the top-down approach. Alternatively, climate models generally do not have the ability to adequately simulate extreme events, and therefore changes in extreme event occurrence and the subsequent impact of this on reservoir turbidity may be more difficult to quantify directly. In such a case, it may be more useful to use the bottom-up approach to understand the amount of change in extreme weather that would pose a risk to reservoir water quality.

Watershed and reservoir water quality model simulations are presented that demonstrate how each approach, top-down and bottom-up, can be employed to further understand the impacts of potential future climate change on the water supply.

American Water Resources Association (AWRA) Annual Conference. November 2013. Portland, OR. (cont'd)

Huang, Y., D. Pierson, and E. Schneiderman 2013. ***Modeling the effect of climate change on reservoir water quality using the projections of multiple general circulation models and Bayesian Model Averaging.***

Abstract:

A number of general circulation models (GCMs) have been developed to predict future climate change, and these data are widely used to predict the effect of climate change on hydrology and water quality. However, the reliability of future predictions is uncertain. The objective of this study is to investigate the effects of climate change on the nutrient and trophic status of Cannonsville Reservoir (one part of the New York City water supply system) using the projections of multiple GCMs and Bayesian Model Averaging. Future climate scenarios are simulated using a watershed model coupled to a reservoir model. These models are driven by meteorological scenarios created from historical measured meteorological data and the outputs of the GCMs contributing to the Fourth Assessment Report of the Intergovernmental Panel on Climate Change (IPCC AR4), under a range of emission scenarios (20C3M, A1B, A2, and B1 scenarios). Output for the 20C3M scenario from the watershed and reservoir models are used to calculated the probabilistic likelihood using the generalized likelihood uncertainty estimation (GLUE), while output for the other scenarios are then processed using Bayesian Model Averaging which is a statistical procedure that infers a consensus prediction by weighing individual predictions based on the probabilistic likelihood measures obtained by GLUE, with the better performing predictions receiving higher weights than the worse performing ones. The results of the BMA scheme have the advantage of generating more reliable predictions than using original GCM data. The findings will be beneficial to the management of the water resources of NYC water supply.

GLEON Annual Meeting. November 2013. Bia Blanco, Argentina

Samal, N. R., K. D. Jöhnk, D. C. Pierson, M. Leppäranta, H. Yao, B. R. Hargreaves, T. Kratz, S. Sharma, A. Laas, D. Hamilton, R. Adrian, J. Rusak, D. Oezkundakci, C. Williamson, D. Vachon, B. Denfeld, G. Kirillin, K. Czajkowski, and L. Camarero.. 2013. ***Modeling long-term trends in ice seasons of seven geographically distributed freshwater lakes.***

Abstract:

Changes in the duration and timing of ice cover are well documented effects of climate change that are expected to continue into the future. Long-term simulations of lake ice timing and duration are essential to understand the mechanisms through which ice cover mediates the effects of climate on lake thermal structure and mixing, and how changing ice cover may ultimately influence phytoplankton succession and trophic status of a lake. In the present study, a simple model that predicts the onset, loss and duration of ice cover and its thickness has been applied to seven freshwater lakes and reservoirs around the globe. The model is driven by readily available daily or hourly measurements of air temperature and wind speed, as these are the most important factors influencing formation and breakup. The effects of snowfall and solar radiation on ice thickness and breakup are not implemented in the simple ice model but can be parameterized. Even though the model does not make detailed calculations of the ice cover energy budget it reproduces long-term trends and allows for historical analysis of ice cover for a >60 years simulation of the ice cover on Otsego lake. The timing and duration of ice cover are also well reproduced in several of the other study sites Work is ongoing to include simple snow cover estimates derived from precipitation and temperature data and expand simulations to a wider set of lakes which will allow more in-depth model inter-comparison.

Soil Science Society of America- Annual Meeting. November 2013. Tampa, FL

Mukundan, R., E. Schneiderman, and D. Pierson 2013. ***Simulating Spatial Sediment Loading in the Esopus Creek Watershed, New York.***

Abstract:

The objective of this study is to develop viable scenarios of sediment load reduction for improvement in stream turbidity levels in the 493 km^2 upper Esopus Creek watershed which is part of the New York City water supply. The SWAT model was parameterized to simulate the relative contribution of suspended sediment from sub-basins to the total suspended sediment loads at the watershed outlet comparable to values from measured data. To achieve this, measured sediment load from each tributary to the Esopus Creek was used to derive channel erosion coefficients for each sub-basin; stream channel erosion being the dominant source of stream sediment in this watershed. Calibrated model performed satisfactorily based on monthly statistics for streamflow (R^2 and NSE = 0.85) and sediment concentration (R^2 = 0.72 and NSE = 0.62). Simulations showed that majority (85%) of the stream sediment originated from stream channels and were consistent with previous estimates. Using a calibrated sediment model as baseline, various sediment load reduction scenarios will be simulated by adjusting the channel erosion parameters for different tributaries to the upper Esopus Creek. The sediment load reduction scenarios are expected to provide guidance on possible alternatives for reducing stream turbidity levels and improvement in water quality.

American Geophysical Union Fall Meeting. December 2013. San Francisco, CA.

Pradhanang, S. M., N. R. Samal, D. C. Pierson, E. M. Schneiderman, and M. S. Zion. 2013. ***Behavior of dissolved and total phosphorus concentration and stream discharge: The form of hysteresis during storm events.***

Abstract:

The forms, rotational patterns and trends of hysteretic loops of dissolved and total phosphorus were investigated in the watershed of a New York City drinking water reservoir. We evaluated two biogeochemical parameters summarizing the changes in solute concentrations and the overall dynamics of each hysteretic loop and seven hydrological parameters that characterize the hydrograph formation of particular storm events. The objectives of this study are: (1) to examine whether the characteristics of solute hysteretic loops monitored during the summer, winter and spring seasons followed a consistent and recurring pattern, (2) to identify hydrological parameters which could potentially influence features of dissolved and total phosphorus hysteresis. Relationships between hysteresis features and hydrological parameters at the watershed outlet were explored using multivariate redundancy analysis (RDA).

Samal, N. R., D. C. Pierson, P. A. Staehr, S. M. Pradhanang, and D. G. Smith. 2013. ***Evaluation of Storm Event Inputs on Levels of Gross Primary Production and Respiration in a Drinking Water Reservoir***

Abstract:

Episodic inputs of dissolved and particulate material during storm events can have important effects on lake and reservoir ecosystem function and also impact reservoir drinking water quality. We evaluate the impacts of storm events using vertical profiles of temperature, dissolved oxygen, turbidity, conductivity and chlorophyll automatically collected at 6 hour intervals in Ashokan Reservoir, which is a part of the New York City drinking water supply. Storm driven inputs to the reservoir periodically result in large input of suspended sediments that result in reservoir turbidity levels exceeding 25 NTU, and substantial reductions in the euphotic depth (Z_{eu}). Dissolved materials associated with these same storms would be expected to stimulate bacterial production. This study involves the use of a conceptual model to calculate depth specific estimates of gross primary production (GPP) and ecosystem respiration (R) using three years of data that included 777 events that increased reservoir turbidity levels to over 25 NTU. Using data from before, during and after storm events, we examine how the balance between GPP and R is influenced by storm related increases in turbidity and dissolved organic matter, which would in turn influence light attenuation and bacterial production.

American Geophysical Union Fall Meeting. December 2013. San Francisco, CA (cont'd)

Huang, Y. 2013. ***Multi-model predictions of local climate change with uncertainty assessment using generalized likelihood uncertainty estimation and Bayesian model averaging.***

Abstract:

A number of general circulation models (GCMs) have been developed to project future global climate change and their outputs are widely used to represent local climate conditions to predict the effect of climate change on hydrology and water quality. Unfortunately, projected results for future climate change are different and it is not known which set of GCM data is better than the others. The objective of this work is to present a Bayesian approach consisting of generalized likelihood uncertainty estimation (GLUE) and Bayesian model averaging (BMA) for the estimation of local climate change with uncertainty assessment. This method is applied to Cannonsville Reservoir watershed. GCM data contributing to the Fourth Assessment Report of the Intergovernmental Panel on Climate Change (IPCC AR4), under a range of emission scenarios (20C3M, A1B, A2, and B1) are used. The GCM data for the 20C3M scenario are used to calculated the posterior probability using GLUE, while outputs for future scenarios (A1B, A2, and B1) are then processed using BMA which is a statistical procedure that infers a consensus prediction by weighing individual predictions based on the posterior probabilities obtained by GLUE, with the better performing predictions receiving higher weights than the worse performing ones. The method has the advantage of generating more reliable predictions than original GCM data. The results also indicate clearly the high reliability of the GCM data for daily average, maximum and minimum temperatures, but the reliability for daily precipitation and wind speed is low. The application supports the method presented.

American Geophysical Union Fall Meeting. December 2013. San Francisco, CA (cont'd)

Mukundan, R. and R. V. Dreason 2013. ***Predicting Trihalomethanes (THMs) in the New York City Water Supply.***

Abstract:

Chlorine, a commonly used disinfectant in most water supply systems, can combine with organic carbon to form disinfectant byproducts, including carcinogenic trihalomethanes. We used water quality data from 24 monitoring sites within the New York City water supply distribution system, measured between January 2009 and April 2012, to develop an empirical model for predicting total trihalomethane (TTHM) levels. Terms in the model included the following water quality parameters: total organic carbon, pH, water age (reaction time), and water temperature. Reasonable estimates of TTHM levels were achieved with overall R^2 of about 0.75, and predicted values on average were within 6 $\mu g \cdot L^{-1}$ of measured values. A sensitivity analysis indicated that total organic carbon and water age are the most important factors for TTHM formation, followed by water temperature; pH was the least important factor within the boundary conditions of observed water quality. Although never out of compliance in 2011, the TTHM levels in the water supply increased after tropical storms Irene and Lee, with 45% of the samples exceeding the 80 $\mu g \cdot L^{-1}$ maximum contaminant level in October and November. This increase was explained by changes in water quality parameters, particularly by the increase in total organic carbon concentration during this period. This study demonstrates the use of an empirical model to understand TTHM formative factors and their relative importance in a drinking water supply. This has implications for simulating management scenarios and real-time estimation of TTHMs in water supply systems under changing environmental conditions.

9. References

Abbaspour, K. C. 2008. SWAT-CUP2: SWAT Calibration and Uncertainty Programs- A User Manual. Department of Systems Analysis, Integrated Assessment and Modelling (SIAM), Eawag, Swiss Federal Institute of Aquatic Science and Technology, Duebendorf, Switzerland, 95pp.

Ahsan, Quamrul A. K. M. and A.F. Blumberg. 1999. Three –dimensional hydrothermal model of Onondaga Lake, New York, *Journal of Hydraulic Engineering*, **125**(9): 912-923.

Anandhi, A., A. Frei, D. C. Pierson, E. M. Schneiderman, M. S. Zion, D. Lounsbury, and A. H. Matonse. 2011. Examination of change factor methodologies for climate change impact assessment. *Water Resources Research*, **47**:W03501. doi:10.1029/2010WR009104.

Anderson, C.W.. 2005. Chapter A6. Section 6.7. Turbidity: USGS Techniques of Water-Resource Investigation: 09-A6.7

Andrea, B., G. Francesc, L. Jérôme, V. Eusebi and S. Francesc. 2006. Cross-site comparison of variability of DOC and nitrate c–q hysteresis during the autumn–winter period in three Mediterranean headwater streams: a synthetic approach. *Biogeochemistry* **77**(3): 327-349

APHA. 1995. Standard Methods for the Examination of Water and Wastewater. 19th Edition. American Public Health Association, Washington, DC.

Arnold, J. G., D.N. Moriasi, P.W. Gassman, K.C. Abbaspour, M.J. White, R. Srinivasan, C. Santhi, R.D. Harmel, A. vanGriensven, M.W. Van Liew, N. Kannan, and M.K. Jha. 2012. SWAT: Model use, calibration, and validation. *Trans. ASABE,* **55**(4): 1494-1508.

Ashton, G.D., *ed.* 1986. *River and Lake Ice Engineering.* Littleton, CO, Water Resources Publications.

ASTM International, 2003, D1889–00 Standard test method for turbidity of water, *in ASTM International, Annual Book of ASTM Standards,* Water and Environmental Technology, 2003, v. 11.01, West Conshohocken, Pennsylvania, 6 p.

Auble G.T., Friedman J.M., M.L. S. 1994 Relating riparian vegetation to present and future streamflows. *Ecological Applications* **4**:544-554.

Austin, J.A. and S.M. Colman. 2007. Lake Superior summer water temperatures are increasing more rapidly than regional air temperature: a positive ice-albedo feedback. *Geophys Res Let* **34**:L06604. Doi:10.1029/2006GL029021.

Austin, J.A. and S.M. Colman. 2008. A century of temperature variability in Lake Superior. *Limnol Oceanogr* **53**(6):2724-2730.

Austin, J. A. and J. Allen, 2011. Sensitivity of Lake Superior Temperature Structure to meteorological forcing. *Limnology and Oceanography* **56**(3): 1141-1154.

Beven, K.J. and M.J. Kirkby. 1979. A physically based, variable contributing area model of basin hydrology. *Hydrological Sciences Bulletin*, **24**(1): 43-69

Bernal, S., A. Butturini and F. Sabater. 2002. Variability of DOC and nitrate responses to storms in a small Mediterranean forested catchment. *Hydrology and Earth System Sciences Discussions* **6**(6): 1031-1041

Blasone, R.S., H. Madsen and D. Rosbjerg. 2008. Uncertainty assessment of integrated distributed hydrological models using GLUE with Markov chain Monte Carlo sampling. *J. Hydrol.* **353**, 18–32.

Bowes, M.J., W.A. House, R.A. Hodgkinson, D.V. Leach 2005. Phosphorus–discharge hysteresis during storm events along a river catchment: the River Swale, UK. *Water Research* **39**(5): 751-762

Brown, L.C. and C.R. Duguay. 2012. Modelling lake ice phenology with an examination of Satellite-Detected Subgrid Cell variability, *Adavnces in Meteorology*, Hindawi Publishing Corporation, doi:10.1155/2012/529064.

Brutsaert, W. 2005. *Hydrology, An Introduction.* Cambridge University Press, NY, NY.

Bunn S.E. and A.H. Arthington. 2002. Basic Principles and Ecological Consequences of Altered Flow Regimes for Aquatic Biodiversity. *Environmental Management* **30**:492-507. DOI: 10.1007/s00267-002-2737-0.

Burns D.A., J. Klaus, and M.R. McHale. 2007. Recent climate trends and implications for water resources in the Catskill Mountain region, New York, USA, *Journal of Hydrology*, **336**, 155-170.

Carey, S.K. 2003. Dissolved organic carbon fluxes in a discontinuous permafrost subarctic alpine catchment. *Permafrost and Periglacial Processes* **14**(2): 161-171

Carey, C. C., B. W. Ibelings, E. P. Hoffmann, D. P. Hamilton, and J. D. Brookes. 2012. Eco-physiological adaptations that favour freshwater cyanobacteria in a changing climate. *Water Research* **46**:1394-1407.

CCE. 2007. Upper Esopus Creek Management Plan. Cornell Cooperative Extension of Ulster County, Technical Report. 225 p.

Chowdhury S. and P. Champagne. 2008. An investigation on parameters for modeling THMs formation. *Global NEST J* **10**(1):80–91.

Chowdhury, S., P. Champagne, and P.J. McLellan. 2009. Models for predicting disinfection byproduct formation in drinking waters: A chronological review. *Science of the Total Environment*. **407**: 4189-4206.

Condie, S.A. and I.T. Webster. 2001. Estimation of stratification in shallow water bodies from mean meteorological conditions, *Journal of Hydraulic Engineering*, **127(**4): 286-292.

Coon W. 2005. Hydrologic Evidence of Climate Change in Monroe County, NYS., US Geological Survey. OFR 2008-1199.

DEP, 2006a. 2006 Long-Term Watershed Protection Program, New York City Department of Environmental Protection, Valhalla, New York.

DEP, 2006b. New York City's 2006 Watershed Protection Program Summary and Assessment. Report, New York City Department of Environmental Protection, Bureau of Water Supply, Valhalla, N.Y.

DEP. 2008a. Upgrades to the Cannonsville Reservoir Eutrophication Model to Allow for Simulation of the Growth and Succession of Phytoplankton Functional Groups. Report, New York City Department of Environmental Protection, Bureau of Water Supply, Valhalla, N.Y.

DEP. 2008b. Evaluation of Turbidity Reduction Potential through Watershed Management in the Ashokan Basin. Valhalla, New York. July 2008

DEP. 2010. Stage 2D/DBP Compliance Study. Bureau of Water Supply, New York

DEP, 2011. New York City's Operations Support Tool (OST) White Paper. http://www.nyc.gov/html/dep/pdf/reports/ost_white_paper.pdf. Accessed 21st August 2012.

Doerr, S.M., E.M. Owens, R.K. Gelda, M.T. Auer and S.W. Effler. 1998. Development and testing of a nutrient-phytoplankton model for Cannonsville Reservoir. *Lake and Reservoir Management* **14**, 301-321.

Du, B., J. G. Arnold, A. Saleh, and D. B. Jaynes. 2005. Development and application of SWAT to landscapes with tiles and potholes. *Transactions of the ASAE*. **48**(3): 1121-1133.

Easterling, D.R. 2002. United States Historical Climatology Network Daily Temperature and Precipitation Data (1871-1997). In. ORNL Oak Ridge National Laboratory (US).

Easton, Z.M., D.R. Fuka, M.T. Walter, D.M. Cowan, E.M. Schneiderman, and T.S. Steenhuis. 2008. Re-conceptualizing the Soil and Water Assessment Tool (SWAT) model to predict runoff from variable source areas. *Journal of Hydrology*. **348**(3-4): 279-291.

Easton, Z.M., M.T. Walter, E.M. Schneiderman, M.S. Zion and T.S. Steenhuis. 2009. Including source-specific phosphorus mobility in a nonpoint source pollution model for agricultural watersheds. *Journal of Environmental Engineering* **135**(1): 25-35

Easton Z.M., M.T. Walter, D.R. Fuka, E.D. White and T.S. Steenhuis. 2010. A simple concept for calibrating runoff thresholds in quasi-distributed variable source area watershed models. *Hydrological Processes* **25**:3131-3143. DOI: 10.1002/hyp.8032.

Effler, S. W., and A. P. Bader. 1998. A Limnological Analysis of Cannonsville Reservoir NY. *Journal of Lake and Reservoir Management* **14**:125-139.

Effler S.W., M.G. Perkins, N. Ohrazda, C.M. Brooks, B.A. Wagner, D.L. Johnson, F. Peng and A. Bennett. 1998. Turbidity and Particle Signatures imparted by Runoff Events in Ashokan Reservoir, NY. *Lake and Reservoir Management* **14**: 254–265.

Elsawwaf, M., P. Willems and J. Feyen. 2010. Assessment of the sensitivity and prediction uncertainty of evaporation models applied to Nasser Lake, Egypt. *Journal of Hydrology* **395**, 10–22.

El-Shehawy, R., E. Gorokhova, F. Fernández-Piñas, and F. F. del Campo. 2012. Global warming and hepatotoxin production by cyanobacteria: What can we learn from experiments? *Water Research* **46**:1420-1429.

Endreny, T.A. and E.F. Wood. 2007. Watershed weighting of export coefficients to map critical phosphorus loading areas. *Journal of the American Water Resources Association* **39**(1): 165-181

Evans, C. and T.D. Davies. 1998. Causes of concentration/discharge hysteresis and its potential as a tool for analysis of episode hydrochemistry. *Water Resources Research* **34**(1): 129-137

Fang, X., C.R. Ellis and H.G. Stefan. 1996. Simulation and observation of ice formation (freeze-over) in a lake. *Cold Reg. Sci. Technol.,* **24**(2), 129–145.

Fang X.and H.G. Stefan. 2009. Simulations of climate effects on water temperature, dissolved oxygen, and ice and snow covers in lakes of the contiguous United States under past and future climate scenarios *Limnol. Oceanogr*., **54**(6, part 2): 2359–2370.

Fiebig, D.M., M.A. Lock and C. Neal. 1990. Soil water in the riparian zone as a source of carbon for a headwater stream. *Journal of Hydrology* **116**(1–4): 217-237

Frankenberger, J.R., E.S. Brooks, M.T. Walter, M.F. Walter and T.S. Steenhuis, 1999. A GIS based variable source area hydrology model, *Hydrological Processes* **13**, 805–822.

Freni, G. and G. Mannina. 2012. Uncertainty estimation of a complex water quality model: The influence of Box–Cox transformation on Bayesian approaches and comparison with a non-Bayesian method. *Physics and Chemistry of the Earth* 42–44, 31–41.

Gan T.Y. 1998. Hydroclimatic trends and possible climatic warming in the Canadian Prairies. *Water Resour. Res.* **34**. DOI: doi:10.1029/98WR01265.

Gassman, P.W., M.R. Reyes, C.H. Green, and J.G. Arnold. 2007. The Soil and Water Assessment Tool: Historical development, applications, and future research directions. *Trans. ASABE* **50**(4):1211–1250.

Gelda, R.K., E.M. Owens and S.W. Effler, 1998. Calibration, verification and an application of a two-dimensional hydrothermal model [CE-QUAL-W2(t)] for Cannonsville Reservoir. *Lake and Reservoir Management*,**14**,186-196.

Gelda, R.K., S.W. Effler, F. Peng, E.M. Owens, and D.C. Pierson. 2009. Turbidity model for Ashokan Reservoir, New York: Case study. *ASCE J. Environ. Eng.*, **135** (9): 885-895.

Gelda, R.K., S.W. Effler, A.R. Prestigiacomo, F. Peng, A.J.P. Effler, B.A. Wagner, M.G. Perkins, D. O'Donnell, S.M. O'Donnell and D.C. Pierson. 2013. Characterizations and modeling of turbidity in a water supply reservoir following an extreme runoff event. *Inland Waters* (in press)

Gibson C.A., J.L. Meyer, N.L. Poff, L.E. Hay and A. Georgakakos. 2005. Flow regime alterations under changing climate in two river basins: implications for freshwater ecosystems. *River Research and Applications* **21**:849-864. DOI: 10.1002/rra.855.

Girod, B., A. Wiek, H. Mieg and M. Hulme. 2009. The evolution of the IPCC's emissions, *Environmental Science & Policy*, **12** (2): 103-118, doi:10.1016/j.envsci.2008.12.006.

Guy, H.P., 1969, Laboratory Theory and Methods for Sediment Analysis: U.S. Geological Survey Techniques of Water-Resources Investigations, Book 5, Chapter C1, 58 p.

Hanrahan, G., M. Gledhill, W.A. House and P.J. Worsfold. 2001. Phosphorus loading in the Frome catchment, UK. *Journal of Environmental Quality* **30**(5): 1738-1746

Hauer F.R., J.S. Baron, D.H. Campbell, K.D. Fausch, S.W. Hostetler, G.H. Leavesley, P.R. Leavitt, D.M. McKnight and J.A. Stanford. 1997. Assessment of Climate Change and Freshwater Ecosystems of the Rocky Mountains, USA and Canada. *Hydrological Processes* **11**:903-924.

Hazen and Sawyer. 2012. CE-QUAL-W2 Upgrade Report – Draft Technical Memorandum.

Health Canada 2006. Guidelines for Canadian Drinking Water Quality: Guideline TechnicalDocument — Trihalomethanes. Water Quality and Health Bureau, Healthy Environments and Consumer Safety Branch, Health Canada, Ottawa, Ontario. http://www.hc-sc.gc.ca/ewh-semt/alt_formats/pdf/pubs/water-eau/trihalomethanes/trihalomethanes-eng.pdf (Accessed January 26, 2014)

Henderson-Sellers, 1977. The thermal structure of small lakes: the influence of a modified wind speed. *Water Resources Research*, **13**(4):791-793.

Hodgkins, G.A., I.C. James, T.G. Huntington. 2002. Historical changes in lake ice-out dates as indicators of climate change in New England, 1850–2000. *International Journal of Climatology* **22**(15): 1819-1827

Hodgkins, G., R. Dudley and T. Huntington. 2003. Changes in the timing of high river flows in New England over the 20th century. *Journal of Hydrology* **278**(1): 244-252

Hodgkins, G.A. and R.W. Dudley. 2006. Changes in late-winter snowpack depth, water equivalent, and density in Maine, 1926–2004. *Hydrological Processes* **20**(4): 741-751

Hondzo, M. and H. Stefan. 1992. Propagation of uncertainty due to variable meteorological forcing in lake temperature models, *Water Resources Research*, **28**(10), 2629-2638.

Hong, H.C., Y. Liang, B.P. Han, A. Mazumder and A.H. Wong. 2007. Modeling of trihalomethane (THM) formation via chlorination of the water from Dongjiang River (source water for Hong Kong's drinking water). *Sci Total Environ* **385**:48–54.

Hooper, R.P. 2003. Diagnostic tools for mixing models of stream water chemistry. *Water Resources Research* **39**(3):

Hornberger, G., K. Bencala, D. McKnight. 1994. Hydrological controls on dissolved organic carbon during snowmelt in the Snake River near Montezuma, Colorado. *Biogeochemistry* **25**(3): 147-165

House W.A. and M.S. Warwick. 1998. Hysteresis of the solute concentration/discharge relationship in rivers during storms. *Water Research* **32**(8): 2279-2290

Huisman, J., J. Sharples, J. M. Stroom, P. M. Visser, W. E. A. Kardinaal, J. M. H. Verspagen, and B. Sommeijer. 2004. Changes in Turbulent Mixing Shift Competition for Light Between Phytoplankton Species. *Ecology* **85**:2960-2970.

Huntington, T., G. Hodgkins and R. Dudley. 2003. Historical trend in river ice thickness and coherence in hydroclimatological trends in Maine. *Climatic Change* **61**(1-2): 217-236

Huntington, T.G., G.A. Hodgkins, B.D. Keim and R.W. Dudley. 2004. Changes in the Proportion of Precipitation Occurring as Snow in New England (1949–2000). *Journal of Climate* **17**(13):

Imberger, J. 1985. The diurnal mixed layer. *Limnol. Oceanogr.* **30**:737-770.

IPCC (Intergovernmental Panel on Climate Change). 2007. Climate Change 2007: The Physical Science Basis. Contribution of Working Group I to the Fourth Assessment Report of the Intergovernmental Panel on Climate Change., in: S. Solomon, D. Qin and M. Manning (Ed.).

Janse, J.H., M. Scheffer, L. Lijklema, L. Van Liere, J.S. Sloot and W.M. Mooij. 2010. Estimating the critical phosphorus loading of shallow lakes with the ecosystem model PCLake: Sensitivity, calibration and uncertainty. *Ecological Modelling* **221**, 654–665.

Jarvis, A.J. and W.J. Davies. 1998. The coupled response to stomatal conductance to photosynthesis and transpiration. *J of Experimental Botany*, **49**: 399-406.

Jeffries, M. O., K. Morris, C.R. Duguay. 2005. Lake ice growth and decay in central Alaska, USA: observations and computer simulations compared, *Annals of Glaciology* **40**: 195-199.

Johnes, P. 1996. Evaluation and management of the impact of land use change on the nitrogen and phosphorus load delivered to surface waters: the export coefficient modelling approach. *Journal of Hydrology* **183**(3): 323-349

Jöhnk, K.D. and L. Umlauf. 2001. Modelling the metalimnetic oxygen minimum in a medium sized alpine lake. *Ecological Modelling* **136**: 67-80.

Jöhnk, K. D., J. E. F. Huisman, J. Sharples, B. E. N. Sommeijer, P. M. Visser, and J. M. Stroom. 2008. Summer heatwaves promote blooms of harmful cyanobacteria. *Global Change Biology* **14**:495-512.

Karl, D.E.-T., J.L.-S. Del Greco, D.P. Kaiser and L.J. Allison. 1999 United States Historical Climatology Network Daily Temperature, Precipitation, and Snow Data for 1871-1997.

Klug, J. L., D.C. Richardson, H.A. Ewing, B.R. Hargreaves, N.R. Samal, D. Vachon, D.C. Pierson, A.M. Lindsey, D.M. O'Donnell, S.W. Effler and K.C. Weathers. 2012. Ecosystem effects of a tropical cyclone on a network of lakes in northeastern North America. Environmental Science & Technology.Ecosystem Effects of a Tropical Cyclone on a Network of Lakes in Northeastern North America. *Environmental Science & Technology* **46** (21), 11693-11701

Komatsu, E., T. Fukushimac. and H. Harasawa. 2007. A modeling approach to forecast the effect of long-term climate change on lake water quality, *Ecological Modelling* **209**: 351–366.

Kosten, S., V. L. M. Huszar, E. Bécares, L. S. Costa, E. van Donk, L.-A. Hansson, E. Jeppesen, C. Kruk, G. Lacerot, N. Mazzeo, L. De Meester, B. Moss, M. Lürling, T. Nõges, S. Romo, and M. Scheffer. 2012. Warmer climates boost cyanobacterial dominance in shallow lakes. *Global Change Biology* **18**:118-126.

Lemke, P., J. Ren, R.B. Alley, I. Allison, J. Carrasco, G. Flato, Y. Fujii, G. Kaser, P. Mote and R.H. Thomas. 2007. Observations: Changes in snow, ice and frozen ground. Titel: Climate change 2007: the physical science basis; summary for policymakers, technical summary and frequently asked questions. Part of the Working Group I contribution to the Fourth Assessment Report of the Intergovernmental Panel on Climate Change: 337-383

Liang, L. and P. C. Singer. 2003. Factors Influencing the Formation and Relative Distribution of Haloacetic Acids and Trihalomethanes in Drinking Water. *Environmental Science Technology* **37**(13): 2920-2928.

Lindenschmidt, K.E., K. Fleischbein and M. Baborowski. 2007. Structural uncertainty in a river water quality modelling system. *Ecological Modelling* **204** (3–4), 289–300.

Livingstone, D. M. and R. Adrian. 2009. Modeling the duration of intermittent ice cover on a lake for climate-change studies. *Limnol. Oceanogr*. **54**: 1709–1722.

Lorke, A., Muller, B., Maerki, M. and Wu¨est, A. 2003. Breathing sediments: The control of diffusive transport across the sediment–water interface by periodic boundary-layer turbulence. *Limnol. Oceanogr.,* **48**(6): 2077–2085.

Lürling, M., F. Eshetu, E. J. Faassen, S. Kosten, and V. L. M. Huszar. 2013. Comparison of cyanobacterial and green algal growth rates at different temperatures. *Freshwater Biology* **58**:552-559.

Markensten, H. and D. Pierson. 2007. Weather driven influences on phytoplankton succession in a shallow lake during contrasting years: Application of PROTBAS. *Ecological Modelling,* **207**, 128-136.

May, L., W.A. House, M. Bowes and J. McEvoy. 2001. Seasonal export of phosphorus from a lowland catchment: upper River Cherwell in Oxfordshire, England. *Science of the Total Environment*, **269**(1): 117-130

McCabe G.J. and D.M. Wolock. 2002. A step increase in streamflow in the conterminous United States. . *Geophysics Research Letters* **29**:2185. DOI: doi:10.1029/2002GL015999.

McGlynn, B.L. and J.J. McDonnell. 2003. Role of discrete landscape units in controlling catchment dissolved organic carbon dynamics. *Water Resources Research* **39**(4): 1090

McHale,,M.R. and J. Siemion, In Press, Turbidity and Suspended Sediment in the Upper Esopus Creek Watershed, Ulster County, NY USGS Open File Report, Troy, New York, 37 pp.

McKay, M.D., R.J. Beckman and W.J. Conover. 1979. A comparison of three methods for selecting values of input variables in the analysis of output from a computer code. *Technometrics* **21**(2), 239–245.

Minella, J.P.G., G.H. Merten and P.F. Magnago. 2011. Qualitative and quantitative analysis of hysteresis between sediment concentration and flow rate during hydrologic events. *Revista Brasileira de Engenharia Agrícola e Ambiental* **15**(12): 1306-1313

Moore, R.J., 2007. The PDM rainfall-runoff model. Hydrol. *Earth Sys. Sci.* **11**(1), 483-499.

Moriasi, D.N., J.G. Arnold, G.G. Vaarquez-Amiaile, B.A. Engel and C.G. Rossi. 2009. Incorporation of a new shallow water table depth algorithm into SWAT2005. *Transactions of the ASABE*. **52**(3): 771-784.

Moriasi, D. N., J.L. Steiner and J.G. Arnold, J. G. 2011a. Sediment measurement and transport modeling: Impact of riparian and filter strip buffers. *Journal of Environmental Quality*, **40**(3), 807-814.

Moriasi, D.N., J.G. Arnold, G.G. Vazquez-Amabile and B.A. Engel. 2011b. Shallow water table depth algorithm in SWAT: Recent developments. *Transactions of the ASABE*. **54**(5): 1705-1711.

Mukundan R., D.C. Pierson, L. Wang, A.H. Matonse, N.R. Samal, M.S. Zion, and E.M. Schneiderman 2013a. Effect of Projected Changes in Winter Streamflow on Stream Turbidity, Esopus Creek Watershed in New York, USA. *Hydrological Processes* **27**: 3014–3023

Mukundan, R., S.M. Pradhanang, E.M. Schneiderman, D.C. Pierson, A. Anandhi, M.S. Zion, A.H. Matonse, D.G. Lounsbury, and T.S. Steenhuis. 2013b. Suspended sediment source areas and future climate impact on soil erosion and sediment yield in a New York City water supply watershed, USA. *Geomorphology*, http://dx.doi.org/10.1016/j.geomorph.2012.06.021.

Mulholland P.J., E.R. Marzolf, J.R. Webster, D.R. Hart and S.P. Hendricks. 1997. Evidence that hyporrheic zones increase heterotrophic metabolism and phosphorus uptake in forest streams. *Limnology and Oceanography* **42**:443-451.

Newbold, J., T. Bott, L. Kaplan, B. Sweeney and R. Vannote. 1997. Organic matter dynamics in White Clay Creek, Pennsylvania, USA. *Journal of the North American Benthological Society*: 46-50

Nokes, C.J., E. Fenton and C.J. Randall. 1999. Modelling the formation of brominated trihalomethanes in chlorinated drinking waters. *Water Res*, **33**(17):3557–68.

Omlin, M., R. Brun and P. Reichert. 2001. Biogeochemical model of Lake Zu¨ rich: sensitivity, identifiability and uncertainty analysis. *Ecological Modelling* **141**, 105–123.

Orlob, G. T. 1983. *Mathematical modeling of water quality: Streams, lakes and reservoirs*. Wiley.

Owens, E.M. 1998a. Thermal and heat transfer characteristics of Cannonsville Reservoir. *Lake and Reservoir Management*, **14**, 152-161.

Owens, E.M. 1998b. Development and testing of a one-dimensional hydrothermal models of Cannonsville Reservoir. *Lake and Reservoir Management*, **14**, 172-185.

Owens, E. M., S. W. Effler, S. M. Doerr, R. K. Gelda, E. M. Schneiderman, D. G. Lounsbury, and C. L. Stepczuk. 1998a. A strategy for reservoir model forecasting based on historic meteorological conditions. *Lake and Reservoir Management* **14**:2-3.

Owens, E. M., R.K. Gelda, S.W. Effler and J.M. Hassett. 1998b. Hydrologic analysis and model development for Cannonsville Reservoir. *Lake Reserv. Manag*. **14** (2–3), 140–151.

Ozekin, K., 1994. Modelling bromate formation during ozonation and assessing its control, Ph.D. Dissertation, University of Colorado, USA.
Paerl, H. W., and J. Huisman. 2008. Blooms Like It Hot. *Science* **320**:57-58.

Paerl, H. W., and J. Huisman. 2009. Climate change: a catalyst for global expansion of harmful cyanobacterial blooms. *Environmental Microbiology Reports* **1**:27-37.

Panguluri, S., G. Meiners, J. Hall, and J. G. Szabo. Distribution system water quality monitoring: sensor technology evaluation methodology and results. U.S. Environmental Protection Agency, Washington, DC, EPA/600/R-09/076, 2009.

Patterson, J.C. and P.F. Hamblin. 1988. Thermal simulation of a lake with winter ice cover, *Limnol. Oceanogr.*, **33**(3): 323-338

Paul, V. J. 2008. Global warming and cyanobacterial harmful algal blooms. Pages 239-256 *in* H. K. Hudnell, editor. Cyanobacterial Harmful Algal Blooms: State of the Science and Research Needs. Springer New York.

Peeters, F., D.M. Livingstone, G.-H. Goudsmit, R. Kipfer and R. Forster, 2002. Modeling 50 years of historical temperature profiles in a large central European lake. *Limnology and Oceanography,* **47**, 186–197.

Pierson, D.C., G. A. Weyhenmeyer, L. Arvola, B. Benson, T. Blenckner, T. Kratz, D.M. Livingstone, H. Markensten, G. Marzec, K. Pettersson, and K. Weathers, 2011. An automated method to monitor lake ice phenology, *Limnol. Oceanogr.: Methods* **9**: 74–83

Pierson, D. C., N. Samal, E. Owens, E. M. Schneiderman, and M. S. Zion. 2013. Changes in the Timing of Snowmelt, and the Seasonality of Nutrient Loading: Can Models Simulate the Impacts on Freshwater Trophic Status? *Hydrologic Processes* **27**:3083-3093.

Poff, N. and J. Ward. 1990. Physical habitat template of lotic systems: Recovery in the context of historical pattern of spatiotemporal heterogeneity. *Environmental Management* **14**:629-645. DOI: 10.1007/bf02394714.

Poff, N.L., J.D. Allan, M.B. Bain, J.R. Karr, K.L. Prestegaard, B.D. Richter, R.E. Sparks and J.C. Stromberg. 1997. The Natural Flow Regime. *BioScience* **47**:769-784.

Pradhanang, S.M., A. Anandhi, R. Mukundan, M.S. Zion, D.C. Pierson, E.M. Schneiderman, A. Matonse, A. Frei. 2011. Application of SWAT model to assess snowpack development and streamflow in the Cannonsville watershed, New York, USA. *Hydrological Processes,* **25**:3268-3277. doi: 10.1002/hyp.8171.

Pradhanang, S.M., A. Frei, M. Zion, E.M. Schneiderman, T.S. Steenhuis, D. Pierson. 2013. Rain-on-snow runoff events in New York. *Hydrological Processes* **27**(21): 3035-3049

Trombulak SC, Wolfson R (2004) Twentieth-century climate change in New England and New York, USA. Geophysical research letters 31(19):

Rao, Y.R., A. Huang, W.M. Schertzer and W.R. Rouse. 2012. Modelling of Physical Processes and Assessment of Climate Change Impacts in Great Bear Lake, *Atmosphere-Ocean*, **50**(3): 317-333, DOI:10.1080/07055900.2012.668492

Rathbun, R.E. 1996. Speciation of trihalomethane mixtures for the Mississippi, Missouri and Ohio rivers. *Sci Total Environ* **180**:125–35.

Reckhow, K.H., M.N. Beaulac and J.T. Simpson. 1980. Modeling phosphorus loading and lake response under uncertainty: A manual and compilation of export coefficients.

Reichwaldt, E. S., and A. Ghadouani. 2012. Effects of rainfall patterns on toxic cyanobacterial blooms in a changing climate: Between simplistic scenarios and complex dynamics. *Water Research* **46**:1372-1393.

Reynolds, C. S., and A. E. Walsby. 1975. Water-blooms. *Biol. Rev.* **50**:437-481.

Reynolds, C.S., A.E. Irish and J.A. Elliott. 2001. The ecological basis for simulating phytoplankton responses to environmental change (PROTECH). *Ecological Modelling,* **140**, 271-291.

Reynolds, C. S. 2006. The Ecology of Phytoplankton. Cambridge Univ Press.

Richter, B.D., J.V. Baumgartner, J. Powell, D.P. Braun. 1996. A Method for Assessing Hydrologic Alteration within Ecosystems. *Conservation Biology* **10**:1163-1174.

Richter, B.D., R. Mathews, D.L. Harrison and R. Wigington. 2003. Ecologically sustainable water management: Managing river flows for ecological integrity. *Ecological Applications* **13**:206-224. DOI: doi:10.1890/1051-0761.

Rigosi, A. and F.J. Rueda, 2012. Propagation of uncertainty in ecological models of reservoirs: From physical to population dynamic predictions. *Ecological Modelling* **247**, 199–209.

Rigosi, A., C. C. Carey, B. W. Ibelings, J. D. Brookes, and 2014. The interaction between climate warming and eutrophication to promote cyanobacteria is dependent on trophic state and varies among taxa. *Limnol. Oceanogr* **59**:99-114.

Risbey, J.S. and D. Entekhabi D. 1996. Observed Sacramento Basin streamflow response to precipitation and temperature changes and its relevance to climate impact studies. *Journal of Hydrology* **184**:209-223.

Robertson, D. M., R. A. Ragotzkie, and J. J. Magnuson. 1992. Lake ice records used to detect historical and future climatic changes. *Clim. Change* **21**:407-427 [doi:10.1007/ BF00 141379].

Rodriguez, M.J. and J.B. Sérodes. 2001. Spatial and temporal evolution of trihalomethanes in three water distribution systems. *Water Res,* **35**(6):1572–86.

Rood, S.B., J.M. Mahoney, D.E. Reid and L. Zilm 1995. Instream flows and the decline of riparian cottonwoods along the St. Mary River, Alberta. *Canadian Journal of Botany* **73**:1250-1260.

Rueda, F.J., W.E. Fleenor and I. Vicente. 2007. Pathways of river nutrients towards the euphotic zone in a deep-reservoir of small size: Uncertainty analysis. *Ecological Modelling* **202**, 345–361.

Sadiq, R., and M.J. Rodriguez. 2004. Disinfection by-products (DBPs) in drinking water and the predictive models for their occurrence: a review, *The Science of the Total Environment*, **321**(1-3): 21-46

Sahoo, G. B., S.G. Schladow, J.E. Reuter and R. Coats. 2011. Effects of climate change on thermal properties of lakes and reservoirs, and possible implications. *Stoch. Environ. Res. Risk Assess.,* **25**: 445–456.

Saltelli A, Chan K, Scott M. (Eds) 2000. Sensitivity Analysis. John Wiley and Sons publishers, Probability and Statistics series.

Saltelli A, M. Ratto, T. Andres, F. Campolongo, J. Cariboni, D. Gatelli, M. Saisana, S. Tarantola. 2008. *Global Sensitivity Analysis. The Primer*, John Wiley and Sons.

Samal, N.R., A. Mazumdar, K. D. J¨ohnk and F. Peeters, 2009. Assessment of ecosystem health of tropical shallow waterbodies in eastern India using turbulence model. *Journal of Aqua. Ecosys. Health & Manage*, Society (AEHMS), Canada. **12**(2), 215–225.

Samal, N.R., D.C. Pierson, Y. Huang, J.S. Read, A. Anandhi, and E.M. Owens, 2012. Impact of climate change on Cannonsville Reservoir thermal structure in the New York City water supply. *Water Quality Research Journal of Canada,* **47**(3-4): 389-405.

Samal, N.R., A.H. Matonse, R. Mukundan, M.S. Zion, D.C. Pierson, R. Gelda, and E.M. Schneiderman, 2013. Modelling potential effects of climate change on winter turbidity loading in the Ashokan Reservoir, NY. *Hydrological Processes* 27, 3061–3074, DOI: 10.1002/hyp.9910.

SAS Institute. 2012. SAS Documentation. Version 9.3. SAS Institute., Cary, NC.

Schneiderman, E.M., D.C. Pierson, D.G. Lounsbury and M.S. Zion. 2002. Modeling the Hydrochemistry of the Cannonsville Watershed with Generalized Watershed Loading Functions (GWLF). *Journal of the American Water Resources Association*, **38**(5):1323-1347.

Schneiderman, E.M., T.S. Steenhuis, D.J. Thongs, Z.M. Easton, M.S. Zion, A.L. Neal, G.F. Mendoza and M.T. Walter, 2007. Incorporating variable source area hydrology into the curve number based Generalized Watershed Loading Function model. *Hydrol. Process.*, **21**:3420-3430.

Semmler, T., B. Cheng, Y. Yang and L. Rontu. 2012. Snow and ice on Bear lake (Alaska)-Sensitivity experiments with two lake ice models, *Tellus A*, **64**, 17339, doi: 10.3402/tellusa.v64i0.17339.

Sharpley, A., P. Kleinman, R. McDowell, M. Gitau and R. Bryant. 2002. Modeling phosphorus transport in agricultural watersheds: Processes and possibilities. *Journal of Soil and Water Conservation* **57**(6): 425-439

Sharpley, A.N., D. Radcliffe and M. Cabrera. 2006. Modeling phosphorus movement from agriculture to surface waters. *Modeling Phosphorus in the Environment*: 3

Sickman, J.O., A. Leydecker, C.C. Chang, C. Kendall, J.M. Melack, D.M. Lucero and J. Schimel. 2003. Mechanisms underlying export of N from high-elevation catchments during seasonal transitions. *Biogeochemistry* **64**(1): 1-24

Sivapalan, M., R.A. Woods, and J.D. Kalma, 1997. Variable bucket representation of Topmodel and investigation of the effects of rainfall heterogeneity, *Hydrological Processes* **11**, 1307–1330.

Siwek, J., J.P. Siwek and M. Żelazny. 2012. Environmental and land use factors affecting phosphate hysteresis patterns of stream water during flood events (Carpathian Foothills, Poland). *Hydrological Processes*:

Steenhuis, T.S., M. Winchell, J. Rossing, J.A. Zollweg, and M.F. Walter. 1995. SCS runoff equation revisited for variable source runoff areas. *J. Irrig. Drain. Eng.* **121**:234–238.

Stefan, H. G., X. Fang and M. Hondzo. 1998. Simulated climate changes effects on year-round water temperatures in temperate zone lakes. *Clim. Chang.* **40**: 547–576.

Stutter, M., S. Langan, R. Cooper. 2008. Spatial contributions of diffuse inputs and within-channel processes to the form of stream water phosphorus over storm events. *Journal of Hydrology* **350**(3): 203-214

SWRC, 2008. Water Quality Monitoring in the Source Water Areas for New York City: An Integrative Watershed Approach. A Final Report on Monitoring Activities, 2000-2005 submitted by Stroud Water Research Center. Avondale, PA.

Tague, C.L. and L.E. Band, 2004. RHESSys: Regional hydro-ecologic simulation system – an object-oriented approach to spatially distributed modeling of carbon, water, and nutrient cycling. *Earth Interactions,* **8** (19): 1-42.

Tyrovola and Diamadopoulos. 2005.. Bromate formation during ozonation of groundwater in coastal areas in Greece. *Desalination* **176**:201–9.

UFI (Upstate Freshwater Institute). 2001. Calibration, Verification of a One-Dimensional Hydrothermal and Eutrophication Model for Catskill/Delaware Reservoirs.

UFI (Upstate Freshwater Institute). 2013a. Implementation of Rondout Reservoir Model in Operation Support Tool, February 2013, Syracuse, NY.

UFI (Upstate Freshwater Institute). 2013b. Implementation of Upgraded Schoharie, Ashokan, and Kensico W2 Models in Operation Support Tool, March 2013, Syracuse, NY.

UFI (Upstate Freshwater Institute). 2013c. Short Circuiting Analysis of Inflow to the East Basin of Ashokan Reservoir, May 2013, Syracuse, NY.

USEPA (U. S. Environmental Protection Agency), 2006. National primary drinking water regulations: stage 2 disinfectants and disinfection by products rule: final rule. Fed Regist;71(2).

USEPA (U. S. Environmental Protection Agency), 2009. National Water Quality Inventory Report to Congress. http://www.epa.gov/305b/, accessed September 23, 2010.

Vadas, P.A., L.B. Owens and A.N. Sharpley. 2008. An empirical model for dissolved phosphorus in runoff from surface-applied fertilizers. *Agriculture, Ecosystems & Environment* **127**(1–2): 59-65

Van Dreason R. 2012 Disinfection Byproducts in the NYC Water Supply System in the aftermath of Tropical Storms Irene and Lee Watershed Science and Technical Conference, September 2012, West Point, NY.

Vazquez-Amabile, G.G. and B. A. Engel. 2005. Use of SWAT to compute groundwater table depth and streamflow in the Muscatatuck River watershed. *Transactions of the ASAE*. **48**(3): 991-1003.

Verstraeten, G. and J. Poesen 2002. Regional scale variability in sediment and nutrient delivery from small agricultural watersheds. *Journal of Environmental Quality* **31**(3): 870-879

Vollenweider, R. A. 1968. Scientific Fundamentals of the Eutrophication of Lakes and Flowing Waters with Particular Reference to Phosphorus and Nitrogen as Factors in Eutrophication. OECD Tech Rep. DAS/CS1 **68**:27.

Wagner, R. J., R.W. Boulger, Jr., C.J. Oblinger and B.A. Smith. 2006. Guidelines and standard procedures for continuous water-quality monitors: station operation, record computation, and data reporting. Techniques and Methods 1-D3. US Department of the Interior, US Geological Survey.

Walsh, S.E., S.J. Vavrus, J.A. Foley, V.A. Fisher, R.H. Wynne and J.D. Lenter. 1998. Global patterns of lake ice phenology and climate: model simulations and observations. *J. Geophys. Res.*, **103**(D22), 28,825–28,837.

Wang, J., X. Bai, G. Leshkevich, M. Colton, A. Clites and B. Lofgren. 2010. Severe Great Lakes ice cover during winter 2008–2009. *AGU EOS* **91** (5), 41–42.

Wang, J., H. Hu, D. Schwab, G. Leshkevich, D. Beletsky, N. Hawley, A. Clites. 2010. Development of the Great Lakes Ice-circulation Model (GLIM): Application to Lake Erie in 2003–2004, *Journal of Great Lakes Research* **36**: 425–436

Weiss, W. J., S. C. Schindler, S. Freud, J. A. Herzner, K. F. Hoek, B. A. Wright, D. A. Reckhow, and W. C. Becker. 2013. Minimizing raw water NOM concentration through optimized source water selection. *Journal of the American Water Works Association* **105**(10):596-608.

Wert, E. C., J. Bolding, D. J. Rexing and R. E. Zegers. 2012. Real-Time Modeling of Trihalomethane Formation in a Full-Scale Distribution System. *Journal of Water Supply: Research and Technology-AQUA* **61**(6): 352-363.

Westerhoff, P., J. Debroux, G. L. Amy, D. Gatel, V. Mary and J. Cavard 2000. Applying DBP Models to Full-Scale Plants. *Journal of the American Water Works Association* **92**(3): 89-102.

White, E.D., Z.M. Easton, D.R. Fuka, A.S. Collick, E. Adgo, M. McCartney, S.B. Awulachew, Y.G. Selassie and T.S. Steenhuis. 2011. Development and application of a physically based landscape water balance in the SWAT model. *Hydrological Processes* **25**:915-925. DOI: 10.1002/hyp.7876.

White, M. J., R. D. Harmel, J. G. Arnold, and J. R. Williams. 2012. SWAT Check: A screening tool to assist users in the identification of potential model application problems. *J. Environ. Quality* (in press). Available at: http://swatmodel. tamu.edu/software/swat-check

Wigmosta, M.S. and D.P. Lettenmaier, 1999. A comparison of simplified methods for routing topographically driven subsurface flow. *Water Resour. Res.*, **35**(1), 255-264.

Wigmosta, M.S., L.W. Vail and D.P. Lettenmaier, 1994. A distributed hydrology-vegetation model for complex terrain. *Water Resour. Res.*, **30**(6), 1666-1679.

Wilde, F.D., D.B. Radtke, J. Gibs and R.T. Iwatsubo. 1999, National field manual for the collection of water-quality data: U.S. Geological Survey Techniques of Water- Resources Investigations, book 9 chap. A4, 103 p.

Williams, G.P. 1989. Sediment concentration versus water discharge during single hydrologic events in rivers. *Journal of Hydrology* **111**(1): 89-106

Williams, C., R. Vose, D. Easterling and M. Menne. 2006. United States historical climatology network daily temperature, precipitation, and snow data. ORNL/CDIAC-118, NDP-070. Available on-line [http://cdiac. ornl. gov/epubs/ndp/ushcn/usa. html] from the Carbon Dioxide Information Analysis Center, Oak Ridge National Laboratory, US Department of Energy, Oak Ridge, Tennessee:

Wood, E.F., D.P. Lettenmaier, and V.G. Zartarian, 1992. A land-surface hydrology parameterization with subgrid variability for general circulation models, *J. Geophysical Res.* **97**, 2717-2728.

Yao, H., N. R. Samal, K. D. Joehnk, X. Fang, L. C. Bruce, D. C. Pierson, J. A. Rusak, A. James. 2014. Comparing ice and temperature simulations by four dynamic lake models in Harp Lake: past performance and future predictions, *Hydrological Proces*ses (In Press), DOI: 10.1002/hyp.10180.

Yoon, B.,and P.A. Raymond. 2012. Dissolved organic matter export from a forested watershed during Hurricane Irene. *Geophysical Research Letters*, **39**(18), L18402.

Zhao, R.J. and Liu, X.R., 1995. The Xinanjiang model. In: Singh, V.P. (Ed.). *Computer Models of Watershed Hydrology*. Water Resources Publication, pp. 215-232.

Zion, M. S., S. M. Pradhanang, D. C. Pierson, A. Anandhi, D. G. Lounsbury, A. H. Matonse, and E. M. Schneiderman. 2011. Investigation and Modeling of winter streamflow timing and magnitude under changing climate conditions for the Catskill Mountain region, New York, USA. *Hydrological Processes*, **25**:3289-3301. DOI: 10.1002/hyp.8174.

Appendix A:

Journal Articles by members of Water Quality Modeling Section

Anandhi, A., M. S. Zion, P. H. Gowda, D. C. Pierson, D. Lounsbury, and A. Frei. 2013. Past and future changes in frost day indices in Catskill Mountain region of New York. *Hydrological Processes* **27**(21):3094-3104.

Gelda, R. K., S. W. Effler, A. R. Prestigiacomo, F. Peng, A. J. P. Effler, B. A. Wagner, M. Perkins, D. M. O'Donnell, S. M. O'Donnell, and D. C. Pierson. 2013. Characterizations and modeling of turbidity in a water supply reservoir following an extreme runoff event. *Inland Waters* **3**:377-390

Matonse, A., and A. Frei. 2013. A seasonal shift in the frequency of extreme hydrological events in southern New York State. *Journal of Climate* **26:** 9577-9593.

Mukundan, R., D. C. Pierson, E. M. Schneiderman, D. M. O'Donnell, S. M. Pradhanang, M. S. Zion, and A. H. Matonse. 2013. Factors affecting storm event turbidity in a New York City water supply stream. *Catena* **107**:80-88.

Mukundan, R., N. R. Samal, D. C. Pierson, M. S. Zion, and E. M. Schneiderman. 2013. Turbidity in a New York City Water Supply Stream: Sensitivity to Projected Changes in Winter Streamflow. *Hydrologic Processes* **27**:3014-3023.

Mukundan, R., S. Pradhanang, E. Schneiderman, D.C. Pierson, A. Anandhi, M. Zion, A. Matonse, D. Lounsbury, and T. Steenhuis. 2013. Suspended Sediment Source Areas and Future Climate Impact on Soil Erosion and Sediment Yield in a New York City Water Supply Watershed, USA. *Geomorphology* 183:110-119.

Pierson, D. C., N. Samal, E. Owens, E. M. Schneiderman, and M. S. Zion. 2013. Changes in the Timing of Snowmelt, and the Seasonality of Nutrient Loading: Can Models Simulate the Impacts on Freshwater Trophic Status? *Hydrologic Processes* **27**:3083-3093.

Pradhanang, S. M., R. Mukundan, E. M. Schneiderman, M. Zion, A. Anandhi, D. C. Pierson, A. Frei, Z. M. Easton, D. Fuka, and T. S. Steenhuis. 2013. Streamflow responses to climate change: Analysis of hydrologic indicators in a New York City Water Supply watershed. *Journal of American Water Resource Association* **49:** 1308-1326

Pradhanang, S. M., E. M. Schneiderman, A. Frei, M. S. Zion, T. S. Steenhuis, and D. C. Pierson. 2013. Rain-On-Snow Events in New York. *Hydrologic Processes* **27**:3035-3049.

Samal, N. R., R. Mukundan, D. C. Pierson, R. K. Gelda, E. M. Schneiderman, M. S. Zion, and A. H. Matonse. 2013. Turbidity in a New York City Water Supply Reservoir: Sensitivity to Anticipated Future Changes in Winter Turbidity Loading. *Hydrologic Processes* **27**:3061-3074.

Schneiderman, E. M., A. H. Matonse, D. G. Lounsbury, S. M. Pradhanang, R. Mukundan, M. S. Zion, and D. C. Pierson. 2013. Comparison of Spatially-Distributed Snowpack Models for New York City Watersheds. *Hydrologic Processes* **27**:3050-3060.

Tilahun, S., R. Mukundan, B. Demisse, T. Engda, C. Guzman, B. Tarakegn, Z. Easton, A. Collick, A. Zegeye, and E. Schneiderman. 2013. A Saturation Excess Erosion Model. *Transactions of the American Society of Agricultural and Biological Engineers (ASABE)* 56:681-695.

HYDROLOGICAL PROCESSES
Hydrol. Process. (2013)
Published online in Wiley Online Library
(wileyonlinelibrary.com) DOI: 10.1002/hyp.9937

Past and future changes in frost day indices in Catskill Mountain region of New York

Aavudai Anandhi,[1]* Mark S. Zion,[2] Prasanna H. Gowda,[3] Donald C. Pierson,[2] David Lounsbury[2] and Allan Frei[4]

[1] *Department of Agronomy, Kansas State University, Manhattan, KS, 66506, USA*
[2] *Water Quality Modeling Group, New York City Department of Environmental Protection, Kingston, NY, USA*
[3] *USDA-ARS Conservation and Production Research Laboratory, Bushland, TX, 79012, USA*
[4] *Department of Geography, Hunter College, City University of New York, New York, NY, USA*

Abstract:

Changes in frost indices in the New York's Catskill Mountains region, the location of water supply reservoirs for New York City, have potentially important implications. Frost day is defined as a day with $T_{min} < 0$ °C. The objective of this study was to investigate past and predicted changes in minimum temperature (T_{min}) and six frost indices in the Catskill Mountains covering six reservoir watersheds. Studied frost indices included (1) number of frost days, (2) number of months with frost, (3) last spring freeze date (LSF), (4) first fall freeze date (FFF), (5) growing season length (GSL), and (6) frost season length. Past changes in the frost indices were studied using observed daily T_{min} for each watershed for the periods 1960–2008. Future changes in frost indices for the periods (2045–2065 and 2080–2100) were studied for emission scenarios (A1B, A2, and B1) downscaled from global climate models (GCMs). Results indicated a general increase in average T_{min} and GSL and a decrease in number of frost days, months with frost, frost season length, earlier LSF, and later FFF from the historical to the future periods, and the magnitude of change varied among the watersheds and GCMs. For the period 1960–2000, in all watersheds (except Cannonsville), LSF occurred earlier by 2.6–4.3 days/decade, FFF occurred later by 2.7–3.2 day/decade, and GSL was longer by 2.4–4 day/decade. Among the scenarios and GCMs, LSF occurred earlier by 4–11 and 4.5–15 days/decade for the periods 2045–2065 and 2081–2100, respectively; FFF occurred later by 1–10 and 4–13 days/decade for the periods 2045–2065 and 2081–2100, respectively; and GSL was longer by 10–25 and 13–40 days/decade for the periods 2045–2065 and 2081–2100, respectively. The increase in GSL is expected to affect hydrologic, ecosystem, and biogeochemical processes with increased net primary productivity and a resulting increase in total annual evapotranspiration. Copyright © 2013 John Wiley & Sons, Ltd.

KEY WORDS Frost day; last spring freeze; first fall freeze; growing season length

Received 28 September 2012; Accepted 10 June 2013

INTRODUCTION

Snow and ice are essential components of the global hydrological and energy cycles, and they are closely associated with the frost occurrence (Jylhä *et al*., 2008). Numerous indices have been used to describe frost's impact on natural and managed ecosystems (Schwartz and Reiter, 2000; Feng and Hu, 2004; Ben-David *et al*., 2010; Zhou and Ren, 2011; Terando *et al*., 2012). Indices make it easier to communicate information about climate anomalies to diverse audiences and allow scientists to assess climate anomalies quantitatively in terms of intensity, duration, frequency, and spatial extent, thereby providing important information useful for planning, designing, and management of applications (Tsakiris and Vangelis, 2005). Commonly used frost indices include the timing of the last frost day in spring and first frost day in fall of each year, number of consecutive frost days, duration of frost-free days, and length of growing season. Many of these indices are calculated using daily minimum air temperature (T_{min}).

Changes in frost indices have important implications in New York's Catskill Mountains region, the location of water supply reservoirs for New York City. More than 90% of the region is covered with forests. Snow is an important component of the region's hydrological systems, ecosystems, infrastructure, travel safety, winter tourism and recreation (Burakowski *et al*., 2008). Studies have shown that an increase in temperature in the region has led to a decrease in snowpack accumulation and duration (Burns *et al*., 2007; Matonse *et al*., 2011; Pradhanang *et al*., 2011; Zion *et al*., 2011). These changes will most likely force changes in the hydrology of the region by decreasing the proportion of precipitation falling as snow, shifting the timing of snowmelt and causing snowmelt-supplemented

*Correspondence to: Aavudai Anandhi, Department of Agronomy, Kansas State University, Manhattan, KS 66506, USA
E-mail: anandhi@ksu.edu

streamflow events to occur earlier in the spring or in late winter, which as a result will decrease the magnitude of traditionally high streamflows in April (Zion *et al.*, 2011). More run-off during winter, in turn, can cause reservoir storage levels, water releases, and spills to increase during the winter and earlier reservoir refill in the spring (Matonse *et al.*, 2011). Changes in last frost day in spring, first frost day in fall, and growing season length (GSL), in turn will change the annual evapotranspiration, streamflow patterns, and the frequency of drought (Huntington *et al.*, 2009). This will have profound direct and indirect effects on forest productivity, nuisance species (including pests, pathogens, and invasive species), wildlife, and forest nutrient cycling (Huntington, 2006; Campbell *et al.*, 2009; Mohan *et al.*, 2009). Hence, investigating current and future climate change on a regional scale is essential to understand potential impacts on humans and the natural environment (Hayhoe *et al.*, 2007). The main objective of this study is to investigate the past and future changes in the frost indices in the Catskill Mountains region of New York State (NY).

STUDY REGION AND DATA

The study region is in the Catskill Mountains, part of the eastern plateau climate region of NY (Figure 1). The study area encompasses an area of about 4100 km^2 and consists of six reservoir watersheds: Cannonsville, Ashokan, Nerversink, Schoharie, Rondout, and Pepacton. The region contributes about 90% of New York City's water supply and has an elevation range of 125–1275 m . These mountainous watersheds are mostly forested with some agricultural land-use (corn, hay, and pasture lands) within the Cannonsville watershed and, to a lesser extent, also within the Schoharie and Pepacton basins. Except for a slight decline in agricultural activity in Cannonsville, there has been little change in land development over the past decade (Schneiderman *et al.*, 2013).

The climate is classified as humid (Keim, 2010) with cool summers (with average minimum, maximum, and mean temperatures of 12, 22, and 18 °C, respectively), colder winters (with average minimum, maximum, and mean temperatures of 0, 10, and 5 °C, respectively), abundant snowfall, and year-round precipitation (Anandhi *et al.* (2011); Figure 2). Typically, total precipitation is about 1000–1200 mm per year, with snowfall accounting for approximately 20% of total precipitation (Anandhi *et al.*, 2011), and snowmelt historically contributes between 24% and 30% of total annual run-off in this region (Schneiderman *et al.*, 2013). The monthly mean snow water equivalent in the six watersheds for December to March are 5.0, 8.1, 9.3, and 2.7 mm/day, respectively (Anandhi *et al.*, 2011). For Cannonsville, the snowfall is ~50 mm/month during winter and contributes about 60% of the total winter precipitation during the 1958–1988 period

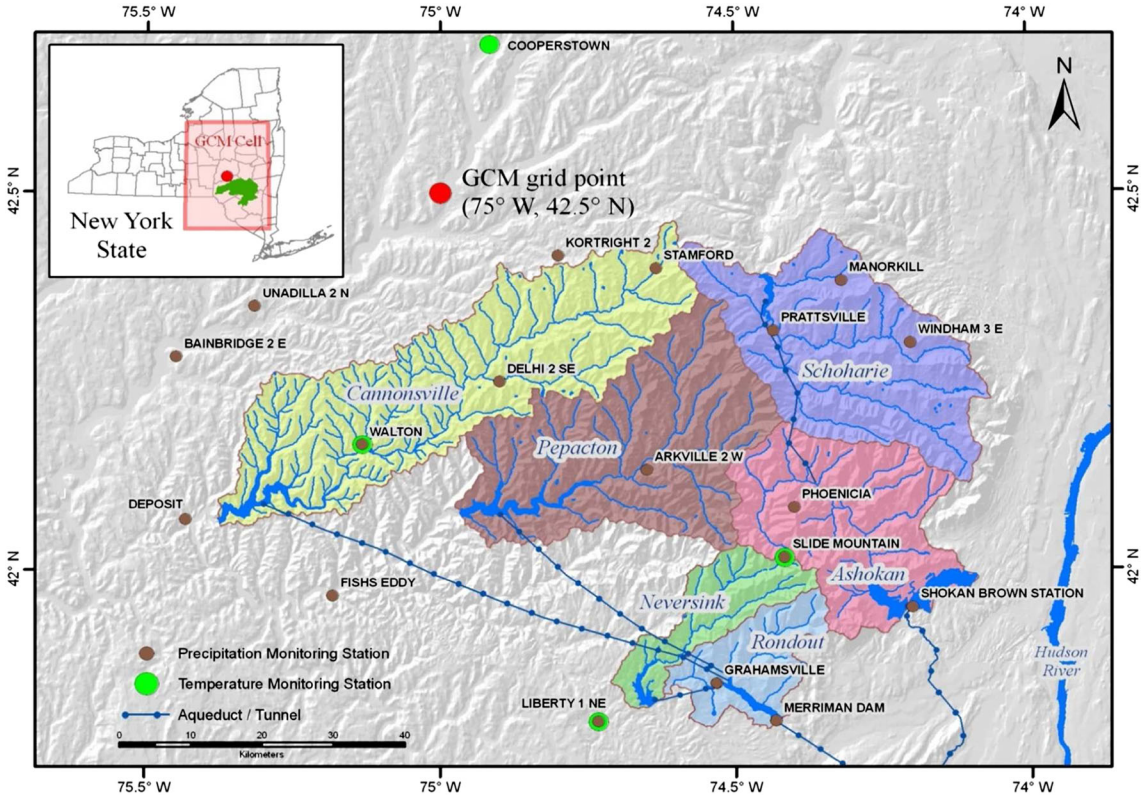

Figure 1. A map of the six reservoir watersheds in the Catskill Mountain region that provides approximately 90% of New York City's drinking water needs. The common grid cell to which all global climate model data were interpolated to is shown in the insert

DOI: 10.1002/hyp

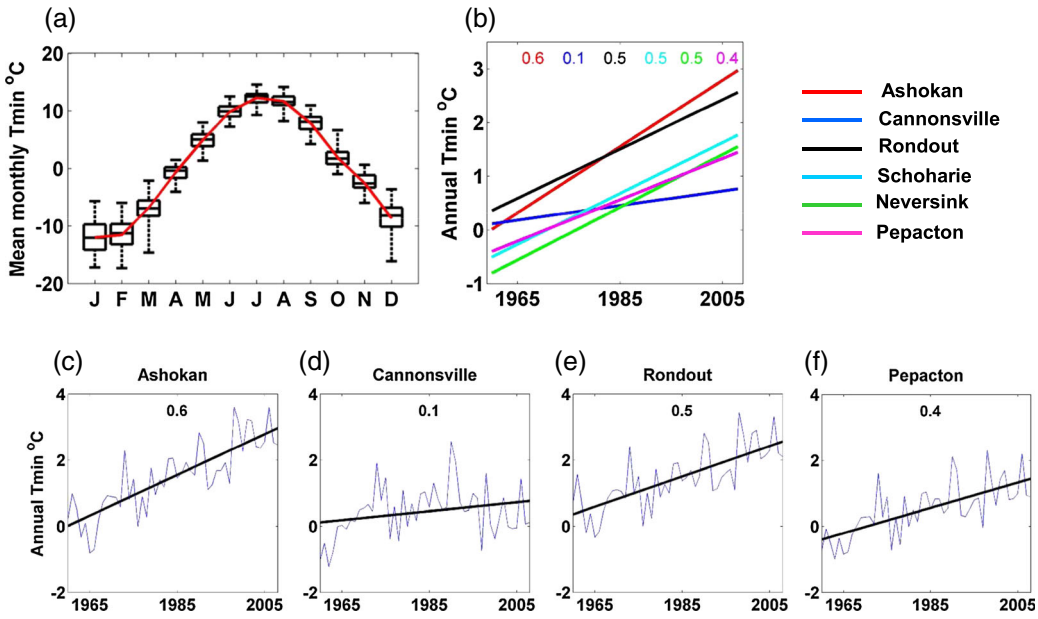

Figure 2. (a) Boxplots of mean monthly T_{min} for the six West of Hudson (WOH) watersheds. Each box is based on 49 years (1960–2008) of data times six watersheds. For this and all subsequent boxplots, the bounds of the box represent the 25th percentile (Q1 quartile) and 75th percentile (Q3 quartile), and the lower whiskers extend from 25th percentile to the minimum value, whereas the upper whisker extends from 75th percentile to the maximum value. The red line is the mean monthly T_{min} for all the six watersheds and all years. (b) Linear trend lines of annual T_{min} calculated as the mean of all daily (January–December) minimum temperatures for each of the six WOH watersheds. (c–f) Linear trend line (black line) and time series plot (blue line) of mean annual T_{min} for each of the six WOH watersheds; the numbers in the top of the subplots (b–f) represent the slope in °C/decade

(Frei *et al*., 2002). Evapotranspiration occurs at a much slower rate during the winter and March and April (periods of spring snowmelt) and occurs the greatest in the summer months with low streamflows (Zion *et al*., 2011).

Observed minimum T_{min} were obtained from the Northeast Regional Climate Center for four stations: Cooperstown, Liberty, Slide Mountain, and Walton (Figure 1), and data for the period 1960–2008 was used in the study. The elevations of these four stations are 366, 472, 808 and 451 m above mean sea level, respectively. Slide Mountain is at a higher elevation when compared with the rest of the stations. Global climate models (GCM) simulations at daily timescale were obtained from the World Climate Research Programme's Coupled Model Intercomparison Project Phase 3 multimodel dataset. The simulations used in the study were for baseline scenario (20C3M), future scenarios (A1B, A2, and B1), and two 21st-century periods (2045–2065 and 2080–2100). A list of the GCM simulations (name and realization number) used in the study is provided in Table I. The data from all the GCMs for the region surrounding the study region were extracted and interpolated to a common 2.5° grid by using bilinear interpolation technique.

Table I. Global climate models, country of origin, and realization numbers for minimum temperatures used in the study

S.N	GCM I.D *	Acronym	T_{min}	Country
1	BCCR-BCM2.0	bcc	1	Norway
2	CGCM3.1(T47)	cc4	1,2,3,4,5	Canada
3	CGCM3.1(T63)	cc6	1	Canada
4	CNRM-CM3	cnr	1	France
5	CSIRO-Mk3.0	cs3	1,2,3	Australia
6	CSIRO-Mk3.5	cs5	1,2,3	Australia
7	ECHAM5/MPI-OM	mpi	1,4	Germany
8	ECHO-G	miu	1,2,3	Germany, Korea
9	FGOALS-g1.0	iap	1,3	China
10	GFDL-CM2.0	gf0	1	USA
11	GFDL-CM2.1	gf1	2	USA
12	GISS-AOM	ga0	1	USA
13	GISS-ER	gir	1	USA
14	INGV-SXG	ing	1	—
15	IPSL-CM4	ips	1,2	France
16	MIROC3.2(hires)	mih	1	Japan
17	MIROC3.2(medres)	mim	1,2,3	Japan
18	MRI-CGCM2.3.2	mri	1,2,3,4,5	Japan
—	Total no. scenarios	—	38	—

*As provided by Lawrence Livermore National Laboratory's Program for Coupled Model Diagnosis and Intercomparison (PCMDI): http://www-pcmdi.llnl.gov/ipcc/model_documentation/ipcc_model_documentation.php.

METHODS

Estimation of daily temperature for a watershed

Frost indices were calculated for the study region (Fig. 1) by using observed and future scenarios of climate inputs. The spatial averaging method includes applying an environmental lapse rate (6 °C/km) to correct for elevation differences between the station and the mean elevation of each reservoir watershed and using inverse

DOI: 10.1002/hyp

distance squared weighting averaging of the four stations (NYCDEP, 2004). A single time series for daily T_{min} for each watershed is obtained after processing the observed T_{min} data from the four observing stations.

Delta change factor methodology

The scenarios of future T_{min} were created using delta change factor methodology. More details of this method can be found in Anandhi *et al*. (2011). In this method, the empirical cumulative distribution function of the simulated baseline (*GCMb*) and future (*GCMf)* climates were estimated. The cumulative distribution function was divided into 25 equal parts (bins), with each bin having four percentile (=100/25). Then, the mean monthly values of *GCMb* and *GCMf* climates were estimated for each bin using Equations (1) and (2).

$$\overline{GCMb_n} = \sum_{i=1}^{Nb} GCMb_{i,n}/Nb \quad (1)$$

$$\overline{GCMf_n} = \sum_{i=1}^{Nf} GCMf_{i,n}/Nf \quad (2)$$

The daily data in a month from all years of a scenario were pooled so *Nb* and *Nf* represent the total number of days associated with a given month during the baseline and future time periods for the *n*th change factor ($n = 1$–25). The *Nb* and *Nf* values varied depending on the month and number of years in the scenario period. Additive change factors associated with each frequency bin ($CF_{add,n}$) were calculated by taking an arithmetic difference between the mean bin value of a GCM variable derived from a current climate simulation and derived for the corresponding bin from a future climate scenario taken at the same GCM grid location (Equation 3). Using the time series of observed local values (*LOb*), pooled monthly data were evaluated to similarly define the range in values associated with each of the 25 bins of the variable frequency distribution. Based on the variable range defining bin (n) during month (m), the appropriate additive change factor was applied to obtain future scaled climate scenarios ($LSf_{add,n,j}$) of the variable for each day (j) of the scenario (Equation 4).

$$CF_{add,n} = \overline{GCMf_n} - \overline{GCMb_n} \quad (3)$$

$$LSf_{add,n,j} = LOb_{n,j} + CF_{add,n} \quad (4)$$

Thus, for each month, 25 CFs are calculated for T_{min} for combinations of GCM, future scenarios (A1B, A2, and B1), and two periods (2045–2065 and 2081–2100) (Table I).

FROST INDICES

A number of definitions of a frost day are available in the literature. In numerous studies, a frost day is defined as a day with a T_{min} less than a base temperature (T_b). Some of the chosen values for T_b are presented in Table IIa. In this study, as with most other studies, a frost day was defined as a day with $T_{min} < 0$ °C ($T_b = 0$ °C). The frost indices used in the study are listed in Table IIb and include the number of frost days (nFDs), number of frost months (nFMs), last spring freeze (LSF), first fall freeze (FFF), GSL, and frost season length (FSL). Trend was estimated using the linear regression method.

RESULTS AND DISCUSSION

Minimum air temperature

Monthly mean daily T_{min} for the six watersheds for the period 1960–2008 is plotted in boxplots in Figure 2a. January had the lowest daily T_{min} values, whereas July recorded the highest value followed closely by August. The range of T_{min} in the boxplots were due to the differences in six watersheds and interannual variations. The range was greatest (10–12 °C) during the winter (December, January, and February), early spring (March), and mid-fall (October), and the difference during the rest of the months was 5–6 °C (Figure 2a). The linear trend lines of the mean annual T_{min} for the six watersheds are plotted in Figures 2b–f. In general, all six watersheds show an increase in T_{min}. Among the watersheds, Cannonsville had the least increase in T_{min} (0.1 °C/decade), and Ashokan had the largest increase (0.6 °C/decade). The differing rates of change in the T_{min} could be due to differences in average elevation and land-use (Table III) between the watersheds.

The oscillations of atmospheric mass between high and midlatitudes are dominant patterns that characterize the northern hemisphere climate variability and are commonly referred to hemispherically as the Arctic Oscillation (AO) and regionally as the North Atlantic Oscillation (NAO) (Gong *et al*., 2002). These oscillations are most prevalent in the winter season and occur over a wide range of timescales, from intraseasonal to interdecadal. The AO exists year-round but is strongest and most variable in winter, and contains expressions in surface air temperatures (Allen and

Table IIa. Frost day definitions and sources

Frost definition	Reference
$T_{min} < 0$ °C	Christidis *et al*., 2007
$T_{min} < -4.4$, –2.2, and 5.6 °C	Robeson 2002
$T_{min} < 2.2$ °C	Schwartz and Reiter, 2000; Goodin *et al*. 1995, 2004
$T_{min} < 2$ °C	Potithep and Yasuoka 2011

DOI: 10.1002/hyp

Table IIb. Definition of the frost indices used in the study

Frost index	Frost index definition
Number of frost days (nFDs)	The number of days with frost
Number of frost months (nFMs)	The number of months with frost
Last spring freeze (LSF)	The last frost (freeze) day is the last day when $T_{min} < 0$ °C in the period starting on 1 March and ending on 30 June.
First fall freeze (FFF)	The first frost (freeze) day is first day when $T_{min} < 0$ °C in the period starting on 1 September and ending on 30 November .
Growing season length (GSL)	The number of days between the LSF and the FFF
Frost season length (FSL)	The number of days between the FFF and the LSF

Table III. General details of the watersheds adapted from Anandhi *et al.* (2011)

S N	Name of reservoir watershed	Elevation range, (mean) m	Watershed area[a] (km^2)	Land-use[b] (%)	
				Forest	Agriculture
1	Ashokan	125–1275 (539)	661	98	1
2	Cannonsville	315–1234 (572)	1177	80	19
3	Neversink	435–1276 (841)	238	98	2
4	Pepacton	353–1181 (633)	961	90	9
5	Rondout	248–1175 (523)	247	96	4
6	Schoharie	315–1234 (632)	817	91	8

[a] Includes the reservoir area.
[b] From Mehaffey *et al.* (2005) (Table I).

Zender, 2010). The positive trend in the winter AO index is associated to warmer winter temperatures in the region in the second half of the 20th century (Overland *et al.*, 2008). At mid to high northern latitudes, the AO statistically explains 31% of the winter temperature and about 40% of the winter temperature trends (Schaefer *et al.*, 2005).

The NAO has been shown to exert a strong influence on climate in eastern North America via latitudinal shifts in the wintertime North Atlantic storm track and associated variations in temperature, precipitation, and cyclonic activity (Gong *et al.*, 2002). For the winter period, the NAO index increased significantly for the period 1948–2001 and has shown to modulate high-frequency (daily) winter climatic variation in high latitude continental regions (Huntington *et al.*, 2004) and influence winter temperatures and precipitation. The positive NAO trends are similar to the AO trends in February and March but different in other months particularly in May and June when NAO trends are negative but AO trends are negligible (Zhou *et al.*, 2001).

Studies have shown that in mountainous terrain such as the study region, the lapse rate vary temporally (e.g. monthly, diurnal, and seasonal cycles) and spatially (e.g. aspect of slope, windward *vs* lee side, location relative to valley, and synoptic types) (Blandford *et al.*, 2008; Minder *et al.*, 2010). However, there is sparsity of long term, high-resolution surface temperature measurements combined with the influences of local factors like cold air pooling and inversions, makes such quantification challenging. Daily T_{min} lapse rates are more variable and tend to be steepest in spring with monthly lapse rate in Idaho during October to April, varied between 0.5 and 3.6 °C/km (Blandford *et al.*, 2008). In another study in Cascade mountain during October to April, the annual mean and seasonal lapse rates in T_{min} were 4.2 °C/km and 4.5–6.0 °C/km, respectively, whereas in the leeward and windward side, the lapse rates were 3.5 to 5.5 °C/km and 2–6.5 °C/km, respectively (Minder *et al.*, 2010). This study assumed a constant environmental lapse rate in estimating the average watershed T_{min}, and so our results are subjective to varying lapse rates.

Boxplots of downscaled future T_{min} for 18 GCMs (Table I), two periods (2045–2065 and 2080–2100), and three special report on emissions scenarios (SRES) (A1B, A2, and B1) are shown in Figure 3 (a, b). In general, all GCMs show an increase in T_{min} except for a few scenarios in June and July for the 2045–2065 period. The magnitude of increase in T_{min} varies with month, GCM, scenario, and time, with a larger increase and range during the period 2080–2100 than in 2045–2065. The increase in T_{min} was 2–3 °C (median values) and 4–6 °C (median values) during the periods 2045–2065 and 2080–2100, respectively. During the 2045–2065 period, winter (December, January, and February) and early spring (March–April) have a greater

DOI: 10.1002/hyp

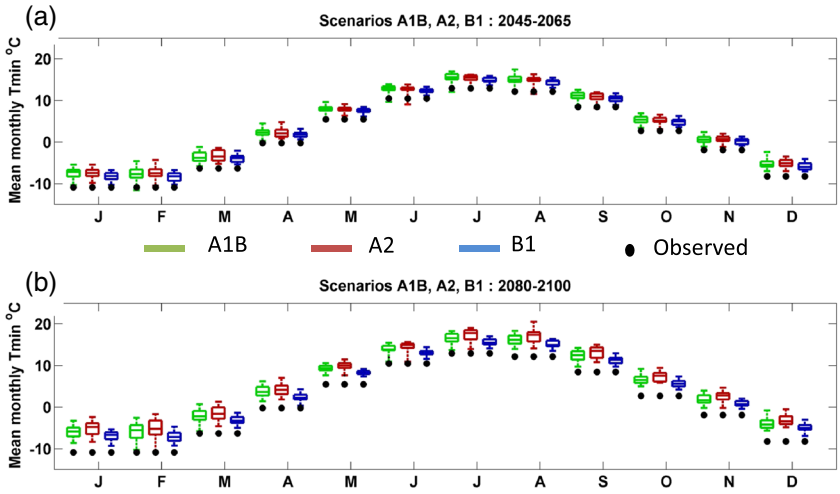

Figure 3. Boxplot of monthly mean downscaled future T_{min} for the six 6 West of Hudson watersheds for 18 global climate models and three emission scenarios (A1B, A2, and B1) for two periods: (a) 2045–2065 and (b) 2080–2100. The daily T_{min} values used to create each box are from multiple scenarios derived from the global climate models in Table I times six watersheds. The black dots in this figure and the red line in the previous figure (2a) represent the monthly mean observed values for the six West of Hudson watersheds

range among GCMs of up to 6 °C. The range of increase among the scenarios also is wider for the period 2080–2100 compared with the period 2045–2065.

Increases in T_{min} during the winter and early spring may influence the timing of snowfall, the number of days of snow cover, frequency of alternating freezing and thawing events, depth, and accumulation and properties of snowpack (Huntington *et al.*, 2009).

NUMBER OF FROST DAYS

The nFDs in a month for the six watersheds for 1960–2008 are plotted in boxplots in Figure 4a. In general, frost occurs in the Catskill Mountains during nine months, September through May; however, a few instances of frost occurred as late as June and as early as August. The variability in nFDs during spring and fall is high compared with the winter months and in general, greatest during the spring of the 1960–2008 historical period. January had the highest nFDs, followed by December, whereas September had the fewest nFDs (median values) during the normal nine-month frost period. The linear trend lines of nFDs in a year for the six watersheds are plotted in Figures 4b–h. In general, all six watersheds show a decrease in nFDs because of a gradual increase in T_{min}. Among the watersheds, Cannonsville showed the lowest decrease in nFDs (−0.3 days/decade), and Ashokan had the highest decrease (−6.6 days/decade). During 1960–2008, on an average, the nFDs in a year for all watersheds in Catskill declined from 177 to 163 days.

Boxplots of nFDs in each month during two future time periods (2045–2065 and 2080–2100) and three SRES scenarios (A1B, A2, and B1) are shown in Figure 5 (a, b). In general, all GCMs showed a decrease in nFDs. The magnitude of the decrease varies with month, GCM, scenario, and time. The differences between A1B and A2 scenarios were less than B1 scenarios during the 2045–2065 period, but during the 2080–2100 period, A2 had the highest decrease followed by A1B and B1 scenarios. The decrease during the period 2080–2100 is generally more than that during the 2045–2065 period, with a median decrease of 5–10 and 8–12 days during the 2045–2065 and 2080–2100 periods, respectively. Winter (December, January, and February) had a lesser decrease in nFDs compared with fall and spring. The range of the decrease is generally wider for 2080–2100 scenarios than for 2045–2065 scenarios.

In mountain valley locations where diurnal temperature ranges can be quite high and the daily average and daily maximum temperatures could conceivably rise in association with greater frequencies of high pressure, while daily minimum temperatures could drop in association with ideal conditions for radiational cooling. Such a scenario could in fact increase the frost indices but result in much lower snowfall and a shorter duration of snow cover. Also, frost (e.g., ice crystals on the vegetation and/or ground surfaces) may still occur even when the 2 m air temperature remains above freezing. So our results are subjective to varying definitions of frost day.

LAST SPRING FROST AND FIRST FALL FROST

Time series and trend lines for LSF and FFF for the six study watersheds are plotted in Figure 6. During 1960–2008, LSF occurred in May in most years (34–39 years out of 49 years) for all six watersheds. LSF occurred in April in about 14–15 years for Ashokan and Rondout watersheds but in June for the remaining four watersheds (7–15 years). All

DOI: 10.1002/hyp

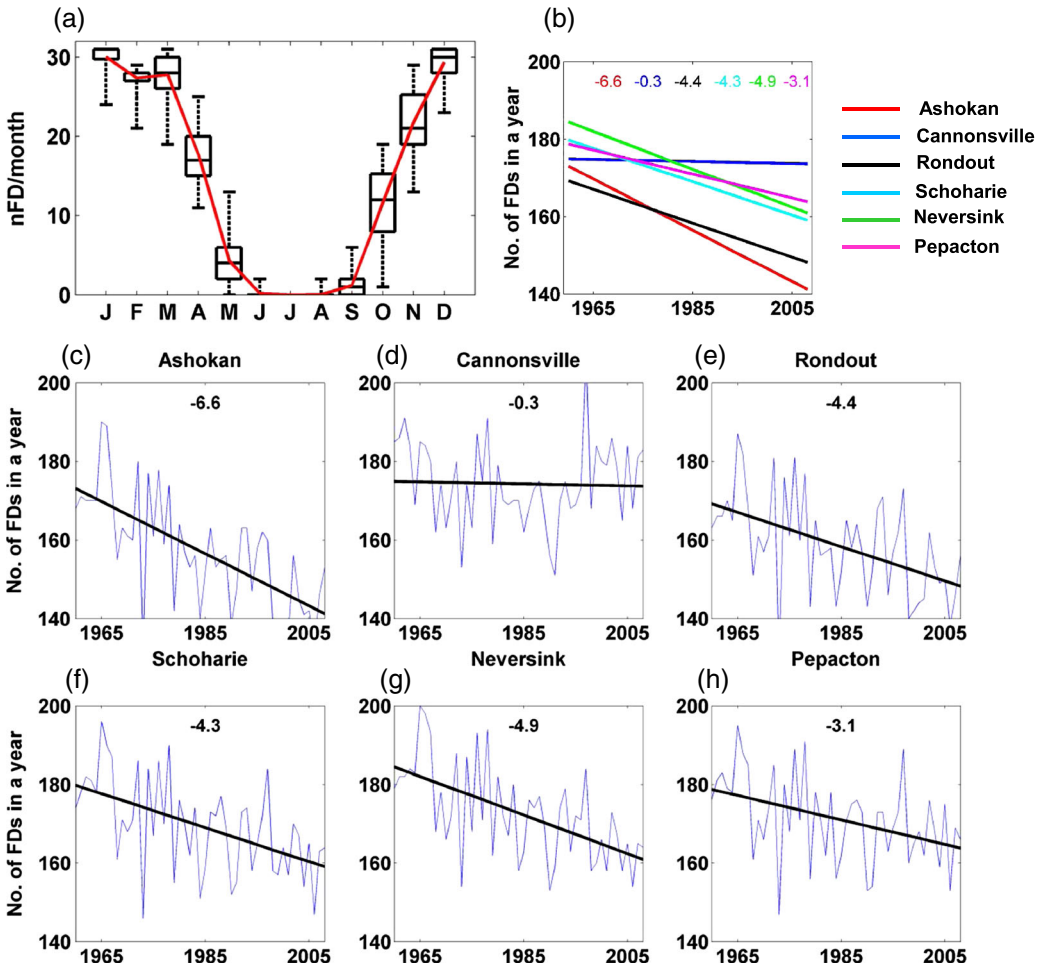

Figure 4. (a) Boxplots of number of frost days (nFDs) in a month for six West of Hudson (WOH) watersheds averaged for 1960–2008. Each box is based on 49 years (1960–2008) of data times six (watersheds) values of nFDs in a year. The red line is the mean nFDs for all six watersheds. (b) Linear trend lines of nFDs for the six WOH watersheds. (c–f) Linear trend line (black line) and time series plot (blue line) of annual nFDs for each of the six WOH watersheds. The numbers in the top of the subplots (b–h) represent the slope in days/decade

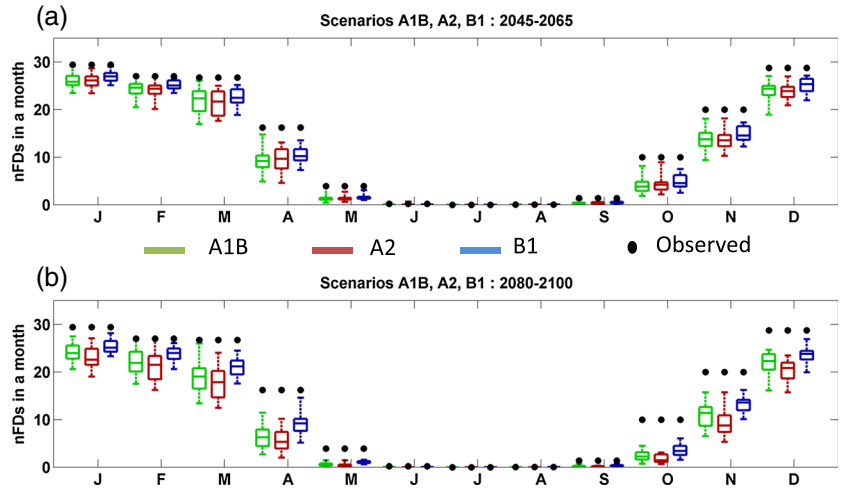

Figure 5. Boxplot of number of frost days in downscaled future T_{min} for six West of Hudson watersheds for three emission scenarios (A1B, A2, and B1) for two periods: (a) 2045–2065 and (b) 2080–2100. Each box is based on the daily data from multiple scenarios derived from the global climate models listed in Table I times six (watersheds). The black dots in this figure and the red line in figure (2a) represent the monthly observed values for the six West of Hudson watersheds

DOI: 10.1002/hyp

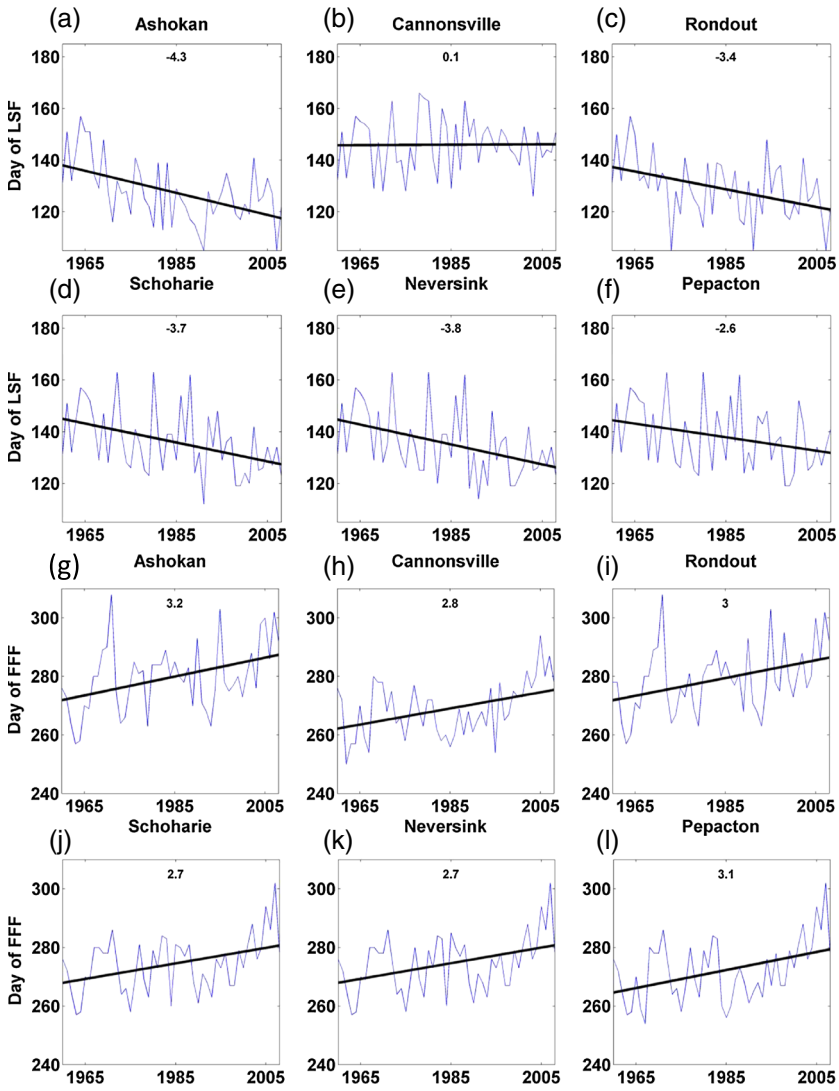

Figure 6. Linear trend line (black line) and time series plot (blue line) for last spring freeze (a–f) and first fall freeze (g–l) for each of the six West of Hudson watersheds. The numbers in the top of the subplots (a–l) represent the slope in days/decade

watersheds except Cannonsville showed a decrease in LSF (−2.6 to −4.3 days/decade; Figure 6a–f), indicating that in general, LSF occurred earlier in the spring season. Cannonsville watershed showed a slight increase of 0.1 day/decade). The earlier occurrence in spring in eastern USA is statistically explained by the increasing trends in the winter AO since the 1960s (Schaefer *et al.*, 2005).

FFF occurred in either October or November in 48 of 49 years for most watersheds. All watersheds experienced an increase in FFF (2.7–3.2 days/decade; Figure 6g–l), indicating that FFF generally occurred later in the fall. The nFMs decreased (figure not shown), with the LSF occurring earlier in the season, and FFF occurring later in the season.

Boxplots of LSF and FFF in future from 18 GCMs for two periods (2045–2065 and 2080–2100) and three SRES scenarios (A1B, A2, and B1) are shown in Figure 7 (a, b). All GCMs showed an earlier LSF and later FFF, which is consistent with historical trends in LSF and FFF. The range of LSF and FFF among the GCMs is higher in 2080–2100 than in 2045–2065 for A1B and A2 emission scenarios. In most GCMs simulations (about 75%), LSF occurred earlier in the spring and FFF occurred later in fall during the 2080–2100. compared to the 2045–2065 period. Among the scenarios and GCMs, LSF occurred earlier by 4–11 and 4.5–15 days / decade for the periods 2045–2065 and 2081–2100, respectively; FFF occurred later by 1–10 and 4–13 days /decade for the periods 2045–2065 and 2081–2100, respectively.

GROWING SEASON LENGTH AND FROST SEASON LENGTH

Time series and trend lines for GSL (Figure 8) and FSL for the six study watersheds are plotted. During the period

DOI: 10.1002/hyp

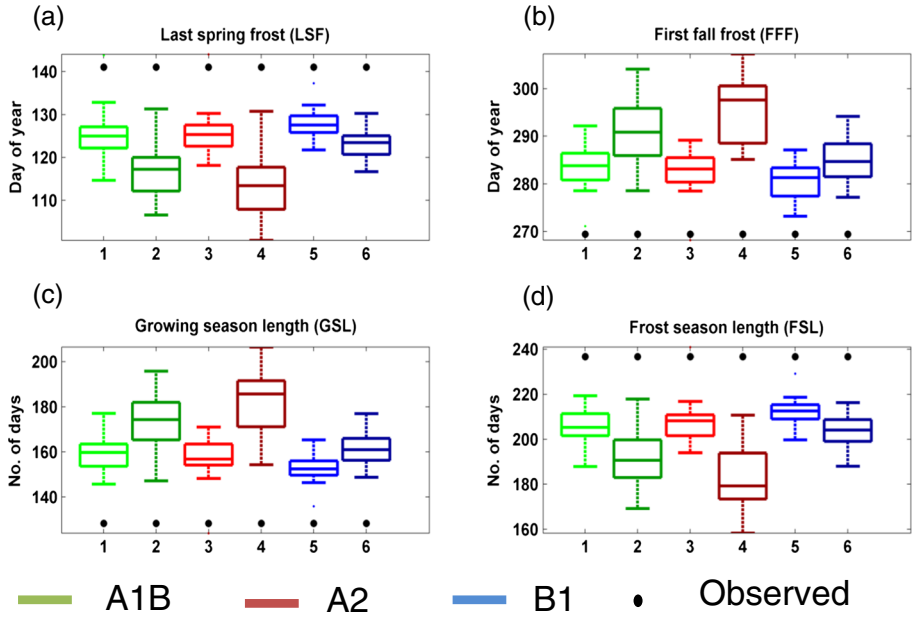

Figure 7. Boxplot of four frost indices (last spring freeze, first fall freeze, growing season length, and frost season length) based on downscaled future values of T_{min} for six West of Hudson watersheds for three emission scenarios (A1B, A2, and B1) for two periods: (a) 2045–2065 (represented as lighter shade) and (b) 2080–2100 (represented as darker shade). Each box is made of ensembles from multiple global climate models explained in Table I times six (watersheds) values. The black dots in this figure represent the mean observed values for the six West of Hudson watersheds. The numbers in the top of subplot (a) represent the slope in days/decade

1960–2008, on an average, the GSL varied from 123–152 days in a year extending from May to late October. All watersheds showed an increase in GSL of about 2.7–7.5 days/decade. With a general increase in GSL, there was a decrease in FSL. On average, the FSL varied from 213–242 days in a year extending from November to May. Among the study watersheds, Cannonsville had the highest FSL (242 days) and least GSL (123 days), whereas Ashokan had the least FSL (213 days) and highest GSL (152 days). Coherent associations between NAO and temperature indices such as nFDs and GSL were observed during 1951–2002 in northeastern USA (Brown *et al.*, 2010), and Cooperstown included in this study was one among the 40 stations used.

Boxplots of GSL and FSL from 18 GCMs for two future periods (2045–2065 and 2080–2100) and three SRES scenarios (A1B, A2, and B1) are shown in Figure 7 (c, d). In general, all GCMs showed a decrease in FSL and an

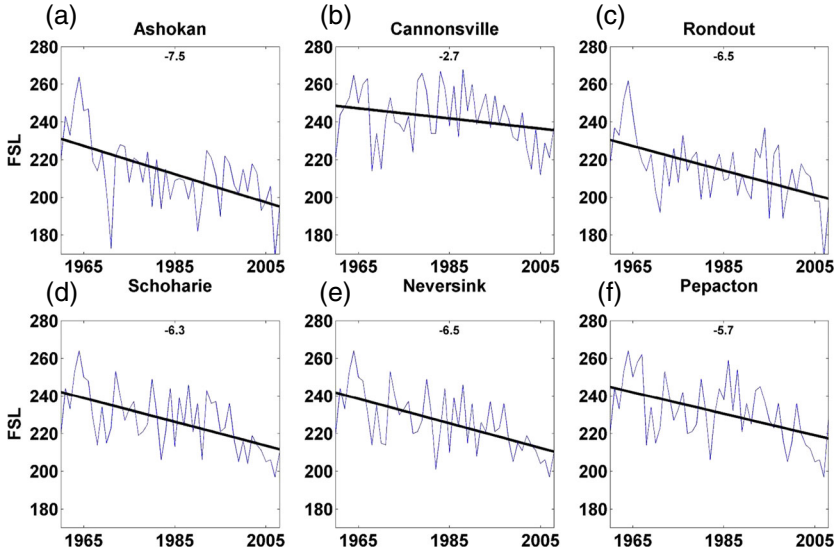

Figure 8. Linear trend line (black line) and time series plot (blue line) for frost season length (a–f) for each of the six West of Hudson watersheds. The numbers in the top of the subplots (a–f) represent the slope in days/decade

DOI: 10.1002/hyp

increase in GSL and were consistent with historical trends. The range in the FSL values obtained among the GCMs was higher in 2080–2100 than in 2045–2065 for A1B and A2 emission scenarios. For most GCMs (about 75 percentile), GSL is longer and FSL is shorter for period 2080–2100 than for 2045–2065. Among the scenarios and GCMs, GSL was longer by 10–25 day /decade and 13–40 days /decade for the periods 2045–2065 and 2081–2100, respectively, and FSL was shorter by the same rate for the two periods.

Increase in GSL will generally lead to an increase in annual evapotranspiration, and changes in LSF and FFF affect phenological events in the region such as bud break in spring and senescence and dormancy in the fall. The decrease in soil moisture during the growing season in substantial parts of eastern USA is likely attributed to increase in evapotranspiration and GSL rather than decreases in rainfall because the historical data do not suggest a decrease in summer rainfall during 1950–2000 period (Huntington *et al*., 2009).

Some of the possible reasons for the variability in the frost indices are discussed. Among the four stations used in the study, Slide Mountain has a higher increase in T_{min} and is at a higher elevation when compared with the rest. While estimating T_{min} for each watershed (using inverse distance squared weighting averaging), Cannonsville is least influenced by Slide Mountain. Also, little change in land development over the past decade is observed in the watershed (Schneiderman *et al*., 2013). Further, Ashokan watershed has a higher precipitation than Cannonsville watershed because of the south-east to north-west precipitation gradient across the region and the high elevation of the Slide Mountain station (Frei *et al*., 2002). The total evapotranspiration in Cannonsville and Askokan are comparable, but the percentage of total precipitation lost as total evapotranspiration is higher for Cannonsville (60%) when compared with Ashokan (30-45%) because the precipitation gradient (Frei *et al*., 2002). However the changes in GSL could change the total evapotranspiration and the period of low streamflow in the region.

Our results add local precision to the earlier findings that encompassed larger areas (Schwartz and Reiter, 2000; Adger *et al*., 2003; Kiktev *et al*., 2003; Feng and Hu, 2004; Christidis *et al*., 2007; Hayhoe *et al*., 2007; Trenberth *et al*., 2007; Hayhoe *et al*., 2008). Earlier LSF, later FFF, and longer GSL could affect the hydrologic, ecosystem, and biogeochemical processes both positively and negatively (Huntington, 2006; Campbell *et al*., 2009; Mohan *et al*., 2009).

CONCLUSION

Overall, our results indicated a general increase in average annual T_{min} and GSL, a decrease in the number of frost-free days (nFFDs) and FSL, earlier occurrence of LSF, and later occurrence of FFF. These trends were detected in the historical record (1960–2008) and were also seen in comparisons between baseline and future climate scenarios. For the period 1960–2000, in all watersheds (except Cannonsvelle), LSF occurred earlier by 2.6–4.3 days/decade, FFF occurred later by 2.7–3.2 days/decade, and GSL was longer by 2.6–7.5 days/decade. The variability in the trends in the frost indices among the watersheds could be due to the variability among the stations, watershed elevation differences, south-east to north-west precipitation gradient across the region, and land development over the past decade in certain regions. The trends in the frost indices are also subjective to varying periods for which the analysis is carried out.

The direction of change in frost indices estimated from the GCM simulations in the region were the same in almost all the scenarios and time periods, however, the magnitude of change varied among the GCMs. A2 scenario during the period 2081–2100 showed a greater change compared to the other emission scenarios. Among the scenarios and GCMs, LSF occurred earlier by 4–11 days /decade and 4.5–15 days /decade for the periods 2045–2065 and 2081–2100, respectively; FFF occurred later by 1–10 days / decade, and 4–13 days /decade for the periods 2045–2065 and 2081–2100, respectively; GSL was longer by 10–25 day /decade and 13–40 days /decade for the periods 2045–2065 and 2081–2100, respectively. Our results add local precision to the earlier findings that encompassed larger areas (Schwartz and Reiter, 2000; Adger *et al*., 2003; Kiktev *et al*., 2003; Feng and Hu, 2004; Christidis *et al*., 2007; Hayhoe *et al*., 2007; Trenberth *et al*., 2007; Hayhoe *et al*., 2008). Some of the implications of these changes in the Catskill Mountains region are discussed.

However, one should be aware that this study assumes a constant environmental lapse rate in estimating the frost indices, and the errors associated with this assumption is unquantified but may be quite important. Also, these results are subjective to the different definitions of frost indices. In future, it would be interesting to correlate the changes in frost indices with the changes in snow statistics and number of days with snow. Also, in future, it would be interesting to study the impact of the changes in GSL on evapotranspiration and the period of low streamflow. Further in-depth study is necessary to understand the direct and indirect effects of these changes on forest productivity, nuisance species (pests, pathogens, and invasive species), wildlife, and forest nutrient cycling.

ACKNOWLEDGEMENTS

This material is based upon work supported by the National Science Foundation under Award No. EPS-0903806 and matching support from the State of Kansas through Kansas Technology Enterprise Corporation. This is the contribution

DOI: 10.1002/hyp

number 13-073-J from the Kansas Agricultural Experiment Station. We thank the anonymous reviewers for helpful and constructive comments and suggestions.

REFERENCES

Adger WN, Huq S, Brown K, Conway D, Hulme M. 2003. Adaptation to climate change in the developing world. *Progress in Development Studies* **3**: 179–195. DOI: 10.1191/1464993403ps060oa.

Allen R, Zender C. 2010. Effects of continental-scale snow albedo anomalies on the wintertime Arctic oscillation. *Journal of Geophysical Research-Atmospheres* **115**: D23105.

Anandhi A, Frei A, Pradhanang SM, Zion MS, Pierson DC, Schneiderman EM. 2011. AR4 climate model performance in simulating snow water equivalent over Catskill Mountain watersheds, New York, USA. *Hydrological Processes* **25**: 3302–3311. DOI: 10.1002/hyp.8230.

Ben-David R, Abbo S, Berger J. 2010. Stress gradients select for ecotype formation in Cicer judaicum Boiss, a wild relative of domesticated chickpea. *Genetic Resources and Crop Evolution* **57**: 193–202. DOI: 10.1007/s10722-009-9461-z.

Blandford TR, Humes KS, Harshburger BJ, Moore BC, Walden VP, Ye H. 2008. Seasonal and synoptic variations in near-surface air temperature lapse rates in a mountainous basin. *Journal of Applied Meteorology and Climatology* **47**: 249–261.

Brown PJ, Bradley RS, Keimig FT. 2010. Changes in extreme climate indices for the northeastern United States, 1870–2005. *Journal of Climate*, **23**: 6555–6572. DOI: 10.1175/2010jcli3363.1.

Burakowski EA, Wake CP, Braswell BH, Brown DP. 2008. Trends in wintertime climate in the northeast United States, 1965–2005. *Journal of Geophysical Research* **113**: D20114. DOI: DOI:10.1029/2008JD009870.

Burns DA, Klaus J, McHale MR. 2007. Recent climate trends and implications for water resources in the Catskill Mountain Region, New York, USA. *Journal of Hydrology* **336**: 155–170.

Campbell JL, Rustad LE, Boyer EW, Christopher SF, Driscoll CT, Fernandez IJ, Groffman PM, Houle D, Kiekbusch J, Magill AH, Mitchell MJ, Ollinger SV. 2009. Consequences of climate change for biogeochemical cycling in forests of northeastern North America. This article is one of a selection of papers from NE Forests 2100: A synthesis of climate change impacts on forests of the Northeastern US and Eastern Canada. *Canadian Journal of Forest Research* **39**: 264–284. DOI: 10.1139/x08-104.

Christidis N, Stott PA, Brown S, Karoly DJ, Caesar J. 2007. Human contribution to the lengthening of the growing season during 1950–99. *Journal of Climate* **20**: 5441–5454. DOI: 10.1175/2007jcli1568.1.

Feng S, Hu Q. 2004. Changes in agro-meteorological indicators in the contiguous United States: 1951–2000. *Theoretical and Applied Climatology* **78**: 247–264. DOI: 10.1007/s00704-004-0061-8.

Frei A, Armstrong RL, Clark MP, Serreze MC. 2002. Catskill Mountain water resources: vulnerability, hydroclimatology, and climate-change sensitivity. *Annals of the Association of American Geographers* **92**: 203–224.

Gong G, Entekhabi D, Cohen J. 2002. A large-ensemble model study of the wintertime AO-NAO and the role of interannual snow perturbations. *Journal of Climate* **15**: 3488–3499.

Goodin DG, Mitchell JE, Knapp MC, Bivens RE. 1995, 2004. Climate and weather atlas of Kansas. Kansas Geological Survey Publications Educational series 12.

Hayhoe K, Wake C, Huntington T, Luo L, Schwartz M, Sheffield J, Wood E, Anderson B, Bradbury J, DeGaetano A, Troy T, Wolfe D. 2007. Past and future changes in climate and hydrological indicators in the US Northeast. *Climate Dynamics* **28**: 381–407. DOI: 10.1007/s00382-006-0187-8.

Hayhoe K, Wake C, Anderson B, Liang X-Z, Maurer E, Zhu J, Bradbury J, DeGaetano A, Stoner A, Wuebbles D. 2008. Regional climate change projections for the Northeast USA. *Mitigation and Adaptation Strategies for Global Change* **13**: 425–436. DOI: 10.1007/s11027-007-9133-2.

Huntington TG. 2006. Evidence for intensification of the global water cycle: review and synthesis. *Journal of Hydrology* **319**: 83–95. DOI: 10.1016/j.jhydrol.2005.07.003.

Huntington TG, Hodgkins GA, Keim BD, Dudley RW. 2004. Changes in the proportion of precipitation occurring as snow in New England (1949–2000). *Journal of Climate* **17**: 2626–2636.

Huntington TG, Richardson AD, McGuire KJ, Hayhoe K. 2009. Climate and hydrological changes in the northeastern United States: recent trends and implications for forested and aquatic ecosystems This article is one of a selection of papers from NE Forests 2100: a synthesis of climate change impacts on forests of the Northeastern US and Eastern Canada. *Canadian Journal of Forest Research* **39**: 199–212.

Jylhä K, Fronzek S, Tuomenvirta H, Carter T, Ruosteenoja K. 2008. Changes in frost, snow and Baltic sea ice by the end of the twenty-first century based on climate model projections for Europe. *Climatic Change* **86**: 441–462. DOI: 10.1007/s10584-007-9310-z.

Keim B. 2010. The lasting scientific impact of the Thronthwaite water-balance model. *Geographical Review* **100**: 295–300.

Kiktev D, Sexton DMH, Alexander L, Folland CK. 2003. Comparison of modeled and observed trends in indices of daily climate extremes. *Journal of Climate* **16**: 3560–3571.

Matonse AH, Pierson DC, Frei A, Zion MS, Schneiderman EM, Anandhi A, Mukundan R, Pradhanang SM. 2011. Effects of changes in snow pattern and the timing of runoff on NYC water supply system. *Hydrological Processes* **25**: 3278–3288. DOI: 10.1002/hyp.8121.

Minder JR, Mote PW, Lundquist JD. 2010. Surface temperature lapse rates over complex terrain: lessons from the Cascade Mountains. *Journal of Geophysical Research* **115**: D14122.

Mohan J, Cox R, Iverson L. 2009. Northeastern forest composition and productivity in a future, warmer world. *Canadian Journal of Forest Research* **39**: 213–230.

NYCDEP. 2004. *"Multi Tiered" Water Quality Modeling Program Semi-Annual Status Report—EPA Filtration Avoidance Deliverable Report*. New York City Department of Environmental Protection (NYCDEP): Valhalla, NY.

Overland J, Wang M, Salo S. 2008. The recent Arctic warm period. *Tellus A* **60**: 589–597.

Pradhanang SM, Anandhi A, Mukundan R, Zion MS, Pierson DC, Schneiderman EM, Matonse A, Frei A. 2011. Application of SWAT model to assess snowpack development and streamflow in the Cannonsville watershed, New York, USA. *Hydrological Processes* **25**: 3268–3277. DOI: 10.1002/hyp.8171.

Potithep S, Yasuoka Y. 2011. Application of the 3-PG model for gross primary productivity estimation indeciduous broadleaf forests: a study area in Japan. *Forests* **2**(2): 590–609.

Robeson SM. 2002. Increasing growing-season length in Illinois during the 20th century. *Clim Chang* **52**(1): 219–238. DOI: 10.1023/a:1013088011223.

Schaefer K, Denning AS, Leonard O. 2005. The winter Arctic Oscillation, the timing of spring, and carbon fluxes in the Northern Hemisphere. *Global Biogeochemical Cycles* **19**: GB3017.

Schneiderman EM, Matonse AH, Zion MS, Lounsbury DG, Mukundan R, Pradhanang SM, Pierson DC. 2013. Comparison of approaches for snowpack estimation in New York City watersheds. *Hydrological Processes*: n/a-n/a. DOI: 10.1002/hyp.9868.

Schwartz MD, Reiter BE. 2000. Changes in North American spring. *International Journal of Climatology* **20**: 929–932.

Terando A, Easterling W, Keller K, Easterling D. 2012. Observed and modeled twentieth-century spatial and temporal patterns of selected agro-climate indices in North America. *Journal of Climate* **25**: 473.

Trenberth K, Jones P, Ambenje P, Bojariu R, Easterling D, Klein Tank A, Parker D, Rahimzadeh F, Renwick J, Rusticucci M, Soden B, Zhai P. 2007. Observations: surface and atmospheric climate change. In Climate Change 2007: The Physical Science Basis. Contribution of Working Group I to the Fourth Assessment Report of the Intergovernmental Panel on Climate Change. Solomon S, Qin D, Manning M, Chen Z, Marquis M, Averyt K, Tignor M, Miller H (eds.).

Tsakiris G, Vangelis H. 2005. Establishing a drought index incorporating evapotranspiration. *European Water* **9–10**: 1–9.

Zhou Y, Ren G. 2011. Change in extreme temperature event frequency over mainland China, 1961–2008. *Climate Research* **50**: 125–139.

Zhou S, Miller AJ, Wang J, Angell JK. 2001. Trends of NAO and AO and their associations with stratospheric processes. *Geophysical Research Letters* **28**: 4107–4110. DOI: 10.1029/2001gl013660.

Zion MS, Pradhanang SM, Pierson DC, Anandhi A, Lounsbury DG, Matonse AH, Schneiderman EM. 2011. Investigation and modeling of winter streamflow timing and magnitude under changing climate conditions for the Catskill Mountain region, New York, USA. *Hydrological Processes* **25**: 3289–3301. DOI: 10.1002/hyp.8174.

Article

Characterizations and modeling of turbidity in a water supply reservoir following an extreme runoff event

Rakesh K. Gelda[1*], Steven W. Effler[1], Anthony R. Prestigiacomo[1], Feng Peng[1], Adam J.P. Effler[1], Bruce A. Wagner[1], MaryGail Perkins[1], David M. O'Donnell[1], Susan M. O'Donnell[1], and Donald C. Pierson[2]

[1] *Upstate Freshwater Institute, PO Box 506, Syracuse, NY 13214*
[2] *New York City Department of Environmental Protection, 71 Smith St, Kingston, NY 12401*
** Corresponding author email: rkgelda@upstatefreshwater.org*

Received 14 January 2013; accepted 24 June 2013; published 15 July 2013

Abstract

The findings from an integrated program of short- and long-term monitoring, individual particle analyses (IPA), and mechanistic modeling to characterize and simulate the turbidity (T_n) effects of an extreme runoff event (2011) on a water supply reservoir were documented. A robotic profiling platform and rapid profiling instrumentation resolved turbidity and temperature (T) patterns in time and space in the reservoir. Metalimnetic enrichment in T_n following the event was reported and attributed to the entry of turbid stream water as density currents, or plunging inflows. The diminishment of high T_n levels following the event was well represented by a first-order loss rate of about 0.023 d^{-1}. The highest T_n levels were avoided in water withdrawn for the water supply following the event by selection of vertical intake alternatives, although T_n values in the withdrawal remained distinctly above typical baseline conditions for nearly 2 months. Based on IPA, the T_n-causing particles were mostly clay minerals in the 1–20 μm size range. The operation of sorting processes determining settling losses from the minerogenic particle population, according to their size and shape, following the runoff event was resolved. The set-up and testing of a mechanistic T_n model, composed of 2 submodels, a 2-dimensional hydrothermal/transport submodel, and a T_n kinetics submodel, is described. The hydrothermal/transport submodel was tested separately and performed well in simulating the dynamics of the reservoir's stratification regime and the entry of the dense streams as plunging inflows during the extreme runoff event. The overall T_n model needed to represent the loss processes of both settling and coagulation to perform well in simulating the in-reservoir and withdrawal T_n patterns following the runoff event.

Key words: aggregation, clay minerals, coagulation, density currents, models, particle size, plunging inflows, settling, turbidity

Introduction

Terrigenous inputs of inorganic, or minerogenic, particles can have important ecological and water quality effects for receiving lakes and reservoirs by (1) influencing the transport and cycling of nutrients (Hupfer et al. 1995) and contaminants (Chapra 1997), (2) affecting metabolic activity (Phlips et al. 1995) and the composition of biological communities (Newcombe 2003), (3) increasing net sedimentation rates (Gelda et al. 2012), and (4) increasing light scattering, with coupled deterioration in related optical metrics of quality (Swift et al. 2006, Effler et al. 2008). Increases in turbidity (T_n), a surrogate metric of the light scattering coefficient (*b*; Kirk 2011), in water supply lakes and reservoirs are particularly problematic in the United States because of regulatory requirements to maintain low T_n levels in water supplied to users. The persistence of minerogenic particles in water columns has been linked to their sizes (Gelda et al. 2009, 2012). Disproportionately large loads of these particles are delivered by streams to many lentic systems during runoff events (Longabucco and Rafferty 1998, O'Donnell and Effler

DOI: 10.5268/IW-3.3.581

2006) because of increases in particle concentrations in tributaries, driven by the energy associated with elevated flows. This problem will be exacerbated in regions with more frequent and intense runoff events associated with ongoing climate changes (Thodsen et al. 2008, Li et al. 2011).

The short time scales of runoff events offer challenges to monitoring programs intended to quantify cause–effect relationships with respect to resolution of patterns of drivers and lake (or reservoir) responses, which cannot be met with common fixed-frequency, limited spatial resolution efforts. Contemporary robotic (O’Donnell and Effler 2006) and rapid profiling technologies are better suited to provide robust representations of the patterns imparted by these events. Moreover, patterns imparted to lentic systems may be vertically and longitudinally complex (Effler et al. 2006, O’Donnell and Effler 2006). Tributaries are often seasonally cooler, and thereby more dense, than the surface waters of receiving lakes and reservoirs in north temperate climates, resulting in a tendency to plunge upon entry (Martin and McCutcheon 1999). Sediment enrichment during runoff events further augments these density differences due to the effect of high suspended solids concentrations (Martin and McCutcheon 1999). A plunging inflow (or density current) generally moves over the bottom in upstream shallow areas of the basin as an underflow, entraining ambient water (Alavian et al. 1992, Rueda and MacIntyre 2010). Upon encountering a depth of equal density, the neutrally buoyant inflow separates from the bottom and intrudes into the water column as an interflow (Martin and McCutcheon 1999). These features of fate and transport are important in water supply lakes and reservoirs related to the position and depth(s) of water supply intakes (Gelda et al. 2009).

Optimal mathematical models of T_n are those that couple the patterns of the driver, terrigenous loads of particles, with those imparted to the receiving lentic system(s) associated with runoff events. Following successful testing, such quantitative frameworks can serve as invaluable management tools to potentially guide short-term management responses to events (Chung et al. 2009, Gelda et al. 2009, Liu and Chen 2013) as well as support the development of long-term strategies (Gelda and Effler 2008). Mechanistic models also serve as valuable research tools (Chapra 1997), which in the case of T_n can be used to investigate influences such as hydrodynamic processes and particle characteristics, including the effects of particle size distribution (PSD; Peng and Effler 2007, Peng et al. 2009).

This paper documents the findings of an integrated program of monitoring, particle characterization, and mechanistic modeling to describe and quantify the turbidity effects of an extreme runoff event (Hurricane Irene, 28 Aug 2011) on a water supply reservoir. Patterns of temperature (T) and T_n are resolved at the necessary fine time and space scales based on monitoring with robotic and rapid profiling technologies. The light scattering (T_n-causing) and settling attributes of particles are characterized with an individual particle analysis (IPA) technique that supports parameterization of the model. The development, testing, and application of a mechanistic T_n model, supported by the detailed monitoring and IPA characterizations, are described.

Methods

System description and Hurricane Irene

Rondout Reservoir (Fig. 1) is one of New York City’s (NYC) 19 water supply reservoirs, located (41°49′21.36″N, 74°28′15.6″W) ~130 km northwest of the city. This narrow (10.5 km long, 1.3 km wide) dimictic reservoir has a volume of 200×10^6 m^3, a surface area of 8.3 km^2, and a maximum depth of 52 m. This is a downstream reservoir in the overall system that receives withdrawals from 3 upstream reservoirs (Cannonsville, Pepacton, and Neversink). The NYC Department of Environmental Protection (NYCDEP) monitors inflows from the upstream reservoirs, outflows from Rondout Reservoir, and its surface elevation daily. Together the upstream reservoir inputs represent more than 80% of the total inflow, on average. The long-term average completely mixed flushing rate is 5 times per year. Four water supply

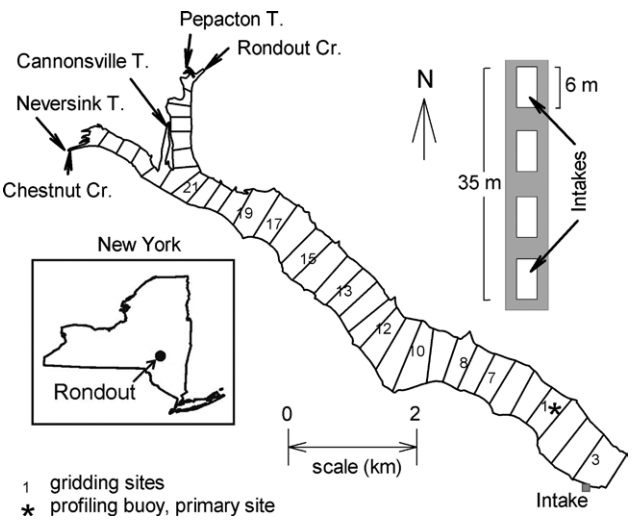

Fig. 1. Rondout Reservoir, robotic profiling platform location, upstream reservoir inflows, 2 natural tributaries, water supply intake position (multiple intake depths, as an inset), model segments, and position in New York (as inset).

 DOI: 10.5268/IW-3.3.581

intakes for the reservoir allow withdrawal from various depth intervals (Fig. 1). Water withdrawn from Rondout Reservoir enters an aqueduct for conveyance to a further downstream reservoir where it mixes with water from other parts of the system before disinfection and supply to NYC (no filtration treatment). NYCDEP has conducted a fixed frequency water quality monitoring program (weekly or biweekly) of the reservoir since the late 1980s that has included T profiles and T_n measurements at selected (n = 3 to 4) depths.

The largest natural inputs to the reservoir are Rondout Creek and Chestnut Creek, which on average contribute 9 and 4% of the total inflow, respectively. Flow (Q) is monitored continuously in both streams by the United States Geologic Survey (USGS site No. 0136500 and 01365500, respectively). The beds and banks of these streams, like most of those in this region (Peng et al. 2009), are positioned in clay mineral-rich glacial deposits. These deposits are subject to mobilization during elevated Q and are the primary source of high T_n levels in the streams during runoff events. NYCDEP also conducts water quality monitoring of these tributaries at variable frequencies and reports measurements of T_n and T on water withdrawn from the reservoir 5 days per week.

Hurricane Irene was a large Atlantic hurricane that was downgraded to a tropical storm just prior to reaching the NYC area on 28 August 2011. Record rainfalls were observed as it moved inland and approached NYC reservoirs, including approximately 20 cm near Rondout Reservoir. The associated runoff event had a recurrence interval of 30 y for Rondout Creek (log Pearson Type III analysis).

Monitoring: robotic and rapid profiling

In 2009, a robotic solar-powered profiling platform (Yellow Springs Instruments [YSI] 6951) was deployed in ~42 m of water along the main axis of the reservoir, approximately 2.2 km from the dam (Fig. 1), to measure T_n (YSI 6136; resolution of 0.3 NTU) and T (YSI 6560; resolution of 0.01 °C). The profiles were conducted at a 1 m depth resolution 4 times a day, separated by ~6 h. The robotic units were maintained weekly, including replacement of probes with newly calibrated ones. The same sensors were deployed in Rondout Creek at the USGS site, with measurements made at 15 min intervals.

Additionally, vertical profiles of T_n (or a surrogate) and T were collected at multiple sites ($n \geq 9$) along the main axis of the reservoir on 8 dates over the 31 August to 9 November 2011 interval to resolve longitudinal patterns. The instrumentation was either (1) a YSI unit (No. 6600), outfitted with the same probes as the profiling platform, with measurements made at 1 m depth intervals (first of 8 surveys), or (2) a SeaBird profiling package, with T and beam attenuation coefficient (at wavelength of 660 nm; c(660), WetLabs C star) sensors configured in a steel cage, with measurements made at a depth resolution of 0.25 m. The c(660) measurement, like T_n, is also a surrogate of b (Babin et al. 2003), and thereby T_n (Effler et al. 2006). A strong linear relationship prevailed between T_n and c(660) ($T_n = 1.84 \times c(660)$; $R^2 = 0.98$; n = 154), which supported reliable specification of T_n patterns from the c(660) measurements.

Particle characterizations related to turbidity and settling

The IPA technique used to characterize the light scattering (i.e., T_n-causing) and settling attributes of the particle populations of number concentration, PSD, and elemental composition, was scanning electron microscopy interfaced with automated image and X-ray analysis (SAX). The sample handling, preparation, and analytical protocols have been described in detail previously (Peng and Effler 2007). Approximately 2000 particles of sizes ≥0.4 µm were characterized for each of the 57 samples; 41 of these were collected from the water column of the reservoir at the primary (robotic buoy) site (Fig. 1), and 4 were collected in Rondout Creek close to its mouth following Hurricane Irene. Reservoir samples were collected at 0, 5, 10, 15, 20, 25, 30, and ~40 m on 31 August and 22 September. Subsequent samples (n = 5) from the primary reservoir site were collected at a depth of 20 m, proximate to the maximum T_n impact.

SAX results were used to make direct estimates of the scattering coefficient associated with minerogenic particles (b_m) through Mie theory calculations (Peng and Effler 2007). Turbidity, T_n, is a surrogate metric of b_m in this system because of the dominance of minerogenic particles (Peng et al. 2009). The SAX characterizations served to support parameterization of the T_n model by guiding partitioning of T_n levels according to different size classes, a major factor influencing the rate of diminishment of the effects following runoff events (Gelda et al. 2009, 2012). The projected area of all particles and the minerogenic subset per unit volume, PAV and PAV_m, respectively, were calculated for each sample as the summation of the projected areas (per unit volume) determined from the SAX analyses. These are fundamental metrics of the optical impacts of these particles because they are linearly related to the associated levels of scattering (i.e., T_n; Peng and Effler 2007).

Numerical model

Hydrothermal/transport submodel

The overall water quality model is composed of 2 submodels, a hydrothermal/transport submodel, and a T_n submodel. The adopted hydrothermal/transport submodel corresponded to that embedded in CE-QUAL-W2 (designated here as W2/T). This is a dynamic, laterally averaged, 2-dimensional model (Cole and Wells 2002) well suited for the morphometry of this reservoir (e.g., long, narrow, lack of dendritic features), with the desired attributes of simulation capabilities for (1) seasonal and shorter-term features of the stratification regime (Gelda and Effler 2007b), (2) behavior of density currents (Chung and Gu 1998), and (3) supporting resolution of longitudinal features of water quality (Gelda and Effler 2007a, Gelda et al. 2009). The model is based on the finite-difference solution of equations for laterally averaged fluid motion and mass transport. The basic equations of the model that describe horizontal momentum, hydrostatic pressure, free water surface elevation, continuity, density dependencies, and constituent transport have been presented previously (Chung and Gu 1998, Cole and Wells 2002). The heat budget of the model represents the effects of evaporative heat loss, short- and long-wave radiation, convection, conduction, and back radiation (Cole and Wells 2002). The equation of state (calculates density) of the model accommodated the effects of T, the concentration of suspended particulate material (SPM), and salinity (Martin and McCutcheon 1999); salinity was not a factor here. SPM was estimated from T_n according to an empirical expression developed for local reservoirs (unpublished data, NYCDEP).

The guidelines of Cole and Wells (2002) were followed in establishing the computational grid, utilizing the bathymetry of the reservoir. The adopted segmentation represented the reservoir by 38 longitudinal segments (Fig. 1), with 1 m thick vertical layers. Features of the outflows were also represented, including the water supply withdrawals (n = 4), dam outlet, and spillway length (Cole and Wells 2002). The model is operated to maintain a hydrologic budget, as described by Owens et al. (1998). The withdrawal algorithm (Cole and Wells 2002) describes the decreasing contributions from water column depths with increasing distances from the intake depths (e.g., “cone effect”). Inputs necessary to drive this submodel include inflows, outflows, inflow T and SPM, the light attenuation coefficient for downwelling irradiance (K_d, specifies light penetration), and meteorological conditions (air temperature, wind speed and direction, dewpoint temperature, and cloud cover, or solar radiation; hourly time step). This submodel has 5 coefficients (Table 1) that may be adjusted in the calibration process, although these are generally observed to not vary greatly among systems (Gelda et al. 2009). The values of the coefficients for longitudinal eddy viscosity, longitudinal eddy diffusivity, the Chezy coefficient, and the wind sheltering coefficient influence simulated features of transport and the distribution of heat. Fraction of solar radiation absorbed at the water surface (Table 1) influences the heat budget of the model. The time step of calculations is automatically adjusted between 1 s and 1 h by the model to maintain numerical stability (Cole and Wells 2002).

The hydrothermal/transport submodel was calibrated for the 1 January 2010–31 December 2011 interval, for

Table 1. Model coefficients for Rondout Reservoirs submodels.

Coefficient	Value
(a) Hydrothermal/transport submodel	
Longitudinal eddy viscosity	1 $m^2 s^{-1}$
Longitudinal eddy diffusivity†	10 $m^2 s^{-1}$
Chezy coefficient	70 $m^{0.5} s^{-1}$
Wind sheltering coefficient†	0.7
Fraction of incident solar radiation absorbed at the water surface	0.45
(b) Turbidity model(s)	
Input T_n fractions (classes 1, 2, 3)	0.2, 0.65, 0.15
Sizes (classes 1, 2, 3)	1, 3.1, 15 µm
Particle density	2.7 g cm^{-3}
Coagulation rates (class 1, 2)*	0.001, 0.0035 m^{-1} day^{-1}
Half-saturation constant*	1 NTU

†calibrated; others set to model default values
*for coagulation/aggregation version of submodel only

 DOI: 10.5268/IW-3.3.581

which the most temporally detailed reservoir monitoring (robotic buoy) was conducted. This submodel was validated for the 1987–2009 period, during which T profiles were collected less frequently. Stream flows (USGS) were specified at a time step of 15 min. Inflows from upstream reservoirs and outflows from Rondout Reservoir were specified as daily averages, based on the daily measurements. The value of K_d (0.4–0.95 m^{-1}) was based on irradiance profiles collected in 2005 and 2006 and 2 profiles during this study, calculated according to standard protocols (Kirk 2011). Meteorological inputs were specified from on-site measurements for the 1995–2011 interval, and by regional observations (Binghamton Airport, 132 km away) for other years.

Turbidity submodel(s)

These submodels adopt T_n as the state variable, conducting mass–balance-type calculations on this metric of light scattering. This approach has previously received extensive support in the literature, which has included review of theoretical and practical advantages over the use of SPM as an alternative and demonstrations of success (Gelda and Effler 2007a, Gelda et al. 2009, 2012). Two interactive ubiquitous processes are primarily responsible for the loss of T_n-causing particles from a water column over time: settling (Davies-Colley et al. 2003) and aggregation (or coagulation; Weilenmann et al. 1989). Two alternative T_n submodels were tested here, one that considers settling only, and the other that includes explicitly both settling and coagulation.

Gelda et al. (2009, 2012) successfully validated a T_n submodel for reservoirs where clay minerals dominated by explicitly representing only the settling process, describing it as a parsimonious (only as complex as necessary to address the issue; Chapra 1997, Martin and McCutcheon 1999) approach. Accordingly, the settling loss of T_n is described by

$$S_i = -v_i \frac{\partial c_i}{\partial z}, \quad (1)$$

where S_i = settling sink term for the i^{th} size class of T_n ($NTUs^{-1}$), v_i = settling velocity of i^{th} size class of T_n ($m \cdot s^{-1}$), c_i = T_n due to i^{th} size class of particles (NTU), and z = vertical coordinate (m). In the finite difference representation, particles (turbidity) settling from one layer serve as a source to the layer below. The settling velocity of the i^{th} size class of turbidity (*ci*; i.e., the associated particles), v_i, is computed for spherical particles according to Stokes Law,

$$v_i = \frac{g\left(\rho_p - \rho_w\right)}{18\mu} d_i^2, \quad (2)$$

where g = gravitational constant ($m \cdot s^{-2}$); ρ_p and ρ_w = densities of particles and water ($kg \cdot m^{-3}$), respectively; d_i = mean diameter of particles responsible for T_n in the i^{th} size class (m); and μ = water viscosity ($kg \cdot m^{-1} \cdot s^{-1}$). Both, ρ_w and μ are temperature dependent (Martin and McCutcheon 1999). The total T_n associated with N size classes of particles is computed according to:

$$T_n = \sum_{i=1}^{N} c_i, \quad (3)$$

consistent with the additivity of the components of inherent optical properties and their surrogates (Kirk 2011). Three size classes were found to represent the observed patterns well in this system (Table 1), as adopted for other nearby reservoirs (Gelda et al. 2009, 2012). Three inputs to this T_n submodel were specified (Table 1) as part of calibration: (1) the sizes of 3 particle size classes (1, 2, and 3), (2) the fractional contributions of these size classes to T_n levels in external loads, and (3) the density of the particles (ρ_p). These specifications were guided by the SAX characterizations (subsequently) that served to constrain the extent of tuning in the calibration process.

The likelihood that effects of particle coagulation were embedded within the above representation of settling has been acknowledged (Gelda et al. 2009) because the platelet morphometry of clay minerals is known to impede settling relative to spheres (Davies-Colley et al. 2003). Hofmann and Filella (1999) reported that sedimentation alone was insufficient to simulate the clay mineral-based decrease in T_n observed in deep portions of the hypolimnion of Lake Lugano (Switzerland, Italy) and concluded that coagulation needed to be represented. They adopted a modeling approach (e.g., O'Melia et al. 1985) that was relatively complex, requiring specification of a number of inputs/coefficients including particle collision frequencies and the efficiency of coagulation associated with the collisions for multiple particle sizes. Such models generally require substantial input adjustments ("tuning") for calibration.

We have instead adopted the following, more parsimonious, approach to accommodate the effects of coagulation in the second T_n submodel, acknowledging an element of empiricism. The same 3 size classes (1, 2, and 3) are considered, and all 3 are subject to continuing settling. The smallest 2 classes (1 and 2) are also subject to coagulation losses through conversion to the largest size class (i.e., source to class 3) that settles the fastest, as described by,

for i = classes 1 and 2: $$S_i = -v_i \frac{\partial c_i}{\partial z} - k'_{c,i} c_i, \text{ and} \quad (4)$$

for class 3: $$S_3 = -v_3 \frac{\partial c_3}{\partial z} + \sum_{i=1}^{2} k'_{c,i} c_i, \quad (5)$$

where $k'_{c,i}$ = coagulation rate constant for i^{th} size class where i = 1 and 2 (s^{-1}). The coagulation rate constant ($k_{c,i}$) is adjusted according to the depth and T_n, as described by:

$$k'_{c,i} = \left(\frac{c_i}{c_i + K} \right) k_{c,i} H, \quad (6)$$

where K = Michaelis-Menten constant (NTU); and H = depth from the surface (m). This last relationship is a form widely used in water quality modeling that here acts to limit the coagulation sink at low T_n levels, a feature consistent with the effects of reduced collision frequencies for lower particle concentrations (O'Melia 1985). The aggregation/coagulation version of the T_n submodel requires 3 additional model inputs, coagulation rates for the 2 smallest size classes, and a half-saturation constant value for T_n (Table 1), which were determined through calibration.

Results and discussion

Runoff event drivers

A typical inflow pattern from the upstream reservoirs was manifested during the 15–27 August 2011 period, before the runoff event, with progressive increases to about 40 $m^3 \cdot s^{-1}$ (as a daily average) and subsequent decreases (Fig. 2a) controlled by reservoir operations to maintain nearly full conditions. The dramatic large and abrupt increases in Rondout Creek and Chestnut Creek Qs from Hurricane Irene represented a strong contrast (Fig. 2a). Peak daily average flows of ~102 and 31 $m^3 \cdot s^{-1}$ and instantaneous peaks of ~ 232 and 74 $m^3 \cdot s^{-1}$ were observed for these 2 streams, respectively. These flows are the highest on record for both streams (since 1987).

The daily average T of Rondout Creek remained in a narrow range of 13.9 to 16.1 °C from 20 August to 5 September. Substantial diurnal variations (e.g., ~3 °C) in the T of the stream prevailed for most days (Fig. 2b), a widely observed phenomenon associated with cyclic variations in heat inputs (e.g., incident radiation, air T) within a day (Sinokrot and Stefan 1993). This variation was modulated on the day of the runoff event. The stream T was distinctly lower (i.e., the stream water was more dense) than the surface waters of the reservoir over the entire 10 d interval, including during the runoff event (Fig. 2b). The stream was also cooler than the 5 m depth of the reservoir, although the difference was diminished relative to the surface waters. These differences establish the propensity of the stream to plunge below the near surface waters of the reservoir over this interval, including during the event. This is a generally recurring feature for the summer to fall interval in the stream–reservoir systems of this area (O'Donnell and Effler 2006, Gelda et al. 2009, O'Donnell et al. 2011). Chestnut Creek T conditions were assumed to track those of Rondout Creek for the model analysis.

Temporal coverage of T_n measurements for Rondout Creek was incomplete for the event (Fig. 2c; disabled from the elevated flow). The abrupt rise of T_n that attended the rising limb of the event hydrograph was captured by the monitoring, but T_n measurements were not available past the time of the peak flow. The observed T_n maximum of ~1000 NTU was at the upper operating bound of the sensor. T_n values for the falling limb of the hydrograph were estimated from Q based on the T_n–Q relationship observed for a 2005 runoff event (Fig. 2c, see inset), the second longest return interval event (14 y) of the record (peak instantaneous flow of 178 $m^3 \cdot s^{-1}$). T_n dynamics for Chestnut Creek were specified based on a T_n–Q relationship developed from long-term monitoring (Fig. 2d, see inset). The extremely high Qs of the Hurricane Irene event required some extension of the T_n–Q relationships beyond the bounds of supporting measurements.

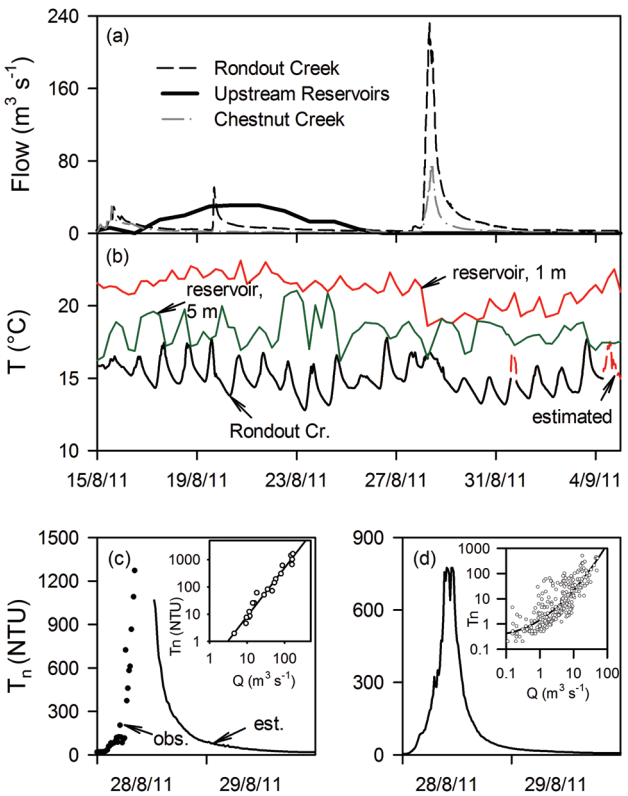

Fig. 2. Inflow conditions to Rondout Reservoir from mid-Aug to early Sep 2011, bracketing the runoff event associated with Hurricane Irene: (a) inflows from upstream reservoirs, Rondout Creek, and Chestnut Creek; (b) temperatures of Rondout Creek (hourly) and the upper waters of Rondout Reservoir (1 and 5 m, two lines) from the robotic profiling platform; (c) T_n in Rondout Creek, measurements combined with estimates, supporting T_n–Q relationship as an inset; and (d) T_n in Chestnut Creek estimated from a T_n–Q relationship (inset).

DOI: 10.5268/IW-3.3.581

Spatial and temporal variations in turbidity

Values of T_n were <2 NTU throughout the water column at the robotic monitoring site before the runoff event (Fig. 3a). Within ~10 h of the peak stream Q, the leading edge of a subsurface turbid plume had reached the downstream position of the buoy deployment in the reservoir, with a T_n maximum of ~15 NTU at a depth of 18 m (Fig. 3a). Approximately 28 h after the peak stream Q, the maximum turbidity impact was observed at that site, with a T_n ~135 NTU at a depth of 11 m; values >100 NTU extended from about 9 to 16 m at that time (Fig. 3b). The impact was clearly localized within stratified (metalimnetic) layers. This vertical T_n signature is compelling evidence for the entry of the streams as turbid plunging inflows, or density currents. This vertical structure could not be well resolved by the long-term monitoring protocols conducted widely for other systems because of the limited number of depths (n = 3 or 4) sampled. Note that while the vast majority of the enrichment in T_n was manifested in subsurface stratified depths, some modest increases to ~5 NTU occurred in the upper waters, consistent with the effects of mixing processes. The substantial thickness of the turbid plume (Fig. 3b) likely reflects not only the effects of mixing but also short-term variations in the density (e.g., T and SPM) differences between the streams and the reservoir during the event. The density current phenomenon occurs widely in lakes and reservoirs (Rueda and MacIntyre 2010, O'Donnell et al. 2011).

Depth–length contours of T_n are presented for 3 d based on observations with rapid profiling instrumentation collected from sites along the main axis of the reservoir (Fig. 4a–c). Corresponding detailed profiles of T and T_n are presented for the robotic site for reference. The highest T_n values were observed on the first of the longitudinal survey days. Variations in the longitudinal direction were manifested for all of these cases, although T_n enrichment extended along the entire reservoir at subsurface metalimnetic depths. The highest T_n levels were positioned upstream of the robotic monitoring site and the intakes for the water supply on 31 August (Fig. 4a) and 9 September (Fig. 4b). On 22 September the highest T_n levels extended to the dam (Fig. 4c). These observations depict a progressive decrease in T_n in the enriched layers

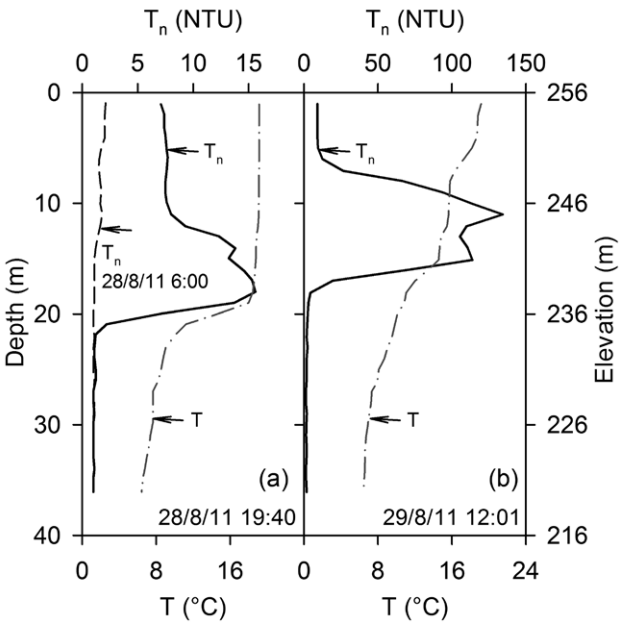

Fig. 3. Turbidity (T_n) and temperature (T) profiles in Rondout Reservoir from the robotic profiling platform: (a) 2 T_n profiles on 28 Aug at 06:00 h and 19:40 h, and the T profile at 19:40 h; and (b) single T_n and T profiles on 29 Aug at 12:01 h. The T_n profiles depict conditions before, soon after, and the peak impact from the turbid density currents from the Hurricane Irene runoff event.

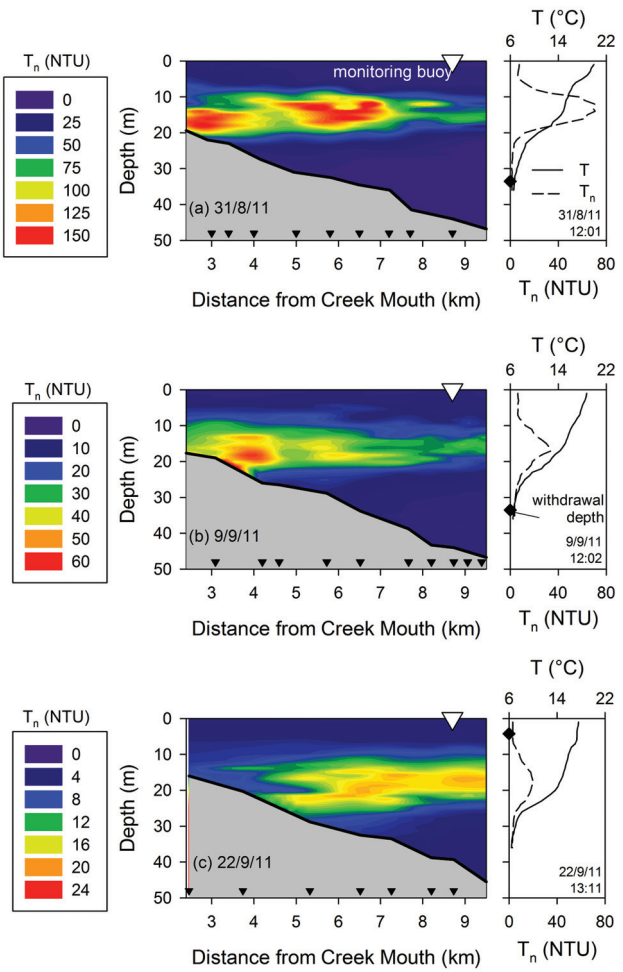

Fig. 4. Depth–length contours of T_n and coincident paired T_n and T profiles at the robotic profiling platform site in Rondout Reservoir for 3 different days following the Hurricane Irene runoff event: (a) 31 Aug, (b) 9 Sep, and (c) 22 Sep.

and a broadening of the affected metalimnetic depths (Fig. 4a–c), features consistent with the progression of particle loss (settling/coagulation) and mixing processes, respectively (Martin and McCutcheon 1999).

The progression of the decrease in T_n for the first 45 d following the event in the most impacted depths (8–18 m), based on robotic monitoring, was well represented by a log-linear relationship (Fig. 5) with a slope consistent with a first-order loss rate (0.024 d^{-1}). This can be considered a lumped, or aggregate, rate that includes the effects of multiple processes (e.g., mixing and particle settling). This rate is within the broad range reported for similarly determined values following multiple runoff events at nearby (60 km) Schoharie Reservoir that receives large quantities of minerogenic sediment during runoff events (Prestigiacomo et al. 2008). Levels of T_n remained relatively uniform after ~45 d (between 3 and 8 NTU), although above pre-event conditions (Fig. 5).

The time series of the withdrawal T_n, extending from approximately 1 month before to 2 months following the runoff event, depicts substantial impacts (Fig. 6a), despite withdrawal from intakes to avoid the most enriched layers. The pre-event levels (0.5–1.5 NTU) are the dominant case for this reservoir. Rarely have levels >2 NTU been observed (unpublished data, NYCDEP). The exceedance of 5 NTU for about 1 month after the event was an unprecedented occurrence for this reservoir. Note that withdrawal T_n values can deviate from those of the water column depths that correspond to the dimensions of the intakes (Fig. 1) because of the cone effect for the withdrawal (Gelda and Effler 2007c). The uppermost intake was being used at the time of the event, which would provide substantial avoidance benefit (Fig. 3b) for static stratification conditions; however, the effects of a seiche, reflected in short-term dynamics in T profiles (Fig. 6c), induced by the hurricane-driven wind even of 28 August, probably caused the abrupt increase in withdrawal T_n to nearly 15 NTU at the time of measurement on 29 August (Fig. 6a). The period of seiche (Wetzel 2001) for the stratification conditions that prevailed was estimated to be 19 h. This high T_n prompted a shift of the withdrawal to the bottom intake for avoidance, a change that was clearly manifested in the abrupt decrease in the withdrawal T (Fig. 6b). Values of T_n in the withdrawal over the following week were in the 6 to 9 NTU range. A change to the top intake on 9 September, depicted by the abrupt increase in the withdrawal T (Fig. 6b), resulted in the second abrupt increase in T_n to ~20 NTU (Fig. 6a) and the subsequent return to use of the deeper intake. This short-term increase in T_n was likely a transitory effect from mid-depth inputs because it exceeded levels that could have been brought into the intake from the upper layers of the reservoir (no seiche at that time). On 16 September there was a return to the use of the upper intake (Fig. 6a), without noteworthy change in the withdrawal T_n, consistent with the similar levels that prevailed in the upper and deep layers of the water column at that time (e.g., Fig. 4c). The return to T_n levels that approached the baseline (~2 NTU) in the withdrawn water took ~50 d following Hurricane Irene.

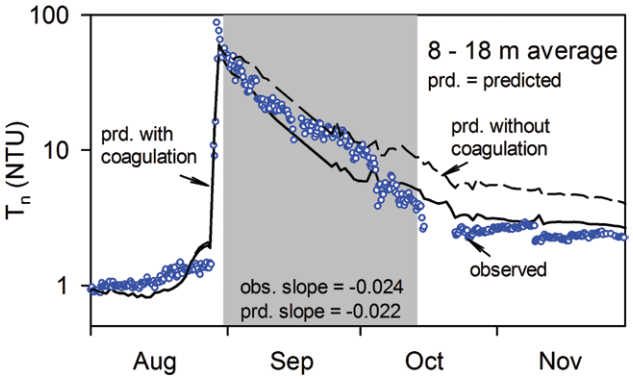

Fig. 5. Time series of volume-weighted T_n in Rondout Reservoir for the 8–18 m depth interval over the Aug–Nov period of 2011, resolved with the robotic monitoring platform, depicting the abrupt increase from the Hurricane Irene runoff event and subsequent attenuation. Simulations of the pattern with the 2 T_n submodels included.

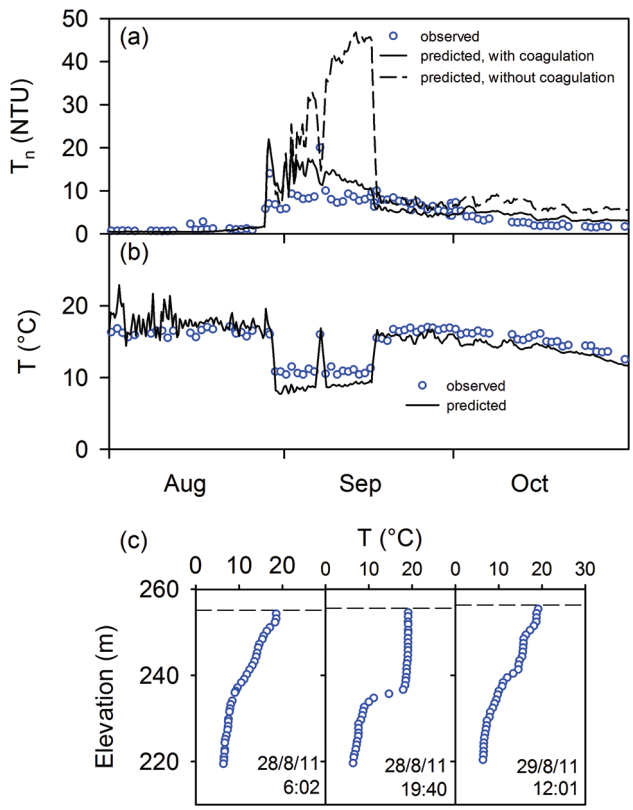

Fig. 6. Time series of measurements and model simulations for water withdrawn from Rondout Reservoir for the water supply for the Aug–Oct interval of 2011: (a) T_n, (b) T, and (c) T profiles at the robotic profiling platform location depicting the effects of a seiche.

DOI: 10.5268/IW-3.3.581

Turbidity-causing particles

The contributions of the various chemical classes to the overall particle populations of Rondout Creek and the reservoir are presented in the context of contributions to PAV (Table 2), which is linearly coupled to b, and thereby T_n (Peng and Effler 2007). Minerogenic particles, particularly clay minerals (Fig. 7a), dominated (i.e., $b \approx b_m$). On average, clay minerals represented 78 and 80% of PAV and PAV_m in the reservoir, respectively, and 75 and 78% in Rondout Creek (Table 2). The second most important minerogenic particle type was quartz. Similar compositions were observed for this stream and the reservoir. Moreover, similar characteristics have been reported for other systems in the region (Peng et al. 2009). Based on this composition breakdown, the T_n-causing particles in Rondout Reservoir primarily had terrigenous origins. Note that over the monitored interval, despite the wide range of T_n, only small variations in the composition of the responsible particles were observed. The dominance of minerogenic particles was further supported by the strong dependence of T_n on PAV_m and the small value of the y-intercept of the best-fit relationship (Fig. 7b). Variations in PAV_m explained 95% ($p < 0.001$) of the differences in T_n according to linear least-squares regression.

Two PSDs are presented from the sampling of 31 August, from depths of 10 and 20 m at primary robotic profiling buoy site (Fig. 7c). All the PSDs demonstrated a general shape found to recur for natural minerogenic particle populations in inland waters (Peng and Effler 2007, Peng et al. 2009). Peaks in number concentrations were observed between ~0.2 and 0.6 µm (Fig. 7c). Distinct differences in the trajectories of the 2 PSDs are evident, with relatively greater contributions by the smaller particles at the 10 m depth where T_n and PAV_m were higher. Corresponding size dependencies of b_m (i.e., T_n; Peng et al. 2009) from Mie theory calculations based on the SAX results are presented for the same 2 samples in a cumulative format (Fig. 7d). The different trajectories are consistent with the differences in the PSDs, with larger particles contributing more to T_n at the deeper depth. The size associated with the 50th percentile of these calculations (d_{50}; Fig. 7d) is a valuable metric of the size dependency of b_m (and T_n; Peng et al. 2009). The higher d_{50} of the 20 m sample (6.06 µm) reflects greater contributions by larger particles. Such high d_{50} values have been

Table 2. Summary of particle compositions according to contributions to PAV for Rondout Reservoir and Rondout Creek, average and standard deviation.

Particle Type	Rondout Reservoir avg. ± st. dev. (%)	Rondout Creek avg. ± st. dev. (%)
clay	78.2 ± 5.5	75.0 ± 3.7
quartz	10.3 ± 3.5	12.9 ± 4.6
Si-rich	3.5 ± 1.5	2.1 ± 0.3
Fe/Mn-rich	2.3 ± 1.9	1.2 ± 0.5
misc.	2.3 ± 0.9	2.5 ± 0.9
organics	1.0 ± 0.8	0.6 ± 0.2
diatom	2.4 ± 3.0	5.7 ± 2.9

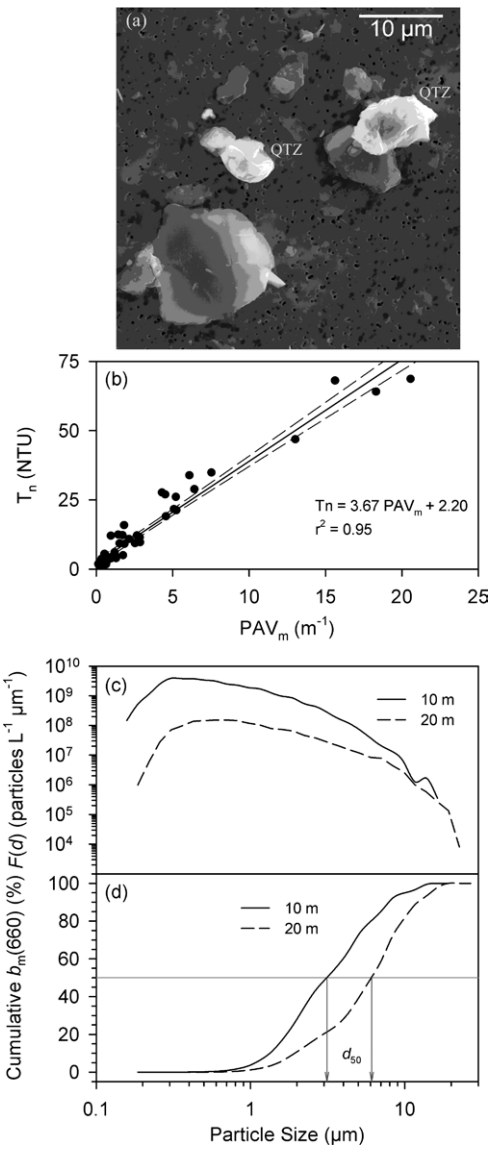

Fig. 7. SAX results and related calculations for Rondout Reservoir following the Hurricane Irene runoff event: (a) micrographs of clay mineral and quartz (bright) particles; (b) strong linear dependence of T_n on PAV_m, with linear least-squares regression fit; (c) PSDs for samples from 2 reservoir depths at the robotic profiling platform site on 31 Aug, where $F(d)$ is the number concentration in a size interval divided by the magnitude of the interval; and (d) associated calculated (according to Mie theory) contributions to light scattering (i.e., T_n) from different size classes, in a cumulative format. The corresponding median particle diameters (d_{50}) are shown.

associated with runoff events elsewhere (Peng and Effler 2012). Nearly 20% of b_m (i.e., T_n) was associated with particles with $d \geq 10$ µm at the 20 m depth (Fig. 7d). The other sample, from 10 m, had a size dependency (d_{50} = 3.12 µm) more commonly reported in SAX characterizations, with much smaller contributions by particles outside of the 1–10 µm range (Peng and Effler 2007, Peng et al. 2009).

Profiles of T (Fig. 8a) and selected features of the SAX results for 2 d following the event, one 3 d after, the other 25 d after (Fig. 8b–8d), provide valuable insights into the behavior of the minerogenic particle population delivered to the reservoir. This representation depicts the entry of minerogenic particles primarily into stratified depths from the event and the subsequent diminishment over the 22 d interval (Fig. 8b), generally consistent with the T_n patterns (Fig. 4). The peak PAV_m decreased ~6-fold and shifted downward ~10 m by the second date, acknowledging these are coarse vertical representations given the 5 m depth interval for SAX samples. Both of these features are qualitatively consistent with the progression of the effects of settling/coagulation losses over the interim.

The quartz (% of PAV_m; Fig. 8c) and d_{50} (Fig. 8d) profiles depict patterns qualitatively consistent with the effects of the operation of morphometry-based sorting in the settling process. Quartz percentages were the highest at a depth below the PAV_m peak and deeper on 31 August. These percentages remained lower in the upper waters 22 d later but with a maximum at mid-depths (Fig. 8c) within stratified layers (Fig. 8a). Despite the similarity in the light-scattering characteristics of clay and quartz for this system (e.g., similar initial PSDs and refractive indices; Peng and Effler 2007), quartz is expected to settle faster because these particles have shapes that more closely approach sphericity compared to the platelet morphometry of clay particles. Thicknesses one-sixth of the length-width dimensions are not unusual for clay particles (Bates 1971). The platelet effect has been described as contributing to the persistence of these particles in water columns and has been represented by a “shape factor” multiplier (<1) in certain settling velocity relationships (Davies-Colley et al. 2003; but not included in equation 2). Size sorting effects were also manifested in the changes in the d_{50} profiles for the same days (Fig. 8d). Distinctly higher d_{50} values were observed on 31 August below the PAV_m (and T_n) peak, presumably as a manifestation of the preferential settling of larger particles of the population from the overlying layers. Moreover, substantial systematic decreases in d_{50} occurred throughout the water column over the subsequent 22 d, depicting a shift to populations with greater contributions from the smaller sizes, consistent with the preferential settling of the larger particles.

Model performance and selected applications

Hydrothermal submodel

Performance of this submodel is depicted through selected graphical representations (Fig. 9) and the root mean square error (RMSE) statistic. The calibrated 2-dimensional hydrothermal/transport model (see Table 1) performed well in tracking the seasonal stratification dynamics of the reservoir in 2010 and 2011, as represented in the patterns of volume-weighted epilimnetic and hypolimnetic Ts (Fig. 9a). The timing of turnovers and T differences between the layers were well simulated, including the warmer hypolimnetic conditions of 2010, although hypolimnetic Ts were somewhat underpredicted in late summer of that year. The RMSE for the 2 calibration years was 0.93 °C. More vertically detailed performance is represented in comparisons of predicted and observed T profiles for months bracketing the runoff event at the robotic monitoring site (Fig. 9b). The vertical details were generally well simulated. The largest deviations were observed in mid-September as somewhat underpredicted upper metalimnetic Ts.

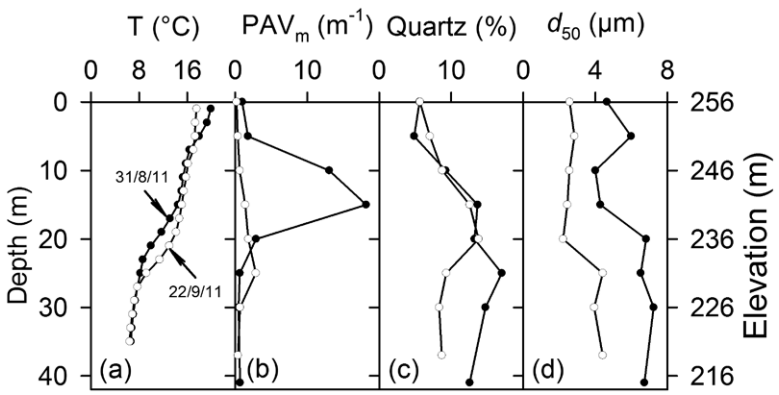

Fig. 8. Profiles of T and selected SAX results for 31 Aug and 22 Sep, at robotic profiling platform site: (a) T, (b) PAV_m, (c) % contribution of quartz to PAV_m, and (d) d_{50}.

 DOI: 10.5268/IW-3.3.581

Validation of the submodel (coefficients from calibration unchanged) is demonstrated for 2 recent years (of the 23 y) for a deep water site, again in the format of seasonal volume-weighted epilimnetic and hypolimnetic Ts (Fig. 9c). Performance for these 2 recent years, as well as for the other 21 y of validation testing, was good. The RMSE for the entire validation period was 1.16 °C. This level of performance compares favorably to other published modeling studies where this metric was reported for multiple years (Gelda et al. 1998, 2009, 2012, Owens 1998, Gelda and Effler 2007a). Moreover, the duration of successful continuous simulations of thermal stratification exceeds the previous maximum of 22 y (Gelda et al. 2012). Finally, the model also performed reasonably well in simulating the temporal pattern of the withdrawal T over the August–October interval of 2011 that bracketed the event, including the abrupt changes in late August through mid-September associated with shifts in the intakes (depths) used (Fig. 6b). Imperfect representation of the cone effect (Gelda and Effler 2007b, 2007c) and input from more than one intake may have contributed to the deviations from observations (Fig. 6b).

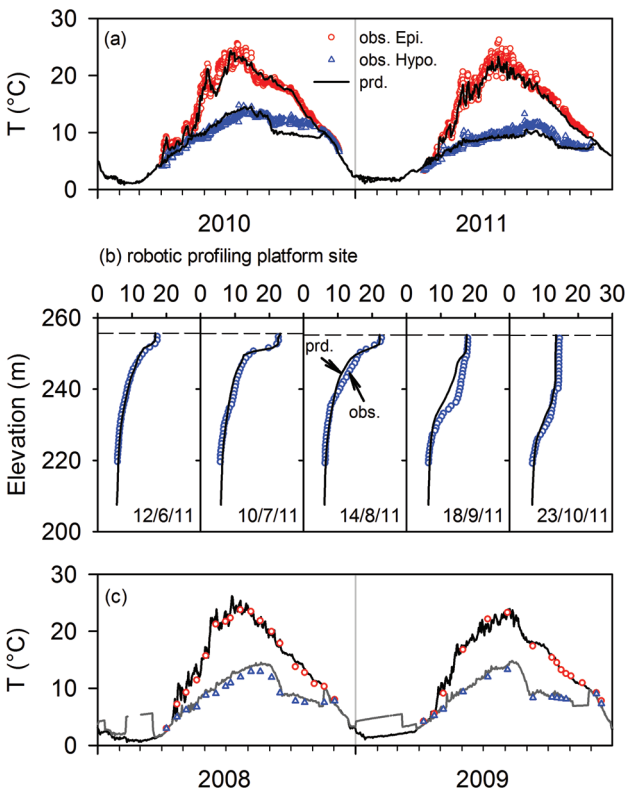

Fig. 9. Performance of the hydrothermal/transport submodel: (a) calibration, comparison of observed and predicted Ts, as volume-weighted epilimnetic and hypolimnetic values, seasonally, in 2010 and 2011; (b) calibration, as detailed vertical profiles for monthly dates bounding the Hurricane Irene runoff event of 2011; and (c) validation (for 2 of the 23 y of testing of the calibrated model), comparison of observed and predicted Ts as volume-weighted epilimnetic and hypolimnetic values, seasonally, in 2008 and 2009.

Overall T_n model(s)

Multiple attributes of the overall T_n model(s) are considered here. The primary longitudinal and vertical features of the T_n plume initially formed from the runoff event, as documented for 31 August (Fig. 10a), was reasonably well simulated by both versions of the T_n model (Fig. 10b; coagulation version shown) in the context of previously published modeling efforts (Gelda and Effler 2007a, Gelda et al. 2009), although vertical gradients were underpredicted. A statistical basis of performance is the normalized RMSE (RMSEN), obtained by dividing the RMSE by the observed peak at each profile site (Gelda and Effler 2007a, Gelda et al. 2009). The average RMSEN for the profile sites of 31 August of 21% compares favorably to the performance reported for T_n modeling at other reservoirs (Gelda and Effler 2007a, Gelda et al. 2009). This primarily reflects good performance of the hydrothermal/transport submodel (e.g., features of transport initially dominate compared to kinetics), not only with respect to the entry of the tributary density currents, but also for transport along the reservoir's primary axis. Moreover, the total T_n content of the reservoir on this date, based on the detailed reservoir-wide profiling, was well matched (within 2%) by the model predictions. This also supports the estimates of T_n loading for the event from the 2 tributaries that were based on the combination of monitoring and T_n–Q relationships. The loads for the event were within 13% of the estimated reservoir-wide increase in T_n assessed from the 31 August observations, adjusted for losses over the intervening 48 h since the event (according to the rate depicted in Fig. 5).

The predicted diminishment of the elevated T_n levels in the most enriched (metalimnetic) reservoir layers (8–18 m) tracked the observations well over the 45 d following the event with both of the T_n submodels (Fig. 5), although T_n predictions were higher for the version without coagulation. The predicted values of the apparent loss rate for the 45 d following the event were within 10% of that based on observations. The somewhat higher T_n levels that persisted into November, relative to the common pre-event baseline (T_n ~ 1 NTU), were also well simulated by the coagulation version, but overpredicted by the version without coagulation (Fig. 5).

Vertical performance was assessed by comparing the simulations to detailed profiles (n = 6) of T_n collected by the robotic monitoring platform (Fig. 10c). The initial vertical pattern was well simulated (30 Aug) by both T_n models, with modest overprediction indicated for the near-surface waters. Differences in predictions of the 2

models became greater thereafter, with generally higher and progressively deeper peaks for the T_n model without coagulation (Fig. 10c). The metalimnetic peaks for both models were somewhat broader than the observations, suggesting vertical mixing may have been somewhat overpredicted. The coagulation version of the model tracked the magnitude and vertical position of the observed peak better starting a week after the event, and was clearly superior in simulating T_n in the deeper near-bottom layers extending later in September and through October (Fig. 10c). These features led us to select the model that includes coagulation as the best of the 2 T_n submodels considered here. This comparative performance of T_n models with and without coagulation is similar to that reported by Hofmann and Filella (1999) for Lake Lugano, where inclusion of the effects of coagulation was necessary to simulate the decrease in clay-based T_n in that lake’s hypolimnion. Inclusion of the effects of coagulation for the Rondout Reservoir model resulted in far better predictions of T_n in the withdrawal during the 18 d interval when the bottom intake was used (Fig. 6a; 30 Aug–16 Sep).

The comprehensive monitoring that supported T_n modeling for this extreme event was not conducted for earlier smaller events for this system; however, the withdrawal T_n record offers an opportunity for further model validation, albeit in a less comprehensive manner. Simulations were conducted for the 2004–2005 interval that included several small events and the major one in April 2005. The T_n model (with coagulation) performed well in simulating the temporal signature of the withdrawal T_n imparted by both the smaller events and the major April 2005 event (Fig. 10d).

Model applications and utility

Selected applications of the tested model are presented here to illustrate the importance of representing both operational conditions (Fig. 11a and b) and the PSD of the minerogenic particles delivered to the reservoir during the runoff event (Fig. 11c). The scenario predictions are compared to those of the calibrated model as vertical profiles for 1 September at the robotic platform site. The operational scenario corresponds to use of the deep intake since 1 January 2011 instead of the upper intake that actually prevailed. A major difference in the reservoir’s stratification (and thereby the attendant mixing; Martin and McCutcheon 1999) regime is predicted for the deep intake scenario, which would have resulted in a substantially warmer water column overall and a deeper hypolimnion (Fig. 11a). Clearly, this operational feature, the intake (i.e., depth of withdrawal) used, has a major effect on the stratification regime consistent with the high flushing rate of the reservoir. Moreover, such an

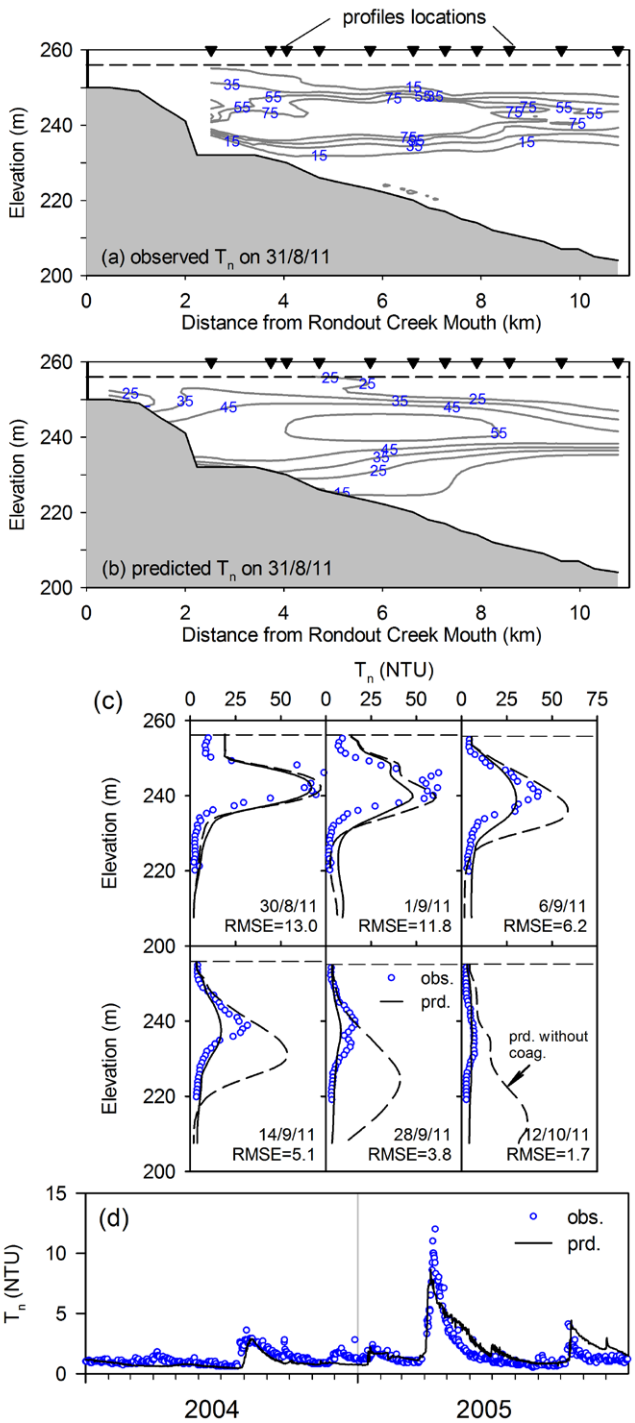

Fig. 10. Performance of the T_n submodel(s): (a) observed depth–length contours of T_n for 31 Aug; (b) simulation of the depth–length contours of T_n (coagulation version) for 31 Aug (compare to Fig. 4a); (c) comparisons of predicted (both with and without coagulation submodels) and observed T_n profiles for 6 dates following the Hurricane Irene runoff event (30 Aug, 1 Sep, 6 Sep, 14 Sep, 28 Sep, and 12 Oct); and (d) comparisons of predictions for withdrawal T_n to observations for an earlier runoff event (with coagulation version).

 DOI: 10.5268/IW-3.3.581

operational mode would have resulted in a different vertical pattern of T_n following the event (Fig. 11b), with somewhat lower levels distributed deeper and over a wider depth interval. The scenarios for PSD illustrate the importance of adopting a representative PSD, in this depiction, soon after the event. Placing all the T_n in the smallest size class causes overprediction on that date, while specifying the largest size class results in gross underprediction for the impact depth and a near bottom peak that was not observed (Fig. 11c). Features of the PSD specifications have importance in simulating the time course of the diminishment of impact over the subsequent interval (Fig. 10), not shown here. These example applications illustrate the utility of the model for investigating the effects of operations, limnological processes, and particle behavior.

The modeling effort has served as an effective integrator of both long-term and event-based monitoring of inputs and the reservoir, detailed characterization of T_n-causing particles, and basic features of transport and the thermal stratification regime. The model has both management and research utility and is recommended for management guidance (e.g., expectations for duration and preferred intake choices) in response to future events for this reservoir and for incorporation into the larger modeling tool under development to support operations of the overall multi-reservoir system (Gannet Fleming & Hazen and Sawyer 2007). This larger modeling framework features the integration of robotic monitoring and modeling to provide near real-time simulations to support operations decisions for the system (Effler et al. 2013). Selected applications of the tested model have illustrated the added value of the tool to provide insights on the influence of various drivers on T_n patterns such as reservoir operations, and the importance of supporting information, particularly PSDs. This model is distinguished from previous T_n modeling contributions by the parsimonious expansion of the kinetic framework of the T_n submodel to explicitly represent the effects of particle coagulation, which is critical to simulating deep layer T_n patterns and T_n dynamics in the withdrawal. Wider applications of this more robust T_n model are recommended where similar issues prevail. The integrated program of contemporary monitoring protocols, individual particle characterization, and modeling (hydrothermal/transport and T_n submodels) is highly transferable to other systems where inorganic particles cause turbidity problems.

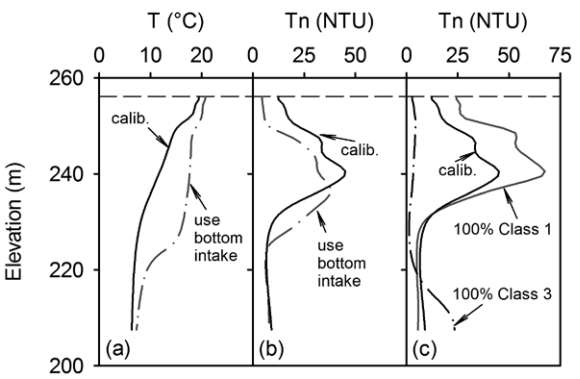

Fig. 11. Applications of the tested model, with scenario simulations compared to those of calibrated model, as vertical profiles for 1 Sep at robotic profiling platform site: (a) T, scenario is use of bottom intake; (b) T_n, scenario is use of bottom intake; and (c) T_n, scenarios are T_n in size classes 1 (smallest) or 3 (largest).

Acknowledgements

Support for this study was provided by the New York City Department of Environmental Protection. This is contribution No. 307 of the Upstate Freshwater Institute.

References

Alavian V, Jirka GH, Denton RA, Johnson MC, Stefan HG. 1992. Density currents entering lakes and reservoirs. J Hydraul Eng. 118:1464–1489.

Babin M, Morel A, Fournier-Siere V, Fell F, Stramski D. 2003. Light scattering properties of marine particles in coastal and open ocean waters as related to the particle mass concentration. Limnol Oceanogr. 48:843–859.

Bates TE. 1971. The kaolin minerals. In: Gard JA, editor. The electron-optical investigation of clays. London: Mineralogical Society. p. 109–157.

Chapra SC. 1997. Surface water-quality modeling. New York: McGraw-Hill. 844 p.

Chung SW, Gu R. 1998. Two-dimensional simulations of contaminant currents in stratified reservoir. J Hydraul Eng. 124:704–711.

Chung SW, Hipsey MR, Imberger J. 2009. Modelling the propagation of turbid density inflows into a stratified lake: Daecheong Reservoir, Korea. Environ Model Softw. 24:1467–1482.

Cole TM, Wells SA. 2002. CE-QUAL-W2: A two-dimensional, laterally averaged, hydrodynamic and water quality model, Version 3.1. Vicksburg (MS): US Army Engineering and Research Development Center. Instruction Report EL-2002-1.

Davies-Colley RJ, Vant WN, Smith DG. 2003. Colour and clarity of natural waters: Science and management of optical water quality. Caldwell (NJ): Blackburn Press. 310 p.

Effler SW, Matthews DA, Kaser J, Prestigiacomo AR, Smith DG. 2006. Runoff event impacts on a water supply reservoir: Suspended sediment loading, turbid plume behavior, and sediment deposition. J Am Wat Resour Assoc. 42:1697–1710.

Effler SW, O'Donnell DM, Matthews DA, Perkins MG, O'Donnell SM, Gelda RK, Prestigiacomo AR, Peng F, Smith DG, Bader AP, Mayfield JD. 2008. Insights for the structure of a reservoir turbidity model from monitoring and process studies. Lake Reserv Manage. 24:69–86.

Effler SW, O'Donnell DM, Prestigiacomo AR, Pierson DC, Zion MS, Pyke GW, Weiss WJ. Forthcoming 2013. Robotic monitoring for turbidity management in a multiple reservoir water supply. J Water Resour Plann Manage.

Gannett Fleming & Hazen and Sawyer. 2007. Catskill turbidity control study: Phase III Final Report. Prepared for New York City Department of Environmental Protection, Bureau of Engineering Design and Construction.

Gelda RK, Effler SW. 2007a. Modeling turbidity in a water supply reservoir: Advancements and issues. J Environ Eng. 133:139–148.

Gelda RK, Effler SW. 2007b. Testing and application of a two-dimensional hydrothermal model for a water supply reservoir: Implications of sedimentation. J Environ Eng Sci. 6:73–84.

Gelda RK, Effler SW. 2007c. Simulation of operations and water quality performance of reservoir multi-level intake configurations. J Water Resour Plann Manage. 133:78–86.

Gelda RK, Effler SW. 2008. Probabilistic model for temperature and turbidity in a reservoir withdrawal. Lake Reserv Manage. 24:219–230.

Gelda RK, Effler SW, Peng F. 2012. Modeling turbidity and the effects of alum application for a water supply reservoir. J Environ Eng. 138:38–47.

Gelda RK, Effler SW, Peng F, Owens EM, Pierson DC. 2009. Turbidity model for Ashokan Reservoir, New York: Case Study. J Environ Eng. 135:885–895.

Gelda RK, Owens EM, Effler SW. 1998. Calibration, verification, and an application of a two-dimensional hydrothermal model [CE-QUAL-W2(t)] for Cannonsville Reservoir. Lake Reserv Manage. 14:186–196.

Hofmann A, Filella M. 1999. Transport of suspended matter in the hypolimnion of Lake Lugano: a comparison of field observations and model predictions. J Great Lakes Res. 25:865–882.

Hupfer M, Gaechter R, Giovanoli R. 1995. Transformation of phosphorus species in settling seston and during early sediment diagenesis. Aquat Sci. 57:305–323.

Kirk JTO. 2011. Light and Photosynthesis in Aquatic Ecosystems, 3rd ed. New York (NY): Cambridge University Press. 662 p.

Li Y, Chen BM, Wang ZG, Peng SL. 2011. Effects of temperature change on water discharge, and sediment and nutrient loading in the lower Pearl River basin based on SWAT modelling. Hydrol Sci J. 56:68–83.

Liu WC, Chen WB. 2013. Modeling hydrothermal, suspended solids transport and residence time in a deep reservoir. Int J Environ Sci Technol. 10:251–260.

Longabucco P, Rafferty MR. 1998. Analysis of material loading to Cannonsville Reservoir: advantages of event-based sampling. Lake Reserv Manage. 14:197–212.

Martin JL, McCutcheon SC. 1999. Hydrodynamics and transport for water quality modeling. Boca Raton (FL): Lewis Publishers. 794 p.

Newcombe CP. 2003. Impact assessment model for clear water fishes exposed to excessively cloudy water. J Am Wat Resour Assoc. 39:529–544.

O'Donnell DM, Effler SW. 2006. Resolution of impacts of runoff events on a water supply reservoir with a robotic monitoring network. J Am Wat Resour Assoc. 42:323–335.

O'Donnell SM, Gelda RK, Effler SW, Pierson DC. 2011. Testing and application of a transport model for runoff event inputs for a water supply reservoir. J Environ Eng. 137:678–688.

O'Melia CR. 1985. The influence of coagulation and sedimentation on the fate of particles, associated pollutants, and nutrients in lakes. In: Stumm W, editor. Chemical processes in lakes. New York (NY): Wiley Interscience. p. 207–224.

Owens EM. 1998. Development and testing of one-dimensional hydrothermal models of Cannonsville Reservoir. Lake Reserv Manage. 14:172–185.

Owens EM, Gelda RK, Effler SW, Hassett JM. 1998. Hydrologic analysis and model development for Cannonsville Reservoir. Lake Reserv Manage. 14:140–151.

Peng F, Effler SW. 2007. Suspended minerogenic particles in a reservoir: light scattering features from individual particle analysis. Limnol Oceanogr. 52:204–216.

Peng F, Effler SW, O'Donnell DM, Weidemann AD, Auer MT. 2009. Characterization of minerogenic particles in support of modeling light scattering in Lake Superior through a two-component approach. Limnol Oceanogr. 54:1369–1381.

Peng F, Effler SW. 2012. Mass-specific scattering coefficient for natural minerogenic particle populations: particle size distribution effect and closure analyses. Appl Optics. 51:2236–2249.

Phlips EJ, Aldridge FJ, Schelske CL, Crisman TL. 1995. Relationships between light availability, chlorophyll *a*, and tripton in a large shallow subtropical lake. Limnol Oceanogr. 40:416–421.

Prestigiacomo AR, Effler SW, O'Donnell DM, Smith DG, Pierson D. 2008. Turbidity and temperature patterns in a reservoir and its primary tributary from robotic monitoring: Implications for managing the quality of withdrawals. Lake Reserv Manage. 24:231–243.

Rueda FJ, MacIntyre S. 2010. Modelling the fate and transport of storm-river-water in small lakes of complex morphometry. Environ Model Softw. 25:146–157.

Sinokrot BA, Stefan HG. 1993. Stream temperature dynamics: Measurements and modeling. Wat Resour Res. 29:2299–2312.

Swift TJ, Joaquim PL, Schladow SG, John ER, Alan DJ, Charles RG. 2006. Water clarity modeling in Lake Tahoe: Linking suspended matter characteristics to Secchi depth. Aquat Sci. 68:1–15.

Thodsen H, Hasholt B, Kjærsgaard JH. 2008. The influence of climate change on suspended sediment transport in Danish rivers. Hydrol Process. 22:764–774.

Weilenmann U, O'Melia CR, Stumm W. 1989. Particle transport in lakes: Models and measurements. Limnol Oceanogr. 34:1–18.

Wetzel RG. 2001. Limnology: lake and reservoir ecosystems. New York (NY): Academic Press.

 DOI: 10.5268/IW-3.3.581

A Seasonal Shift in the Frequency of Extreme Hydrological Events in Southern New York State

ADÃO H MATONSE

Institute for Sustainable Cities, City University of New York, New York, New York

ALLAN FREI

Institute for Sustainable Cities, City University of New York, and Department of Geography, Hunter College of the City University of New York, New York, New York

(Manuscript received 16 November 2012, in final form 13 June 2013)

ABSTRACT

The recent sequence of extreme hydrological events across the eastern United States (e.g., Hurricane Irene in August 2011, Tropical Storm Lee in September 2011, and Hurricane Sandy in October 2012), which led to unprecedented flooding including in various parts in the study region, the Catskill Mountains, and Hudson River Valley in southern New York State, have raised the question of whether the frequency of extreme events across the region is changing. In this study variations in the frequency of extreme precipitation and streamflow events available from historical records are analyzed. This study finds that there has been a marked increase in the frequency of warm season (June–October) extreme hydrologic events during the last two decades, with an accelerated rate of increase since the mid-1990s. The most recent decade has the highest frequency of extreme warm season events in the last 100 years across the study region. No such trend is observed between November and May; in fact the frequency of 4-day extreme precipitation events during the cold period has declined during the last two decades.

1. Introduction

In August and September of 2011, Hurricane Irene and Tropical Storm Lee dropped large amounts of rain across various parts of the eastern US, including our study region that includes the Catskill Mountains and Hudson River Valley of southern New York State. Prior to fall 2011, the most recent flooding event approaching such magnitudes in this region occurred in April 2005, when the Delaware River basin was hit by heavy rain that led to a total of 20 New York Counties being declared federal disaster areas. This event forced more than 1000 residents to evacuate their homes and approximately $35 million (U.S. dollars) in recovering cost mostly from flood damage (Suro and Firda 2006). Peak water surface elevations exceeding the 100- to 500-yr flood mark were registered in some areas across the region. More recently, in late October 2012, our region was affected by Hurricane Sandy, although the worst impacts of that storm in the northeast occurred as a result of storm surge along the coasts of New Jersey and New York State.

In light of the public perception within our study region of a recent increase in the frequency of extreme precipitation and hydrological events, we examine the hypothesis that there has been a change in the frequency of extreme events in this region. We employ a suite of parametric and nonparametric statistics to precipitation and stream gauge records, some of which extend back over a century.

Historically, the occurrence of extreme weather and climate events such as these storms has been associated with losses of human life, waterborne disease outbreaks, water quality issues, and high cost for damage recovery (Curriero et al. 2001; Easterling et al. 2000; Karl and Easterling 1999; Kunkel et al. 1994; Weniger et al. 1983; Towler et al. 2010). Despite their common association with physical processes, the severity of flood impacts are also a function of human development, land use patterns, exposure, and vulnerability (Allen et al. 2012;

Corresponding author address: Adão H. Matonse, CUNY Institute for Sustainable Cities, 71 Smith Ave., Kingston, NY 12401. E-mail: amatonse@hunter.cuny.edu

DOI: 10.1175/JCLI-D-12-00810.1

Kunkel 2003b; Changnon and Demissie 1996). Pielke and Downton (2000) indicate that differences in flood damage at a regional scale appear more correlated with differences in precipitation while differences in flood damage at a local scale are more related to other factors. Apart from direct catastrophic damage, tropical storms, floods, and droughts can affect human welfare indirectly through low yields/failed crops, waterborne disease outbreaks resulting in humanitarian crises with a higher number of lives lost. Such threats are likely to occur disproportionately in developing countries given the limited resources for mitigation and adaptation (Arnell et al. 2001; Curriero et al. 2001; Manabe et al. 2004; Huntington 2006). Recently, the Intergovernmental Panel on Climate Change (IPCC) has emphasized the importance of new approaches to address the management of risks associated with extreme events as these may be directly affected by climate change (Allen et al. 2012).

A number of studies have shed light on trends in extreme events across the globe (for example, Knutson and Manabe 1998; Dai et al. 1997; Kunkel 2003a). Results from instrumental records and climate model simulations suggest that human-induced climate change is responsible for more intense precipitation over many extratropical regions, including the United States (Min et al. 2011; Groisman et al. 2005). At regional scales the results are highly variable with zonally averaged precipitation showing an increase by 7%–12% between 30° and 85°N, while an increase by 2% between 0° and 55°S and a decrease in other regions (Folland et al. 2001; Zhang et al. 2007). Analyses of multiday extreme precipitation events (Kunkel et al. 1999) and 1-day duration with a 20-yr return period (Zhang et al. 2001) found no statistically significant long-term trend for Canada. However, other studies found statistically significant trends including, in the average annual precipitation (Zhang et al. 2000), precipitation events exceeding a 2-month return period (Stone et al. 2000) for most areas in Canada, and precipitation of 5-yr return period associated with tropical cyclones (Kunkel et al. 2010). Across the United States, a number of studies have identified trends in extreme events during the last few decades (e.g.: Kunkel et al. 1999; Karl et al. 1995; Karl and Knight 1998; Novotny and Stefan 2007; Burns et al. 2007), though their analysis periods all end prior to 2005. Novotny and Stefan (2007) analyzed 36 stream gauge records distributed across five major river basins in Minnesota and found that peak flows due to rainfall and the number of days with high extreme flows in summer are increasing after 1980 but found no trend in snowmelt related runoff. In most studies the observed changes in precipitation are occurring in conjunction with increasing air temperature; for example Burns et al. (2007) studied the Catskill Mountain region in New York and found a 0.6°C increase in mean annual temperature associated with 136 mm increase in yearly cumulative precipitation in the past 50-yr period.

Two recent studies of precipitation and drought over the Catskill Mountains region demonstrate that the period since the 1970s has been particularly wet when viewed in the context of station observations since the early twentieth century (Seager et al. 2012), as well as in the context of longer-term hydrological variations based on tree ring reconstructions (Pederson et al. 2012). These studies show that both the drought of the 1960s and the subsequent wet period (which continues until today) were caused by internal atmospheric variability (Seager et al. 2012) and that periods of more extensive drought have occurred in earlier centuries (Pederson et al. 2012). Assuming that tree ring growth index and streamflow are both integrators of the available moisture and energy Devineni et al. (2013) applied a hierarchical Bayesian regression (HBR) model to tree-ring chronologies from different species to reconstruct the average concurrent summer streamflow in five basins across the upper Delaware River basin (which is part of our study region). Focusing on the summer months of June, July, and August they studied the frequency and recurrence of 1960s-like severe droughts at each basin in past centuries. They used the HBR model to generate a thousand realizations of a 247-yr simulation. From a count of the number of events exceeding the duration and severity of the 1960s at each gauge they estimated the median return period of the 1960s drought in the region to be around 80 years. A Mann–Kendall test on the time series revealed lack of evidence of a trend in the occurrence of the 1960s-like droughts. Thus, based on climatology and hydrology data reconstruction, the implication is that water resources in this region are vulnerable to significant drought events beyond what has been experienced during the last 100 years. In any case, the relationship between drought and flood events and climate change and how they directly affect society and sustainable development remains uncertain. Reducing uncertainty will require (among other things) more data on extreme events covering longer periods of record to become available; as well as a better understanding of the physical processes and evidence linking extreme events to climate change (Allen et al. 2012).

2. Study area and data description

a. Study area

The study area encompasses the mid–Hudson Valley and Catskill Mountain regions in southern New York

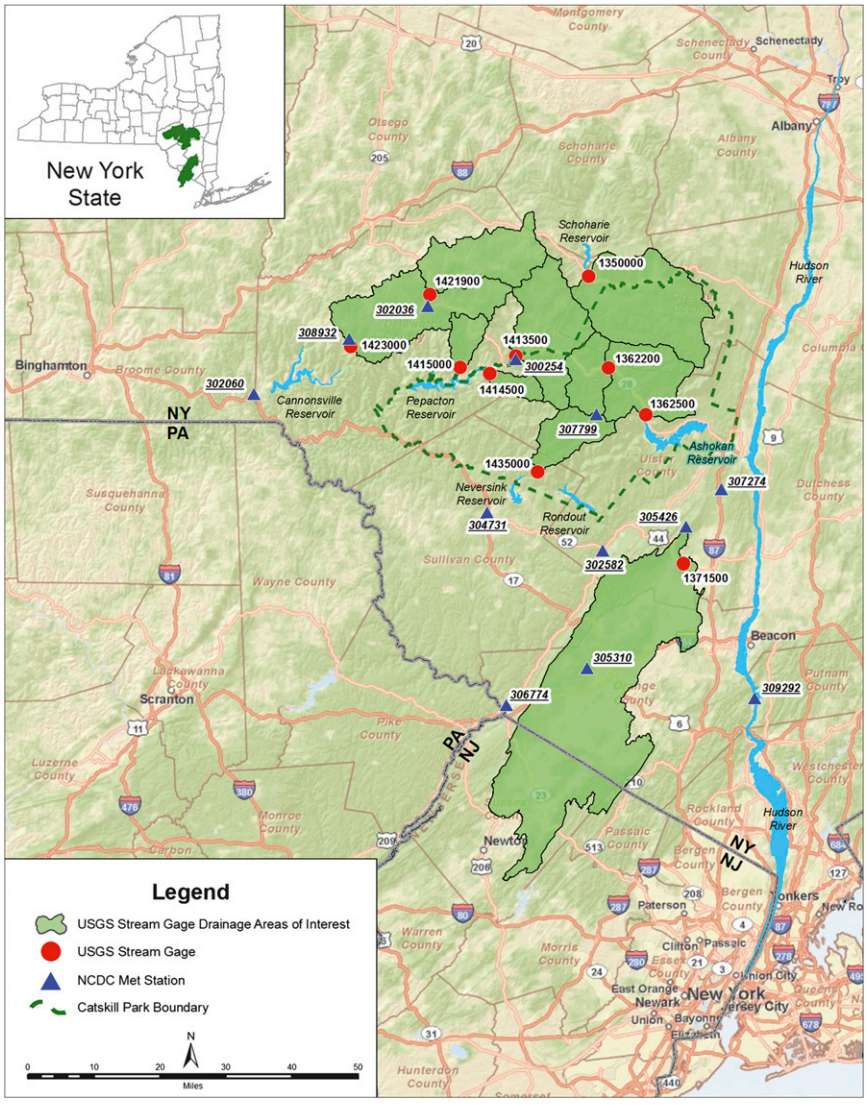

FIG. 1. The study area with the drainage areas for the stream gauges, the location of the rain, and stream gauges used in this study, state boundaries, and a few local geographic features.

State. Fig. 1 shows a map of the study area with the drainage areas for the stream gauges, and the location of the rain gauges and stream gauges used in this study.

The Catskill Mountain region is part of the Allegheny Plateau consisting mainly of sedimentary bedrock (Burns et al. 2007) and contains rugged topography through which numerous tributaries drain naturally into the Hudson and Delaware Rivers. The study area, located between 80 and 250 km north of New York City, extends through Delaware, Greene, Orange, Ulster, Schoharie, and Sullivan counties of New York State. The climate of the region is humid continental with mean daily winter temperatures ranging between −5° and 0°C and mean daily summer temperatures ranging between 15° and 20°C. The temperature of the Catskill Mountain region is strongly impacted by elevation that rises to approximately 1200 m from the Hudson River. Regional hydrology is influenced by snow and snowmelt during winter and early spring particularly at higher elevations (Frei et al. 2002; Matonse et al. 2012). Average annual precipitation from the stations included in this study ranges from 1005 to 1580 mm. Average daily streamflow for the selected gauges ranges from 1.6 to 31 $m^3 s^{-1}$.

b. *Data description*

Historical long-term precipitation records from rain gauge stations across our region were obtained from

TABLE 1. List of precipitation stations used in this study, including the average total annual rainfall, and average totals for August and September.

Station ID number	Station name	County	Record period available	Average total annual rainfall (cm)	Average total august rainfall (cm)	Average total september rainfall (cm)
300254	Arkville	Delaware	1948–2011	102.41	9.44	9.97
302036	Delhi	Delaware	1926–2011	108.53	10.15	9.79
302060	Deposit	Delaware	1962–2011	111.64	10.38	10.30
302582	Ellenville	Ulster	1948–2011	113.73	10.15	10.39
304731	Liberty	Sullivan	1950–2011	128.92	12.13	11.66
305310	Middletown	Orange	1951–2011	109.46	10.37	10.46
305426	Mohonk Lake	Ulster	1896–2011	122.41	11.20	11.16
306774	Port Jervis	Orange	1893–2011	111.99	10.34	10.10
307274	Rosendale	Ulster	1956–2011	113.43	10.37	10.07
307799	Slide Mtn	Ulster	1948–2011	158.70	13.51	13.82
308932	Walton 2	Delaware	1956–2011	112.62	10.39	9.60
309292	West Point	Orange	1890–2011	119.00	10.76	10.92

Northeast Regional Climate Center (NRCC) at Cornell University, Ithaca, New York. Daily total precipitation for the entire period of record at each station is used to evaluate historical variations in extreme values. A total of 12 rain gauge stations with historical precipitation records met our criteria for inclusion in this study (Table 1): stations must have at least 30 yr of continuous data with no extended gaps, and must be currently active. Three stations have >100 yr of data. All trace precipitation was set to zero as these have no effect on the maximum precipitation time series.

Historical daily average and annual peak streamflow records are obtained from the U.S. Geological Survey (USGS) surface water website (http://waterdata.usgs.gov/nwis/sw) for all stream gauge stations used in this study. Ten USGS gauges are selected in the Greater Catskill and mid–Hudson Valley watersheds for use in this analysis (Table 2). The selection is based on the following two criteria: 1) the gauge is presently active and has 30 or more years of annual maximum streamflow records; and 2) the streamflow at the site is natural or is minimally impacted by regulation. No processing was performed to replace missing values.

3. Methods

A suite of parametric and nonparametric statistics is applied to precipitation and streamflow records to evaluate extreme events. All analyses are performed for annual, warm season, and cold season separately. Annual analyses include data from all months of a calendar year. Warm season analyses include data from 1 June through 31 October, and cold season analyses include data from 1 November through 31 May 31st. These seasonal definitions effectively separate events associated with snow (i.e., melt and rain-on-snow events) from those associated only with heavy rain. For much of the nonparametric analysis, our definition of ''extreme

TABLE 2. List of USGS gauges used in this study, including the drainage area, gauge elevation, basin slope, and average annual streamflow.

USGS ID Number	Gauge name	County	Record period available	Drainage area (sq. km)	Gauge elevation (m)	Basin average slope (%)	Average annual streamflow ($m^3 s^{-1}$)
1350000	Schoharie Creek at Prattsville	Greene	1936–2011	613.8	344.9	21.1	13.6
1362200	Esopus Creek at Allaben	Ulster	1964–2011	165.0	304.2	32.0	4.4
1362500	Esopus Creek at Coldbrook	Ulster	1936–2011	497.3	189.4	31.5	21.5
1371500	Wallkill River at Gardiner	Ulster	1936–2011	1800.0	56.6	4.6	31.4
1421900	West Branch Delaware River Upstream from Delhi	Delaware	1937–2011	347.1	411.9	17.4	7.0
1423000	West Branch Delaware River at Walton	Delaware	1937–2011	859.9	362.8	18.4	17.3
1413500	East Branch Delaware River at Margaretville	Delaware	1937–2011	422.2	397.0	23.5	9.0
1414500	Mill Brook Near Dunraven	Delaware	1958–2011	65.3	395.8	25.8	1.6
1415000	Tremper Kill Near Andes	Delaware	1951–2011	86.0	391.9	21.6	1.7
1435000	Neversink River Near Claryville	Sullivan	1939–2011	172.5	464.0	23.3	5.6

event'' includes all events with magnitudes greater than or equal to the 95th percentile of the empirical distribution of all events at a given station. This definition is applied to each station individually; then, for some parts of the analysis, results from all stations are averaged.

Parametric statistics include hydrologic frequency analysis (HFA) using annual-maximum series (AMS) (El Adlouni and Ouarda 2010). In addition, HFA is also employed using seasonal-maximum time series from warm season and cold season separately. HFA provides the magnitude of events as a function of average return period (also known as recurrence interval). For this study we estimated return periods from 2 to 100 yr.

a. Annual streamflow HFA

For annual streamflow HFA, at each gauge location annual peak discharges are fitted to a log-Pearson type III distribution (LP3) (Stedinger et al. 1993; Interagency Advisory Committee on Water Data 1982—Bulletin 17B). This distribution is chosen because it has been recommended by the Interagency Advisory Committee on Water Data (1982) as a uniform technique for developing flood flow frequency analysis in the United States. Peak streamflows are used in this study for developing annual streamflow frequency analysis while daily average streamflows are applied to compare annual and seasonal flood flow estimates. Our application of the LP3 model followed the description in Stedinger et al. (1993) with the return period T calculated using Eq. (1):

$$T = \frac{1}{1-p} \tag{1}$$

where p is the cumulative probability of the pth quantile, and x_p, which represents the streamflow event that will be exceeded on average once every T years [also called the 100(1-p) percent exceedance event]. To implement the LP3 distribution the AMS series are transformed to a logarithmic space resulting in a three parameter log-normal distribution. Assuming the log-transformed series follow a normal distribution the pth quantile can be estimated from Eq. (2):

$$x_p = \log(Q_T) = \mu + \sigma K_p(\gamma), \tag{2}$$

where Q_T is the discharge associated with return period T, μ is the mean of the log-transformed annual maximum peak streamflow, σ is the standard deviation, and $K_p(\gamma)$ is the frequency factor. The frequency factor represents the pth quantile of a standard Pearson type-3 distribution with skew coefficient γ, mean zero, and variance 1. For the selected quantile the corresponding streamflow estimate is calculated as

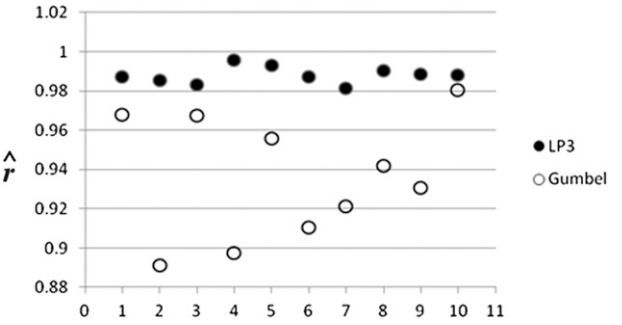

FIG. 2. Probability-plot correlation coefficient ($\hat{r}$) for the warm season maximum streamflows assuming a LP3 and Gumbel probability distributions. The number in the x axis are Schoharie Creek at Prattsville (1), Esopus Creek at Allaben (2), Esopus Creek at Coldbrook (3), Wallkill River at Gardiner (4), East Branch Delaware River at Margaretville (5), Mill Brook near Dunraven (6), Tremper Kill near Andes (7), West Branch Delaware River upstream from Delhi (8), West Branch Delaware River at Walton (9), and Neversink River near Claryville (10).

$$Q_T = \exp(x_p). \tag{3}$$

b. Warm season streamflow HFA

To determine the most appropriate probability distribution to be used for the warm season maximum flows, a probability-plot correlation-coefficient (PPCC) (Vogel and Kroll 1989) is calculated by fitting the log-Pearson type III (LP3) and the extreme value type I or Gumbel distributions. The Gumbel distribution is among the extreme value (EV) distributions described by Gumbel (Gumbel 1958; Stedinger et al. 1993). The Gumbel distribution, which is further discussed in section 3c, is used to describe a large number (n) of annual maximum streamflow values assuming these are independent and identically distributed random variables. This distribution is unbounded above and is characterized by an ''exponential-like'' upper tail.

The PPCC test statistic that provides a measure of the linearity probability plot is $\hat{r}$. The metric $\hat{r}$ is defined as the product moment correlation coefficient between the ordered observations and the order statistic means for each distribution function assumed.

At all sites the PPCC statistic for the LP3 distribution is higher than for the Gumbel distribution (Fig. 2) indicating that the LP3 is a better fit to warm season streamflow time series. Based on these results we adopt the LP3 distribution assumption for warm season maximum streamflow.

c. Annual and warm season precipitation HFA

For precipitation frequency analysis of 24-h rainfall AMS are assumed to follow a Gumbel distribution

(Stedinger et al. 1993). The Gumbel distribution has been most often used with precipitation AMS and was applied for developing a rainfall frequency atlas in the United states including for our region of study (Hershfield 1961; El Adlouni and Ouarda 2010; Frederick et al. 1977; Smith 1993).

The Gumbel Distribution represents a good approximation for annual maxima 24-h rainfall. Its pdf has the following form:

$$f_X(x) = \frac{dF_X(x)}{dx} = \frac{1}{\alpha}\exp\left[-\frac{x-\xi}{\alpha} - \exp\left(-\frac{x-\xi}{\alpha}\right)\right] \quad -\infty < x < \infty, \tag{4}$$

and the cdf

$$F_X(x) = P(X \le x) = \exp\left[-\exp\left(-\frac{x-\xi}{\alpha}\right)\right]. \tag{5}$$

The cdf can be inverted to obtain $x_p = \xi - \alpha \ln[-\ln(p)]$ as

$$F_X(x_p) = p. \tag{6}$$

To solve for the rainfall values associated with a return period defined by p we estimated parameters α and ξ using the sample estimators of first and second moments according to the following relationship:

$$\hat{\alpha} = \frac{s\sqrt{6}}{\pi} = 0.7797s \tag{7}$$

and

$$\xi = \overline{X} - 0.5772\,\hat{\alpha} \tag{8}$$

where $\overline{X}$ and s are the sample mean and standard deviation.

The same Gumbel distribution that is used for annual maximum precipitation is also applied to warm and cold season analyses.

d. Nonparametric data analysis and event definition

Prior to applying nonparametric statistics, we use daily total precipitation data to calculate 4-day, 30- and 30-day antecedent, and 60-day events. Here, 4-day events represent individual storms. We chose the 4-day-averaging period because precipitation from many storms occurs over a period between one and two days for smaller storms to three or four days for larger storms (e.g., both Hurricane Irene and Tropical Storm Lee resulted in precipitation over 4 days at most stations used in this study). An event is defined as any series of consecutive days (including only one day) with precipitation. Thus, 4-day events include all events in which precipitation occurred on one, two, three, or four consecutive days. All events included in this analysis are nonoverlapping. The procedure used to calculate multiday precipitation totals is described below using the 4-day averaging period as an example, but other averaging periods are calculated in an equivalent fashion. Also, time series for individual seasons are calculated in an equivalent fashion by including only days during the season in question.

The procedure used to calculate 4-day events is as follows:

First, calculate the total precipitation over all 4-day intervals, including overlapping intervals, which is equivalent to the 4-day running sum of the daily precipitation time series.

Second, identify all 4-day events in the resultant time series by eliminating all zero running sum values. Thus, an ''event'' is any group of four consecutive days with nonzero total precipitation. By this definition, events that last less than four days are still included as part of a 4-day event, and are not excluded from the analysis.

Third, we exclude overlapping events so that the final dataset is made up of discrete individual events. Two overlapping events might include, for example, a 4-day event ending on 20 January (which is the total precipitation for 17–20 January) and a 4-day event ending on 21 January (which is the total precipitation for 18–21 January). For all such overlapping events, only the one with the largest precipitation amount is retained for analysis; others are set to zero, and are therefore no longer considered in the analysis. This procedure results in a time series for each station, and for each period of analysis. Extreme events are defined from these time series as any event greater than or equal to the 95th percentile of the empirical distribution of all 4 day values, which is calculated for each station, and each season, individually. While this explanation uses 4-day events as an example, we perform the identical procedure for 30- and 60-day events.

4. Results and discussion

a. Historical climatology of extreme precipitation and streamflow

Climatologies of extreme precipitation and streamflow events for each month are presented using boxplots

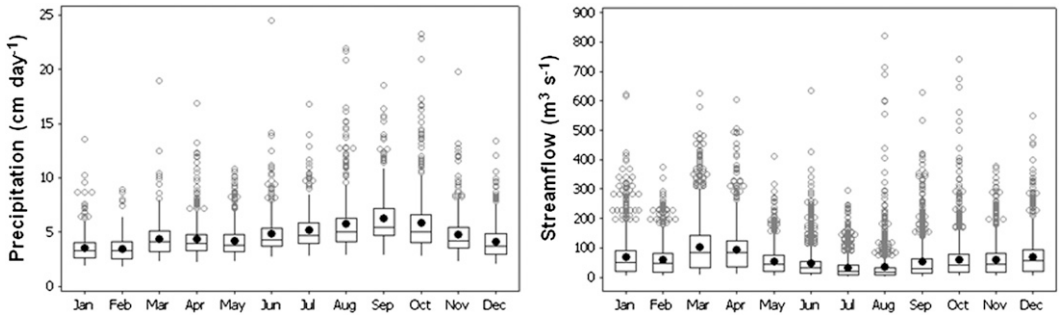

FIG. 3. Seasonal variations of (a) extreme daily precipitation and (b) streamflow (including only values equal to or greater than the 95th percentile). The 95th percentile was calculated for each station and month, separately; boxplots represent data from all stations. The horizontal line in each boxplot is the median while the solid dot is the mean.

of daily total precipitation (Fig. 3a) and daily mean streamflow (Fig. 3b). In these and all subsequent boxplots, the lower and higher ends of the boxes represent the 25th (Q1) and 75th (Q3) quartiles, respectively; the whiskers represent the lowest and highest data values within the lower [Q1 − 1.5(Q3 − Q1)] and upper [Q3 + 1.5(Q3 − Q1)] limits. The horizontal lines in the boxplots represent the median, and the dots the mean. Each panel shows the distribution of daily events, including values from all stations that match or exceed the 95th percentile value for each month (i.e., the 95th percentile values for each station are calculated individually). The seasonal cycle of extreme precipitation events is unimodal, with the largest events tending to occur between August and October (Fig. 3a), including but not limited to the direct influence of tropical storms and hurricanes in this region.

In contrast, streamflow events exhibit a bimodal distribution, in particular for the largest events (outliers) with peak values occurring between March and April as well as between August and October (Fig. 3b). Spring time extreme streamflow events result largely from snowmelt and rain-on-snow events, while late summer/fall extreme streamflow events are associated with rain. Over basins in which snow accumulation is significant compared to the amount of water in extreme rainfall events, the largest flood events tend to be snow related during spring. These include colder basins, which are generally smaller in size and at higher elevations. The selection of basins in this study includes examples of these colder basins, which have large streamflow events during the cold season (November through May) as well as basins in which the peak flood events occur during the warm season (June through October).

The magnitudes of streamflow events resulting from precipitation during either season are also influenced by antecedent conditions. During spring antecedent conditions include the mass of water stored in the snowpack as well as the thermal states of the snowpack and underlying surface (Leathers et al. 1998; Todhunter 2001). During late summer/fall, the most important antecedent condition affecting the magnitude of extreme streamflow events is the amount of moisture in the near-surface soil layers, which determines the amount of saturation excess runoff.

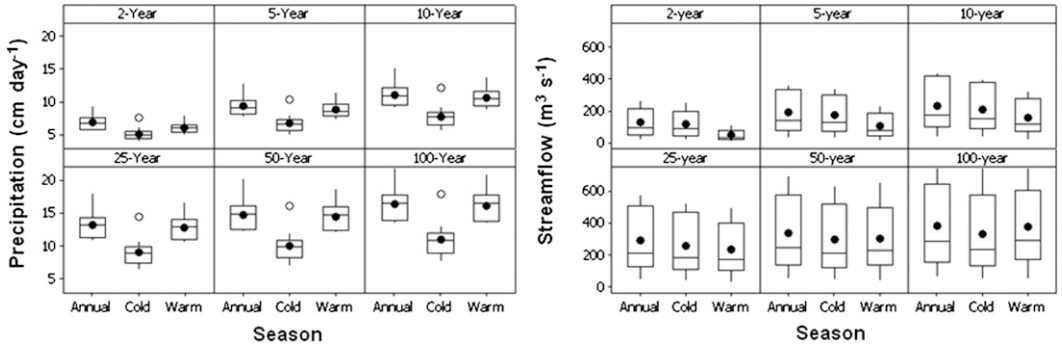

FIG. 4. Magnitude of events as a function of season and return period for (a) precipitation and (b) streamflow. Boxplots represent variations in frequency statistics from 12 rain gauges and 10 stream gauges used in this study. The horizontal line in each boxplot represents the median and the dark dot represents the mean.

TABLE 3. Average annual peak flow for the long-term historical and five 30-yr periods for each of the six gauge stations included to study changes in flood frequency estimates over time.

Time Period	Average annual peak flow ($m^3 s^{-1}$)						
	Prattsville	Gardiner	Coldbrook	Margaretville	Mill Brook	Tremper Kill	Median
Long-term historical	160.5	101.6	152.6	15.8	13.9	12.8	58.7
1940–70	130.4	94.9	127.7	15.7	13.1	11.9	55.3
1950–80	159.8	101.6	156.7	15.8	12.8	11.9	58.7
1960–90	145.9	91.9	136.8	15.8	11.3	10.9	53.9
1970–2000	165.3	98.5	155.7	15.9	12.9	12.0	57.2
1980–2011	190.7	106.0	180.7	16.0	15.5	13.7	61.0

We also compare the magnitudes of events associated with various recurrence intervals during the cold and warm seasons (Fig. 4). For all precipitation return periods between 2 and 100 yr, warm season events are larger than cold season events (Fig. 4a). For example, the 100-yr precipitation event during the warm season varies at different stations between approximately 14 and 20 cm day^{-1}, while in the cold season the 100-yr event is smaller, varying between approximately 8 and 13 cm day^{-1} at the same group of stations. In contrast, for streamflow the relative magnitude between the seasons is a function of return period: the magnitude of frequent (i.e., small) streamflow events is smaller during the warm season; but the magnitudes of streamflow events at larger return periods are comparable in the two seasons (Fig. 4b). For example, the magnitude of the 2-yr cold season flood flow varies between 40 and 250 $m^3 s^{-1}$ at different stations, while the largest warm season 2-yr return period event for any station is only ~100 $m^3 s^{-1}$. This reflects the fact that, when examining relatively frequent events, warm season flow is dominated by base flow, while cold season flow is strongly influenced by snowmelt and is therefore of a greater magnitude.

b. *Has the frequency of extreme events changed during the period of record?*

In this section we examine variations in the frequency of extreme events during the periods of record for stations in this region. Two approaches are applied for this analysis: one based on parametric frequency analysis of streamflow and a second based on nonparametric statistics of precipitation and streamflow.

1) PARAMETRIC STATISTICS

Using time series of annual peak flows from gauges with the longest records, we compare flood flow frequencies from five overlapping 30-yr periods [1940–70 (hereafter called the 1950s); 1950–80 (1960s); 1960–90 (1970s); 1970–2000 (1980s); and 1980–2011 (1990s)]. Average annual peak flows from these periods exhibit an increasing pattern over time (Table 3). Our objective is to detect temporal changes in flow magnitudes associated with different return periods using these overlapping periods that begin 10 yr apart from each other.

In our study region, 30-yr flood frequency estimates vary over time, as demonstrated by Fig. 5a. In general, streamflow events were large during the 1950s and

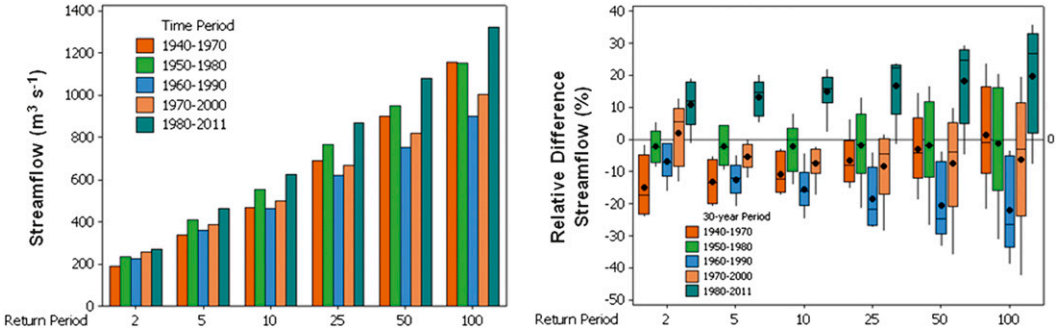

FIG. 5. Flood flow magnitude as a function of return period and analysis data time period. (a) Average of stream gauges flood flow analyses and (b) relative difference flood flow in percentage [(30-yr based flood flow – long-term-based flood flow)(long-term-based flood flow)$^{-1}$ × 100]. These results are based on flood frequency estimates from the following six streamflow gauges: Schoharie Creek at Prattsville, Esopus Creek at Coldbrook, Wallkill River at Gardiner, Millbrook near Dunraven, Tremper Kill near Andes, and Neversink River near Claryville.

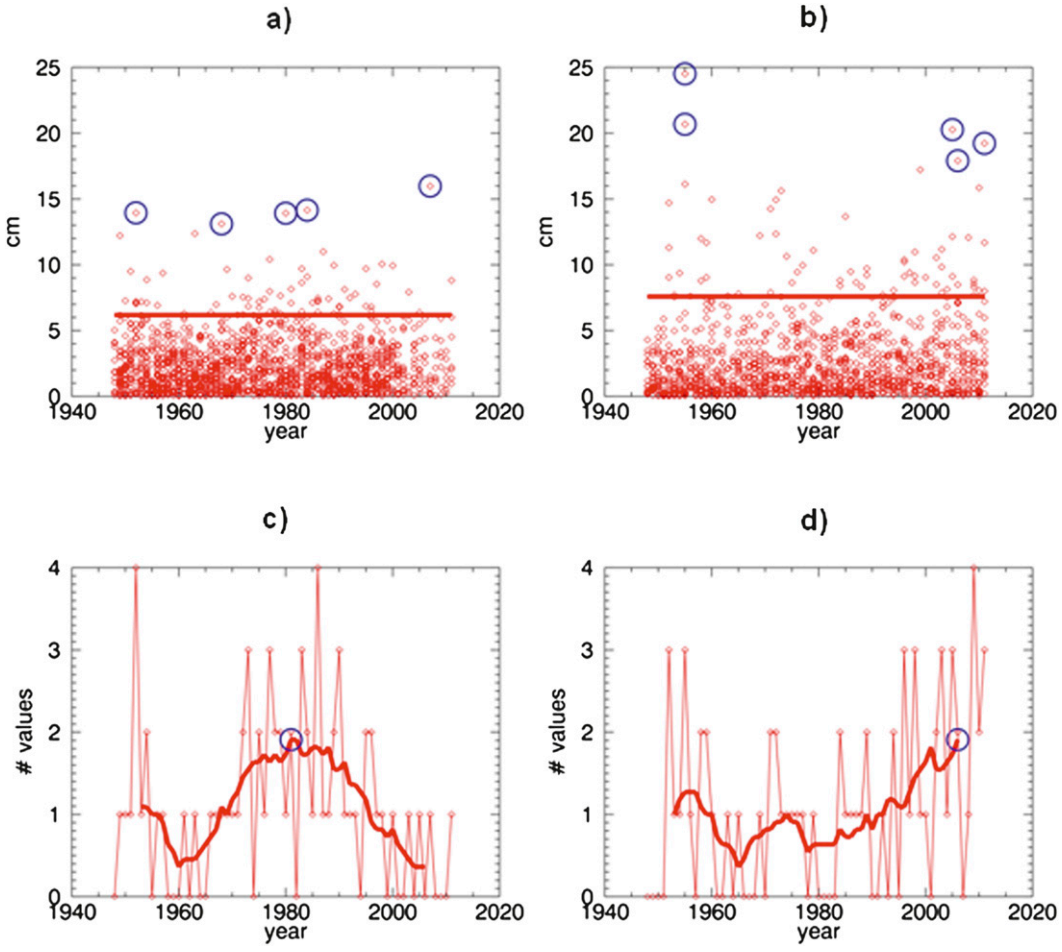

FIG. 6. Example of nonparametric analysis for the Ellenville precipitation record. Magnitudes of every 4-day precipitation event on record during (a) cold and (b) warm seasons; the 95th percentile value (horizontal line); and the top-five historical events (blue circles). The number of extreme (i.e., >=95th percentile) events per year in the (c) cold and (d) warm seasons; 11-yr-centered mean line (bold); year(s) of maximum smoothed value (blue circles).

1960s; smallest during the 1970s and 1980s; and have increased to their highest magnitudes on record in recent decades (Fig. 5a). Boxplots showing the range of values for all stations indicate that flood magnitude is a function of both the period used for the analysis and gauge location across the region (Fig. 5b). These variations can be attributed to differences in weather patterns and other watershed hydrological characteristics including the size of the gauge contributing area. The 1970s-based estimates have the smallest relative flood magnitudes by an average 5%–25% where the difference increases proportional to the return period. The period 1980–2011 has the largest flood estimates for all return periods by approximately 10%. In any case, it is difficult to identify trends at time scales less than 30 yr using this sort of analysis. Hence, we turn to the nonparametric analysis in the next section.

2) NONPARAMETRIC STATISTICS

For each precipitation and streamflow gauge station we calculate the magnitude of the 95th percentile events of different durations (4-, 30-, and 60-day total precipitation or daily mean streamflow) using all events from the period of record and then make a yearly count of how many events exceed the 95th percentile threshold value. (Note that the number of 95th percentile events is a function of the total number of events, which depends on whether one is considering precipitation or streamflow, the extent of available record, and on the duration of the event being analyzed. The important aspect of the results presented in this section are the changes over time.)

Starting with 4-day events, an example of such an analysis for one precipitation station (Ellenville in Orange

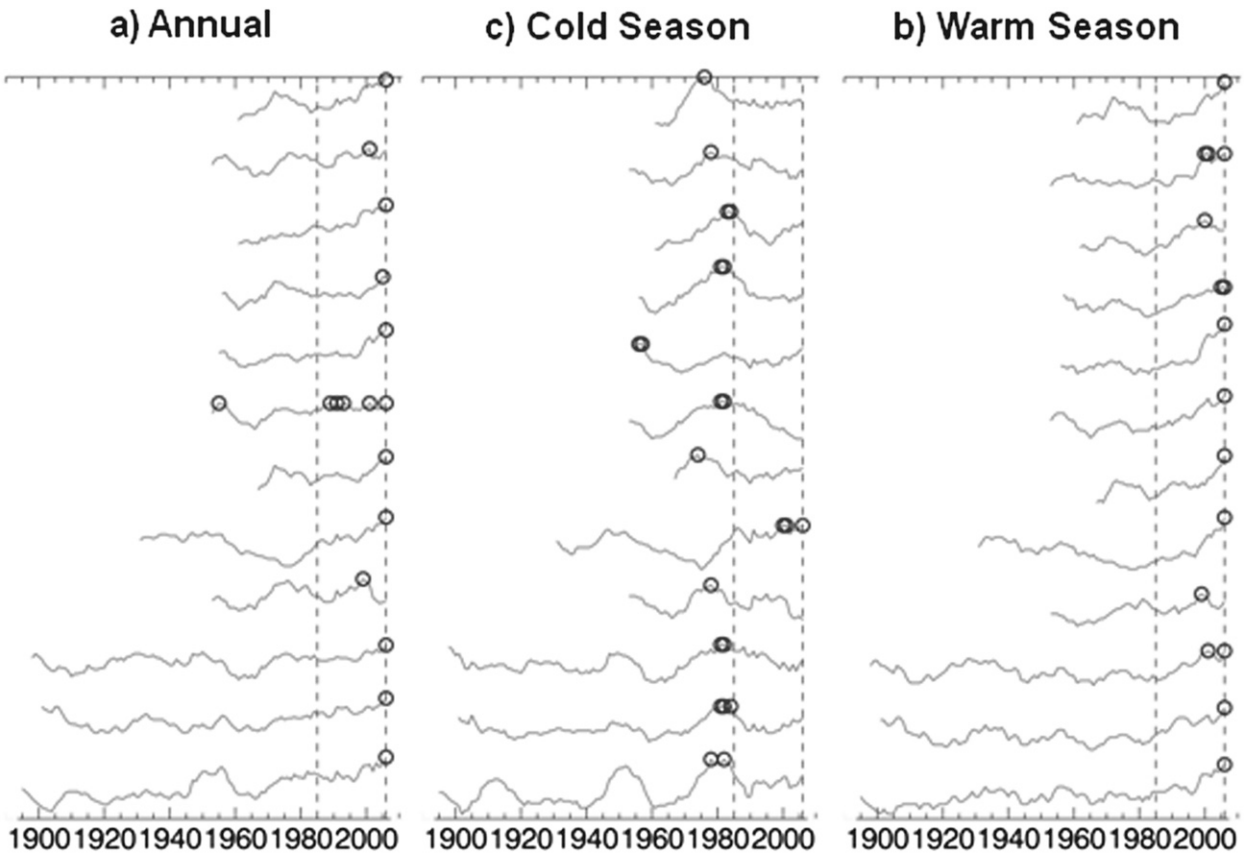

FIG. 7. Eleven-year smoothed centered running means of number of 4-day precipitation events per year equaling or exceeding the 95th percentile value for the entire record at 12 precipitation stations. Results from (a) annual, (b) cold season, and (c) warm season analyses are shown. The *y* axes are not shown. In each panel left vertical dashed line shows 1985; right vertical dashed line shows 2006. Blue circles on time series indicate year(s) of maximum value. (top to bottom) The 12 stations include the following: West Point, Mohonk, Port Jervis, Arkville, Delhi, Deposit, Ellenville, Liberty, Middletown, Rosendale, Slide, and Walton.

County) is shown in Fig. 6. Figs. 6a and 6b show scatterplots of 4-day precipitation for each season (with one diamond for each event); the 95th percentile value is indicated by the horizontal line. Warm season extreme (95th percentile) events are greater than cold season extreme events at this station (and, in fact, at all stations), which is consistent with the unimodal pattern of monthly precipitation (Fig. 3b). The time series of the number of extreme events per year in each seasonal period are shown in Figs. 6c and 6d. Superimposed on the annual time series is the smoothed (11-yr centered mean) time series, which we use to represent decadal-scale fluctuations in the frequency of extreme events. The maximum smoothed value (or values, if two or more years had the same maximum value) is indicated with a circle. For this station, one can see that while there are significant interannual variations, it appears that the frequency of extreme events during the cold season peaked near 1980, while the frequency of extreme events during the warm season has increased and reached historical highest values on record during the most recent decade.

To provide an overview of the variation of the frequency of extreme events at all stations, 11-yr running mean time series (such as shown for the Ellenville station in Figs. 6c,d) from all precipitation stations are shown in Fig. 7 for annual values (Fig. 7a), cold season (Fig. 7b), and warm season (Fig. 7c). Also indicated on each panel are maximum smoothed value(s) (blue circles), and the years 1985 (left vertical dashed line) and 2006 (the most recent year for which 11-yr-centered running means can be calculated; right vertical dashed line).

Annual time series (Fig. 7a) indicate an increase in the frequency of extreme precipitation events in recent years. The maximum smoothed value on record at all stations occurs during the post-1985 period. At 9 of 12 stations the maximum value is 2006, which means that the most recent period has the most frequent extreme events. Nine stations display an increasing trend since

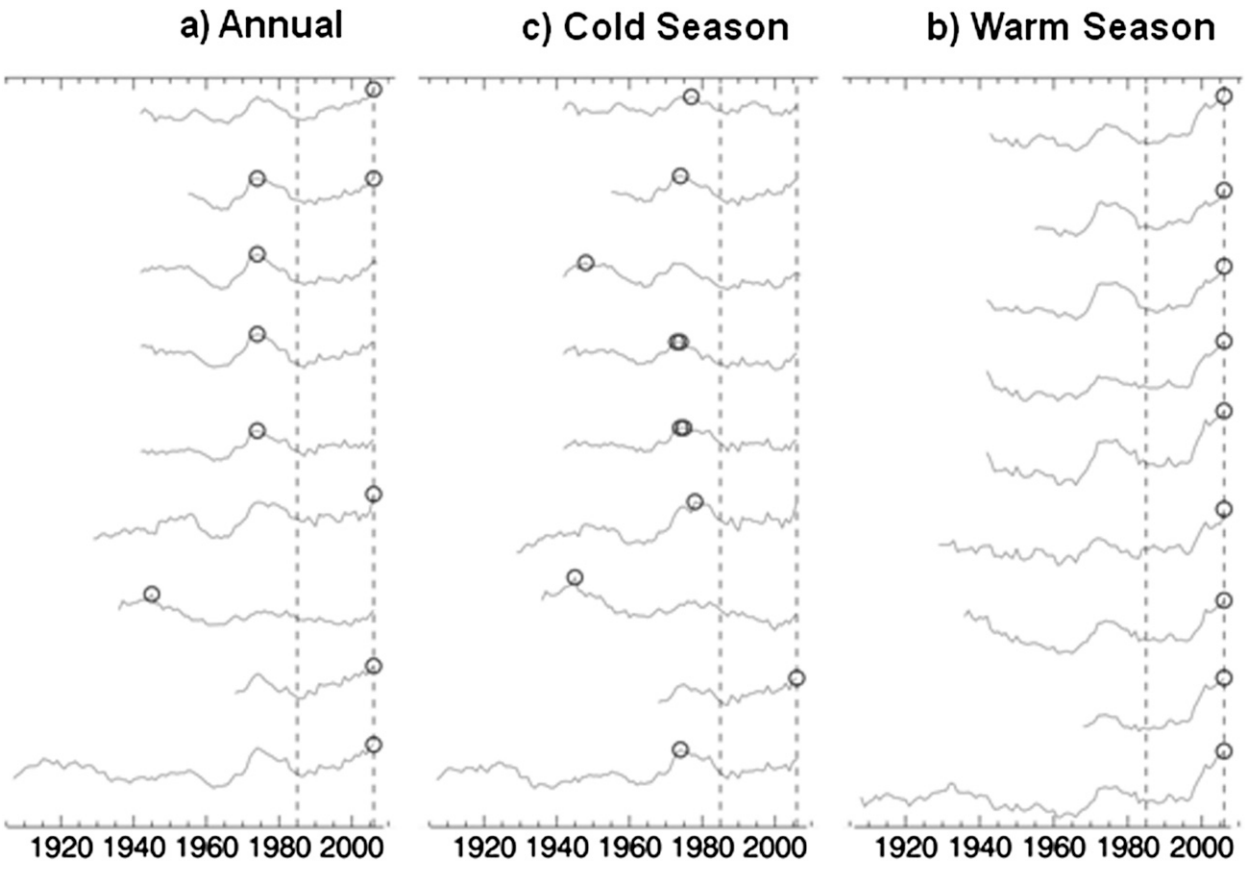

FIG. 8. As in Fig. 7, but for streamflow. (top to bottom) The 9 gauge stations include the following: 01350000, 1362200, 1362500, 01371500, 01413500, 01414500, 01415000, 01423000, and 01435000.

1985; seven stations show an accelerated rate of increase since the mid1990s.

The same analysis is performed using data from only the cold (Fig. 7b) and warm (Fig. 7c) seasons independently. Since 1985, a consistent seasonal shift appears in these records. The frequency of cold season extreme precipitation events at most stations either decreased or displayed no visual trend. At all stations except one (Delhi), the highest smoothed cold season value occurs prior to 1985. In contrast, the frequency of warm season extreme precipitation events has increased in all stations except Arkville during this post-1985 period; at many stations the frequency of extreme events has continued to increase, or has increased at an accelerated rate, since the mid-1990s. All stations experienced the maximum warm season value after 1985. In fact, 10 of 12 stations experienced the highest value in 2006 (the most recent 11-yr period). Thus, the frequency of extreme warm season precipitation events in this region has increased during the last 1–2 decades to levels unprecedented in the historical record.

During the pre-1985 period, no obvious or consistent long-term trend is observed, although a number of possible cold season decadal-scale variations may be gleaned from these records. For example there is evidence of decadal-scale periods of more frequent cold season extreme events centered around 1950 and around 1980, although not all stations are in agreement. It should be noted that the 1950s results are limited by the reduced number of stations with data covering that period (see period of record in Tables 1 and 2). A period of less frequent extreme events appear to have occurred in the 1960s, the time of the most extreme drought of the twentieth century in this region. During the warm season, no consistent or obvious regional-scale variations prior to 1985 are revealed by this analysis.

Recent increases in the frequency of extreme streamflow values (Fig. 8) are even more pronounced than for precipitation. Smoothed annual values (Fig. 8a) peak in 2006 at some stations and in the 1970s at others; at one station, annual values peaked in the 1940s. Cold season results (Fig. 8b) differ markedly from warm season results (Fig. 8c). Most cold season smoothed values peak during the 1970s; at only one station do cold season values increase and peak during the post-1985 period. However, at all stations, warm season values increase

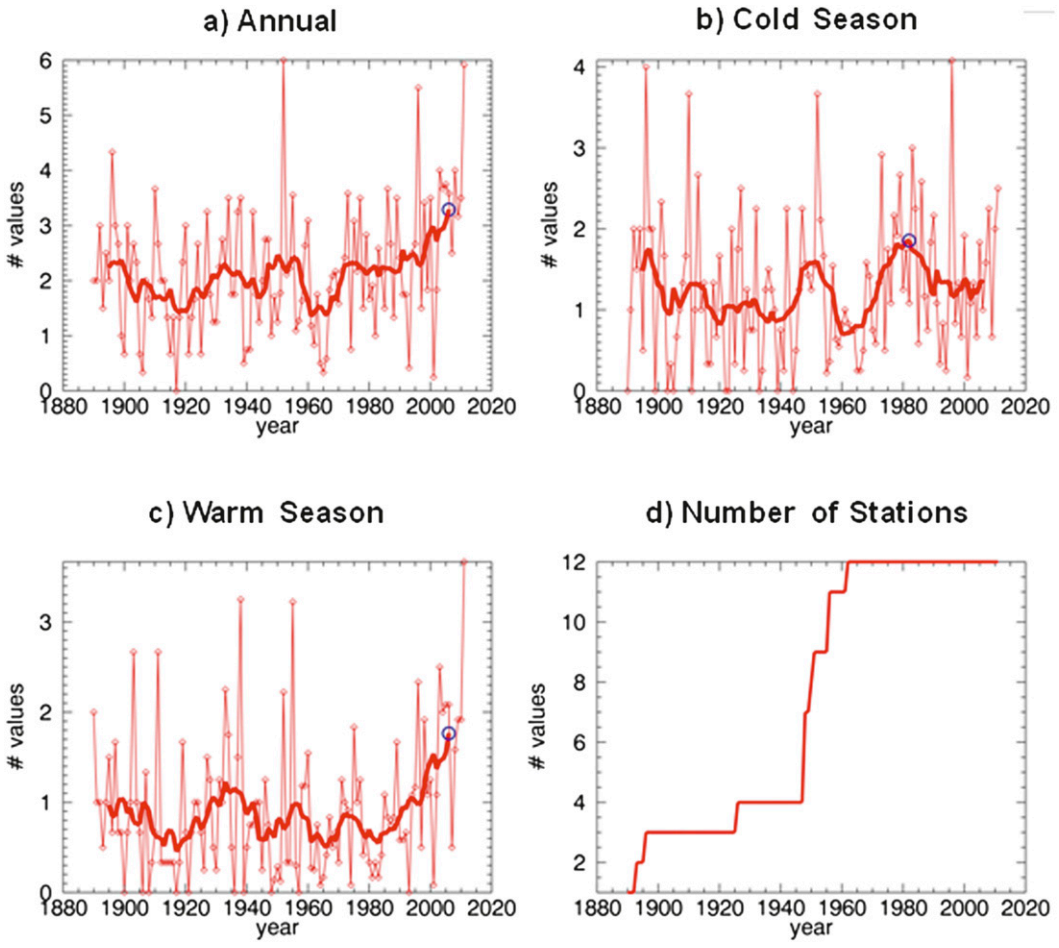

FIG. 9. Regional mean number of 95th percentile 4-day precipitation values per year. For each year, the number of 95th percentile values per year, averaged over all stations available, is shown (solid line with diamonds) along with the 11-yr running mean (bold line) and a (blue) circle indicating the year with the highest smoothed value. (a) Values from all months, (b) cold season values only, (c) warm season values only, and (d) the number of stations per year are shown.

during the post-1985 period and increase most consistently since 1995; at all stations warm season highest values occur in 2006 (which is the center value of the most recent 11-yr period).

During the pre-1985 period, a consistent regional-scale warm season signal appears at these stations: the 1960s had less frequent extreme streamflow events, and the 1970s had more frequent extreme events. These are consistent with the precipitation results described above.

To provide a single time series that represents regional-scale variations in the frequency of extreme events, results from individual stations are combined for precipitation (Fig. 9) and streamflow (Fig. 10). These are produced by calculating the mean, for each year, of the number of extreme events at all available stations. The dry 1960s are apparent during both seasons (Figs. 9b,c). However, the wet 2000s are only apparent during the warm season (Fig. 9c). A consistent increase in extreme precipitation frequency since the 1980s is apparent during the warm season (and in the annual mean records) but not during the cold season (Fig. 9b). The mean number of warm season extreme precipitation events per year has increased from approximately 0.6 during the early 1980s to approximately 1.8 during the most recent decade. Also shown is the time series of number of stations per year included in the regional mean (Fig. 9d).

The regional mean frequency of extreme streamflow events was relatively high during the 1970s and low during the 1960s in both the cold and warm seasons (Figs. 10c,d). During the warm season only (Fig. 10c) the occurrence of extreme streamflow has increased considerably since the mid-1990s, and has reached historical highest values in the most recent decade. The regional mean frequency of extreme events during the warm period has increased from approximately six per year in the mid-1990s to approximately sixteen per year during

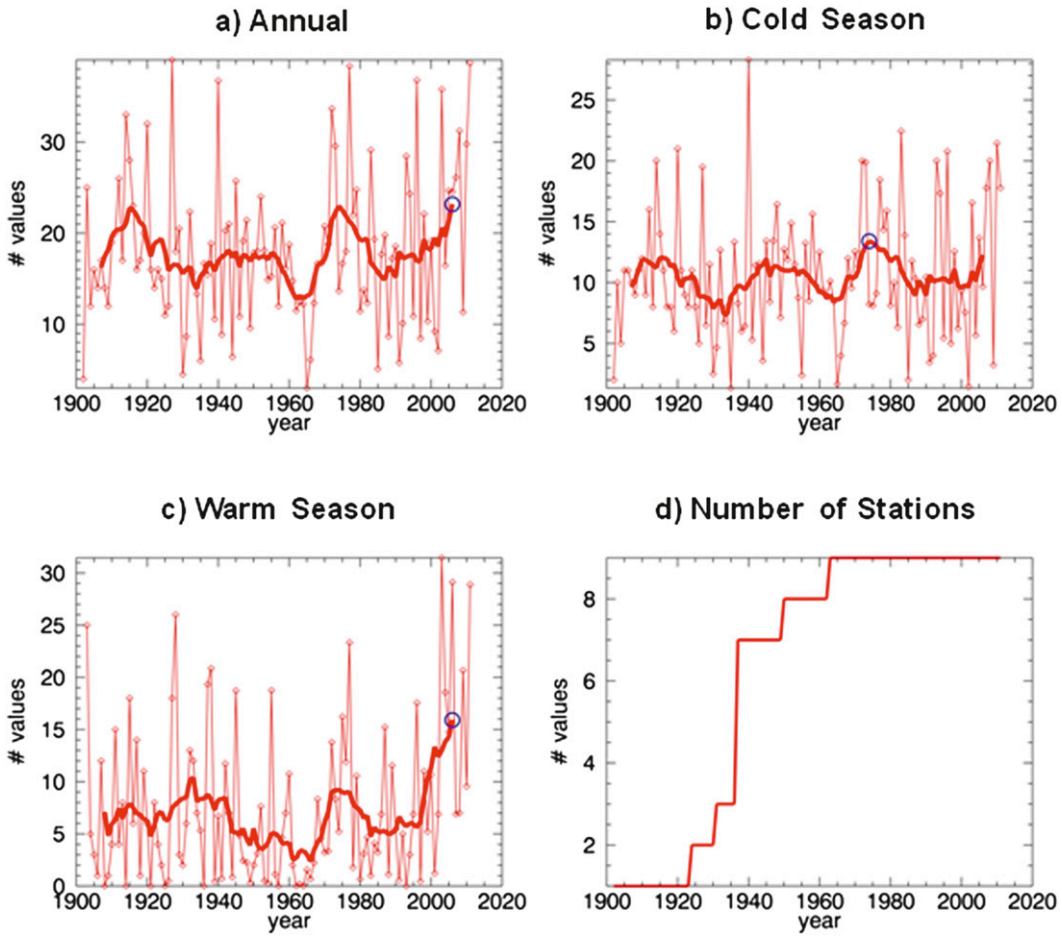

FIG. 10. As in Fig. 9, but for daily streamflow.

the most recent decade. This pattern is not unique to our region: for example, Novotny and Stefan (2007) studied streamflow in Minnesota and found similar results of increasing trend in summer peak rainfall events as well as in the number of days with higher flows starting from the 1980s while observing no trend in snowmelt related (cold season) streamflow events.

We applied the same nonparametric analysis to 30- and 60-day precipitation and streamflow events, with results similar to those discussed above. Cold season extreme event frequencies peak in the 1970s and 1980s (Figs. 11a,c and 12a,c), and warm season frequencies peak in the most recent decade (Figs. 11b,d and 12b,d). Stone et al. (2000) found a similar increasing trend in precipitation events exceeding a 2-month return period for most areas in Canada.

5. Summary and conclusions

Anecdotal evidence of a recent increased frequency of extreme hydrologic events in the Catskill Mountains and Hudson River Valley of southern New York State are evaluated by applying parametric and nonparametric statistics to precipitation and streamflow time series. The periods of record for these stations varies between approximately 50 and 120 yr. Thus, for some stations we are able to analyze the changing frequencies of extreme events since the late nineteenth century.

In our region, the seasonal cycle of extreme (i.e., ≥95th percentile) precipitation events is unimodal, peaking between August and October. In contrast, extreme streamflow events exhibit a bimodal distribution, peaking in March and April as well as between August and October. Spring time extreme streamflow events result largely from snowmelt and rain-on-snow events, while late summer/fall extreme streamflow events are associated with liquid precipitation only.

Parametric results of regional mean peak streamflow frequency estimates from five overlapping 30-yr periods reveal an increasing pattern in flood flows from the 1970s to 1990s for all return periods, in particular for flow magnitudes of 25 yr or greater return period. Flood flow

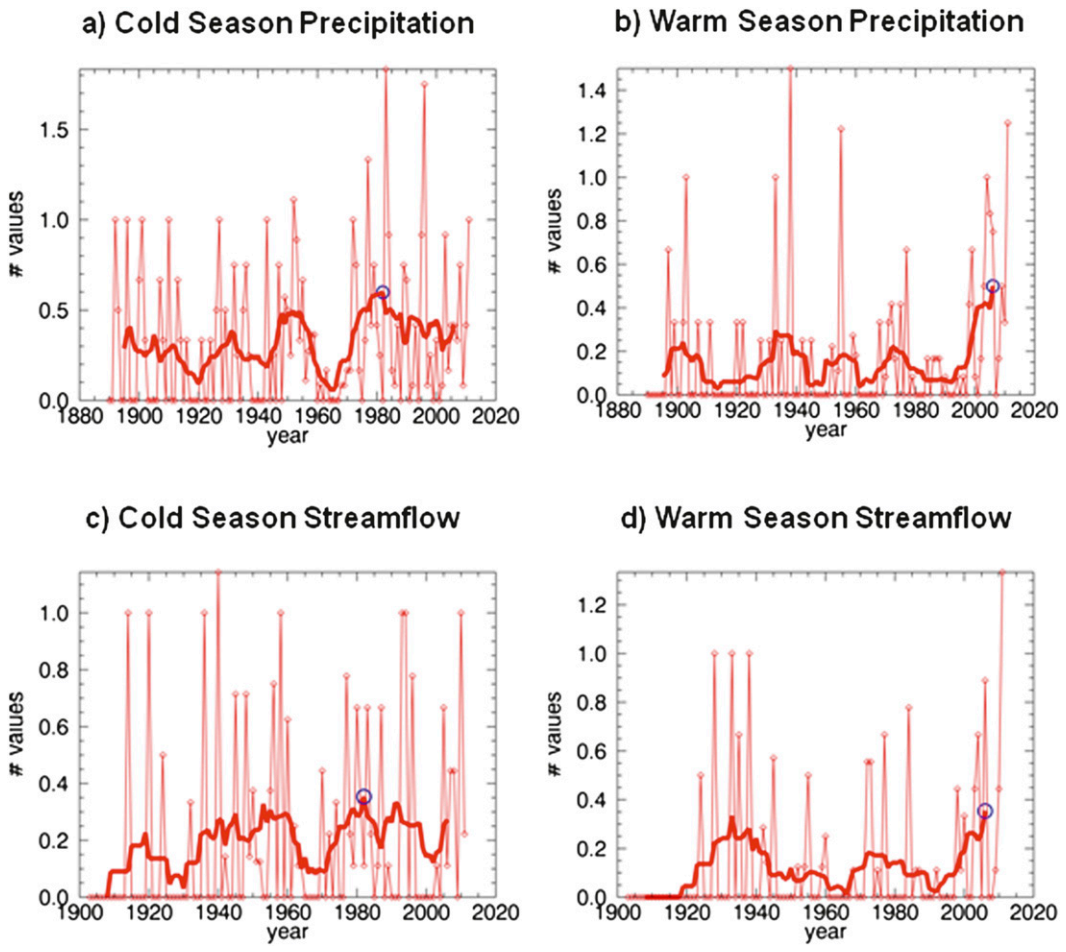

FIG. 11. Regional annual mean number of 95th percentile 30-day events for (a) cold season precipitation, (b) warm season precipitation, (c) cold season streamflow, and (d) warm season streamflow. Each panel includes regional annual mean values (solid line with diamonds); 11-yr running mean (bold line); and maximum running mean values (blue circles).

magnitude is a function of station location as well as the particular 30-yr period included for analysis. Temporal variations in flood flow magnitude also depend on the return period of interest. The Interagency Advisory Committee on Water Data (1982) recommends a minimum of 25-yr record to perform flood frequency estimates corresponding to a 100-yr or larger return period (Pilgrim and Cordery 1993) but with an assumption of invariance in climate. The assumption of stationarity in hydrological processes has become a major topic of discussion in recent years (Galloway 2011; Hirsh 2011; Vogel et al. 2011; Milly et al. 2008). Our 30-yr-based results appear to support those who advocate for a new, nonstationarity based approach to modeling fundamental hydrological processes including flood flow frequency analysis. Among all 30-yr periods in this analysis 1950–80 provides estimates most similar to long-term flood flow estimates; 1960–90 and 1980–2011 reveal to be the driest and wettest periods, respectively.

Nonparametric analysis demonstrates that in our region extreme warm season hydrological events have been more frequent during the last decade than at any time on record. The frequency of 4-day precipitation and daily streamflow extreme warm period events during the first decade of the twenty-first century has risen by 150%–200% in the last two decades, to levels 40%–70% higher than at any earlier time on record. Based on 30- and 60-day results, the wettest years on record are the 2000s during the warm season and the 1980s during the cold season.

The causes of the increasing frequency of extreme hydrological events are uncertain and outside the scope of this paper. However, various studies have linked such changes globally to changes in atmospheric composition, including water vapor (Min et al. 2011; Kunkel et al. 2013a) and regionally to extratropical and tropical cyclones, mesoscale convective systems, and North American Monsoon (Kunkel et al. 2013a, 2012, 2010). It remains unclear whether this recent increase in extreme

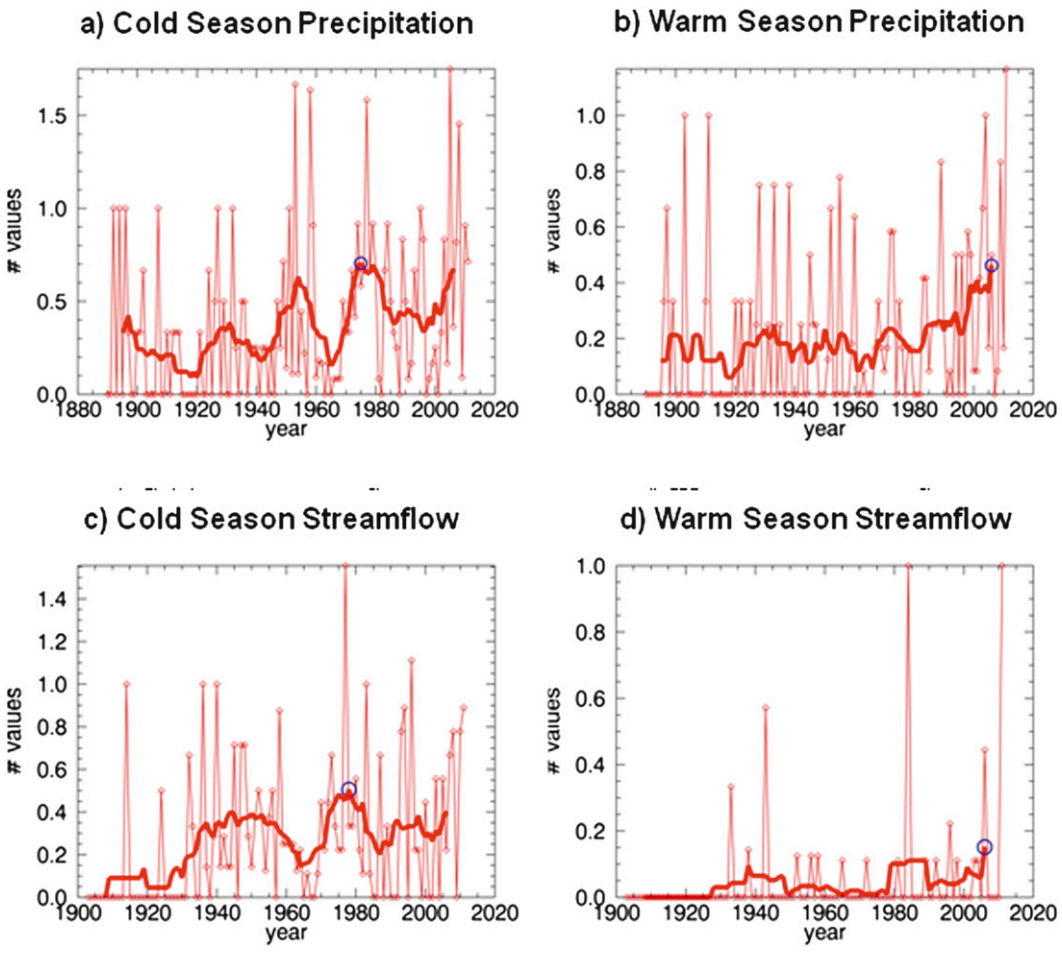

FIG. 12. As in Fig. 11, but for 60-day events.

events is part of a trend that will continue, or just a short-term fluctuation. However, these results are consistent with an increase in the frequency of extreme climatic events in the northeastern United States as indicated by National Oceanic and Atmospheric Administration (NOAA)'s climate extremes index (http://www.ncdc.noaa.gov/extremes/cei/graph/ne/4/09-11, accessed 15 April 2013) and twenty-first-century predictions based on climate model results (Kunkel et al. 2013b).

Acknowledgments. The authors are grateful to the New York State Energy Research and Development Authority (NYSERDA) for providing funding for part of the research that let to this manuscript. This paper does not necessarily reflect the official views of NYSERDA and no endorsement should be inferred. Thanks to Donald Pierson, Elliot Schneiderman, and David Lounsbury of the NYC DEP water quality modeling group for their inputs and technical support; and to Neil Pederson, Rajith Mukundan, and David Smith for their input that helped improve this manuscript.

REFERENCES

Allen, S. K., and Coauthors, 2012: Managing the risks of extreme events and disasters to advance climate change adaptation. *Summary for Policymakers,* C. B. Field et al., Eds., Cambridge University Press, 1–19.

Arnell, N., and Coauthors, 2001: Hydrology and water resources. *Climate Change 2001: The Scientific Basis,* J. T. Houghton et al., Eds., Cambridge University Press, 133–233.

Burns, D. A., J. Klaus, and M. R. McHale, 2007: Recent climate trends and implications for water resources in the Catskill Mountain region, New York, USA. *J. Hydrol.,* **336,** 155–170, doi:10.1016/j.jhydrol.2006.12.019.

Changnon, S. A., and M. Demissie, 1996: Detection of changes in streamflow and floods relating from climate fluctuations and land use changes. *Climatic Change,* **32,** 411–421.

Curriero, F. C., J. A. Patz, J. B. Rose, and S. Lele, 2001: The association between extreme precipitation and waterborne disease outbreaks in the United States, 1948 – 1994. *Amer. J. Public Health,* **91,** 1194–1199.

Dai, A., I. Y. Fung, and A. D. DelGenio, 1997: Surface observed global land precipitation variations during 1900–1988. *J. Climate,* **10,** 2943–2962.

Devineni, N., U. Lall, N. Pederson, and E. Cook, 2013: A tree ring–based reconstruction of Delaware River basin Streamflow

using hierarchical Bayesian regression. *J. Climate,* **26,** 4357–4374.

Easterling, D. R., J. L. Evans, P. Ya Groisman, T. R. Karl, K. E. Kunkel, and P. Ambenje, 2000: Observed variability and trends in extreme climate events: A brief review. *Bull. Amer. Meteor. Soc.,* **81,** 417–425.

El Adlouni, S., and T. B. M. J. Ouarda, 2010: Frequency analysis of extreme rainfall events. *Rainfall: State of the Science, Geophys. Monogr.,* Vol. 191, Amer. Geophys. Union, 171–188.

Folland, C. K., and Coauthors, 2001: Observed climate variability and change. *Climate Change 2001: The Scientific Basis,* J. T. Houghton et al., Eds., Cambridge University. Press, 99–181.

Frederick, R. H., V. A. Meyers, and E. P. Auciello, 1977: Five- to 60-minute precipitation frequency for the Eastern and Central United States. NOAA Tech. Memo NWS HYDRO-35, 35 pp.

Frei, A., R. L. Armstrong, M. P. Clark, and M. C. Serreze, 2002: Catskill Mountain water resources vulnerability, Hydroclimatology, and climate-change sensitivity. *Ann. Assoc. Amer. Geogr.,* **92,** 203–224.

Galloway, G. E., 2011: If stationarity is dead, what do we do now? *J. Amer. Water Resour. Assoc.,* **47,** 563–570, doi:10.1111/j.1752-1688.2011.00550.x.

Groisman, P. Ya., R. W. Knight, D. R. Easterling, T. R. Karl, G. C. Hegerl, and V. N. Razuvaev, 2005: Trends in intense precipitation in the climate record. *J. Climate,* **18,** 1326–1350.

Gumbel, E. J., 1958: *Statistics of Extremes*. Columbia University Press, 375 pp.

Hershfield, D. M., 1961: Rainfall frequency atlas of the United States for durations from 30 minutes to 24 hours and return periods from 1 to 100 Years. U.S. Weather Bureau Tech. Paper 40, 34 pp. [Available online at http://www.nws.noaa.gov/oh/hdsc/PF_documents/TechnicalMemo_HYDRO35.pdf.]

Hirsh, R. M., 2011: A perspective on nonstationarity and water management. *J. Amer. Water Resour. Assoc.,* **47,** 436–446, doi:10.1111/j.1752-1688.2011.00539.x.

Huntington, T. G., 2006: Evidence for intensification of the global water cycle: Review and synthesis. *J. Hydrol.,* **319,** 83–95.

Interagency Advisory Committee on Water Data, 1982: Guidelines for determining food flow frequency. U.S. Department of the Interior, U.S. Geological Survey, Office of Water Data Coordination Bull. 17B, 186 pp. [Available online at http://water.usgs.gov/osw/bulletin17b/dl_flow.pdf.]

Karl, T. R., and R. W. Knight, 1998: Secular trends of precipitation amount, frequency, and intensity in the USA. *Bull. Amer. Meteor. Soc.,* **79,** 231–241.

——, and D. R. Easterling, 1999: Climate extremes: Selected review and future research directions. *Climatic Change,* **42,** 309–325.

——, R. W. Knight, D. R. Easterling, and R. G. Quayle, 1995: Trends in U.S. climate during the twentieth century. *Consequences,* **1,** 2–12.

Knutson, T. R., and S. Manabe, 1998: Model assessment of decadal variability and trends in the tropical Pacific Ocean. *J. Climate,* **11,** 2273–2296.

Kunkel, K. E., 2003a: North American trends in extreme precipitation. *Nat. Hazards,* **29,** 291–305.

——, 2003b: Sea surface temperature forcing of the upward trend in U.S. extreme precipitation. *J. Geophys. Res.,* **108,** 4020–4030, doi:10.1029/2002JD002404.

——, S. A. Changnon, and J. R. Angel, 1994: Climatic aspects of the 1993 upper Mississippi River basin flood. *Bull. Amer. Meteor. Soc.,* **75,** 811–822.

——, K. Andsager, and D. R. Easterling, 1999: Long-term trends in extreme precipitation events over the conterminous United States and Canada. *J. Climate,* **12,** 2515–2527.

——, D. R. Easterling, D. A. R. Kristovich, B. Gleason, L. Stoecker, and R. Smith, 2010: Recent increases in U.S. heavy precipitation associated with tropical cyclones. *Geophys. Res. Lett.,* **37,** L24706, doi:10.1029/2010GL045164.

——, ——, ——, ——, ——, and ——, 2012: Meteorological causes of the secular variations in observed extreme precipitation events for the conterminous United States. *J. Hydrometeor.,* **13,** 1131–1141.

——, and Coauthors, 2013a: Monitoring and understanding trends in extreme storms: State of knowledge. *Bull. Amer. Meteor. Soc.,* **94,** 499–514.

——, T. R. Karl, D. R. Easterling, K. Redmond, J. Young, X. Yin, and P. Hennon, 2013b: Probable maximum precipitation and climate change. *Geophys. Res. Lett.,* **40,** 1402–1408, doi:10.1002/grl.50334.

Leathers, D. J., D. R. Kluck, and S. Kroczynski, 1998: The severe flooding event of January 1996 across north-central Pennsylvania. *Bull. Amer. Meteor. Soc.,* **79,** 785–797.

Manabe, S., R. T. Wetherald, P. C. D. Milly, T. L. Delworth, and R. J. Stouffer, 2004: Century-scale change in water availability: CO_2-quadrupling experiment. *Climatic Change,* **64,** 59–76.

Matonse, A. H., D. C. Pierson, A. Frei, M. S. Zion, A. Anandhi, E. Schneiderman, and B. Wright, 2012: Investigating the impact of climate change on New York City's primary water supply. *Climatic Change,* **116,** 437–456, doi:10.1007/s10584-012-0515-4.

Milly, P. C. D., J. Betancourt, M. Falkenmark, R. M. Hirsch, Z. W. Kundzewicz, D. P. Lettenmaier, and R. J. Stouffer, 2008: Stationarity is dead: Whither water management? *Science,* **319,** 573–574, doi:10.1126/science.1151915.

Min, S. K., X. Zhang, F. W. Zwiers, and G. C. Hegerl, 2011: Human contribution to more intense precipitation extremes. *Nature,* **470,** 378–381.

Novotny, E. V., and H. G. Stefan, 2007: Streamflow in Minnesota: Indicator of climate change. *J. Hydrol.,* **334,** 319–333, doi:10.1016/j.jhydrol.2006.10.011.

Pederson, N., A. R. Bell, E. R. Cook, U. Lall, N. Devineni, R. Seager, K. Eggleston, and K. J. Vranes, 2012: Is an epic pluvial masking the water insecurity of the Greater New York City Region? *J. Climate,* **26,** 1339–1354.

Pielke, R. A., Jr., and M. W. Downton, 2000: Precipitation and damaging floods: Trends in the United States, 1932–1997. *J. Climate,* **13,** 3625–3637.

Pilgrim, D. H., and I. Cordery, 1993: Flood runoff. *Handbook of Hydrology,* D. R. Maidment, Ed., McGraw-Hill Inc., 9.1–9.42.

Seager, R., N. Pederson, Y. Kushnir, J. Nakamura, and S. Jurburg, 2012: The 1960s drought and the subsequent shift to a wetter climate in the Catskill Mountains region of the New York City watershed. *J. Climate,* **25,** 6721–6742.

Smith, J. A., 1993: Precipitation. *Handbook of Hydrology,* D. R. Maidment, Ed., McGraw-Hill Inc., 3.1–3.47.

Stedinger, J. R., R. M. Vogel, and E. Foufoula-Georgiou, 1993: Frequency analysis of extreme events. *Handbook of Hydrology,* D. R. Maidment, Ed., McGraw-Hill Inc., 18.1–18.66.

Stone, D. A., A. J. Weaver, and F. W. Zwiers, 2000: Trends in Canadian precipitation intensity. *Atmos.–Ocean,* **38,** 321–347.

Suro, T. P., and G. D. Firda, 2006: Flood of April 2–3, 2005, Neversink River Basin, New York. U.S. Department of

Interior, U.S. Geological Survey, Open-file Rep. 2006-1319, 98 pp. [Available online at http://pubs.usgs.gov/of/2006/1319/pdf/OFR2006-1319_Neversink_report.pdf.]

Todhunter, P. E., 2001: A hydroclimatological analysis of the Red River of the North snowmelt flood catastrophe of 1997. *J. Amer. Water Resour. Assoc.,* **37,** 1263–1278.

Towler, E., B. Rajagopalan, E. Gilleland, R. S. Summers, D. Yates, and R. W. Kats, 2010: Modeling hydrologic and water quality extremes in a changing climate: A statistical approach based on extreme value theory. *Water Resour. Res.,* **46,** W11504, doi:10.1029/2009WR008876.

Vogel, R. M., and C. N. Kroll, 1989: Low-flow frequency analysis using probability-plot correlation coefficients. *J. Water Resour. Plan. Manage.,* **115,** 338–357.

——, C. Yaindl, and M. Walter, 2011: Nonstationarity: Flood magnification and recurrence reduction factors in the United States. *J. Amer. Water Resour. Assoc.,* **47,** 464–474, doi:10.1111/j.1752-1688.2011.00541.x.

Weniger, B. G., M. J. Blaser, J. Gedrose, E. C. Lippy, and D. D. Juranek, 1983: An outbreak of waterborne giardiasis associated with heavy water runoff due to warm weather and volcanic ashfall. *Amer. J. Public Health,* **73,** 868–872.

Zhang, X., L. A. Vincent, W. D. Hogg, and A. Niitsoo, 2000: Temperature and precipitation trends in Canada during the 20th century. *Atmos.–Ocean,* **38,** 395–429.

——, W. D. Hogg, and E. Mekis, 2001: Spatial and temporal characteristics of heavy precipitation events over Canada. *J. Climate,* **14,** 1923–1936.

——, F. W. Zwiers, G. C. Hegerl, F. H. Lambert, N. P. Gillett, S. Soloman, P. A. Stott, and T. Nozawa, 2007: Detection of human influence on twentieth-century precipitation trends. *Nature,* **448,** 461–466.

Catena xxx (2013) xxx–xxx

Contents lists available at SciVerse ScienceDirect

Catena

journal homepage: www.elsevier.com/locate/catena

Factors affecting storm event turbidity in a New York City water supply stream

R. Mukundan [a,*], D.C. Pierson [b], E.M. Schneiderman [b], D.M. O'Donnell [c], S.M. Pradhanang [a], M.S. Zion [b], A.H. Matonse [a]

[a] Institute for Sustainable Cities, City University of New York, NY 10065, USA
[b] New York City Department of Environmental Protection, Kingston, NY 12401, USA
[c] Upstate Freshwater Institute, Syracuse, NY 13214, USA

ARTICLE INFO

Article history:
Received 29 April 2012
Received in revised form 16 November 2012
Accepted 7 February 2013
Available online xxxx

Keywords:
Turbidity
Automated monitoring
Hysteresis
Rating curve
New York City water supply

ABSTRACT

Stream turbidity levels tend to increase during high stream discharge events, and it is important to quantify the suspended sediment flux during these events that could potentially lead to water quality problems. Here, a case study for estimating suspended sediment loads (as a product of turbidity and stream discharge) in streams that are part of the New York City (NYC) water supply in the Catskill region of New York State is presented. Over the 8 year study period 80% of the suspended sediment load was transported during less than 4% of the time, indicating the importance of estimating storm event suspended sediment loads. The objective of this study was to understand the underlying factors controlling the uncertainty in the discharge vs turbidity relationship at the outlet of the watershed draining into the NYC Ashokan Reservoir. High frequency (15-min) automated monitoring of stream turbidity was combined with stream discharge measurements of a similar frequency to provide an estimate of the true suspended sediment load that could be used for model testing and verification at two time scales; daily and events. Multivariate statistical analyses indicate that average daily stream turbidity during storm events can be influenced by the spatial variability in runoff, antecedent conditions, and season. A predictive relationship of event mean stream turbidity based on stream discharge alone led to a strong predictive relationship ($r^2 = 0.81$), but also a 10% underestimation of the cumulative measured event mean suspended sediment load. Inclusion of information on the time between events improved the regression equation ($r^2 = 0.89$), and reduced the cumulative difference between estimated and measured event mean suspended sediment loads to 7% underestimation.

1. Introduction

Sediment loads can exert an important control on drinking water supply and other designated water uses (Walling, 2009). High river sediment loads and the resulting sedimentation of water resources is a major water quality issue in the United States (USEPA, 2009). The economic impact of sedimentation in the United States is estimated to be billions of dollars annually (Larsen et al., 2010; Osterkamp, 2004; Pimentel et al., 1995). The vast majority of the suspended sediments are transported during high flow events (Wolman and Miller, 1960) and therefore it is important to quantify the sediment flux during these events. Improved capability to quantify sediment flux in large events may help in developing predictive models that can support management of water resources.

Methods to calculate sediment loads make use of multiple instantaneous measurements of sediment concentration/turbidity and stream discharge. Suspended sediment transport rating curves are widely used by hydrologists for predicting sediment concentrations during unsampled periods (Asselman, 2000; Horowitz, 2003; Walling, 1977; Walling and Webb, 1988). Most of these methods involve developing a regression line relating suspended sediment concentration to discharge followed by interpolation and extrapolation. The accuracy of this empirical method depends largely on the availability of data over all ranges of flow and sediment concentration (Horowitz et al., 2001), and the underlying variability in the processes which regulate erosion and sediment transport. The daily sediment load, S (T d^{-1}) of a stream can be estimated using a simple power function of discharge, Q (m^3 s^{-1}) (Nash, 1994):

$$S = aQ^b \quad (1)$$

where a and b are empirically determined constants. Nash (1994) used the same function to establish a relationship between sediment transport rate and discharge for 55 streams across the United States. A fairly good fit was obtained for the observed data for all streams. Improvement in sediment transport rate predictions can be made by constructing separate rating curves for different seasons and by

* Corresponding author. Tel.: +1 845 340 7791.
E-mail address: Rajith.Mukundan@hunter.cuny.edu (R. Mukundan).

0341-8162/$ – see front matter © 2013 Elsevier B.V. All rights reserved.
http://dx.doi.org/10.1016/j.catena.2013.02.002

separating storm hydrographs into rising and falling limbs (Walling, 1974, 1977).

A shortcoming in the use of a sediment rating curve is caused by hysteresis, a phenomenon where the rate of sediment transport for a given discharge during the rising limb of the hydrograph will be different from that of the falling limb. In such cases the rates of sediment transport between rising and falling limbs of the hydrograph frequently vary by as much as several orders of magnitude. Several studies discuss hysteresis and its causes (Asselman, 1999; Lenzi and Marchi, 2000; Walling and Webb, 1988). Hysteresis can be observed as a loop in time series plots of discharge vs suspended sediment over the course of a storm event. A clockwise loop which is due to depletion of sediment sources is the most common. Counter-clockwise loops can be observed when the sediment source inputs increase over the duration of the storm event. Factors that can lead to this behavior include sediment sources that are located far away from the monitoring station, or sources that may increase during the storm event such as actively eroding channel banks and hill slopes. Hysteresis does not invalidate the use of a power function sediment rating curve if the variation about this function is symmetrically distributed at all discharges. However, if the predicted and observed sediment transport rates systematically diverge above a threshold value of discharge, then the rating curve cannot be used for extrapolation beyond that value (Nash, 1994). The rating curve method in general tends to under predict sediment concentrations during high flows and over predict during low flows (Horowitz et al., 2001).

A direct method of estimating suspended sediment loads is to use the weighted sum of all instantaneous loads. This method has advantages over the rating curve approach in that it requires few assumptions about the underlying physical processes and is not subject to bias due to transformation of data (Cohn, 1995). However, this method requires high frequency sampling of suspended sediment for accurate estimation of loads which in turn will make monitoring programs more expensive. For automated measurement of instantaneous loads, use of turbidity as a surrogate for suspended sediment may be a good alternative (Jastram et al., 2010; O'Donnell and Effler, 2006; Pierson et al., 2008; Stubblefield et al., 2007).

Differences between turbidity or suspended sediment loads estimated using discharge rating curves and loads based on actual measurements may be caused by missing explanatory variables in addition to discharge (Colby, 1956; Syvitski et al., 2000; Thomas, 1988), which may also result in inter-event variability in the sediment rating relationship (Asselman, 1999; Lenzi and Marchi, 2000; Seeger et al., 2004; Zabaleta et al., 2007). Recent studies have considered additional predictors of suspended sediment which include antecedent soil moisture conditions and event variables such as maximum stream discharge and precipitation (Seeger et al., 2004; Zabaleta et al., 2007). Hicks et al. (1996) observed spatial variability in sediment yield due to variations in rainfall and geology. The underlying assumption is that sediment yield at the watershed outlet is controlled by factors related to sediment supply rather than just transport capacity represented by stream discharge at the outlet. Therefore, inclusion of predictors of sediment supply in addition to measurements of stream discharge may improve the predictive models for event mean turbidity or suspended sediment loads.

A case study from the Catskill region of New York State is presented in this paper, using data collected from the Esopus Creek watershed that is part of the New York City (NYC) drinking water supply system. The focus of this paper is on the estimation of stream water turbidity and estimates of suspended sediment loads (using product of turbidity and stream discharge) entering the Ashokan Reservoir (Fig. 1). Turbidity measures the light-scattering effects of suspended particulate material (SPM) and is, therefore, related to suspended sediment concentrations and loading rates. Turbidity, however, depends not only on the concentration of the SPM, but also on the characteristics of the SPM (particle size distribution and refractive index) and color of water. These characteristics will change with turbidity source and stream discharge making turbidity a useful proxy, but less than the perfect measurement of SPM. Previous studies in this region support the concept of suspended sediment loading estimates using turbidity measurements (i.e., units of NTU $\cdot$ m^3 s^{-1}), with turbidity being the regulatory pollutant of concern although the product of turbidity and stream discharge is not a strict mass loading rate (Peng et al., 2009). Additional support for this approach is provided by the additive nature of turbidity i.e., the turbidity of a mixture of two volumes can be computed by volume averaging (Davies-Colley et al., 2003). Being an optical measurement, turbidity can be measured in situ and at higher sampling frequency than is possible with manual sampling and laboratory analysis of SPM. Automated high frequency monitoring of turbidity (*Tn*, NTU) can therefore be used to provide high frequency estimates of suspended sediment loads that are an important input to predictive models (Gelda and Effler, 2007) used to guide reservoir operations and minimize the impact of turbid inputs on the water delivered to New York City consumers.

Multivariate statistical analyses are frequently applied to study environmental problems (e.g., Boyacioglu and Boyacioglu, 2008; Zeng and Rasmussen, 2005). However, the use of this type of analysis is less common for evaluating watershed suspended sediment dynamics and understanding the main controlling processes (e.g., Seeger et al., 2004; Zabaleta et al., 2007).

We hypothesize that the event mean turbidity is determined by a combination of factors such as: (1) spatial distribution of precipitation, (2) geologic sources of sediment, (3) antecedent soil moisture condition of the watershed, (4) stream power generated during the event, (5) flow regime, and (6) season. The purpose of this study is to identify the factors that cause variability in discharge–turbidity relations using multivariate analyses which can be used to develop improved turbidity predictions that include factors in addition to stream discharge. Incorporation of additional factors that may influence stream turbidity in a predictive model could potentially improve our understanding of stream turbidity variability in space as well as in time. This knowledge is critical in the development and evaluation of operational predictive models and in the design of watershed management strategies (Giménez et al., 2012). Information gained from this study is expected to provide insight on developing operational predictive models of turbidity for NYC water supply watersheds. A similar approach could be used in any watershed or region with similar water quality problems.

2. Materials and methods

2.1. Description of study site

The Esopus Creek is a major source of water to the NYC water supply Ashokan Reservoir (Fig. 1). The Esopus watershed drains an area of 493 km^2 and is dominated by forests which occupy more than 90% of the watershed area. The elevation of the watershed ranges from about 194 m near the watershed outlet at Coldbrook to 1275 m at the headwaters. During and following high levels of stream discharge increases in reservoir turbidity can impact water quality and potentially affect a portion of the drinking water supply (Effler et al., 1998; Gelda et al., 2009). Widespread stream channel erosion of glacial clay deposits has been identified as the primary cause of high levels of turbidity in many of the tributaries draining the Catskill watersheds (Nagle et al., 2007). However, these clay exposures are not uniformly distributed across the watershed. Stream discharge–turbidity relations from the outlet of this watershed show wide variability (Fig. 2). Similar turbidity–discharge relations also occur in an adjacent stream Schoharie Creek that drains to the Schoharie Reservoir and water from the Schoharie Reservoir can be diverted into the Esopus Creek and Ashokan Reservoir (Fig. 1).

2.2. Turbidity monitoring

An automated *Tn* monitoring system was installed on the main tributary entering the Ashokan Reservoir near the confluence of the

Please cite this article as: Mukundan, R., et al., Factors affecting storm event turbidity in a New York City water supply stream, Catena (2013), http://dx.doi.org/10.1016/j.catena.2013.02.002

Fig. 1. Location map of the Esopus Creek watershed showing tributary stream gauge stations and diversion tunnel from the Schoharie Reservoir.

creek and with the reservoir. Water was pumped into a riverside hut where measurements of *Tn*, specific conductivity and water temperature were made using a YSI water quality sonde. Water samples were also periodically collected and analyzed for *Tn* and TSS in the laboratory. The laboratory measured *Tn* data were then used to correct the automated data to account for drift in the turbidity measurements. A U. S. Geological Survey (USGS) gauging station at the watershed outlet provided discharge data at a daily and a 15 minute interval. Turbidity measurements were made at intervals between 15 min and 1 h and flow-weighted to provide daily average values, comparable in frequency to the most widely available daily USGS discharge data, and are also the time step used by New York City Department of Environmental Protection (NYCDEP) reservoir water quality models. In this study turbidity measurements during storm events are defined in two time scales; daily (mean daily turbidity for the day that accounted for the greatest proportion of the load during an event) and events (based on the entire hydrograph) whose start times were determined graphically by rise in hydrograph above baseflow and end time determined by the inflection point in the falling limb of the hydrograph similar to the method used by Stuntebeck et al. (2008). Mean daily turbidity (MDT) and event mean turbidity (EMT) were calculated by summing the measurements of discharge and turbidity that were collected at 15 minute frequency intervals (Eqs. (2) and (3)).

$$\mathrm{MDT} = \frac{\sum_{i=1}^{96} [(\mathrm{NTU_i}) \times (\mathrm{Q_i})]}{\sum_{i=1}^{96} [(\mathrm{Q_i})]} \tag{2}$$

$$\mathrm{EMT} = \frac{\sum_{i=1}^{n} [(\mathrm{NTU_i}) \times (\mathrm{Q_i})]}{\sum_{i=1}^{n} [(\mathrm{Q_i})]} \tag{3}$$

where $\mathrm{NTU_i}$ is the instantaneous turbidity (NTU), $\mathrm{Q_i}$ is the instantaneous discharge ($\mathrm{m^3\ s^{-1}}$) and n is the number of 15 minute intervals during an event.

Please cite this article as: Mukundan, R., et al., Factors affecting storm event turbidity in a New York City water supply stream, Catena (2013), http://dx.doi.org/10.1016/j.catena.2013.02.002

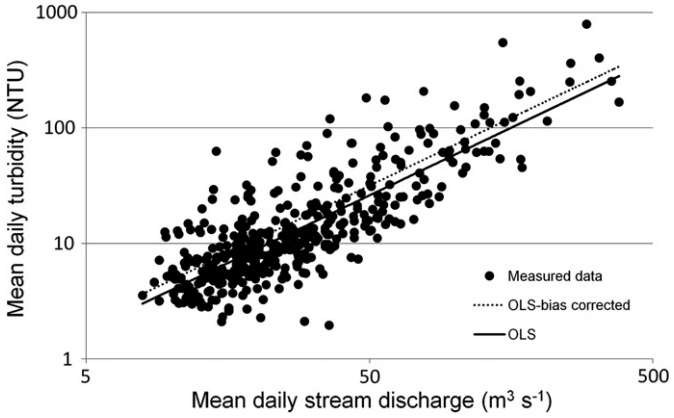

Fig. 2. Discharge–turbidity relations at Coldbrook outlet. OLS is ordinary least square.

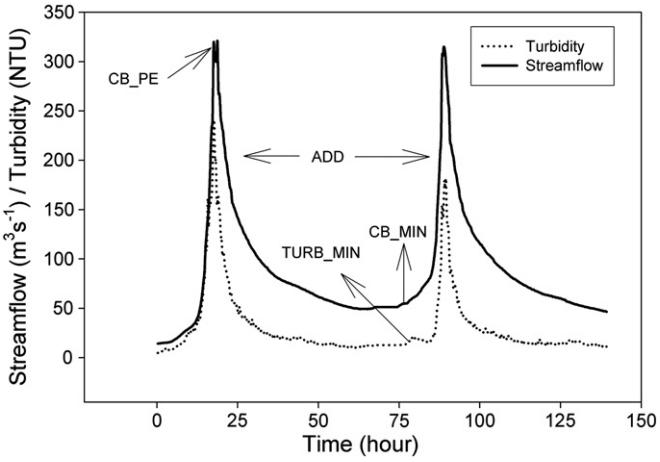

Fig. 3. Illustration of variables that may influence temporal variability in stream turbidity. Abbreviations used are explained in Table 1; ADD is antecedent dry days; CB_PE is mean daily flow during the previous event; CB_MIN is the flow at the onset of an event; TURB_MIN is the turbidity at the onset of an event.

Suspended sediment loads were calculated for 30 event days (where MDT could be calculated) and 27 events (where EMT could be calculated) between 11/19/2003 and 04/17/2011. Although many events were characterized at both time scales, some events were not captured over the entire hydrograph due to storm related damage and fouling of turbidity sensors.

2.3. Analysis of turbidity events

A description of the suite of variables used as possible predictors of mean daily turbidity (MDT) is presented in Table 1 and Fig. 3. In the absence of rain gauges, mean daily stream discharge at the tributaries (Fig. 1) was used to represent the spatial variability of rainfall and the contributions of water and sediment from different parts of the watershed, where differences in geologic sources of sediment, and the processes regulating stream channel erosion could occur. For each event day, the total stream discharge at the tributaries ($m^3\ d^{-1}$) was divided by the corresponding sub-basin area (m^2) to get the water yield for the day ($m\ d^{-1}$). Relative water yield (dimensionless) for a tributary was calculated by dividing the tributary water yield with the whole watershed water yield.

2.4. Principal component analysis (PCA)

Principal component analysis was used to determine the variability in the potential explanatory variables that may influence outlet turbidity. This method is widely used in multivariate statistical analysis of water quality data (Boyacioglu and Boyacioglu, 2008; Zeng and Rasmussen, 2005). Data for the variables listed in Table 1 and Fig. 3 were used in the analysis. Potential explanatory variables for MDT were grouped into two classes; variables that influence spatial variability in suspended sediment loads during individual events (Table 1 variables 1–7) and variables that may influence watershed-wide variability in suspended sediment loads between events (Table 1 variables 8–12 and Fig. 3). Separate PCA were performed on the correlation matrix of the two classes of variables with the JMP 7.0 software (SAS Institute, 2007).

2.5. Cluster analysis

Cluster analysis was performed on the same dataset used for PCA using the JMP 7.0 software (SAS Institute, 2007). Cluster analysis is another data reduction technique used to group entities with similar properties. The objective of cluster analysis is to identify complex multivariate relationships in the dataset under study and assist in the further development of hypothesis about the phenomenon (Zeng and Rasmussen, 2005). Several authors have used cluster analysis in studies on ground water (Colby, 1993) and surface water quality (Boyacioglu and Boyacioglu, 2008; Momen et al., 1999; Salmaso, 1996). Once the events were grouped into clusters, the predictor values associated with events falling within the different clusters were compared.

2.6. Development of regression equations

A step-wise regression approach was implemented on the potential predictor variables listed in Table 1 and Fig. 3 to determine the optimum combination of variables capable of predicting mean daily turbidity (MDT) during the 30 identified event days. Separate multiple regression models were developed with the two classes of predictors, and a seasonal term was included in the analysis (0 for May–October and 1 for November–April). This multivariate approach has been used to analyze variations in sediment yield (Restrepo et al.,

Table 1
Potential predictors of mean daily turbidity at the Esopus Creek watershed outlet.

No	Predictor	Indicator
1	Mean daily flow at USGS station (#01362500) near Coldbrook (CB)	Energy/stream power
2	Mean daily flow at USGS station (#01362465) at Beaverkill (BK) above Lake Hill	Precipitation, geologic sediment source, and sediment supply
3	Mean daily flow at USGS station (#01362497) near Little Beaverkill (LBK)	Precipitation, geologic sediment source, and sediment supply
4	Mean daily flow at USGS station (#01362370) near Stony Clove (SC)	Precipitation, geologic sediment source, and sediment supply
5	Mean daily flow at USGS station (#0136230002) near Woodland Creek (WC)	Precipitation, geologic sediment source, and sediment supply
6	Mean daily flow at USGS station (#013621955) near Birch Creek (BC)	Precipitation, geologic sediment source, and sediment supply
7	Mean daily flow at USGS station (#01362342) near Hollow tree brook (HB)	Precipitation, geologic sediment source, and sediment supply
8	Antecedent dry days (ADD)	Soil moisture condition/sediment supply
9	Mean daily flow at Coldbrook during the previous event (CB_PE)	Soil moisture condition and sediment supply in the watershed
10	Mean daily flow at Coldbrook at the onset of an event (CB_MIN)	Flow regime
11	Mean daily turbidity at Coldbrook at the onset of an event (TURB_MIN)	Sediment supply
12	Time of year (SEASON)	Seasonal effect on sediment supply

Please cite this article as: Mukundan, R., et al., Factors affecting storm event turbidity in a New York City water supply stream, Catena (2013), http://dx.doi.org/10.1016/j.catena.2013.02.002

2006; Tamene et al., 2006). A similar approach was used for predicting the event mean turbidity (EMT) for the 27 events.

2.7. Stream discharge-Tn rating curve

Stream discharge versus turbidity relations were developed using data from days when the flow diversion from the Schoharie Reservoir was less than 20% of the total Esopus Creek daily discharge. In all cases suspended sediment inputs to Esopus Creek from the Schoharie watershed were a very small component (<1%) of the event loads. Daily suspended sediment loads were estimated based on a relationship between discharge and *Tn* derived from 415 paired observations of mean daily discharge and mean daily turbidity (Eq. (4)). In the absence of automated *Tn* monitoring, a common approach to account for intra- and inter-storm variations in *Tn* (Crawford, 1991; Horowitz, 2003) expresses mean daily turbidity (NTU) as a function of discharge (Q).

$$\text{Log NTU} = 1.17\,\text{Log Q} - 0.575 \quad \left(r^2 = 0.66\right) \tag{4}$$

A rating curve in the form of an ordinary least square (OLS) regression (Eq. (4) and Fig. 2) on log-transformed mean daily stream discharge (Q, $m^3\ s^{-1}$) and log-transformed mean daily turbidity (NTU) was used. A bias correction factor (β) (Ferguson, 1986) estimated based on the variance in the regression equation in the form $\beta = \exp(2.65\ \sigma^2)$, was multiplied by the OLS estimated turbidity value to reduce the expected under prediction in suspended sediment loads due to retransformation bias.

3. Results and discussion

3.1. Hysteresis in discharge–turbidity relationship

Analysis of discharge–turbidity relations during each of the individual storm events shows a hysteretic behavior with the rising and falling limbs of the hydrograph transporting suspended sediment at different rates, and also showed that the pattern of hysteresis varied between events (Fig. 4). The most common type of hysteresis, the clockwise hysteresis was observed during most events, and is illustrated by an event in February, 2008 (Fig. 4a). Such phenomenon indicates that the rate of suspended sediment transport in the falling limb is lower than the rising limb due to sediment source depletion (Seeger et al., 2004; Steegen et al., 2000). An event in July 2004 (Fig. 4b) showed counter-clockwise hysteresis, which showed that the rate of suspended sediment transport is higher during the falling limb of the hydrograph, and that there is a time lag between the peaks of stream discharge and turbidity as a result of sediment sources being located far away from the watershed outlet, or new sediment sources becoming available as the event progressed (Seeger et al., 2004; Zabaleta et al., 2007). Events from March 2007 and June 2007 (Fig. 4c and d) illustrated more complex hysteresis due to the effects of sediment depletion, which can decrease turbidity when multiple and frequent storm events occur at relatively short time intervals (Doomen et al., 2008). The March 2007 storm event showed sediment depletion in the second storm whereas the June 2007 event showed sediment depletion in the third storm. During multiple storm events such as those illustrated by Fig. 4c and d, baseflow becomes an increasingly greater component of the later discharge peaks, and dilution by baseflow may influence the suspended sediment transported by a stream (Bača, 2008). Fig. 4a–d illustrates event to event variations of the relation between stream discharge and turbidity suggesting the uncertainty in stream discharge–turbidity relations that may arise due to the spatial location of sediment sources and the available sediment supply in the watershed during an event.

3.2. Principal component analysis

Principal component analysis using relative water yield (tributary water yield ($m\ d^{-1}$) divided by water yield ($m\ d^{-1}$) at the watershed outlet) as the independent variable indicates that patterns of regional runoff showed variability during the period of study (Table 2). Based on the principal component weights, three turbidity source regions were identified. PC1 is related to the region that includes the Beaverkill (BK) and the Little Beaverkill (LBK) sub-basins, PC2 is related to the region centered on the Woodland Creek (WC) sub-basin, and PC3 is related to the region near the Stony Clove (SC) sub-basin. The three principal components were able to explain 80% of the variability in relative amount of runoff. This spatial difference in the relative amount of runoff indicates spatial differences in turbidity sources and transport resulting from variation in stream discharge itself, and also since there are variations in glacial geology between regions.

Principal component analysis using variables related to records of stream discharge and turbidity measured at the watershed outlet was also used to gain insights into the relative importance of factors influencing the discharge turbidity relation (Table 3). The PC1 is related to the moisture condition of the watershed based on the high principal component weights for variables antecedent dry days (ADD) and mean daily flow during the previous event (CB_PE) in Table 1. The PC2 is related to sediment supply based on the high principal component weights for variable turbidity at the onset of an event (TURB_MIN) and seasonal effect (SEASON). The PC3 is related to the flow regime based on the high principal component weight for streamflow at the onset of an event (CB_MIN). The first three principal components were able to explain 82% of the variability in the data. Maximum variability was observed due to moisture condition followed by sediment supply and flow regime.

3.3. Cluster analysis

The 30 storm event days were grouped into 4 clusters based on the predictor variables in Table 4. Cluster 1 showed the lowest median turbidity value and cluster 2 showed the highest median turbidity value. The observed turbidity value for cluster 2 was expected since high stream discharge should generate high turbidity. The observed median turbidity value for cluster 1 is in contrast to the remaining clusters that showed higher turbidity values for a much lower stream discharge. For cluster 3 the high turbidity levels may be due to the high median value for the variable antecedent dry days (ADD) suggesting that the replenishment and availability of turbidity sources were of importance, since an increase in low stream discharge days between events can result in accumulation of sediment in the stream channels as discussed in Doomen et al. (2008). For cluster 4 the relatively high turbidity levels may be due to the high median value for the variable representing minimum turbidity at the onset of an event (TURB_MIN), suggesting that the relative contribution of turbidity sources at the onset of an event (background turbidity) impacts the turbidity during the event. These findings are consistent with observations of high suspended sediment concentrations under low runoff made in other studies (Giménez et al., 2012; Mateos and Giráldez, 2005; Nadal-Romero et al., 2008). High stream turbidity at the onset of a storm event is an indication of increased sediment mobilization within the channel and therefore its availability for transport.

3.4. Step-wise multiple regression

Use of additional variables identified in the analyses above improved the explanatory power of the stream discharge-based turbidity model. The average daily stream discharge, Q_D, ($m^3\ s^{-1}$) alone as a predictor could explain only 39% of the variance in mean daily turbidity (MDT) prediction for the 30 event days (Eq. (5)). A multiple regression model (Eq. (6)) that included the variable seasonal effect

Please cite this article as: Mukundan, R., et al., Factors affecting storm event turbidity in a New York City water supply stream, Catena (2013), http://dx.doi.org/10.1016/j.catena.2013.02.002

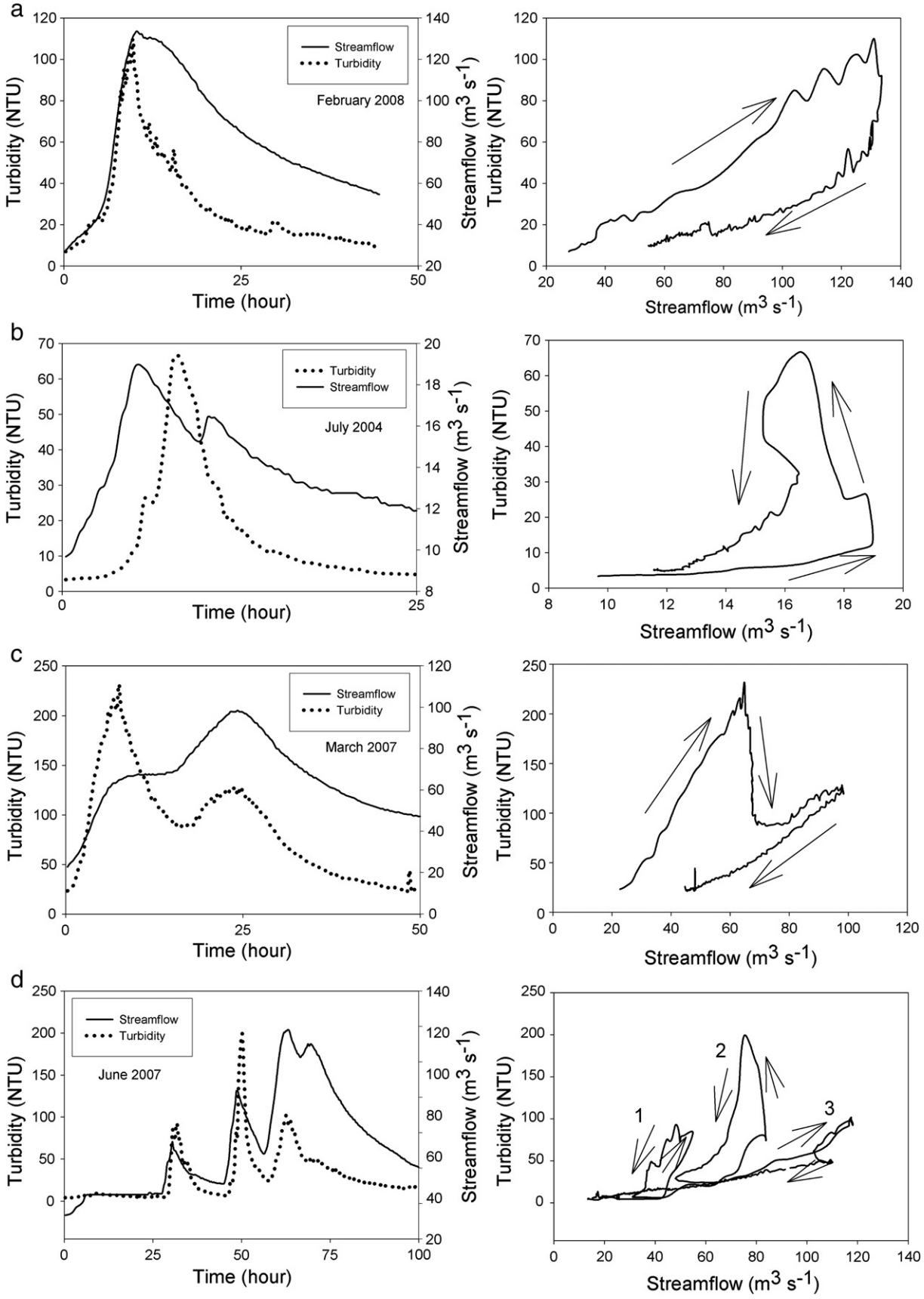

Fig. 4. Hysteresis in discharge–turbidity relations. Figures on the left have time on horizontal axis with each unit equal to a 15-min interval.

Table 2
Principal component weights, eigenvalues and variance explained using relative water yields at the tributaries (water yield at the tributaries divided by the total water flow into the Reservoir). See Fig. 1 and Table 1 for tributary location and gauging station number. Bold values indicate strong linear correlation.

Tributary	PC1	PC2	PC3
Beaverkill (BK)	**0.90**	−0.03	0.21
Little Beaverkill (LBK)	**0.94**	0.07	0.09
Stony Clove (SC)	0.22	0.09	**0.91**
Birch Creek (BC)	−0.02	**−0.79**	0.14
Woodland Creek (WC)	0.07	**0.84**	0.19
Hollow tree brook (HTB)	−0.63	−0.27	**0.53**
Eigenvalue	2.3	1.3	1.2
Variance explained (%)	38.0	22.0	20.0

(SEASON) and antecedent dry days (ADD) in addition to stream discharge could explain 67% of the variance in mean daily turbidity prediction.

$$\mathrm{Log(MDT)} = 1.26\ \mathrm{Log(Q_D)} - 0.694\ \left(r^2 = 0.39, P<0.0001\right) \quad (5)$$

$$\mathrm{Log(MDT)} = 1.43\ \mathrm{Log(Q_D)} - 0.272\ \mathrm{SEASON} + 0.0029\ \mathrm{ADD} - 1.06\ \left(r^2 = 0.67, P<0.0001\right) \quad (6)$$

$$\mathrm{Log(MDT)} = 1.33\ \mathrm{Log(Q_D)} - 0.46\ \mathrm{SCr} - 0.61\ \mathrm{BCr} + 0.045\ \left(r^2 = 0.65, P<0.0001\right) \quad (7)$$

A second regression model (Eq. (7)) that included relative water yield from the tributaries (SCr and BCr representing Stony Clove and Birch Creek) with respect to the watershed outlet could explain 65% of the variance in turbidity prediction. The two tributaries used in the regression model showed marked differences in relative water yield (tributary water yield divided by the water yield at the watershed outlet) with Stony Clove (SC) sub-basin generating a relatively high proportion of the total runoff compared to the Birch Creek (BC) sub-basin (Fig. 5). Such differences suggest that variations in the hydrologic pathways/response from the two sub-basins that can affect the amount of generated sediment.

In comparison to turbidity predictions based on stream discharge alone, multiple regression models were able to better capture the variability in stream discharge–turbidity relations within a given range of flow. This analysis illustrates the multiple factors that may influence stream turbidity, which make predictions using a single explanatory variable inaccurate. Our findings are in line with those reported in the literature that concluded that sediment yield from a watershed can be influenced by a number of factors in addition to stream discharge such as season (Casalí et al., 2010; Steegen et al., 2000), antecedent soil conditions (Giménez et al., 2012; Seeger et al., 2004) and rainfall characteristics (Nadal-Romero et al., 2008).

While the above analyses explains the importance of multiple factors that may influence daily stream turbidity, event to event variability in total event suspended sediment load is important in the Esopus Creek watershed, as the magnitude of suspended sediment loading can impact reservoir operations. We predicted the event mean turbidity (EMT) for 27 events using multiple regressions and compared the results with the measured EMT (Fig. 6). A predictive relationship of EMT based on event mean stream discharge (Q_E, derived from 15-min data) alone led to a strong predictive relationship ($r^2 = 0.81$), but also a 10% underestimation of the cumulative measured event mean suspended sediment load calculated as the product of EMT and event mean stream discharge. Using the same relationship, the deviation in predicted event mean suspended sediment loads ranged from −71% to 166% when compared to the measured loads (Table 5). Inclusion of the variable antecedent dry days (ADD) improved the regression equation ($r^2 = 0.89$), reducing the cumulative underestimation to 7%, and also reducing the uncertainty in predicted event mean suspended sediment loads to −48% to 104%. Other variables that were significant at the daily scale did not improve the regression model at the event scale.

$$\mathrm{Log(EMT)} = 1.67\ \mathrm{Log(Q_E)} - 1.43\ \left(r^2 = 0.81, P<0.0001\right) \quad (8)$$

$$\mathrm{Log(EMT)} = 1.84\ \mathrm{Log(Q_E)} + 0.0051\ \mathrm{ADD} - 1.92\ \left(r^2 = 0.89, P<0.0001\right) \quad (9)$$

Table 3
Principal component weights, eigenvalues and variance explained using variables influencing turbidity at the watershed outlet. See Table 1 for variable explanation. Bold values indicate strong linear correlation.

Variable (Range)	PC1	PC2	PC3
CB_MIN (8–57)	0.01	−0.02	**0.96**
TURB_MIN (3–65)	−0.08	**0.86**	−0.04
CB_PE (36–492)	**0.86**	0.22	0.29
ADD (1–180)	**0.81**	−0.12	−0.45
SEASON (0 or 1)	−0.19	**−0.80**	−0.05
Eigenvalue	1.44	1.43	1.22
Variance explained (%)	28.8	28.7	24.4

Table 4
Summary of cluster analysis using predictor variables of mean daily turbidity values (n = 30).

	Variables (median values)				
	Description	Turbidity (NTU)	FLOW ($m^3\ s^{-1}$)	ADD (days)	TURB_MIN (NTU)
Cluster 1 (n = 12)	High flow low turbidity	119	152	13	8
Cluster 2 (n = 6)	High flow high turbidity	309	274	2	14
Cluster 3 (n = 6)	Low flow high turbidity	134	76	108	10
Cluster 4 (n = 6)	Low flow high turbidity	135	102	3	61

3.5. Comparison of rating curve estimates with automated monitoring

The OLS regression (Eq. (4)) rating curve underestimated the total measured suspended sediment loads by 30% for the study period. This underestimation was not surprising and is consistent with other studies (Asselman, 2000; Horowitz et al., 2001; Skarbøvik et al., 2012). Use of a

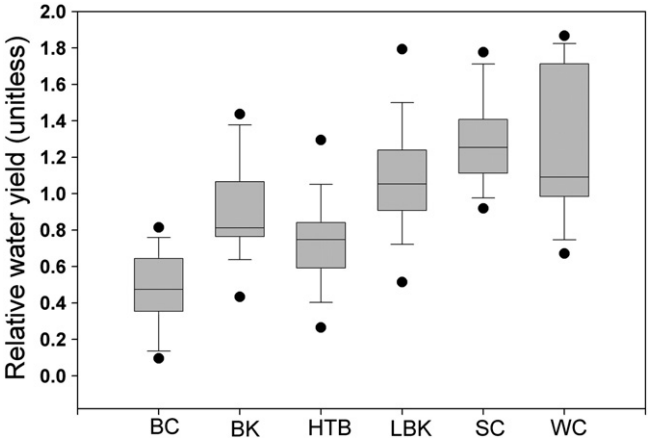

Fig. 5. Boxplot showing relative water yields from tributaries (water yield from tributaries divided by total water yield to the Reservoir) during event days (n = 30). Range of values includes 5th to 95th percentiles. See Fig. 1 and Table 1 for abbreviations used.

Please cite this article as: Mukundan, R., et al., Factors affecting storm event turbidity in a New York City water supply stream, Catena (2013), http://dx.doi.org/10.1016/j.catena.2013.02.002

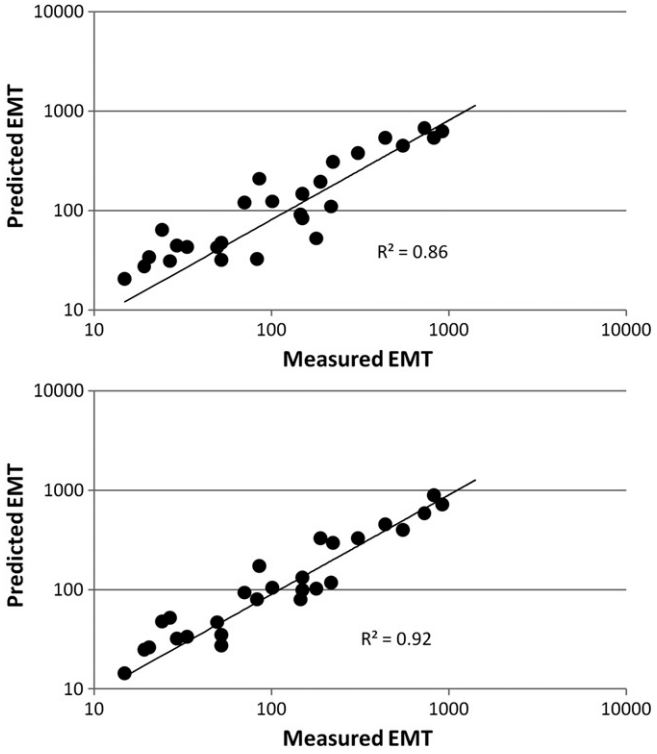

Fig. 6. Predicted vs measured event mean turbidity (EMT) using Eq. (8) (top) and Eq. (9) (bottom).

retransformation bias correction factor ($\beta = 1.22$) reduced the under prediction to 16%. Most of the underprediction was due to the two data points that had the highest turbidity values whose corresponding stream discharge values were not the highest. Without those two points the bias corrected rating curve was able to predict the actual total load with high accuracy whereas the OLS regression rating curve underestimated the measured load by 18%. A suspended sediment load duration curve derived from rating curve (Eq. (4)) estimate of daily turbidity showed that as much as 80% of the total suspended sediment load during the 8 year study period was transported in a short period of the total time (4%) when the stream discharge was $>100\ m^3\ s^{-1}$. Therefore, accurate turbidity estimation at high stream discharges is critical as high levels of turbidity inputs lead to water quality problems. Automated turbidity monitoring clearly provides a better estimate of the turbidity inputs to the reservoir under periods of high discharge. This is illustrated by the hysteresis curves (Fig. 4) based on high frequency monitoring data that shows wide variability in stream discharge–turbidity relation.

4. Conclusions

A multivariate analysis was used to identify the factors causing variability in stream discharge–turbidity relation in the Esopus Creek watershed in New York State. Analyses using high frequency turbidity monitoring data show that this relation can be influenced by watershed, as well as event characteristics related to sediment supply and transport. This was illustrated by multiple regression equations that showed improved predictions when using variables in addition to only stream discharge. In the study watershed these variables relate to spatial variability in runoff and thus sediment sources, antecedent conditions, and season. These additional variables, to a certain extent, explain the episodic nature of erosion and its variability in space and time which makes prediction using a single explanatory variable inaccurate. The study also highlights the importance of collecting high-frequency spatially-distributed precipitation (we used tributary stream discharge data in the absence of rain gauges), stream discharge, and water quality data for quantifying pollutant loads and for distributed watershed modeling for water quality. Results from this study may also be applicable in other watersheds where stream turbidity problems exist.

Table 5
Predicted vs measured event mean suspended sediment loads for the 27 events and percent deviation from measured loads.

Event #	Date	Event mean discharge ($m^3\ s^{-1}$)	Event mean turbidity (NTU)	Suspended sediment load ($NTU \cdot m^3\ s^{-1}$)	Suspended sediment load ($NTU \cdot m^3\ s^{-1}$)	Suspended sediment load	Suspended sediment load ($NTU \cdot m^3\ s^{-1}$)	Suspended sediment load
		Measured	Measured	Measured	Eq. (8)	Eq. (8) % deviation	Eq. (9)	Eq. (9) % deviation
1	11/19/2003	106	145	15,354	9662	−37.1	8416	−45.2
2	9/17/2004	248	306	76,018	94,280	24.0	81,888	7.7
3	11/28/2004	167	188	31,369	32,495	3.6	54,801	74.7
4	4/22/2006	76	178	13,564	3989	−70.6	7762	−42.8
5	5/12/2006	141	149	21,085	20,913	−0.8	18,647	−11.6
6	2/4/2006	67	33	2252	2888	28.3	2258	0.3
7	6/28/2006	307	436	133,668	165,534	23.8	138,644	3.7
8	10/19/2006	52	19	988	1418	43.6	1281	29.7
9	10/28/2006	174	85	14,792	36,308	145.5	30,116	103.6
10	11/8/2006	86	24	2067	5491	165.7	4110	98.9
11	11/16/2006	125	70	8758	15,007	71.4	11,661	33.2
12	3/14/2007	57	82	4705	1853	−60.6	4561	−3.1
13	3/27/2007	72	52	3722	3407	−8.5	2507	−32.7
14	4/15/2007	220	222	48,685	67,907	39.5	65,026	33.6
15	6/2/2007	67	49	3325	2883	−13.3	3167	−4.7
16	11/15/2007	59	20	1193	1983	66.3	1533	28.6
17	1/7/2008	43	15	643	887	38.0	623	−3.1
18	2/5/2008	57	52	2935	1804	−38.5	1541	−47.5
19	2/18/2008	69	29	2013	3081	53.1	2227	10.6
20	3/4/2008	127	101	12,800	15,721	22.8	13,300	3.9
21	3/9/2009	56	27	1482	1724	16.3	2902	95.8
22	1/25/2010	334	912	304,759	208,542	−31.6	240,371	−21.1
23	3/14/2010	101	149	14,958	8393	−43.9	9953	−33.5
24	3/26/2010	275	549	151,123	124,129	−17.9	109,625	−27.5
25	12/1/2010	306	819	250,572	164,906	−34.2	272,866	8.9
26	3/11/2011	350	725	253,790	236,122	−7.0	204,453	−19.4
27	4/17/2011	118	216	25,576	13,009	−49.1	13,923	−45.6

Please cite this article as: Mukundan, R., et al., Factors affecting storm event turbidity in a New York City water supply stream, Catena (2013), http://dx.doi.org/10.1016/j.catena.2013.02.002

Acknowledgments

We thank Dr. Allan Frei (Institute for Sustainable Cities, City University of New York) and David Lounsbury (GIS-specialist, NYCDEP) for their support in this project.

Appendix A. Supplementary data

Supplementary data to this article can be found online at http://dx.doi.org/10.1016/j.catena.2013.02.002.

References

Asselman, N.E.M., 1999. Suspended sediment dynamics in a large drainage basin: the River Rhine. Hydrological Processes 13, 1437–1450.
Asselman, N., 2000. Fitting and interpretation of sediment rating curves. Journal of Hydrology 234, 228–248.
Bača, P., 2008. Hysteresis effect in suspended sediment concentration in the Rybárik basin, Slovakia. Hydrological Sciences Journal 53, 224–235.
Boyacioglu, H., Boyacioglu, H., 2008. Water pollution sources assessment by multivariate statistical methods in the Tahtali Basin, Turkey. Environmental Geology 54, 275–282.
Casalí, J., Giménez, R., Díez, J., Álvarez-Mozos, J., Valle, Del, de Lersundi, J., Goñi, M., Campo, M., Chahor, Y., Gastesi, R., López, J., 2010. Sediment production and water quality of watersheds with contrasting land use in Navarre (Spain). Agricultural Water Management 97, 1683–1694.
Cohn, T., 1995. Recent advances in statistical methods for the estimation of sediment and nutrient transport in rivers. Reviews of Geophysics 33, 1117–1124.
Colby, B.R., 1956. The relationship of sediment discharge to streamflow. U. S. Geological Survey Open File Report, Reston, VA.
Colby, N., 1993. The use of 2-way cluster analysis as a tool for delineating trends in hydrogeologic units and development of a conceptual model. International Ground Water Modeling Center (IGWMC), Proceedings of the 1993 Ground Water Modeling Conference, pp. 91–100.
Crawford, C.G., 1991. Estimation of suspended-sediment rating curves and mean suspended-sediment loads. Journal of Hydrology 129, 331–348.
Davies-Colley, R.J., Vant, W.N., Smith, D.G., 2003. Colour and Clarity of Natural Waters: Science and Management of Optical Water Quality. The Blackburn Press, Caldwell, NJ.
Doomen, A., Wijma, E., Zwolsman, J.J.G., Middelkoop, H., 2008. Predicting suspended sediment concentrations in the Meuse River using a supply-based rating curve. Hydrological Processes 22, 1846–1856.
Effler, S., Perkins, M., Ohrazda, N., Brooks, C., Wagner, B., Johnson, D., Peng, F., Bennett, A., 1998. Turbidity and particle signatures imparted by runoff events in Ashokan Reservoir, NY. Lake and Reservoir Management 14, 254–265.
Ferguson, R., 1986. River loads underestimated by rating curves. Water Resources Research 22, 74–76.
Gelda, R.K., Effler, S.W., 2007. Modeling turbidity in a water supply reservoir: advancements and issues. Journal of Environmental Engineering 133, 139–148.
Gelda, R.K., Effler, S.W., Peng, F., Owens, E.M., Pierson, D.C., 2009. Turbidity model for Ashokan Reservoir, New York: case study. Journal of Environmental Engineering 135, 885–895.
Giménez, R., Casalí, J., Grande, I., Díez, J., Campo, M., Álvarez-Mozos, J., Goñi, M., 2012. Factors controlling sediment export in a small agricultural watershed in Navarre (Spain). Agricultural Water Management 110, 1–8.
Hicks, D.M., Hill, J., Shankar, U., 1996. Variation of Suspended Sediment Yields Around New Zealand: The Relative Importance of Rainfall and Geology. IAHS Publication, pp. 149–156.
Horowitz, A.J., 2003. An evaluation of sediment rating curves for estimating suspended sediment concentrations for subsequent flux calculations. Hydrological Processes 17, 3387–3409.
Horowitz, A.J., Elrick, K.A., Smith, J.J., 2001. Estimating suspended sediment and trace element fluxes in large river basins: methodological considerations as applied to the NASQAN programme. Hydrological Processes 15, 1107–1132.
Jastram, J.D., Zipper, C.E., Zelazny, L.W., Hyer, K.E., 2010. Increasing precision of turbidity-based suspended sediment concentration and load estimates. Journal of Environmental Quality 39, 1306–1316.
Larsen, M., Gellis, A., Glysson, G., Gray, J., Horowitz, A., 2010. Fluvial sediment in the environment: a national problem. Proceedings, 2nd Joint Federal Interagency Conference, Las Vegas, Nevada, June (http://kleene.er.usgs.gov/sdct/images/9/90/Larsen.et.al.Sediment.FISC.2010.pdf, accessed August 11, 2012, 15 pp.).
Lenzi, M.A., Marchi, L., 2000. Suspended sediment load during floods in a small stream of the Dolomites (northeastern Italy). Catena 39, 267–282.
Mateos, L., Giráldez, J.V., 2005. Suspended load and bed load in irrigation furrows. Catena 64, 232–246.
Momen, B., Zehr, J.P., Boylen, C.W., Sutherland, J.W., 1999. Determinants of summer nitrate concentration in a set of Adirondack lakes, New York. Water, Air, and Soil Pollution 111, 19–28.
Nadal-Romero, E., Regüés, D., Latron, J., 2008. Relationships among rainfall, runoff, and suspended sediment in a small catchment with badlands. Catena 74, 127–136.
Nagle, G.N., Fahey, T.J., Ritchie, J.C., Woodbury, P.B., 2007. Variations in sediment sources and yields in the Finger Lakes and Catskills regions of New York. Hydrological Processes 21, 828–838.
Nash, D.B., 1994. Effective sediment-transporting discharge from magnitude–frequency analysis. Journal of Geology 79–95.
O'Donnell, D.M., Effler, S.W., 2006. Resolution of impacts of runoff events on a water supply reservoir with a robotic monitoring network. Journal of the American Water Resources Association 42, 323–335.
Osterkamp, W., 2004. An invitation to participate in a North American sediment-monitoring network. EOS. Transactions of the American Geophysical Union 85, 386.
Peng, F., Effler, S.W., Pierson, D.C., Smith, D.G., 2009. Light-scattering features of turbidity-causing particles in interconnected reservoir basins and a connecting stream. Water Research 43, 2280–2292.
Pierson, D., Gelda, R., Effler, S., O'Donnell, D., Prestigiacomo, A., 2008. Use of automated monitoring to estimate the load of turbidity entering a drinking water reservoir. Verhandlungen der Internationalen Vereinigung für Theoretische und Angewandte Limnologie 30, 113.
Pimentel, D., Harvey, C., Resosudarmo, P., Sinclair, K., Kurz, D., McNair, M., Crist, S., Shpritz, L., Fitton, L., Saffouri, R., 1995. Environmental and economic costs of soil erosion and conservation benefits. Science 1117–1123.
Restrepo, J.D., Kjerfve, B., Hermelin, M., Restrepo, J.C., 2006. Factors controlling sediment yield in a major South American drainage basin: the Magdalena River, Colombia. Journal of Hydrology 316, 213–232.
Salmaso, N., 1996. Seasonal variation in the composition and rate of change of the phytoplankton community in a deep subalpine lake (Lake Garda, Northern Italy). An application of nonmetric multidimensional scaling and cluster analysis. Hydrobiologia 337, 49–68.
SAS Institute, 2007. JMP 7 User Guide. SAS Publishing.
Seeger, M., Errea, M.P., Begueria, S., Arnáez, J., Mart, C., Garcıa-Ruiz, J.M., 2004. Catchment soil moisture and rainfall characteristics as determinant factors for discharge/suspended sediment hysteretic loops in a small headwater catchment in the Spanish Pyrenees. Journal of Hydrology 288, 299–311.
Skarbøvik, E., Stålnacke, P., Bogen, J., Bønsnes, T.E., 2012. Impact of sampling frequency on mean concentrations and estimated loads of suspended sediment in a Norwegian river: implications for water management. The Science of the Total Environment 433, 462–471.
Steegen, A., Govers, G., Nachtergaele, J., Takken, I., Beuselinck, L., Poesen, J., 2000. Sediment export by water from an agricultural catchment in the Loam Belt of central Belgium. Geomorphology 33, 25–36.
Stubblefield, A.P., Reuter, J.E., Dahlgren, R.A., Goldman, C.R., 2007. Use of turbidometry to characterize suspended sediment and phosphorus fluxes in the Lake Tahoe basin, California, USA. Hydrological Processes 21, 281–291.
Stuntebeck, T.D., Komiskey, M.J., Owens, D.W., Hall, D.W., 2008. Methods of Data Collection, Sample Processing, and Data Analysis for Edge-of-field, Streamgaging, Subsurface-tile, and Meteorological Stations at Discovery Farms and Pioneer Farm in Wisconsin, 2001–7. US Department of the Interior, US Geological Survey.
Syvitski, J.P., Morehead, M.D., Bahr, D.B., Mulder, T., 2000. Estimating fluvial sediment transport: the rating parameters. Water Resources Research 36, 2747–2760.
Tamene, L., Park, S., Dikau, R., Vlek, P., 2006. Analysis of factors determining sediment yield variability in the highlands of northern Ethiopia. Geomorphology 76, 76–91.
Thomas, R.B., 1988. Monitoring baseline suspended sediment in forested basins: the effects of sampling on suspended sediment rating curves. Hydrological Sciences Journal 33, 499–514.
USEPA, 2009. National water quality inventory report to Congress. Available at http://www.epa.gov/305b/ (verified 23 Sep. 2010).
Walling, D., 1974. Suspended sediment and solute yields from a small catchment prior to urbanization. Fluvial Processes in Instrumented Watersheds 6, 169–192.
Walling, D., 1977. Assessing the accuracy of suspended sediment rating curves for a small basin. Water Resources Research 13, 531–538.
Walling, D.E., 2009. The impact of global change on erosion and sediment transport by rivers: current progress and future challenges. UNESCO-IHP. The United Nations World Water Development Report 3. (URL: http://unesdoc.unesco.org/images/0018/001850/185078e.pdf . Accessed September 23, 2010).
Walling, D., Webb, B., 1988. The reliability of rating curve estimates of suspended sediment yield: some further comments. Sediment Budgets. IAHS Publication.
Wolman, M.G., Miller, J.P., 1960. Magnitude and frequency of forces in geomorphic processes. Journal of Geology 54–74.
Zabaleta, A., Martínez, M., Uriarte, J.A., Antigüedad, I., 2007. Factors controlling suspended sediment yield during runoff events in small headwater catchments of the Basque Country. Catena 71, 179–190.
Zeng, X., Rasmussen, T.C., 2005. Multivariate statistical characterization of water quality in Lake Lanier, Georgia, USA. Journal of Environmental Quality 34, 1980–1991.

Please cite this article as: Mukundan, R., et al., Factors affecting storm event turbidity in a New York City water supply stream, Catena (2013), http://dx.doi.org/10.1016/j.catena.2013.02.002

HYDROLOGICAL PROCESSES
Hydrol. Process. (2013)
Published online in Wiley Online Library
(wileyonlinelibrary.com) DOI: 10.1002/hyp.9824

Effect of projected changes in winter streamflow on stream turbidity, Esopus Creek watershed in New York, USA

Rajith Mukundan,[1]* Donald C. Pierson,[2] Lucien Wang,[3] Adao H. Matonse,[1] Nihar R. Samal,[1] Mark S. Zion[2] and Elliot M. Schneiderman[2]

[1] *Institute for Sustainable Cities, City University of New York, New York, NY, 10065, USA*
[2] *New York City Department of Environmental Protection, Kingston, NY, 12401, USA*
[3] *Hazen and Sawyer, P.C., , New York, NY, 10018, USA*

Abstract:

This study focuses on the impact of changes in winter streamflow on in-stream turbidity in the Esopus Creek watershed, one of the New York City water supply watersheds. Projected changes in daily precipitation and air temperature from a suite of five global climate models and three emission scenarios for future periods 2046–2065 and 2081–2100 were downscaled for the study region. The simulated climate scenarios were used to project future streamflows using the Generalized Watershed Loading Functions – Variable Source Area watershed model. Seasonal turbidity rating curves based on measured historical streamflow and stream turbidity were used in combination with the simulated streamflow for generating future stream turbidity scenarios. Results indicate an increase in future ambient stream turbidity from November to March and a decrease during April. These results are the effects of increased winter rainfall, reduced snowfall, and a shift to early timing of spring snowmelt runoff, causing an increase in streamflow during early winter. It also suggests a reduction in the traditional peak streamflow around April that is expected to occur in this region. As a result, our models simulate a consistent increase in the low to medium percentile range of turbidity values associated with low to medium range of streamflows and no apparent change in high-percentile turbidity values associated with high streamflows. Our results may be applicable in regions where snowmelt runoff is an important process and turbidity caused by the suspension of fine clay particles is a water quality concern. Copyright © 2013 John Wiley & Sons, Ltd.

KEY WORDS climate change; snowmelt runoff; turbidity load; time series model; autocorrelation; rating curves

Received 21 August 2012; Accepted 8 March 2013

INTRODUCTION

High suspended sediment loads and the resulting turbidity can impact the sustained use of rivers for water supply and other designated uses. Changes in stream turbidity can be an indication of changes in material fluxes, aquatic geochemistry, water quality, channel morphology, and aquatic habitats (Walling, 2009). Snowmelt runoff is an important component of the hydrologic cycle in many places, and changes in the timing and extent of snowmelt can alter the quantity and quality of seasonal distribution of the streamflow captured for water supply (Marshall and Randhir, 2008) and also influence seasonal variations in landscape and channel erosion. McDonald and Lamoureux (2009) found non-linear increase in sediment yield with increasing snowpack in the Canadian High Arctic due to channel erosion caused by discharge from melting snowpack. Evrard *et al*. (2011), based on a study in south-eastern France, found a decrease in sediment yield in the presence of deep snow cover that protected the soil against erosion. Riverson *et al*. (2013) discuss the impact of projected climate change on the spatial distribution of snowpack development and its impact on water quality including sediment in the Sierra Nevada, USA.

Understanding the processes and quantifying stream turbidity under present and future conditions will be valuable for watershed-scale management of stream turbidity and maintaining high water quality. In particular, the regional impacts of future climate variability and its seasonal effects on sediment transport need further attention. Regional variations in the direction and magnitude of hydroclimatic signal especially snow processes have been observed (Stewart, 2009); however, very few studies have reported on the potential impact of climate change on sediment loads of streams and rivers (Intergovernmental Panel on Climate Change (IPCC), 2007).

The New York City (NYC) water supply is currently the largest unfiltered water supply in the USA, operating under a renewable filtration avoidance determination granted by the New York State Department of Health and the US

*Correspondence to: Rajith Mukundan, City University of New York, New York, NY 10065, USA.
E-mail: Rajith.Mukundan@hunter.cuny.edu

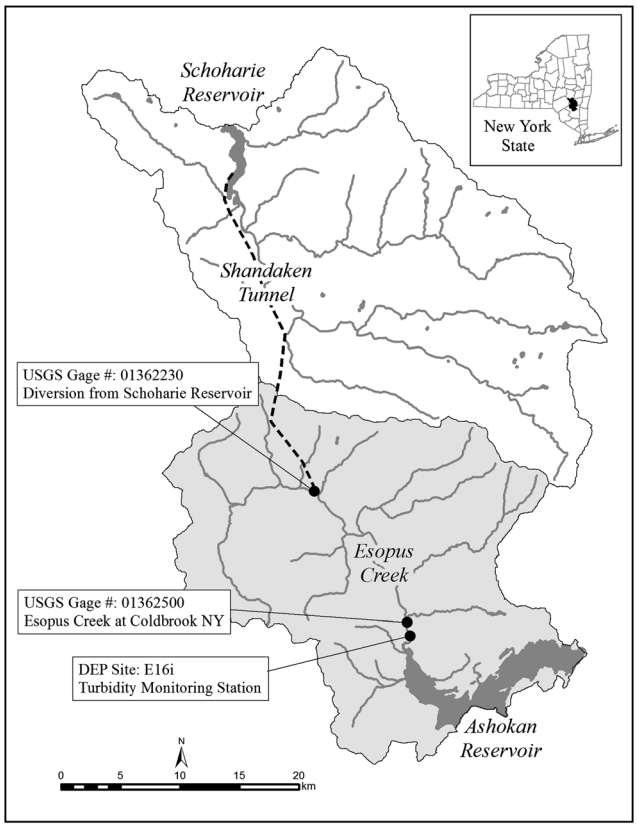

Figure 1. The Esopus Creek watershed, New York, showing the location of the Coldbrook sampling area and the diversion tunnel from the adjacent Schoharie Reservoir

Environmental Protection Agency. Historically, Catskill Mountain streams provide approximately 90% of the municipal water supply for about 9 million residents of NYC and upstate communities through a network of six reservoirs draining approximately 3885 km^2. The Upper Esopus Creek that drains into the Ashokan Reservoir along with water diverted from the nearby Schoharie Reservoir (via the Shandaken Tunnel) provides approximately 40% of this unfiltered drinking water supply (Figure 1).The water quality is typically high in the Catskill streams. However, high-magnitude runoff events can cause significant increases in stream and reservoir turbidity, which at times limits the use of this unfiltered drinking water supply (Effler *et al.*, 1998; Gelda *et al.*, 2009). For example, late in the winter of 2010, a large snowstorm in early March created an unusually large snowpack, with a March 1 volume of snowpack snow water equivalent (SWE) for the Esopus Creek watershed of approximately 110 million m^3 compared to a historical average of about 40 million m^3. During March, a series of rain and snowmelt events occurred, and measured in-stream turbidity in the Esopus Creek went as high as 1000 nephelometric turbidity units (NTU).

The Catskills have typical geology of a glaciated landscape where the glacial till tends to be enriched with clay and silt from the eroded bedrock. As glacial ice-melted, fine sediment was entrained in melt water that discharged into lakes impounded by the ice, recessional moraines, and mountain topography. The sediment deposited in these *pro-glacial* lakes is lacustrine sediment. The silt and clay in these Pleistocene deposits are the principal geologic sources of turbidity in Catskill Mountain streams. Eroding glacial deposits dominate sediment loads in many watersheds in the Catskills (Nagle *et al.*, 2007).

An examination of historical data for the Catskill region has shown an increasing trend in mean annual precipitation (8–26 cm/50 years) and streamflow over the past 50 years (Burns *et al.*, 2007). With increased annual precipitation and streamflows, one would expect a corresponding increase in stream turbidity. However, the generation and transport of high turbidity in the Esopus Creek watershed are not easily defined by changes in annual meteorological forcing, but rather, the stream turbidity is controlled more by the magnitude and seasonal timing of individual events. Major climate change impacts identified and predicted for this region include reduced snowfall and an earlier timing of snowmelt-driven runoff due to mean annual air temperature increasing at the rate of 0.5–2.0 °C over a 50-year period (Burns *et al.*, 2007). Ongoing research efforts on climate change impact on water resources in NYC watersheds include selecting global climate models (GCMs) reasonable for the region, detecting changes in seasonal streamflow, and predicting future changes in water supply and water quality (Anandhi *et al.*, 2011; Matonse *et al.*, 2011; Zion *et al.*, 2011; Mukundan *et al.*, 2013a). The potential impact of changes in winter stream event timing and magnitude due to climate change on stream turbidity in the region is not well understood. This analysis is particularly important because there are differences in sources of turbidity due to land use and geology between the NYC water supply watersheds. In this study, we performed a sensitivity analysis of stream turbidity to ongoing and anticipated changes in the seasonality of streamflow, with a focus on the winter period, using data from the Esopus Creek watershed. Stream channel processes are a major contributor of stream turbidity in this watershed (DEP, 2008). The long-term (1931–2010) record of measured streamflow data from the US Geological Survey (USGS) gauge (#1362500) at Coldbrook, where the Esopus Creek enters the Ashokan Reservoir, shows that the majority of bankfull discharge events with a 1.5-year return interval occur during the period from the beginning of November to the end of April. Snowfall, snowpack, rain, and snowmelt play an important role in the frequency and magnitude of bankfull stream discharges during the winter period. Therefore, it is important to have a better understanding of potential changes in stream turbidity during this period, when major changes in streamflows are observed and predicted due to changes in timing of snowmelt runoff.

METHODS

Turbidity monitoring in the Esopus Creek watershed

The Esopus Creek watershed drains an area of 493 km^2 and is dominated by forests, which occupy more than 90% of the watershed area. The elevation of the watershed ranges from about 194 m near the watershed outlet at Coldbrook to 1275 m at the headwaters. An automated turbidity monitoring system was installed on the main tributary entering the Ashokan Reservoir near the confluence of the creek and the reservoir (Figure 1). Water was pumped into a riverside hut where measurements of turbidity, specific conductivity, and water temperature were made using a YSI water quality sonde. Water samples were also periodically collected and analysed for turbidity (*Tn*, NTU) and total suspended solids in the laboratory. These data were then used to correct the automated data to account for any drift in the turbidity measurements. Just upstream of the turbidity monitoring station, a USGS gauging station provides streamflow data at daily and 15-min intervals. Since 2003, turbidity measurements were made at intervals between 15 min and 1 h. Sub-daily observations were flow-weighted to provide daily average values, which are comparable in frequency to the most widely available daily USGS streamflow data, and are at the time step used by NYC Department of Environmental Protection (NYCDEP) reservoir water quality models (e.g., see Samal *et al.*, 2013).

Time series model of average daily turbidity

Although continuous turbidity measurements were made for most periods between June 2003 and August 2011, there were periods where turbidity measurements could not be made due to storm-related damage and fouling of turbidity sensors. Therefore, turbidity values for missing days were estimated using a time series model, which was used because ordinary least square regression models on time series data often show highly correlated residuals, particularly for daily time series data (Richards *et al.*, 2008; Walker *et al.*, 2009). Because the ordinary regression residuals are not independent for time series data, they contain information that can be used to improve the prediction of future values (Reed *et al.*, 2008). More importantly, addressing autocorrelation can avoid incorrect conclusions on significance of parameters, confidence limits for predicted values, and estimates of regression coefficients. The AUTOREG procedure in SAS statistical software was used to fit a linear regression with autoregressive errors. Three predictor variables were used for the linear regression; streamflow at the Coldbrook gauge, daily point source turbidity measurements from the Shandaken Tunnel (Figure 1), and hysteresis effects in streamflow–turbidity relation. The hysteresis effect on stream turbidity was derived using the method proposed by Hirsch (1988). Our previous analysis has shown that for a given value of streamflow, the rising limb of streamflow hydrograph contributed higher turbidity compared to the falling limb (Mukundan *et al.*, 2013b). The hysteresis term will account for such differences due to sediment source depletion as an event progresses. A detailed description on the development of the time series turbidity model and its use as an operational predictive tool is outlined in Wang *et al.* (2012).

The Generalized Watershed Loading Functions – Variable Source Area (GWLF-VSA) model

The GWLF-VSA model (Schneiderman *et al.*, 2007) is a modified version of the original GWLF watershed model (Haith and Shoenaker, 1987) capable of simulating streamflow and nutrients at a daily time step. Major modifications include accounting for surface runoff distribution across the landscape based on saturation-excess hydrology. This modification is important because saturation excess is the dominant runoff generation mechanism in north-eastern USA (Steenhuis *et al.*, 1995; Frankenberger *et al.*, 1999; Walter *et al.*, 2003; Lyon *et al.*, 2006). For simulating daily streamflow, major inputs to the GWLF model include daily precipitation and daily minimum and maximum air temperature time series. The model has been successfully calibrated and applied in NYC water supply watersheds (Schneiderman *et al.*, 2007; Matonse *et al.*, 2011; Zion *et al.*, 2011). In this study, we applied the calibrated model for simulating daily streamflow using daily time series of baseline and simulated future precipitation and air temperature.

Table I. List of GCMs, scenarios, and time slices used in this study

	GCM ID	Country	Scenario	Time slice
1	CGCM3.1	Canada	A1B, A2, B1	2046–2065, 2081–2100
2	CNRM CM3	France	A1B, A2, B1	2046–2065, 2081–2100
3	GFDL CM2.1	USA	A1B, A2, B1	2046–2065, 2081–2100
4	ECHO-G	Germany/Korea	A1B, A2, B1	2046–2065, 2081–2100
5	MRI-CGCM2.3.2	Japan	A1B, A2, B1	2046–2065, 2081–2100

Future climate scenarios

The potential effect of climate change on in-stream turbidity was evaluated using baseline and future climate scenarios derived from a suite of five global climate models (GCMs) and three greenhouse gas emission scenarios that represent a wide range of future climate conditions, during the 2046–2065 and 2081–2100 time slices (Table I) and a baseline (20C3M) scenario representing historical (1960–2000) conditions. In this study, the A1B, A2, and B1 scenarios from the Special Report on Emission Scenarios in the IPCC Fourth Assessment Report (IPCC, 2007) were used. Projected values from the selected GCMs for the region surrounding the NYC water supply were extracted and interpolated to a common 2.5° grid using bilinear interpolation for the baseline and future emission scenarios. Climate scenarios were downscaled using a 25-bin change factor (CF) methodology. This methodology divides the cumulative distribution function of a given meteorological variable associated with measurements made in a given month into 25 equally spaced percentiles, and a monthly delta CF (Anandhi *et al.*, 2011) is developed for each bin. Monthly CFs were calculated from the difference between baseline and each future GCM/scenario simulation. These monthly CFs were used to adjust the locally measured meteorological data from 1927 to 2009 and used to generate future climate conditions associated with a given GCM. The use of long-term observed data in generating future climate scenarios has an advantage of representing the observed regional climate patterns but has the disadvantage of relying only on the local historical variability of events (Matonse *et al.*, 2012).

Developing future stream turbidity scenarios

A combination of measured and interpolated daily in-stream turbidity time series and measured streamflow time series was used to derive empirical relationships that relate a wide range of streamflow to stream turbidity (rating curves). To reduce the effect of regulated releases from the Schoharie Reservoir via the Shandaken Tunnel particularly on low flow turbidity, only streamflow–turbidity pairs from days when the flow diversion from Schoharie Reservoir was less than 10% of the total Esopus Creek daily streamflow were used. Separate turbidity rating curves were developed for the winter (November–April) and summer (May–October) periods to account for seasonal variability in turbidity inputs. As stream channel erosion is the primary source of turbidity in this watershed, seasonal variability in turbidity rating curves will be due to seasonal differences in stream channel processes (e.g. freeze thaw cycles in the winter and desiccation in the summer). Another possible factor that may result in seasonal differences in turbidity is seasonal variations in the amount of organic matter in the sediment. The two seasonal rating curves were then applied to baseline and future time series of streamflow simulated by the GWLF-VSA model to develop baseline and future stream turbidity scenarios. These scenarios were analysed for average daily turbidity, average daily turbidity loads, and annual cumulative turbidity loads. In addition, exceedance probability curves of predicted daily winter in-stream turbidity for baseline and future climate scenarios were compared. Previous studies in this region support the concept of turbidity 'loading' (i.e. units of NTU $m^3 s^{-1}$), with turbidity being the regulatory pollutant of concern although the product of turbidity and streamflow is not a strict mass loading rate (Peng *et al.*, 2009). Additional support for this approach is provided by the additive nature of turbidity, i.e. the turbidity of a mixture of two volumes can be computed by volume averaging (Davies-Colley *et al.*, 2003).

RESULTS

Stream turbidity time series

A continuous time series of average daily stream turbidity from 13 June 2003 to 31 August 2011 was used for this analysis. Missing turbidity data were estimated using the time series model described in the Methods section. Residual analysis from the ordinary least square regression model using the three predictor variables showed a lag of

Table II. Autoregressive time series model parameters

Variable	DF	Estimate	Standard error	*t*-value	Approx Pr > |*t*|
Intercept	1	0.3490	0.0514	6.78	<0.0001
Log (Q^2)	1	0.3042	0.0065	46.12	<0.0001
Log PS-turb	1	0.0845	0.0200	4.22	<0.0001
HE	1	0.2564	0.0110	23.25	<0.0001
AR1	1	–0.6348	0.0227	–27.98	<0.0001
AR2	1	–0.1197	0.0273	–4.38	<0.0001
AR3	1	–0.1102	0.0272	–4.05	<0.0001
AR4	1	–0.0774	0.0228	–3.39	0.0007

*Q = mean daily streamflow at the watershed outlet; PS-turb = measured turbidity at the diversion tunnel inlet; HE = hysteresis effect; DF = degrees of freedom.

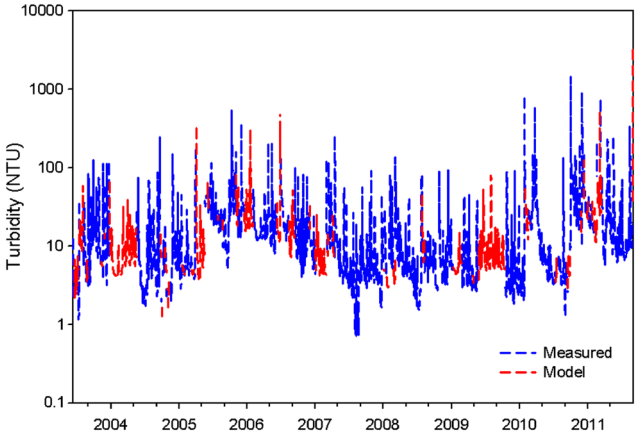

Figure 2. Continuous time series (2003–2011) of average daily turbidity at Coldbrook showing the range in observed (blue) and missing turbidity values replaced by regression model results (red)

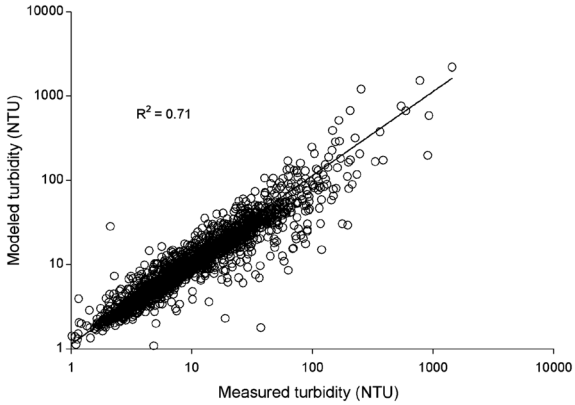

Figure 3. Scatter plot of measured and modelled turbidity

4 days in the autocorrelation function (AR4 error). This information was used in selecting an autoregressive model capable of predicting log-transformed daily turbidity. The selected regression model with AR4 error is as follows:

$$Y(t) = \beta x(t) + v(t)$$

$$v(t) = \sum_{i=1}^{4} \phi_i v(t-i) + \epsilon_t$$

$x(t)$ is a vector of predictor variables at time t.
β is a vector of regression parameters.
ϕ_i represent the autoregressive parameters.
$v(t)$ is the model error at time t.
ϵ_t is 'white noise', which is normally distributed with a mean of 0 and a variance of σ^2.

Parameter estimates for the selected model is presented in Table II, and a plot of continuous time series of daily turbidity, including both measured data and missing values replaced by model results at the Coldbrook outlet,

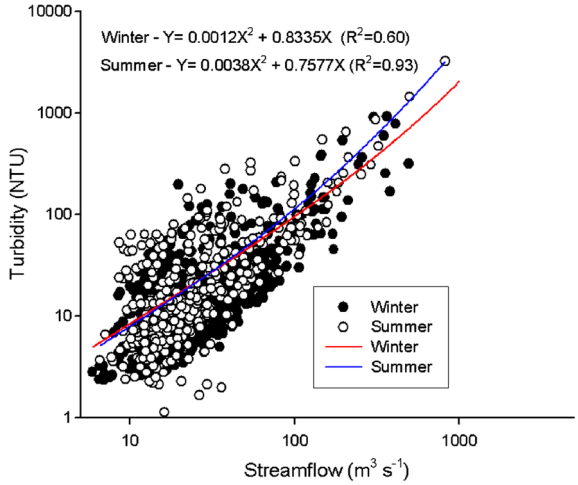

Figure 4. Streamflow–turbidity relationship at the Coldbrook outlet, summer *versus* winter comparison. X and Y in the equations are the average daily streamflow and the average daily turbidity, respectively

is presented in Figure 2. The selected model was evaluated for its performance in predicting mean daily stream turbidity using coefficient of determination (R^2), Nash–Sutcliffe efficiency (NSE) (Nash and Sutcliffe, 1970), and percent bias (PBIAS). The autoregressive daily time series model performed reasonably well with an R^2 of 0.71 (Figure 3), an NSE of 0.46, and a PBIAS less than 2%. Model performance was affected by predictions for two data points, without which the R^2 and NSE improved to 0.82 and 0.62, respectively. The model-predicted average daily turbidity for 16 April 2007 was 1205 NTU when the measured value was only 253 NTU, and for 25 January 2010, the predicted value was 196 NTU when the measured value was 904 NTU. Certain watershed processes, such as streambank collapse occurring under baseflow conditions resulting in high stream turbidity or the travel times of highly turbid water from point sources to the watershed outlet, cannot be explicitly captured by a time series regression model.

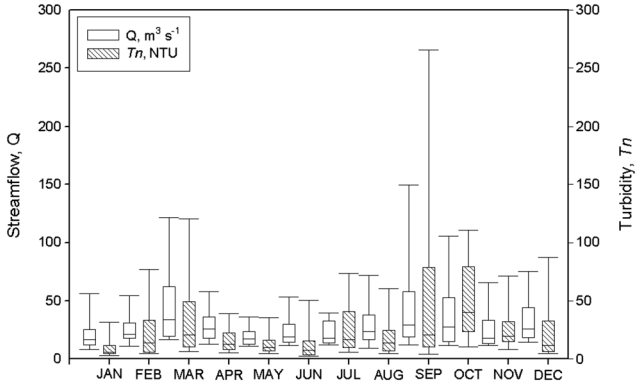

Figure 5. Box plots of observed average daily stream turbidity and corresponding streamflow by month. Boxes represent inter-quartile range and whiskers represent 10th and 90th percentile values

Moreover, uncertainty due to errors in turbidity measurements can affect the quantitative results presented.

Streamflow–turbidity relationship

A scatter plot of average daily streamflow and average daily in-stream turbidity is presented in Figure 4. A second-order polynomial gave the best-fit deterministic rating curve for daily stream turbidity prediction from daily streamflow. This form of rating curve has been previously reported in other studies (Horowitz, 2003) and is used in predictive models for this watershed (Gannett Fleming & Hazen and Sawyer, 2008). Comparison of rating curves for the winter (November–April) and summer (May–October) periods did not show much difference during low-flow periods (e.g. $<100\,m^3\,s^{-1}$). However, at high-flow periods, higher turbidity values per unit streamflow were observed during the summer period. Although limited turbidity observations are available under high-flow conditions compared to low-flow periods, predictions of lower high-flow turbidity levels during winter are supported by the fact that more frequent precipitation events observed in the winter can reduce sediment supply and hence turbidity compared to fewer and more intense storm events observed in the summer resulting in higher turbidity. Longer periods of low streamflow between events can result in accumulation of sediment in the stream channels and replenishment of turbidity sources as discussed in Doomen *et al.* (2008). During the period of our turbidity record, major storm events including tropical storms and hurricanes were observed in September–October after the seasonal lower flow period from May to August (Figure 5). One such event occurred on 1 October 2010, when the stream turbidity increased as high as 2300 NTU and another event occurred between 26 and 29 August 2011 in the form of Hurricane Irene, when sediment concentrations of

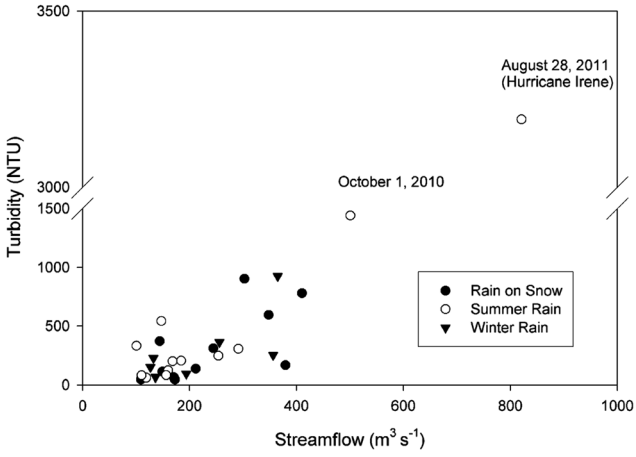

Figure 6. Bankfull events in the Esopus Creek between June 2003 and August 2011 and associated mean daily streamflows and turbidity

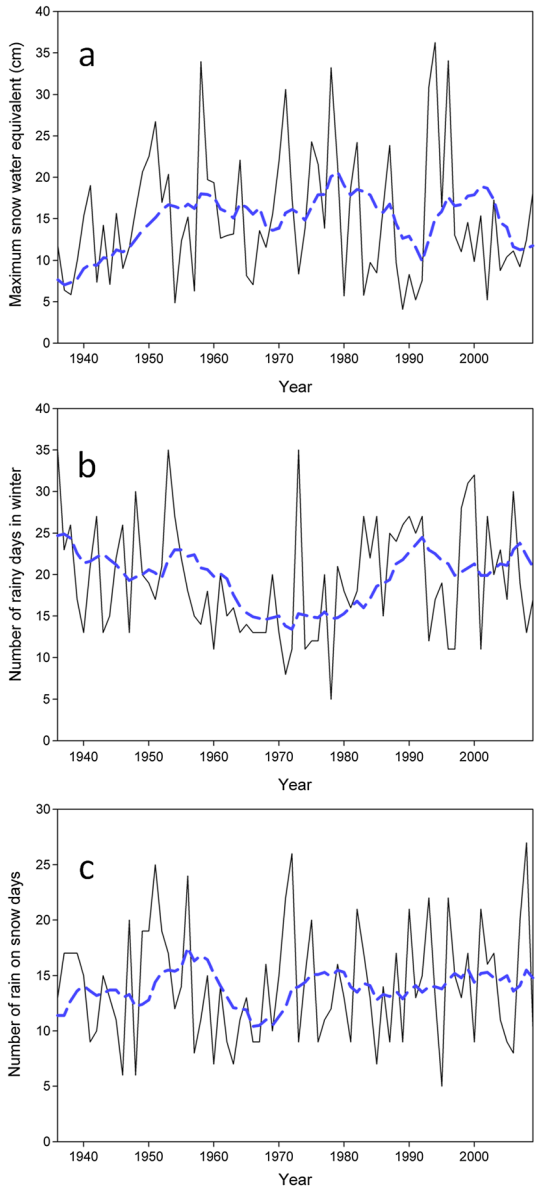

Figure 7. Modelled trend in (a) maximum basin-wide SWE between November and April; (b) number of rainy days in winter when there was no snow cover on ground; (c) number of rain on snow days. Blue line represents 10-year moving average from 1936 to 2009

over 6000 mg/l were measured in the Esopus Creek. Sustained high levels of turbidity were observed in the Ashokan Reservoir for over a month following this event. Selective use of water from the system of inter-connected reservoirs that make up the NYC water supply is the management strategy of choice to provide high-quality drinking water to NYC consumers.

Wynn *et al.* (2008), based on a study in south-western Virginia, USA, found that desiccation of streambank soils in the summer can increase channel erodibility and decrease critical shear stress. Confirmation on occurrence of such processes in our study region needs further investigation. Moreover, our observations are based on the most recent

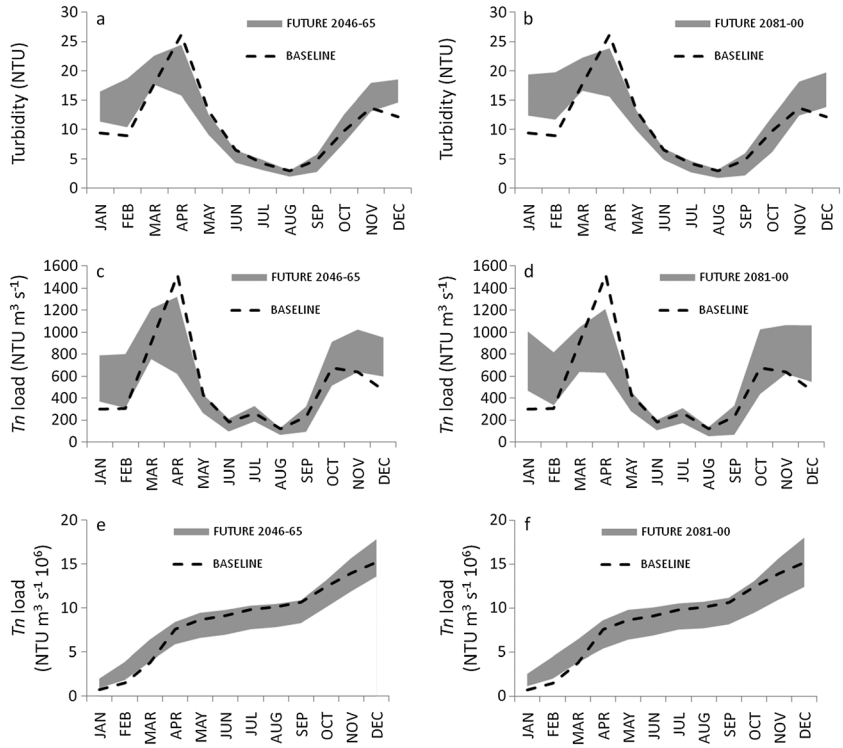

Figure 8. Comparison of baseline *versus* future estimates of stream turbidity for the 2046–2065 period (a) and the 2081–2100 period (b); projected change in average monthly turbidity load for the 2046–2065 period (c) and the 2081–2100 period (d); projected change in average annual cumulative turbidity loads (e and f). The dashed line shows the monthly mean values calculated for the baseline time period; the grey shading shows the range in monthly means calculated for different future scenarios

decadal seasonal pattern in stream turbidity, and this could potentially change in the long term depending on the number and size of events that may occur.

Bankfull events in the winter

For the Esopus Creek at Coldbrook, streamflow greater than about 200 $m^3 s^{-1}$ is considered as bankfull (Mulvihill *et al.*, 2009). During the period of monitoring, a total of 31 events with peak flows exceeding the bankfull threshold were observed, of which 19 were in the winter (Figure 6), and in general, the events occurring in winter were events with the greatest associated streamflows. In fact, eight out of the ten next largest bankfull events (excluding the two tropical storms discussed above) occurred in the winter, with five of these events associated with rain on snow processes. Unlike watersheds with significant upland erosion where snow cover tends to protect the soil, snowmelt runoff and the resulting increase in stream discharge can increase stream turbidity through stream channel erosion in the Esopus Creek watershed.

Long-term trend in snowpack, winter rainy days, and rain on snow days

The lumped-parameter temperature index snowpack algorithm in the GWLF model is described in Schneiderman

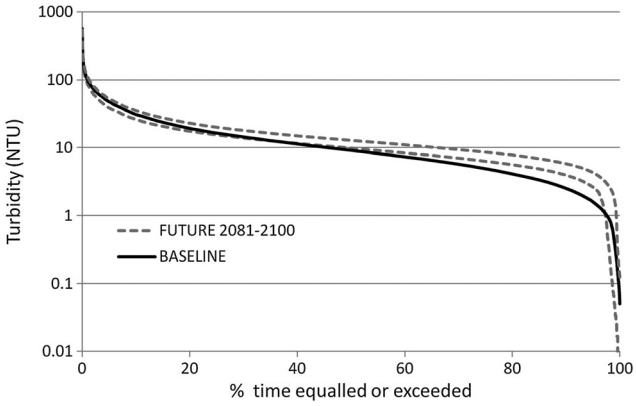

Figure 9. Winter stream turbidity exceedance curves for baseline (solid) and future (dashed) scenarios. The future scenario curves show the maximum and minimum values of all 2081–2100 time slice scenarios

et al. (2013). In the absence of a long-term record of watershed snow measurements, a time series of watershed-wide SWE for November–April was estimated using the GWLF model for the historical baseline scenario (1927–2009). Annual maximum in SWE showed a general increase from the 1940s through 1980 after which a decreasing trend was observed from 1980 to 2009 (Figure 7a). The number of winter rainy days (rain when there was no snow on ground) generally decreased from the

Table III. Exceedance probability of modelled winter stream turbidity (NTU)

% time equalled or exceeded	Baseline turbidity	Future turbidity 2046–65		Future turbidity 2081–00	
		Minimum	Maximum	Minimum	Maximum
5	47.35	41.87	53.12	38.68	53.07
10	30.58	28.06	34.83	26.01	35.31
25	16.29	16.59	19.88	15.44	19.98
50	9.11	10.10	12.35	9.86	12.82
75	4.87	5.91	7.92	6.31	8.64
90	2.48	3.31	5.14	3.94	5.83
95	1.55	2.19	3.76	2.64	4.32

1940s through the early 1970s and then tended to increase thereafter (Figure 7b). Winter precipitation on frozen snow-free ground can increase peak discharges that can potentially lead to higher stream turbidity. The number of rain on snow days showed no clear trend over the simulation period (Figure 7c), which could be due to an increasing number of rain event acting on the diminished snow cover.

Projected changes in stream turbidity

Modelled long-term monthly average turbidity for the baseline scenario showed a peak in April, and this peak was also evident in the future scenarios (Figures 8a and 8b). However, the height of the peak was reduced in the future time slices (2046–2065 and 2081–2100), and there was a projected increase in stream turbidity during January and February. As a result of this shift, January–February turbidity was up to 45% higher for the 2046–2065 period and up to 68% higher for the 2081–2100 period compared to baseline. These changes in turbidity are clearly related to a shift in timing of snowmelt runoff and the resulting increase in streamflow in earlier months, and are also consistent with predictions of a decrease in the amount of precipitation received as snow reported by other studies from the same region (Frei *et al*., 2002; Mukundan *et al*., 2013a). Projected changes in average daily stream turbidity loads yielded similar results (Figures 8c and 8d). The maximum increase in winter turbidity loads is projected for the month of January, and the maximum decrease is projected to occur in April. Figures 8e and 8f show the modelled long-term average annual cumulative turbidity load for baseline and future scenarios developed from average monthly values. The percent change in average annual cumulative turbidity load was only +3% and +5% for the 2046–2065 and 2081–2100 time slices and corresponds well with the projected average annual change in streamflow volumes (+4% and +6%, respectively) for the same time period. Therefore, climate change effects on turbidity loads at the annual time scale are simulated to have no major effects despite a major seasonal effect in the winter due to a shift in the timing of snowmelt runoff. Similar results where there was a shift in the timing of snowmelt runoff causing significant seasonal changes in nutrient and sediment loads under projected climate with no major change in annual loads were observed by Riverson *et al*. (2013) in Lake Tahoe basin and Bouraoui *et al*. (2004) in a Finnish drainage basin.

Figure 9 shows the modelled winter in-stream turbidity exceedance probability curves for baseline and future scenarios for the 2081–2100 time slice. The predicted future probability curves (based on maximum and minimum of all GCMs and all scenarios) were well above the baseline curve, particularly for low values of turbidity (<10 NTU). A similar pattern was observed for time slice 2046–2065 (not shown in Figure 9). However, at higher turbidity values, this pattern was not evident. Table III shows the maximum and minimum winter in-stream turbidity values (based on all GCMs and all scenarios) associated with the 5th to the 95th percentile exceedance probability for both time slices. It appears that the baseline stream turbidity values are within the range of predicted future values for the 5th to 25th percentiles, associated with the highest turbidity levels. Below this, the predicted range of future values is well above the baseline values, which indicates that the projected impact of climate change on winter stream turbidity appears to be more prominent at medium to low streamflows. Part of this change could be due to reduced snowpack development and early melting of snow particularly in January and February, resulting in higher ambient streamflow and thus higher stream turbidity values for these months compared to the baseline scenario. The model-predicted reductions in snowpack during these months are about 50% and 70% for the two future time slices when compared to the historical baseline scenario. In our study region, a number of runoff events are observed throughout the winter period, many of which are associated with snowpack and snowmelt. A combination of reduced snowpack development and fewer number of snowmelt-driven runoff events during winter may result in a cumulative period under higher stream turbidity comparable to baseline conditions. These results may be applicable to a wide range of landscapes with similar hydroclimatology and sources of stream turbidity.

SUMMARY AND CONCLUSIONS

Snowfall is an important and variable component of total precipitation in the Catskill Mountains of New York, where the major NYC water supply watersheds are located. Previous studies reporting the impact of climate change in this region and north-eastern USA in general have concluded that changes in temperature and precipitation may lead to changes in snowpack development and winter rainfall and more importantly a shift in the timing of snowmelt runoff. Our study reports the effects of these changes on winter stream turbidity in the Upper Esopus Creek watershed, one of the NYC water supply watersheds. We use both measured historical data and simulated future scenarios to compare differences in stream turbidity between present and future climate scenarios. Results of model simulations using a suite of five GCMs, three emission scenarios, and two time slices indicate a future increase in ambient stream turbidity from November to March and a decrease during April. These results are the consequence of a strong relationship between streamflow and turbidity, and changes in the seasonality of streamflow that are the effects of increased winter rainfall, reduced snowfall, and an earlier occurrence of snowmelt runoff. Changes in turbidity loads followed the same pattern as simulated stream turbidity for most months. Changes in average annual cumulative turbidity loads were minimal. This is due to the fact that despite predicted future winter streamflow patterns showing a redistribution of discharge and turbidity loads to earlier in the year, future annual loading was only slightly increased.

Our projected changes in winter stream turbidity are consistent with the projected changes in winter hydrology as discussed in Matonse *et al*. (2011) and Zion *et al*. (2011) for the same region. However, the results presented here should be viewed as a general sensitivity analysis rather than absolute numerical predictions, given the uncertainty in future climate projections, particularly the difficulties in predicting changes in the frequency of extreme events that are not well captured by GCMs or the downscaling method used in this study. Our study is an example of a regional study on the impact of projected climate on water resources with a focus on stream turbidity. The tools and methods used in this study may be applied in other watersheds to understand the seasonality, magnitude, and direction of hydroclimatic signal on regional water resources. Future research on the impact of changing watershed hydrology on water quality and quantity may provide more insight into mitigation strategies and sustainable management of water resources.

ACKNOWLEDGEMENTS

The authors thank Dr Allan Frei (Hunter College, City University of New York) for his support in this project, Dr David Smith (Hunter College, City University of New York) for his valuable review comments, and Mr David Lounsbury (NYCDEP) for GIS support.

REFERENCES

Anandhi A, Frei A, Pierson DC, Schneiderman EM, Zion MS, Lounsbury DG, Matonse AH. 2011. Examination of change factor methodologies for climate change impact assessment. *Water Resources Research* **47**: W03501. DOI:10.1029/2010WR009104.

Bouraoui F, Grizzetti B, Granlund K, Rekolainen S, Bidoglio G. 2004. Impact of climate change on the water cycle and nutrient losses in a Finnish catchment. *Climatic Change* **66**: 109–126.

Burns DA, Klaus J, McHale MR. 2007. Recent climate trends and implications for water resources in the Catskill Mountain region, New York, USA. *Journal of Hydrology* **336**: 155–170.

Davies-Colley RJ, Vant WN, Smith DG. 2003. Colour and Clarity of Natural Waters: Science and Management of Optical Water Quality. Blackburn Press: Caldwell; NJ.

DEP. 2008. Evaluation of Turbidity Reduction Potential through Watershed Management in the Ashokan Basin. Valhalla, New York, July 2008.

Doomen AMC, Wijma E, Zwolsman JJG, Middelkoop H. 2008. Predicting suspended sediment concentrations in the Meuse River using a supply-based sediment rating curve. *Hydrological Processes* **22**: 1846–1856.

Effler SW, Perkins MG, Ohrazda N, Brooks CM, Wagner BA, Johnson DL, Peng F, Bennett A. 1998. Turbidity and Particle Signatures imparted by Runoff Events in Ashokan Reservoir, NY. *Lake and Reservoir Management* **14**: 254–265.

Evrard O, Navratil O, Ayrault S, Ahmadi M, Némery J, Legout C, Lefèvre I, Poirel A, Bonté P, Esteves M. 2011. Combining suspended sediment monitoring and fingerprinting to trace the spatial origin of fine sediment in a mountainous river catchment. *Earth Surface Processes and Landforms* **36**: 1072–1089.

Frankenberger JR, Brooks ES, Walter MT, Walter MF, Steenhuis TS. 1999. A GIS-based variable source area model. *Hydrological Processes* **13**(6): 804–822.

Frei A, Armstrong RL, Clark MP, Serreze MC. 2002. Catskill Mountain Water Resources: Vulnerability, Hydroclimatology, and Climate-Change Sensitivity. *Annals of the Association of American Geographers* **92**(2): 203–224.

Gannett Fleming & Hazen and Sawyer. 2008. Catskill turbidity control studies: Phase III Implementation Plan, Prepared for New York City Department of Environmental Protection, Bureau of Engineering Design and Construction.

Gelda RK, Effler SW, Peng F, Owens EM, Pierson DC. 2009. Turbidity Model for Ashokan reservoir, New York: Case study. *Journal of Environmental Engineering* **135**(9): 885-895.

Haith DA, Shoenaker LL. 1987. Generalized Watershed Loading Functions for stream flow nutrients. *Water Resources Bulletin* **23**(3): 471–478.

Hirsch RM. 1988. Statistical Methods and Sampling Design for Estimating Step Trends in Surface-Water Quality. *Journal of the American Water Resources Association* **24**: 493–503.

Horowitz AJ. 2003. An evaluation of sediment rating curves for estimating suspended sediment concentrations for subsequent flux calculations. *Hydrological Processes* **17**:3387-3409.

IPCC- Intergovernmental Panel on Climate Change. 2007. IPCC Fourth Assessment Report: Climate Change 2007, Cambridge University Press: Cambridge, United Kingdom and New York, NY, USA.

Lyon SW, Lembo AJ, Walter MT, Steenhuis TS. 2006. Defining probability of saturation with indicator kriging on hard and soft data. *Advances in Water Resources* **29**(2): 181–193.

Marshall E, Randhir T. 2008. Effect of climate change on watershed system: a regional analysis. *Climatic Change* **89**: 263–280.

Matonse AH, Pierson DC, Frei A, Zion MS, Schneiderman ES, Anandhi A, Mukundan R, Pradhanang SM. 2011. Effects of changes in snow pattern and the timing of runoff on NYC water supply system. *Hydrological Processes* **25**: 3278–3288.

Matonse AH, Pierson DC, Frei A, Zion MS, Anandhi A, Schneiderman E, Wright B. 2012. Investigating the impact of climate change on New York City's primary water supply. *Climatic Change* **116**:437–456.

McDonald DM, Lamoureux SF. 2009. Hydroclimatic and channel snowpack controls over suspended sediment and grain size transport in a High Arctic catchment. *Earth Surface Processes and Landforms* **34**:424–436.

Mukundan R, Pradhanang SM, Schneiderman EM, Pierson DC, Anandhi A, Zion MS, Matonse AH, Lounsbury DG, Steenhuis TS. 2013a. Suspended sediment source areas and future climate impact on soil erosion and sediment yield in a New York City water supply watershed, USA. *Geomorphology* **183**: 110–119.

Mukundan R, Pierson DC, Schneiderman EM, O'Donnell DM, Pradhanang SM, Zion MS, Matonse AH. 2013b. Factors Affecting Storm Event Turbidity in a New York City Water Supply Stream. *Catena*, In press. http://dx.doi.org/10.1016/j.catena.2013.02.002.

Mulvihill CI, Baldigo BP, Miller SJ, DeKoskie D, Joel D. 2009. Bankfull discharge and channel characteristics of streams in New York State: U. S. Geological Survey Scientific Investigations Report 2009–5144, 51 p.

Nagle GN, Fahey TJ, Ritchie JC, Woodbury PB. 2007. Variations in sediment sources and yields in the Finger Lakes and Catskills Regions of New York. *Hydrological Processes* **21**: 828–838.

Nash JE, Sutcliffe JV. 1970. River flow forecasting through conceptual models – Part I: A discussion of principles. *Journal of Hydrology* **10**: 282–290.

Peng F, Effler SW, Pierson DC, Smith DG. 2009. Light-scattering features of turbidity-causing particles in interconnected reservoir basins and a connecting stream. *Water Research* **34**(8): 2280–2292.

Reed RE, Dickey DA, Burkholder JM, Kinder CA, Brownie C. 2008. Water level variations in the Neuse and Pamlico Estuaries, North Carolina due to local and remote forcing. *Estuarine, Coastal and Shelf Science* **76**(2): 431–446.

Richards RP, Baker DB, Crumrine JP, Kramer JW, Ewing DE, Merryfield BJ. 2008. Thirty-year trends in suspended sediment in seven Lake Erie tributaries. *Journal of Environmental Quality* **37**: 1894–1908.

Riverson J, Coats R, Costa-Cabral M, Dettinger M, Reuter J, Sahoo G, Schladow G. 2013. Modeling the transport of nutrients and sediment loads into Lake Tahoe under projected climatic changes. *Climatic Change* **116**(1): 35–50.

Samal NR, Matonse AH, Mukundan R, Zion MS, Pierson DC, Gelda RK, Schneiderman EM. 2013. Modeling Potential Effects of Climate Change on Winter Turbidity Loading in the Ashokan Reservoir, NY, (In this issue).

Schneiderman EM, Steenhuis TS, Thongs DJ, Easton ZM, Zion MS, Neal AL, Mendoza GF, Walter MT. 2007. Incorporating variable source area hydrology into a curve-number-based watershed model. *Hydrological Processes* **21**: 3420–3430.

Schneiderman EM, Matonse AH, Zion MS, Lounsbury DG, Mukundan R, Pradhanang SM, Pierson DC. 2013. Comparison of Snowpack Models for New York City Watersheds (Submitted).

Steenhuis TS, Winchell M, Rossing J, Zollweg JA, Walter MF. 1995. SCS runoff equation revisited for variable-source runoff areas. *Journal of Irrigation and Drainage Engineering* **121**: 234–238.

Stewart IT. 2009. Changes in snowpack and snowmelt runoff for key mountain regions. *Hydrological Processes* **23**: 78–94.

Walker JT, Vose JM, Knoepp J, Geron CD. 2009. Recovery Of Nitrogen Pools And Processes In Degraded Riparian Zones In The Southern Appalachians. *Journal of Environmental Quality* **38**(4): 1391–1399.

Walling DE. 2009. The Impact of Global Change on Erosion and Sediment Transport by Rivers: Current Progress and Future Challenges. UNESCO-IHP The United Nations World Water Development Report 3 Available at http://unesdoc.unesco.org/images/0018/001850/185078e.pdf (Accessed Sept 23, 2010)

Walter MT, Mehta VK, Marrone AM, Boll J, Gérard-Marchant P, Steenhuis TS, Walter MF. 2003. Simple estimation of prevalence of Hortonian flow in New York City watersheds. *Journal of Hydrologic Engineering* **8**: 214–218.

Wang L, Mukundan R, Zion MS, Pierson DC. 2012. Beyond Rating Curves: Time Series Models for in-Stream Turbidity Prediction. *American Geophysical Union Annual Meeting 2012*, San Francisco, CA, USA.

Wynn T, Henderson M, Vaughan D. 2008. Changes in streambank erodibility and critical shear stress due to subaerial processes along a headwater stream, southwestern Virginia, USA. *Geomorphology* **97**: 260–273.

Zion MS, Pradhanang SM, Pierson DC, Anandhi A, Lounsbury D, Matonse AH, Schneiderman ES. 2011. Investigation and modelling of winter streamflow and timing and magnitude under changing climate conditions for the Catskill mountain region, New York, USA. *Hydrological Processes* **25**: 3289–3301.

Geomorphology 183 (2013) 110–119

Contents lists available at SciVerse ScienceDirect

Geomorphology

journal homepage: www.elsevier.com/locate/geomorph

Suspended sediment source areas and future climate impact on soil erosion and sediment yield in a New York City water supply watershed, USA

Rajith Mukundan [a,*], Soni M. Pradhanang [a], Elliot M. Schneiderman [b], Donald C. Pierson [b], Aavudai Anandhi [c], Mark S. Zion [b], Adão H. Matonse [a], David G. Lounsbury [b], Tammo S. Steenhuis [d]

[a] Institute for Sustainable Cities, City University of New York New York City, NY, USA
[b] New York City Department of Environmental Protection, Kingston, NY, USA
[c] Department of Agronomy, Kansas State University, Manhattan, KS, USA
[d] Department of Biological and Environmental Engineering, Cornell University, Ithaca, NY, USA

ARTICLE INFO

Article history:
Received 2 June 2011
Received in revised form 2 February 2012
Accepted 22 June 2012
Available online 28 June 2012

Keywords:
Suspended sediment
Climate change
SWAT-WB
Saturation excess
New York City water supply

ABSTRACT

High suspended sediment loads and the resulting turbidity can impact the use of surface waters for water supply and other designated uses. Changes in fluvial sediment loads influence material fluxes, aquatic geochemistry, water quality, channel morphology, and aquatic habitats. Therefore, quantifying spatial and temporal patterns in sediment loads is important both for understanding and predicting soil erosion and sediment transport processes as well as watershed-scale management of sediment and associated pollutants. A case study from the 891 km^2 Cannonsville watershed, one of the major watersheds in the New York City water supply system is presented. The objective of this study was to apply Soil and Water Assessment Tool-Water Balance (SWAT-WB), a physically based semi-distributed model to identify suspended sediment generating source areas under current conditions and to simulate potential climate change impacts on soil erosion and suspended sediment yield in the study watershed for a set of future climate scenarios representative of the period 2081–2100. Future scenarios developed using nine global climate model (GCM) simulations indicate a sharp increase in the annual rates of soil erosion although a similar result in sediment yield at the watershed outlet was not evident. Future climate related changes in soil erosion and sediment yield appeared more significant in the winter due to a shift in the timing of snowmelt and also due to a decrease in the proportion of precipitation received as snow. Although an increase in future summer precipitation was predicted, soil erosion and sediment yield appeared to decrease owing to an increase in soil moisture deficit and a decrease in water yield due to increased evapotranspiration.

1. Introduction

Many recent studies have focused on the potential effects of climate change on water resources including water quality, hydrology, water demand, and socio-economic changes (Aber et al., 1995; Christensen et al., 2004; Parry et al., 2004; Bates et al., 2008). However, little research has been undertaken on the potential impact of climate change on sediment loads of streams and rivers (IPCC, 2007). High sediment loads and the resulting turbidity can impact the sustained use of rivers for water supply and other designated uses. Changes in fluvial sediment loads influence material fluxes, aquatic geochemistry, water quality, channel morphology, and aquatic habitats. Therefore, quantifying spatial and temporal patterns in sediment loads under present and future conditions will be valuable in both understanding and predicting sediment transport processes as well as watershed-scale management of sediment for maintaining high water quality.

Although it is impossible to predict the exact climate of the future, past climate trends combined with improved knowledge of global climatology, atmospheric processes and socio-economic changes have been used to develop future climate scenarios. The climate change scenarios recognized by the Intergovernmental Panel for Climate Change (IPCC) are widely used for modeling purposes. A limited number of studies have reported on the potential impact of climate change on soil erosion (Nearing, 2001; Yang et al., 2003; Nearing et al., 2004; O'Neal et al., 2005; Zhang and Nearing, 2005; Zhang, 2007; Nunes et al., 2009; Maeda et al., 2010; Nunes et al., 2011). While there is a general consensus that increasing rainfall intensity will increase watershed sediment loads (Kostaschuk et al., 2002; Bouraoui et al., 2004) through hillslope erosion (due to high rainfall erosivity) and channel erosion (due to high stream velocity), the regional impacts of future climate on erosion and sediment transport need further attention. Watershed sediment transport in response to changes in precipitation depends on the dominant sediment

* Corresponding author.
E-mail address: Rajith.Mukundan@hunter.cuny.edu (R. Mukundan).

0169-555X/$ – see front matter © 2012 Elsevier B.V. All rights reserved.
doi:10.1016/j.geomorph.2012.06.021

generation process. Soil erosion is closely linked to watershed sediment transport as it is a dominant process in watersheds where hillslope erosion is the primary source of sediment. The rate and magnitude of sediment transport are dependent on flow velocity in the channel, erodibility of the channel material as well as sediment delivery from upstream. A decrease in sediment supply combined with increased peak stream discharges can create imbalance between sediment supply and sediment transport capacity leading to channel instability (Rakovan and Renwick, 2011). Nunes and Nearing (2011) discuss the impact of climate change on erosion using multiple case studies. Knowledge gaps identified in their analysis include fewer studies at the watershed scale, uncertainty in climate change impact estimates, and links and feedbacks between erosion and land use/land cover.

Asselman et al. (2003) used UK Hadley Centre's high-resolution atmospheric general circulation model (UKHI) climate change scenario, in combination with land use changes to evaluate changes in sediment yield in the Rhine basin of the Dutch–German border. Although erosion rates were predicted to increase by 12% they found no significant effect on sediment yield at the basin outlet due to insufficient sediment delivery. Lawler et al. (2003) conducted a study in three catchments in Iceland and concluded that in response to climate change there was a decline in sediment yield in all catchments predominantly in the spring and in autumn. This decline in sediment yield was related to river flow reductions driven by significant cooling in spring and decreases in heavy daily precipitation events in autumn. Zhu et al. (2008) performed a climate change sensitivity analysis on measured sediment flux during the period 1960–1990 in a tributary of the Upper Yangtze River in China. They concluded that a combination of rainfall and temperature changes resulted in changes in the sediment flux of the river. Higher sediment flux is expected to appear under wetter and warmer climate, when higher transport capacity is accompanied by a higher erosion rate. Thodsen et al. (2008) used the HIRHAM regional climate model to study the influence of climate change on suspended sediment transport in Danish Rivers. Model simulations incorporating projected changes in land use/land cover scenarios for the period 2071–2100 suggested an increase in suspended sediment transport in the winter months as a result of the increase in river discharge caused by increase in precipitation, and decreases during summer and early autumn months. Li et al. (2011) based on Soil and Water Assessment Tool (SWAT) model simulations in the lower Pearl River Basin, South China concluded that a 3 °C increase in average annual air temperature would increase the sediment load by about 13%. Warming climate can reduce vegetation and slow plant growth resulting in increased soil loss.

Models such as ANSWERS (Beasley et al., 1980); AGNPS (Young et al., 1987); WEPP (Nearing et al., 1989); EuroSEM (Morgan et al., 1990); HSPF (Bicknell et al., 1993); RUSLE (Renard et al., 1997); and SWAT (Neitsch et al., 2005) are often used in combination with geographic information systems (GIS) in sediment transport studies. In the SWAT model sediment is generated by hillslope and stream channel erosion and routed through the stream which is explicitly characterized as a network of connected reaches. The model has been shown to simulate sediment loads at the outlet of the watershed fairly well for a variety of catchment types (Santhi et al., 2001; Cerucci and Conrad, 2003; Cotter et al., 2003; Arabi et al., 2006; Jha et al., 2007; Tolson and Shoemaker, 2007). Previous studies using SWAT model to simulate the impact of climate change on sediment transport have shown both increases as well as decreases in sediment transport rates depending on characteristics of the location of study (Hanratty and Stefan, 1998; Varanou et al., 2002; Nearing et al., 2005).

In this paper we apply the Soil and Water Assessment Tool-Water Balance (SWAT-WB) model (White et al., 2011) to simulate sediment transport and quantify the potential impact of climate change on soil erosion and sediment yield in the Cannonsville watershed. The watershed drains into the Cannonsville Reservoir, one of the drinking water supply reservoirs for New York City (NYC), USA. This catchment was chosen because a SWAT-2005 model application has been developed that simulates hydrology at the catchment outlet fairly well (Pradhanang et al., 2011), and a long term record of stream water suspended sediment data was available. An examination of historical data and results of model simulations for this region have both shown an increasing trend in precipitation and streamflow over the past fifty years (Burns et al., 2007; Zion et al., 2011). Our goal in this study is to examine how changes in precipitation and streamflow translate into changes in soil erosion and sediment transport in the Cannonsville catchment using a physically based semi-distributed model. Our study assumes stationary land use/cover for the study region. The specific objectives of this study are:

(1) To identify the major sediment source areas within the Cannonsville watershed
(2) To quantify the impact of future climate on long-term soil erosion and sediment yields at the watershed outlet

2. Study site

The Cannonsville watershed, one of the major NYC water supply watersheds is located in the Catskill region of New York State (Fig. 1). The watershed drains an area of 891 km^2 above the USGS gauging station at Walton and is predominantly forested (67%). Other major land uses include agriculture (23%) and brush lands (6%). Agricultural land use in this watershed consists primarily of dairy farms and includes hay lands, pastures, and Corn row crops. The elevation of the watershed ranges from about 300 m near the watershed outlet to about 1100 m near the headwaters. The mean annual rainfall in this region is about 1100 mm (Pradhanang et al., 2011) and the mean annual streamflow is about 601 mm of which 64% can be considered baseflow and 36% as surface runoff based on standard hydrograph separation techniques (Arnold and Allen, 1999). Saturation excess is the dominant runoff generation mechanism in NYC water supply watersheds (Walter et al., 2000; Schneiderman et al., 2007; Easton et al., 2008).

Previous studies in this watershed concluded that majority (95–100%) of the stream sediment in this watershed originated from surface erosion of hillslopes and agricultural fields (Nagle et al., 2007; Tolson and Shoemaker, 2007). The Catskill region has shown changes in regional water balance in recent years (Burns et al., 2007). An increasing trend in mean air temperature during 1952–2005 has caused an increase in potential evapotranspiration (PET) as a result of which one would expect decreases in watershed water yield. However, an increasing trend in precipitation has nullified this effect and actually resulted in a net increase in water yield. Such changes in water balance are expected to have a direct impact on soil erosion and sediment yield.

3. Methods

3.1. SWAT-water balance model

The SWAT-WB (White et al., 2011) is a modified version of the SWAT-2005 model (Neitsch et al., 2005). The original SWAT model uses Hydrologic Response Units (HRU) to define the scale at which precipitation is partitioned into runoff and infiltration. Each HRU is defined based on land use and soil, while the runoff curve number method is used to partition precipitation into runoff and infiltration. In SWAT-WB each HRU is defined based on land use and topographic location which define surface soil moisture pattern, and the partitioning of precipitation into runoff and infiltration is calculated based on daily soil water balance for the HRU. The modified version (SWAT-WB) has been found to perform well in simulating streamflow and sediment

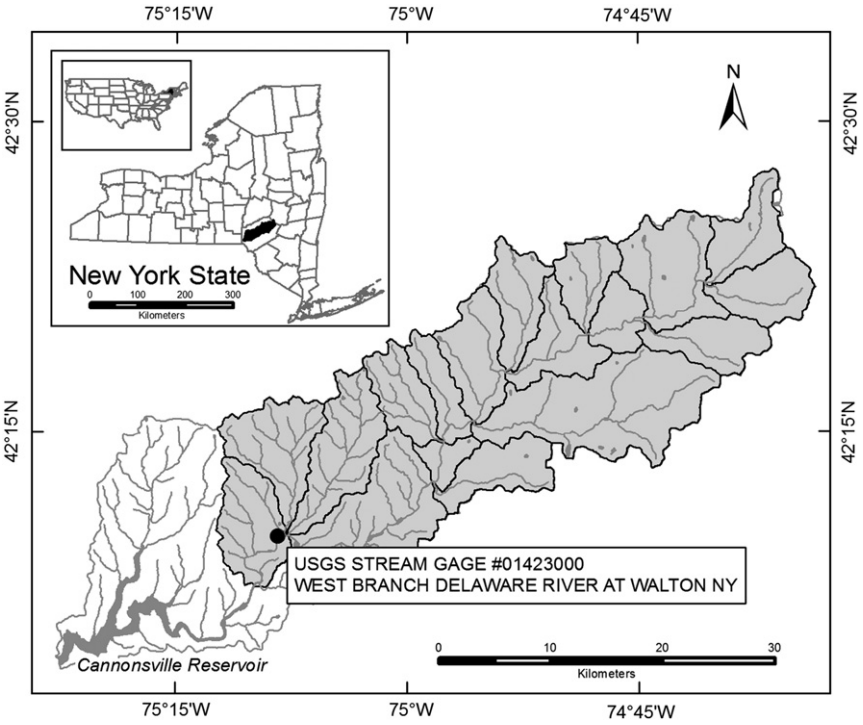

Fig. 1. Location of Cannonsville watershed in New York State, USA.

yield in watersheds, where saturation excess runoff process is dominant runoff generation mechanism (Easton et al., 2010; White et al., 2011).

SWAT's existing soil moisture routines are used by SWAT-WB to determine the degree of saturation-deficit for each soil profile for each day of simulation. This saturation-deficit (in mm of water) is termed the available soil storage, τ_i and is a function of soil properties and watershed soil moisture status (White et al., 2011).

$$\tau_i = (EDC_i \varepsilon_i - \Theta i, t) d_i \quad (1)$$

where EDC_i is the effective depth of a given soil profile i, (unitless), ε_i is the soil porosity (unitless) of a given soil i, $\theta_{i,t}$ is the volumetric soil moisture of a given soil i, for each day, t, (unitless), and d_i is the soil profile depth of soil i (mm). The porosity, ε_i, is a constant value for each soil type, whereas $\theta_{i,t}$ varies in time and is determined by SWAT's soil moisture routines. The effective depth coefficient, EDC_i, a parameter ranging from zero to one, is used to partition soil moisture in excess of ε_i into infiltrating (groundwater) and runoff fractions (including rapid shallow interflow). EDC_i is spatially varied based on a saturation probability defined by a soil wetness index (Easton et al., 2008). This spatially adjusted available storage is then used to partition rainfall into infiltration and runoff, q_i (mm):

$$q_i = \begin{cases} 0 & if\ P < \tau_i \\ P - \tau_i & if\ P > \tau_i \end{cases}. \quad (2)$$

The available soil storage, τ_i, is calculated each day and once precipitation starts, a portion of the rain, equal in volume to τ_i, will infiltrate the soil. If the rainfall event is larger in volume than τ_i, the soil profile will saturate and surface runoff will occur. If the rainfall is less than τ_i, the soil will remain unsaturated and there will be no surface runoff and SWAT's internal soil moisture routing will calculate the flux.

3.2. HRU definition

HRUs are defined in SWAT as unique combinations of soil type, land cover, and slope class. However, in basins dominated by variable source area (VSA) hydrology this HRU definition has been insufficient for describing the spatial variations in runoff generating areas (Schneiderman et al., 2007; Easton et al., 2008). Runoff-generating areas are likely to occur in portions of the landscape with shallow, low conductive soils, large upslope contributing areas, mild slopes, or any combination of the three. To include upslope contributing area while defining HRUs, a topographic index was integrated with existing soil data to create a soil topographic index (*STI*), which is then used in the SWAT-WB HRU definition process (Easton et al., 2008). The *STI* is defined as (Beven, 1986):

$$\lambda = \ln\left(\frac{\alpha}{T_0 \tan\beta}\right). \quad (3)$$

The upslope contributing area, α, and the slope, $\tan(\beta)$, were both obtained from a DEM, while the lateral transmissivity (L^2T^{-1}) of the soil profile, T_0, when water table intersects the soil surface (Beven, 1986) is a function of the soil layer depth, D_0, and soil layer saturated hydraulic conductivity, K_{s0}, ($T_0 = K_{s0} \cdot D_0$), and are obtained from the SSURGO database (USDA-NRCS, 2000). The *STI* values relate to a location's likelihood of saturation, and therefore the likelihood to contribute surface runoff. Values of STI are used to create wetness classes and are used to represent a location's likelihood to saturate. This wetness class map is then substituted for the soil map in the HRU definition process. While the wetness classes were used in HRU delineation instead of a soil type, SWAT still requires specific soil properties. Thus, in SWAT-WB soil properties obtained from the SSURGO database were areally weighted and averaged for each wetness class.

3.3. Sediment transport in SWAT

The SWAT model simulates soil erosion and sediment export from hillslopes as well as in-stream channel processes (Neitsch et al.,

2005). Erosion caused by rainfall and runoff is calculated with the Modified Universal Soil Loss Equation (MUSLE) as:

$$sed = 11.8 \cdot \left(Q_{surf} \cdot q_{peak} \cdot area_{hru}\right)^{0.56} \cdot K \cdot C \cdot P \cdot LS \cdot CFRG \quad (4)$$

where *sed* is the sediment exported from a HRU to the channel on a given day (metric tons), Q_{surf} is the surface runoff volume (mm ha^{-1}), q_{peak} is the peak surface runoff rate (m^3 s^{-1}), $area_{hru}$ is the area of the HRU (ha), *K* is the USLE soil erodibility factor (T h MJ^{-1} mm^{-1}), *C* is the USLE cover and management factor (dimensionless), *P* is the USLE support practice factor (dimensionless), *LS* is the USLE topographic factor (dimensionless) and *CFRG* is the coarse fragment factor (dimensionless). The use of a runoff term in the equation avoids the use of a sediment delivery ratio.

Watershed models widely used in sediment source assessment use various forms of the Universal Soil Loss Equation (USLE) for soil loss and sediment yield estimates. The use of these algorithms, developed from field scale evaluations, in watershed scale models has been cautioned by several researchers (Wischmeier and Smith, 1978; Risse et al., 1993; Kinnell, 2004). This is because of the need for validating these empirically derived equations at the watershed scale. However, a physically based hydrology model such as the SWAT-WB when coupled with the MUSLE may reduce uncertainty in soil erosion and sediment yield prediction when compared to the original USLE based calculations of long term sediment yields that are highly sensitive to topographic factors. Given the episodic nature of erosion and its variability in space, it is important to develop deterministic models capable of predicting the location and extent of sediment source areas. In many cases the eroded sediment originates from a small fraction of the landscape. Such information is required by watershed managers for effective implementation of sediment control practices.

Deposition and degradation are the dominant channel processes influencing sediment yield at the basin outlet. These channel processes are determined by the upland sediment loads and also the transport capacity of the channel network. The transport capacity of the channel segment is determined by the simplified Bagnold's equation (Bagnold, 1977):

$$T_{ch} = a \cdot v^b \quad (5)$$

where T_{ch} (T m^{-3}) is the transport capacity of a channel segment, *a* and *b* are user defined coefficients, and *v* (m s^{-1}) is the peak channel velocity. In addition parameters related to channel cover and channel erodibility that have a linear influence on channel contribution of sediment can be adjusted in SWAT.

3.4. SWAT model set up and calibration

A digital elevation model (DEM) of the basin obtained from the New York City Department of Environmental Protection (NYCDEP) with 10 m horizontal and 0.1 m vertical resolutions was used to delineate the watershed into 19 sub-basins. The sub-basins were further divided into 554 HRUs based on the method outlined above. A land use map derived by supervised classification of 2001 Landsat Enhanced Thematic Mapper Plus (ETM+) imagery was obtained from NYCDEP. Samples for each land use class were selected from the classification. An equalized random sampling approach was used, with 150 samples specified for each class. The sample pixels were compared with the original Landsat image and the reference 2001 orthoimagery to visually interpret their true land cover type. The generated land use map had an overall classification accuracy of 57%. SWAT simulations require daily meteorological data including precipitation, temperature, wind, humidity and solar radiation. Daily precipitation data were obtained from cooperator stations recognized by the National Climate Data Center (NCDC) and through the Northeast Regional Climate Center (NRCC). Minimum and maximum daily air temperatures for model input were derived from four stations in the NRCC data set. All other regional weather parameters were simulated by the model using a weather generator encoded within SWAT.

The model was calibrated for streamflow and sediment yield at the watershed outlet for the 1991–1995 water years and validated for the 2000–2002 water years. Measured daily streamflow data was obtained from the USGS gauging station (#01423000) located at the watershed outlet near Walton. Daily time series of total suspended solids (TSS) collected near the Walton stream monitoring station using a sampling protocol that allowed accurate estimation of both baseflow and storm event sediment loads (Longabucco and Rafferty, 1998). The calibrated streamflow and sediment models were used to simulate a historical baseline scenario (1965–2008) of sediment yield using measured meteorological forcing.

3.5. Future climate scenarios

The potential effect of climate change on soil erosion and sediment yield was evaluated using scenarios derived from a suite of nine Global Climate Model (GCMs) that represent a wide range of future climate conditions, during the 2081–2100 future period (Table 1). In this study, the A1B scenario from the Special Report on Emission Scenarios (SRES) in the IPCC Fourth Assessment Report (AR4) was used. This greenhouse gas emission scenario represents rapid economic growth with balanced emphasis on all energy sources. Data from the selected GCMs for the region surrounding the NYC water supply were extracted and interpolated to a common 2.5° grid using bilinear interpolation for baseline scenario (20C3M) for the period 1960–2000 and a future A1B emission scenario for the period 2081–2100. Climate scenarios were downscaled using change factor methodology described in Anandhi et al., 2011. Monthly change factors (CFs) were calculated from the difference between baseline (20C3M) and future GCM simulations. These monthly CFs were used to adjust the same local meteorological data used for the baseline simulation to represent the future climate conditions associated with a given GCM. Use of long term observed data in generating future climate scenarios ensured that the scenarios were representative of the observed climate patterns in the region. The nine GCMs selected in this study have high skill in simulating the observed precipitation or temperatures (Anandhi et al., in review).

4. Results and discussion

4.1. Model calibration for hydrology and sediment

Both hydrology and sediment calibration used the goal of maximizing the coefficient of determination (R^2), maximizing Nash–Sutcliffe efficiency (NSE) (Nash and Sutcliffe, 1970), and minimizing percent bias. In addition, hydrology calibration was optimized so that the runoff and baseflow components of streamflow were simulated reasonably well compared to values derived from measured

Table 1
GCMs used in this study.

GCM ID[a]	Acronym used
CGCM3.1 (T47)	CC4
CGCM3.1 (T63)	CC6
CSIRO-MK 3.0	CS0
GISS-AOM	GAO
GFDL-CM 2.0	GF0
IPSL-CM4	IPS
MIROC3.2 (HIRES)	MIH
ECHAM5/MPI-OM	MPI
MRI-CGCM 2.3.2	MRI

[a] As provided by Lawrence Livermore National Laboratory's Program for Coupled Model Diagnosis and Intercomparison (PCMDI): http://www-pcmdi.llnl.gov/ipcc/model_documentation/ipcc_model_documentation.php.

Table 2
Monthly model calibration statistics.

	Calibration 1991–1995	Validation 2000–2002
Streamflow		
R^2	0.76	0.71
NSE	0.76	0.68
% bias	+2.0%	−2.0%
Sediment		
R^2	0.62	0.70
NSE	0.61	0.70
% bias	−6.0%	−4.0%

data using standard baseflow separation techniques (Arnold and Allen, 1999).

In addition to the *EDC*, twenty parameters were calibrated which controls the hydrologic processes involved in streamflow generation including partitioning precipitation into infiltration and runoff, baseflow recession, and the rates of snowpack development and depletion. The calibrated model simulated streamflow reasonably well as evident from the monthly statistics for the calibration and validation period (Table 2). Predicted and measured monthly streamflow for the calibration and validation periods are presented in Fig. 2. Although the model was able to capture most peaks, it underestimated the measured streamflow during certain periods.

Soil erodibility, cover and management factors in the MUSLE equation, parameters related to sediment transport capacity (Eq. (5)), the channel cover parameter and the channel erodibility parameter were calibrated to optimize sediment yield results. The simulated contribution of stream channel processes to total sediment yield was only about 6% which is consistent with previous studies in the same watershed (Nagle et al., 2007; Tolson and Shoemaker, 2007). The calibrated model simulated suspended sediment load at the watershed outlet with acceptable model performance (Table 2). Predicted and measured sediment loads for the calibration and validation periods are presented in Fig. 3. Any discrepancy observed between measured and simulated sediment loads were either related to error in stream flow prediction or due to some inherent deficiency in the model especially during winter months.

4.2. Spatial variability in runoff and sediment source areas

Figs. 4 and 5 show the spatial variability in runoff and sediment generating areas across the watershed. The sub-basins generating maximum runoff were also found to generate maximum sediment through surface/hillslope erosion. The model computes the sediment generated from each HRU and thereby enabling identification of the actual location of erosion within a sub-basin. The high sediment generating areas would be a combination of relatively high surface runoff and erosive land cover (e.g.; agricultural field). The HRU maps of the highest sediment generating sub-basins were visualized to locate the sites of maximum erosion.

The long-term (1965–2008) average annual sediment export (transport of eroded sediment from hillslopes to stream channels) from each combination of wetness index class and major land use is presented in Table 3. The highest sediment export rate was from a combination of wetness class one and agricultural land use and progressively decreasing to higher wetness classes. In our classification scheme wetness class one has the highest probability of getting saturated followed by two, three and so on. As expected forests and brush lands produced less erosion than agricultural land use in addition to following the same pattern for the wetness index classes. Erosion from the last four wetness classes was minimal. A combination of wetness class seven with agricultural or brush land did not exist anywhere in the watershed.

4.3. Model evaluation of future climate impact on soil erosion and sediment yield

Simulated future changes in watershed water balance that may influence soil erosion and sediment yield are presented in Fig. 6. Our analysis of future climate impact on sediment included changes in basin wide average annual sediment export from HRUs as well as changes in average annual sediment yield (sediment exiting the watershed outlet) (Table 4). Future sediment export from HRUs based on the wide range of future climate conditions represented by the GCMs showed wide variability. The ensemble mean showed a net increase in future sediment export by 49% from average historical values indicating the possibility of higher rates of soil erosion in the future (2081–2100). The results are biased by one of the GCMs (MIH) without which the increase in future sediment export dropped to 27%. Such increasing rates of sediment export due to soil erosion are comparable with Nearing et al. (2004) who predicted similar rates of increase to occur in multiple sites across the U.S., based on two GCMs. In comparison, the sediment yield from the watershed outlet showed only a 3.9% increase in the ensemble mean compared to average historical values. Sediment export from HRUs is influenced by precipitation and surface runoff while sediment yield at the watershed outlet is primarily influenced by stream flow. Decreased sediment yield at the watershed outlet relative to the soil erosion rates predicted by the model under simulated future climate could be due to the inability of the model to account for sediment deposited in the channel. The model works on daily time steps and sediment deposited in the channel is not considered in subsequent time steps.

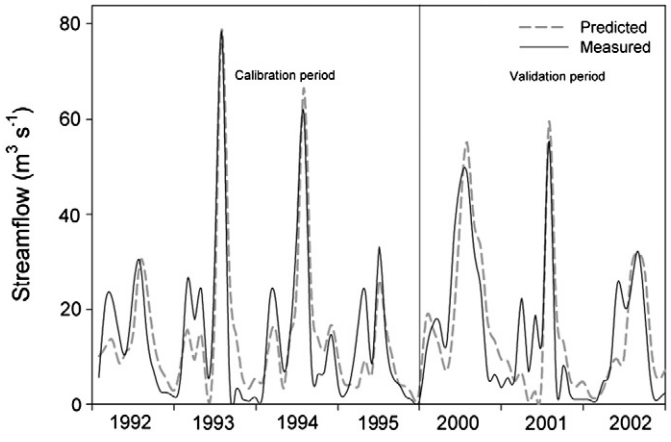

Fig. 2. Predicted vs measured streamflow.

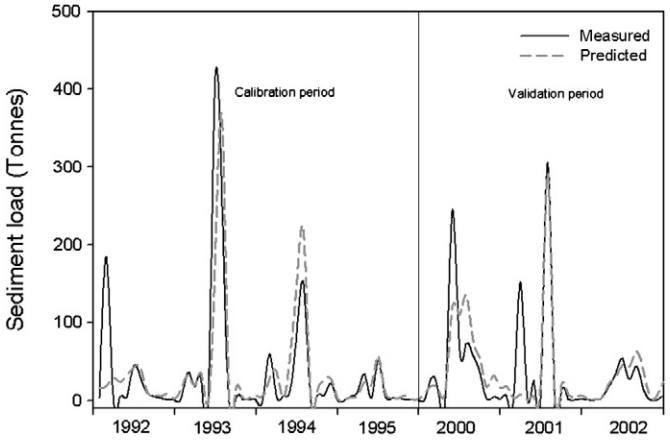

Fig. 3. Predicted vs measured sediment load.

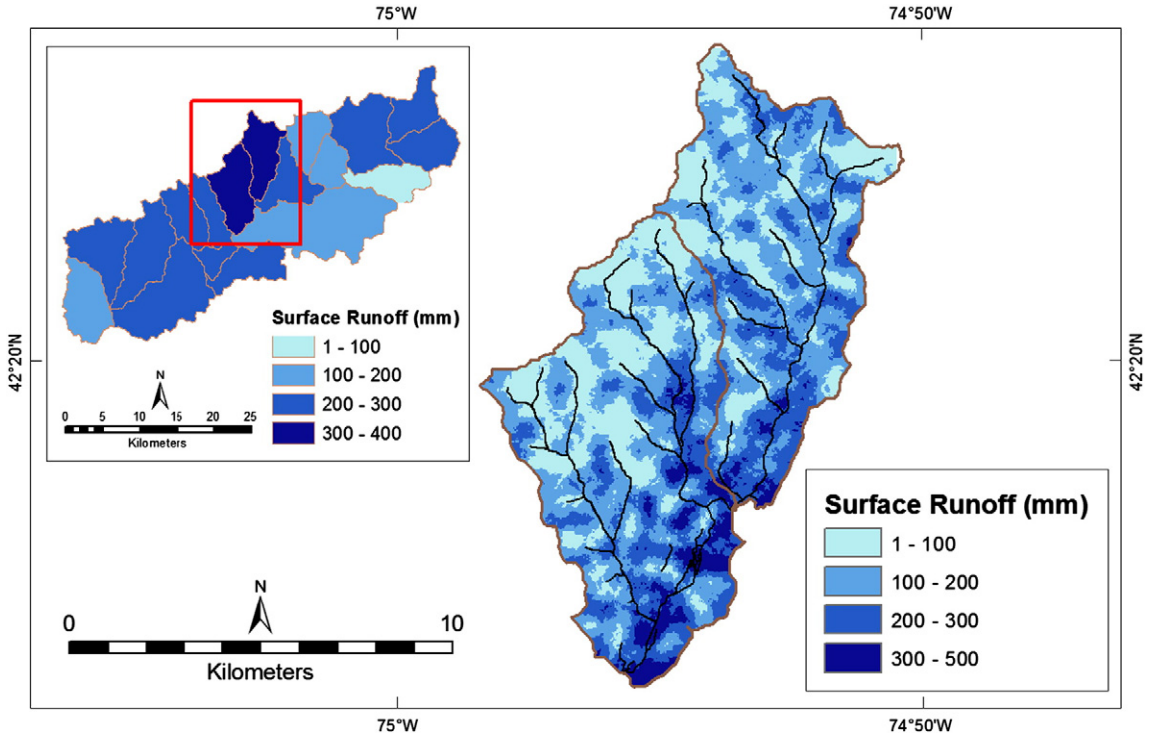

Fig. 4. Map showing spatial distribution of runoff generating areas at sub-basin level (inset) and HRUs from the dominant runoff generating region. Values are average annual estimates.

Analysis of seasonal changes in basin wide sediment export from HRUs showed increases in the winter and in the early spring and decreases in the summer and in early fall season (Fig. 7). The increase was much higher in magnitude compared to the decrease. This increase is due to the combined effect of increase in precipitation (Fig. 6a) and also the decrease in precipitation falling as snow. The existence of this phenomenon has already been detected in northeast U.S. catchments over the past fifty years (Hodgkins et al., 2003; Burns et al., 2007). The SWAT model predicts less erosion in the presence of snow. A comparison of the cumulative annual proportion of precipitation received as snow predicted by the model between the historical and future scenarios showed a sharp decline by 46% in the ensemble

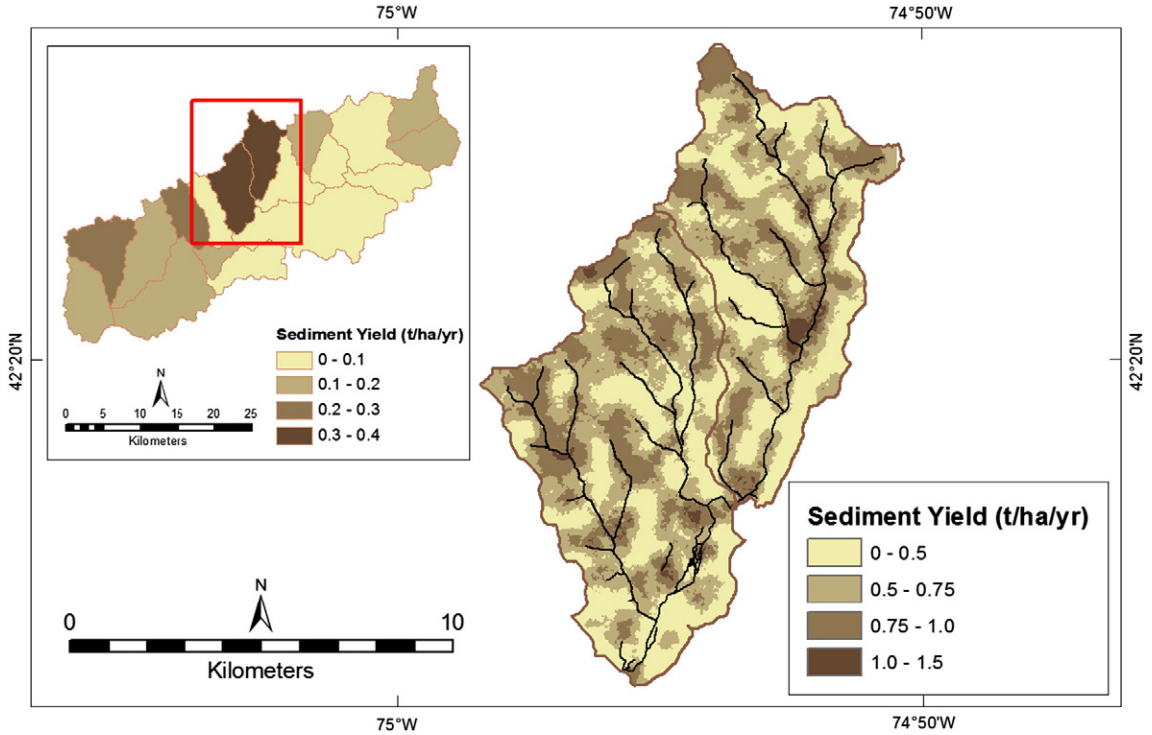

Fig. 5. Map showing spatial variability in average annual sediment export from sub-basins (inset) and HRUs expressed as sediment yield to stream channels from the dominant sediment generating region.

Table 3
Average annual sediment export from land use wetness index combinations. Wetness class one indicates the wettest conditions and class ten indicates the driest conditions.

Land use	Sediment export from wetness index class (t ha^{-1} year^{-1})									
	One	Two	Three	Four	Five	Six	Seven	Eight	Nine	Ten
Forest	0.04	0.05	0.02	0.02	0.02	0.02	0.00	0.00	0.00	0.00
Agriculture	1.03	0.74	0.43	0.37	0.34	0.46	–	0.00	0.00	0.00
Brush land	0.10	0.09	0.04	0.04	0.02	0.02	–	0.00	0.00	0.00

Table 4
Table showing average annual sediment export from HRUs and watershed outlet.

Scenario	Sediment export (t ha^{-1} year^{-1}) (2081–2100)	% change from baseline	Sediment yield (t ha^{-1} year^{-1}) (2081–2100)	% change from baseline
CC4	0.143	+6	0.085	−2.1
CC6	0.158	+18	0.106	+22.6
CS0	0.076	−43	0.069	−20.7
GAO	0.079	−41	0.085	−2.6
GFO	0.214	+59	0.091	+5.4
IPS	0.311	+131	0.081	−6.5
MIH	0.445	+231	0.100	+15.3
MPI	0.287	+113	0.109	+25.5
MRI	0.093	−31	0.085	−1.6
Average	0.194	+49	0.090	+3.9

mean with a range of 38–62% decline predicted by the nine GCMs (Fig. 6c).

Decrease in erosion during summer and early fall period may be related to the changes in antecedent soil water content during rainfall events under future conditions. Although an increase in summer rainfall was predicted by the GCMs (Fig. 6b) increases in evapotranspiration (Fig. 6d) can cause reduction in soil water content which may result in increased saturation deficit (τ_i in Eq. (1)). This means that more rainfall is required to bring the soil to saturation and generate equal amount of runoff as the current conditions. The importance of antecedent soil moisture on erosion from saturation excess dominated landscapes has been previously reported (Fitzjohn et al., 1998). Analysis of one of the HRUs under agricultural land use and soil wetness class one revealed an increase in crop biomass productivity during the months July and August by 19% and 29% respectively suggesting an earlier onset of growing season due to warmer climate. Such phenological changes are expected to affect the amount and timing of residue going back to the soil and thus soil erosion. These results are consistent with the finding of Nunes et al. (2011) using a SWAT model application for climate change assessment of soil erosion in two Mediterranean watersheds.

Future trends in sediment yield at the watershed outlet followed the soil erosion trends for most months except for March and April

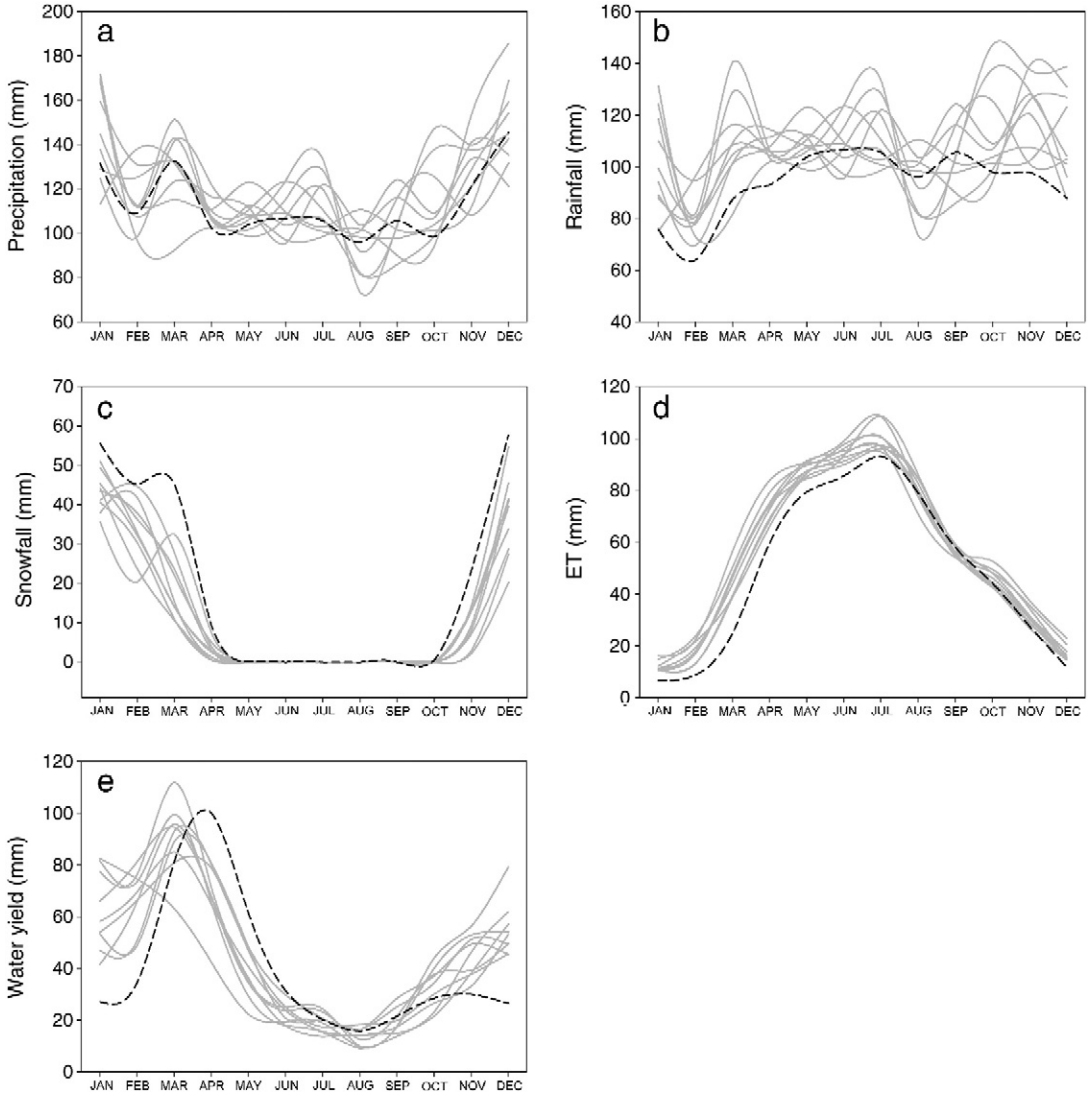

Fig. 6. Monthly simulated components of the watershed water balance, Historical (1965–2008) in dark dotted lines versus Future (2081–2100) in gray lines.

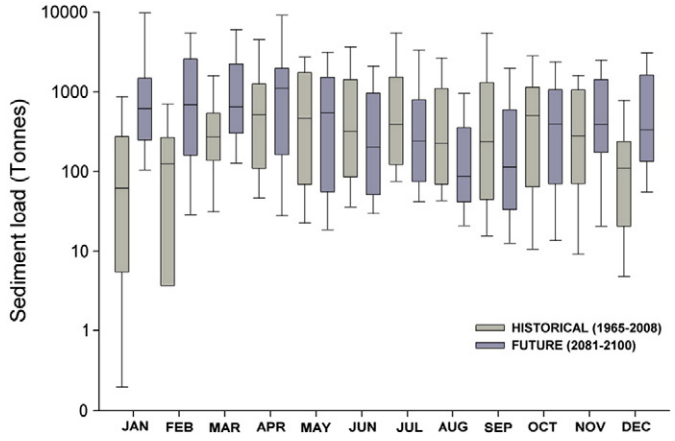

Fig. 7. Boxplot of average monthly basin wide sediment export from HRUs expressed as sediment load to stream channels. Boxes represent the 25th and the 75th percentile and whiskers represent the 10th and 90th percentile values.

(Fig. 8). These two months transported the maximum amount of sediment through the watershed outlet as seen in the historical scenario. Decline in sediment yield in these months during future periods explains to a certain extent the relatively small increase in average annual sediment yield at the watershed outlet (Table 3). The decrease in sediment yield is related to the decrease in basin wide streamflow during this period. This decrease in sediment yield predicted is consistent with the findings of Burns et al. (2007) who found a sharp decreasing trend in streamflow during April in the same region although a similar trend in precipitation was not evident. The decrease in April streamflow results from early snowmelt being observed in the region (Burns et al., 2007; Matonse et al., 2011; Zion et al., 2011). Although summer precipitation appeared to increase in the future scenarios, a decrease in water yield resulting from an increase in saturation deficit (described above) predicted by the model (Fig. 6d and e) coupled with a decrease in erosion resulted in less sediment yield at the watershed outlet in the summer.

4.4. What to expect in the future?

The results of this study indicate that under future climate scenarios the rate of surface erosion from fields and hillslopes may increase; however there may not be a significant increase in sediment yield at the watershed outlet. This conclusion depends on a number of assumptions within the modeling scheme. Our modeling indicated that majority of the stream sediment yield originated from surface erosion of hillslopes. This finding was consistent with the conclusions drawn by Nagle et al. (2007) and Tolson and Shoemaker (2007) for the same watershed. Other factors related to the fraction of sediment yield at the outlet due to stream channel sources versus landscape erosion sources may alter the quantitative results presented here.

We analyzed long term records of measured flow and stream water sediment concentration (1991–2008). For low flow (days when base flow was >90% of total flow) the median base flow TSS value was consistently below 3.0 mg L^{-1} between 1991 and 2005; however, in recent years (2007–2008) a relatively high median TSS value of 4.4 mg L^{-1} has occurred (Fig. 9). This increase might be attributed to an extreme event that occurred in June 27 of 2006 that generated the highest streamflow in a record that goes back to the early 1950s. This event created major changes in the watershed landscape in the form of hillslope erosion and mass wasting of tributaries and subsequent deposition of sediment in the main stem of the watershed (Eskeli, *Personal communication*). The long-term memory in stream TSS during low flows could be the result of re-suspension and subsequent transport of sediment that was deposited in the channel bed during this extreme event. A non-parametric Wilcoxon test on low flow TSS values two years prior (n = 355) and two years (n = 327) after 2006 indicated that this change in low flow TSS was statistically significant ($P<0.0001$). These results are indicative of the existence of a geomorphic threshold capable of altering the sediment transport rates and sediment supply in the fluvial system. Such thresholds could be either intrinsic (related to the geomorphic structure of the system such as critical shear stress of the stream banks) or extrinsic (related to changes in climate forcing) (Phillips, 2006).

Although the SWAT-WB model is capable of providing a general sensitivity on the effect of future climate, it is not developed to capture the subtle changes in the rate of sediment transport resulting from events such as the one in 2006. Depending on the frequency of such extreme events, the major sediment source in the Cannonsville watershed might shift in the future with eroding stream channels becoming the primary source. Such geomorphic changes could lead to non-stationarity in sediment transport rates, which is not represented in the SWAT-WB model.

Another area for improvement deals with the implications of the methods of producing future climate scenarios. Our study examines the effect of changes in magnitude of precipitation and air temperature on sediment loads; however the climate scenarios do not change the frequency of storm events and its effect on sediment loads are not represented here. In order to assume a one-to-one correlation between environmental forcing and sediment response, it is required that the sedimentary system remains in equilibrium or respond to the forcing in a linear fashion (Swenson, 2005). However, in reality potential changes in intensity and frequency of storm events as a

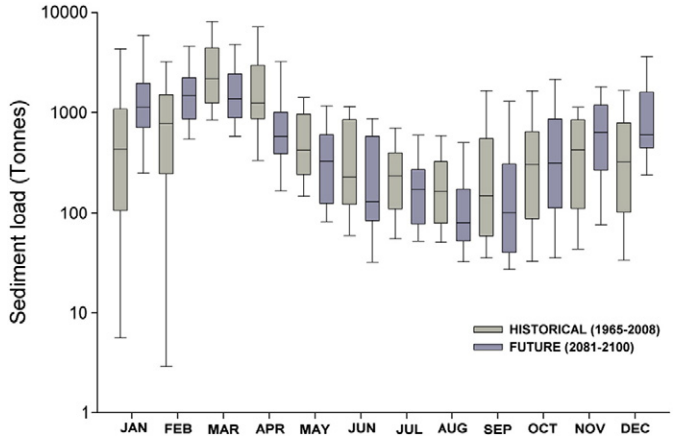

Fig. 8. Boxplot of average monthly sediment yield from watershed outlet. Boxes represent the 25th and the 75th percentile and whiskers represent the 10th and 90th percentile values.

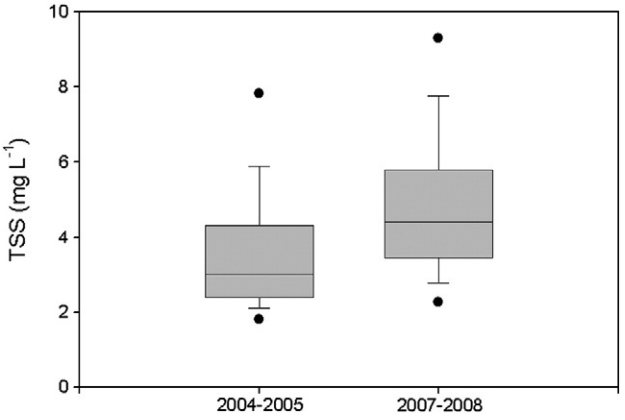

Fig. 9. Box plot showing shift in low flow suspended sediment concentration due to an extreme event in 2006.

result of global climate change may have varying impact on suspended sediment transport and the resulting turbidity. Increased precipitation following prolonged period of low flows are projected to exacerbate many forms of water pollution including sediment (Bates et al., 2008). However, one could argue that the impact of storm frequency on turbidity is influenced by several independent hydrological processes such as wetness/saturation of soils in watersheds with relatively high hillslope erosion or baseflow dilution and sediment supply in channel erosion dominated watersheds. Therefore, future changes in storm event frequency will make turbidity prediction difficult especially in channel erosion dominant watersheds.

5. Summary and conclusions

A physically based watershed model was used to identify the location of major sediment generating areas in a NYC water supply watershed. To evaluate the effect of future climate on soil erosion and sediment yield, the model output was compared using historical (1965–2008) and future (2081–2100) climate scenarios. The predictions presented here should be viewed as qualitative trends, rather than as absolute numerical predictions, given the uncertainty in future climate predictions, particularly since potential changes in extreme events are not completely captured by GCMs and downscaling method used in this study. Results indicate a sharp increase in the annual rates of soil erosion although a similar result in sediment yield at the watershed outlet was not evident. Analysis of seasonal changes in basin wide soil erosion and sediment export from HRUs showed an increase in the winter and in the early spring and a decrease in the summer and early fall seasons. Future simulated sediment yield at the watershed outlet followed the soil erosion results for most months except for March and April. Future climate related changes in soil erosion and sediment yield were more significant in the winter due to a shift in the timing of snowmelt and also due to a decrease in the proportion of precipitation received as snow. Although an increase in future summer precipitation was predicted, soil erosion and sediment yield appeared to decrease owing to an increase in soil moisture deficit and a decrease in water yield due to increased evapotranspiration.

Acknowledgment

We thank Dr. Allan Frei (Hunter College, City University of New York) for his support in this research project.

References

Aber, J.D., Ollinger, S.V., Federer, C.A., Kicklighter, D.W., Melillo, J.M., Lathrop Jr., R.G., Ellis, J.M., 1995. Predicting the effects of climate change on water yield and forest production in the Northeastern U.S. Climate Research 5, 207–222.

Anandhi, A., Frei, A., Pierson, D.C., Schneiderman, E.M., Zion, M.S., Lounsbury, D., Matonse, A.H., 2011. Examination of change factor methodologies for climate change impact assessment. Water Resources Research 47, W03501, http://dx.doi.org/10.1029/2010WR009104.

Arabi, M., Govindaraju, R.S., Hantush, M.M., Engel, B.A., 2006. Role of watershed subdivision on modeling the effectiveness of best management practices with SWAT. Journal of the American Water Resources Association 42, 513–528.

Arnold, J.G., Allen, P.M., 1999. Methods for estimating baseflow and groundwater recharge from streamflow. Journal of the American Water Resources Association 35, 411–424.

Asselman, N.E.M., Middelkoop, H., van Dijk, P.M., 2003. The impact of changes in climate and land use on soil erosion, transport and deposition of suspended sediment in the River Rhine. Hydrological Processes 17, 3225–3244.

Bagnold, R.A., 1977. Bedload transport in natural rivers. Water Resources Research 13, 303–312.

Bates, B.C., Kundzewicz, Z.W., Wu, S., Palutikof, J.P., 2008. Climate change and water. Technical Paper of the Intergovernmental Panel on Climate Change. Geneva, 210 pp.

Beasley, D.B., Huggins, L.F., Monke, E.J., 1980. ANSWERS: a model for watershed planning. Transactions of ASAE 23, 938–944.

Beven, K.J., 1986. Runoff production and flood frequency in catchments of order n: an alternative approach. In: Gupta, V.K., Rodriguez-Iturbe, I. (Eds.), Scale Problems in Hydrology. Reidel, Dordrecht, pp. 107–131.

Bicknell, B.R., Imhoff, J.C., Kittle Jr., J.L., Donigian Jr., A.S., Johanson, R.C., 1993. Hydrologic Simulation Program — FORTRAN (HSPF) User's Manual for Release 10. Report No. EPA/600/R-93/174. U.S. EPA Environmental Research Lab., Athens, GA.

Bouraoui, F., Grizzetti, B., Granlund, K., Rekolainen, S., Bidoglio, G., 2004. Impact of climate change on the water cycle and nutrient losses in a Finnish catchment. Climatic Change 66, 109–126.

Burns, D.A., Klaus, J., McHale, M.R., 2007. Recent climate trends and implications for water resources in the Catskill Mountain region, New York, USA. Journal of Hydrology 336, 155–170.

Cerucci, M., Conrad, J.M., 2003. The use of binary optimization and hydrologic models to form riparian buffers. Journal of the American Water Resources Association 39, 1167–1180.

Christensen, N.S., Wood, A.W., Lettenmaier, D.P., Palmer, R.N., 2004. Effects of climate change on the hydrology and water resources of the Colorado River Basin. Climatic Change 62, 337–363.

Cotter, A.S., Chaubey, I., Costello, T.A., Soerens, T.S., Nelson, M.A., 2003. Water quality model output uncertainty as affected by spatial resolution of input data. Journal of the American Water Resources Association 39, 977–986.

Easton, Z.M., Fuka, D.R., Walter, M.T., Cowan, D.M., Schneiderman, E.M., Steenhuis, T.S., 2008. Re-conceptualizing the Soil and Water Assessment Tool (SWAT) model to predict runoff from variable source areas. Journal of Hydrology 348, 279–291.

Easton, Z.M., Fuka, D.R., White, E.D., Collick, A.S., Biruk Asharge, B., McCartney, M., Awulachew, S.B., Ahmed, A.A., Steenhuis, T.S., 2010. A multi basin SWAT model analysis of runoff and sedimentation in the Blue Nile, Ethiopia. Hydrology and Earth System Sciences 7, 3837–3878.

Fitzjohn, C., Ternan, J.L., Williams, A.G., 1998. Soil moisture variability in a semi-arid gully catchment: implications for runoff and erosion control. Catena 32, 55–70.

Hanratty, M.P., Stefan, H.G., 1998. Simulating climate change effects in a Minnesota agricultural watershed. Journal of Environmental Quality 27, 1524–1532.

Hodgkins, G.A., Dudley, R.W., Huntington, T.G., 2003. Changes in the timing of high river flows in New England over the 20th Century. Journal of Hydrology 278, 244–252.

IPCC (Intergovernmental Panel on Climate Change), 2007. Climate change: impacts, adaptation and vulnerability. Contribution of Working Group II to the Fourth Assessment Report of IPCC. Cambridge, United Kingdom and New York, USA, 976 pp.

Jha, M., Gassman, P.W., Arnold, J.G., 2007. Water quality modeling for the Raccoon River Watershed using SWAT. Transactions of the ASABE 50, 479–493.

Kinnell, P.I.A., 2004. Letter to the editor on the mathematical integrity of some universal soil loss variants. Soil Science Society of America Journal 68, 336–337.

Kostaschuk, R., Terry, J., Raj, R., 2002. Suspended sediment transport during tropical-cyclone floods in Fiji. Hydrological Processes 17, 1149–1164.

Lawler, D.M., McGregor, G.R., Phillips, I.D., 2003. Influence of atmospheric circulation changes and regional climate variability on river flow and suspended sediment fluxes in southern Iceland. Hydrological Processes 17, 195–223.

Li, Y., Chen, B.M., Wang, Z.G., Peng, S.L., 2011. Effects of temperature change on water discharge, and sediment and nutrient loading in the lower Pearl River basin based on SWAT modelling. Hydrological Sciences Journal 56, 68–83.

Longabucco, P., Rafferty, M.R., 1998. Analysis of material loading to Cannonsville Reservoir: advantages of event-based sampling. Lake and Reservoir Management 14, 197–212.

Maeda, E.E., Pellikka, P.K.E., Siljander, M., Clark, B.J.F., 2010. Potential impacts of agricultural expansion and climate change on soil erosion in the Eastern Arc Mountains of Kenya. Geomorphology 123, 279–289.

Matonse, A.H., Pierson, D.C., Frei, A., Zion, M.S., Schneiderman, E.S., Anandhi, A., Mukundan, R., Pradhanang, S.M., 2011. Effects of changes in snow pattern and the timing of runoff on NYC water supply system. Hydrological Processes 25, 3278–3288.

Morgan, R.P.C., Quinton, J.N., Rickson, R.J., 1990. Structure of the soil erosion prediction model for the European community. Proceedings of International Symposium on Water Erosion, Sedimentation and Resource Conservation, 9–13 Oct 1990, Dehradun, India. Central Soil and Water Conservation Research and Training Institute, CSWCRTI, Dehradun, India, pp. 49–59.

Nagle, G.N., Fahey, T.J., Ritchie, J.C., Woodbury, P.B., 2007. Variations in sediment sources and yields in the Finger Lakes and Catskills Regions of New York. Hydrological Processes 21, 828–838.

Nash, J.E., Sutcliffe, J.V., 1970. River flow forecasting through conceptual models — part I: a discussion of principles. Journal of Hydrology 10, 282–290.

Nearing, M.A., 2001. Potential changes in rainfall erosivity in the United States with climate change during the 21st century. Journal of Soil and Water Conservation 56, 229–232.

Nearing, M.A., Foster, G.R., Lane, L.J., 1989. A process-based soil erosion model for USDA water erosion prediction project. Transactions of ASAE 32, 1587–1593.

Nearing, M.A., Pruski, F.F., O'Neal, M.R., 2004. Expected climate change impacts on soil erosion rates: a review. Journal of Soil and Water Conservation 59, 43–50.

Nearing, M.A., Jetten, V., Baffaut, C., Cerdan, O., Couturier, A., Hernandez, M., Le Bissonais, Y., Nichols, M.H., Nunes, J.P., Renschler, C.S., Souchère, V., Van Oost, K., 2005. Modelling response of soil erosion and runoff to changes in precipitation and cover. Catena 61, 131–154.

Neitsch, S.L., Arnold, J.G., Kiniry, J.R., Williams, J.R., 2005. Soil and water assessment tool: theoretical documentation — version 2005. Grassland, Soil and Water Research Laboratory, Agricultural Research Service. January 2005, 494 pp.

Nunes, J.P., Nearing, M.A., 2011. Modelling impacts of climatic change. In: Morgan, R.P.C., Nearing, M.A. (Eds.), Handbook of Erosion Modelling. Wiley-Blackwell, Oxford, pp. 289–312.

Nunes, J.P., Seixas, J., Keizer, J.J., Ferreira, A.J.D., 2009. Sensitivity of runoff and soil erosion to climate change in two Mediterranean watersheds. Part II: assessing impacts from changes in storm rainfall, soil moisture and vegetation cover. Hydrological Processes 23, 1212–1220.

Nunes, J.P., Seixas, J., Keizer, J.J., 2011. Modeling the response of within-storm runoff and erosion dynamics to climate change in two Mediterranean watersheds: a multi-model, multi-scale approach to scenario design and analysis. Catena, http://dx.doi.org/10.1016/j.catena.2011.04.001.

O'Neal, M.R., Nearing, M.A., Vining, R.C., Southworth, J., Pfeifer, R.A., 2005. Climate change impacts on soil erosion in Midwest United States with changes in crop management. Catena 61, 165–184.

Parry, M.L., Rosenzweig, C., Iglesias, A., Livermore, M., Fischer, G., 2004. Effects of climate change on global food production under SRES emissions and socioeconomic scenarios. Global Environmental Change 14, 53–67.

Phillips, J.D., 2006. Evolutionary geomorphology: thresholds and nonlinearity in landform response to environmental change. Hydrology and Earth System Sciences 10, 731–742.

Pradhanang, S.M., Anandhi, A., Mukundan, R., Zion, M.S., Pierson, D.C., Schneiderman, E.S., Matonse, A.H., Frei, A., 2011. Application of SWAT model to assess snowpack development and streamflow in the Cannonsville watershed, New York, USA. Hydrological Processes 25, 3268–3277.

Rakovan, M.T., Renwick, W.H., 2011. The role of sediment supply in channel instability and stream restoration. Journal of Soil and Water Conservation 60, 40–50.

Renard, K.G., Foster, G.R., Weesies, G.A., McCool, D.K., Yoder, D.C., 1997. Predicting soil erosion by water: a guide to conservation planning with the Revised Universal Soil Loss Equation (RUSLE). Agriculture Handbook N.703. U.S. Department of Agriculture Research Service, Washington, DC, USA. 348 pp.

Risse, L.M., Nearing, M.A., Nicks, A.D., Laflen, J.M., 1993. Error assessment in the universal soil loss equation. Soil Science Society of America Journal 57, 825–833.

Santhi, C., Arnold, J.G., Williams, J.R., Dugas, W.A., Hauck, L., 2001. Validation of the SWAT Model on a large river basin with point and nonpoint sources. Journal of the American Water Resources Association 37, 1169–1188.

Schneiderman, E.M., Steenhuis, T.S., Thongs, D.J., Easton, Z.M., Zion, M.S., Neal, A.L., Mendoza, G.F., Walter, M.T., 2007. Incorporating variable source area hydrology into a curve-number-based watershed model. Hydrological Processes 21, 3420–3430.

Swenson, J.B., 2005. Fluviodeltaic response to sea level perturbations: amplitude and timing of shoreline translation and coastal onlap. Journal of Geophysical Research 110, F03007, http://dx.doi.org/10.1029/2004JF000208.

Thodsen, H., Hasholt, B., Kjærsgaard, J.H., 2008. The influence of climate change on suspended sediment transport in Danish rivers. Hydrological Processes 22, 764–774.

Tolson, B.A., Shoemaker, C.A., 2007. Cannonsville Reservoir Watershed SWAT2000 model development, calibration and validation. Journal of Hydrology 337, 68–86.

USDA-NRCS, 2000. Soil Survey Geographic (SSURGO) Database for Delaware County, New York.

Varanou, E., Gkouvatsou, E., Baltas, E., Mimikou, M., 2002. Quantity and quality integrated catchment modeling under climate change with use of soil and water assessment tool model. Journal of Hydrologic Engineering 7, 228–244.

Walter, M.T., Walter, M.F., Brooks, E.S., Steenhuis, T.S., Boll, J., Weiler, K.R., 2000. Hydrologically sensitive areas: variable source area hydrology implications for water quality risk assessment. Journal of Soil and Water Conservation 3, 277–284.

White, E.D., Easton, Z.M., Fuka, D.R., Collick, A.S., Adgo, E., McCartney, M., Awulachew, S.B., Selassie, Y.G., Steenhuis, T.S., 2011. Development and application of a physically based landscape water balance in the SWAT model. Hydrological Processes 25, 915–925.

Wischmeier, W.H., Smith, D.D., 1978. Predicting rainfall erosion losses; a guide to conservation planning, U.S. Department of Agriculture, Agricultural Handbook No. 537. 58 pp.

Yang, D., Kanae, S., Oki, T., Koike, T., Musiake, K., 2003. Global potential soil erosion with reference to land use and climate changes. Hydrological Processes 17, 2913–2928.

Young, R.A., Onstad, C.A., Bosch, D.D., Anderson, W.P., 1987. AGNPS, agricultural nonpoint source pollution model: a watershed analytical tool. U.S. Department of Agriculture Conservation Research Report, 35.

Zhang, X.C., 2007. A comparison of explicit and implicit spatial downscaling of GCM output for soil erosion and crop production assessments. Climate Change 84, 337–363.

Zhang, X.C., Nearing, M.A., 2005. Impact of climate change on soil erosion, runoff, and wheat productivity in Central Oklahoma. Catena 61, 185–195.

Zhu, Y.M., Lu, X.X., Zhou, Y., 2008. Sediment flux sensitivity to climate change: a case study in the Longchuanjiang catchment of the upper Yangtze River, China. Global and Planetary Change 60, 429–442.

Zion, M.S., Pradhanang, S.M., Pierson, D.C., Anandhi, A., Lounsbury, D., Matonse, A.H., Schneiderman, E.S., 2011. Investigation and modelling of winter streamflow and timing and magnitude under changing climate conditions for the Catskill mountain region, New York, USA. Hydrological Processes 25, 3289–3301.

HYDROLOGICAL PROCESSES
Hydrol. Process. (2013)
Published online in Wiley Online Library
(wileyonlinelibrary.com) DOI: 10.1002/hyp.9894

Changes in the timing of snowmelt and the seasonality of nutrient loading: can models simulate the impacts on freshwater trophic status?

Donald C. Pierson,[1]* Nihar R. Samal,[2] Emmet M. Owens,[3] Elliot M. Schneiderman[1] and Mark S. Zion[1]

[1] *New York City Environmental Protection, Kingston, NY, USA*
[2] *Institute for Sustainable Cities, Hunter College, City University of New York, New York City, NY, USA*
[3] *Upstate Freshwater Institute, Syracuse, NY, USA*

Abstract:

The New York City water supply region, located in the Catskill Mountains in upstate New York, has always had a historically variable snow cover, with consequent effects on the magnitude of spring runoff and the relative importance of winter *versus* spring periods on annual hydrologic and nutrient budgets. Simulations show that under present conditions (1966–2005), on average 38% (12%–70%) of the annual total dissolved phosphorus load occurs during winter (Nov–Feb), while future predictions (2046–2065 and 2081–2100) show winter nutrient loads may account for an average of 46% (18%–73%) of the annual load. It is expected that changes in the importance of winter nutrient loading will lead to some increase in phytoplankton growth under isothermal conditions prior to the onset of thermal stratification, a reduced bloom coinciding with the onset of thermal stratification, and on an annual basis somewhat lower levels of biomass. However, future climate simulations using two different one-dimensional reservoir water quality models show no strong relationship between changes in algal biomass and the proportion of winter nutrient loading. The lack of a winter response calls into question model assumptions concerning the growth potential of phytoplankton under deeply mixed low light conditions, as well as factors influencing the bioavailability of nutrients input during the winter period. This illustrates the pitfalls of simulating future climate conditions, when the seasonality of model drivers has changed, and processes regulating winter conditions are not strongly represented. Copyright © 2013 John Wiley & Sons, Ltd.

KEY WORDS winter; hydrology; limnology; snowmelt; phytoplankton; nutrients; reservoirs

Received 19 August 2012; Accepted 2 May 2013

INTRODUCTION

The geographic distribution and quantity of lakes are strongly influenced by glacial processes, so that the greatest number of the world's lakes are located in formally glaciated areas particularly in areas across the Northern Hemisphere such as the Boreal region (Wetzel, 2001; Lehner and Doll, 2004). These northern locations today are ones where snow has an important influence on the annual hydrologic cycle, and where the seasonality of the hydrologic and biogeochemical processes regulating nutrient delivery to lakes are influenced by the accumulation and melting of snow. Despite a strong geographic relationship between the distribution of lakes and the occurrence of snow, there is surprisingly little information on the influence of snowmelt hydrology on limnology. This is no doubt due to the fact that rates of biological processes are greatest during the summer in north-temperate lakes and are strongly regulated by seasonal patterns of thermal stratification. However, there are many well-documented examples of microbial (e.g. Tulonen *et al*., 1994; Reitner *et al*., 1997; Straskrabova *et al*., 2005), algal (e.g. Phillips and Fawley, 2002; Kiili *et al*., 2009; Vehmaa and Salonen, 2009; Twiss *et al*., 2012), and zooplankton activity under winter conditions (e.g. Vanderploeg *et al*., 1992; DeBates *et al*., 2003; Balayla *et al*., 2010), and there is also an increasing appreciation of how conditions in the winter can have long-lasting effects that carry forward through the spring and into the period of summer stratification (Dokulil *et al*., 2006; Blenckner *et al*., 2007; Blank *et al*., 2009)

One consistent outcome of studies of the effects of climate change on watershed hydrology is a pronounced shift in the timing of streamflow due to increased winter air temperature and rain, decreased snow, and earlier snowmelt. Such changes have been found for NYC water supply watersheds (Matonse *et al*., 2011; Zion *et al*., 2011) and other watersheds across the United States and Europe (Andreasson *et al*., 2004; Barnett *et al*., 2005; Pierson *et al*., 2010). Such a shift in the timing of streamflow will lead to a

*Correspondence to: Donald Pierson, New York City Environmental Protection, Kingston, NY, USA.
E-mail: DPierson@dep.nyc.gov

greater proportion of the yearly nutrient load being delivered to a lake or reservoir during cold, deeply mixed, and possibly ice-covered conditions that would not be expected to lead to the highest rates of phytoplankton growth. Furthermore, decreased water residence time associated with the higher winter flows could increase nutrient loss from the system prior to more favorable growing conditions that develop in the spring. Consequently, for lakes and reservoirs in Northern climates where snow presently constitutes an important component of the hydrological cycle, it can be hypothesized that: (1) variations in the amount and timing of snowmelt runoff can affect the seasonal and annual levels of phytoplankton biomass; and (2) that under future climate conditions increases in winter nutrient loading could lead to reduced levels of eutrophication, or lessen eutrophication effects that may result from increased nutrient loading associated with future increases in precipitation.

Water quality models play an important role in evaluating the impacts of nutrient management on lake/reservoir quality under current conditions (e.g. Summer *et al*., 1990; Owens *et al*., 1998), and models are the only way to evaluate the future impacts of climate change on eutrophication (Elliott *et al*., 2005; Komatsu *et al*., 2007; Markensten *et al*., 2010). Most eutrophication models, however, focus on the period of summer stratification when phytoplankton growth is greatest and problems associated with eutrophication are most evident. The suitability of lake models to simulate the effects of changing winter processes that are expected to be strongly affected by climate change has been less rigorously tested. The purpose of this paper is to test the ability of two reservoir eutrophication models used by the New York City Department of Environmental Protection (DEP), to simulate the above hypothesized relationship between the magnitude and timing of snowmelt runoff and simulated levels of phytoplankton biomass.

METHODS

Study area

This study is based on model simulations of water quality in the Cannonsville Reservoir, which is part of the NYC water supply system (Figure 1). The Cannonsville watershed is 1178 km^2 and is predominately forested, but also has a significant proportion of agricultural landuse (10.1%). The reservoir has a surface area of 19.1 km^2, an average depth of 20.7 m, and a maximum depth of 52 m. The water residence time of the reservoir normally varies between 120 and 210 days. The regional climate is characterized as humid continental with cool summers (with average minimum, maximum, and mean temperatures of 12 °C, 22 °C, and 18 °C), and cold winters (with average minimum, maximum, and mean temperatures −10 °C, 0 °C, and −5 °C). This region experiences a uniform distribution of precipitation throughout the year. Typically, total precipitation is about 1000–1200 mm per year, with snowfall accounting for approximately 15–20% of total precipitation (Frei *et al*., 2002; Burns *et al*., 2007).

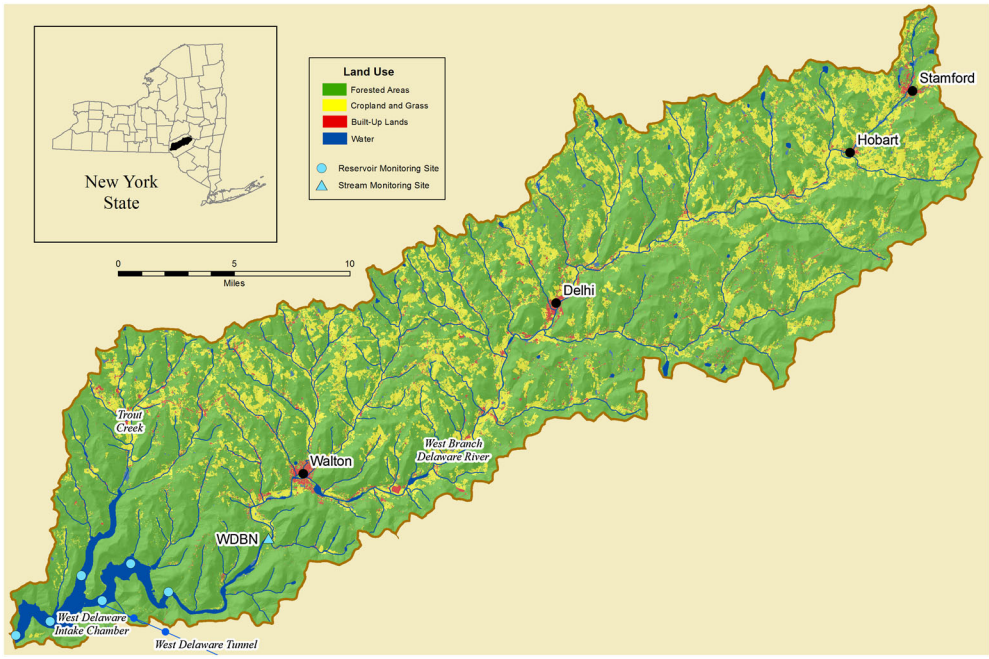

Figure 1. Cannonville reservoir and watershed

DOI: 10.1002/hyp

However, in this portion of New York State, snow accumulation and the importance of snow to the annual watershed water budget are quite variable. Based on 55 years of metrological data collected from the central portion of the Cannonsville watershed, Pierson and Kick (1995) estimated that peak snow water equivalent (SWE) accounted for between 1.2% and 18% of the total annual precipitation input to the watershed. Snowcourse measurements made between 1965 and 2012 within the Cannonsville watershed show peak SWE varying from less than 1 cm to nearly 15 cm, and also show that the timing and duration of snow cover can be quite variable. The onset, loss, and timing of lake ice cover can also be quite variable in this region. Unfortunately, ice cover has not been extensively monitored on Cannonsville reservoir. There are a limited amount of data collected over 5–7 years from Cannonsville and two nearby reservoirs in the NYC water supply which suggests that the duration of ice cover can vary between approximately 40 and 70 days. Ice development usually occurs between mid-December and mid-February, while ice loss usually occurs between late-March and mid-April. The Cannonsville reservoir was once eutrophic because of relatively high levels of agricultural activity, and other point and nonpoint source nutrient inputs. Following an aggressive program of watershed management and point source treatment upgrades, the reservoir water quality has now improved to mesotrophic quality.

Modeling framework

The models used in this study consist of the GWLF VSA watershed model to simulate reservoir inflow and nutrient load, and two versions of a one-dimensional reservoir water quality model that focuses on phytoplankton growth and eutrophication (Figure 2). GWLF VSA is a version of the GWLF model (Haith and Shoemaker, 1987; Schneiderman *et al.*, 2002; Schneiderman *et al.*, 2007), which is a lumped parameter model that simulates total watershed streamflow as the sum of a subsurface/delayed flow component based on a single basin-wide ground water reservoir, and land use specific surface runoff, that is further distributed based on a soil topographic index. GWLF VSA is driven by daily variations in air temperature and precipitation which can either be obtained from historical data measured in the reservoir watershed, or based on future climate scenarios. Nutrient export is estimated from the product of the simulated flow components and source specific nutrient concentrations. In GWLF VSA, snow is simulated using a simple temperature-based approach that assumes all precipitation entering the watershed when mean daily air temperature is less than 0 °C is snow and that the rate of snow melt above 0 °C is a function of the mean daily air temperature and a degree day melt factor. Zion *et al.* (2011) describe the GWLF VSA snow model in more detail and showed that the model reproduced historical trends in the timing of spring snowmelt runoff.

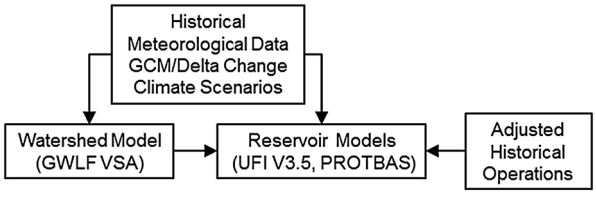

Figure 2. Models and data sources used to simulate changes in reservoir phytoplankton and trophic status. Both watershed and reservoir models are driven by daily changes in meteorological data that are either measured or derived from future climate scenarios. Daily variations in reservoir conditions also depend on reservoir operations, which determine reservoir outflow

The two reservoir water quality models used by DEP are built upon the same one-dimensional hydrothermal framework that was developed for DEP by the Upstate Freshwater Institute (Owens, 1998) The hydrothermal sub-model simulates the reservoir thermal structure and the rate of inflow, outflow, and vertical exchange between one meter vertical cells. GWLF VSA provides the hydrologic inputs to the reservoir model as well as dissolved and particulate loads of nitrogen, phosphorous, and silica. The concentration of nutrients in the reservoir are dependent on the transformation and biological uptake of the nutrients simulated by the water quality sub-models, as well as mixing and redistribution as simulated by the hydrothermal sub-models. Both water quality models examined here simulate phytoplankton growth as a function of water temperature, light, and nutrients.

The UFI version 3.5 (UFI V3.5) water quality sub-model is based on the model described by Doerr *et al.* (1998). This model has a single phytoplankton component which has a maximum growth rate that varies as a function of temperature and a single rate of light limited growth that occurs below a fixed light threshold. Growth is further related to the concentration of the growth-limiting nutrient, based on a Michaelis–Menten relationship between ambient nutrient concentration and growth.

The second model is based on the PROTECH model as developed by Reynolds *et al.* (2001), and later modified by Markensten and Pierson (2007) and renamed PROTBAS. In PROTBAS, there are eight major algal functional groups, each of which has distinct allometric characteristics parameterized by the algal surface area, volume, and axial length, characteristics that define the need for silica, the ability to fix nitrogen, and information related to rates of motility and sinking. For each functional group, the maximum temperature-dependent rate of growth and rate of light-limited growth are based on allometric relationships. In PROTBAS, the uptake of nutrients is related to growth using a fixed stoichiometric ratio between algal carbon and nutrients, so that growth continues until the nutrient in lowest supply is depleted to

DOI: 10.1002/hyp

below a threshold concentration. When comparing these two models, V3.5 has more detailed and realistic algorithms describing the transformations of nutrients and the effects of nutrient concentration on algal growth, while PROTBAS has a better description of the diversity of phytoplankton and the effects of phytoplankton characteristics on growth.

Climate scenarios

Future Climate Scenarios were based on Global Climate Models (GCM) data obtained from the World Climate Research Program's Coupled Model Intercomparison Project Phase 3 multi-model dataset. Daily datasets were downloaded for the baseline scenario (20C3M) during the period 1960–2000 and three future emission scenarios (A1B, A2, and B1) during two time periods (2045–2065 and 2081–2100), and all data sets were extrapolated to a common model grid (Anandhi *et al*., 2011). For this study, GCM/emission scenarios were chosen which contained all the meteorological variables (air temperature, precipitation, solar radiation, and wind speed) needed to drive both the watershed and reservoir models in the baseline and two future time periods (Table I). To create future climate scenarios, we made use of the frequency distribution-based change factor methodology proposed by Anandhi *et al*. (2011). Using this method, the monthly data from each time period are pooled, and for each month, a 25-bin frequency distribution is created from the pooled data. Twenty-five bins were suggested as an optimal number from the analysis presented by Anandhi (2011), and accordingly, 25 change factors are calculated for each month as the difference in the frequency distributions calculated under baseline and future time periods (Equation (1)).

$$CF_{add,n} = \overline{GCMf_n} - \overline{GCMb_n} \tag{1}$$

Where:

$CF_{add,n}$ is an additive change factor for bin n (1–25).

$\overline{GCMb_n}$ is the mean value of the meteorological variable of interest in bin n of the pooled monthly data from the GCM future scenario.

$\overline{GCMb_n}$ is the mean value of the meteorological variable of interest in bin n of the pooled monthly data from the GCM baseline scenario.

To create future scenarios, the change factors are added to historical climate data collected in the Cannonsville reservoir watershed. To do this, the historical data are again pooled on a monthly basis so that a 25-bin frequency distribution can be developed and each day in the historical record can be ranked by its position in the pooled monthly frequency distribution. Based on this rank the appropriate change factor is applied (Equation (2))

$$LSf_j = LOb_{n,j} + CF_{add,n} \tag{2}$$

Where:

LSfj is the future value of the meteorological variable of interest on day j scaled to local conditions

$LObn,j$ is the historical observed value of the meteorological variable of interest on day j that is ranked to be in bin n (1–25) in the pooled observed data for a given month.

$CF_{add,n}$ is an additive change factor for bin n (1–25).

This method retains the simplicity of the change factor approach that has been widely used for creating future climate scenarios (e.g. Hay *et al*., 2000), while at the same time allowing the change factors to be dependent on event magnitude as well as being seasonally variable.

Reservoir operations are an important determinant of reservoir water quality and will depend on variations in reservoir inputs, which are in turn affected by climate. Since the change factor approach of creating climate scenarios retains the historical sequence of events, historical records of reservoir operations can be used as the basis for future climate simulations. Scenarios of future operations (Figure 2) were created for the future

Table I. GCM models used to produce future climate scenarios. For each model scenarios were created for three emission scenarios (A1B, A2, and B1) and two future time periods (2045–2065 and 2081–2100)

GCM	Model name	Source/Country
CCSM3	Community Earth System Model	NCAR/USA
CNRM-CM3	Global Coupled System model Ver 3	CNRM/France
CSIRO-Mk3.0	CSIRO Mark 3	CSIRO/Australia
ECHO-G	ECHAM4 + HOPE-G	Germany/Korea
GFDL-CM2.0	Geophysical Fluid Dynamic Lab CM2	NOAA/USA
MRI CGCM2.3.2	Meteorological Research Institute CGCM2.3.2	MRI/Japan

DOI: 10.1002/hyp

climate scenarios using a preprocessor that calculated the reservoir water balance using scenario inputs and simulated future water surface elevation and spill. If necessary, the preprocessor also reduced the historical outflow from the reservoir to prevent storage from falling below a minimum level. The preprocessor used a simple model to estimate future inflowing water temperature as a function of scenario air temperature.

RESULTS AND DISCUSSION

All future climate scenarios simulated increased temperature in all months of the year with mean monthly winter (Nov–Feb) temperatures coming closer to, and in some cases, even exceeding 0 °C (Figure 3A). Changes in precipitation between present and future conditions were not as consistent, but in general, the GCM simulations suggest greater amounts of precipitation particularly in the fall and winter (Figure 3B). One of the most pronounced effects of climate change as discussed by Matonse *et al*. (2011) and shown here in Figure 3C was on the simulated level of snowpack SWE. As a result of the warmer winter air temperatures, all future climate scenarios simulated lower levels of snow accumulation, with anywhere from a 40% to 90% reduction in the mean monthly SWE (Figure 3D).

The effects of these changes on the seasonality of stream discharge and phosphorus loading, as simulated by GWLF VSA, are illustrated in Figure 4. Increased fall–winter precipitation, lower levels of snow accumulation, and earlier snowmelt all result in increased winter (Nov–Feb) streamflow and a somewhat decreased spring (Mar–Apr) runoff period. These results are consistent with many other climate change simulations in areas where snow influences the seasonality of streamflow (e.g. Barnett *et al*., 2005), and also with studies of the Catskill region (Burns *et al*., 2007; Zion *et al*., 2011), which show a shift in the timing of the spring runoff peak and increased winter levels of streamflow. The Catskill region of New York is an area where the snowpack can play an important role in the yearly hydrologic cycle, but also where the snow accumulation and melt can be highly variable. Consequently, variations in the seasonality of flow, particularly in regards to winter streamflow, are also highly variable.

Figure 5A and 5B summarizes results from GWLF VSA simulations and shows the proportion of annual streamflow and total dissolved phosphorus loading to the reservoir that occur during the winter months (Nov – Feb) under present baseline conditions and under future conditions based on data from the 36 future scenarios associated with the six GCMs (Table I), three emission scenarios, and two future time periods. Even under present conditions, the importance of the winter months

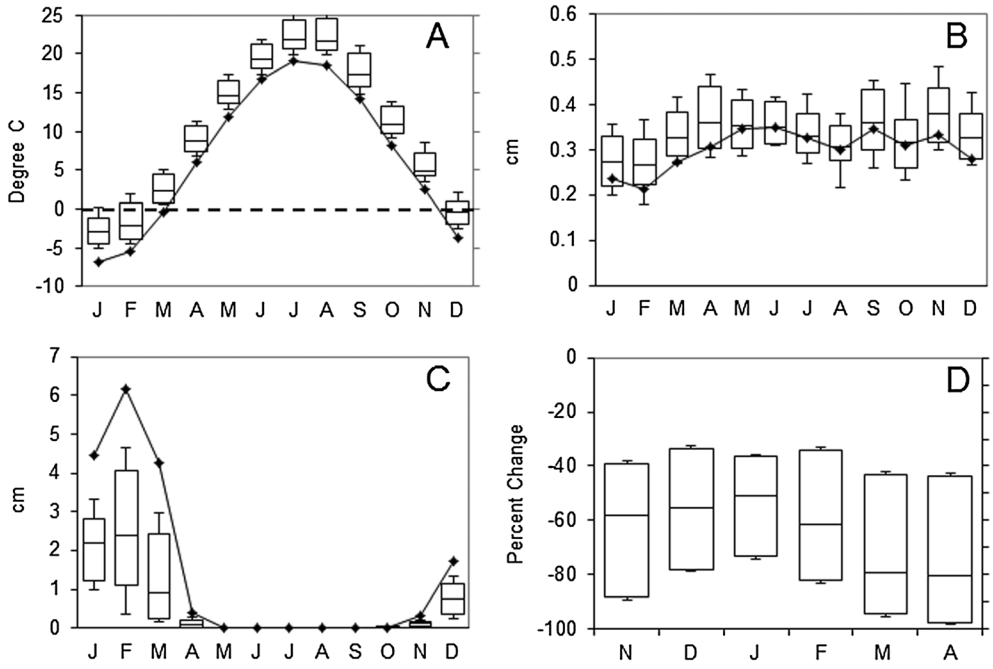

Figure 3. Seasonal variations in future climate scenarios and snowpack simulated using the GWLF VSA model. (A) Mean daily air temperature; solid line is the mean value for each month in the baseline scenario Dashed line shows 0 °C as a reference. Boxplots show the variability of the 36 future scenarios. (B) shows a similar plot for mean daily precipitation, and (C) shows the expected changes in mean snow water equivalent. (D) shows the percent change in the mean snow water equivalent between baseline and future conditions. Scenario box plots show the median, 90th percentile, 10th percentile, maximum and minimum values of the mean monthly values from the 36 future scenarios

DOI: 10.1002/hyp

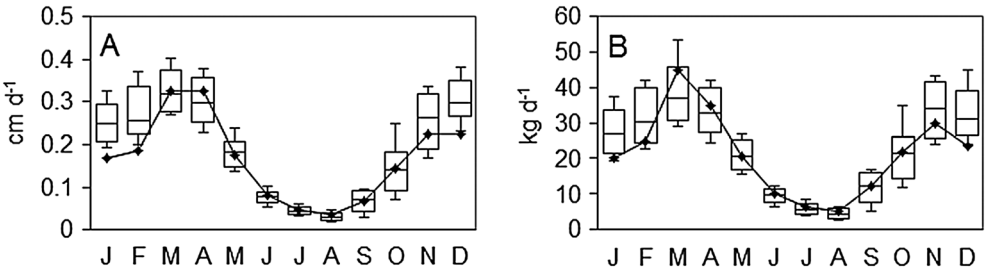

Figure 4. Simulated seasonal variation in streamflow (A) and TDP loading (B) under present and future conditions. The line shows the mean daily values for calculated each month, based on the pooled data from all months in the baseline scenario. Boxplots show the variability of the 36 future scenarios

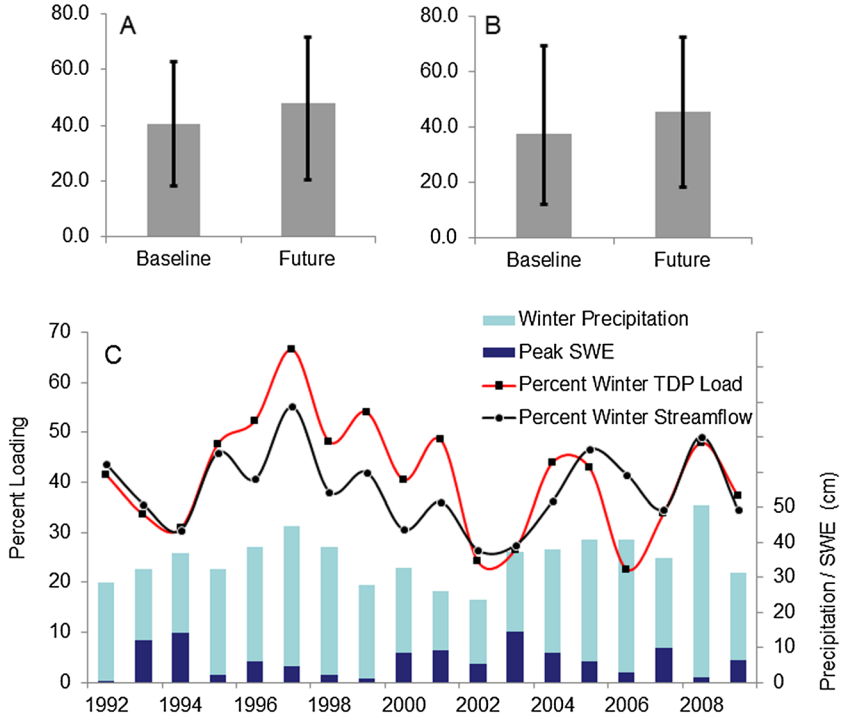

Figure 5. The percentage of the simulated total annual streamflow (A) or TDP load (B) that occurred during the winter months (Nov–Feb). Graphs show the median and maximum and minimum values of the baseline scenario, and the combined results of all future scenarios. Measured values of the percent winter streamflow and TDP loading from the Cannonsville watershed (C), as well as annual variations in winter total precipitation and peak SWE

in affecting the annual reservoir inputs is highly variable. Our simulations (Figure 5A and 5B) suggest that anywhere from 18% to 63% of the annual streamflow and 12% to 70% of the annual TDP, inputs can occur in the winter, while actual measurements (Figure 5C) confirm that between 26% and 55% of the annual streamflow and between 23% and 66% of the annual TDP, input occurs in the winter, and it is winters with relatively large amounts of precipitation and relatively low amounts of SWE that have the greatest percent export. With increasing winter flows in the future, there is also an increasing contribution of the winter months to the annual reservoir inputs. Median winter streamflow increases from 40% to 48% (Figure 5A) of the annual inflows, while the median winter TDP inputs increase from 38% to 46% of the annual values (Figure 5B). High levels of variability remain in the future simulations, with anywhere from 20% to 72% of the future streamflow and 18% to 73% of the future TDP inputs occurring in winter.

Given that phosphorus is the limiting nutrient that regulates phytoplankton biomass in the NYC water supply reservoirs, shifts in the timing of TDP inputs could be expected to impact overall levels of biomass as well as the seasonal patterns of phytoplankton biomass and succession. To examine how climate change will impact reservoir chlorophyll levels, reservoir model simulations were run under baseline conditions and compared to simulations driven by climate scenarios associated with the GCM models in Table I. The results of these simulations are shown in Figure 6, using both the

DOI: 10.1002/hyp

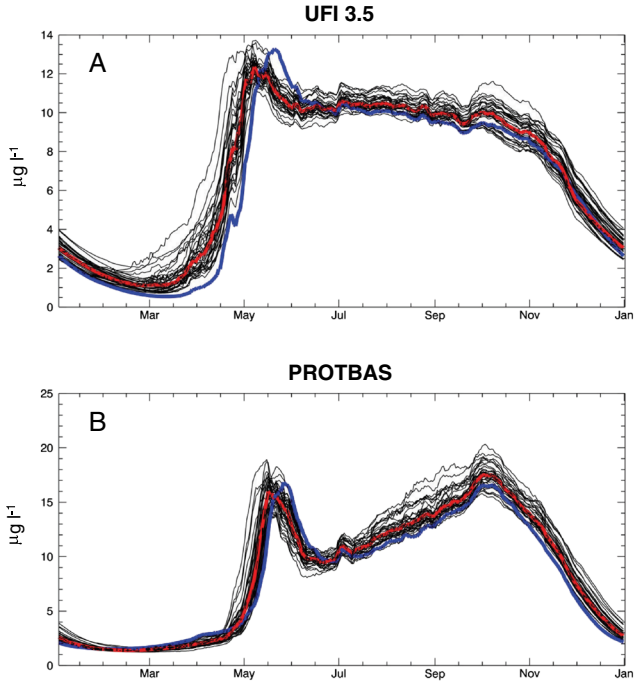

Figure 6. Seasonal variations in mixed layer chlorophyll concentration simulated with the UFI 3.5 (A) and PROTBAS (B) models. Each line is the mean daily value of the data from all years in a given scenario. Blue line is the baseline scenario, thinner black lines are associated with each of the 36 future scenarios, and the red line is the median of the future scenarios

UFI 3.5 and PROTBAS water quality models, and compare the seasonal patterns associated with baseline conditions (blue line) with the seasonal patterns associated with individual future scenarios or the median of the future scenarios (red line).

Both models show moderate (up to 10–15%) increases in mixed layer chlorophyll concentrations for the future scenarios, and both models also predict that the timing of the spring bloom will move forward by approximately 10–14 days. In general, the simulated increases were lowest during the winter period of isothermal mixing (Nov–Feb), and the shift in the timing of the spring bloom was related to simulated changes in the onset of thermal stratification, which is also expected shift forward in time as a result of climate change (Samal *et al.*, 2012). The somewhat different levels of biomass and slightly different seasonal patterns simulated by the two models are the result of differing modeling assumptions, particularly those affecting phosphorus uptake and phytoplankton settling. Both models, however, produce credible patterns of phytoplankton succession and levels of biomass. Comparison to measured data verifies that the levels of chlorophyll simulated are reasonable and that seasonal variations in chlorophyll follow the timing of thermal stratification as shown in Figure 6A. However, since available measured chlorophyll data are highly variable and collected at a 0.5 to 1.0 month frequency, it is not possible to determine which of the two seasonal patterns is most accurate.

The patterns in Figure 6 are average seasonal patterns, with each trace based on 39 simulation years. Between years, there are significant variations in the levels of biomass, as well as the timing and magnitude of the spring peak and fall bloom (Figure 7). Nutrients added to the reservoir during winter should be less likely to increase phytoplankton biomass since cold water temperature, deep mixing, ice cover, and low light exposure would all be expected to limit phytoplankton growth. We hypothesized that a relationship would exist between the proportion of TDP loading that occurred in the winter and the mean annual mixed layer chlorophyll simulated by our models, with years having a relatively high proportion of winter TDP loading having less annual biomass. In Figure 8, mean annual mixed layer chlorophyll concentration is plotted against the proportion of winter TDP load using data output from both the UFI 3.5 and PROTBAS models. In both cases, there is no clear relationship between the average annual chlorophyll concentration and the proportion of winter TDP loading, despite a large range in the proportion of TDP loading that occurs in the winter.

In an exercise such as this, it is difficult to determine if our hypothesis fails as a result of an incorrect theory, or as a result of the models not correctly representing the lake processes upon which the theory is based. To gain greater insight into model performance, we systematically varied the timing of nutrient input, without changing the amount of annual loading or the meteorological forcing affecting the reservoir model. A number of synthetic loading time series were created from the historical reservoir input data by taking 50% of the combined water and material loads from March and April and redistributing these into a

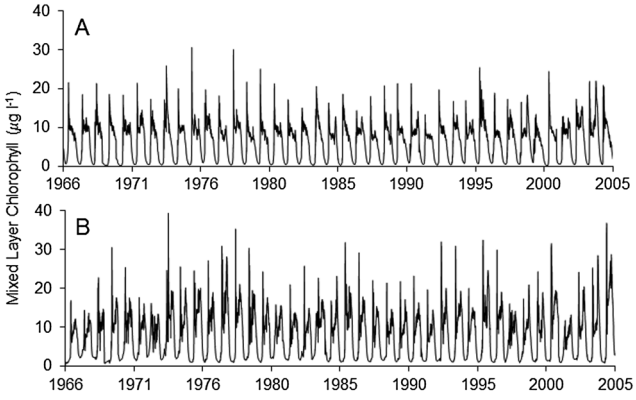

Figure 7. Daily variations the simulated mixed layer chlorophyll concentration produced using the UFI V3.5 (A) and PROTBAS (B) models for Cannonsville reservoir. The simulation shown here is based on historical (baseline) conditions

DOI: 10.1002/hyp

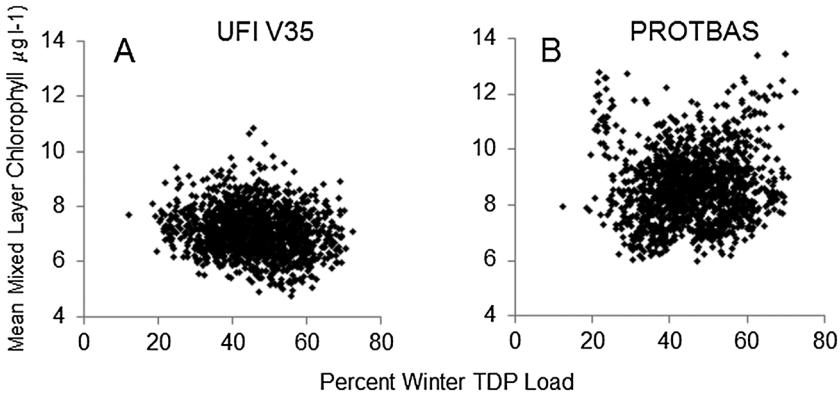

Figure 8. The relationship between mean annual mixed layer chlorophyll concentration and the percent of the annual TDP load that occurs in Nov–Feb. Each point is for a single year's data in the baseline and 36 future climate scenarios. The results from UFI V3.5 are shown in A and PROTBAS are shown in B

different month. In all, five synthetic loading records were created which redistributed the March–April loads into January and February, to simulate the expected future shift to earlier winter runoff, and also forward in time to May, June, and July to examine differences in response to shifting the loads to stratified as opposed to isothermal conditions.

Shifting 50% of the spring nutrient load to January or February (Figure 9A) resulted in virtually no change in the annual pattern of mixed layer chlorophyll or in the magnitude of the chlorophyll concentrations, which is consistent with the lack of relationship in Figure 8. On the other hand, the model predicts significant changes in the timing of peak biomass, as well as levels of biomass (Figure 9B) when the spring nutrient loading is shifted forward into thermally stratified period. Further analysis of the results from the sensitivity analysis shows that the timing of thermal stratification is critical for explaining the different responses in Figures 9A and 9B. During winter, the average light exposure experienced by the phytoplankton is low as a consequence of deep isothermal mixing, and light exposure is also limited due to lower incident irradiance during the winter months and the presence of lake ice and snow cover. Under such conditions, simulated rates of phytoplankton growth are strongly light limited, and the input TDP is not utilized and remains biologically available. Following the onset of thermal stratification, the mixed layer becomes shallower, and the phytoplankton circulating through this mixed layer are exposed to much higher average light intensity. Growth can then proceed until limited by nutrient availability. This is the classic explanation for the timing of the spring bloom (Riley, 1947; Sommer *et al.*, 1986) and its coincidence with the transition from light-limited to nutrient-limited growth.

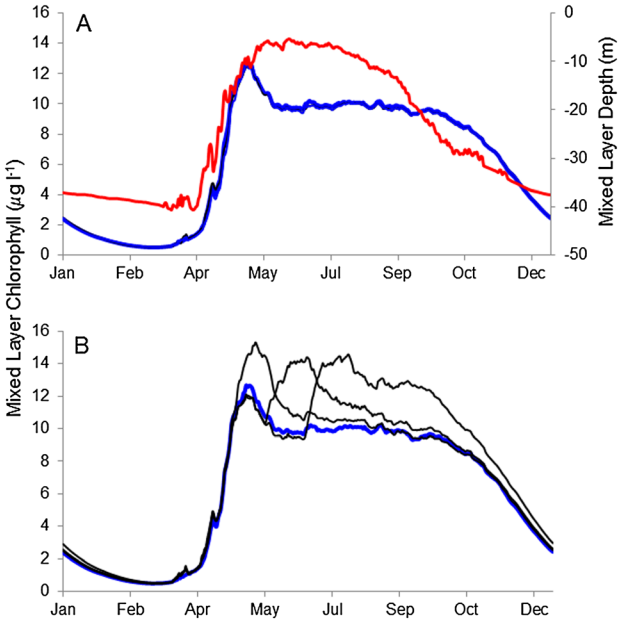

Figure 9. Sensitivity analysis which examined the effects of shifting 50% of the March + April nutrient load to winter conditions (A January and February) and summer conditions (B May, June, and July). Figures show mean daily patterns calculated from the full simulation time period. Thick blue line shows results under baseline conditions with no redistribution of the nutrient loads. Thin black lines show traces associated with redistributed loads. In part A, the simulated depth of the mixed layer is also plotted, as a red line. These are results using the UFI V3.5 model. The PROTBAS model showed similar results

Our models correctly simulate this transition, as can be seen from the strong relationship between the depth of the mixed layer and the onset of the spring bloom in Figure 9A, and a shift in the timing of the spring bloom that corresponds to an earlier onset of thermal stratification in future scenarios (Figure 6). In our models, it is the change in mixed layer depth and the consequent increase in light availability that determine the timing of the spring phytoplankton bloom. What is less clear is whether the models are correctly simulating the conditions that occur during the winter that affect phytoplankton growth and TDP bioavailability. For the models to be completely insensitive to the timing of TDP inputs during the winter period

DOI: 10.1002/hyp

(Figure 9A) requires that virtually no phytoplankton growth occurs and that no processes impact the bioavailability of TDP inputs during the winter. Both assumptions are not supported by lake studies under winter conditions. There are a number of studies that suggest microbial (Tulonen *et al.*, 1994; Reitner *et al.*, 1997) and phytoplankton (Phillips and Fawley, 2002; Kiili *et al.*, 2009) growth under winter conditions which would reduce the store of bioavailable TDP prior to the onset of thermal stratification. Furthermore, there are also numerous studies that have reported the phytoplankton blooms occurring under ice cover, e.g. (Catalan, 1992; Pettersson *et al.*, 2003; Twiss *et al.*, 2012) or during deeply mixed ice free conditions prior to the onset of thermal stratification (Horn *et al.*, 2011). Correctly simulating these effects would require accurately simulating the onset and loss of lake ice, stratification and mixing under ice, phytoplankton light adaptation to deeply mixed low light conditions, and the effects of microbial activity on phosphorus bioavailability. These are processes that are not well simulated or simulated at all in the two models tested here.

The lack of sensitivity of our models to the changes in winter nutrient loading should not, however, be seen as a failure of the models, since they were developed to simulate peak phytoplankton concentrations during the period of thermal stratification when drinking water concerns and the effects of watershed management would be most evident. Emphasis was placed on simulating the processes that occur during this period, and model process studies and calibration (Auer and Forrer, 1998; Doerr *et al.*, 1998) were almost entirely focused on the stratified period. As a result, the models do respond as expected when spring nutrient loads are shifted into the summer period (Figure 9B). Studies of climate change focused attention on the winter and the effects of processes whose importance is changing as the seasonality of model drivers changes with the climate. This study illustrates the importance of carefully examining model assumptions and testing the sensitivity of models to changes that would be expected as a consequence of future climate change. This study also illustrates the added advantage of testing models beyond the realm of typical concern. Considering the effects of climate change on snow, snowmelt hydrology, and the seasonality of nutrient loading focused our attention on the winter period and illuminated model processes that need further investigation even under contemporary conditions. In the NYC water supply region, snow accumulation and melt are naturally variable, so that the proportion of winter nutrient loading is highly variable even today (Figure 5). As a result, the need for studies examining the relative importance of the timing of nutrient loading as well as the magnitude of nutrient loading on the NYC water supply reservoirs has become clear.

CONCLUSIONS

The results of this study support the conclusion drawn by many groups (e.g. Andreasson *et al.*, 2004; Barnett *et al.*, 2005), working in regions where snow plays an important role in defining the seasonality of the hydrologic cycle, that future climate change will lead to increased winter runoff and a shift in the timing of the contemporary spring runoff peak. Some of the predicted changes are the result of increased winter precipitation; however, an important component of the expected change is the result of rising air temperature on snow accumulation and melt.

One aspect of this change which has not been widely considered is the concurrent change in the timing of nutrient delivery on the ecology and productivity of lakes and reservoirs, even though regions where snow has an important influence on hydrology tend to be rich in lakes. In this paper, an attempt was made to simulate how increasing winter nutrient loads would affect annual levels of reservoir chlorophyll using two different models developed for NYC water supply reservoirs. Our initial simulations were not able to simulate any clear effect between the proportion of nutrient loading occurring in the winter and the magnitude of reservoir chlorophyll. This challenges our understanding of the limnology of these systems and has caused us to examine factors not considered important in the original model development process; namely processes influencing the bio-availability of nutrients entering the reservoirs during the winter and the ability of phytoplankton to adapt and grow under winter conditions prior to the onset of thermal stratification. This indicates the need for additional studies of such processes under the ice in winter.

This study highlights the challenges and pitfalls associated with simulating the future impacts of climate change using complex ecosystem models. Such models are by necessity simplifications of the lake/reservoir system and focus on the processes considered most important for the question/interest at hand. Phytoplankton models, therefore, often focus on processes affecting growth and succession during the period of thermal stratification when biomass is greatest and blooms could become problematic. Climatic impacts affecting winter processes in these models may not be well represented. As model use shifts to simulating expected effects of climate change, impacts need to be clearly articulated, and the model structure and algorithms simulating these impacts need to be systematically evaluated.

ACKNOWLEDGEMENTS

We thank NYCDEP for supporting this project and the comments by Lorraine Janus and Steve Schindler of NYCDEP, and two anonymous reviewers. This is contribution number 314 from the Upstate Freshwater Institute.

DOI: 10.1002/hyp

REFERENCES

Anandhi A, Frei A, Pierson DC, Schneiderman EM, Zion MS, Lounsbury D, Matonse AH. 2011a. Examination of change factor methodologies for climate change impact assessment. *Water Resources Research* **47**: W03501. DOI: 10.1029/2010wr009104.

Anandhi A, Frei A, Pradhanang SM, Zion MS, Pierson DC, Schneiderman EM. 2011b. AR4 climate model performance in simulating snow water equivalent over Catskill Mountain watersheds, New York, USA. *Hydrological Processes*, **25**: 3302–3311. DOI: 10.1002/hyp.8230.

Andreasson J, Bergstroem S, Carlsson B, Graham LP, Lindstroem G. 2004. Hydrological Change - Climate Change Impact Simulations for Sweden. *Ambio* **33**: 228–234.

Auer MT, Forrer BE. 1998. Development and parameterization of a kinetic framework for modelling light and phosphorus limited limited phytoplankton growth in Cannonsville Reservoir. *Lake and Reservoir Managment* **14**: 290–300.

Balayla D, Lauridsen TL, Sondergaard M, Jeppesen E. 2010. Larger zooplankton in Danish lakes after cold winters: are winter fish kills of importance? *Hydrobiologia* **646**: 159–172. DOI: 10.1007/s10750-010-0164-4.

Barnett TP, Adam JC, Lettenmaier DP. 2005. Potential impacts of a warming climate on water availability in snow-dominated regions. *Nature* **438**: 303–309.

Blank K, Haberman J, Haldna M, Laugaste R. 2009. Effect of winter conditions on spring nutrient concentrations and plankton in a large shallow Lake Peipsi (Estonia/Russia). *Aquatic Ecology*, **43**: 745–753. DOI: 10.1007/s10452-009-9283-2.

Blenckner T, Adrian R, Livingstone DM, Jennings E, Weyhenmeyer GA, George DG, Jankowski T, Jarvinen M, Aonghusa CN, Noges T, Straile D, Teubner K. 2007. Large-scale climatic signatures in lakes across Europe: a meta-analysis. *Global Change Biology*, **13**: 1314–1326. DOI: 10.1111/j.1365-2486.2007.01364.x.

Burns DA, Klaus J, McHale MR. 2007. Recent climate trends and implications for water resources in the Catskill Mountain region, New York, USA. *Journal of Hydrology*, **336**: 155– 170.

Catalan J 1992. Evolution of dissolved and particulate matter during the ice-covered period in a deep, high-moutain lake. *Canadian Journal of Fisheries and Aquatic Sciences* **49**: 945–955. DOI: 10.1139/f92-105.

DeBates TJ, Chipps SR, Ward MC, Werlin KB, Lorenzen PB. 2003. Cladoceran zooplankton abundance under clear and snow-covered ice. *Journal of Freshwater Ecology* **18**: 169–170. DOI: 10.1080/02705060.2003.9663963.

Doerr SM, Owens EM, Gelda RK, Auer MT, Effler SW. 1998. Development and testing of a nutrient-phytoplankton model for Cannonsville Reservoir. *Lake and Reservoir Management* **14**: 301–321.

Dokulil MT, Jagsch A, George GD, Anneville O, Jankowski T, Wahl B, Lenhart B, Blenckner T, Teubner K. 2006. Twenty years of spatially coherent deepwater warming in lakes across Europe related to the North Atlantic Oscillation. *Limnology and Oceanography* **51**(6), 2787–2793.

Elliott JA, Thackeray SJ, Huntingford C, Jones RG. 2005. Combining a regional climate model with a phytoplankton community model to predict future changes in phytoplankton in lakes. *Freshwater Biology* **50**: 1404–1411.

Frei A, Armstrong RL, Clark MP, Serreze MC. 2002. Catskill Mountain Water Resources:Vulnerability, Hydroclimatology, and Climate--Change Sensitivity. *Annal. of the Association of American Geographers.* **92**: 203–224.

Haith DA, Shoemaker LL. 1987. Generalized Watershed Loading Functions for stream flow nutrients. *Water Resources Bulletin* **23**: 471–478.

Hay LE, Wilby RJL, Leavesley GH. 2000. A comparison of delta change and downscaled GCM scenarios for three mountainous basins in the United States. *Journal of the American Water Resources Association* **36**: 387–397.

Horn H, Paul L, Horn W, Petzoldt T. 2011. Long-term trends in the diatom composition of the spring bloom of a German reservoir: is Aulacoseira subarctica favoured by warm winters? *Freshwater Biology* **56**: 2483–2499. DOI: 10.1111/j.1365-2427.2011.02674.x.

Kiili M, Pulkkanen M, Salonen K. 2009. Distribution and development of under-ice phytoplankton in 90-m deep water column of Lake Paijanne (Finland) during spring convection. *Aquatic Ecology* **43**: 707–713. DOI: 10.1007/s10452-009-9262-7.

Komatsu E, Fukushima T, Harasawa H. 2007. A modeling approach to forecast the effect of long-term climate change on lake water quality. *Ecological Modelling* **209**: 2–4.

Lehner B, Doll P. 2004. Development and validation of a global data base of lakes, reservoirs and wetlands. *Journal of Hydrology* **296**: 1–22.

Markensten H, Pierson DC. 2007. Weather driven influences on phytoplankton succession in a shallow lake during contrasting years. Application of PROTBAS. *Ecology Modeling* **207**: 128–136.

Markensten H, Moore K, Persson I. 2010. Simulated lake phytoplankton composition shifts toward cyanobacteria dominance in a future warmer climate. *Ecological Applications* **20**: 752–767. DOI: 10.1890/08-2109.1.

Matonse AH, Pierson DC, Frei A, Zion MS, Schneiderman EM, Anandhi A, Mukundan R, Pradhanang SM. 2011. Effects of changes in snow pattern and the timing of runoff on NYC water supply system. *Hydrological Processes* **25**: 3278–3288. DOI: 10.1002/hyp.8121.

Owens EM. 1998. Development and testing of a one-dimensional hydrothermal models of Cannonsville Reservoir. *Lake and Reservoir Managment* **14**: 172–185.

Owens EM, Effler SW, Doerr SM, Gelda RK, Schneiderman EM, Lounsbury DG, Stepczuk CL. 1998. A strategy for reservoir model forecasting based on historic meteorological conditions. *Lake and Reservoir Management [Lake Reserv. Manage.]* **14**: 2–3.

Pettersson K, Grust K, Weyhenmeyer G, Blenckner T. 2003. Seasonality of chlorophyll and nutrients in Lake Erken - effects of weather conditions. *Hydrobiologia* **506**: 75–81. DOI: 10.1023/b:hydr.0000008582.61851.76.

Phillips KA, Fawley MW. 2002a. Winter phytoplankton blooms under ice associated with elevated oxygen levels. *Journal of Phycology* **38**: 1068–1073. DOI: 10.1046/j.1529-8817.2002.01044.x.

Phillips KA, Fawley MW. 2002b. Winter phytoplankton community structure in three shallow temperate lakes during ice cover. *Hydrobiologia* **470**: 97–113. DOI: 10.1023/a:1015667803372.

Pierson DC, Kick JW. 1995. Use of a GIS to develop a statified snow survey in a mountainous agricultural landscape. In Proceedings 52nd Eastern Snow Conference p. 59–58.

Pierson D, Arvola L, Allott N, Järvinen M, Jennings E, May L, Moore K, Schneiderman E, George G. 2010. *Modeling the Effects of Climate Change on the Supply of Phosphate-Phosphorus The Impact of Climate Change on European Lakes*. Springer Netherlands; 139–159.

Reitner B, Herzig A, Herndl GJ. 1997. Microbial activity under the ice cover of the shallow Neusiedler See (Austria, Central Europe). *Hydrobiologia* **357**: 173–184. DOI: 10.1023/a:1003151323756.

Reynolds CS, Irish AE, Elliott JA. 2001. The ecological basis for simulating phytoplankton responses to environmental change (PROTECH). *Ecological Modelling* **140**: 271–291.

Riley GA. 1947. Factors controlling phytoplankton populations on Georges Bank. *Journal of Marine Research* **6**: 54–73.

Samal NR, DC Pierson, E Schneiderman, Y Huang, JS Read, A Anandhi, Owens EM. 2012. Impact of climate change on Cannonsville reservoir thermal structure in the New York City Water Supply. *Water Quality Research Journal of Canada* **47**: 389–405. DOI: 10.2166/wqrjc.2012.020.

Schneiderman EM, Pierson DC, Lounsbury DG, Zion MS. 2002. Modeling the hydrochemistry of the Cannonsville watershed with Generalized Watershed Loading Functions (GWLF). *Journal of the American Water Resources Association* **38**: 1323–1347.

Schneiderman EM, Steenhuis TS, Thongs DJ, Easton ZM, Zion MS, Neal AL, Mendoza GF, Todd WM. 2007. Incorporating variable source area hydrology into a curve-number-based watershed model. *Hydrological Processes* **21**: 3420–3430. DOI: 10.1002/hyp.6556.

Sommer UZ, Gliwcz M, Lampert W, Duncan A. 1986. The PEG model of seasonal succession of planktonic events in fresh waters. *Archives of Hydrobiology* **106**: 433–471.

Straskrabova V, Izmest'yeva LR, Maksimova EA, Fietz S, Nedoma J, Borovec J, Kobanova GI, Shchetinina EV, Pislegina EV. 2005. Primary production and microbial activity in the euphotic zone of Lake Baikal (Southern Basin) during late winter. *Global and Planetary Change* **46**: 57–73. DOI: 10.1016/j.gloplacha.2004.11.006.

Summer RM, Alonso CV, Young RA. 1990. Modeling linked watershed and lake processes for water quality management decisions. *Journal of Environmental Quality* **19**: 421–427.

Tulonen T, Kankaala P, Ojala A, Arvola L. 1994. Factors controling production of phytoplankton and bacteria under-ice in a humic, boreal lake. *Journal of Plankton Research* **16**: 1411–1432. DOI: 10.1093/plankt/16.10.1411.

Twiss MR, McKay RML, Bourbonniere RA, Bullerjahn GS, Carrick HJ, Smith REH, Winter JG, D'Souza NA, Furey PC, Lashaway AR, Saxton MA, Wilhelm SW. 2012. Diatoms abound in ice-covered Lake Erie: An investigation of offshore winter limnology in Lake Erie over the period 2007 to 2010. *Journal of Great Lakes Research* **38**: 18–30. DOI: 10.1016/j.jglr.2011.12.008.

Vanderploeg HA, Bolsenga SJ, Fahnenstiel GL, Liebig JR, Gardner WS. 1992. Plankton ecology in an ice covered bay of Lake-Michigan - Utilization of a winter phytoplankton bloom by reproducing copepods. *Hydrobiologia* **243**: 175–183. DOI: 10.1007/bf00007033.

Vehmaa A, Salonen K. 2009. Development of phytoplankton in Lake Paajarvi (Finland) during under-ice convective mixing period. *Aquatic Ecology* **43**: 693–705. DOI: 10.1007/s10452-009-9273-4.

Wetzel RG. 2001. *Limnology Lake and River Ecosystems*. 3rd Edn, Academic Press.

Zion MS, Pradhanang SM, Pierson DC, Anandhi A, Lounsbury DG, Matonse AH, Schneiderman EM. 2011. Investigation and Modeling of winter streamflow timing and magnitude under changing climate conditions for the Catskill Mountain region, New York, USA. *Hydrological Processes* **25**: 3289–3301. DOI: 10.1002/hyp.8174.

JOURNAL OF THE AMERICAN WATER RESOURCES ASSOCIATION

AMERICAN WATER RESOURCES ASSOCIATION

STREAMFLOW RESPONSES TO CLIMATE CHANGE: ANALYSIS OF HYDROLOGIC INDICATORS IN A NEW YORK CITY WATER SUPPLY WATERSHED[1]

Soni M. Pradhanang, Rajith Mukundan, Elliot M. Schneiderman, Mark S. Zion, Aavudai Anandhi, Donald C. Pierson, Allan Frei, Zachary M. Easton, Daniel Fuka, and Tammo S. Steenhuis[2]

ABSTRACT: Recent works have indicated that climate change in the northeastern United States is already being observed in the form of shorter winters, higher annual average air temperature, and more frequent extreme heat and precipitation events. These changes could have profound effects on aquatic ecosystems, and the implications of such changes are less understood. The objective of this study was to examine how future changes in precipitation and temperature translate into changes in streamflow using a physically based semidistributed model, and subsequently how changes in streamflow could potentially impact stream ecology. Streamflow parameters were examined in a New York City water supply watershed for changes from model-simulated baseline conditions to future climate scenarios (2081-2100) for ecologically relevant factors of streamflow using the Indicators of Hydrologic Alterations tool. Results indicate that earlier snowmelt and reduced snowpack advance the timing and increase the magnitude of discharge in the winter and early spring (November-March) and greatly decrease monthly streamflow later in the spring in April. Both the rise and fall rates of the hydrograph will increase resulting in increased flashiness and flow reversals primarily due to increased pulses during winter seasons. These shifts in timing of peak flows, changes in seasonal flow regimes, and changes in the magnitudes of low flow can all influence aquatic organisms and have the potential to impact stream ecology.

(KEY TERMS: flow regimes; hydrologic modeling; SWAT-WB; indicator of hydrologic alterations; aquatic biota.)

Pradhanang, Soni M., Rajith Mukundan, Elliot M. Schneiderman, Mark S. Zion, Aavudai Anandhi, Donald C. Pierson, Allan Frei, Zachary M. Easton, Daniel Fuka, and Tammo S. Steenhuis, 2013. Streamflow Responses to Climate Change: Analysis of Hydrologic Indicators in a New York City Water Supply Watershed. *Journal of the American Water Resources Association* (JAWRA) 1-19. DOI: 10.1111/jawr.12086

INTRODUCTION

Assessment of the seasonality and variability in streamflow is essential for drinking water supply watersheds, not only to ascertain long-term supply of water to the public but also to assess the aquatic health of watershed streams. Water resources are highly sensitive to climate change with many studies cautioning of pending water shortages and of

[1]Paper No. JAWRA-12-0094-P of the *Journal of the American Water Resources Association* (JAWRA). Received April 23, 2012; accepted March 20, 2013. **Discussions are open until six months from print publication.**

[2]Research Associate (Pradhanang, Mukundan) and Professor (Frei), Institute for Sustainable Cities, City University of New York, 695 Park Ave., New York, New York 10065; Senior Research Scientist (Schneiderman, Zion) and Section Chief (Pierson), Water Quality Modeling, New York City Department of Environmental Protection, Kingston, New York 12401; Research Assistant Professor (Anandhi), Department of Agronomy, Kansas State University, Manhattan, Kansas 66506; Assistant Professor (Easton), Department of Biological and Environmental Engineering, Virginia Tech, Painter, Virginia 23420; Ph.D Candidate (Fuka) and Professor (Steenhuis), Department of Biological and Environmental Engineering, Cornell University, Ithaca, New York 14853 (E-Mail/Pradhanang: spradh@hunter.cuny.edu).

increased flooding or extreme events (WMO, 1987). In addition to the these quantity-related issues, the seasonal pattern of flows; timing of extreme flows; frequency and duration of floods, droughts; daily, seasonal, and annual flow variability; and rates of streamflow change are critical to ecosystem function (Poff *et al.*, 1997). Small perturbations in precipitation frequency, magnitude, and type can impact streamflow patterns (Risbey and Entekhabi, 1996). Such variability occurs at many time scales, from hourly to daily, and from seasonal to interannual. Streamflow characterization and classification using hydrologic indices can foster an understanding of the characteristics of streamflow variability that are believed important in shaping ecological processes in streams.

An examination of historical data and results of model simulations in the northeastern United States (U.S.) has shown an increasing trend in precipitation and streamflow during the last 50 years (Burns *et al.*, 2007; Zion *et al.*, 2011). Numerous studies have suggested different variables for detecting the impact of climate change. For instance, Burn and Soulis (1992) suggested studying a suite of hydrologic variables, as climatic change is expected to affect many components of the hydrologic regime. Streamflow and its components represent a good proxy of the combined impact of climate change because of the spatially integrated hydrologic response that they provide. Characteristics related to the amount and variability of discharge are considered the most fundamental variables influencing the stream ecosystem (Poff and Ward, 1990; Bunn and Arthington, 2002) and the alteration of flow regimes is identified as a serious threat to the ecological sustainability of rivers (Richter *et al.*, 1996). Ecologists have consistently identified flow magnitude, duration, frequency, timing, and rate of change (Risbey and Entekhabi, 1996; Poff *et al.*, 1997) as the most influential hydrologic factors to consider in ecological studies. To quantify these five classes of hydrologic affect, Risbey and Entekhabi (1996) focused on flow parameters that represented the variability and predictability of low-, average-, and high-flow conditions.

Our goal is to examine how changes in precipitation and temperature translate into changes in streamflow responses in a watershed located in the Catskill Mountains in New York state. A physically based semidistributed model, Soil Water Assessment Tool-Water Balance (SWAT-WB) model (Easton *et al.*, 2011; White *et al.*, 2011), is applied to simulate hydrology and to assess the streamflow responses due to climate change. Distributed, physically based watershed hydrologic models use the spatial and temporal characters of topography, land use, soils, meteorological variables, and precipitation in the simulation of hydrologic processes. The hydrology model streamflow results were then analyzed for a collection of statistics encompassing the important components of the hydrologic regime that influence stream ecology including frequency, magnitude, and duration of hydrologic events using the Indicators of Hydrologic Alterations (IHA) tool (Richter *et al.*, 1996). This method is used to gain an overall indication of the extent of hydrologic change from reference baseline conditions with an emphasis on the quantification and identification of streamflow variables that are known to have ecological implications.

STUDY SITE

The West Branch of the Delaware River (WBDR) is the major tributary to the Cannonsville Reservoir, a part of the New York City (NYC) water supply located in the Catskill region of New York state (Figure 1). The watershed drains an area of 891 km^2 above the U.S. Geological Survey (USGS) gauging station 01423000 at Walton, New York and land use is predominantly forested (67%), agriculture (23%), and brush lands (6%). The elevation of the watershed ranges from about 300 m near the watershed outlet to about 1,100 m near the headwaters. The mean annual rainfall in this region is 1,100 mm (Pradhanang *et al.*, 2011) and the mean annual streamflow is 601 mm of which 64% is base flow and 36% surface runoff based on standard hydrograph separation techniques (Arnold and Allen, 1999). Saturation excess is the dominant runoff generation mechanism in NYC water supply watersheds (Schneiderman *et al.*, 2007; Easton *et al.*, 2008; Pradhanang *et al.*, 2011).

Recently, Burns *et al.* (2007) identified changes in the regional water balance of the Catskill Mountain region, and following this work hydrologic models such as Generalized Watershed Loading Function (GWLF) and Soil and Water Assessment Tool (SWAT) have been applied to evaluate the changes in winter streamflow timing (Zion *et al.*, 2011) and snowpack development (Pradhanang *et al.*, 2011). An increasing trend in mean air temperature during 1952-2005 has caused an increase in potential evapotranspiration (PET) as a result of which one would expect decreases in watershed water yield. However, an increasing trend in precipitation has offset the impact of increased PET and, in fact, resulted in a net increase in water yield. These trends demonstrate that recent changes in precipitation and temperature are leading temporal shifts in the water balance (Burns *et al.*, 2007) that could potentially cause changes in hydrologic regimes, stream habitat,

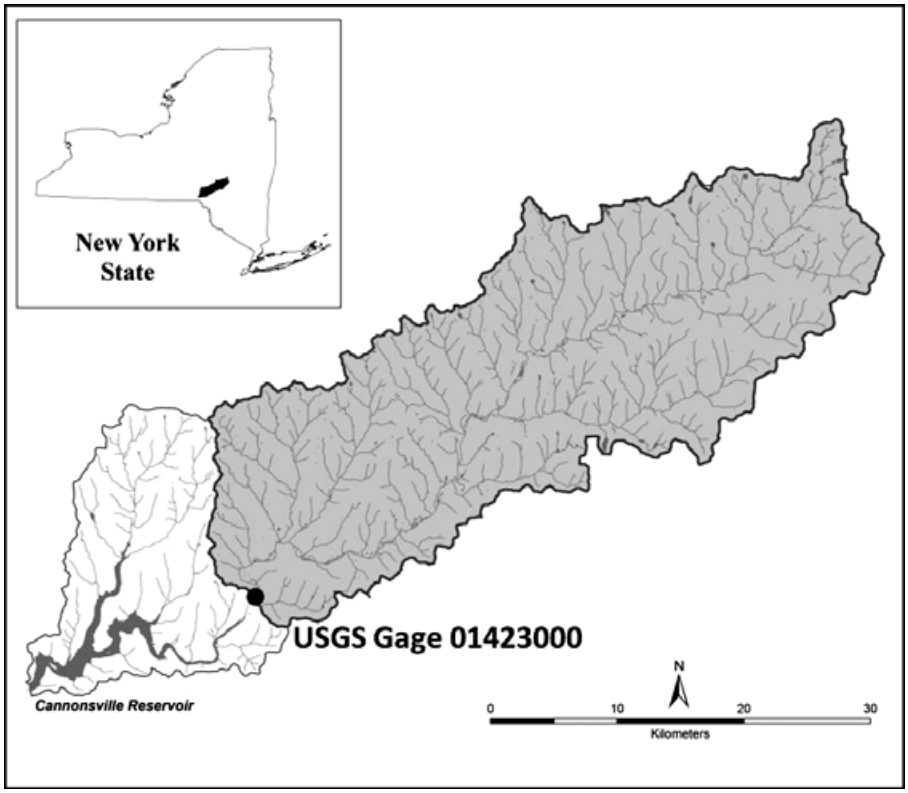

FIGURE 1. Location of West Branch of the Delaware River (WBDR) Watershed (shaded) and Cannonsville Reservoir in New York State, U.S.

ecosystem diversity, and water resource management (Gibson *et al.*, 2005).

METHODS

SWAT-Water Balance Model

Watershed-scale hydrologic models have been developed to simulate the surface runoff from a watershed over various time periods. The SWAT (Arnold *et al.*, 1999) is well-supported and one of the most widely used watershed models that simulates hydrology (Arnold and Allen, 1996; Arnold *et al.*, 1999; Bouraoui *et al.*, 2005; Abbaspour *et al.*, 2007); channel flow routing through stream reaches; utilizes an ecosystem approach to simulating watershed and stream chemistry (Brown and Hollis, 1996; Benaman and Shoemaker, 2005; Bouraoui and Grizzetti, 2008; Santhi *et al.*, 2008) by dynamic simulation of storages and fluxes; and is integrated with GIS by a user-friendly interface. To assess the impact of climate change on the water budget of the WBDR, we employ the SWAT-WB model (Easton *et al.*, 2011; White *et al.*, 2011; Zion *et al.*, 2011). The dominant stormflow generation process in humid temperate landscapes is saturation excess runoff (Dunne and Black, 1970). The response of streams to rainfall or snowmelt is largely dependent on the extent of saturated surface and the amount of water needed to achieve this condition at any given point. Tracking the extent of saturated areas and the amount of saturation is an important addition to the SWAT-WB model, which is being applied at this watershed. SWAT-WB is a modified version of the SWAT-2005 model (Neitsch *et al.*, 2005) that incorporates a daily water balance for each Hydrologic Response Unit (HRU) to predict the partitioning of precipitation into runoff and percolation. Following this partitioning, the existing SWAT soil moisture routines are used by SWAT-WB to determine the degree of saturation deficit for each soil profile for each day of simulation. SWAT-WB has been found to perform well in simulating streamflow in watersheds where a saturation excess runoff process is the dominant runoff generation mechanism (Easton *et al.*, 2011; White *et al.*, 2011).

To include the landscape features most important in runoff generation (e.g., upslope contributing area, soil depth, and slope) a topographic index was integrated with existing soils data to create a soil topographic index (STI) (Walter *et al.*, 2002), which is then used in the SWAT-WB HRU definition process (Easton *et al.*, 2008). The STI is calculated for each 10-m grid cell (aligned with the watershed digital

elevation model [DEM]) within the watershed and is a function of upslope contributing area, the local slope, and the lateral transmissivity of the soil profile. The upslope contributing area, α, and the local slope, tan(β), are both obtained from a DEM. The lateral transmissivity of the soil profile, T_0, when water table intersects the soil surface (Walter *et al.*, 2002), is the product of the soil layer depth and soil layer saturated hydraulic conductivity, which are both obtained from the SSURGO database (USDA-NRCS, 2000). Grid cells with larger upslope areas, flatter slopes, and lower transmissivity tend to be more saturated and therefore, generate runoff through saturation excess more frequently. The grid-cell STI values are partitioned based on numerical ranges into equal area zones to create 10 wetness classes. The SWAT model's existing soil moisture routines are used by SWAT-WB to determine the degree of saturation deficit for each soil profile for each day of simulation. This saturation deficit (in mm of water) is termed the available soil storage, τ_i and is a function of soil properties and watershed soil moisture status (White *et al.*, 2011).

$$\tau_{\mathrm{i}} = (\mathrm{EDC}_i \varepsilon_i - \Theta_{i,t})d_i \tag{1}$$

where EDC_i is the effective depth of a given soil profile i (unitless), ε_i is the soil porosity (unitless) of a given soil i, $\Theta_{i,t}$ *is the volumetric soil moisture of a given soil* i for each day, t (unitless), and d_i is the soil profile depth of soil i (mm). The porosity, ε_i, is a constant value for each soil type, whereas $\Theta_{i,t}$ varies in time and is determined by SWAT's soil moisture routines. The EDC_i, a parameter ranging from 0 to 1, is used to partition soil moisture in excess of soil porosity into infiltrating and runoff fractions. EDC_i is spatially varied based on a saturation probability defined by a soil wetness index (Easton *et al.*, 2008). This spatially adjusted available storage is then used to partition rainfall into infiltration and runoff, q_i (mm):

$$q_i = \begin{cases} 0 & \text{if } P < \tau_i \\ P - \tau_i & \text{if } P > \tau_i \end{cases} \tag{2}$$

The available soil storage, τ_i, is calculated each day and once precipitation begins, a portion of the rain, equal in volume to τ_i, will infiltrate the soil. If the rainfall event is larger in volume than τ_i, the soil profile will saturate and surface runoff will occur. If the rainfall is less than τ_i, the soil will remain unsaturated and there will be no surface runoff and SWAT's internal soil moisture routing will calculate the flux. Through this method, a location's likelihood to saturate is determined by its wetness class value. This wetness class map is then integrated with the soils map in the HRU definition process by areally weighting and averaging soil properties for each wetness class obtained from the SSURGO database.

A DEM of the basin, obtained from the New York City Department of Environmental Protection (NYCDEP) with 10-m horizontal and 0.1-m vertical resolutions, was used to delineate the watershed into 19 subbasins. A land use map derived by supervised classification of 2001 Landsat thematic mapper imagery was obtained from the NYCDEP. The subbasins were further discretized into 554 HRUs per the method outlined above. Measured daily streamflow data for 1991-2000 were obtained from the USGS gauging station 01423000 located at the watershed outlet near Walton. The model results at the watershed outlet will be used for this study.

The model was calibrated for streamflow at the watershed outlet from 1991-2000 using the Parameter Solution (ParaSol) method (Van Griensven *et al.*, 2006), using Shuffled Complex Evolution algorithm (SCE-UA) developed by Duan *et al.* (1994) to get a group of optimized parameters. In a first step (zero-loop), SCE-UA selects an initial "population" by random sampling throughout the feasible parameters space for p parameters to be optimized (delineated by given parameter ranges). The population is portioned into several "complexes" that consist of $2p + 1$ points. Each complex evolves independently using the simplex algorithm. The complexes are periodically shuffled to form new complexes to share information between the complexes. The objective function used in ParaSol is sum of square of the residuals (SSQ). The SCE-UA will find a parameter set consisting of a number of free parameters that correspond to the minimum of the SSQ. The uncertainty analysis divides the simulations that have been performed by SCE-UA optimization into "good" and "not good" simulations. The algorithm samples over the entire parameter space with focus of solutions near optimum (Van Griensven *et al.*, 2006). The maximum number of trials allowed before optimization is terminated is 2,000 for this model run. Using optimized parameter values, the model was validated for streamflow from 1981 to 1989. Model performance metrics such as the coefficient of determination (R^2) and Nash-Sutcliffe efficiency (NSE) (Nash and Sutcliffe, 1970), and the percent bias were calculated for the model output. The coefficient of determination (R^2), which describes the degree of collinearity between the simulated and measured values (Moriasi *et al.*, 2007), is computed as the squared ratio between the covariance and the multiplied standard deviations of the observed and predicted values (Krause *et al.*, 2005). It is interpreted as the proportion of the variation in the dependent variable that is accounted for by the independent variable. The NSE,

widely used to evaluate hydrologic model performance (Wilcox *et al.*, 1990), shows how well the plot of observed *vs.* simulated data conforms to the 1:1 line (Krause *et al.*, 2005; Moriasi *et al.*, 2007). Bias is defined as the relative percentage difference between the average modeled and measured data time series over n time steps. The overall objective of the calibration was to maximize the coefficient of determination (R^2) and NSE (Nash and Sutcliffe, 1970), and to minimize the percent bias. The calibrated streamflow was then used to simulate a historical (actual) baseline scenario (1964-2008) of streamflow using measured meteorological data. In the baseline simulation, the SWAT-WB model was forced with observed temperature and precipitation obtained from the National Climate Data Center (NCDC) and through the Northeast Regional Climate Center (NRCC). Solar radiation and wind speed are calculated by the SWAT model based on daily temperature and precipitation (Neitsch *et al.*, 2005).

Future Climate Scenarios

The potential effect of climate change on streamflow was assessed using scenarios derived from a suite of nine Global Climate Models (GCMs) that represent a wide range of simulated future (2081-2100) climate conditions (Table 1). The major assumption of this study is that the calibrated parameter set is still valid under climate change, and there is no assumed land use change in the future scenario. In this study, the A1B Emission Scenario (representing rapid economic growth with balanced emphasis on all energy sources) from the Special Report on Emission Scenarios (SRES) in the IPCC Fourth Assessment Report (IPCC, 2007) was used. The scenarios and assumptions behind the carbon emissions are all the same in each GCM model in this study. It is important to note that the model results are obtained with a single emission scenario, and therefore, only give a sampling of of potential climate change impacts and do not encompass the full range of potential outcomes due to various emission scenarios. In addition, the changes in temperature and precipitation pattern may have considerable impacts on the land cover within the watersheds, providing further feedback on streamflow which is not included in this analysis. Data from the selected GCMs were extracted and interpolated to a common 2.5° grid using bilinear interpolation for a control period in the late 20th Century (20C3M) between 1960 and 2000 and a future A1B emission scenario for the period 2081-2100. Climate scenarios were downscaled using change factor methodology (CFM) described in Anandhi *et al.* (2011).

The CFM is an empirical (as compared with dynamical) downscaling technique (Hay *et al.*, 2000; Prudhomme *et al.*, 2002; Wilby *et al.*, 2004; Hayhoe, 2010). CFM uses the difference between the monthly statistics for current and future time slices of a single GCM/Emission Scenario model run, to derive change factors for a meteorological variable for the future relative to current time slice as projected by that GCM. The change factors are then added to the observed historical meteorology (which serves as a baseline or current conditions scenario) to derive a projected future meteorological scenario. Traditional CFM derives a single change factor for each month based on the difference of monthly averages between current and future time slices (Wilby *et al.*, 2004). We utilize a statistically distributed version of CFM as described in Anandhi *et al.* (2011), hereto referred to as CFM-SD. In CFM-SD, the frequency distributions of a meteorological variable in current and future time slices of model output from a single

TABLE 1. Climate Models Used in This Study.

GCM ID*	Center/Country	Spatial Resolution (lat × lon)	Reference
CGCM3.1 (T47)	Canadian Centre for Climate Modeling and Analysis	~3.75° × 3.75°	Flato and Boer (2001)
CGCM3.1 (T63)	Canadian Centre for Climate Modeling and Analysis	~2.8° × 2.8°	Flato and Boer (2001)
CSIRO-MK 3.0	CSIRO/Australia	~1.88° × 1.88°	Gordon *et al.* (2000)
GISS-AOM	GISS/United States	3.0° × 4.0°	Russell *et al.* (1995)
GFDL-CM 2.0	GFDL/United States	2.0° × 2.5°	Delworth *et al.* (2006)
IPSL-CM4	IPSL/France	~2.5° × 3.75°	Marti *et al.* (2006)
MIROC3.2 (HIRES)	CCSR/NIES/FRCGC/Japan	~1.125° × 1.125°	K-1 Model Developers (2004)
ECHAM5/MPI-OM	MPI/Germany	~1.88° × 1.88°	Jungclaus *et al.* (2006)
MRI-CGCM 2.3.2	MRI/Japan	~2.8° × 2.8°	Yukimoto *et al.* (2001)

Note: GCM, Global Climate Model.
*From information at Lawrence Livermore National Laboratory's Program for Coupled Model Diagnosis and Intercomparison (PCMDI): http://wwwpcmdi.llnl.gov/.

GCM/Emission Scenario model run are compared to derive a series of change factors across a set of percentile range bins for each month. This is in contrast to simply comparing monthly averages and deriving a single monthly change factor as in traditional CFM. For our application the frequency distribution was divided into 25 equal range bins, so each change factor represents a 4th percentile range in the distribution of GCM output for a given time slice and month. The change factor for a particular bin is taken as the difference in the average values within the bin's percentile range between the current *vs.* future time slice. The method as employed here produces a single future time series meteorological scenario as a permutation of the historical time series, although it should be noted that one could do a stochastic sampling with this technique to simulate multiple trajectories of different percentiles from the climate model output distributions.

Daily meteorological values in the projected future time series scenario for a given GCM/Emission Scenario are thus defined by the following equation

$$F_d = O_{p,m} + (G_{p,m,fut} - G_{p,m,cur}) \quad (3)$$

where F_d is the daily value for a given future scenario based on a particular GCM; $O_{p,m}$ is the observed daily value from the historical data time series which falls within the percentile range, p, of the historical data during a given month; G_{fut} is the average GCM meteorological value for the same percentile range, p, for the given month, m, for a given future time slice, *fut*, of the GCM model output; $G_{p,m,cur}$ is the GCM meteorological value for the same percentile, p, for the given month, m for the current time slice (20C3M) GCM output. In this way, the statistically distributed change factors are applied to the appropriate percentile ranges of the historical data to produce the future time series scenario as a permutation of the historical time series. It should be noted that in this methodology no attempt is made to compare the frequency distributions of the historical data time series *vs.* the current time slice (20C3M) GCM output nor to bias correct the GCM future output as in alternative statistical downscaling methods (Wilby *et al.*, 1999; Fowler *et al.*, 2007; Piani *et al.*, 2010). Rather, it is assumed that any bias in GCM output in relation to observed data will consistently be present in both current and future time slices of the same GCM; i.e., we assume that the relative change projected by a single GCM is bias free.

Through this method the observed dataset becomes a current conditions, or baseline, scenario of model input, and the observed data with the prescribed current to future changes incorporated defines the future scenario. GCMs contain significant uncertainties and IPCC (2007) recommends that the results of different models and scenarios should be considered in climate change studies. It has become standard practice to use several climate scenarios to characterize uncertainty in future climate (Arnell *et al.*, 2004). The skill of a multimodel ensemble is known to consistently outperform individual models for detection and attribution studies (Brekke *et al.*, 2008; Gleckler *et al.*, 2008; Pierce *et al.*, 2009). According to Najafi *et al.* (2010), the hydrologic uncertainty is considerably smaller than climate uncertainty where the total uncertainty for dry season is higher than the one in the wet season in the Pacific Northwest U.S. Recent study on headwater basins across British Columbia conducted by Bennett *et al.* (2012) found that the hydrologic parameter uncertainty ranged up to 55% (average 31%) for winter runoff anomalies, which was less than the uncertainty associated with GCMs and emissions scenarios that ranged up to 135% and 78% (average 84% and 58%, respectively). In a hydrologic impact study of climate change, the most important sources of uncertainty may arise from, in decreasing order, the emission scenarios (Arnell *et al.*, 2004), climate model parameterization (particularly for precipitation), downscaling (Wilby and Harris, 2006), and the hydrologic model parameterization (Wilby and Harris, 2006; Caballero *et al.*, 2007). The climate change ensemble average scenario presented in this study was calculated by averaging the SWAT model output on daily streamflow from all future scenarios.

Hydrologic Assessment

The general approach for hydrologic assessment consisted of defining a series of 33 hydrologic attributes that characterize the seasonality and variability in streamflow conditions and then comparing how these attributes vary between simulated baseline and climate changed streamflow. The hydrologic attributes are based on five characteristics of hydrologic regimes, known as Indicators of Hydrologic Alterations (IHA) (Richter *et al.*, 1996). A summary of the parameters, and their characteristics, used in the IHA is provided in Table 2. The IHA analysis statistically characterizes interannual variation in flow regimes. Seventeen of the 33 IHA parameters (Groups 2, 3, and 4 in Table 2) focus on the magnitude, duration, timing, and frequency of extreme events, whereas the other 16 parameters (Groups 1 and 5 in Table 2) are measures of the median of the magnitude of flows or the rate of change in streamflow conditions.

The following sections summarize the descriptions of the five groups and the associated statistical parameters given by Richter *et al.* (1996) and Richter *et al.* (1997, 1998).

TABLE 2. Indicators of Hydrologic Alterations (Richter *et al.*, 1996).

IHA Group	Hydrologic Parameters	Ecosystem Influences
Group 1: Magnitude of monthly water conditions	Median value for each calendar year (12 parameters)	1. Availability of habitat for aquatic organisms 2. Availability of soil moisture for plants 3. Availability of water 4. Reliability of water supplies for wildlife 5. Effects of water temperature and dissolved oxygen
Group 2: Magnitude and duration of annual extreme water conditions (median daily flow)	1. Annual one-day minima 2. Annual three-day minima 3. Annual seven-day minima 4. Annual 30-day minima 5. Annual 90-day minima 6. Annual one-day maxima 7. Annual three-day maxima 8. Annual seven-day maxima 9. Annual 30-day maxima 10. Annual 90-day maxima 11. Number of zero-flow days 12. Seven-day minima/mean for year	1. Balance of competitive and stress tolerant organisms 2. Creation of sites for plant colonization 3. Structure of river channel morphology and physical habitat conditions 4. Soil moisture stress in plants 5. Dehydration of wildlife 6. Duration of stressful conditions 7. Distribution of plant communities
Group 3: Timing of annual extreme of high and low pulses	1. Julian date of each annual one-day maxima 2. Julian date of each annual one-day minima	1. Predictability and avoidability of stress for organisms 2. Spawning cues for migratory fish
Group 4: Frequency and duration of high and low pulses	1. Number of low pulses within each year 2. Median duration of low pulses each year 3. Number of high pulses within each year 4. Median duration of high pulses each year	1. Frequency and magnitude of soil moisture stress for plants 2. Availability of floodplain habitat for aquatic organisms 3. Effects of bed-load transport and channel sediment distribution, and duration of substrate disturbance
Group 5: Rate and frequency of water condition changes	1. Medians of all positive difference between consecutive daily values within each year 2. Medians of all negative difference between consecutive daily values within each year 3. Number of hydrologic reversals within each year	1. Drought stress on plants 2. Desiccation stress on low-mobility stream-edge organisms

Note: IHA, Indicators of Hydrologic Alterations.

Group 1: The magnitude of the monthly median of daily flows represents normal daily flow conditions for the month and indicates suitability of flow levels for supporting aquatic habitats. The degree to.which monthly medians vary from month to month indicates the intraannual variation in streamflow conditions, whereas the extent to which flows vary from year to year indicates the interannual variation in streamflow conditions.

Group 2: The magnitude and duration of extreme annual conditions measures different environmental disturbances that can occur throughout the year. The durations represent cycles of interest to natural or man-made systems and consider the one-day, three-day, seven-day (weekly), 30-day (monthly), and 90-day (seasonal) extremes. The one-day events are the maximum and minimum daily flow values that occur in any given year and the multiday events are

the highest and lowest multiday means occurring in any given year. The number of zero-flow days, characteristic of nonperennial rivers, is also included in this group. An index of base-flow conditions is calculated as the seven-day annual minimum flow divided by the annual mean daily flow. The interannual variation in the magnitude of these extreme conditions influences the extent to which environmental variation occurs within ecosystems.

Group 3: The Julian date of the one-day maximum and minimum flow events represents the timing of the annual extreme conditions and provides a measure of the seasonal nature of environmental stress or disturbances. The timing of these flows can influence the life cycles of aquatic organisms. The interannual variation in the timing of these extremes influences the extent to which environmental variation occurs within ecosystems. This may have greater significance in more temperate regimes where melting snow consistently influences the date of maximum flow and also significantly reduces water temperatures and increases dissolved oxygen concentration.

Group 4: The numbers of continuous occurrences during which the magnitude of streamflow exceeds an upper threshold or falls below a lower threshold within an annual cycle and the mean duration of such episodes together reflect the pulsing behavior of environmental variation within a given year. Richter *et al.* (1996, 2003) define high pulses as those periods within a year when the daily streamflow rises above the 75th percentile of all daily values, and low pulses as those periods within a year when the daily streamflow falls below the 25th percentile of all daily values.

Group 5: The rate and frequency of change in conditions measure the number and median rate of both positive and negative changes in the streamflow between consecutive days. These changes in the hydrograph indicate the rate and frequency of intraannual environmental variability.

The steps used in hydrologic assessment are as follows:

1. The streamflow time series for baseline simulation (1964-2008) and nine climate change scenarios were defined. During the data set up, baseline simulation is treated as preimpact scenario and each climate change scenario as postimpact scenario.
2. The values for ecologically relevant 33 parameters (Table 2) for each year in each time series were calculated.
3. Interannual statistics such as measures of central tendency, variance, and ranges were calculated for each time series for 33 parameters.
4. The medians, coefficients of dispersion, minimum, and maximum for each parameter were then compared between simulated baseline and future scenario streamflow results.

Due to the skewed nature of hydrologic dataset, we employ nonparametric statistics in this study. Monthly median of daily flows were calculated for streamflow from baseline condition and ensemble scenario. Ensemble scenario is the scenario obtained from averaging eight climate models used in this study. The median (50th percentile) is used as the measure of central tendency for the IHA parameters; the spread between the 25th and 75th percentiles, divided by the median, is the measure of dispersion called the "coefficient of dispersion." The deviation of the streamflow under climate scenarios from the baseline condition is presented as deviation factor. The ranges of variation between the simulated streamflow and streamflow under climate scenarios were assessed for each of the variables described above and in Table 2. We averaged the model outputs from eight climate models to get climate change ensemble average scenario for comparison with baseline condition. In addition to the streamflow statistics described above, other flow components such as floods, and flow duration curves are also analyzed.

RESULTS AND DISCUSSIONS

SWAT Model Calibration

In addition to the effective depth coefficient (EDC), 20 parameters (listed in Table 3) were calibrated which control the hydrologic processes involved in streamflow generation including partitioning precipitation into infiltration and runoff, base-flow recession, and the rates of snowpack development and depletion. Streamflow parameters included Manning's n value for main channel (Ch_N2), base-flow alpha factor (Alpha-bf), and snowpack temperature lag factor (TIMP), the parameters surface runoff lag time (SURLAG), threshold depth of water in the shallow aquifer required for return flow to occur (GWQMN), threshold depth of water in the shallow aquifer for revaporization to occur (REVAPMN), soil evaporation compensation factor (ESCO), and other groundwater-, channel-, and basin-related parameters were also adjusted. The EDC values ranged from 0.1 to 1.0 (Easton *et al.*, 2011).

Predicted and measured monthly streamflow for the calibration and baseline periods are presented in Figure 2. Although the model was able to capture most peaks, it underestimated the measured streamflow

TABLE 3. Calibration Parameters and Their Best Parameter Ranges for SWAT Model Simulations.

SWAT Input Variables*	Description	Parameter Range	Best Parameter Values
ALPHA_BF.gw	Base-flow alpha factor [days]	0.01-0.056	0.054
GW_DELAY.gw	Groundwater delay [days]	0.01-8.0	5.920
GW_REVAP.gw	Groundwater revaporization coefficient	0.01-0.2	0.193
GWQMN.gw	Threshold depth of water in the shallow aquifer required for return flow to occur [mm]	0.01-0.01	0.008
REVAPMN.gw	Threshold depth of water in the shallow aquifer for revaporization to occur [mm]	0-1,000	499.7
RCHRG_DP.gw	Deep aquifer percolation fraction	0.15	0.145
GW_SPYLD.gw	Specific yield of shallow aquifer [m^3/m^3]	0-0.3	0.271
DEEPST.gw	Initial depth of water in the deep aquifer [mm H_2O]	0-2700	2,681.0
SHALLST.gw	Initial depth of water in the shallow aquifer [mm H_2O]	0-600	580.1
SMTMP.bsn	Snowmelt base temperature [°C]	−5.0-0.08	0.081
SFTMP.bsn	Snowfall temperature [°C]	−5.0-0.4	0.343
SMFMX.bsn	Melt factor for snow on June 21 [mm H2O/°C-day]	0.01-0.5	0.492
TIMP.bsn	Snowpack temperature lag factor	0.01-0.5	0.431
SURLAG.bsn	Surface runoff lag time [days]	0-1.0	1.0
LAT_TTIME.bsn	Lateral flow travel time [days]	0-0.5	0.015
CH_N2.rte	Manning's n value for main channel	0.01-0.031	0.203
CH_K2.rte	Effective hydraulic conductivity in main channel alluvium [mm/h]	0.01-85.2	85.13
ESCO.bsn	Soil evaporation compensation factor	0.01-0.17	0.029
EPCO.bsn	Plant water uptake compensation factor	0.01-0.815	0.264
EDC.bee	Effective depth coefficient used to partition soil moisture in excess of soil porosity into infiltration and runoff fraction	0.01-1.0	0.195-1.0 (Above range are for EDC1 and EDC10)

*Groundwater (.gw), channel (.rte) parameters are at HRU level, while basin (.bsn) parameters are a watershed scale parameter. EDC.bee represents 10 wetness classes in SWAT-WB.

during certain periods. The baseline simulation represents observed conditions under current climate scenario. In addition, hydrology calibration was optimized so that the runoff and base-flow components of streamflow were simulated reasonably well compared with values derived from measured data using standard base-flow separation techniques (Arnold and Allen, 1999). The final calibrated streamflow for the Cannonsville watershed had a mean absolute bias of 7.0%, a NSE of 0.63 and R^2 of 0.64 for daily streamflow, and a NSE of 0.76 and R^2 of 0.77 for monthly streamflow. Model validation was carried out by comparing simulated and measured data from 1981 to 1989. The validation statistics gave a mean absolute bias in the annual flow volume of 3.0%, a NSE of 0.64 and R^2 of 0.64 for daily streamflow, and NSE of 0.76 and R^2 of 0.77 for monthly streamflow. The model performance is in agreement with the work that has been done in Cannonsville and other subwatersheds by Easton *et al.* (2011), White *et al.* (2011), and Mukundan *et al.* (2013). According to our results, the SWAT-WB performed good in simulating streamflow in Cannonsville watershed. The model

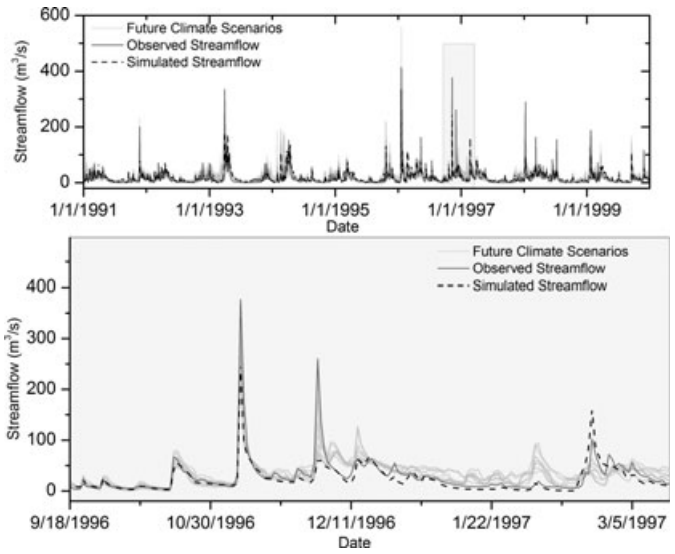

FIGURE 2. Predicted *vs.* Measured Monthly Streamflow for (a) Baseline Period (1991-2000). Gray lines represent streamflow predictions from eight climate models, dashed black line represents simulated streamflow, and solid black line represents observed streamflow and (b) hydrograph from 9/1996 to 4/1997 zoomed in show rising and falling limbs of hydrograph.

performance ranking method complies with the guidelines provided by Moriasi *et al.* (2007).

Baseline and Climate Change Scenarios

When examining the hydrologic effects of climate change scenarios, the change in the hydrologic responses were calculated relative to the results from a baseline scenario, which is the calibrated model simulation described above. Using baseline model results, rather than historic observations for comparison with future model scenarios provides a more consistent approach and avoids having to account for model effects in addition to changes due to climate. The simulated water balance is controlled by moisture inputs such as precipitation and snowfall; and internal model flows including base flow, evapotranspiration (ET), direct runoff; and model state conditions such as soil moisture storage. Based on analysis of the downscaled GCM data, by the end of the century, temperature is projected to increase for all seasons with this increase being present in all of the GCMs presented here (Figure 3b). Predicted future precipitation is expected to generally increase in most months for most GCMs. Some scenarios show decreased precipitation in some months, especially during the summer and early fall (Figure 2). These findings are consistent with other analyses that have suggested a shift in precipitation from summer to winter (Burns *et al.,* 2007; Zion *et al.*, 2011).

Future simulations suggest an increase in ET in the spring, and decrease during August and September to levels similar to those measures under baseline conditions. This can be attributed to increased temperature and reduced soil moisture during these periods (Figure 3). Both meteorological forcings, precipitation as rainfall and temperature, increased in the spring which also led to a reduction in snow cover and reduced albedo. Decreased summer precipitation may also result in decreased plant ET as a result of water stress reducing transpiration. The ensemble climate scenario showed annual water yield increasing by up to ~25% at the watershed outlet. The ensemble data also suggest that winter and spring flow increased on average by ~70% for the late century period (Figure 3). With an increase in local winter air temperature, there was an increase in winter snowmelt events and a corresponding increase in rainfall. Our study showed a decrease in streamflow during the spring and summer and a subsequent increase during the winter and fall (Figure 5), similar to Lettenmaier *et al.* (1994). The decreases in summer streamflow were minimal and may indicate that the wetter spring conditions were not sufficient to offset the seasonal drying.

Total annual snowfall also decreased for all climate change scenarios. Figure 4c shows overall reduction in snow water equivalent for all the climate model simulations and for all the months. The GWLF and SWAT simulation driven using A2 and B1 emission scenarios showed that future snowmelt and snowpack is expected to substantially decrease (Pradhanang *et al.*, 2011; Zion *et al.*, 2011). Climate warming during the winter and early spring is expected to influence timing of snowfall snowpack accumulation, and the number of snow days (Burakowski *et al.*, 2008; Hayhoe *et al.*, 2008). Snow insulates the soil, so a reduction in snowpack may lead to an increase in soil freezing (Shanley and Chalmers,

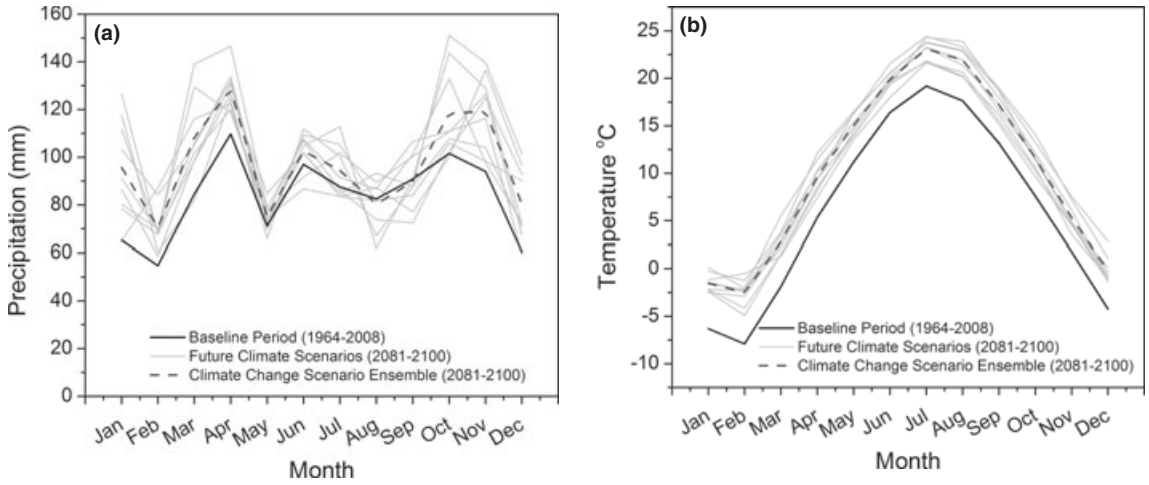

FIGURE 3. Average (a) Precipitation and (b) Temperature Plots for Baseline and Climate Change Scenario. The gray lines represent eight climate change models, dark dashed line represents climate change scenarios ensemble, and the black solid line represents baseline period.

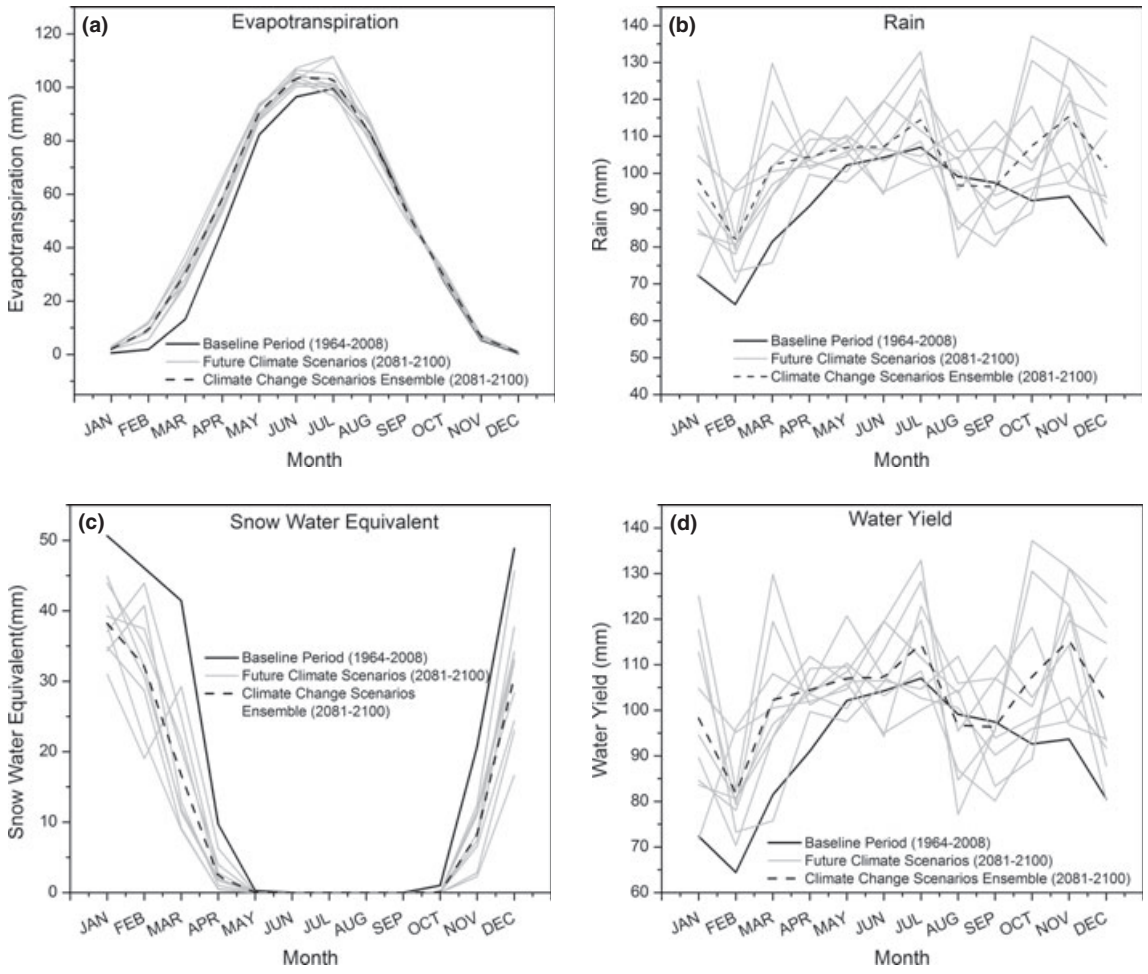

FIGURE 4. Water Balance Components: (a) Evapotranspiration, (b) Rain, (c) Snow Water Equivalent, (d) Water Yield (output from SWAT model) for Baseline Period and Climate Scenarios. The gray lines represent eight climate change models output, dark dashed line represents climate change scenarios ensemble, and the black solid line represents model output of the baseline period.

1999) or, under scenarios of more extreme warming, no soil freezing at all. These changes in snow processes will likely affect the intensity and depth of soil freezing and thawing and the frequency of alternating freezing and thawing events in a given winter-spring season (Shanley and Chalmers, 1999; Groffman *et al.*, 2001). Xu (2000) investigated the influences of climate changes on the flow regimes for 25 catchments in central Sweden using a conceptual monthly water balance model, suggesting that significant increase in winter streamflow and decrease in spring and summer streamflow occurred during most scenarios. Nearly, all of the studies that have focused on the northeastern U.S. have estimated that, on average, annual streamflow should change (Neff *et al.*, 2000; Frei *et al.*, 2002; Hayhoe *et al.*, 2008) and project increased late winter and spring flows, and a shift in the timing of spring snowmelt. This indicates that there will be both a shift in timing and a change in volume of annual streamflow, with slightly lower flows in the summer and early autumn, lower flows in mid-spring, and higher flows in the winter and early spring.

Hydrologic Assessment of Streamflow Parameters and Potential Ecological Implications

We used median as an estimate of central tendency and the variance as an estimate of dispersion. For each 33 hydrologic parameters listed in Table 2, the differences between median of the baseline condition and climate change ensemble scenario are presented as both a magnitude of difference and a deviation percentage (Table 3). It is expected that the hydrologic indicators examined here have biological relevance, as many studies have linked estimates of stream health with streamflow, and there are fundamental reasons to believe this would be the case. The potential ecological implication of future streamflow

changes discussed here for the Cannonsville Reservoir watershed is based primarily on available relevant literature, from New York and other geographic regions, and further field research is needed to establish cause-and-effect relationships between hydrologic indicators and ecological responses in the Catskill Mountain Region. The value of this study is to demonstrate the possible changes in streamflow that could be of ecological concern, and therefore serve as justification for needed research on the ecological implications of potential change in the seasonality and variability of streamflow.

Magnitude of the Monthly Median of Daily Flows

The hydrologic assessment showed an increase in median monthly streamflow for winter months (Figure 5), with the highest increase during January (Table 3). Table 3 also shows the variability in the absolute magnitude of median streamflow for baseline and ensemble climate change scenarios. The values in parenthesis in Table 3 show the range of median and dispersion for eight climate models that were used in this study. The change in dispersion was minimal for June, July, November, and December streamflows. The largest decrease in dispersion was observed in January through March which is possibly due to the shifted snowmelt changing the variability during winter months. Gan (1998), in a study of the Canadian Prairies, found that over the last 40-50 years many stream and river gauging stations observed an increase in streamflow during March, attributed to earlier snowmelt, followed by reduced flow in May and June. Hydrologic changes accompanying increase in winter flow are likely to impact aquatic macroinvertebrate communities; however, little work has been done linking stream biota and effects of changes in stream flow in the Northeast U.S. Warren *et al.* (2009) assessed fish community data documenting winter and spring high flows and salmonid species in two the Catskill Mountain streams. They reported that the abundance of fall-spawning age-0 salmonids was significantly and inversely related to maximum winter-spring discharge, although the number of spring-spawning age-0 fish was not. High peak flow rates result in high-flow velocities and shear stresses that transport sediments (Poff *et al.*, 2006) and displace benthic organisms (Poff and Ward, 1990) and small aquatic fauna (Harvey, 1987). High shear stresses also increase the depth of bed scour and increase mortality of benthic invertebrates (Palmer *et al.*, 1992; Townsend *et al.*, 1997). Warren *et al.* (2009) reported that the decline in the total abundance of fall-spawning age-0 salmonids in the Catskill Mountain system during their study period was largely due to streambed scour during winter floods. In winter, more frequent rain-on-snow events could increase the incidence and magnitude of winter flooding in snow-dominated basins (Wigmosta and Leung, 2003); flooding degrades water quality by transporting silt into streams, and can also scour the streambed, washing away small organisms and organic matter that serve as important food resources for other species (Waters, 1995; Poff *et al.*, 1997).

The streamflow decreased from April through September with the greatest reduction in streamflow in April/May (Figure 5) which is probably due to reduced snow accumulation and melt. A study specific to the Catskill Mountain region of New York (Burns

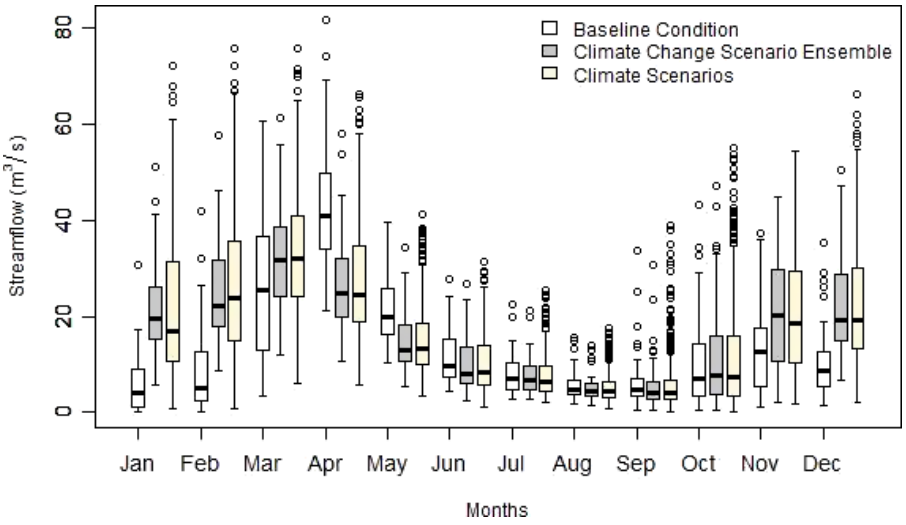

FIGURE 5. Monthly Median Streamflow (Group 1 Indicators) Box Plots for Baseline Scenario (hollow box), Average of Ensemble Climate Scenarios (gray box), and Climate Scenarios (bisque box). Climate scenario boxplot contains all the data points (monthly medians) for eight climate models showing the range of streamflow simulations using eight climate models.

et al., 2007) noted increasing trends in annual temperature, precipitation, PET, and runoff over a 50-year period starting in the 1950s. They also reported that there was notable (from 5 days to 15 days) backward shift in peak snowmelt from early April at the beginning of the historic record to late March by the end of the record and a decrease in runoff from June to October. Maurer (2007) reported that the A2 and B1 emissions pathways show some differing impacts with high confidence in Sierra Nevada, California: the degree of warming expected, the amount of decline in summer low flows, the shift to earlier streamflow timing, and the decline in end-of-winter snowpack, with more extreme impacts under higher emissions in all cases. Mantua *et al.* (2010) evaluated that extreme daily high and low streamflows are evaluated under multimodel composites for A1B and B1 greenhouse gas emissions scenarios and reported that the combined effects of warming summertime stream temperatures and altered streamflow will likely reduce the reproductive success for many Washington salmon populations, with impacts varying for different life-history types and watershed types. The amount of water available in a river defines the suitability of a habitat to aquatic organisms, therefore, streamflow alteration, especially low flows, can have profound impacts on native species. Wills *et al.* (2006) reported in their study in streams of Michigan that flow reductions can reduce the density of many benthic insect species, particularly filter feeding and grazing taxa, and those taxa that typically use erosional habitats. Lower summer flows can lead to increased water temperatures and reduced dissolved oxygen, which in turn lead to reduce instream habitat for invertebrates and fish, and may increase mortality of certain juvenile fish species (Meyer and Edwards, 1990; Stromberg *et al.*, 1996; Scott *et al.*, 1999), increase rate of microbial activity and decomposition resulting in decrease in food available for invertebrates and fish (Meyer and Edwards, 1990). Lower flows also indicate a reduced wetted perimeter, which would decrease habitat availability and impact lateral exchanges between the riparian zone and the stream and less water for sustaining riparian tree communities. Because low flows are less effective at diluting pollutants, lower instream flows in summer months could contribute to lowered water quality (especially if the timing of pollution events coincide with reduced flows), resulting in decreased macroinvertebrate and fish populations (IPCC, 2007).

Magnitude and Duration of Extreme Annual Conditions

Our study indicates increased future streamflow, particularly the streamflow occurring during low-flow periods. For example, the consecutive seven-day low flow increased by only 124% from baseline conditions whereas the seven-day high-flow discharge increased by only 2.7% from baseline under different climate scenarios (Table 3), similar to the observations made by McCabe and Wolock (2002) for the conterminous U.S. In general, the longer the time period examined the smaller the percent change between baseline and future conditions. All time periods showed increases except the 90-day minimum and maximum streamflow which decreased from baseline to ensemble scenarios; while at the same time showing an increase in variability. The base-flow coefficient increased from 0.05 to 0.07 and may result from the change in projected climate effecting soil moisture and soil water storage. A study in Monroe County, New York by Coon (2005) assessing trends from 1965 to 2005 noted an increase in temperature, precipitation, and seven-day low flows in rural streams; consistent with trends observed elsewhere in the U.S. Hodgkins *et al.* (2003) documented that peak river flows occurred several weeks earlier throughout the Northeast. McCabe and Wolock (2002) assessed streamflow at 400 sites in the conterminous U.S. from 1941 to 1999 and documented an increase in annual minimum and median daily streamflow beginning in 1970, and the trend was particularly strong in the East (also corroborated by Baker *et al.*, 2004). This finding matches results of other studies that found low flows increasing in the upper Midwest (Lins and Slack, 1999; Douglas *et al.*, 2000).

Timing of the Annual Extremes and Rate and Frequency of Change

The timing of the maximum one-day flow shifted backward by approximately six days for future scenarios, while there was a forward shift in the timing of minimum flow (from early February to September) (Table 4). The streamflow output for GCM scenarios, however, showed wide range of maximum flow showing timing as early as late December as indicated in parentheses of Table 4. Such wide range indicates that the climate models are bound with uncertainty and therefore, using multiple climate models provide possible ranges of certain hydrologic alterations. This effect is mainly the result of increased winter flow rather than decreased fall streamflow. Such temporal shift in the water balance was also reported by Burns *et al.* (2007) in the NYC watersheds. A preliminary investigation of potential climate change using both the GWLF-VSA and the SWAT models by Zion *et al.* (2011) showed that there was a shift in winter-spring center of volume of streamflow of about 15-20 days earlier for A2 and B1 emission scenarios 100 years

TABLE 4. Results of Indicators of Hydrologic Alteration Analysis for Stream at Walton, New York. Values in the Parenthesis Are the Minimum and Maximum Values Obtained from Eight GCMs for the Corresponding Parameters.

	Medians			Dispersion		
	Streamflow[1] (m^3/s)					
	Baseline Condition (1964-2008)	Ensemble Scenario (2081-2100)	Deviation[2]/ Magnitude %	Baseline Condition (1964-2008)	Ensemble Scenario (2081-2100)	Deviation/ Magnitude %
Parameter Group #1: Monthly magnitude						
January	4.07	19.5 (10.6-30.1)	15.4/379	2.10	1.02 (0.75-1.25)	−1.08/−51.4
February	4.99	22.2 (13.4-28.5)	17.2/344	2.44	0.81 (0.66-1.02)	−1.63/−66.9
March	25.5	31.6 (19.6-39.5)	6.10/23.9	0.98	0.47 (0.37-0.60)	−0.51/−52.0
April	40.8	24.7 (15.1-34.5)	−16.1/−39.5	0.40	0.52 (0.40-0.67)	0.12/29.2
May	19.9	12.9 (8.81-15.3)	−7.03/−35.3	0.47	0.67 (0.54-0.90)	0.20/41.5
June	9.69	8.06 (6.72-10.3)	−1.63/−16.8	0.81	1.01 (0.81-1.13)	0.20/24.6
July	7.00	6.58 (4.97-8.38)	−0.42/−6.0	0.84	0.83 (0.65-1.04)	−0.01/−1.20
August	4.71	4.44 (3.02-5.89)	−0.27/−5.8	0.68	0.65 (0.50-0.80)	−0.03/−5.00
September	4.61	4.11 (2.87-6.34)	−0.50/−10.9	0.88	0.91 (0.79-1.02)	0.02/2.80
October	7.12	7.59 (4.16-10.1)	0.47/6.6	1.63	1.74 (1.46-1.90)	0.11/6.80
November	12.5	20.2 (14.8-25.1)	7.68/61.2	0.99	0.98 (0.80-1.36)	−0.02/−1.50
December	8.73	19.2 (15.0-34.7)	10.5/120	0.82	0.82 (0.64-0.94)	0.00/−0.20
Group averages[3]			**68.4%**			**−6.11%**
Parameter Group #2: Magnitude and duration of annual extremes						
One-day minimum	0.21	0.50 (0.17-0.77)	0.29/140	2.81	1.38 (0.96-1.63)	−1.49/−50.8
Three-day minimum	0.27	0.65 (0.25-1.02)	0.38/144	2.55	1.27 (0.91-1.48)	−1.28/−50.2
Seven-day minimum	0.47	1.04 (0.50-1.68)	0.58/124	2.16	0.89 (0.67-1.08)	−1.27/−58.8
30-day minimum	2.44	2.73 (1.82-3.90)	0.29/12.0	0.95	0.70 (0.56-0.88)	−0.20/−26.3
90-day minimum	5.20	5.11 (3.64-5.93)	−0.09/−1.80	0.46	0.49 (0.39-0.65)	0.03/6.8
One-day maximum	130.0	137.4 (116.0-154.0)	7.40/5.70	0.59	0.57 (0.49-0.64)	−0.02/−4.0
Three-day maximum	98.3	105 (91.7-114.7)	6.57/6.70	0.54	0.49 (0.43-0.58)	−0.05/−9.0
Seven-day maximum	80.2	82.4 (72.5-88.5)	2.17/2.70	0.54	0.39 (0.34-0.44)	−0.15/−27.7
30-day maximum	51.7	53.5 (46.3-58.3)	1.80/3.50	0.49	0.37 (0.25-0.47)	−0.12/−24.5
90-day maximum	36.5	35.3 (33.4-39.3)	−1.14/−3.10	0.30	0.35 (0.27-0.40)	0.05/16.6
Base flow	0.02	0.07 (0.03-0.09)	0.05/222	2.41	0.80 (0.63-0.97)	−1.61/66.8
Group averages[3]			**54.6%**			**−31.0%**
Parameter Group #3: Timing of annual extremes						
Date of minimum	50.0	253.5 (248.0-257.0)	202.5/397	0.14	0.11 (0.09-0.14)	−0.03/−23.6
Date of maximum	84.0	79.8 (33.0-349.0)	−4.22/−5.0	0.14	0.19 (0.16-0.29)	0.04/29.2
Group averages[3]			**196%**			**2.80%**
Parameter Group #4: Frequency and duration of high and low pulses						
Low pulse count	11.0	9.11 (8.0-10.0)	−1.89/−17.20	0.55	0.56 (0.40-0.75)	0.02/3.30
Low pulse duration	5.00	4.67 (4.0-6.0)	−0.33/−6.70	0.60	0.68 (0.44-0.88)	0.08/13.9
High pulse count	12.0	14.2 (13.0-15.0)	2.22/18.50	0.42	0.44 (0.36-0.53)	0.027/5.1
High pulse duration	4.00	3.94 (3.5-4.0)	−0.66/−1.40	0.50	0.58 (0.50-0.69)	0.08/16.9
Group averages[3]			**−1.7%**			**9.80%**
Parameter Group #5: Rate and frequency of change in conditions						
Rise rate	2.16	2.33 (2.05-2.58)	0.17/8.1	0.61	0.42 (0.29-0.55)	−0.19/−31.5
Fall rate	−1.12	−1.37 (−1.50 - −1.20)	−0.25/22.5	−0.28	−0.35 (−0.40 - −0.30)	−0.07/24.3
Reversals	116	126.2 (119.0-131.0)	10.22/8.8	0.15	0.11 (0.09-0.13)	−0.04/−24.5
Group averages[3]			**13.1%**			**10.57%**

Note: Bold values in the table indicate group averages of magnitude (%).
[1]Daily median streamflow in cubic meter per second.
[2]The deviations represent the Indicators of Hydrologic Alterations.
[3]Group averages are computed as the mean of all deviations within the group.

into the future. Some potential impacts of this shift in streamflow timing include changes in the timing of water supply reservoir filling and spills (Matonse *et al.*, 2011), and changes in the timing of sediment and nutrient delivery to reservoirs impacting reservoir water quality. According to Warren *et al.* (2009), rainbow trout in the Catskill Mountain system spawn from late March to the second week in April, followed by emergence three or more weeks later, depending on stream temperature, whereas brook trout and brown trout in New York streams emerge from March through May (Smith, 1985). Shift in timing of maximum flow therefore may delay emergence of rainbow trout in these streams. A shift in the timing of peak flow can also

change the retention time of organic matter (Mulholland *et al.*, 1997), disrupting the recruitment of riparian species that depend on high flows to disperse seeds on the floodplain (Auble *et al.*, 1994; Rood *et al.*, 1995).

The behavior of the stream at the USGS gauge in Walton, shows a reduced (17.2%) number of low pulse events, but an increase of 18.5% in high pulse events compared to the baseline scenario (Table 4). The median duration of both low and high pulse flows, however, was reduced. Our results showed an increase in both rise and decrease in the fall rate of the hydrograph (e.g., steeper rising and receding limbs) resulting in increase in number of reversals. Increase in rising limb of hydrograph may affect aquatic organisms as there will be less time to find refuge and avoid being flushed out by the approaching high-flow conditions. This variability in the rate of hydrograph rise and fall may affect aquatic invertebrates inhabiting the littoral zone along the river's edge (Richter *et al.*, 1996).

Flow Components and Duration

Flow conditions such as low and high flows or floods are important consequences of the nonlinear change that can result in small climatic perturbations leading to more extreme impacts. Our analyses show that there will be shifts in timing and duration of flow peaks. Both the 2-year return interval storm (small flood) and the 10-year return interval storm (moderate flood) will increase by 8.6% and 11.9%, respectively, and both will shift in timing from spring to winter. A small flood includes all river rises that overtop the main channel but does not include more extreme and less frequent floods. The 10-year storms will decrease in duration and show a more flashy response, with the rates at which the hydrograph rises and falls increasing (Figure 6). As a result, even though the duration of the large floods is expected to decrease, the intensity (peak flow) is expected to increase. Increases in flashy short duration floods can pose threats to streambank stability near stream habitat depending on the streambank characteristics. Small floods correspond to a two-year return period, often referred to as bankfull flow or channels forming flow are important indicators of increased stream channel erosion. Wolman and Miller (1960) reported that flows with a one to five-year return period are important to stream geomorphology being capable of moving significant amounts of sediment. Increased frequency of substrate-disturbing events can lead to a shift toward "weedy" invertebrate species and loss of species with poor recolonization ability.

The final analysis included evaluation of seasonal flow duration curves (FDC). FDC methods are commonly used in a variety of streamflow assessments (Vogel and Fennessey, 1995; Acreman, 2005) because they provide a graphical illustration of the hydrologic conditions of a river system. Using probability of exceedance or frequency of streamflow as a common index, FDCs were plotted (Figure 7) for climate change scenarios. These curves represent cumulative probability distribution of seasonal streamflow. Results show an increase in streamflow during January, February, and March months for all the flow regimes, with greater impact on the low to medium flows. Streamflow during summer and fall months showed minimal change from the baseline scenario.

The indicators of hydrologic alteration provide a link between river flow and river condition by identifying critical variations in magnitude, timing, duration, frequency, and rate of change in streamflow. These indicators offer water resource managers a preliminary assessment tool of the range of flow characteristics that can influence aquatic ecosystems.

CONCLUSIONS

This study used SWAT-WB model to simulate streamflow and to evaluate effects of climate change on streamflow characteristics influencing stream ecology. The effects of climate on the seasonality and variability in hydrologic flow regime were estimated using the IHA tool (Richter *et al.*, 1996). Comparative analyses between the streamflow for a baseline period (1964-2008) and climate change simulations were then carried out for different streamflow indicators, which are important for understanding how river flow dynamics will impact the health of the aquatic environment as well as water supply and other

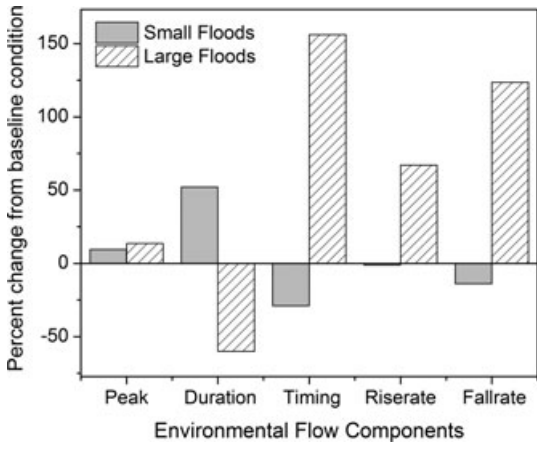

FIGURE 6. Percent Change in Magnitude, Duration, Timing, and Rate of Small and Large Flood.

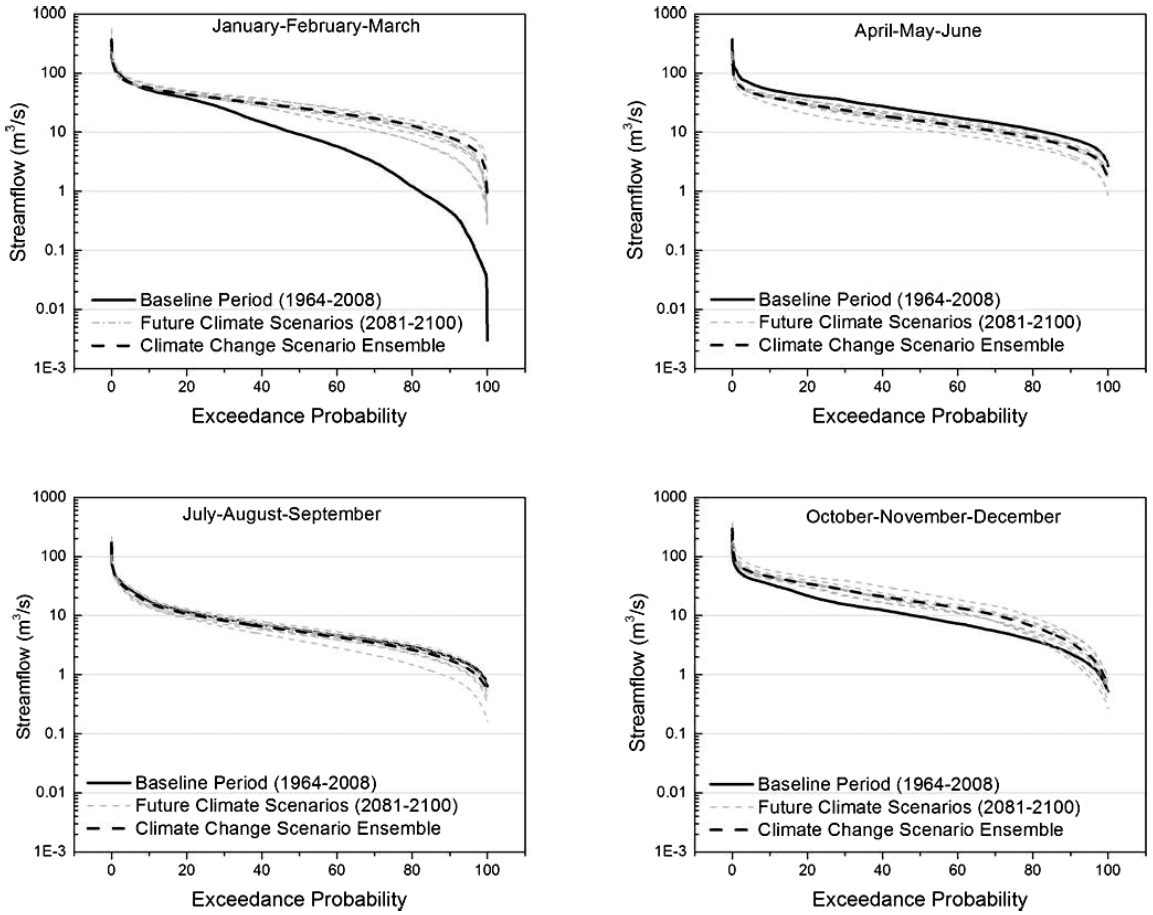

FIGURE 7. Flow Duration Curve of Seasonal Streamflow in WBDR. The gray dotted lines represent eight climate change models output, dark dashed line represents climate change scenarios ensemble, and the black solid line represents model output of the baseline period.

infrastructure. The generally good performance over the calibration and validation periods suggested that the model could be used to simulate the impact of climate change scenarios. The results suggest that water yield is expected to increase at annual scale, and that winter and early spring streamflow will increase, but that summer is expected to become slightly drier in future. Our study predicted increased monthly streamflow during late fall and winter (November through March), with the remaining months often showing a decrease in monthly flow especially during April, May, and June. These are times when water management will become increasingly important, and could also have potential impacts on crop growth due to water stress during summer months. The magnitude and duration of annual extremes, i.e., daily minimum and maximum, are also expected to increase due to climate change. Lower flows would result in a smaller wetted perimeter, which would decrease habitat availability and impact lateral exchanges between the near-stream zone and the stream channel. The timing of annual maximum flows is projected to shift backwards in time by six days. The minimum flow is projected to shift forward, from February to September. Such shifts in high- and low-flow periods would likely adversely affect the fall spawning of species such as brook trout due to reduced habitat availability resulting from extended low-flow conditions, or other species that time their spawning behavior relative to peak spring flows. Both the rise and fall rates of the hydrograph will increase resulting in increased flashiness and a greater number of flow reversals primarily due to increased pulses during winter seasons.

Changes in land surface hydrology due to climate change, such as changes in the discharge of large rivers, have potentially far reaching implications both for human populations and for regional-scale physical and ecological processes. The geographic and topographic characteristics of watersheds and the climatic variations that determine their hydrologic characteristics often constitute the defining features of the regions they occupy. They govern to a considerable extent the development of ecosystems, as well as human communities and their activities. These regional ecosystems and human activities are usually reasonably well adapted to the current climate conditions, but may be vulnerable to large

or rapid changes in climate. It should also be noted that future flow conditions cannot be projected exactly due to the uncertainty in GCM outputs and scenarios. However, the results obtained in this study are expected to provide more insights into the availability of future streamflow, and to provide local water management authorities with the planning tool.

ACKNOWLEDGMENTS

The authors would like to thank the New York City Department of Environmental Protection for providing funds and necessary support to conduct this research. The authors are also grateful to David Lounsbury, NYCDEP for GIS support and two anonymous reviewers for their valuable comments and suggestions.

LITERATURE CITED

Abbaspour, K.C., J. Yang, I. Maximov, R. Siber, K. Bogner, J. Mieleitner, J. Zobrist, and R. Srinivasan, 2007. Modelling Hydrology and Water Quality in the Pre-Alpine/Alpine Thur Watershed Using SWAT. Journal of Hydrology 333:413-430.

Acreman, M., 2005. Linking Science and Decision-Making: Features and Experience From Environmental River Flow Setting. Environmental Modeling & Software 20:99-109.

Anandhi, A., A. Frei, D.C. Pierson, E.M. Schneiderman, M.S. Zion, D. Lounsbury, and A.H. Matonse, 2011. Examination of Change Factor Methodologies for Climate Change Impact Assessment. Water Resources Research 47:10.

Arnell, N.W., M.J.L. Livermore, S. Kovats, P.E. Levy, R. Nicholls, M.L. Parry, and S.R. Gaffin, 2004. Climate and Socio-Economic Scenarios for Global-Scale Climate Change Impacts Assessments: Characterising the SRES Storylines. Global Environmental Change 14:3-20.

Arnold, J. and P. Allen, 1996. Estimating Hydrologic Budgets for Three Illinois Watersheds. Journal of Hydrology 176:57-77.

Arnold, J.G. and P.M. Allen, 1999. Automated Methods for Estimating Baseflow and Groundwater Recharge From Streamflow. Journal of the American Water Resources Association 35(2):411-424.

Arnold, J.G., R. Srinivasan, R.S. Muttiah, and P.M. Allen, 1999. Continental Scale Simulation of the Hydrologic Balance. Journal of the American Water Resources Association 35:1037-1051.

Auble, G.T., J.M. Friedman, and M.L. Scott, 1994. Relating Riparian Vegetation to Present and Future Streamflows. Ecological Applications 4:544-554.

Baker, D.B., P. Richards, T.L. Loftus, and J.W. Kramer, 2004. A New Flashiness Index: Characteristics and Applications to Midwestern Rivers and Streams. Journal of the American Water Resources Association 40:503-522.

Benaman, J. and C.A. Shoemaker, 2005. An Analysis of High-Flow Sediment Event Data for Evaluating Model Performance. Hydrological Processes 19:605-620.

Bennett, K.E., A.T. Werner, and M. Schnorbus, 2012. Uncertainties in Hydrologic and Climate Change Impact Analyses in Headwater Basins of British Columbia. Journal of Climate 25:5711-5730.

Bouraoui, F., S. Benabdallah, A. Jrad, and G. Bidoglio, 2005. Application of the SWAT Model on the Medjerda River Basin (Tunisia). Physics and Chemistry of the Earth, Parts A/B/C 30:497-507.

Bouraoui, F. and B. Grizzetti, 2008. An Integrated Modelling Framework to Estimate the Fate of Nutrients: Application to the Loire (France). Ecological Modelling 212:450-459.

Brekke, L.D., M.D. Dettinger, E.P. Maurer, and M. Anderson, 2008. Significance of Model Credibility in Estimating Climate Projection Distributions for Regional Hydroclimatological Risk Assessments. Climatic Change 89:371-394.

Brown, C.D. and J.M. Hollis, 1996. SWAT—A Semi-Empirical Model to Predict Concentrations of Pesticides Entering Surface Waters From Agricultural Land. Pesticide Science 47:41-50.

Bunn, S.E. and A.H. Arthington, 2002. Basic Principles and Ecological Consequences of Altered Flow Regimes for Aquatic Biodiversity. Environmental Management 30:492-507.

Burakowski, E.A., C.P. Wake, B. Braswell, and D.P. Brown, 2008. Trends in Wintertime Climate in the Northeastern United States: 1965–2005. Journal of Geophysical Research 113: D20114.

Burn, D.H. and E.D. Soulis, 1992. The Use of Hydrologic Variables in Detecting Climatic Change: Possibilities for Single Station and Regional Analysis. *In:* Using Hydrometric Data to Detect and Monitor Climatic Change, G.W. Kite and K.D. Harvey (Editors). Proceedings of NHRI Workshop No. 8 National Hydrology Research Institute, Saskatoon, Saskatchewan, pp. 121-130.

Burns, D.A., J. Klaus, and M.R. McHale, 2007. Recent Climate Trends and Implications for Water Resources in the Catskill Mountain Region, New York, USA. Journal of Hydrology 336:155-170.

Caballero, Y., S. Voirin-Morel, F. Habets, J. Noilhan, P. LeMoigne, A. Lehenaff, and A. Boone, 2007. Hydrological Sensitivity of the Adour-Garonne River Basin to Climate Change. Water Resources Research 43:W07448.

Coon, W., 2005. Hydrologic Evidence of Climate Change in Monroe County, NYS. US Geological Survey, OFR 2008-1199.

Delworth, T.L., A.J. Broccoli, A. Rosati, R.J. Stouffer, V. Balaji, J.A. Beesley, W.F. Cooke, K.W. Dixon, J. Dunne, K.A. Dunne, J.W. Durachta, K.L. Findell, P. Ginoux, A. Gnanadesikan, C.T. Gordon, S.M. Griffies, R. Gudgel, M.J. Harrison, I.M. Held, R.S. Hemler, L.W. Horowitz, S.A. Klein, T.R. Knutson, P.J. Kushner, A.R. Langenhorst, H.-C. Lee, S.-J. Lin, J. Lu, S.L. Malyshev, P.C.D. Milly, V. Ramaswamy, J. Russell, M.D. Schwarzkopf, E. Shevliakova, J.J. Sirutis, M.J. Spelman, W.F. Stern, M. Winton, A.T. Wittenberg, B. Wyman, F. Zeng, and R. Zhang, 2006. GFDL's CM2 Global Coupled Climate Models. Part I: Formulation and Simulation Characteristics. Journal of Climate 19:643-674.

Douglas, E.M., R.M. Vogel, and C.N. Kroll, 2000. Trends in Floods and Low Flows in the United States: Impact of Spatial Correlation. Journal of Hydrology 240:90-105.

Duan, Q., S. Sorooshian, and V.K. Gupta, 1994. Optimal Use of the SCE-UA Global Optimization Method for Calibrating Watershed Models. Journal of Hydrology 158:265-284.

Dunne, T. and R.D. Black, 1970. Partial Area Contributions to Storm Runoff in a Small New England Watershed. Water Resources Research 6:1296-1311.

Easton, Z.M., D.R. Fuka, M.T. Walter, D.M. Cowan, E.M. Schneiderman, and T.S. Steenhuis, 2008. Re-Conceptualizing the Soil and Water Assessment Tool (SWAT) Model to Predict Runoff From Variable Source Areas. Journal of Hydrology 348:279-291.

Easton, Z.M., M.T. Walter, D.R. Fuka, E.D. White, and T.S. Steenhuis, 2011. A Simple Concept for Calibrating Runoff Thresholds in Quasi-Distributed Variable Source Area Watershed Models. Hydrological Processes 25:3131-3143.

Flato, G.M. and G.J. Boer, 2001. Warming Asymmetry in Climate Change Simulations. Geophysical Research Letters 28:195-198.

Fowler, H., S. Blenkinsop, and C. Tebaldi, 2007. Linking Climate Change Modelling to Impacts Studies: Recent Advances in Downscaling Techniques for Hydrological Modelling. International Journal of Climatology 27:1547-1578.

Frei, A., R.L. Armstrong, M.P. Clark, and M.C. Serreze, 2002. Catskill Mountain Water Resources: Vulnerability, Hydroclimatology, and Climate-Change Sensitivity. Annals of the Association of American Geographers 92:203-224.

Gan, T.Y., 1998. Hydroclimatic Trends and Possible Climatic Warming in the Canadian Prairies. Water Resources Research 34(11):3009-3015.

Gibson, C.A., J.L. Meyer, N.L. Poff, L.E. Hay, and A. Georgakakos, 2005. Flow Regime Alterations Under Changing Climate in Two River Basins: Implications for Freshwater Ecosystems. River Research and Applications 21:849-864.

Gleckler, P.J., K.E. Taylor, and C. Doutriaux, 2008. Performance Metrics for Climate Models. Journal of Geophysical Research 113:D06104.

Gordon, C., C. Cooper, C.A. Senior, H. Banks, J.M. Gregory, T.C. Johns, J.F.B. Mitchell, and R.A. Wood, 2000. The Simulation of SST, Sea Ice Extents and Ocean Heat Transports in a Version of the Hadley Centre Coupled Model Without Flux Adjustments. Climate Dynamics 16:147-168.

Groffman, P.M., C.T. Driscoll, T.J. Fahey, J.P. Hardy, R.D. Fitzhugh, and G.L. Tierney, 2001. Colder Soils in a Warmer World: A Snow Manipulation Study in a Northern Hardwood Forest Ecosystem. Biogeochemistry 56:135-150.

Harvey, B.C., 1987. Susceptibility of Young-of-the-Year Fishes to Downstream Displacement by Flooding. Transactions of the American Fisheries Society 116:851-855.

Hay, L.E., R.L. Wilby, and G.H. Leavesley, 2000. A Comparison of Delta Change and Downscaled GCM Scenarios for Three Mountain Basins in the United States. Journal of the American Water Resources Association 36:387-397.

Hayhoe, K., C. Wake, B. Anderson, X.-Z. Liang, E. Maurer, J. Zhu, J. Bradbury, A. DeGaetano, A. Stoner, and D. Wuebbles, 2008. Regional Climate Change Projections for the Northeast USA. Mitigation and Adaptation Strategies for Global Change 13:425-436.

Hayhoe, K.A., 2010. A Standardized Framework for Evaluating the Skill of Regional Climate Downscaling Techniques. Ph.D. Thesis, University of Illinois at Urbana-Champaign. Publication Number: AAT 3430975, ISBN: 9781124315010, Source: Dissertation Abstracts International, Volume 71-12, Section B, 158 pp.

Hodgkins, G.A., R.W. Dudley, and T.G. Huntington, 2003. Changes in the Timing of High River Flows in New England Over the 20th Century. Journal of Hydrology 278:244-252.

IPCC, 2007. Climate Change 2007: The Physical Sciencebasis. Contribution of Working Group I to the Fourth Assessment. *In*: Report of the Intergovernmental Panel on Climate Change, S. Solomon, D. Qin, M. Manning, Z. Chen, M. Marquis, K.B. Averyt, M. Tignor, and H.L. Miller (Editors). Cambridge University Press, Cambridge, United Kingdom and New York.

Jungclaus, J.H., M. Botzet, H. Haak, N. Keenlyside, J.J. Luo, M. Latif, J. Marotzke, U. Mikolajewicz, and E. Roeckner, 2006. Ocean Circulation and Tropical Variability in the Coupled Model ECHAM5/MPI. Journal of Climate 19(16):3952-3972.

K-1 Model Developers, 2004. K-1 Coupled Model (MIROC) Description, K-1 Technical Report, 1, H. Hasumi and S. Emori (Editors). Center for Climate System Research, University of Tokyo, Japan, 34 pp.

Krause, P., D.P. Boyle, and F. Bäse, 2005. Comparison of Different Efficiency Criteria for Hydrological Model Assessment. Advances in Geosciences 5:89-97.

Lettenmaier, D.P., E.F. Wood, and J.R. Wallis, 1994. Hydro-Climatological Trends in the Continental United States 1948-1988. Journal of Climate 7(4):586-607.

Lins, H.F. and J.R. Slack, 1999. Stream Flow Trends in the United States. Geophysical Research Letters 26:227-230.

Mantua, N., I. Tohver, and A. Hamlet, 2010. Climate Change Impacts on Streamflow Extremes and Summertime Stream Temperature and Their Possible Consequences for Freshwater Salmon Habitat in Washington State. Climatic Change 102:187-223.

Marti, O., P. Braconnot, J. Bellier, R. Benshila, S. Bony, P. Brockmann, P. Cadule, A. Caubel, S. Denvil, J.L. Dufresne, L. Fairhead, M.A. Filiberti, M.A. Foujols, T.T. Fichefet, P. Friedlingstein, H. Gosse, J.Y. Grandpeix, F.F. Hourdin, G. Krinner, C. Lévy, G. Madec, I. Musat, N. de Noblet, J. Polcher, and C. Talandier, 2006. The New IPSL Climate System Model: IPSL-CM4. Institut Pierre-Simon Laplace (IPSL), Notes Sci. Pole Model Climate, Ref. Manual, Vol. 26, Institut Pierre-Simon Laplace, Gif sur Yvette, France.

Matonse, A.H., D.C. Pierson, A. Frei, M.S. Zion, E.M. Schneiderman, A. Anandhi, R. Mukundan, and S.M. Pradhanang, 2011. Effects of Changes in Snow Pattern and the Timing of Runoff on NYC Water Supply System. Hydrological Processes 25:3278-3288.

Maurer, E.P., 2007. Uncertainty in Hydrologic Impacts of Climate Change in the Sierra Nevada, California, Under two Emissions Scenarios. Climatic Change 82:309-325.

McCabe, G.J. and D.M. Wolock, 2002. A Step Increase in Streamflow in the Conterminous United States. Geophysics Research Letters 29: 2185.

Meyer, J.L. and R.T. Edwards, 1990. Ecosystem Metabolism and Turnover of Organic Carbon Along a Blackwater River Continuum. Ecology 60:1255-1269.

Moriasi, D.N., J.G. Arnold, M.W. Van Liew, R.L. Bingner, R.D. Harmel, and T.L. Veith, 2007. Model Evaluation Guidelines for Systematic Quantification of Accuracy in Watershed Simulations. Transactions of ASAE 50:885-900.

Mukundan, R., S.M. Pradhanang, E.M. Schneiderman, D.C. Pierson, A. Anandhi, M.S. Zion, A.H. Matonse, D.G. Lounsbury, and T.S. Steenhuis, 2013. Suspended Sediment Source Areas and Future Climate Impact on Soil Erosion and Sediment Yield in a New York City Water Supply Watershed, USA. Geomorphology 183:110-119.

Mulholland, P.J., G.R. Best, C.C. Coutant, G.M. Hornberger, J.L. Meyer, P.J. Robinson, J.R. Steinberg, R.E. Turner, F. Vera-Herrera, and R.G. Wetzel, 1997. Effects of Climate Change on Freshwater Ecosystems of the South-Eastern United States and the Gulf Coast of Mexico. Hydrological Processes 11:949-970.

Najafi, M.R., H. Moradkhani, and I.-W. Jung, 2010. Combined Effect of Global Climate Projection and Hydrologic Model Uncertainties on the Future Changes of Streamflow. *In:* World Environmental and Water Resources Congress 2010, Providence, Rhode Island, May 16-20, R.N. Palmer (Editor). American Society of Civil Engineers, pp. 81-91.

Nash, J.E. and J.V. Sutcliffe, 1970. River Flow Forecasting Through Conceptual Models. Part I: A Discussion of Principles. Journal of Hydrology 10:282-290.

Neff, R., H. Chang, C.G. Knight, R.G. Najjar, B. Yarnal, and H.A. Walker, 2000. Impact of Climate Variation and Change on Mid-Atlantic Region Hydrology and Water Resources. Climate Research 14:207-218.

Neitsch, S.L., J.G. Arnold, J.R. Kiniry, R. Srinivasan and J.R. Williams, 2005. Soil and Water Assessment Tool: Theoretical Documentation. Blackland Research Center, Texas Agricultural Experiment Station, Temple, Texas. Version 2005.

Palmer, M.A., A.E. Bely, and K.E. Berg, 1992. Response of Invertebrates to Lotic Disturbances - A Test of the Hyporheic Refuge Hypothesis. Oecologia 89(2):182-194.

Piani, C., G. Weedon, M. Best, S. Gomes, P. Viterbo, S. Hagemann, and J. Haerter, 2010. Statistical Bias Correction of Global Simulated Daily Precipitation and Temperature for the Application of Hydrological Models. Journal of Hydrology 395:199-215.

Pierce, D.W., T.P. Barnett, B.D. Santer, and P.J. Gleckler, 2009. Selecting Global Climate Models for Regional Climate Change Studies. Proceedings of the National Academy of Sciences 106:8441-8446.

Poff, N.L., J.D. Allan, M.B. Bain, J.R. Karr, K.L. Prestegaard, B.D. Richter, R.E. Sparks, and J.C. Stromberg, 1997. The Natural Flow Regime. BioScience 47:769-784.

Poff, N.L., B.P. Bledsoe, and C.O. Cuhaciyan, 2006. Hydrologic Variation With Land Use Across the Contiguous United States: Geomorphic and Ecological Consequences for Stream Ecosystems. Geomorphology 79:264-285.

Poff, N.L. and J.V. Ward, 1990. Physical Habitat Template of Lotic Systems: Recovery in the Context of Historical Pattern of Spatiotemporal Heterogeneity. Environmental Management 14:629-645.

Pradhanang, S.M., A. Anandhi, R. Mukundan, M.S. Zion, D.C. Pierson, E.M. Schneiderman, A. Matonse, and A. Frei, 2011. Application of SWAT Model to Assess Snowpack Development and Streamflow in the Cannonsville Watershed, New York, USA. Hydrological Processes 25:3268-3277.

Prudhomme, C., N. Reynard, and S. Crooks, 2002. Downscaling of Global Climate Models for Flood Frequency Analysis: Where Are We Now? Hydrological Processes 16:1137-1150.

Richter, B., J. Baumgartner, R. Wigington, and D. Braun, 1997. How Much Water Does a River Need? Freshwater Biology 37:231-249.

Richter, B.D., J.V. Baumgartner, D.P. Braun, and J. Powell, 1998. A Spatial Assessment of Hydrologic Alteration Within a River Network. Regulated Rivers: Research & Management 14:329-340.

Richter, B.D., J.V. Baumgartner, J. Powell, and D.P. Braun, 1996. A Method for Assessing Hydrologic Alteration Within Ecosystems. Conservation Biology 10:1163-1174.

Richter, B.D., R. Mathews, D.L. Harrison, and R. Wigington, 2003. Ecologically Sustainable Water Management: Managing River Flows for Ecological Integrity. Ecological Applications 13:206-224.

Risbey, J.S. and D. Entekhabi, 1996. Observed Sacramento Basin Streamflow Response to Precipitation and Temperature Changes and Its Relevance to Climate Impact Studies. Journal of Hydrology 184:209-223.

Rood, S.B., J.M. Mahoney, D.E. Reid, and L. Zilm, 1995. Instream Flows and the Decline of Riparian Cottonwoods Along the St. Mary River, Alberta. Canadian Journal of Botany 73:1250-1260.

Russell, G.L., J.R. Miller, and D. Rind, 1995. A Coupled Atmosphere-Ocean Model for Transient Climate Change Studies. Atmosphere-Ocean 33:683-730.

Santhi, C., N. Kannan, J.G. Arnold, and M. Di Luzio, 2008. Spatial Calibration and Temporal Validation of Flow for Regional Scale Hydrologic Modeling. Journal of the American Water Resources Association 44:829-846.

Schneiderman, E.M., T.S. Steenhuis, D.J. Thongs, Z.M. Easton, M.S. Zion, A.L. Neal, G.F. Mendoza, and M. Todd Walter, 2007. Incorporating Variable Source Area Hydrology Into a Curve-Number-Based Watershed Model. Hydrological Processes 21:3420-3430.

Scott, M.L., P.B. Shafroth, and G.T. Auble, 1999. Responses of Riparian Cottonwoods to Alluvial Water Table Declines. Environmental Management 23:347-358.

Shanley, J.B. and A. Chalmers, 1999. The Effect of Frozen Soil on Snowmelt Runoff at Sleepers River, Vermont. Hydrological Processes 13:1843-1857.

Smith, C.L., 1985. The Inland Fishes of New York. New York State Department of Environmental Conservation, Albany, New York.

Stromberg, J.C., R. Tiller, and B.D. Richter, 1996. Effects of Groundwater Decline on Riparian Vegetation of Semi-Arid Regions: The San Pedro River, Arizona, USA. Ecological Applications 6:113-131.

Townsend, C.R., S. Doledec, and M.R. Scarsbrook, 1997. Species Traits in Relation to Temporal and Spatial Heterogeneity in Streams: A Test of Habitat Template Theory. Freshwater Biology 37:367-387.

USDA-NRCS, 2000. Soil Survey Geographic (SSURGO) Database for Delaware County, New York.

Van Griensven, A., T. Meixner, S. Grunwald, T. Bishop, M. Diluzio, and R. Srinivasan, 2006. A Global Sensitivity Analysis Tool for the Parameters of Multi-Variable Catchment Models. Journal of Hydrology 324:10-23.

Vogel, R.M. and N.M. Fennessey, 1995. Flow Duration Curves II: A Review of Applications in Water Resources Planning. Water Resources Bulletin 31:1029-1039.

Walter, M.T., T.S. Steenhuis, V.K. Mehta, D. Thongs, M. Zion, and E. Schneiderman, 2002. Refined Conceptualization of TOPMOD-EL for Shallow Subsurface Flows. Hydrological Processes 16:2041-2046.

Warren, D.R., A.G. Ernst, and B.P. Baldigo, 2009. Influence of Spring Floods on Year-Class Strength of Fall- and Spring-Spawning Salmonids in Catskill Mountain Streams. Transactions of the American Fisheries Society 138:200-210.

Waters, T.F., 1995. Sediment in Streams—Sources, Biological Effects and Control: Monograph 7. American Fisheries Society, Bethesda, Maryland, 249 pp.

White, E.D., Z.M. Easton, D.R. Fuka, A.S. Collick, E. Adgo, M. McCartney, S.B. Awulachew, Y.G. Selassie, and T.S. Steenhuis, 2011. Development and Application of a Physically Based Landscape Water Balance in the SWAT Model. Hydrological Processes 25:915-925.

Wigmosta, M. and R. Leung, 2003. Impacts of Climate Change on Streamflow and Flooding in Snow Dominated Basins. *In:* Environmental Change and Geomorphic Hazards in Forests IUFRO Research Series, No. 9, R.C. Sidle (Editor), CABI Publishing, Wallingford, United Kingdom, pp. 7-24.

Wilby, R., S. Charles, E. Zorita, B. Timbal, P. Whetton, and L. Mearns, 2004. Guidelines for Use of Climate Scenarios Developed From Statistical Downscaling Methods. IPCC Task Group on Data and Scenario Support for Impacts and Climate Analysis. Available from the Data Distribution Center of IPCC TGCIA.

Wilby, R.L. and I. Harris, 2006. A Framework for Assessing Uncertainties in Climate Change Impacts: Low-Flow Scenarios for the River Thames, UK. Water Resources Research 42: W02419.

Wilby, R.L., L.E. Hay, and G.H. Leavesley, 1999. A Comparison of Downscaled and Raw GCM Output: Implications for Climate Change Scenarios in the San Juan River Basin, Colorado. Journal of Hydrology 225:67-91.

Wilcox, B.P., W.J. Rawls, D.L. Brakensiek, and J.R. Wight, 1990. Predicting Runoff From Rangeland Catchments: A Comparison of Two Models. Water Resources Research 26:2401-2410.

Wills, T.C., E.A. Baker, A.J. Nuhfer, and T.G. Zorn, 2006. Response of the Benthic Macroinvertebrate Community in a Northern Michigan Stream to Reduced Summer Streamflows. River Research and Applications 22:819-836.

WMO, 1987. Water Resources and Climate Change. Sensitivity of Water Resources Systems to Climate Change and Variability. World Meteorological Organization (WMO/TO), Geneva, Switzerland.

Wolman, M.G. and W.P. Miller, 1960. Magnitude and Frequency of Forces in Geomorphic Processes. Journal of Geology 68:54-74.

Xu, C., 2000. Modelling the Effects of Climate Change on Water Resources in Central Sweden. Water Resources Management 14:177-189.

Yukimoto, S., A. Noda, A. Kitoh, M. Sugi, Y. Kitamura, M. Hosaka, K. Shibata, S. Maeda, and T. Uchiyama, 2001. The New Meteorological Research Institute Global Ocean-Atmosphere Coupled GCM (MRI-CGCM2)–Model Climate and Variability. Papers in Meteorology and Geophysics 51:44-88.

Zion, M.S., S.M. Pradhanang, D.C. Pierson, A. Anandhi, D.G. Lounsbury, A.H. Matonse, and E.M. Schneiderman, 2011. Investigation and Modeling of Winter Streamflow Timing and Magnitude Under Changing Climate Conditions for the Catskill Mountain Region, New York, USA. Hydrological Processes 25:3289-3301.

HYDROLOGICAL PROCESSES
Hydrol. Process. **27**, 3035–3049 (2013)
Published online 18 June 2013 in Wiley Online Library
(wileyonlinelibrary.com) DOI: 10.1002/hyp.9864

Rain-on-snow runoff events in New York

Soni M. Pradhanang,[1]* Allan Frei,[1] Mark Zion,[2] Elliot M. Schneiderman,[2] Tammo S. Steenhuis[3] and Donald Pierson[2]

[1] *Institute for Sustainable Cities, Department of Geography, Hunter College, City University of New York, New York, NY, USA*
[2] *Bureau of Water Supply, New York City Environmental Protection, Kingston, NY, USA*
[3] *Department of Biological and Environmental Engineering, Cornell University, Ithaca, NY, USA*

Abstract:

Rain-on-snow (ROS) runoff events are important hydro-meteorological phenomenon due to their association with flooding. The severity of ROS runoff events depends on the magnitude of the precipitation, air temperature elevation, snow water equivalent (SWE), and areal extent of the antecedent snowpack. Examining the consequences of these factors acting together creates challenges for both flood prediction and flood risk assessments. This study provides information on the spatial patterns, and seasonality of ROS events in New York. We examine the spatial and temporal variability of ROS events for water years 2004 to 2012 from SNOw Data Assimilation System products for New York. Liquid and solid precipitation, snow depth, snowmelt, SWE, maximum and minimum temperature, hydrograph characteristics, and annual peak flow are examined. There is significant positive correlation of ROS days and ROS triggered events with elevation and negative correlation of these events with increasing air temperature. Our study shows that ROS events are dominant in high elevation areas of Adirondack and Catskill regions, and their distribution varies with month. Cumulative runoffs from ROS events are generally greater than the rain-only runoff events. The majorities of annual peak flows in the study watersheds are the results of ROS events and lasted from a few days to many weeks. Copyright © 2013 John Wiley & Sons, Ltd.

KEY WORDS runoff events; rain-on-snow; precipitation; temperature; elevation; peak flow

Received 20 August 2012; Accepted 15 April 2013

INTRODUCTION

Rain-on-snow (ROS) is an important winter and spring phenomenon that plays a significant role in generating high streamflow and has greater potential for generating serious floods than does radiation-induced snowmelt (Kattelmann, 1985; Huntington *et al*., 2004). The term 'ROS' is interpreted in many different ways. While the literal meaning of the term 'ROS' would be snow melted by warm rain, many researchers have recognized that this is not entirely the case (McCabe *et al*., 2007). Rain contributes to some snowmelt while the heat transferred to the snowpack during the condensation of water vapor on the snowpack surface may be the greatest contributor of heat for snowmelt (USACE, 1956). Introduction of liquid water into snow weakens the bond between grains and alters the snow texture which results in reduced mechanical strength of the snowpack. In ROS events, the amount of runoff from the snowpack is maximized and added to the precipitation-induced runoff, such that excess runoff is generated quickly and extreme flooding can occur (Singh *et al*., 1997; Leathers *et al*., 1998). During ROS event, the potential for flooding is increased if the soil is frozen (Dunne and Black, 1971; Shanley and Chalmers, 1999; Niu and Yang, 2006) and if snow cover extends over whole basin accompanied by high wind (Marks *et al*., 2001). ROS effects have been documented for coastal areas of western North America where large floods are commonly associated with ROS (Kattelmann, 1987; Brunengo, 1990; Leathers *et al*., 1998; Graybeal and Leathers, 2006). ROS is an important process for flooding in the eastern United States as well (Graybeal and Leathers, 2006). For example, in January 1996, more than 11.5 cm of rain fell on the Catskill Mountain region during January 18–19, combined with melting of as much as 115 cm of snow resulting in major flooding throughout the region. Record peak discharges occurred at 57 U.S. Geological Survey (USGS) streamflow-gaging stations throughout New York (USGS, 1997). This increased the levels of streams and lakes causing massive flooding in many parts of the Northeastern US (Leathers *et al*., 1998). In this case, the runoff from the snowmelt and the heavy rainfall, which may have been enhanced by orographic effects, combined to create the severe flooding. Runoff from ROS may trigger landslides and, in some areas, is

*Correspondence to: Soni M. Pradhanang, Research Associate, Institute for Sustainable Cities, City University of New York, New York, NY, USA
E-mail: spradh@hunter.cuny.edu

also considered to be the primary cause of increased erosion that leads to changes in channel morphology in some areas (Harr, 1981; Chirstner and Harr, 1982; Harr, 1986; Bergman, 1987). Harr (1981) reported that in the Oregon Cascades, 85% of the landslides were associated with rainfall causing snowmelt.

Rain or snowmelt generated at the snow surface passes through the porous snowpack before appearing as streamflow. The major factors affecting the timing of the runoff response include surface melt, snow metamorphism, water movement through the wet snow, interaction of melt water with the underlying soil, and overland flow at the snow cover base (Singh *et al.*, 1998). In order to improve streamflow prediction for reservoir operation, flood control, and engineering design, models are needed to estimate the timing, amount, and rate of outflow from the snowpack under ROS events (McCabe *et al.*, 2007). Such knowledge is enhanced by a thorough understanding of processes associated with liquid water storage, natural and rain-induced melting, and transmission through the snowpack. Wankiewicz (1978) emphasized the quantitative effect of snow cover on the various runoff mechanisms, and Kattelmann (1985) discussed the necessity of accurate forecasting of snowmelt particularly during rainy conditions. Peak flows that result from small amounts of precipitation are of little consequence in terms of erosional damage in upland areas or downstream flooding. However, if rapid snowmelt occurs during such rainfall, the erosional potential of storm runoff may increase. Conversely, in the case of high daily rainfall rates and streamflow, even a small addition of snowmelt water could increase storm runoff above thresholds of volume and peak flow, thereby increasing the chance of not only channel erosion and landslides in upland watersheds but also downstream flooding (Harr, 1981).

Limited documentation of ROS events makes anticipation and mitigation of potential hazards difficult. To help overcome the lack of useful information, this investigation provides basic information on the spatial and temporal patterns of ROS events in New York. This study is one of the first of its kind in the Northeastern U. S., and it provides important information on ROS events, their frequency of occurrence, seasonal patterns, magnitude of mean snowpack, snow depth, and snow-water equivalent information necessary for water managers to improve on their management plans.

METHODS

Streamflow and climate records for watersheds upstream of 31 USGS gage stations in New York State (Figure 1; Table I) were used to determine frequency of runoff events resulting from rainfall and/or snowmelt. The area

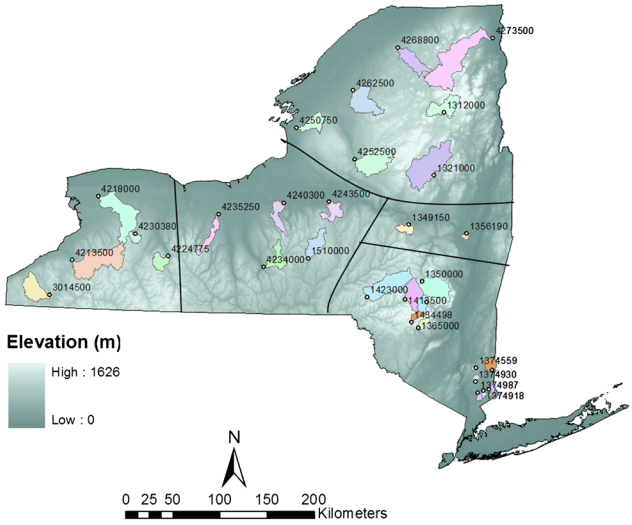

Figure 1. Map of New York State with 31 USGS gaged watersheds for rain-on-snow runoff events study. [Digital Elevation Model Source: (USGS, 2007)]

of these watersheds ranged from as small as 29 km^2 to 1574 km^2 and the mean elevation ranged from 105 m to 788 m.

Daily streamflow data were downloaded from the USGS National Water Information System for each of 31 USGS gaged watersheds. The first step in hydrograph analysis entails separation of stream flow into surface runoff and base flow components. Baseflow separation is done using the filter method outlined in (Arnold *et al.*, 1995). Event runoff is defined as the cumulative surface runoff estimated from the flow-separated daily hydrograph over a period between the first day of surface runoff rise (t_1) until the beginning of the next event (t_2) when a rapid rise in streamflow leads to a new peak in surface runoff (Hewlett and Hibbert, 1967).The length of the runoff event is defined as the period between the first day of streamflow rise (t_1) until the beginning of the next event (t_2) as illustrated in Figure 2.

Snow characteristics prior to runoff events were derived from the data in the Snow Data Assimilation System (SNODAS) (NOHRSC, 2010). SNODAS is a modeling and data assimilation system developed by the National Weather Service's National Operational Hydrologic Remote Sensing Center (NOHRSC) to provide estimates of snow cover, snow water equivalent (SWE), snowmelt, and associated snowpack variables at a 1-km spatial resolution to support hydrologic modeling and analysis. SNODAS includes procedures to ingest and downscale output from Numerical Weather Prediction models; a physically based, spatially distributed energy-and-mass-balance snow model; and procedures to assimilate satellite-derived, airborne, and ground-based observations of snow-covered area and SWE. For this

Table I. Watershed area and average elevation of 31 USGS gaged watersheds. The watersheds are arranged by regions and in ascending order of elevation

USGS gage	USGS gage	Area (sq. km)	Basin mean elevation (m)	Elevation range (m)	Region
4250750	Sandy Creek near Adams	354.8	331.4	74–521	Adirondack
4262500	West Branch Oswegatchie River	668.2	399.9	181–538	Adirondack
4268800	West Branch Regis	442.9	474.9	89–838	Adirondack
4273500	Saranac at Plattsburgh	1574.7	499.5	29–501	Adirondack
4252500	Blackriver near Boonville	787.4	499.9	220–645	Adirondack
1321000	Sacandaga River near Hope	1271.7	581.4	235–668	Adirondack
1312000	Hudson River near Newcomb	497.3	660	456–1095	Adirondack
1423000	West Br Delaware River at Walton	859.9	592.1	350–777	Catskill
1365000	Rondout Creek near Lowes Corners	99.2	628.6	256–1173	Catskill
1350000	Schoharie Creek at Prattsville	613.8	652.6	344–956	Catskill
1413500	East Br Delaware R. at Margaretteville	422.2	667.3	390–1057	Catskill
1362200	Esopus Creek at Alaben	165	671.5	180–1042	Catskill
1434498	West Br. Neversink at Claryville	87.5	788.2	439–903	Catskill
1356190	Lishakill NW of Niskayuna	40.4	104.9	55–154	East
1349150	Canajoharie Creek at Canajoharie	154.6	310.5	86–703	East
4235250	Flint Creek at Phelps	264.2	338.1	139–654	Finger Lake
4240300	Ninemile Creek at Lakeland	297.9	272.2	110–582	Finger Lake
4243500	Oneida Creek at Oneida	292.7	312.3	112–162	Finger Lake
4234000	Fall Creek at Ithaca	326.3	414.7	116–575	Finger Lake
1510000	Ostellic River at Cincinnatus	380.7	483.2	286–636	Finger Lake
1374987	Kisco River below Mt. Kisco	45.6	137.8	63–245	Southeast
1374918	Stonehill River South of Katonah	48.4	146.2	66–265	Southeast
1374890	Cross River near Cross River	44.3	169.3	103–304	Southeast
1374930	Muscoot River near Baldwin Place	35	204.7	155–344	Southeast
13744980	East Br. Croton River near Putnam Lake	160.8	213.6	117–406	Southeast
1374559	West Br. Croton River at Richardsville	28.5	257.1	155–357	Southeast
4218000	Tonawanda Creek at Rapids	903.9	236.7	173–244	West
3014500	Chadokoin River at Falconer	502.5	454.6	377–568	West
4230380	Oatka Creek at Warsaw	101.3	468.7	156–588	West
4213500	Cattaraugus Creek at Gowanda	1129.2	492.1	174–709	West
4224775	Canaseraga Creek above Dansville	230.3	498.6	160–690	West

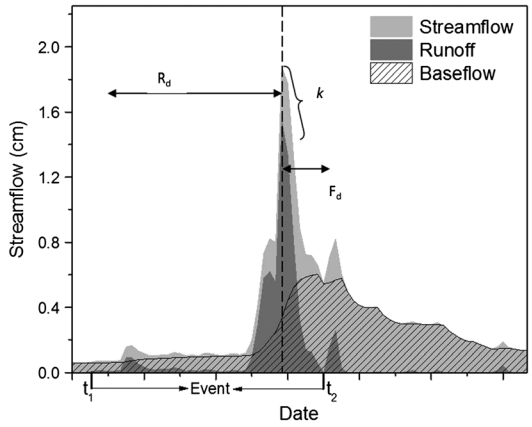

Figure 2. Example hydrograph showing streamflow in depth, baseflow separated runoff depth, and event. t_1 is the beginning of the event, and t_2 is the end of the event. R_d is the length of the rising limb in days, F_d is the length of the falling limb in days, and k is slope of the falling limb for first few days

study, we analyzed liquid precipitation, snowpack depth, snowmelt, and SWE from October to April (2003–2012). To obtain averages or totals for desired parameters representative of the USGS basins, the gridded (~1 km) SNODAS data were extracted based on the areal extent of the watersheds. Since air temperature is not one of the output variables of SNODAS, we used spatially distributed air temperature data from the Northeast Regional Climate Center at Cornell University, Ithaca, NY ((DeGaetano and Belcher, 2007). The 4 km resolution air temperature data was spatially averaged for the 31 USGS gaged watersheds.

ROS runoff events were characterized based on snowmelt, snow depth, liquid precipitation (rain), and solid precipitation (snow) information obtained from SNODAS. Two ROS variables were calculated for each watershed. First, a ROS day was defined as a day when precipitation occurred as rain and snowpack was present. Second, a ROS-induced event was defined by satisfying the following two conditions (1) precipitation as rain, (2) rain on snowpack, events that consisted at least one ROS day, and/or ROS that initiated runoff event to occur, i.e. when snow ripened or melted and resulted in runoff. For all ROS events, rain amount and snowmelt were calculated. The ROS initiated runoff events were defined as the condition when an event begins in the presence of rain and snow on the ground. Each ROS runoff event usually consisted of more than one day of ROS.

The Spearman rank correlation test was used for exploratory data analysis. Correlation analysis was done to understand relationships between elevation, temperature, ROS, and precipitation characteristics. Spearman rank correlation is often used as a statistical tool to detect monotonic relationships. It is a non-parametric technique and therefore not affected by the statistical distribution of the population. Because the technique operates on ranks of the data, it is relatively insensitive to the outliers, and there is no requirement that the data be collected over regularly spaced temporal intervals (Helsel and Hirsch, 1992). The Spearman rank correlation coefficient (r) is calculated using Equation (1):

$$r = 1 - \frac{6\sum_{i=1}^{n} d_i^2}{n^3 - n} \quad (1)$$

where, d_i is the difference between rank for each x_i, y_i data pair, and n is the number of data pairs. The strength of the relation is indicated by r, which ranges from -1 (strong negative correlation) to +1 (strong positive correlation) with a value of 0 denoting no correlation. A two-tailed significance test ($\alpha = 0.05$) was done to assess the significance of a correlation between two variables.

Annual peak flow for the 31 watersheds was analyzed for the periods of record for available data. Peak flows were ranked by size over the periods of record, and SNODAS from between 2003 and 2012 were used, where possible, to separate peak flows caused by rainfall from peak flows caused by ROS. The peak flow event hydrograph was characterized by analyzing hydrograph parameters (Figure 2), including the length of the rising limb (R_d) in days, length of the falling limb (F_d) in days, the ratio between the length of the rising limb, and the falling limb of the storm hydrograph denoted by R_d:F_d. Peak flow return period was calculated using Log Pearson Type III analysis (Graybeal and Leathers, 2006).

RESULTS AND DISCUSSIONS

Spatial and temporal patterns of ROS events

Daily precipitation as rain and snowfall, SWE, and snowmelt of the 31 USGS gauged watersheds in New York were used to examine the spatial and temporal patterns of ROS runoff events for water years 2003 through 2012 (Tables II and III). Figure 3 illustrates the total number of ROS runoff initiated events on a monthly basis that occurred during the period of study. ROS runoff events are found to be most frequent in the Western, Adirondack, and Catskill regions of New York during December and varied spatially. The number of ROS initiated runoff events that occurred at any individual watershed over the nine year study period ranged from 0 to 25, and varied by location and elevation (Figure 3, Table III). Only one site (located in the southeast region-Cross River near Cross River; elevation 169 m) showed no ROS that initiated runoff events [Note: considering events that are started by ROS, i.e. ROS initiated runoff event]. Percent of runoff events that are rain to ROS ranged from as low as 22 (in USGS gage 1374930 located in Southern region of NY) to 62 (in USGS gage 1423000

Table II. Snowpack and snow cover characteristics of 31 USGS gaged watersheds. The watersheds are arranged by regions and in ascending order of elevation

USGS gage	Annual total liquid precipitation (2003–2012)	Annual total snowpack (cm) (2003–2012)	Annual average snow depth (cm) (2003–2012)	Annual average SWE (cm) (2003–2012)
4250750	429.2	257.7	142.1	29.4
4262500	377.7	255.7	147.7	30.0
4268800	353.4	260.5	160.8	32.7
4273500	324.5	257.2	161.9	33.7
4252500	419.1	299.1	225.0	50.4
1321000	408.1	295.5	258.3	60.0
1312000	354.8	298.1	240.2	54.5
1423000	384.5	213.8	82.5	14.8
1365000	513.9	233.6	110.6	24.5
1350000	406.4	211.6	93.5	18.0
1413500	425.1	234.0	96.0	18.2
1362200	451.3	243.7	119.6	24.3
1434498	503.4	249.7	125.6	25.5
1356190	378.3	132.8	53.0	9.7
1349150	347.8	196.6	78.7	14.6
4235250	305.2	149.6	46.1	7.7
4240300	353.3	193.0	73.4	13.1
4243500	374.4	190.1	74.6	13.6
4234000	342.1	189.5	66.8	11.7
1510000	375.7	229.7	114.5	22.8
1374987	523.6	89.1	31.5	6.0
1374918	529.8	89.4	32.8	6.2
1374890	522.2	101.7	32.8	5.9
1374930	493.1	114.7	32.4	5.7
13744980	478.7	129.9	38.6	7.0
1374559	475.2	123.8	35.2	6.1
4218000	341.8	183.1	61.0	10.5
3014500	388.4	238.6	81.4	14.0
4230380	335.9	216.3	65.4	10.7
4213500	363.4	257.8	94.8	16.7
4224775	310.4	187.8	60.2	10.2

Table III. Precipitation characteristics and rain-on-snow runoff events in 31 USGS gaged watersheds. The watersheds are arranged by regions and in ascending order of elevation. (2003–2012)

U S G S gage	Total rain days	Rain-on-snow days	Percent of days that are ROS days to total rain	Total number of events (Oct–April)	Runoff event consisting at least one ROS day	Percent of runoff events that are rain to rain-on-snow	Rain-on-snow initiating runoff event
4250750	725	408	56	156	86	55	14
4262500	712	434	61	112	66	59	16
4268800	674	410	61	127	74	58	15
4273500	750	554	74	168	78	46	22
4252500	708	481	68	154	90	58	13
1321000	692	470	68	143	80	56	20
1312000	659	482	73	110	63	57	24
1423000	670	379	57	157	98	62	12
1365000	632	361	57	170	71	42	11
1350000	661	398	60	163	79	48	15
1413500	656	388	59	149	70	47	13
1362200	645	392	61	141	69	49	13
1434498	589	326	55	182	78	43	6
1356190	552	181	33	217	46	21	6
1349150	650	302	46	197	78	40	13
4235250	715	322	45	159	64	40	9
4240300	752	378	50	170	74	44	10
4243500	715	330	46	208	75	36	15
4234000	687	327	48	207	76	37	8
1510000	724	392	54	183	85	46	12
1374987	602	136	23	144	44	31	3
1374918	600	135	23	127	43	34	1
1374890	577	139	24	154	36	23	0
1374930	569	135	24	170	38	22	3
13744980	582	110	19	134	42	31	4
1374559	577	136	24	140	44	31	4
4218000	776	356	46	146	68	47	21
3014500	868	457	53	95	57	60	11
4230380	679	259	38	207	68	33	13
4213500	799	436	55	200	103	51	20
4224775	702	338	48	138	58	42	10

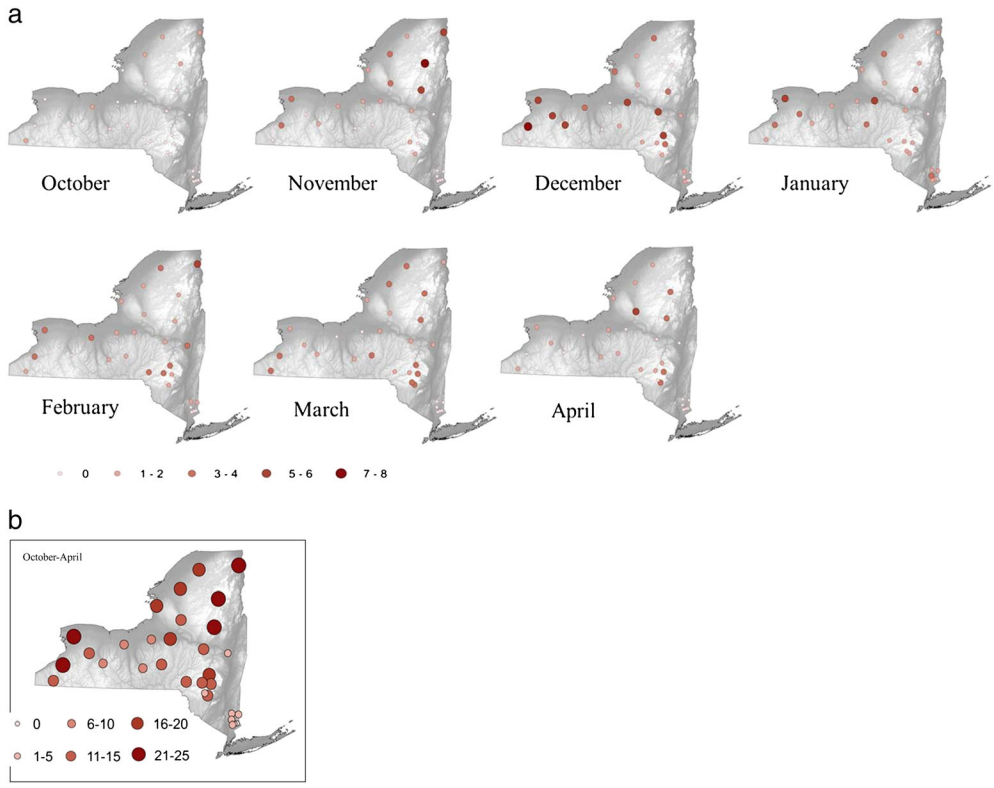

Figure 3. a) Total number of rain-on-snow that initiated events from October to April during 2003–2012; b) total number of rain-on-snow initiated runoff events summed over October to April

located in Catskill Region of NY) (Table III). The number of events that consisted of at least one day of rain that fell on an existing snowpack or snowmelt varied spatially and by month (Figure 4). December has more ROS runoff events than other months followed by March and April. In general, ROS events are less frequent in southeastern New York and the Finger Lakes regions. The ROS runoff events generally occur in most watersheds as early as October and as late as April. Although it is quite possible that some watersheds in the far north and west of New York may experience snowfall and subsequent runoff as early as September and as late as May, these earlier and later months were not investigated as these events generally represented a small fraction of ROS events.

It is also apparent from Figures 3 and 4 that ROS runoff events and ROS days are relatively greater in the Adirondack region and the Catskill (New York City water supply watershed) region as compared to other regions of NY. In March and April, the largest snowmelt per ROS runoff event occurred in the Central and Northern New York. The magnitude of snow depth is largest in northern NY during spring, thus, ROS events in these locations can still melt a significant amount of snow. The 31 USGS gaged watersheds represented a variety of elevation ranges. Figure 5 shows boxplot of distribution of October –April number of ROS variables and show apparent decrease in ROS days in low elevation sites. However, other variables such as rain days, ROS during runoff events, and ROS causing events showed variable distribution. Average snow depth, SWE, and snowmelt decrease in low elevation sites. Table II shows snowpack and snow cover characteristics for 31 USGS gaged watersheds. The annual total snowpack and snow depth was highest in the Adirondack followed by Catskill regions and Western region. Generally, the lowest elevation watersheds were found in the southern part of NY.

The Spearman correlation analysis between elevation and rain days, ROS days, ROS during runoff events, and ROS that initiated runoff events is presented in Table IV. The analysis was done for two seasons, i.e. OND (October–November–December), JFMA (January–February–March–April), and for all months (October–April). All variables are positively correlated with elevations. ROS days showed the highest positive correlation (0.72 for JFMA, 0.55 for OND, and 0.65 for October–April) with elevation and were significant at the 0.05 level. Similar significant positive correlations were observed for ROS during runoff events during all three seasonal periods. The runoff events that were initiated due to ROS were positively correlated with elevation for JFMA and October to April analysis, possibly since the amount of snow on the ground during this period is high relative to the OND period. Snow on the ground days were

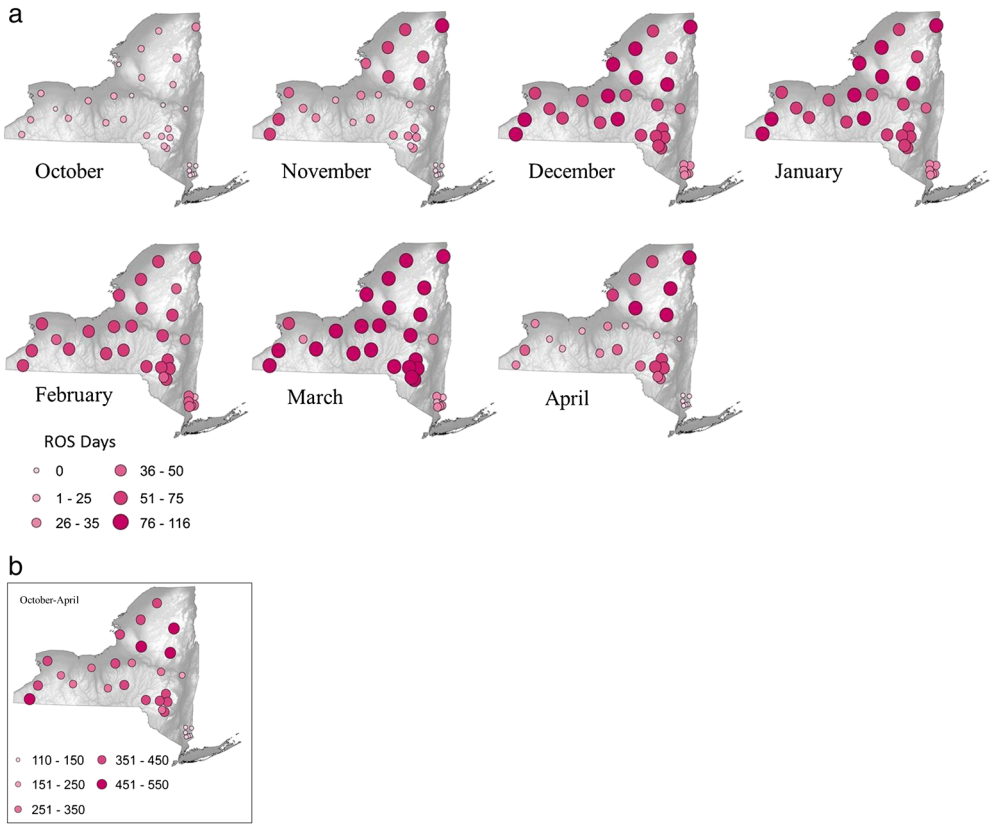

Figure 4. Total number of events that had at least one rain-on-snow from October to April during 2003–2012; b) total number of events that had at least rain-on-snow (summed over October to April)

positively correlated to elevation and negatively correlated with temperature during all seasonal periods. Average SWE showed similar trends as snow on the ground days.

During the cool months (i.e. January–March), lower elevations tend to experience more frequent snow days. In contrast, during the warm months (October and April), the elevation distribution of snow days is relatively uniform. The temperatures at low-elevation sites are warmer which affect the apportioning of precipitation between rain and snow and the frequency of their occurrence. The number of rain days at a site is an important statistic that is related to the frequency of ROS events. For the study period, the percentage of ROS days is about 19–24% of total rain days at the lowest elevation basins (located in the southeast region), and this percentage increases with increased elevation and location of the watersheds to greater than 60% in the Adirondack Region (Table III). Another important condition for ROS runoff events is an accumulation of snow on the ground. Temperatures at the lower elevation sites are warmer, reducing the number of days with snowpack on the ground, and thus reducing the number of potential ROS days. During the late fall (late October and November) and winter (December–February), the frequency of ROS runoff events increased with elevation, and the percentage ROS days increased at higher elevations. At the lowest elevations, the percentage of cool months, i.e. January to March precipitation days that are ROS runoff events is close to zero for most of the sites. This elevation relation with ROS runoff events at certain high elevation sites during the relatively warm months (October and April) is primarily related to the number of days and amount of snow on the ground.

The frequency of occurrence of ROS days showed a locational pattern. Figure 4 shows ROS days for each month and summed ROS days from October to April for 31 USGS gaged watersheds. The frequency of ROS days from October to April was highest in the Adirondack, and Western region followed by Catskill regions (Figure 4b). On the monthly basis, the highest ROS days for most of the watersheds were observed from December to March. The numbers of ROS runoff events was greater in the Adirondack, Western and Catskill regions while there were less ROS runoff events in the Southeastern region. The relatively small differences in elevation in the Southeastern Region may also mean that the observed

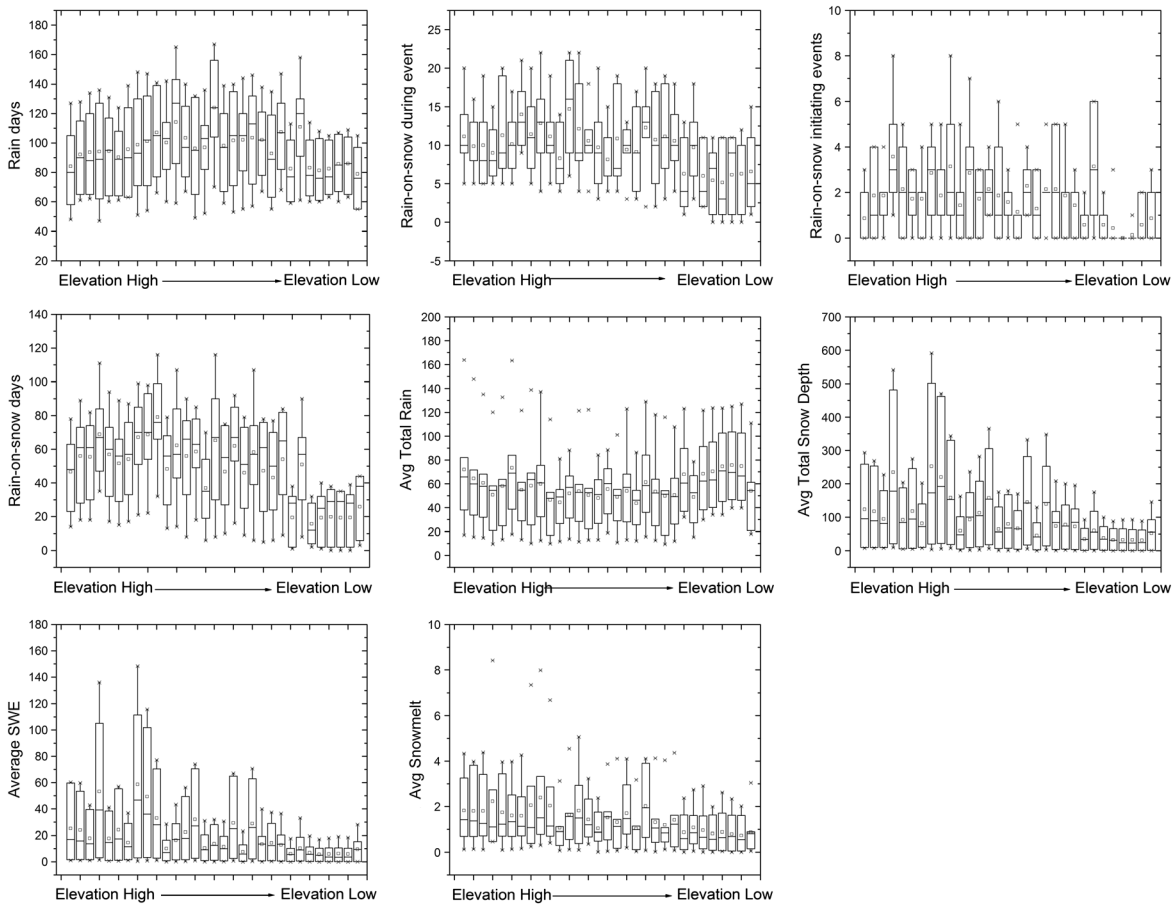

Figure 5. Box plots of the distribution of October to April number of rain days, number of ROS initiating runoff events, number of events with at least one ROS day, number of ROS days, rain (mm/d), average snow depth (mm), average SWE (mm), and average snowmelt (mm/day). Values are calculated from SNODAS product. The boxes/whiskers show the interannual variability for each of the 31 study watersheds (The boxes indicate the range of values between the 25th and 75th percentiles, the dark horizontal lines indicate the median, the ends of the dashed lines indicate the 1st and the 99th percentiles of the distribution, and the small square shows the average)

differences in ROS days and runoff events are better indexed by the location of these watersheds than by elevation.

ROS runoff events and temperature relations

The Spearman correlation analysis between number of rain days, ROS days, ROS during runoff events, and ROS that initiated events and the average maximum and minimum temperature is presented in Table IV. The analysis was done for three seasonal periods similar to the analysis for elevation, i.e. JFMA and OND and the entire period of time between October and April. In general, ROS days, ROS during runoff events, and ROS initiating runoff events were negatively correlated with average maximum temperature during all time periods and the correlations were usually found to be significant at the 0.05 level. Average minimum temperature showed significant negative correlation with ROS days and ROS initiating runoff events, but as expected, the minimum temperature was often not strongly correlation with melt events. The negative correlations between average winter temperatures and the occurrence of ROS runoff event indicate that as temperature increases, ROS runoff events become less frequent, presumably as a result of a shorter period of snow cover. The negative correlations are most common for low elevation sites that are located in the southern part of NY.

Many studies that have shown that temperatures have been increasing in the Northeastern United States during the past several decades with subsequent effects on hydrological conditions, including a decreasing snowpack and shifts to earlier snowmelt runoff (Burns *et al.*, 2007; Hayhoe *et al.*, 2008). Warming winter temperature trends and decreases in number of days with snow cover in Northeastern US in recent decades are also documented in Burakowski *et al.* (2008). Modeling studies in watersheds in New York have also indicated that climate change may result in a decrease in snowpack and a shift in the timing of annual peak and annual low flows (Pradhanang *et al.*, 2011; Zion *et al.*, 2011).

Table IV. Spearman rank correlation coefficients for elevation, maximum and minimum temperature and rain-on-snow variables

Variables	Elevation			Average maximum temperature			Average minimum temperature		
	OND	JFMA	Oct–Apr	OND	JFMA	Oct–Apr	OND	JFMA	Oct–Apr
Rain days	0.24	0.22	0.19	−0.47*	−0.25	−0.40*	−0.16	−0.34	−0.28
ROS days	0.55*	0.72*	0.65*	−0.73*	−0.75*	−0.80*	−0.78*	−0.79*	−0.78*
ROS event	0.68*	0.46*	0.57*	−0.78*	−0.49*	−0.67*	−0.54*	−0.71*	−0.64*
ROS initiating event	0.30	0.60*	0.50*	−0.51*	−0.67*	−0.71*	−0.44	−0.66*	−0.61*
Snow on theground days	0.79*	0.79*	0.79*	−0.91*	−0.79*	−0.90*	−0.89*	−0.91*	−0.92*
Average SWE	0.67*	0.54*	0.75*	−0.90*	−0.85*	−0.94*	−0.63*	−0.74*	−0.71*

Two-tailed test of significance is used
*Correlation is significant at the 0.05 level

Figure 6 shows scatter plots of average October–April maximum and minimum temperatures against ROS days, ROS occurring during runoff events, and ROS causing runoff events. With increase in temperature, there is a decrease in ROS frequencies. In theory, warmer temperatures could affect ROS days either by increasing the frequency of rain events in the presence of snow cover, or by decreasing the duration of snow cover and therefore the probability of ROS days. The fact that a negative relationship is found between air temperature and ROS statistics in Figure 6 and Table IV suggest that it is the effect of winter temperature on the duration of snow cover that is the dominate mechanism in controlling the occurrence of ROS days. Mote *et al.* (2005) reported a similar relationship occurs between increased air temperature and decreased snowpack in

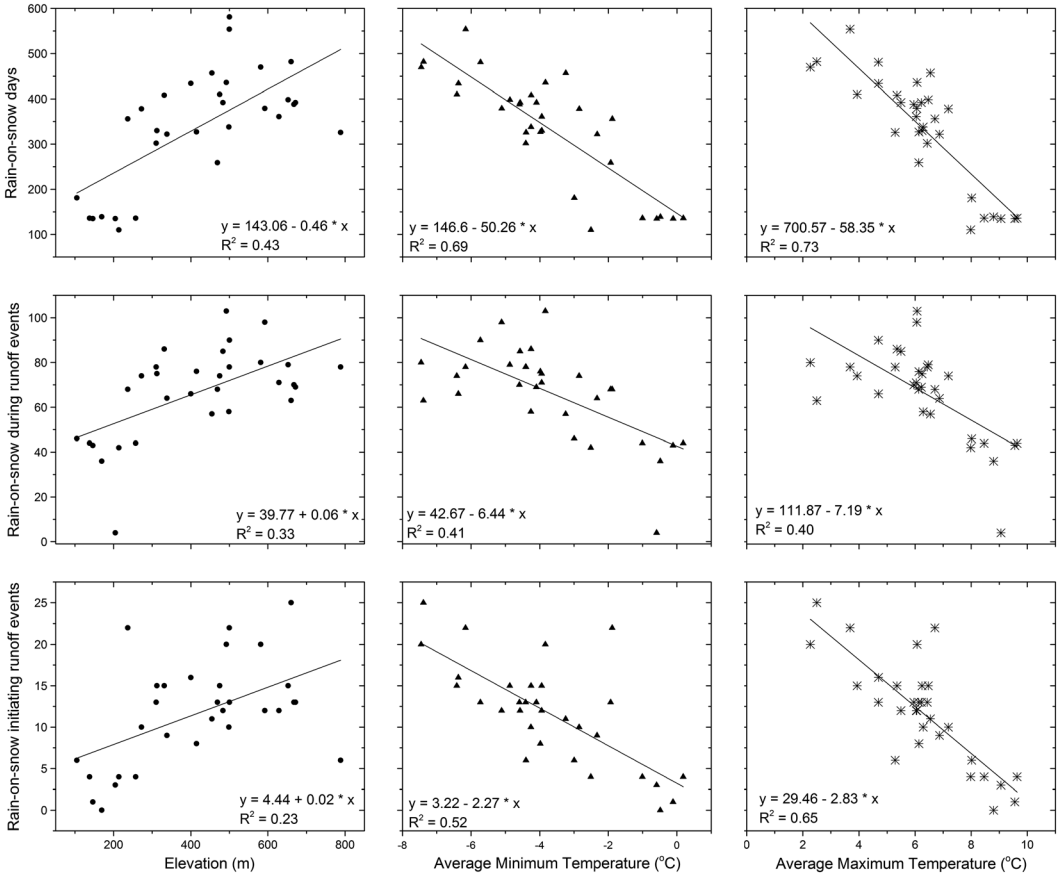

Figure 6. Scatter plots of elevation, average maximum, and minimum temperature (October–April) against rain-on-snow days, rain-on-snow during runoff events, and rain-on-snow initiating runoff events

western United States, and that the relationship of temperature to ROS event frequency appears to be through the effects of temperature on the number of precipitation days with snow on the ground.

Streamflow characteristics

ROS conditions produce streamflow hydrographs that generally differ from hydrographs caused by rain alone. Figure 7 shows typical examples of hydrographs resulting from ROS, as compared to snowmelt and rain only runoff events. During the winter spring period, rising limbs of ROS hydrographs are generally steeper than those of rain hydrographs. Differences in size of peak flows and rates of hydrograph rise would be expected due to differences in rate of water input. The additional water stored in a ripened snowpack, and the snowmelts from ROS generate relatively large flows compared to the runoff from snowmelt or rain alone.

Seasonal and spatial variation in snow accumulation, rain on snowpack, or snowmelt can all possibly play an important role in regulating the extent of flooding that occurred in New York State during the years of this study. Watershed streamflow responses to the changes in rate of water input are also highly variable. There is a variable time lag between the onset of rain and/or melt and the increase in streamflow corresponding to that input. The length of lag is affected by many factors, such as relative levels of soil moisture conditions, land cover, and the size of the area producing runoff (Harr, 1981). High air and dewpoint temperatures, and high wind speeds can induce large surface energy fluxes that lead to the rapid ablation of the snowpack and result in flooding events (Leathers *et al.*, 1998). Singh *et al.* (1998) studied the role of snowpack on producing runoff and reported that the development of preferential flow paths in the snowpack due to differential snow settlement during the ROS tend to reduce the transient storage and travel time of water in the snowpack in comparison to that which would occur if uniform melting is taking place on the surface. They also concluded that the role of rainwater is much more important for the conditioning of a snowpack to yield maximum runoff rather than contributing to additional melting of snow.

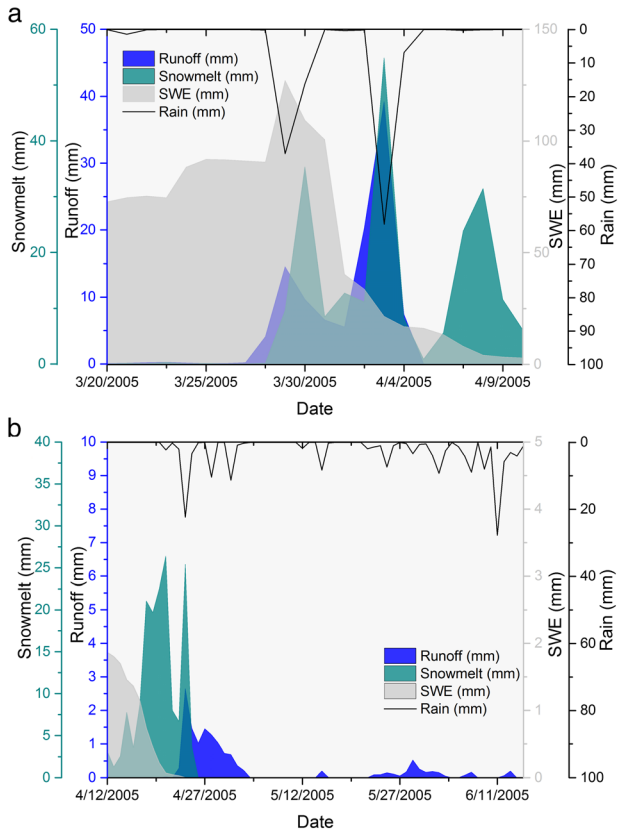

Figure 7. Hydrograph characteristics of a) rain-on-snow, and b) snowmelt and rain-induced streamflow

Peak flow sources were identified for 2003–2012 period using SNODAS model information. Table V shows the return intervals for two selected events: one that is the result of ROS, and the other the result of rain only. For the snowmelt-affected event ranking of peak flow, whether or not snowmelt contributed substantially to peaks was done. The causes of peak flow were then identified based on rain and snow information from SNODAS. There is evidence that snowmelt during rainfall added to many annual peaks from 2003 to 2011. On average, 7 of 10 annual peaks were the result of ROS events in the study sites (Table V). The sites that had fewer ROS events-related annual peaks were located in southeastern NY. Most of the ROS-related peaks ranked highest in the record of study (Figure 8). A peak flow runoff hydrograph (Figure 2) extends from the date at which the flows first begin to increase to the date that the discharge returns to base flow. The river rises rapidly after runoff reaches the channel, attaining peak flow after the peak of the rainfall itself. The magnitude of the runoff increase may be greatly augmented by snowmelt during ROS events (Floyd and Weiler, 2008). Annual peak flow runoff event caused by rain on snow showed longer rising and falling limb compared to annual peak flow events that were caused by rain only. The steeper nature of the recession limbs in annual peak flow runoff events caused by rain exhibited (Table V) is indicative of fast receding hydrograph in the absence of additional melt water inputs. ROS and snowmelt hydrographs often have a long, gradual rising limb and may occur over weeks as a result of the slow release of snowmelt inputs.

Peak flow and return interval analysis showed that most of the highest annual peak flow events occurred during mid-to-late March and were augmented by melt inputs.

Table V. Annual peak flow hydrograph characteristics 31 USGS gaged watersheds. The watersheds are arranged by regions and in ascending order of elevation. (2003–2012)

USGS gage	Annual peak flow caused by rain-on-snow (WY2003–WY2012)	Average length of rising limb (days)		Average length of falling limb (days)		Average ratio of rising and falling limb		Average slope of the recession limb	
		ROS	Rain	ROS	Rain	ROS	Rain	ROS	Rain
04250750	9	9.33	0.00	10.89	0.00	1.69	0.00	−1.98	0.00
04262500	9	10.13	3.00	17.38	10.00	1.36	0.30	−4.86	−3.92
04268800	9	13.75	11.00	9.38	13.00	1.78	1.01	−6.44	−3.66
04273500	8	15.13	9.00	15.00	6.00	1.01	1.50	−10.47	−4.48
04252500	5	8.67	3.67	14.33	5.33	0.65	0.70	−2.39	−1.63
01321000	8	13.00	3.00	12.43	10.50	1.46	0.29	−1.75	−1.81
01312000	8	14.00	3.33	10.33	10.33	1.40	0.38	−10.89	−83.20
01423000	6	9.00	4.25	10.00	11.25	1.13	0.38	−4.51	−1.44
01365000	7	10.60	4.00	7.80	7.00	2.00	0.78	−0.71	−0.47
01350000	7	9.00	2.00	16.71	8.00	1.02	0.25	−2.26	−0.38
01413500	7	9.00	3.25	13.20	9.25	1.05	0.34	−1.23	−0.85
01362200	7	9.60	6.00	11.00	11.00	1.95	0.91	−0.73	−0.58
01434498	7	7.60	4.25	10.00	7.75	1.31	0.65	−0.51	−0.34
01356190	7	11.14	5.67	8.57	4.67	1.16	1.78	−1.35	−7.10
01349150	6	7.60	3.00	10.00	8.75	0.63	0.39	−0.85	−0.53
04235250	8	11.38	2.00	7.00	3.00	2.13	0.67	−2.65	−1.28
04240300	8	11.50	8.00	9.38	16.00	1.43	0.50	−7.82	−5.99
01510000	7	6.83	3.67	8.00	7.00	0.83	0.54	−2.13	−1.24
04234000	9	7.00	4.00	7.25	6.00	1.28	0.67	−2.46	−0.79
04230380	8	7.57	3.50	5.43	9.00	1.64	0.46	−2.09	−0.63
01374987	3	8.40	3.00	6.80	7.00	1.76	0.44	−1.03	−1.40
01374918	3	6.40	5.50	10.40	8.00	1.28	0.75	−1.95	−1.83
01374890	6	8.75	9.00	14.25	9.00	0.59	1.00	−2.50	−1.32
01374930	5	7.14	4.00	6.86	10.50	1.71	0.40	−2.11	−1.84
013744980	6	10.00	8.00	13.50	8.00	0.66	1.00	−2.18	−1.63
01374559	6	9.88	20.00	11.88	7.00	0.85	2.86	−2.22	−0.68
04218000	9	13.63	4.00	10.00	6.00	1.71	0.67	−4.40	−2.49
03014500	5	28.00	12.67	22.67	10.67	1.09	1.17	−41.75	−16.13
04243500	7	11.67	4.33	8.17	7.33	2.52	0.90	−1.53	−1.12
04213500	7	4.63	4.00	6.00	3.00	0.91	1.33	−1.31	−0.91
04224775	9	4.00	1.50	15.33	11.00	0.40	0.18	−6.26	−15.38

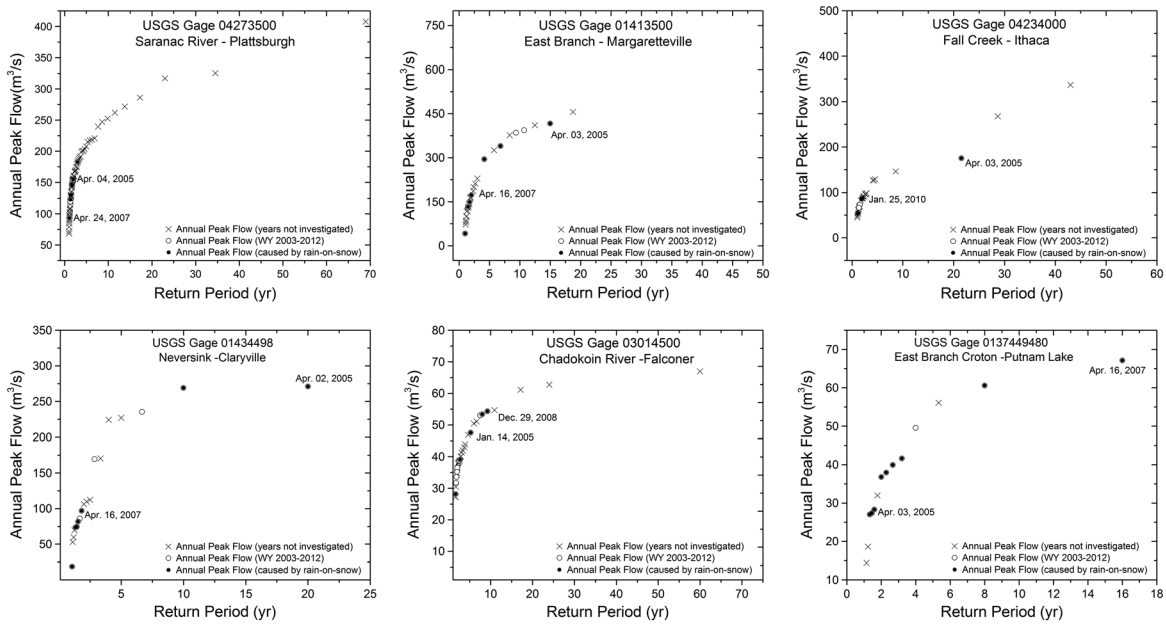

Figure 8. Plot of annual peak flow *versus* return period for selected USGS gages. Circles indicate annual peak flow, solid circle indicate annual peak flow due to rain-on-snow as indicated through SNODAS results

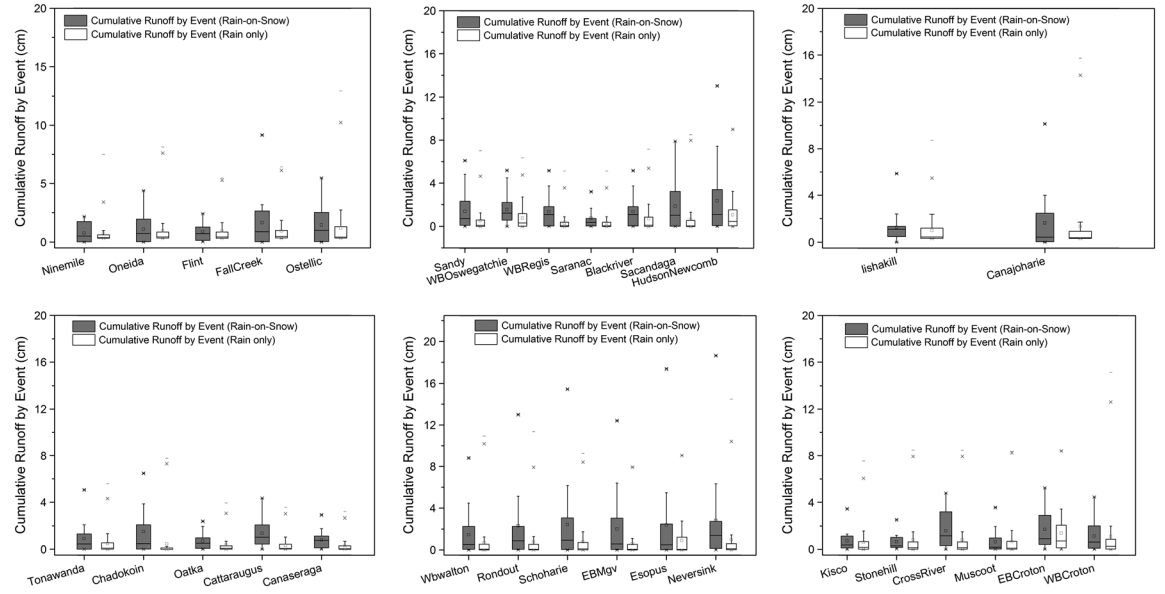

Figure 9. Boxplots of cumulative runoff by event for events due to rain-on-snow (grey-shaded box) *versus* events due to rain-only. The boxes indicate the range of values between the 25th and 75th percentiles, the dark horizontal lines indicates the median, the ends of the dashed lines indicate the 1st and the 99th percentiles of the distribution, and the small squares show the average

Figure 8 shows annual peak flow plotted against return interval for selected sites in NY. The peak flows that were the result of ROS (2003–2012) are shown as solid circles. The majority of annual peak flows during the study period are found to be ROS peak flow events. For example, the majority of annual peak flows in Adirondack and Catskill regions were due to ROS event (Table V). This was confirmed through the analysis of SNODAS products. The comparison of the boxplots of event cumulative runoff identified as generated by ROS and runoff generated by rain only is shown in Figure 9. The intensity of ROS events compared to rain only events tended to be

greater in the Adirondack and Catskill regions of NY and increased with elevation. The southeastern region showed greater cumulative runoff for rain only events. Other regions showed mixed results.

CONCLUSIONS

A first attempt has been made in documenting frequency of ROS events and their spatial and temporal distribution in New York. The period of 2003–2012 was selected to examine the spatial and temporal patterns of ROS events, their correlation with temperature, and hydrologic characteristics of ROS events and rain only events. Our study showed that although the number of ROS events that were initiated by precipitation falling as rain on snowpack, the number of runoff events that actually had at least one ROS day were numerous. The majority of annual peak flow events measured in 31 USGS gaged watersheds distributed throughout New York State were due to ROS events. The ROS runoff events were longer lasting and consequently had slower and less steep rising and falling hydrograph limbs than rain only runoff events.

Total amounts of seasonal snowfall the occurrence of rain on the snowpack and snowmelt all had an important influence on flooding events that occurred in most of the areas in NY during 2005, 2007, and 2010. Flooding events associated with ROS are devastating from the human and economic perspectives and are a hydrologic phenomenon that deserves greater analysis in New York State. Our analyses of ROS runoff events appear to follow logical climate relationships and have provided one of the first inventories of the magnitude and variability of these relationships, as well as a description of elevation and regional differences. This information is useful as a basis for additional research into ROS events, which should improve both flood forecasts and flood risks assessments.

ACKNOWLEDGEMENT

I would like to thank David Lounsbury from New York City, Department of Environmental Protection for GIS support.

REFERENCES

Arnold JG, Allen PM, Muttiah R, Bernhardt G. 1995. Automated Base Flow Separation and Recession Analysis Techniques. *Ground Water* **33**: 1010–1018.

Bergman JA. 1987. Rain-on-snow and soil mass failure in the Sierra Nevada of California. In Landslide Activity in the Sierra Nevada during 1982 and 1983, DeGraff JV (ed.), Earth Resources Monograph 12. USDA Forest Service: Pacific Southwest Region; 15–26.

Brunengo MJ. 1990. A method of modelling the frequency characteristics of daily snow amount for stochastic simulation of rain-on-snowmelt events. *58th Western Snow Conference Proceedings*; 110–121.

Burakowski EA, Wake CP, Braswell B, Brown DP. 2008. Trends in wintertime climate in the northeastern United States: 1965-2005. *Journal of Geophysical Research* **113**: D20114.

Burns DA, Klaus J, McHale MR. 2007. Recent climate trends and implications for water resources in the Catskill Mountain region, New York, USA. *Journal of Hydrology* **336**: 155–170.

Chirstner J, Harr RD. 1982. Peak streamflow from transient snow zone Western Cascades, Oregon. *50th Western Snow Conference*; 27–38.

DeGaetano AT, Belcher BN. 2007. Spatial Interpolation of Daily Maximum and Minimum Air Temperature Based on Meteorological Model Analyses and Independent Observations. *Journal of Applied Meteorology and Climatology* **46**: 1981–1992.

Dunne T, Black RD. 1971. Runoff processes during snowmelt. *Water Resources Research* **7**: 1160–1172.

Floyd W, Weiler M. 2008. Measuring snow accumulation and ablation dynamics during rain-on-snow events: innovative measurement techniques. *Hydrological Processes* **22**: 4805–4812.

Graybeal DY, Leathers DJ. 2006. Snowmelt-Related Flood Risk in Appalachia: First Estimates from a Historical Snow Climatology. *Journal of Applied Meteorology and Climatology* **45**: 178–193.

Harr RD. 1981. Some characteristics and consequences of snowmelt during rainfall in western Oregon. *Journal of Hydrology*, **53**: 277–304.

Harr RD. 1986. Effects of clearcutting on rain-on-snow runoff in western Oregon: a new look at old studies. *Water Resources Research* **22**: 1095–1100.

Hayhoe K, Wake C, Anderson B, Liang X-Z, Maurer E, Zhu J, Bradbury J, DeGaetano A, Stoner A, Wuebbles D. 2008. Regional climate change projections for the Northeast USA. *Mitigation and Adaptation Strategies for Global Change* **13**: 425–436.

Helsel DR, Hirsch RM. 1992. *Statistical Methods in Water Resources*. Vol. **49**. Elsevier Science, ISBN 0444885285.

Hewlett JD, Hibbert AR. 1967. Factors affecting the response of small watersheds to precipitation in humid areas. In *Forest hydrology*, Sopper WE, Lull HW (eds.) Pergamon Press: New York; 275–290.

Huntington TG, Hodgkins GA, Keim BD, Dudley RW. 2004. Changes in the Proportion of Precipitation Occurring as Snow in New England (1949–2000). *Journal of Climate* **17**: 2626–2636.

Kattelmann RC. 1985. Macropores in snowpacks of Sierra Nevada. *Annals of Glaciology* **6**: 272–273.

Kattelmann RC. 1987. Water release from a forest snowpack during rainfall. In *Forest Hydrology and Watershed Management*, Swanson RH, Bernier PY, Woodard PD (eds), Proc. Vancouver Symposium, August. IAHS Publ. no. 167; 265–272. Vancouver, BC, Canada.

Leathers DJ, Kluck DR, Kroczynski S. 1998. The Severe Flooding Event of January 1996 across North-Central Pennsylvania. *Bulletin of the American Meteorological Society* **79**: 785–797.

Marks D, Link T, Winstral A, Garen D. 2001. Simulating snowmelt processes during rain-on-snow over a semi-arid mountain basin. *Annals of Glaciology* **32**: 195–202.

McCabe GJ, Hay LE, Clark MP. 2007. Rain-on-Snow Events in the Western United States. *Bulletin of the American Meteorological Society* **88**: 319–328. DOI: 10.1175/bams-88-3-319.

Mote PW, Hamlet AF, Clark MP, Lettenmaier DP. 2005. Declining mountain snowpack in Western North America. *Bulletin of the American Meteorological Society* **86**: 39–49. DOI: 10.1175/bams-86-1-39.

Niu G-Y, Yang Z-L. 2006. Effects of frozen soil on snowmelt runoff and soil water storage at a continental scale. *Journal of Hydrometeorology* **7**: 937–952.

NOHRSC. 2010. Snow Data Assimilation System (SNODAS) Data Products at NSIDC. National Snow and Ice Data Center: Boulder, Colorado USA. Digital media.

Pradhanang SM, Anandhi A, Mukundan R, Zion MS, Pierson DC, Schneiderman EM, Matonse A, Frei A. 2011. Application of SWAT model to assess snowpack development and streamflow in the Cannonsville watershed, New York, USA. *Hydrological Processes* **25**: 3268–3277.

Shanley JB, Chalmers A. 1999. The effect of frozen soil on snowmelt runoff at Sleepers River, Vermont. *Hydrological Processes* **13**: 1843–1857.

Singh P, Spitzbart G, Hübl H, Weinmeister HW. 1997. Hydrological response of snowpack under rain-on-snow events: a field study. *Journal of Hydrology* **202**: 1–20.

Singh P, Spitzbart G, Hubl H, Weinmeister HW. 1998. The role of snowpack in producing floods under heavy rainfall. In Proceedings of the HcadWater'98 Conference: Hydrology, Water Resources and Ecology in Headwaters. IAHS Publ. no. 248; 89–95. Meran, Italy.

USACE. 1956. *Snow hydrology*. North Pacific Division: Portland, Oregon.

USGS. 1997. Flood of January 19-20, 1996 in New York State. U.S. Geological Survey prepared in cooperation with New York State Department of Transportation. *Water Resource Investigation Report 97-4252*.

USGS. 2007. Digital elevation models (DEM). http://eros.usgs.gov/#/Find_Data/Products_and_Data_Available/DEMs (accessed 20 May 2012).

Wankiewicz A. 1978. Water pressure in ripe snowpacks. *Water Resources Research* **14**: 593–600.

Zion MS, Pradhanang SM, Pierson DC, Anandhi A, Lounsbury DG, Matonse AH, Schneiderman EM. 2011. Investigation and Modeling of winter streamflow timing and magnitude under changing climate conditions for the Catskill Mountain region, New York, USA. *Hydrological Processes* **25**: 3289–3301.

HYDROLOGICAL PROCESSES
Hydrol. Process. (2013)
Published online in Wiley Online Library
(wileyonlinelibrary.com) DOI: 10.1002/hyp.9910

Modelling potential effects of climate change on winter turbidity loading in the Ashokan Reservoir, NY

Nihar R. Samal,[1,2]* Adao. H. Matonse,[1] Rajith Mukundan,[1] Mark S. Zion,[3] Donald C. Pierson,[3] Rakesh K. Gelda[4] and Elliot M. Schneiderman[3]

[1] *Institute for Sustainable Cities, City University of New York, NY 10065, USA*
[2] *Department of Civil Engineering, National Institute of Technology, Durgapur 713209, India*
[3] *New York City Department of Environmental Protection, Kingston, NY 12401, USA*
[4] *Upstate Freshwater Institute, Syracuse, NY 13204, USA*

Abstract:

Recent studies have indicated that potential future climate change may lead to changes in the timing and quantity of snowpack accumulation and winter (November to April) streamflow patterns including increased streamflow and turbidity in early winter and a slight reduction in turbidity loads at the time of traditional early spring run-off. In this study, we examine the potential effects of these predicted changes on reservoir turbidity levels. Our analysis focuses on Ashokan Reservoir, NY, which can at times receive significant watershed turbidity inputs mainly from stream channel erosion from the Esopus Creek. Both measured and simulated turbidity loads and climatology are input to CE-QUAL-W2 (W2), a reservoir turbidity transport model that can simulate reservoir turbidity and other water quality parameters. The W2 model is applied to estimate the effects of hydroclimatology on effective settling rates and turbidity transport as a result of differences in reservoir thermal structure during summer and winter events. Simulations suggest that the effective settling velocity is substantially lower at low temperatures during winter time. Winter average stream flow is simulated to increase by 12% and 20%, which leads to increases in reservoir turbidity by 11% and 17% for the future period 2046–2065 and 2081–2100, respectively. From a seasonal perspective, a change in timing of peak streamflow with increased flows during the winter and slightly reduced flows during early spring leads to increased average reservoir turbidity during winter and slightly decreased in-reservoir turbidity during early spring and summer.

KEY WORDS stream turbidity; reservoir turbidity; W2 model; climate change; winter settling rate; snowmelt run-off

Received 24 August 2012; Accepted 14 May 2013

INTRODUCTION

Transport of high concentrations of suspended particles is one of the major water quality concerns for water supply reservoirs, including the New York City (NYC) unfiltered water supply. Of concern are conditions during high streamflow events when high loads of inorganic particles are transported and can cause elevated turbidity (T_n, NTU) levels with complex spatial pattern in downstream lakes and reservoirs (Effler *et al*., 2006a, b; Gelda and Effler, 2007; Prestigiacomo *et al*., 2008; Gelda *et al*., 2012). Turbid water in a reservoir has negative aesthetic and recreational appeal and may have adverse effect on biodiversity, in addition to increasing water treatment costs in drinking water supply systems (Chung *et al*., 2009). The presence of increased turbidity in many water supply reservoirs also influences the ecological behaviour of cyanobacteria (Dzialowski *et al*., 2011). Therefore, aquatic ecosystems may be threatened by the redistribution of sediments and the associated transport of contaminants (Lou and Schwab, 2000). The dynamics of the turbid inflows from the stream discharge during the period of spring snowmelt or torrential rains can be a dominant physical phenomenon for reservoir sedimentation (Chikita and Okumura, 1990). Distribution and transport of particles in lakes and reservoirs are time and space varying (Casamitjana and Schladow, 1993) and are further influenced by the extrinsic variables of hydrometeorological forcing. Changes in meteorological forcing can lead to reservoir thermal stratification (Samal *et al*., 2009; 2012) resulting in changing the distribution of turbidity, although high levels of particle concentration may sometimes occur because of episodic mixing during upwelling (Lou and Schwab, 2000). In the unstratified winter period, a reservoir is well mixed, and high turbidity levels may be observed because of winter storm events (Lou and Schwab, 2000).

*Correspondence to: Nihar R. Samal, Research Associate, City University of New York, NY 10065, USA.
E-mail: nsamal@hunter.cuny.edu

Various studies have been undertaken on particle size, particle distribution and transport processes at surface and boundary layer mixing (Weilenmann *et al.*, 1989; Casamitjana and Schladow, 1993; MacIntyre *et al.*, 1999; Brach-Papa *et al.*, 2006; Chung *et al.*, 2009; Gelda *et al.*, 2009; 2012). However, specific mechanisms occurring at times of low and high water temperature with an effect on particle transport following large and small events (due to the changes in snowmelt and seasonality of streamflow) in a large reservoir system are not well understood and require further investigation. Of particular interest is how potential decrease in winter snowpack and earlier snowmelt in our study region due to climate change (Matonse *et al.*, 2011; Mukundan *et al.*, 2012a, b) will affect the process of particle transport in NYC water supply reservoirs. Historical data analysis in the northeastern USA indicates a warming in surface air temperatures with a rate of winter warming that was greater than 0.7 °C/decade over the period 1970–1999, 0.12 °C/decade over the period 1900–1999 (Hayhoe *et al.*, 2007) and 0.42–0.46 °C/decade over the period 1965–2005 (Burakowski *et al.*, 2008). At most stations in the northeastern USA, the average number of snow-covered days has declined by 8.9 days/decade at the same time that averaged winter snowfall has decreased by about 4.6 cm/decade (Burakowski *et al.*, 2008). Also, long-term records of ice research indicate that warmer winter temperatures have been associated with earlier river (Hodgkins *et al.*, 2003) and lake ice loss (Hodgkins *et al.*, 2002). A warmer climate across North America also leads to earlier snowmelt, a decrease in the extent of deeper snowpacks (Dyer and Mote, 2006; Milly *et al.*, 2008; Wake *et al.*, 2008) and more winter precipitation falling as rain instead of snow (Zion *et al.*, 2011). Increased winter rain and snowmelt leads to greater winter stream discharge and turbidity in our study region (Mukundan *et al.*, 2012a, b), which in turn causes greater loading of turbidity-causing particles into the reservoir system.

Further, potential changes in extreme events that may accompany climate change are of particular concern and important to consider. Our current knowledge about the impact of climate change on extreme precipitation events are limited (Kharin *et al.*, 2007). Event processes occur at too fine a spatial or temporal scale to be properly represented in a single global circulation model (GCM). One partial solution to this problem is to obtain multiple realizations of differing combination of emissions scenarios and GCMs resulting in multiple scenarios in the period of interest. Historical event analysis is also important because a good understanding of the streamflow–turbidity relationship is needed to plan water supply reservoir system operations. Because water supply reservoirs are designed to store water over long periods for later use, turbidity problems may endure long past the storm events that seed the reservoir with large amounts of turbidity-causing materials. Considering the variability and changing seasonality of streamflow and associated changes in stream turbidity, the goals of this paper are as follows: (1) to document specific summer and winter events during the historical record; (2) to assess the impact of turbidity and temperature distributions in the reservoir prior and after the occurrence of peak summer and winter events; (3) to investigate the effects of temperature on effective settling rates in the reservoir following the summer and winter events; and (4) to assess the potential impact of climate change on future turbidity levels in the reservoir.

STUDY AREA: NEW YORK CITY WATER SUPPLY RESERVOIR

The NYC water supply system is one of the largest unfiltered surface water supplies in the USA. The system combines 19 reservoirs that supply more than 3.8 million cubic metres of drinking water per day to about nine million people in the metropolitan NYC and outside communities along the system aqueducts (NYCDEP 2006). The Ashokan Reservoir is one of the major NYC water supply reservoirs, located approximately 115 km northwest of New York City (Figure 1). The reservoir is divided into two basins, the West and the East, which are separated by a dividing weir (Figure 1). Most of the water enters Ashokan Reservoir through the West Basin where it can be stored and released, or transferred to the East Basin. A gate in the dividing weir is usually used to regulate water transfer to the East Basin; however, during large events, water can also spill over the dividing weir once the West Basin is filled. Water is normally diverted from the East Basin (although it can also be taken from the West Basin) via an aqueduct (120 km) to Kensico Reservoir, where it mixes with water from other parts of the system before being disinfected and conveyed to NYC. The focus of this study is the West Basin of Ashokan Reservoir, which can at times receive significant watershed turbidity inputs. Table I shows West Basin Ashokan Reservoir characteristics. The West Basin of Ashokan Reservoir receives most of its water (85%) from Esopus Creek, the smaller Bush Kill tributary and other local ungauged flows. The Esopus Creek flow consists of both natural watershed flow and water diverted from the nearby Schoharie Reservoir via the Shandaken Tunnel (Figure 1, inset). The major source of highly elevated turbidity in the West Basin of Ashokan Reservoir is clay mineral particles (1–10 μm diameter) (Gelda *et al.*, 2009) that are transported from Esopus Creek watershed into the reservoir during large storm events.

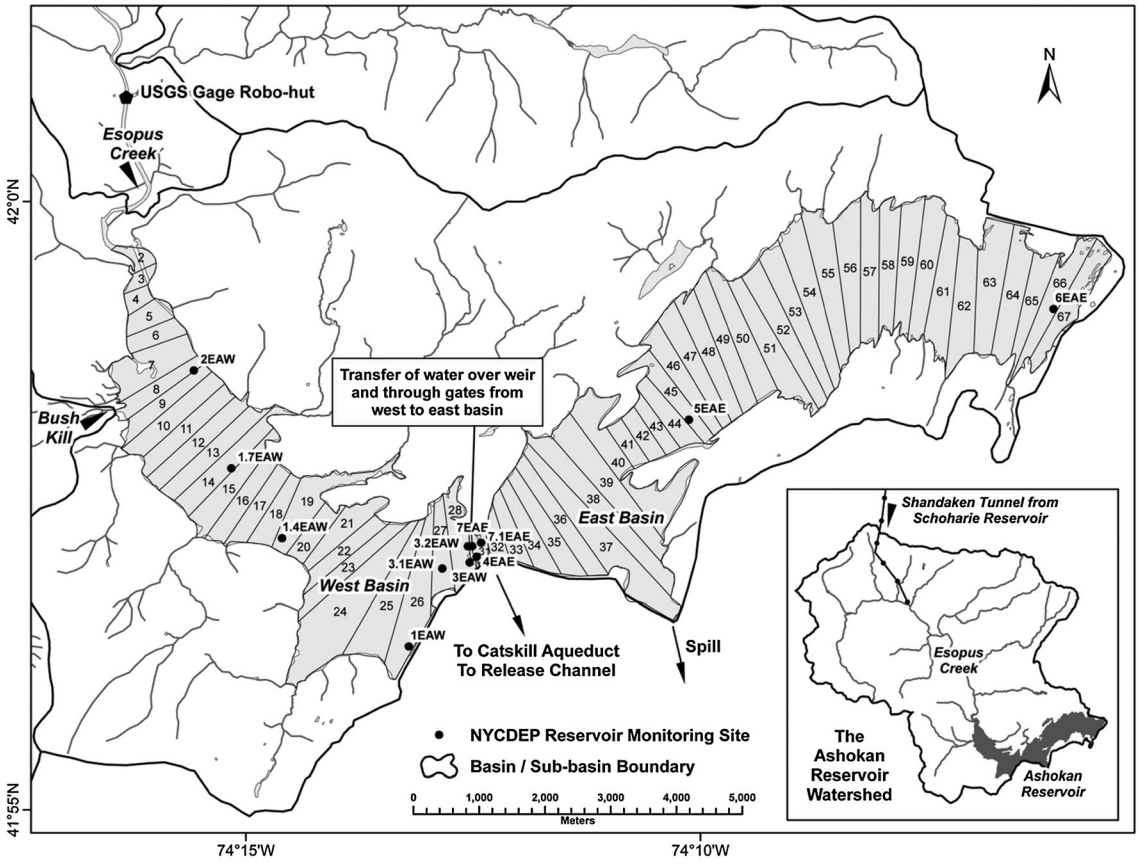

Figure 1. Ashokan Reservoir (West and East Basin): mouth of Esopus Creek and Bush Kill with model segment identification number

Table I. West Basin of Ashokan Reservoir

Reservoir characteristics	Value
Max length (m)	7400
Max depth (m)	58
Mean depth (m)	14
Surface areas (km^2)	12.18
Watershed areas (km^2)	616.34
Number tributaries	2
Number outflows	3
Spillway/dam elevation (m)	179.83
Residence time (days)	76.7
Volume at maximum (m^3) ($\times 10^6$)	178.576

DATA AND METHODS

Reservoir segmentation and turbidity transport modelling description

For this study, the two-dimensional reservoir hydrodynamic and turbidity model, CE-QUAL-W2 (W2; Cole and Buchak, 1995; Cole and Wells, 2004; Kim and Kim, 2006), is applied for both hindcasting historical events and future climate change simulations. The W2 model is a two-dimensional reservoir hydrodynamic and water quality model that has been widely used in many reservoirs to describe thermal regimes, water quality and also particle transport (Chung and Gu, 1998; Gu and Chung, 1998; Kim and Kim, 2006) and has been further adapted to model turbidity for the Ashokan Reservoir by Gelda *et al*. (2009). Cole and Wells (2004) describe the basic hydrodynamic and transport equations of the model.

Turbidity is a measure of the magnitude of light side scattering in the water and a rough surrogate measure of total suspended solids (Gelda *et al*., 2009; 2012). The turbidity submodel adopts T_n as the state variable as described in Gelda *et al*. (2009, 2012). In particular, the T_n is discretized into three size classes of turbidity-causing particles (1, 3.14 and 8.11 μm). The relative contribution of the turbidity level of each particle size class is calculated within each grid of the model on the basis of mass balance. The settling rate of T_n is based on the settling rates of the three-component particle sizes and is calculated using Stokes law:

$$v_i = \frac{g\left(\rho_p - \rho_w\right)}{18\mu} d_i^2 \quad (1)$$

Table II. Two-dimensional hydrothermal/hydrodynamic model (W2) coefficients for Ashokan (West Basin) (Gelda *et al.* 2009)

Coefficient	Value
Longitudinal eddy viscosity (m^2/s)	1
Longitudinal eddy diffusivity (m^2/s)	1
Chezy coefficient ($m^{0.5}/s$)	70
Wind sheltering coefficient	0.9
Fraction of incident solar radiation absorbed at the water surface	0.45
Coefficient of bottom heat exchange ($W/m^2/°C$)	7.0×10^{-8}

where v_i is the settling velocity for the ith particle size class; g is the gravitational constant (m/s^2); ρ_p and ρ_w are densities of particle and water (kg/m^3), respectively; d_i is the geometric mean diameter of particles in the ith size class of particles (μm); and μ is the viscosity of water (kg/m/s). Both ρ_w and μ are temperature dependent (Martin and McCutcheon, 1999).

The W2 model has been adapted, calibrated and rigorously tested for the Ashokan Reservoir (Gelda *et al.*, 1998; 2009). The model represents Ashokan Reservoir (West Basin under study) in the form of a grid of cells with 28 longitudinal segments and vertical layers of 1 m thickness with a top surface boundary layer and varying bottom boundary layer depending on the depth of each segment (Figure 1). The inflows and outflows directly enter or exit model segments according to segment depth and location relative to the density of inflow water or the depth of withdrawal. Six coefficients were adjusted to calibrate the W2 hydrothermal submodel (Table II). Coefficients defining the partitioning of turbidity into three different size classes and the particle size associated with those classes were developed from extensive field studies and particle size analysis (Peng *et al.*, 2002; 2004).

For this study, the W2 model is used to run hindcasting simulations that are driven by actual input conditions for the reservoir from 1948 to 2011 and to also produce a series of future simulations driven by locally downscaled climate scenarios. The data inputs and modelling methods for each case are described in the following text.

Historical simulations

The driving data for the model under historical conditions (1948–2011) include measured time series of daily reservoir inflows with associated stream temperature (T) and turbidity T_n, meteorological data (hourly air temperature, dew point, solar radiation, wind speed and wind direction) and daily records of operational information [withdrawal, spill and release volumes, and reservoir water surface elevation (WSE)].

Model results for in-reservoir water temperature and turbidity for more recent years (2003–2011) were compared with data collected at automated profile buoys located within the reservoir (Figure 1). The two buoys were located at sites about midway longitudinally from the Esopus Creek inflow to the dam (site 1.4) and near the dam (site 3.1). Data were collected four times a day (6-h increments) and include water temperature and turbidity measured from the surface to the bottom of the reservoir at 1-m depth increments (Gelda *et al.*, 2009). Event-based sampling was also conducted in order to support our modelling study.

Future climate simulations

The modelling framework applied for the future climate change simulations is illustrated in Figure 2. Inputs to W2 model include downscaled GCM/emission scenarios climate data, simulated hourly climate developed using various methods on the basis of simulated daily hydrology and climatology, watershed model-simulated daily streamflow, daily stream turbidity simulated as a function of streamflow and daily reservoir operations simulated by the Operational Analysis and Simulation of Integrated Systems (OASIS; Hydrologics Inc., 2007) reservoir system model. Future climate scenarios were developed using a 25-bin change factor (CF) methodology (Anandhi *et al.*,

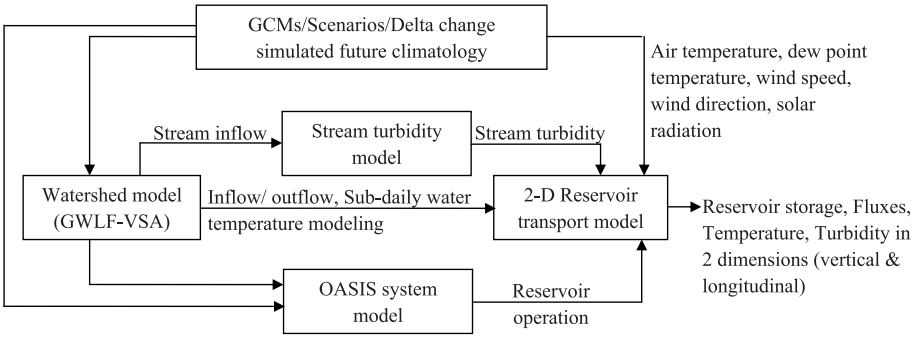

Figure 2. Modelling frame work: model connection and data flow

2011). For GCM baseline and future scenarios, associated with three GCMs, two future time slices and three future emission scenarios are detailed in Table III. Data from each unique future scenario were compared with the GCM baseline scenario, by grouping data from the future scenario by individual months and calculating the frequency distribution of a meteorological variable during the future months and the same months in the baseline scenario. For each month, 25 CFs were calculated by taking the difference between the same 4 percentile ranges in the baseline and future scenarios. Locally scaled future scenarios of daily air temperature and precipitation were created by adding the created CFs to historical records of daily meteorological data. For each month, the CF applied to any given day's data corresponded to that day's position in the frequency distribution of the historical measurements for that month. This CF methodology (Anandhi *et al*., 2011) maintains the temporal pattern of the historical meteorological events while modifying the magnitude of the individual events consistent with the changes indicated by the GCM simulations. Scaling the CFs by position in the monthly frequency distribution of events allows event size to influence the magnitude of the derived CF.

Inflow

Climate change inflows to the West Basin Ashokan Reservoir are simulated on a daily time step using the Generalized Watershed Loading Functions-Variable Source Area (GWLF-VSA) watershed model (Haith and Shoemaker, 1987; Schneiderman *et al*., 2002; Schneiderman *et al*., 2007). The GWLF-VSA is a lumped-parameter continuous simulation model that simulates daily stream flow, nutrients and sediment loads on a watershed scale. Inputs include daily air temperature, precipitation, incoming solar radiation and daily average relative humidity. The GWLF-VSA model was calibrated over a 6-year period (1997–2002) to minimize the differences between measured and simulated streamflow for the Esopus Creek at Coldbrook, which is the major tributary to West Basin Ashokan Reservoir. The Nash–Sutcliffe coefficient comparing the measured with simulated daily flows for the calibration period was 0.74. In addition, inflow from ungauged areas draining to the reservoir is estimated on the basis of the simulated discharge and a ratio between gauged and ungauged drainage areas. To produce scenarios of future inflows to Ashokan Reservoir, the GWLF-VSA model was driven using the future simulated inputs of daily air temperature and precipitation, which are produced using the CF methodology described earlier.

Table III. General circulation models (GCM), emission scenarios and time slices applied in this study

GCM	Emission scenario	Time slices
CGCM3.1 (Canada)	A1B, A2, B1	2081–2100
	B1	2046–2065
CNRM-CM3 (France)	B1	2046–2065
		2081–2100
MRI-CGCM2.3.2 (Japan)	B1	2081–2100

Inflow water quality

A rating curve (Gannett Fleming & Hazen and Sawyer, 2008) developed empirically using historical data is used to estimate turbidity level, T_n, based on the GWLF-VSA-simulated Esopus Creek flow Q_{Esp} and has the form

$$\log T_n = 1.033 - 0.986 \log Q_{\mathrm{Esp}} + 0.691 \left(\log Q_{\mathrm{Esp}}\right)^2 \quad (2)$$

A lower bound $T_n = 4.8$ is used for $Q_{\mathrm{Esp}} < 5.17\ \mathrm{m}^3/\mathrm{s}$. Total daily turbidity is then partitioned into three particle sizes using the following criteria:

$$T_{n1} = 0.10 * T_n \quad (3a)$$

$$T_{n2} = 0.45 * T_n, \text{and } T_{n3} = 0.45 * T_n \text{ if } Q_{\mathrm{Esp}} > 40\ \mathrm{m}^3/\mathrm{s} \quad (3b)$$

$$T_{n2} = 0.65 * T_n \text{ and } T_{n3} = 0.25 * T_n \text{ if } Q_{\mathrm{Esp}} \le 40\ \mathrm{m}^3/\mathrm{s} \quad (3c)$$

Inflow temperature

Esopus Creek water temperature at hour i (T_i) is calculated in °C using the following regression equation developed by the Upstate Freshwater Institute and published in NYCDEP (2007)

$$T_i = a_0 + a_1 * T_{\mathrm{air},i-2} + a_2 * \log Q_{\mathrm{Esp}} + a_3 * a_5 * T_{\mathrm{STP},i}^{a_4} \quad (4)$$

where $T_{\mathrm{air},i-2}$ is the simulated local air temperature of 2 h back in time (°C), a_0–a_5 are the model coefficients calibrated on a monthly basis using historical data, Q_{Esp} is the simulated Esopus Creek daily average streamflow (m^3/s) and $T_{\mathrm{STP},i}$ is the Shandaken Tunnel portal (Figure 1, inset) temperature at the ith hour. Coefficient a_5 is 0 when the Shandaken Tunnel is off and 1 when the tunnel is on. Because the effects of the T_{STP} were relatively small, for these simulations, the same historical record of T_{STP} was used to produce both present and future scenarios of Esopus Creek stream temperature.

Reservoir meteorology

The W2 reservoir model requires hourly meteorological data as input. Hourly air temperatures are obtained from the daily scenario data using future simulated daily

minimum (T_{min}) and maximum (T_{max}) air temperatures and the WAVE model as described in Reicosky *et al.* (1989). The WAVE model uses today's T_{min} and T_{max} together with next day T_{min} to compute hourly air temperature from today's sunrise (Rise) to 1400 h and from 1400 h to sunrise of the next day. Hourly temperature ($T(H)$) is estimated as follows:

$$T(H) = T_{ave} + \mathrm{Amp}(\cos(\pi H'/\mathrm{Rise})) \quad \text{for } 0 \le H < \mathrm{Rise} \text{ and } 1400 \text{ h} < H \le 2400 \text{ h} \tag{5a}$$

$$T(H) = T_{ave} - \mathrm{Amp}(\cos(\pi(H - \mathrm{Rise})/(14 - \mathrm{Rise}))) \quad \text{for } \mathrm{Rise} \le H \le 1400 \text{ h} \tag{5b}$$

where H is the time in hours; $H' = H + 10$ if $H <$ Rise; $H' = H - 14$ if $H > 1400$ h; $T_{ave} = (T_{min} + T_{max})/2$ and $\mathrm{Amp} = (T_{max} - T_{min})/2$.

The dew point temperature for W2 climate change simulations is set equal to the scenario values of daily T_{min}. For these simulations, we did not attempt to create future scenarios of wind and solar radiation. Consequently, the same local historical hourly values were used in both baseline and future simulations.

Reservoir operations

As part of the NYC water supply operations, water from the nearby Schoharie Reservoir can be routed through Shandaken Tunnel to the Esopus Creek (Figure 1, inset), which subsequently enters the West Basin of Ashokan Reservoir. These and other operational flows are obtained from the NYC OASIS model (Hydrologics Inc., 2007) simulations. For the West Basin Ashokan Reservoir, these include the Shandaken Tunnel flows, the gate flows in the dividing weir between the West and East Basins of the Ashokan Reservoir and the release channel withdrawals from West Basin Ashokan. The time series for these flows are obtained from OASIS on a daily time step. The OASIS model takes daily reservoir inflows throughout the entire NYC water supply system as inputs, and these inflows were in turn simulated using GWLF-VSA with either historical baseline or future scenario meteorological data.

RESULTS AND DISCUSSIONS

Evaluation of W2 model's performance using historical data

The W2 model was previously calibrated and validated for the Ashokan Reservoir by comparing measured temperature and turbidity collected using an automated reservoir monitoring system with simulated values in the reservoir and also by comparing measured and simulated temperature and turbidity levels from the reservoir effluent withdrawals. On the basis of these comparisons, the model has been found to predict the spatial variations in turbidity and the timing of turbidity transport well (Gelda *et al.*, 2009). Prior to further analysis in this study, the W2 model results for the study period (2003–2011) are evaluated. During this study period, the model was driven with the actual observed streamflow and the best possible continuous time series of turbidity input based on a combination of automated monitoring with missing values filled in with modelled information (Mukundan *et al.* (2012a, b)). The model results were compared with both reservoir WSE as measured by NYCDEP for June 2003 to November 2011 (Figure 3(a)) and reservoir turbidity measured at automated in-lake monitoring sites 1.4 and 3.1 for 2006 to 2011 (Figure 4(a)).

The model simulates well the fluctuations in WSE both during low and high flow event periods (Figure 3(a)). Three occurrences of reservoir drawdown below 174 m are observed on 23 September 2007, 19 October 2008 and 04 September 2010, and all are well reflected by the model simulation. Large storm events, which result in sharp rises in WSE, are also well simulated. The high model performance in simulating the WSE is reflected in Figure 3(b) with $R^2 = 0.99$.

Figure 4(a) illustrates how the model-simulated reservoir turbidity compares with observed data at buoys 3.1 and 1.4 of the West Basin available for the period 2006–2011. The model-simulated turbidity levels are generally of a similar magnitude as the buoy measured data. In addition, the timing of the increases and decreases in simulated and the measured turbidity matches well. Some potential causes for differences between model simulation and buoy measurements include uncertainties in the particle size distribution of the turbidity-causing material flowing into the reservoir, the magnitude of the loading estimates from the Esopus Creek under extreme flow conditions when the automated monitoring system may have been inoperable, potential errors in the buoy measurements and possible model errors in turbidity transport for individual events.

Event sampling from simulated time series

To investigate and better understand the seasonal pattern between streamflow, stream turbidity and reservoir turbidity, we separated the model results into two seasons: summer (May to October) and winter (November to April) during more than six decades of model hindcasts using input based on the historical record (1948–2011). A total of 12 events (six in each season) spanning a wide range of measured streamflow inputs and simulated reservoir turbidity levels are considered for this analysis. The simulated turbidity is that near the surface at

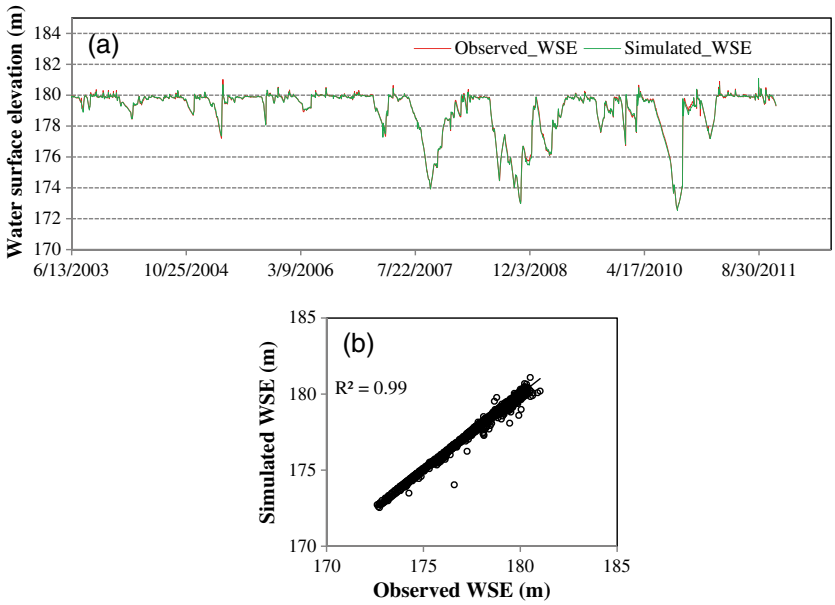

Figure 3. (a) Model simulated and observed WSE in Ashokan Reservoir for the period 2003–2011; (b) scatter plot observed and simulated WSE pairs

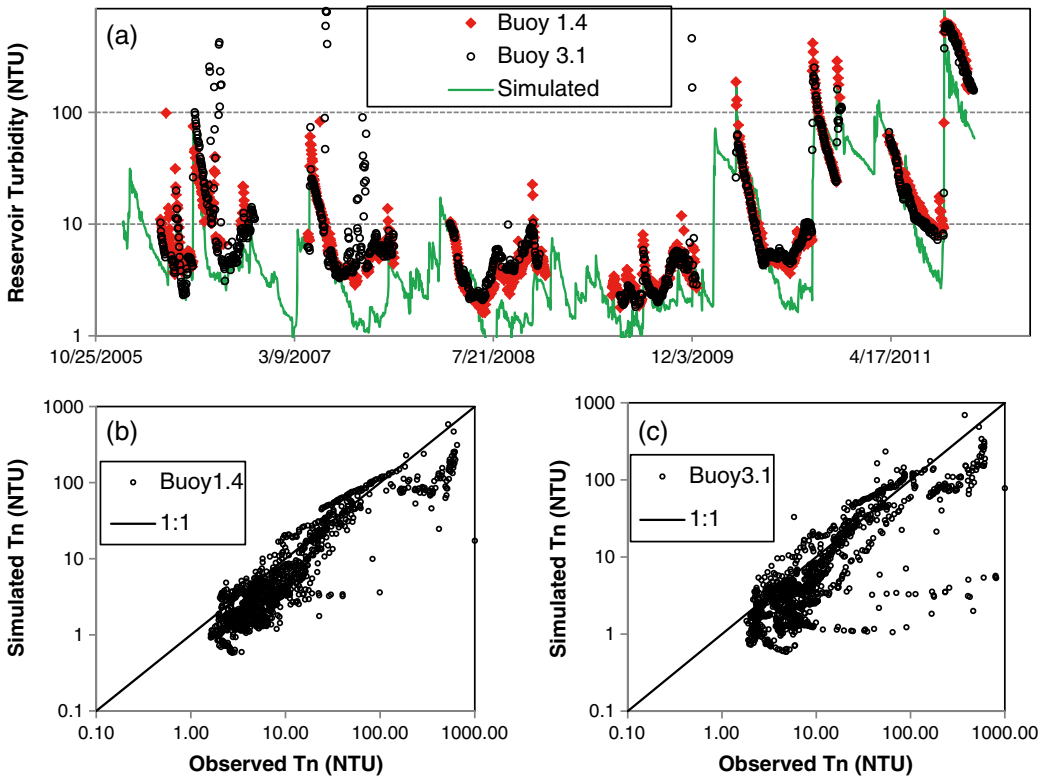

Figure 4. (a) Model *versus* observed turbidity (T_n, NTU) in Ashokan Reservoir, 2006–2011, where the green line represents the model turbidity at segment 28 (withdrawal point); (b) buoy1.4 (segment 19); (c) buoy3.1 (near the dividing weir, segment 28). The figures in (b) and (c) include 1 : 1 line

the end of the West Basin opposite the inflow (segment 28, Figure 1). This would be representative of the turbidity that would be transferred from West Basin to East Basin by spilling over the reservoir dividing weir during storm events and thereby influence the turbidity of water withdrawn from the East Basin reservoir.

The minimum streamflow that causes the simulated reservoir turbidity to rise above 10 NTU (146 m^3/s) was used as a lower bound for selecting these storm events.

For these two events with similar streamflow, the simulated peak reservoir turbidity is found to be higher in the winter event compared with the event in summer (Table IV), largely as a result of somewhat greater turbidity inputs to the reservoir and higher background turbidity in the reservoir prior to the winter event. In addition to differences in magnitude, an anecdotal example of differences in transport time is illustrated in Figure 5. Reservoir turbidity appears to peak 2–3 days after the peak stream turbidity in the summer example, whereas the turbidity peaks within 1 day in the winter event example (Figure 5(b,d)). Such differences in turbidity transport would primarily be expected to result from seasonal differences in the water temperature and thermal stratification and can also be affected from differences in the pre-event reservoir storage levels, the vertical distribution of the turbidity relative to the crest of the reservoir dividing weir and inter-storm variations in particle size and settling rates. All of these factors can all have an impact on the height of the peak and the lag

Table IV. Similar size paired events during summer and winter

Summer				Winter			
Date of peak streamflow	Streamflow (m^3/s)	Peak stream turbidity (NTU)	Peak reservoir turbidity (NTU)	Date of peak streamflow	Streamflow (m^3/s)	Peak stream turbidity (NTU)	Peak reservoir turbidity (NTU)
07-09-1999	191	228	12	28-11-1993	233	283	83
18-09-2004	250	15	12	08-12-1974	240	306	58
21-10-1995	254	351	28	02-12-1996	271	413	92
07-09-2011	312	860	352	08-11-1977	304	557	95
28-06-2006	322	468	68	23-03-2010	350	595	165
01-10-2010	500	1440	138	03-04-2005	500	315	69

Streamflow and stream turbidity are measured at the Esopus Creek inflow to the reservoir. Peak reservoir turbidity is that simulated at the upper layer of segment 28.

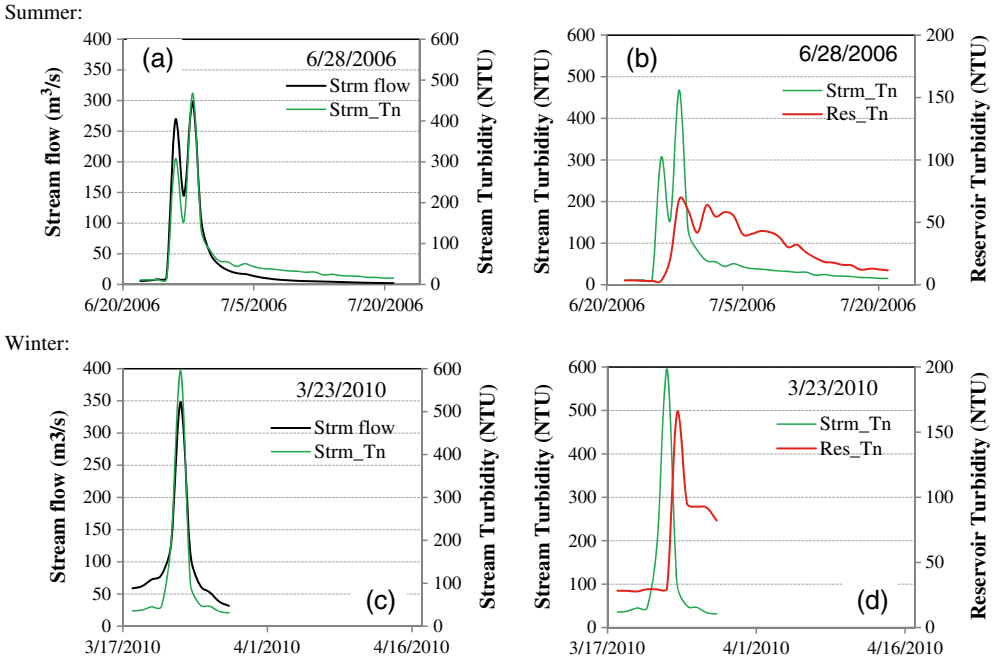

Figure 5. (a,c) Measured inputs to the reservoir from paired summer and winter events with similar peak stream discharge; (b,d) the simulated reservoir turbidity in the upper layer of segment 28. (Strm flow, streamflow; Strm_Tn, stream turbidity; Res_Tn, reservoir turbidity)

(transport time) between peak stream and reservoir turbidity. The relatively small difference in turbidity transport between these summer and winter events suggests that at least in this case, secondary effects other than those directly related to thermal stratification were of greater importance. Another potential difference between winter and summer occurs because of high turbidity events tending to be more frequent during winter. Because of the winter isothermal condition, the turbidity plumes have a longer travel time in the reservoir resulting in overlapping effects between consecutive turbidity events; thus, it is more likely that one event will influence the initial conditions of the reservoir prior to the next event. For example, for the event depicted in Figure 5, the summer-event initial T_n was 5 NTU (Figure 5(b)), whereas the winter-event initial T_n was 25 NTU (Figure 5(d)).

To further investigate inter-event differences during winter, streamflow events of similar size during winter were compared. Twelve winter events were selected from the hindcasting model results and were grouped into six pairs of similarly sized flows. Results in Table V show that winter events with the highest streamflow and turbidity levels are those with the greatest event precipitation and snowmelt; however, there is high variability in reservoir turbidity for similar size streamflow events, which are complexly related to watershed snow and reservoir ice conditions during each winter event as well as the total precipitation and weather conditions occurring during each event. This suggests that winter events are sensitive to the antecedent conditions. It is difficult to understand the reservoir response from the individual characteristic of any storm, the reservoir initial conditions, subsequent reservoir forcing or operations alone. Rather, the reservoir response is the result of complex interactions of all these and other factors. Therefore, to further understand the reservoir response to any individual storm event, a detailed analysis of the model results is necessary.

Table V. Paired winter events of similar size and pre-event snow/ice conditions

Similar size paired events	Date of peak streamflow	Streamflow (m^3/s)	Peak stream turbidity	Reservoir water surface elevation (m)	Initial reservoir turbidity*	Peak reservoir turbidity*	Turbidity sources	Event snowpack melt (mm)	Pre-event snowpack SWE (mm)	Storm event precipitation (mm)	Reservoir ice cover	Event type
1	26-02-1961	167	172	177.91	11.2	12	R	15.0094	96.4364	0	#	A
	10-03-1964	147	132	178.49	33.8	45	R	15.1841	148.795	5.85429	#	C
2	16-04-2007	350	253	180.44	36.5	56	M	11.2369	12.2724	7.80572	No	C
	01-12-2010	350	925	180.39	46.8	252	M	0.42774	0.427742	0	Yes	A
3	20-02-1981	371	961	180.16	37.5	196	R	23.0397	148.039	0	#	A
	11-03-2011	400	780	180.0	121.0	127	M	0	122.985	7.32178	Yes	B
4	21-12-1957	450	1677	180.02	94.3	255	R	36.6577	8.36197	28.2957	#	C
	11-12-1952	475	1976	180.48	18.7	284	R	19.7692	37.6682	0	#	A
5	05-04-1984	507	2325	180.02	312	322	R	13.5488	60.8674	5.85429	#	C
	04-04-1987	493	2197	180.08	206	409	R	24.9145	28.2957	14.6357	#	C
6	21-03-1980	622	4574	179.93	14.8	1130	R	12.7025	51.5164	0	#	A
	19-01-1996	616	4417	179.54	168	928	R	20.0466	246.333	0	#	A

Turbidity sources are M for measured and R for Regression when measured data were not available. Event types are A, snowmelt; B, rain-on-snow; and C, snow-dominated mixed rain event. Snowpack melt and Snow Water Equivalent (SWE) are from a GWLF-VSA simulation.
*Turbidity at the upper layer of segment 28.
Information not available.

Event-specific temperature–turbidity profiles in Ashokan reservoir

Distribution of temperature in reservoir is an important factor in determining the transport of turbidity within the reservoir and, in turn, critical to understanding the potential turbidity in reservoir effluents. Simulated reservoir water temperature and turbidity profiles during example summer and winter events are shown in Figures 6 and 7. In the case of the summer event, the reservoir temperature is clearly stratified before the occurrence of an event (Figure 6(a)). Warmer epilimnetic temperature forms an upper mixed layer, and the wind-induced turbulence energy is not sufficient to allow surface waters to mix with colder and less dense deeper water. During

the example winter event, the reservoir is isothermal with near-zero vertical temperature gradient so the reservoir remains well mixed throughout the entire water column.

This difference in thermal structure has a large impact on the reservoir response to a turbidity loading event. Although the summer (Figure 5(a)) and winter streamflow events (Figure 5(c)) are of similar size (Table IV), the simulated reservoir response to these events is quite different. During the summer event, turbidity forms a plume with the higher (>100 NTU) levels in a layer between 5 and 10 m and with lower levels (<5 NTU) below the upper mixed layer (Figure 6(b)). The turbidity loading from the stream enters the reservoir in the upper layer because the temperature (density) of the inflowing stream water matches the temperature of the epilimnion. The turbidity is then concentrated within this upper mixed layer because the horizontal transport through the reservoir is much faster than the slow settling of turbidity-causing clay particles. This process forms a turbidity plume above the thermocline.

In the case of the winter event (Figure 7), the pre-event turbidity appears evenly distributed at about 30–40 NTU throughout the reservoir because of the preceding turbidity loading history. At first, turbidity is simulated to move from the stream mouth (segment 1) to the dividing weir (segment 28, where $T_n > 100$ NTU) as a surface plume associated with inverse stratification. During this time, the reservoir was nearly isothermal (Figure 7(a)), and the turbidity is soon mixed throughout the full vertical profile of the reservoir (Figure 7(b)).

Examination of the full longitudinal distribution of turbidity in Figures 6 and 7 provides a clearer explanation for the summer *versus* winter differences in turbidity illustrated in Figure 5. The apparently more rapid turbidity transport under winter conditions is actually a result of the summer turbidity plume illustrated in Figure 6. Simulated turbidity spilling over the dividing weir and in the upper metres of the reservoir remained low as a consequence of the vertical structure of the turbidity plume even though turbidity was rapidly transported in this concentrated plume. In the winter example (Figure 7), the complete vertical mixing of the turbidity ensured that it would be rapidly detected at all levels in the reservoir.

Thus, in both winter and summer, the initial turbid plume and peak T_n in the reservoir following an event is a result of variations in the relative rates of horizontal and vertical advection. The location of the plume is dependent on the ambient stratification regime and the density of the inflow waters, whereas the magnitude of the peak impact is a

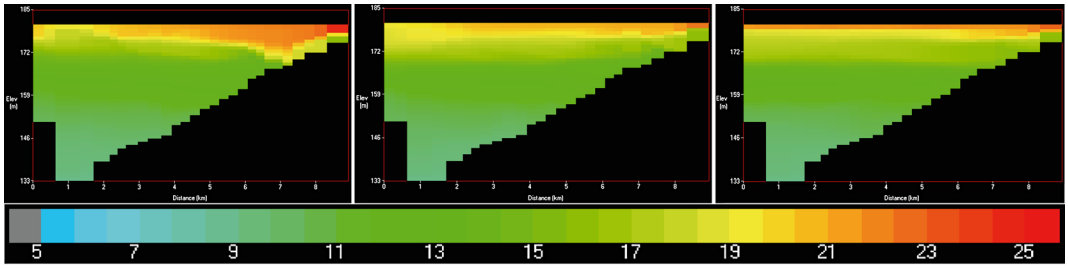

a. Simulated temperature distribution 24 h before, during and 24 h after a summer event (06/28/2006)

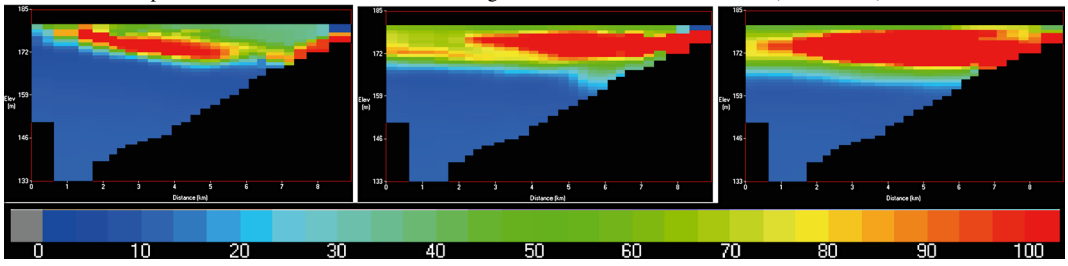

b. Simulated turbidity distribution 24 h before, during and 24 h after a summer event that occurred on 06/28/2006.

X-axis: Distance (in km) from 0 (model segment 28) to 9 (segment 1) with 1 km increment;
Y-axis: Elevation (meters above sea level) from bottom (133 m) to top (185 m) with 13 meter increment.

This figure is centered around the day of peak event stream discharge. The turbidity plume in the first panel is associated with an increase in discharge prior to the event peak stream discharge (see also figure 5a). This is the turbidity at the upper layer of segment 28.

Figure 6. (a) Temperature distribution 24 h before, during and 24 h after a summer event (28/06/2006). (b) Simulated turbidity distribution 24 h before, during and 24 h after a summer event that occurred on 28/06/2006.

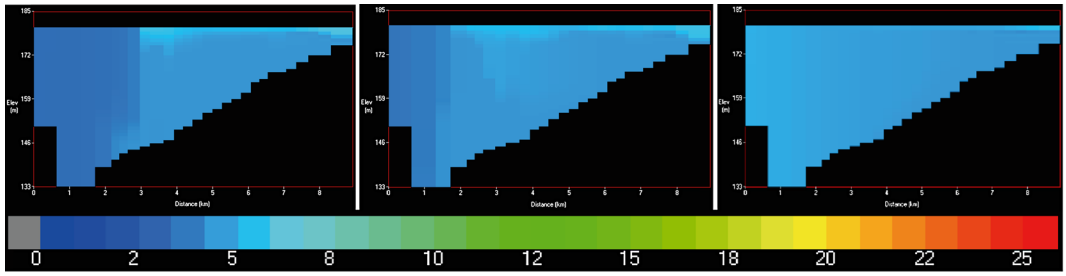

a. Simulated temperature distribution 24 h before, during and 24 h after a winter event (03/23/2010)

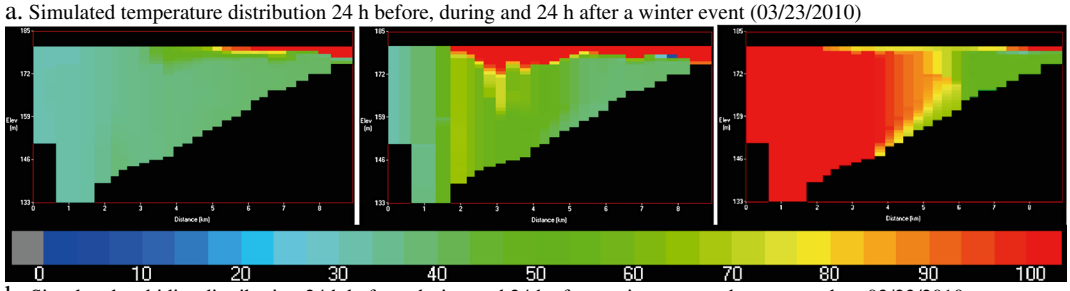

b. Simulated turbidity distribution 24 h before, during and 24 h after a winter event that occurred on 03/23/2010.

X-axis: Distance (in km) from 0 (model segment 28) to 9 (segment 1) with 1 km increment;
Y-axis: Elevation (meters above sea level) from bottom (133 m) to top (185 m) with 13 meter increment.

This is the turbidity at the upper layer of segment 28.

Figure 7. (a) Temperature distribution 24 h before, during and 24 h after a winter event (23/03/2010). (b) Simulated turbidity distribution 24 h before, during and 24 h after a winter event that occurred on 23/03/2010.

function of the loading. Furthermore, the ensuing attenuation of turbidity is often different in winter and summer because of the different settling rates (Figure 8). A measure of this attenuation in T_n levels between two seasons for different events is interesting and needs further investigation.

Driving parameters and reservoir turbidity under future climate

We have shown how Ashokan Reservoir experiences elevated turbidity levels following summer and winter events under current climate conditions. In Figures 9–12, we compare monthly boxplots calculated from simulated daily future period 2046–2065 and 2081–2100, respectively, and baseline (1980–2000) conditions for air temperature, streamflow, stream turbidity, reservoir WSE, water temperature and reservoir turbidity. The boxplots represent the 25th ($Q1$) and 75th ($Q3$) quartiles (or the interquartile range) from six GCM/emission scenarios (Table III); run for the two future periods and under present baseline conditions, the whiskers represent the lowest and highest data values within the lower ($Q - 1.5 \times (Q3 - Q1)$) and upper ($Q3 + 1.5 \times (Q3 - Q1)$) limits; the dark horizontal lines in the boxplots represent the median, and the individual plotted points (□, Δ and ○) represent outliers.

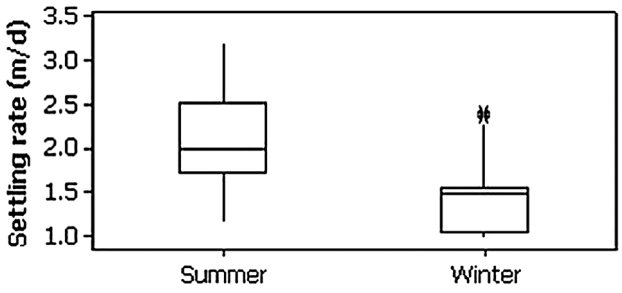

Figure 8. Summer and winter settling velocities based on Stokes law

The air temperature as shown in Figure 9 is projected to increase under future climate conditions with the difference from the baseline being slightly higher for the future period 2081–2100. The projected average annual increase in air temperature is +2.0 and +3.5 °C by the future period 2046–2065 and 2081–2100, respectively. The summer and winter season average annual air temperatures is projected to increase by +2.1 and +1.8 °C by future period 2046–2065, whereas it is +3.3 and +3.7 °C by future period 2081–2100. These values are consistent with seasonal trends in historical temperature, which suggest that average increases in winter temperature are slightly higher than those occurring during summer (Hayhoe *et al.*, 2007; Matonse *et al.*, 2011). The higher winter temperature will lead to a reduction in snowpack and may cause more precipitation to fall as rain

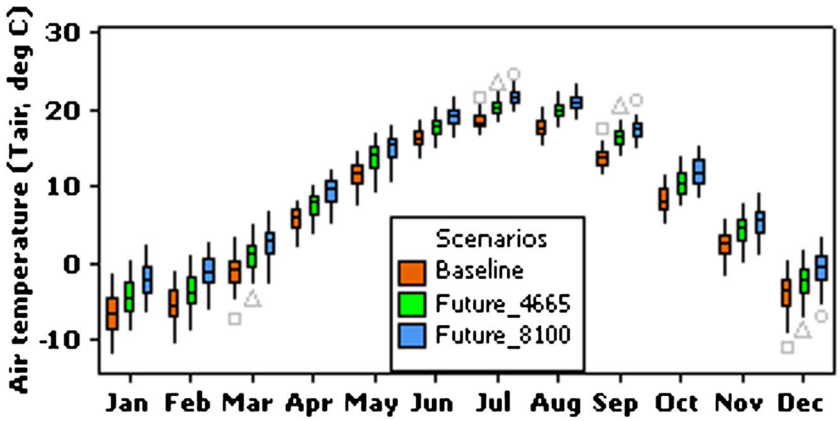

Figure 9. Average monthly air temperature (°C) for the baseline and simulated future period (2046–2065: Future_4665) and 2081–2100: Future_8100

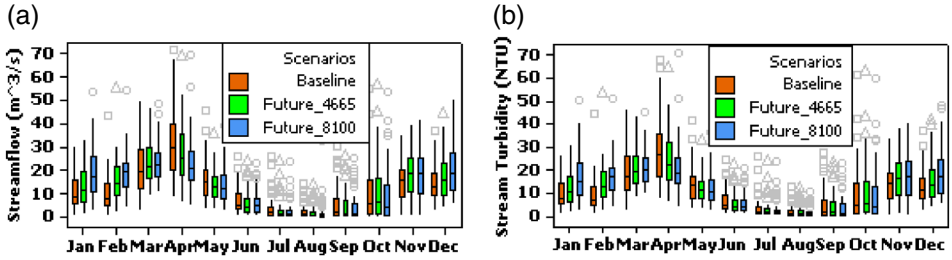

Figure 10. (a) Average monthly streamflow (m^3/s); (b) average monthly stream turbidity (T_n, NTU) for the baseline and simulated future period (2046–2065: Future_4665) and 2081–2100: Future_8100

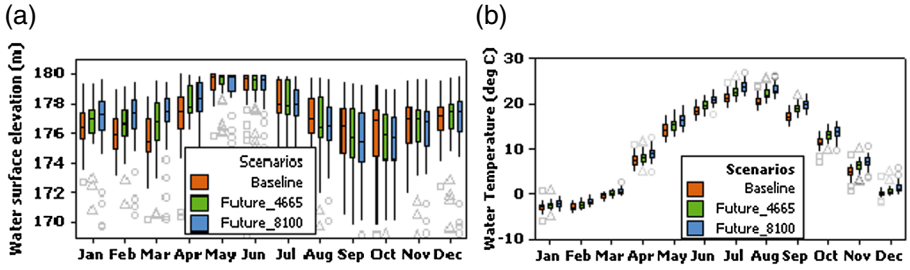

Figure 11. (a) Average monthly WSE (m); (b) average monthly in-reservoir water temperature (°C) for the baseline and simulated future period 2046–2065: Future_4665 and 2081–2100: Future_8100

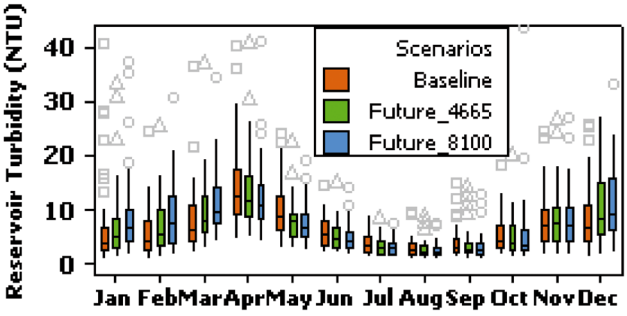

Figure 12. Average monthly reservoir turbidity (T_n, NTU) under baseline and simulated future period 2046-2065: Future_4665 and 2081-2100: Future_8100

(Matonse *et al.*, 2012). As a result of these changes in snow and precipitation, early winter streamflow is projected to increase, whereas the streamflow during April is projected to decrease (Figure 10(a)) under future climate conditions. Similar changes are projected to occur in seasonal patterns of stream turbidity (Figure 10(b)).

Ashokan Reservoir seasonal WSE (Figure 11(a)) is simulated to increase during the winter period because of increased winter streamflow. The reservoir water temperature (Figure 11(b)) shows a similar seasonal pattern of variation as air temperature (Figure 9). On average, the reservoir water temperature is increased by +1.0 °C (+1.8 °C), +1.4 °C (+2.4 °C) during summer months and +0.6 °C (+1.3 °C) during winter months by future period 2046–2065 (and 2081–2100). This is an indication of stronger stratification during summer under future climate.

Under future scenarios, the average annual streamflow is increased by 5% and 7%, which results in an annual increase in reservoir turbidity by 3% and 5% for the future period 2046–2065 and 2081–2100, respectively. However, the average winter reservoir turbidity is increased by 11% and 17% as result of an increase in winter stream flow by 12% and 20% for the future period 2046–2065 and 2081–2100, respectively. The future scenarios clearly show a shift in timing of streamflow and turbidity loading to the reservoir from a peak in April to higher values earlier in the winter (December to March). This shift to winter events causes increased in-reservoir turbidity during December to March and decreased turbidity in April to May (Figure 12). However, despite the future reductions in April loads, the peak average in-reservoir turbidity still occurs in April under the future conditions. This is because turbidity loading during late winter will continue to affect reservoir turbidity into the early spring because of the lag time associated with slow-settling turbidity-causing particles within the reservoir.

SUMMARY AND CONCLUSIONS

In this study, historical and simulated future streamflows and simulated stream turbidity were input to a two-dimensional hydrodynamic transport model to estimate water quality variables in the Ashokan Reservoir. Simulated inputs represent baseline and future climate scenarios. Our objectives were to (1) further understand the critical processes in both summer and winter that govern the fate and transport of turbidity within the Ashokan Reservoir and (2) study the effects of climate change on reservoir turbidity with a focus on the winter period.

Under future climate conditions, reservoir turbidity is expected to change because of greater winter precipitation, reduction in snowpack and earlier snowmelt resulting in increased winter streamflow and turbidity loading. This is expected to increase average Ashokan Reservoir turbidity during winter and slightly decrease in-reservoir turbidity during early spring.

On the basis of seasonal and event-based comparisons, a tendency towards higher reservoir turbidity during winter compared with summer was found when examining simulations driven by historical data. As a result of seasonal differences in thermal stratification reservoir, turbidity generally moved as a plume above the thermocline in summer following a storm event, whereas in winter, turbidity generally mixed throughout the water column. Within winter, similar size large streamflow events often showed marked differences in average reservoir turbidity depending on the sequence of previous turbidity events and the effect on background reservoir turbidity levels prior to an event.

ACKNOWLEDGEMENTS

The authors are grateful to the New York City Department of Environmental Protection (NYCDEP) for providing funding to carry out this research investigation. The authors acknowledge Ben Wright of Hazen and Sawyer for providing future simulated reservoir operation data. The authors also extend their thanks to Dr. David Smith, Hunter College, City University of New York, for his valuable review comments, Mr. David Lounsbury (NYCDEP) for GIS support and Donald Kent for various hydrometeorological data support. This is Contribution No. 313 of the Upstate Freshwater Institute.

REFERENCES

Anandhi A, Frei A, Pierson DC, Schneiderman EM, Zion MS, Lounsbury D, Matonse AH. 2011. Examination of change factor methodologies for climate change impact assessment. *Water Resources Research* **47**: W03501, DOI: 10.1029/2010WR009104.

Brach-Papa C, Boyer P, Ternat F, Amielh M, Anselmet F. 2006. Settling classes for fine suspended particles. *Comptes Rendus Mecanique* **334**: 560–567.

Burakowski EA, Wake CP, Braswell B, Brown DP. 2008. Trends in wintertime climate in the northeastern United States: 1965–2005. *Journal of Geophysical Research* **113**: D20114, DOI: 10.1029/2008JD009870.

Casamitjana X, Schladow G.1993. Vertical distribution of particles in stratified lake. *Journal of Environmental Engineering* **119**(3): 443–462.

Chikita K, Okumura Y. 1990. Dynamics of turbidity currents measured in Katsurazawa reservoir, Hokkaido, Japan. *Journal of Hydrology* **117**: 323–338.

Chung SW, Gu R. 1998. Two-dimensional simulations of contaminant currents in stratified reservoir. *Journal of Hydraulic Engineering* **12**(7): 704–711.

Chung SW, Hipsey MR, Imberger J. 2009. Modelling the propagation of turbid density inflows into a stratified lake: Daecheong Reservoir, Korea. *Environmenta Modelling Software* **24**: 1467–1482.

Cole T, Buchak EM. 1995. CE-QUAL-W2: a two-dimensional, laterally averaged, hydrodynamic and water quality model, version 2.0 (June 1995), *User Manual. U.S. Army Corps of Engineers*, Waterways Experiment Station, Vicksburg, MS 39180–6199.

Cole TM, Wells SA. 2004. Water quality and hydrodynamic modeling using CE-QUAL-W2 (Version 3.2 workshop manual) Portland State University.

Dyer JL, Mote TL. 2006. Spatial variability and trends in observed snow depth over North America. *Geophysical Research Letters* **33**: L16503, DOI: 10.1029/2006GL027258.

Dzialowski AR, Smith VH, Wang SH, Martin MC, Jr., de Noyelles F. 2011. Effects of non-algal turbidity on cyanobacterial biomass in seven turbid Kansas reservoirs. *Lake and Reservoir Management* **27**1: 6–14.

Effler SW, Matthews DA, Kaser J, Prestigiacomo AR, Smith DG. 2006a. Runoff event impacts on a water supply reservoir: suspended sediment loading, turbid plume behavior, and sediment deposition. *Journal of the American Water Resources Association* **42**(6): 1697–1710.

Effler SW, Prestigiacomo A, Peng F, Bulygina KB, Smith DG. 2006b. Resolution of turbidity patterns from runoff events in a water supply reservoir, and the advantages of in situ beam attenuation measurements. *Lake and Reservoir Management* **22**: 79–93.

Gannett Fleming & Hazen and Sawyer. 2008. Catskill turbidity control studies: phase III implementation plan, Prepared for New York City Department of Environmental Protection, Bureau of Engineering Design and Construction.

Gelda RK, Effler SW. 2007. Modeling turbidity in a water supply reservoir: advancements and issues. *Journal of Environmental Engineering Division ASCE* **133**: 139–148.

Gelda RK, Owens EM, Effler SW. 1998. Calibration, verification and an application of a two-dimensional hydrothermal model [CE-QUAL-W2(t)] for Cannonsville Reservoir. *Lake and Reservoir Management* **14**: 186–196.

Gelda RK, Effler SW, Peng F, Owens EM, Pierson DC. 2009. Turbidity model for Ashokan Reservoir, New York: case study. *Journal of Environmental Engineering Division ASCE* **135**(9): 885–895.

Gelda RK, Effler SW, Peng F. 2012. Modeling turbidity and the effects of alum application for a water supply reservoir. *Journal of Environmental Engineering Division ASCE* **138**(1): 38–47.

Gu R, Chung SW. 1998. Reservoir flow sensitivity to inflow and ambient parameters. *Journal of Water Resources Planning Management* **124**: 119–128.

Haith DA, Shoemaker LL. 1987. Generalized watershed loading functions for stream flow nutrients. *Water Resources Bulletin* **23**(3): 471–478.

Hayhoe K, Wake CP, Huntington TG, Luo L, Schwartz MD, Sheffield J, Wood E, Anderson B, Bradbury J, DeGaetano A, Troy TJ, Wolfe D. 2007. Past and future changes in climate and hydrological indicators in the US Northeast. *Climate Dynamics* **28**: 381–407.

Hodgkins GA, James IC, Huntington TG. 2002. Historical changes in ice-out dates as indicators of climate change in New England. *International Journal of Climate* **22**: 1819–1827.

Hodgkins GA, Dudley RW, Huntington TG. 2003. Changes in the timing of high river flows in New England over the 20th Century. *Journal of Hydrology* **278**: 244–252.

Hydrologics Inc. 2007. User manual for OASIS with OCL, Columbia, MD.

Kharin VV, Zwiers FW, Zhang X, Hegerl GC. 2007. Changes in temperature and precipitation extremes in the IPCC ensemble of global coupled model simulations. *Journal of Climate* **20**: 1419–1444.

Kim Y, Kim B. 2006. Application of a 2-dimensional water quality model (CE-QUAL-W2) to the turbidity interflow in a deep reservoir (Lake Soyang, Korea). *Lake and Reservoir Management* **22**(3): 213–222.

Lou J, Schwab DJ. 2000. A model of sediment resuspension and transport dynamics in southern Lake Michigan. *Journal of Geophysical Research* **105**(C3): 6591–6610.

MacIntyre S, Flynn KM, Jellison R, Romero JR. 1999. Boundary mixing and nutrient fluxes in Mono Lake, California. *Limnology and Oceanography* **44**(3): 512–529.

Martin JL, McCutcheon SC. 1999. Hydrodynamics and Transport for Water Quality Modeling. Lewis Publishers: Boca Raton, Fla.

Matonse AH, Pierson DC, Frei A, Zion MS, Schneiserman EM, Anandhi A, Mukundan R, Pradhanang SM. 2011. Effects of changes in snow pattern and the timing of run off on NYC water supply system. *Hydrological Processes* **25**: 3278–3288. DOI: 10.1002/hyp.8121.

Matonse AH, Pierson DC, Frei A, Zion MS, Anandhi A, Schneiserman EM, Wright B. 2012. Investigating the impact of climate change on New York City's primary water supply. *Climatic Change* DOI: 10.1007/s10584-012-0515-4.

Milly PCD, Betancourt J, Falkenmark M, Hirsch RM, Kundzewicz ZW, Lettenmaier DP, Stouffer RJ. 2008. Stationarity is dead: whither water management? *Science* **319**(5863): 573–574.

Mukundan R, Pierson DC, Wang L, Matonse AH, Samal NR, Zion MS, Schneiderman EM. 2012a. Effect of projected changes in winter streamflow on stream turbidity, Esopus Creek watershed in New York, USA. *Hydrological Processes* DOI: 10.1002/hyp.9824.

Mukundan R, Pradhanang SM, Schneiderman EM, Pierson DC, Anandhi A, Zion MS, Matonse AH, Lounsbury DG, Steenhuis TS. 2012b. Suspended sediment source areas and future climate impact on soil erosion and sediment yield in a New York City water supply watershed, USA. Geomorphology. http://dx.doi.org/10.1016/j.geomorph.2012.06.021.

NYCDEP. 2006. New York City water supply system reference guide, NYCDEP Bureau of Water Supply, Valhalla, New York.

NYCDEP. 2007. CAT-211 Catskill turbidity control study - Phase III final report, NYCDEP Bureau of Water Supply, Valhalla, New York.

Peng F, Johnson DL, Effler SW. 2002. Suspensoids in New York City's drinking water reservoirs: turbidity apportionment. *Journal of the American Water Resources Association* **38**: 1453–1465.

Peng F, Johnson DL, Effler SW. 2004. Characterization of inorganic particles in selected reservoirs and tributaries of the New York City water supply. *Journal of the American Water Resources Association* **40**: 663–676.

Prestigiacomo AR, Effler SW, O'Donnell DM, Smith DG, Pierson DC. 2008. Turbidity and temperature patterns in a reservoir and its primary tributary from robotic monitoring: implications for managing the quality of withdrawals. *Lake and Reservoir Management* **24**: 231–243.

Reicosky DC, Winkelman LJ, Baker JM, Baker DG. 1989. Accuracy of hourly air temperatures calculated from daily minima and maxima. *Agricultural and Forest Meteorology* **46**: 193–209.

Samal NR, Mazumdar A, Joehnk KD, Peeters F. 2009. Assessment of ecosystem health of tropical shallow waterbodies in eastern India using turbulence model. *Journal Aquatic Ecosystem Health Management Society* **12**(2): 215–225.

Samal NR, Pierson DC, Huang Y, Read J, Anandhi A, Owens EM. 2012. Impact of climate change on Cannonsville reservoir thermal structure in the New York City Water Supply. *Water Quality Research Journal, Canada* **47**(3–4): 389–405.

Schneiderman EM, Pierson DC, Lounsbury DG, Zion MS. 2002. Modeling the hydrochemistry of the Cannonsville watershed with generalized watershed loading functions (GWLF). *Journal of the American Water Resources Association* **38**(5): 1323–1347.

Schneiderman EM, Steenhuis TS, Thongs DJ, Easton ZM, Zion MS, Neal AL, Mendoza GF, Walter MT. 2007. Incorporating variable source area hydrology into the curve number based Generalized Watershed Loading Function model. *Hydrological Processes* **21**: 3420–3430.

Wake CP, Frumhoff P, McCarthy J, Melillo J, Moser S, Wuebbles D (Eds). 2008. Special issue: assessment of climate change, impacts, and solutions in the Northeast United States. *Mitigation and Adaptation Strategies for Global Change* **13**(5–6): 419–660.

Weilenmann U, O'Melia CR, Stumm W. 1989. Particle transport in lakes: models and measurements. *Limnology and Oceanography* **34**(1): 1–18.

Zion MS, Pradhanang SM, Pierson DC, Aavudai A, Lounsbury DG, Matonse A, Schneiderman E. 2011. Investigation and modeling of winter streamflow timing and magnitude under changing climate conditions for the Catskill Mountain region, New York, USA. *Hydrological Processes* **25**: 3289–3301.

HYDROLOGICAL PROCESSES
Hydrol. Process. (2013)
Published online in Wiley Online Library
(wileyonlinelibrary.com) DOI: 10.1002/hyp.9868

Comparison of approaches for snowpack estimation in New York City watersheds

Elliot M. Schneiderman,[1]* Adao H. Matonse,[2] Mark S. Zion,[1] David G. Lounsbury,[1] Rajith Mukundan,[2] Soni M. Pradhanang[2] and Donald C. Pierson[1]

[1] *Bureau of Water Supply, New York City Environmental Protection, Kingston, NY, USA*
[2] *Institute for Sustainable Cities, Hunter College, City University of New York, New York City, NY, USA*

Abstract:

Snow is a substantial component of historical annual precipitation in New York City (NYC) water supply watersheds in the Catskill Mountains, and the pattern of snow accumulation and snowmelt has important implications for the management of the reservoirs and watersheds that are part of the NYC water supply. NYC currently estimates reservoir basin-scale snowpack throughout the snow season by extrapolation from biweekly snow survey data. These estimates are complemented by the NOAA Snow Data Assimilation System (SNODAS) product. Snowpack models are used in short-term projections to support reservoir operations and long-term simulations to evaluate the potential effects of climate change, land use change, and watershed management on the water supply. We tested three snowpack estimation approaches compared with snow survey data: the lumped-parameter temperature index approach from the Generalized Watershed Loading Function (GWLF) watershed model, a spatially distributed temperature index (SDTI) model, and the spatially distributed NOAA SNODAS product. Of the spatially distributed approaches, SNODAS estimated the spatial variability of snow water equivalent (SWE) among snow survey sites within a basin better than the SDTI model. All three snowpack estimation approaches, including the lumped-parameter GWLF model, performed well in estimating basin-wide SWE for most of the basins studied. Copyright © 2013 John Wiley & Sons, Ltd.

KEY WORDS snowpack; snow modelling; SNODAS; GWLF; Catskill Mountains

Received 27 August 2012; Accepted 22 April 2013

INTRODUCTION

Snow is a substantial component of annual precipitation in New York City (NYC) water supply watersheds in the Catskill Mountains, and snowmelt historically contributes between 24% and 30% of total annual runoff in this region (Frei *et al*., 2002). The pattern of snow accumulation and snowmelt has important implications for the management of water resources (Lundquist *et al*., 2005; Vicuna and Dracup, 2007; Matonse *et al*., 2011). NYC currently estimates snowpack for the six major reservoirs in the Catskill and Delaware systems of the NYC water supply from biweekly snow survey data (Figure 1). These data are complemented by the NOAA National Operational Hydrologic Remote Sensing Center (NOHRSC) Snow Data Assimilation System (SNODAS), which combines the NYC snow survey data with observer station and remote sensing data and with simulation modelling to produce 1-km gridded near-real-time and historical sub-daily snow, snowpack, and snowmelt estimates. Basin-scale near-real-time snowpack estimates are used to optimize reservoir storage for spring melt (Matonse *et al*., 2011).

The potential effects of climate change on snowpack and the subsequent effect on water supply quantity and quality are actively being investigated for NYC and elsewhere (New York City Department of Environmental Protection (NYCDEP), 2008; Stewart, 2009; Matonse *et al*., 2011; Zion *et al*., 2011; Matonse *et al*., 2012). An increasing trend in air temperature has been observed for the Catskill region (Burns *et al*., 2007), and simulated climatology and hydrology for the region have suggested a measurable impact on snowpack and streamflow in the NYC watersheds (Matonse *et al*., 2011; Pradhanang *et al*., 2011; Zion *et al*., 2011). An observed shift in the timing of snowmelt-driven runoff associated with warmer winters, lower snowpacks, and shift from snowfall to rain events in winter/spring is expected to intensify under climate change (Matonse *et al*., 2011; Pradhanang *et al*., 2013).

Simulation models are used to predict snowpack and snowmelt at both basin and finer scales for potential future conditions of climate and land use. Basin-scale snowpack projections provide guidance for future operational

*Correspondence to: Elliot M. Schneiderman, Bureau of Water Supply, NYC Department of Environmental Protection, 71 Smith Ave, Kingston, NY 12401, USA.
E-mail: eschneiderman@dep.nyc.gov

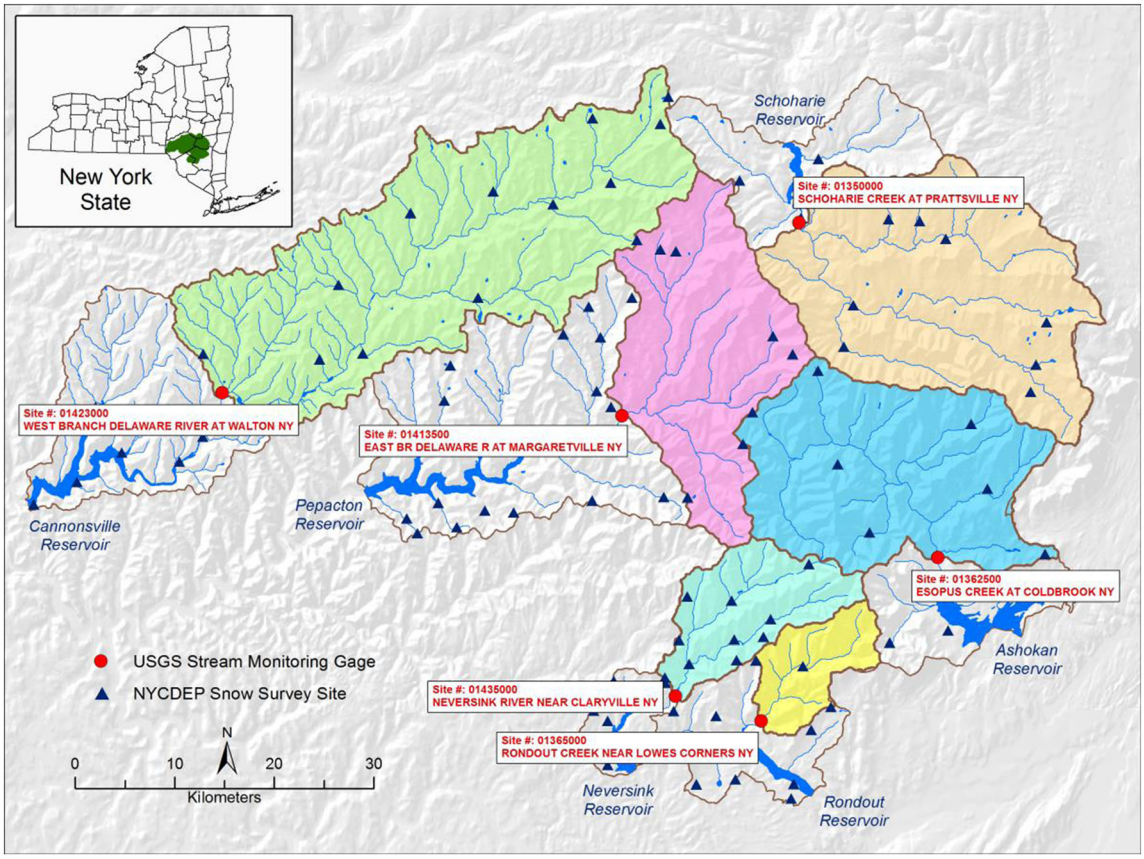

Figure 1. Snow survey sites and major gauged reservoir watersheds in NYC West of Hudson water supply

strategies for optimizing reservoir storage. On a finer scale, the spatial distribution of snowmelt within a basin has important consequences for water quality through its role in diluting and transporting pollutants (Johannessen and Henriksen, 1978; Watson and Putz, 2012). Snowpack estimates are used in long-term hydrologic model simulations to evaluate the potential effects of changing land use and climate on water quantity and quality (Johannessen and Henriksen, 1978; Stottlemyer and Toczydlowski, 1999; Suzuki, 2003; Matonse *et al.*, 2011; Pradhanang *et al.*, 2011; Pierson *et al.*, 2013; Samal *et al.*, 2013).

Snowpack models vary in complexity and resolution. The simplest is the daily lumped-parameter temperature index approach, where the snowpack for a basin is a single storage of snow water equivalent (SWE) to which precipitation as snowfall is added and from which water as snowmelt is removed daily. A melt parameter that linearly relates snowmelt to air temperature is empirically determined (Fontaine *et al.*, 2002). This approach has minimal data requirements and has been incorporated into watershed water quality simulation models like the Generalized Watershed Loading Function (GWLF) (Haith *et al.*, 1992; Schneiderman *et al.*, 2002; Schneiderman *et al.*, 2007) and the soil water assessment tool (SWAT) (Arnold and Allen, 1996; Neitsch *et al.*, 2005; Arnold *et al.*, 2007). More complex snow models explicitly simulate an energy balance of snowpack and upper soil layers, at sub-daily time steps, and as a spatially distributed process such as in the regional hydro-ecologic simulation system (RHESSys) model (Band *et al.*, 2002; Tague and Band, 2004). With the added complexity come increasing data requirements, and depending on the objectives of the model application, sometimes, the end results may not justify the additional effort (Watson and Putz, 2012).

We tested three approaches for estimating snowpack SWE by comparing SWE estimates to measured snow survey data for six major NYC reservoir watersheds. The three approaches are the spatially distributed NOAA SNODAS product and two snowpack simulation models – the temperature index model from the lumped GWLF watershed model (Haith *et al.*, 1992) and a spatially distributed temperature index (SDTI) model. The SDTI model was evaluated both in terms of its ability to simulate basin-average SWE and the spatial variability of SWE within a basin.

STUDY SITE

For this study, we used six watersheds that are major tributaries to water supply reservoirs for New York City within the Catskill Mountain region of New York State (Figure 1). These mountainous watersheds range in size from 100 to 859 km^2 and span an elevation range of 188–1276 m (Table I). The watersheds are mostly forested with some agricultural land use (corn, hay, and pasture lands) within the Cannonsville watershed and, to a lesser extent, also within the Schoharie and Pepacton basins. A number of small hamlets are also scattered throughout the area. Except for a slight decline in agricultural activity in Cannonsville, there has been little change in land development over the past decade.

DATA AND METHODS

Meteorological data

Gridded 4-km-resolution daily precipitation and air temperature data were obtained from the Northeast Regional Climate Center (NRCC) at Cornell University, Ithaca, NY. The product is available in near-real-time for the entire Northeast USA starting in 2005 (http://compag.tc.cornell.edu/sciencegateway/). The precipitation data were developed using radar-guided interpolation in which radar-based precipitation is adjusted on a daily time step using unadjusted rain-gauge observations to reduce spatially varying errors in the radar estimates (DeGaetano and Wilks, 2009). Radar-based interpolation helps reduce estimation uncertainty by reducing interpolation errors independently from season or precipitation magnitude. Spatially distributed air temperatures are estimated at grid points by interpolation from observation stations and application of an environmental lapse rate that adjusts for elevation effects on temperature. The precipitation data obtained in a polar coordinate system were re-gridded to match the air temperature 4-km grid by nearest-neighbour analysis, and the final grid was clipped to produce a consistent spatial distribution of 324 4-km grid cells that covered the area of the entire NYC west of the Hudson watershed area.

Snow survey data

The NYC Department of Environmental Protection (DEP) snow survey at 76 established sites (Figure 1) has been conducted biweekly since 2005. Snow cores are taken at each site and measured for SWE, starting around 1 January and continuing through April. 67 sites with contiguous records from 2005 to 2011 were used in this study. The sample sites are located throughout the west of Hudson watersheds at varying elevations from 257 to 826 m above sea level. For the purpose of analysing model performance in simulating snow survey site to site variability, the snow survey sites were characterized by elevation band (low: 250–450 m, medium: 451–650 m, and high: 651–850 m), land use [forest (evergreen, deciduous, and mixed); agriculture (row crop, pasture, and hay], commercial (high intensity commercial/industrial), and aspect (eight compass directions).

SNODAS product

Gridded SNODAS SWE and snowmelt estimates were downloaded from the NOHRSC web site (www.nohrsc.noaa.gov). SNODAS is a snow data assimilation system developed by the NOAA National Weather Service's (NWS) NOHRSC to provide users with the best possible estimates of snow cover and associated parameters (NOHRSC, 2010). SNODAS aims to achieve a physically consistent framework that integrates measured snow data from satellite, airborne platforms, and ground stations with model-simulated estimates of snow cover from the numerical weather prediction (NWP) model for the conterminous U.S. (CONUS) (Carroll *et al.*, 2001; Carroll, 2005).

Temperature index snowpack models

The lumped-parameter temperature index snowpack algorithm in the GWLF model (Haith *et al.*, 1992;

Table I. List of study watershed characteristics

Reservoir watershed name	USGS gauge no.	Watershed description	Watershed area (km^2)	Mean elevation (m)	Min. elevation (m)	Max. elevation (m)
Ashokan	01362500	Esopus Creek at Coldbrook	493.2	600	188	1276
Cannonsville	01423000	West Branch Delaware River at Walton	859.3	592	360	1020
Neversink	01435000	Neversink River near Claryville	172.5	770	463	1275
Pepacton	01413500	East Branch Delaware River at Margaretville	421.7	668	396	1181
Rondout	01365000	Rondout Creek near Lowes Corners	99.5	629	263	1175
Schoharie	01350000	Schoharie Creek at Prattsville	612.5	653	344	1234

Schneiderman *et al.*, 2007) is as follows. Daily precipitation is snowfall that is added to the snowpack if mean daily air temperature (T) $\leq 0\,^{\circ}$C; otherwise, it is rain. Daily snowmelt occurs when T exceeds $0\,^{\circ}$C at the rate of the product of the melt coefficient and air temperature (cm·day^{-1}) but does not exceed the available water in the Snowpack. The Snowpack is a storage term that is updated daily by snowfall additions and snowmelt withdrawals.

$$\text{Snowfall}(t) = P(t) \text{ if } T(t) \leq 0\ ^{\circ}\text{C, else } 0 \quad (1)$$

$$\text{Rain}(t) = P(t) \text{ if } T(t) > 0\ ^{\circ}\text{C, else } 0 \quad (2)$$

$$\text{Snowpack}(t) = \text{Snowpack}(t-1) + \text{Snowfall}(t) - \text{Snowmelt}(t) \quad (3)$$

$$\text{Snowmelt}(t) = \text{Melt Coeff} * T(t) \text{ if } T(t) > 0\ ^{\circ}\text{C},$$

$$\text{If Snowmelt } (t) > \text{Snowpack } (t-1) \text{ then}$$
$$\text{Snowmelt } (t) = \text{Snowpack } (t-1),$$
$$\text{If } T(t) < 0 \text{ then Snowmelt } (t) = 0 \quad (4)$$

where (t) denotes current time step (day) and ($t-1$) denotes the previous day. Note that rain does not explicitly interact with the snowpack in the temperature index model.

An SDTI model based on the GWLF algorithm was developed and applied by first dividing up the watershed into 4-km grid cells that correspond to the grid of available spatially distributed meteorological (precipitation and air temperature) data from the NRCC. Each 4-km grid cell is further sub-divided by elevation band. Air temperature for each grid cell/elevation band is calculated from the grid cell air temperature modified by the product of a lapse rate and elevation difference between the grid cell centroid and the mean elevation of the elevation band. The model calculates air temperature, snowfall vs. rain, snowpack, and snowmelt for each grid cell/elevation band in the watershed, using Equations (1)–(4). A single calibration melt coefficient is used for all grid cell/elevation band zones.

Model calibration and testing

Model calibration compared simulated basin-average SWE to basin-average estimates from snow survey measurements for each of the major reservoir watersheds of the NYC West of Hudson water supply. The 6-year period of available snow survey data was split into a 3-year calibration period (2005–2008) and 3-year validation period (2008–2011). The two temperature index models were calibrated by adjusting the melt coefficient to maximize the Nash–Sutcliffe coefficient (NS) of model efficiency (Nash and Sutcliffe, 1970) for observed (snow survey) SWE vs. modelled SWE for the calibration period. The NS model efficiency and differences in mean basin SWE were used to evaluate model fit during the calibration and validation periods.

The ability of the SDTI model to simulate spatial variations in SWE was evaluated by comparison of the SDTI simulated spatial distribution of SWE to that estimated by SNODAS and by also comparing simulated estimates of SWE to SWE measurements at snow survey locations across the West of Hudson watershed area; and by comparison of the SDTI simulated distributions of SWE within selected reservoir watershed basins with similar distributions derived from the SNODAS data.

RESULTS

Daily basin-averaged SWE

The basin averages of DEP snow survey data from 2006 to 2011 are compared with the results of the lumped-parameter GWLF-VSA watershed model, the SDTI model, and the SNODAS product. For each date with available data, all of the snow survey measurements of SWE within each watershed were averaged to obtain a basin-average SWE value.

In order to produce model-simulated or SNODAS-estimated values of SWE corresponding in time to the snow survey dates, the SWE values simulated by SDTI and estimated by SNODAS were averaged over each watershed. GWLF being a lumped model produced a single SWE value for each date. The scatter plots of the daily results of the three snowpack estimation approaches versus the basin-averaged snow survey SWE are shown in Figure 2; the NS efficiency and mean values for each basin and model are shown in Figure 3. Overall, the scatter plots show that all three approaches reasonably capture the temporal variability found in the average snow survey data, despite the difference in performance at individual watersheds (Figure 2). The NS efficiency coefficients for the lumped GWLF model appears to perform similarly to SDTI for most watersheds except in the Schoharie watershed, where the NS efficiency for the GWLF model during the validation period is quite weak (0.05). Much of this low value is due to an individual point at Schoharie in March of 2010, when the survey recorded 15.3 cm of SWE and the model has melted the snowpack completely. The NS efficiency for the SNODAS data is also fairly consistent across each of the basins, except for Schoharie and Neversink, where the SNODAS tends to result in lower NS values.

Looking at the mean results for the full period (Figure 3), the average basin SWE derived from the SNODAS product tends to be approximately 15% greater than both the snow survey average and the average from

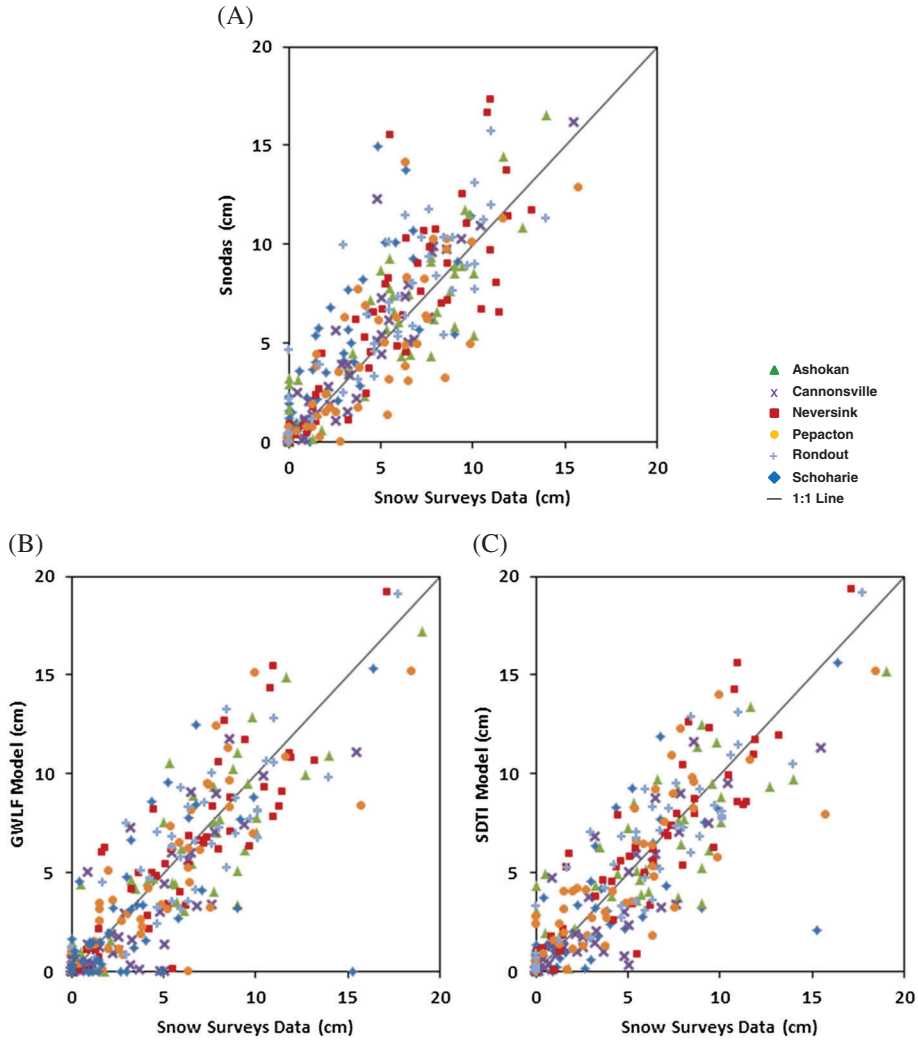

Figure 2. Scatter plots of daily average SWE as estimated by (A) SNODAS, (B) the GWLF model, and (C) the SDTI model versus daily average SWE as measured at DEP snow survey sites

the GWLF and SDTI models. This higher estimation is also evident in the scatter plot (Figure 2A). This result is not surprising; since the models were calibrated to the snow survey data, it makes some sense that the model average estimate would better match the snow survey data. However, it is important to note that given the spatial variability of snowpack within each watershed, it is not clear how adequately the survey sites represent this variability, so it is possible that the simple arithmetic average of the survey site measurements might be biased versus the 'true' basin-average SWE. Clow *et al.* (2012) compared SNODAS estimates with ground-based observations in the Colorado Rocky Mountains and found that SNODAS showed a poor performance in alpine areas, but the applicability of this finding to NYC watersheds is uncertain. For our study region, the differences in SNODAS and snow survey average could be due to a low bias in the survey average due to a limited areal coverage and higher snowpack in other parts of the watershed.

A closer inspection of example winter time series of model, SNODAS, and survey results illustrates some other issues with each of the SWE estimations. Figure 4 shows the winter time series of average basin SWE for the Schoharie and Neversink watersheds for the winters of 2008–2009 and 2009–2010. It is important to notice that the Schoharie and Neversink watersheds have different characteristics; Schoharie has an area that is more than three times larger than Neversink's (Table I), while Neversink's minimum and average elevations are approximately 100 m higher than Schoharie's. These characteristics will result in different topographic gradients across these two watersheds. As noted previously, the high estimate of the SNODAS product as compared to

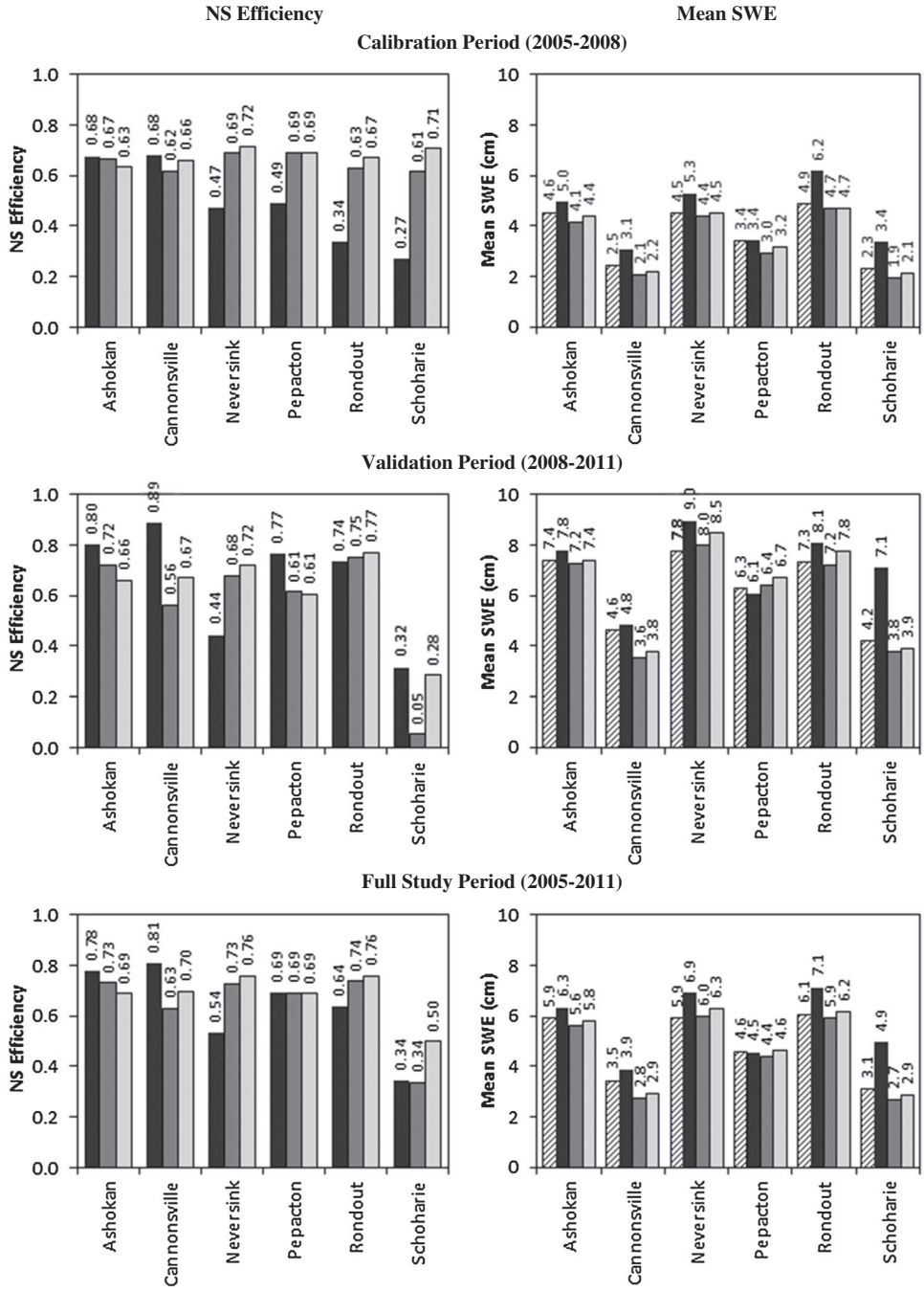

Figure 3. NS efficiency and mean values for each basin for SNODAS product (black), GWLF model (medium grey), and SDTI model (light grey) compared to DEP snow survey basin-average values (striped)

the survey data is quite apparent for the Schoharie watershed for these winters, in particular during snow accumulation events in winter 2009–2010. However, for these winters in Neversink, the SNODAS product tracks well with the average survey data. The discrepancies in SWE estimation for these basins and time periods could be due to SNODAS error or to biases in basin-wide SWE estimation due to a limited number of snow survey sites.

In each of these cases illustrated in Figure 4, the two models, GWLF and SDTI, seem to track closely. This makes sense, as the models use similar temperature index algorithms and the input meteorological forcings are based on the same underlying data. The only difference between these two models is the spatial resolution of the snowpack algorithm. This difference results in GWLF melting faster than SDTI, which is most apparent at the

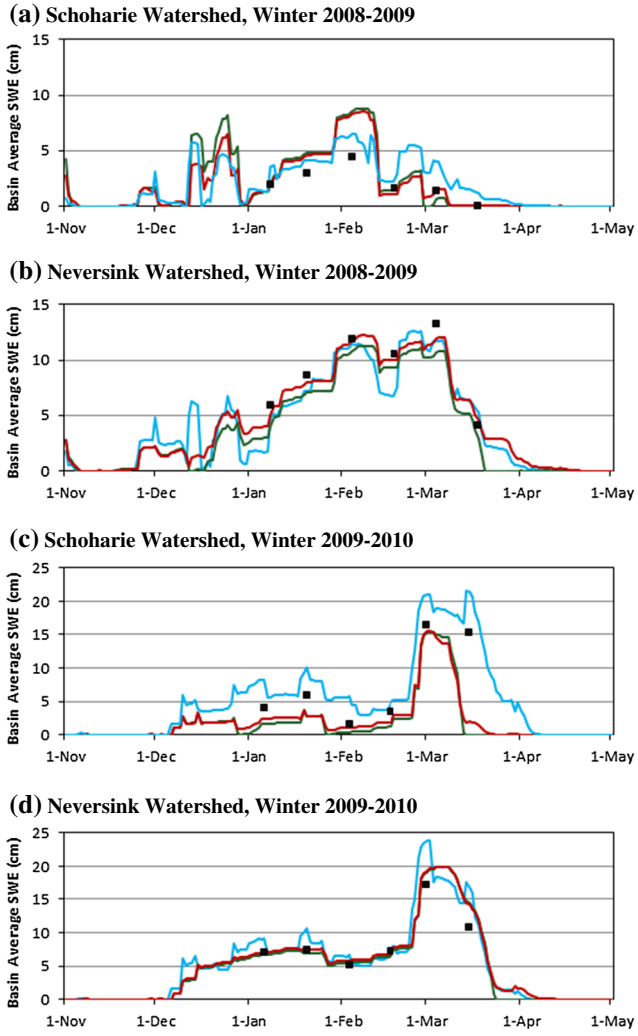

Figure 4. Example time series of basin-average SWE with average of DEP snow survey measurements (black squares), SNODAS product (light blue), GWLF model results (green), and SDTI model results (red) for Schoharie and Neversink watershed for winters of 2008–2009 and 2009–2010

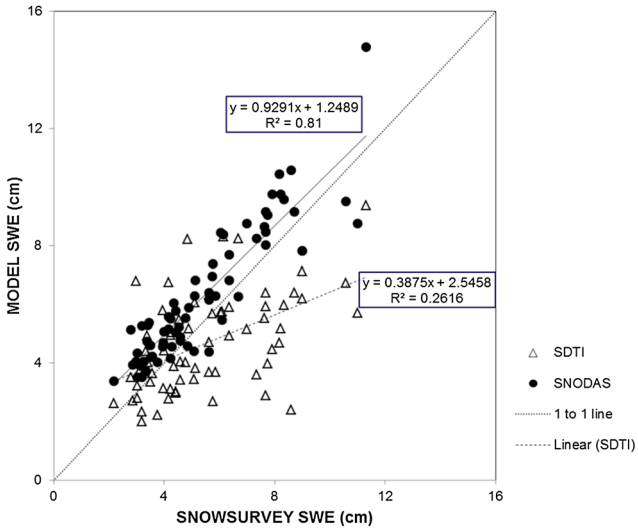

Figure 5. Scatter plot of model versus snow survey SWE in centimetres

end of the season, when the SDTI model tends to continue to show SWE values for a few extra weeks in the spring. This is due to the SDTI model having areas of snowpack at higher elevations that take longer to melt, while the lumped GWLF model, with its average snowpack and average temperature forcings, does not explicitly account for the colder portion of the watershed. This simulated spatial variation in snow distribution during melt is consistent with observations made in the watersheds. In the Neversink examples, it is interesting to note that the timings of the spring melt for the SDTI model and the SNODAS match quite well, suggesting that the spatially distributed component of the SDTI model is helpful in accounting for this elevation-related process.

Unlike SNODAS, the GWLF- and SDTI-simulated snowpack is not updated or nudged to be consistent with the measured snow survey data as they become available. Therefore, differences between model-simulated and measured SWE can persist for long periods into the winter. For example, in the Neversink watershed (winter 2008–2009), the GWLF model estimated about 1.5 cm less SWE than the survey data indicated by mid-January 2009. This difference then persisted and remained about the same through late March. Although the number of events analysed is limited, the results from Figure 4 show the difficulty in comparing snow survey (point) data with model (gridded) aggregates. The differences between the two appear to be basin specific as survey point density and locations, and other topographic and physiographic characteristics vary from one basin to another. In general, SNODAS appears to be more sensitive to small snow events during the accumulation period, as shown during the 2009–2010 winter events.

Spatially distributed SWE

The SDTI model and SNODAS produce estimates of SWE on a gridded format across the six watersheds. GWLF is a lumped model that simulates basin-average SWE and is thus not included in analyses of spatially distributed SWE. Figure 5 compares the SWE values for each snow survey site versus the SWE values for the SDTI or SNODAS grid locations corresponding to the survey point locations. Each dot in the scatter plot represents the average for all snow survey measurements taken from 2008 to 2011 at an individual survey point versus the average of the same survey days for the appropriate SDTI and SNODAS grid location. In general, the SNODAS results appear to systematically overestimate SWE but with a slope closer to the 1 : 1 line and show a similarly small spread at all ranges of SWE. The SDTI performance seems to be dependent on SWE magnitude; for lower SWE (below around 7 cm),

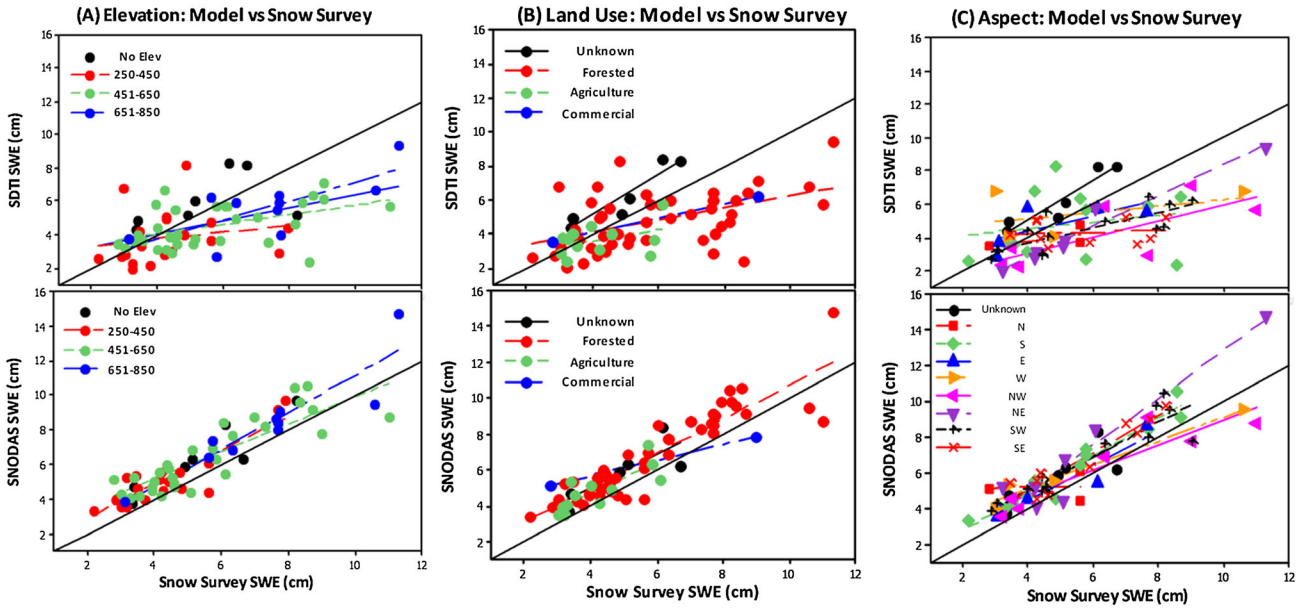

Figure 6. Scatter plots of model versus snow survey SWE in centimetres. The plots illustrate the model performance as a function of (A) elevation, (B) land use, and (C) aspect. The upper row shows the SDTI results; the bottom row shows the SNODAS results. The black diagonals represent a 1 : 1 line

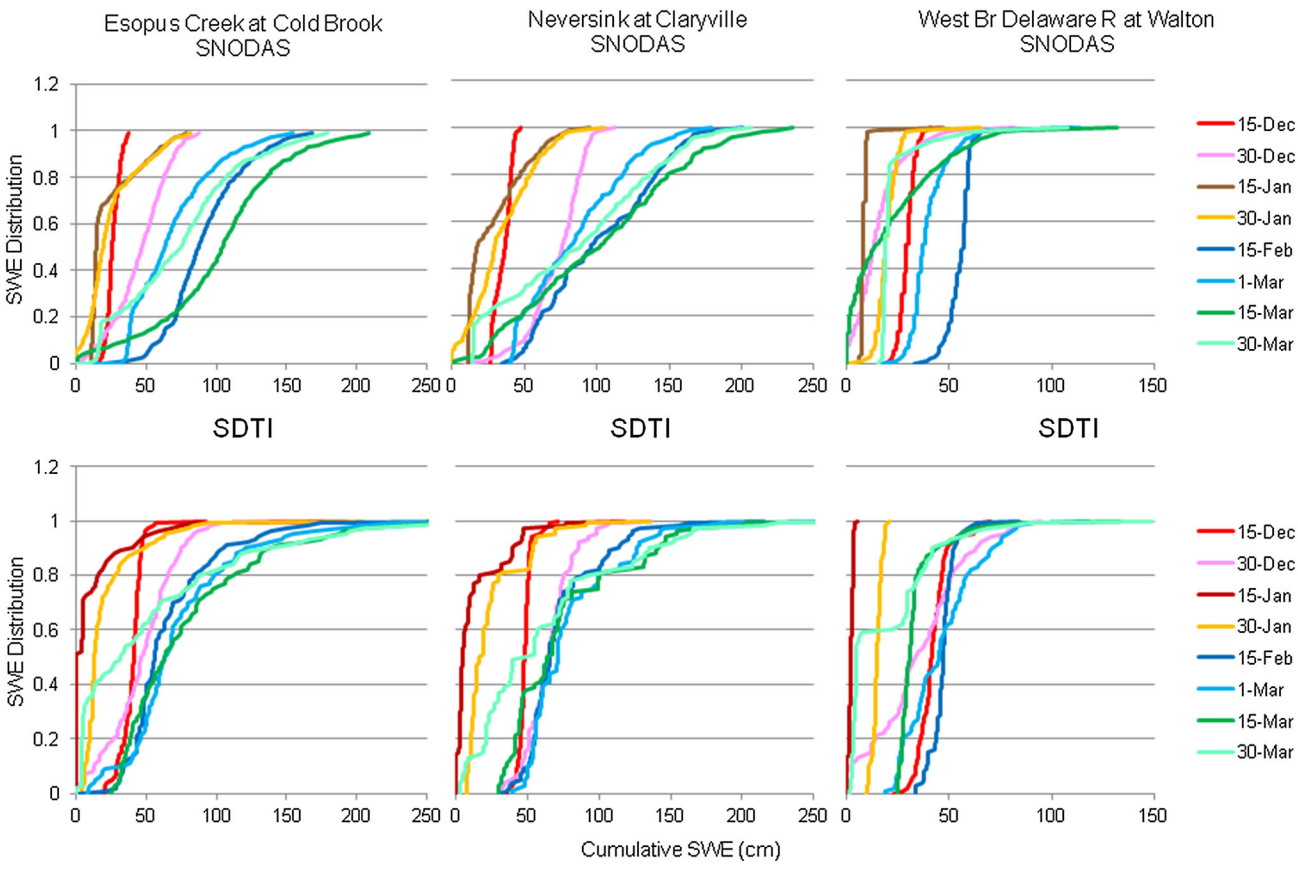

Figure 7. Comparison of SDTI and SNODAS SWE distributions for selected days during the winter of 2007–2008

SDTI simulations are around the 1 : 1 line, while this model systematically underpredicts SWE for the survey sites with greater snowpack. In addition, the SDTI results show a much greater range of variability between simulated and measured SWE. Figure 5 illustrates that SNODAS estimates site-to-site variability in SWE quite well, while SDTI model simulation does not demonstrate this capability, especially at locations with higher SWE.

The scatter plots in Figure 6 present the same data points as in Figure 5, except that the SDTI and SNODAS data are plotted separately, and we highlight points in differing land use, elevation, and aspect classes. With respect to elevation, SNODAS appears to slightly and systematically overestimate SWE at all elevation ranges (bottom part of Figure 6A), whereas the SDTI-simulated SWE values both over- and underestimate the measured SWE, following a pattern that is generally independent of elevation (upper part of Figure 6A). A combination of factors, including faster simulation of melt processes (e.g. mid-March 2010; Figure 4c), and underestimation of small snow events during accumulation (Figures 4c and 4d) may be responsible for the varied SDTI results. Similarly, Figure 6B reveals that, irrespective of land use, SNODAS tends to overestimate SWE while SDTI underestimates SWE. With regard to aspect (Figure 6C), there are differences between the two approaches: SDTI shows no pattern for S, E, SE, and SW facing sites (although with SWE of most locations below the 1 : 1 line, except for S facing sites, where values are more evenly distributed above and below the 1 : 1 line) while SNODAS systematically overestimates SWE on these sites. SDTI underestimates NE while SNODAS overestimates NE. SDTI underestimates NW while SNODAS shows no pattern. Both approaches show no pattern for N and W facing sites. In total, these figures indicate that SDTI performance depends on SWE magnitude rather than elevation, aspect, or land use.

In Figure 7, we compare empirical cumulative distributions of SWE calculated using the gridded SNODAS and SDTI SWE values from three watersheds. The distributions are estimated between the onset and loss of snow cover at 15-day intervals during the 2007–2008 winter periods. The two approaches result in similar watershed-wide frequency distributions of SWE. SNODAS appears to add more SWE during accumulation events than SDTI. Changes in the frequency distributions are basin dependent where the difference in pattern among basins can originate from different basin location, topography and timing of snowfall, as well as other basin characteristics.

SUMMARY AND CONCLUSIONS

In this study, we compared three different snowpack estimation approaches – the NOAA SNODAS product, a lumped-parameter basin-scale temperature index model (GWLF), and an SDTI model – against measured snow survey data. The approaches were tested based on the estimation of basin-scale average snowpack SWE, the spatial distribution of SWE within each watershed, and SWE measured at point locations within a basin. The SNODAS product is fundamentally different from the lumped and distributed temperature index–based models, in that SNODAS combines simulation model results with both remotely sensed and observer station snowpack data to produce historical and near-real-time estimates of the snowpack and other snow variables (Houser *et al*., 1998; Mandapaka and Germann, 2010; Clow *et al*., 2012). In the data assimilation approach, the model effectively extends the data beyond the spatial location(s) of data sampling points while the data is used to nudge fit the model results (Simanton and Osborn, 1980; Paniconi *et al*., 2003). It is challenging for even SNODAS to estimate the spatial distribution of SWE particularly in areas with high spatial variability of SWE. Nevertheless, this approach should provide the best available SWE estimates, based on both data and modelling. The disadvantage of SNODAS is that it is by nature retrospective and not useful for forecasting and simulating future scenarios. Thus, there is a need to develop models driven only by commonly available meteorological data. In this paper, we examined two temperature index models that meet this need and are being used by DEP for long-term historical simulations and future climate simulations where measured snow cover data are not available.

All three snowpack estimation approaches performed well in estimating basin-wide SWE for most of the basins studied. Comparison of estimated SWE vs. snow survey data (Figure 3) showed better NS fit by SNODAS for some but not all basins. SNODAS tended to estimate a higher basin SWE when compared to average measured SWE in five of the six basins, and both temperature index models yielded similar basin-average estimates. It must be noted that the basin-average SWE estimated from snow survey measurements assumes that the snow survey provide an unbiased representation of the entire basin area, which is an unverified assumption. Results were somewhat equivocal regarding a 'best approach' for basin-scale estimation. Basin-scale SWE is important for estimating basin-outlet streamflow. Several widely used continuous simulation watershed models utilize a temperature index approach for snowpack modelling. Our results suggest that for NYC reservoir watersheds, the simplest lumped GWLF basin-scale temperature index approach with the least data requirements may be sufficient for the purpose of estimating basin-average SWE.

In estimating the spatial distribution of SWE in the NYC watersheds, the SNODAS product performed well and clearly showed better agreement with snow survey

data than the SDTI approach (Figure 5). The performance of SNODAS may reflect the retrospective assimilation of SWE data from the Catskill Mountain region in the gridded SWE estimates and/or better performance of the process-based simulation model component of SNODAS relative to the temperature index approach. We did not find that the systematic errors in the SDTI model results were related to aspect or vegetative cover (Figure 6), suggesting that incorporation of these variables into the SDTI model would probably not improve its performance. An area of future study could incorporate more process-based snowpack models for improved simulation of site-specific SWE (Fuka *et al*., 2012).

Overall, our initial results from an ongoing investigation of use of lumped and SDTI snowpack estimation approaches illustrate that for basin-wide SWE estimation, both the lumped and spatially distributed approaches yield reasonable results, with the main differences in results occurring late in the snow season, when there is potentially more spatial variability in SWE due to higher elevation snow persisting longer into the spring. The SDTI model did not simulate site-to-site variability in SWE effectively, and therefore, an improvement in model structure is warranted.

REFERENCES

Arnold J, Allen P. 1996. Estimating hydrologic budgets for three Illinois watersheds. *Journal of Hydrology* **176**: 57–77.

Arnold JG, Srinivasan R, Muttiah RS, Williams J. 2007. Large area hydrologic modeling and assessment part I: Model development1. *JAWRA Journal of the American Water Resources Association* **34**: 73–89.

Band LE, Tague CL, Brun SE, Tenenbaum DE, Fernandes RA. 2002. Modelling watersheds as spatial object hierarchies: structure and dynamics. *Transactions in GIS* **4**: 181–196.

Burns DA, Klaus J, McHale MR. 2007. Recent climate trends and implications for water resources in the Catskill Mountain region, New York, USA. *Journal of Hydrology* **336**: 155–170. DOI: 10.1016/j.jhydrol.2006.12.019.

Carroll T. 2005. Overview of the Center's Web Site and Products. National Operational Hydrologic Remote Sensing Center, 15 pp.

Carroll T, Cline D, Fall G, Nilsson A, Li L, Rost A. 2001. NOHRSC operations and the simulation of snow cover properties for the coterminous US. In: Proceedings of the 69th Western Snow Conference, pp: 16–19.

Clow DW, Nanus L, Verdin KL, Schmidt J. 2012. Evaluation of SNODAS snow depth and snow water equivalent estimates for the Colorado Rocky Mountains, USA. *Hydrological Processes* **26**: 2583–2591.

DeGaetano AT, Wilks DS. 2009. Radar-guided interpolation of climatological precipitation data. *International Journal of Climatology* **29**: 185–196.

Fontaine T, Cruickshank T, Arnold J, Hotchkiss R. 2002. Development of a snowfall–snowmelt routine for mountainous terrain for the soil water assessment tool (SWAT). *Journal of Hydrology* **262**: 209–223.

Frei A, Armstrong RL, Clark MP, Serreze MC. 2002. Catskill Mountain Water Reseources Vulnerability, Hydroclimatology, and Climate-Change Sensitivity. *Annals of the Association of American Geographers* **92**(2): 203–224.

Fuka DR, Easton ZM, Brooks ES, Boll J, Steenhuis TS, Walter MT. 2012. A Simple Process-Based Snowmelt Routine to Model Spatially Distributed Snow Depth and Snowmelt in the SWAT Model1. *JAWRA Journal of the American Water Resources Association* **48**: 1151–1161.

Haith DA, Mandel R, Wu RS. 1992. Generalized Watershed Loading Functions Version 2.0 User's Manual. Cornell University, Ithaca, New York.

Houser PR, Shuttleworth WJ, Famiglietti JS, Gupta HV, Syed KH, Goodrich DC. 1998. Integration of soil moisture remote sensing and hydrologic modeling using data assimilation. *Water Resources Research* **34**: 3405–3420.

Johannessen M, Henriksen A. 1978. Chemistry of snow meltwater: changes in concentration during melting. *Water Resources Research* **14**: 615–619.

Lundquist JD, Dettinger MD, Cayan DR. 2005. Snow-fed streamflow timing at different basin scales: Case study of the Tuolumne River above Hetch Hetchy, Yosemite. *California. Water Resources Research* **41**: W07005.

Mandapaka P, Germann U. 2010. Radar-rainfall error models and ensemble generators. *Geophysical Monograph Series* **191**: 247–264.

Matonse AH, Pierson DC, Frei A, Zion MS, Schneiderman EM, Anandhi A, Mukundan R, Pradhanang SM. 2011. Effects of changes in snow pattern and the timing of runoff on NYC water supply system. *Hydrological Processes* **25**: 3278–3288.

Matonse AH, Pierson DC, Frei A, Zion MS, Anandhi A, Schneiderman E, Wright B. 2012. Investigating the impact of climate change on New York City's primary water supply. *Climatic Change* **116**: 437–456.

Nash J, Sutcliffe J. 1970. River flow forecasting through conceptual models part I—A discussion of principles. *Journal of Hydrology* **10**: 282–290.

National Operational Hydrologic Remote Sensing Center (NOHRSC). 2010. Snow Data Assimilation System (SNODAS) Data Products at NSIDC. Boulder, Colorado USA: National Snow and Ice Data Center. Digital media.

Neitsch S, Arnold J, Kiniry J, Williams J, King K. 2005. Soil and water assessment tool theoretical documentation, version 2005. In: Texas, USA, Grassland, Soil and Water Research Laboratory, Agricultural Research Service. Available at: www.brc.tamus.edu/swat/doc.html. Accessed 1 February 2010.

New York City Department of Environmental Protection (NYCDEP). 2008. Climate change program: assessment and action plan. May 2008. Report 1. A report based on the ongoing work of the DEP climate change task force. http//www.nyc.gov/html/dep/pdf/climate/climate_complete.pdf. Accessed 21 August 2012.

Paniconi C, Marrocu M, Putti M, Verbunt M. 2003. Newtonian nudging for a Richards equation-based distributed hydrological model. *Advances in Water Resources* **26**: 161–178.

Pierson D, Samal N, Owens E, Schneiderman E, Zion M. 2013. Changes in the timing of snowmelt, and the seasonality of nutrient loading: Can models simulate the impacts on freshwater trophic status?. *Hydrological Processes* (submitted).

Pradhanang SM, Anandhi A, Mukundan R, Zion MS, Pierson DC, Schneiderman EM, Matonse A, Frei A. 2011. Application of SWAT model to assess snowpack development and streamflow in the Cannonsville watershed, New York, USA. *Hydrological Processes* **25**: 3268–3277. DOI: 10.1002/hyp.8171.

Pradhanang S, Mukundan R, Zion M, Scheiderman E, Anandhi A, Pierson D, Frei A, Easton Z, Fuka D, Steenhuis T. 2013. Streamflow responses to climate change: Analysis of hydrologic indicators in a New York City water supply watershed. *Journal of American Water Resource Association* (*in production*).

Samal N, Matonse A, Mukundan R, Pierson D, Gelda R, Zion M, Schneiderman E. 2013. Potential effects of climate change on winter turbidity loading in the Ashokan Reservoir, NY. *Hydrological Processes* (*submitted).*

Schneiderman EM, Pierson DC, Lounsbury DG, Zion MS. 2002. Modeling the hydrochemistry of the Cannonsville watershed with Generalized Watershed Loading Functions (GWLF). *JAWRA Journal of the American Water Resources Association* **38**: 1323–1347.

Schneiderman EM, Steenhuis TS, Thongs DJ, Easton ZM, Zion MS, Neal AL, Mendoza GF, Todd Walter M. 2007. Incorporating variable source area hydrology into a curve-number-based watershed model. *Hydrological Processes* **21**: 3420–3430. DOI: 10.1002/hyp.6556.

Simanton JR, Osborn HB. 1980. Reciprocal-distance estimate of point rainfall. *Journal of the Hydraulics Division* **106**: 1242–1246.

Stewart IT. 2009. Changes in snowpack and snowmelt runoff for key mountain regions. *Hydrological Processes* **23**: 78–94.

Stottlemyer R, Toczydlowski. 1999. Seasonal change in precipitation, snowpack, snowmelt, soil water and streamwater chemistry, northern Michigan. *Hydrological Processes* **13**: 2215–2231.

Suzuki K. 2003. Chemistry of stream water in a snowy temperate catchment. *Hydrological Processes* **17**: 2795–2810.

Tague C, Band L. 2004. RHESSys: regional hydro-ecologic simulation system-an object-oriented approach to spatially distributed modeling of carbon, water, and nutrient cycling. *Earth Interactions* **8**: 1–42.

Vicuna S, Dracup J. 2007. The evolution of climate change impact studies on hydrology and water resources in California. *Climatic Change* **82**: 327–350.

Watson BM, Putz G. 2012. Comparison of Temperature-Index Snowmelt Models for Use within an Operational Water Quality Model.

Zion MS, Pradhanang SM, Pierson DC, Anandhi A, Lounsbury DG, Matonse AH, Schneiderman EM. 2011. Investigation and Modeling of winter streamflow timing and magnitude under changing climate conditions for the Catskill Mountain region, New York, USA. *Hydrological Processes* **25**: 3289–3301.

A SATURATION EXCESS EROSION MODEL

S. A. Tilahun, R. Mukundan, B. A. Demisse, T. A. Engda, C. D. Guzman, B. C. Tarakegn, Z. M. Easton, A. S. Collick, A. D. Zegeye, E. M. Schneiderman, J.-Y. Parlange, T. S. Steenhuis

ABSTRACT. *Scaling-up sediment transport has been problematic because most sediment loss models (e.g., the Universal Soil Loss Equation) are developed using data from small plots where runoff is generated by infiltration excess. However, in most watersheds, runoff is produced by saturation excess processes. In this article, we improve an earlier saturation excess erosion model that was only tested on a limited basis, in which runoff and erosion originated from periodically saturated and severely degraded areas, and apply it to five watersheds over a wider geographical area. The erosion model is based on a semi-distributed hydrology model that calculates saturation excess runoff, interflow, and baseflow. In the development of the erosion model, a linear relationship between sediment concentration and velocity in surface runoff is assumed. Baseflow and interflow are sediment free. Initially during the rainy season in Ethiopia, when the fields are being plowed, the sediment concentration in the river is limited by the ability of the surface runoff to move sediment. Later in the season, the sediment concentration becomes limited by the availability of sediment. To show the general applicability of the Saturation Excess Erosion Model (SEEModel), the model was tested for watersheds located 10,000 km apart, in the U.S. and in Ethiopia. In the Ethiopian highlands, we simulated the 1.1 km^2 Anjeni watershed, the 4.8 km^2 Andit Tid watershed, the 4.0 km^2 Enkulal watershed, and the 174,000 km^2 Blue Nile basin. In the Catskill Mountains in New York State, the sediment concentrations were simulated in the 493 km^2 upper Esopus Creek watershed. Discharge and sediment concentration averaged over 1 to 10 days were well simulated over the range of scales with comparable parameter sets. The Nash-Sutcliffe efficiency (NSE) values for the validation runs for the stream discharge were between 0.77 and 0.92. Sediment concentrations had NSE values ranging from 0.56 to 0.86 using only four calibrated sediment parameters together with the subsurface and surface runoff discharges calculated by the hydrology model. The model results suggest that correctly predicting both surface runoff and subsurface flow is an important step in simulating sediment concentrations.*

Keywords. *Monsoon climates, Partial area hydrology, Sediment, USLE, Variable source areas.*

The success of soil and water conservation practices depends on the understanding of the processes involved in the generation and transport of sediment (Ciesiolka et al., 1995). Most of existing models use the Universal Soil Loss Equation (USLE) for predicting sediment loads, which assumes that rainfall intensity is one of the main driving forces causing erosion. Although this might be a reasonable assumption for areas with limited infiltration capacity and/or extremely high-intensity storms, it is not applicable for humid climates, where soils are well structured and rainfall intensities are usually less than the infiltration capacity of the soil (Bayabil et al., 2010; Engda et al., 2011). Models that are based on USLE also assume that steep slopes produce more sediment than gentle slopes, while in humid areas runoff is generated from saturated and degraded areas of the landscape, and the amount of runoff is a function of cumulative precipitation depth and available soil storage (Liu et al., 2008; Steenhuis et al., 2009; Tilahun et al., 2012). Because of such limitations, existing models do not predict the optimal locations within the landscape for erosion control.

The limitation of USLE urged modelers to come up with alternative hillslope erosion models that are less complex than physically based models but applicable to monsoon climates. One attempt is the work of Rose et al. (1983) and Hairsine and Rose (1992). The former defined a mathematical model of sediment transport from a sloping plain by

Submitted for review in March 2012 as manuscript number SW 9668; approved for publication by the Soil & Water Division of ASABE in January 2013. Presented at the 2011 Symposium on Erosion and Landscape Evolution (ISELE) as Paper No. 11061.

The authors are **Seifu Admassu Tilahun,** Assistant Professor, School of Civil and Water Resources Engineering, Bahir Dar University, Bahir Dar, Ethiopia; **Rajith Mukundan,** Research Associate, CUNY Institute for Sustainable Cities, Hunter College, City University of New York, New York; **Bezawit A. Demisse,** Graduate Student, and **Tegenu A. Engda,** Graduate Student, Cornell Master Program in Integrated Watershed Management and Water Supply, Bahir Dar, Ethiopia; **Christian D. Guzman, ASABE Member,** Research Assistant, Department of Biological and Environmental Engineering, Cornell University, Ithaca, New York, **Birara C. Tarakegn,** Graduate Student, Cornell Master Program in Integrated Watershed Management and Water Supply, Bahir Dar, Ethiopia; **Zachary M. Easton, ASABE Member,** Assistant Professor, Department of Biological Systems Engineering, Virginia Tech, Blacksburg, Virginia; **Amy S. Collick,** Scientist, USDA-ARS Pasture Systems and Watershed Management Research Unit, University Park, Pennsylvania; **Assefa D. Zegeye,** Research Assistant, Department of Biological and Environmental Engineering, Cornell University, Ithaca, New York (on leave from Adet Research Center, Amhara Regional State Agricultural Research Institute, Adet, Ethiopia); **Elliot M. Schneiderman,** Senior Research Scientist, New York City Department of Environmental Protection, Kingston, New York; **Jean-Yves Parlange,** Professor Emeritus, Department of Biological and Environmental Engineering, Cornell University, Ithaca, New York; and **Tammo S. Steenhuis,** Professor, Department of Biological and Environmental Engineering, Cornell University, Ithaca New York, and School of Civil and Water Resources Engineering, Bahir Dar University, Bahir Dar, Ethiopia. **Corresponding author:** Tammo S. Steenhuis, 206 Riley Robb Hall, Cornell University, Ithaca, NY 14853; phone: 607-255-2489; e-mail: tss1@cornell.edu.

  ISSN 2151-0032

determining sediment concentration as a function of overland flow, while the latter developed a new model to determine sediment concentration from physical principles that depends on the overland flow rate and a coefficient dependent on landscape and sediment characteristics. Models that are based on Hairsine and Rose (1992), such as Griffith University Erosion System Template (GUEST) technology, were found to be suitable for monsoonal climates (Kandel et al., 2001; Rose, 2001). Tilahun et al. (2012) further refined the GUEST technology and applied it to the monsoonal humid climate in the Ethiopian highlands. For simplicity, the Tilahun et al. (2012) hillslope erosion model assumed that, throughout the rainy phase of the monsoon, the sediment concentration from uplands is at the transport limit (i.e., the ability of overland flow to move sediment). The model performed reasonably well in simulating sediment concentration in the Anjeni watershed (1.13 km^2) and Blue Nile basin (174,000 km^2).

In reality, however, the sediment concentration decreases to the sediment source limit as sediment sources decline after a certain time during the rainy period (Ciesiolka et al., 1995). This phenomenon is well documented for the Ethiopian highlands by Tebebu et al. (2010), Zegeye et al. (2010), and Vanmaercke et al. (2010). The objective of this article is therefore to add this detail to the erosion model of Tilahun et al. (2012) and to validate the modified model for a wider set of watersheds in Ethiopia and in New York State. At the same time, we will test the modified model to determine if it performs better for the previously tested watersheds.

SATURATED EXCESS EROSION MODEL (SEEMODEL) DEVELOPMENT

The amount of erosion is predicted as a function of the (daily) amounts of surface runoff, interflow, and baseflow. These fluxes are obtained from the relatively simple hydrology model shown in figure 1 (Steenhuis et al., 2009; Tesemma et al., 2010) that divides the watershed into three zones. Two are runoff-producing zones: one becomes saturated during the wet monsoon period, and the other is the degraded hillslope. The remaining hillslope area (fig. 1) forms the third zone, where rainwater infiltrates and becomes either interflow (zero-order reservoir) or baseflow (first-order reservoir) depending on its path to the stream. Each zone is not necessarily continuous. Parameter values are averages for each of the three zones. A daily water balance is kept for each of the zones using the Thornthwaite-Mather procedure, in which actual evaporation has a linear relationship with the available water storage in the root zone. At maximum storage (S_{max}), actual evaporation is equal to the potential evaporation (Steenhuis and van der Molen, 1986). More information about the hydrology model can be found in Steenhuis et al. (2009) and Tesemma et al. (2010). Erosion originates from the runoff-producing zones. Erosion is negligible from the non-degraded hillslopes because almost all water infiltrates before it reaches the stream.

In calculating the erosion from runoff-producing areas, we assume that the rate of erosion depends on the stream power (Ω) per unit area. The maximum sediment concentration that a stream can carry (called the transport limiting capacity (C_t, g L^{-1}) can be derived from the stream power function, as shown by Hairsine and Rose (1992), Siepel et al. (2002), Ciesiolka et al. (1995), and Yu et al. (1997):

$$C_t = a_t q_r^{\,n} \tag{1}$$

where q_r is the runoff rate per unit area from each runoff-producing area (mm d^{-1}), and a_t is a variable derived from the stream power [(g L^{-1})(mm d^{-1})$^{-n}$]. Variable a_t is a function of the slope, Manning's roughness coefficient, slope length, and effective depositability (Yu et al., 1997). As water depth increases, a_t essentially becomes independent of the runoff rate per unit area and can be taken as a constant (Yu et al., 1997). In this article, where the smallest watershed considered is 113 ha, the water in the channel is sufficiently deep so that a_t is constant.

For erosion of cohesive soils, the sediment concentration will not always reach the transport limit. The sediment concentration is at the transport limit only when rills are actively formed in newly plowed soils. Tebebu et al. (2010) and Zegeye et al. (2010) found that, once the rill network has been fully established, no further erosion takes place, the sediment source becomes limited, and the sediment concentration (C, g L^{-1}) falls below the transport limit. For cases in which the sediment concentration becomes lower than the transport limit (C_t, g L^{-1}), Ciesiolka et al. (1995) found, based on the work of Hairsine and Rose (1992), that the sediment concentration will not decline below the source limit (C_s, g L^{-1}):

$$C_s = a_s q_r^{\,n} \tag{2}$$

where a_s is the source limit and is assumed to be independent of the flow rate for a particular watershed (as compared to plots). Introducing a new variable, H, defined as the fraction of the runoff-producing area with active rill formation, the sediment concentration from the runoff-producing area (C_r, g L^{-1}) can then be written as:

$$C_r = C_s + H\left(C_t - C_s\right) \tag{3}$$

Combining equation 3 with equations 1 and 2, the sediment concentration from the runoff-producing area becomes:

$$C_r = \left[a_s + H\left(a_t - a_s\right)\right] q_r^{\,n} \tag{4}$$

Finally, baseflow and interflow play an important role in the calculation of the daily sediment concentration. In a monsoon climate, baseflow at the end of the rainy season can be a significant portion of the total flow. Thus, in the last part of the rainy season, subsurface flow dilutes the peak storm sediment concentration from the runoff-producing zones when simulated on a daily basis. It is therefore important to incorporate the contribution of baseflow in the prediction of sediment concentration.

Next, we calculate the sediment concentration yield in the stream. Since the interflow and baseflow are sediment

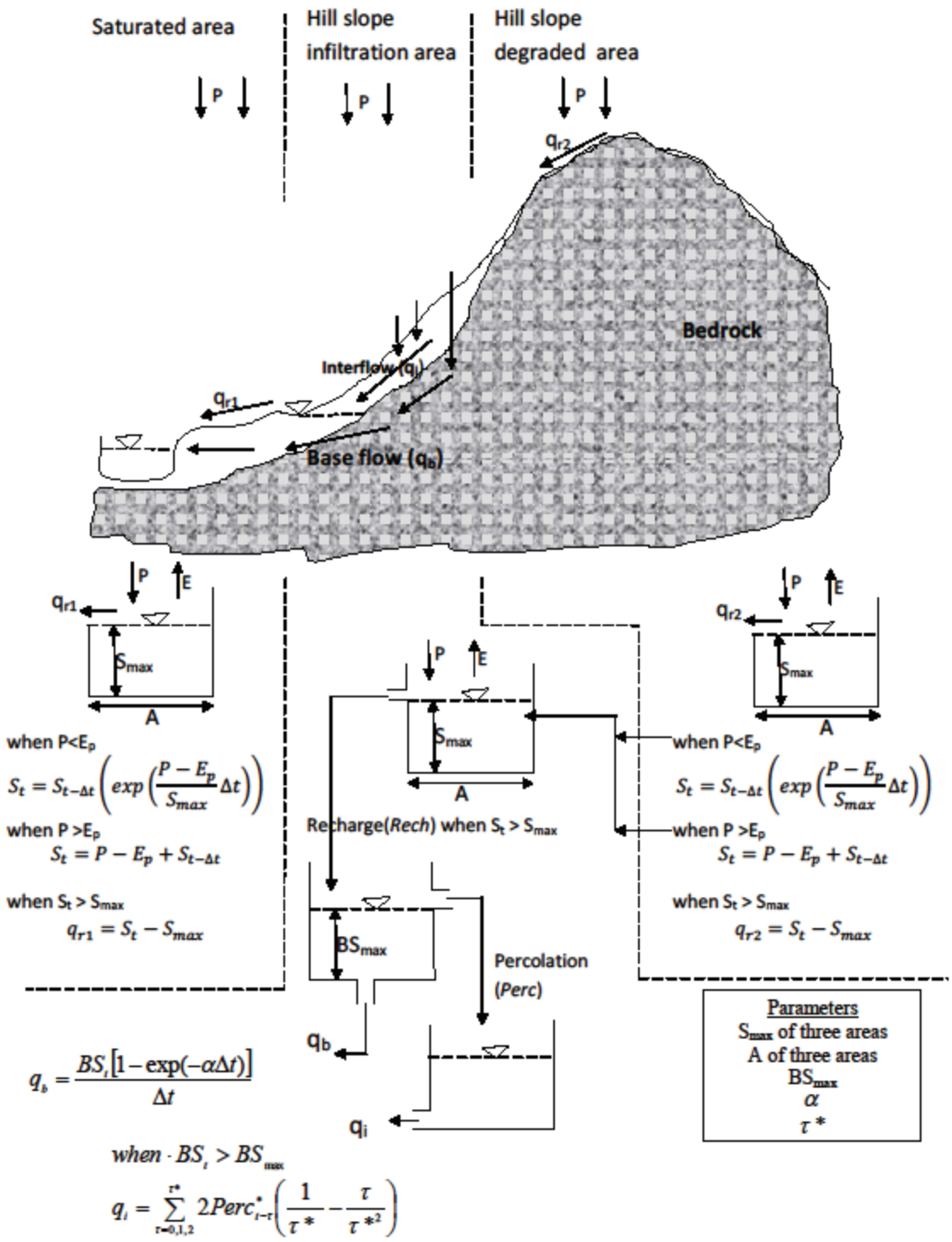

Figure 1. Schematic of the hydrology model: P is precipitation; E_p is potential evaporation; A is area fraction for zones 1 (saturated area), 2 (degraded area), and 3 (infiltration area); S_{max} is maximum water storage capacity of the three areas; BS_{max} is maximum baseflow storage of the linear reservoir; $t_{1/2}$ (= 0.69/α) is the time (in days) required to reduce the volume of the baseflow reservoir by a factor of 2 under no-recharge conditions, and τ* is the duration of the period after a single rainstorm until interflow ceases.

free, the sediment load per unit watershed area (Y, g m^{-2} d^{-1}) can be obtained by multiplying C_r in equation 4 by the relative area and the flux per unit area:

$$Y = A_1 q_{r1}\left[a_{s1} + H\left(a_{t1} - a_{s1}\right)\right] {q_{r1}}^n + A_2 q_{r2}\left[a_{s2} + H\left(a_{t2} - a_{s2}\right)\right] {q_{r2}}^n \quad (5)$$

where q_{r1} and q_{r2} are the runoff rates expressed in depth units for contributing area A_1 (fractional saturated area) and A_2 (fractional degraded area), respectively. Theoretically, for both turbulent flow and a wide field, n is equal 0.4 (Tilahun et al., 2012; Ciesiolka et al., 1995; Yu et al., 1997). The sediment concentration in the stream can be obtained by dividing the sediment load (Y in eq. 5) by the total watershed discharge:

$$C = \left(A_1 {q_{r1}}^{1.4} \left[a_{s1} + H\left(a_{t1} - a_{s1}\right) \right] + A_2 {q_{r2}}^{1.4} \left[a_{s2} + H\left(a_{t2} - a_{s2}\right) \right] \right) \div \left[A_1 q_{r1} + A_2 q_{r2} + A_3 \left(q_b + q_i\right) \right] \quad (6)$$

where q_b is the baseflow (mm d^{-1}) and q_i is the interflow (mm d^{-1}) per unit area of the non-degraded hillslope (A_3), where the water is being recharged to the subsurface (baseflow) reservoir.

Therefore, equation 6 was tested in four watersheds in the Ethiopian highlands (Anjeni, Andit Tid, Enkulal, and the Blue Nile basin) and one watershed in New York State (Esopus Creek), ranging in size from 1.13 to 174,000 km^2. There are four parameters in equation 6 that need to be calibrated (a_{s1}, a_{t1}, a_{s2}, and a_{t2}). The fraction (H) with active rill formation is not calibrated and is determined *a priori* based on field observations.

Watershed Descriptions

The Anjeni watershed (fig. 2) covers an area of 1.13 km^2 with elevations ranging between 2405 and 2507 m. It is located in the sub-humid northwestern part of Ethiopia near Debre Markos, 370 km northwest of the city of Addis Ababa. The mean annual rainfall is 1690 mm, which lasts from the middle of May to the middle of October. Ninety percent of the watershed is cultivated land (Guzman, 2011). Both discharge and sediment concentrations were measured during storm events. Daily average discharge and sediment concentrations were calculated. Rainfall, potential evaporation, stream discharge, and sediment concentrations were collected from 1988 to 1997. In 1986, soil and water conservation practices were installed, resulting in a decrease in soil loss for two years (Bosshart, 1997). Periods for which there are incomplete data were excluded. The model for discharge was calibrated for 1988 and 1990 and validated for 1989, 1991-1993, and 1997. Only four years were available for sediment concentration: 1990 was used for calibration, and 1991 to 1993 were used for validation.

The Andit Tid watershed (fig. 2) covers an area of 4.8 km^2. It is situated 180 km northeast of Addis Ababa in the North Shewa Administrative Zone adjacent to the Debre Birhan-Mekelle Highway. The catchment has a relatively high bimodal rainfall pattern with annual rainfall of 1400 mm. Hillslopes are very steep and degraded, with elevations ranging between 3040 and 3548 m. Only 15% of the watershed is cultivated land (Guzman, 2011). As in Anjeni, both discharge and sediment concentrations were measured during storm events. Daily average discharge and sediment concentrations were calculated. Rainfall, potential evaporation, stream discharge, and sediment concentrations were collected from 1986 to 1994. The model for discharge was calibrated for 1986, 1988, and 1989 and validated for 1990 to 1994. The model for erosion was calibrated for 1986 and 1988, while the years 1989 and 1991 to 1993 were used for validation.

The Enkulal catchment (fig. 2) is a small tributary of the Gumara watershed, located approximately 80 km northeast of Bahir Dar. The Enkulal watershed covers an area of 4.0 km^2. The elevation ranges from 2306 to 2528 m. The average annual rainfall is 1577 mm. Most of the rainfall is concentrated from June to September. More than three-quarters of the watershed is low-yielding oxen-plowed agriculture. Discharge and sediment concentration data were available twice a day, at 6:00 a.m. and 6:00 p.m., for the year 2010. However, many storms occurred at night, especially at the end of the rainy season, and the peak flows were not recorded. The rivers in the watershed are stable and run over bedrock in the lower part.

The last watershed modeled in Ethiopia is the entire Blue Nile basin (fig. 2) in Ethiopia. It is 174,000 km^2 in area and encompasses the Anjeni, Andit Tid, and Enkulal watersheds. It is commonly believed that the source of the Blue Nile is a spring located about 100 km south of Lake

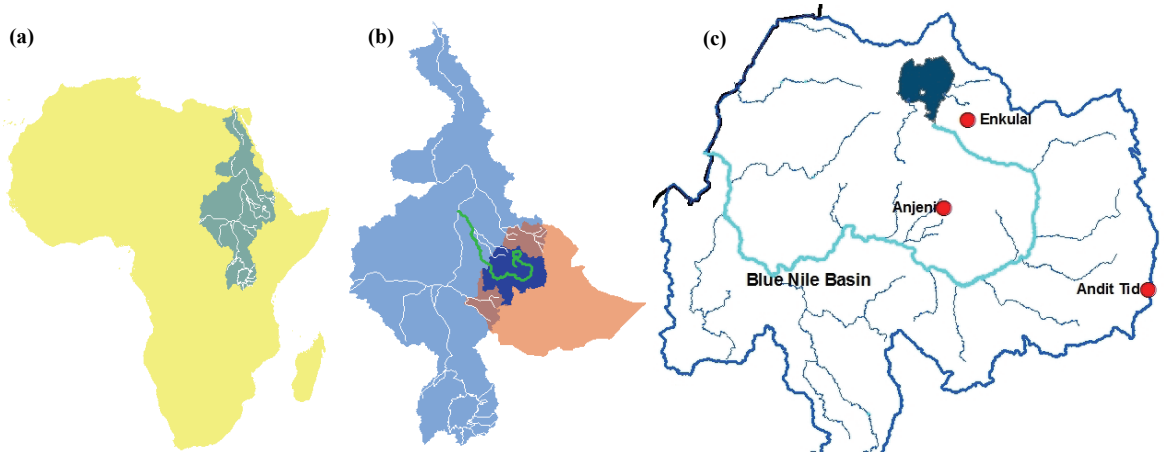

Figure 2. Location map of (a) the Nile basin in Africa, (b) the Blue Nile basin within the Nile basin and Ethiopia, and (c) the three watersheds (Anjeni, Andit Tid, and Enkulal) within the Blue Nile basin.

Tana at an elevation of 2900 m. This spring is the beginning of the Gilgil Abbay, which flows into Lake Tana. After Lake Tana, the Nile flows through a 1 km deep gorge, mostly over bedrock, to the Sudanese border. The Blue Nile leaves the highlands near the western border of Ethiopia and enters Sudan at an elevation of 490 m. The annual rainfall varies from less than 1000 mm near the Sudanese border to over 1800 mm in the highlands south of Lake Tana. Three years (1997, 2003, and 2004) of discharge and sediment data were available at the Sudanese border. The year 1993 was used for calibration, and 2003 and 2004 were used for validation. Tesemma et al. (2010) found that the degraded soils had increased by 10% during a 25-year time span. For that reason, the degraded hillslope area was increased by 3% from 1997 to 2003 and 2004.

The final watershed is the Esopus Creek watershed, located in the Catskill region of New York State. This watershed drains 493 km^2 and is dominated by forests, which occupy more than 90% of the watershed area. The elevation of the watershed ranges from 194 m near the watershed outlet at Coldbrook to 1275 m at the headwaters. The average annual rainfall is 1450 mm. Widespread stream channel erosion of glacial clay deposits has been identified as the primary cause of high levels of turbidity. For the Esopus Creek watershed, we used measured daily stream discharge data from the USGS gauging station at the watershed outlet near Coldbrook. Turbidity measurements were taken at intervals between 15 min and 1 h using a YSI water quality sonde from which flow-weighted average daily values were calculated. The measured stream discharge was separated into baseflow and surface runoff components using a baseflow filter program (Arnold and Allen, 1999). The values for the surface runoff region (A_1) and hillslope recharge region (A_3) were derived as the long-term (1931-2011) mean proportions of runoff and baseflow to total streamflow. Degraded areas were not identified in the watershed, as the hillslope is covered by forest. The surface runoff-producing area in this watershed is the saturated zone observed along the streambank. Observed daily turbidity and daily stream discharge from March 2003 to March 2004 were used for calibration of sediment in the SEEModel, and a power function and data from March 2007 to March 2008 were employed for validation. Esopus Creek is at times fed by a diversion tunnel operated from the nearby Schoharie reservoir that contributes to stream discharge. Therefore, all calculations were confined to days when the tunnel contribution to stream discharge was insignificant.

RESULTS AND DISCUSSION

HYDROLOGY MODEL

The model calibrations over a wide range of scales have some remarkable similarities (table 1). In particular, the fraction of surface runoff zones (areas A_1 and A_2) in four of the watersheds is between 0.3 and 0.4. Only in the Anjeni watershed is this fraction smaller and equal to 16% of the watershed. Small changes in the relative extent of surface runoff zones and permeable hillslopes greatly affect the shape of the hydrograph (Tilahun et al., 2012). The small Ethiopian watersheds are located in the upper reaches of the Blue Nile basin, and it is likely that some of the subsurface water passes under the gauging station and provides water for springs below. The sum of the fractional areas for the small watersheds is therefore less than one. The hillslope infiltration area is especially small for the Enkulal watershed (table 1), which is in accordance with data from piezometer readings that indicated disconnection between the top and bottom parts of the watershed (Demisse, 2011). The maximum storage of water in the root zone (S_{max}) and shallow aquifer (BS_{max}) varies among the watersheds. However, the hydrology model (fig. 1) is relatively insensitive to the S_{max} and BS_{max} values since they only affect the amount of surface runoff at the beginning of the rainfall season (Tilahun et al., 2012). Variations in these values between watersheds are therefore not significant, with the exception of the maximum storage for the hillslope infiltration area and saturated area of the Blue Nile basin, which are larger.

Two parameters determine subsurface flow (fig. 1): τ^* for interflow and $t_{1/2}$ (= 0.69/α) for baseflow. While the baseflow contribution to streamflow decreases slowly depending on the amount of water in the aquifer, the interflow decreases as a linear function of time for a particular storm and stops after time τ^*. As expected, τ^* increases with watershed size because more deep flow paths are intercepted

Table 1. Calibrated hydrology and erosion model parameters for the five watersheds.[a]

Description		Parameter	Unit	Calibrated Values				
				Anjeni	Andit Tid	Enkulal	Blue Nile	Esopus
Hydrology component	Saturated area	Area A_1	fraction	0.02	0.1	0.1	0.2	0.32
		S_{max} in A_1	mm	200	70	50	200	-
	Degraded area	Area A_2	fraction	0.14	0.15	0.2	0.2	-
		S_{max} in A_2	mm	10	10	10	10	-
	Infiltration area	Area A_3	fraction	0.5	0.75	0.3	0.6	0.68
		S_{max} in A_3	mm	100	80	50	300	-
	Subsurface	BS_{max}	mm	100	100	500	20	
		$t_{1/2}$	days	70	100	120	35	-
		τ^*	days	10	10	100	140	-
Erosion component								
Sediment transport limit for A_1 and A_2		a_t	(g L^{-1})(mm d^{-1})$^{-0.4}$	4	2.2	17	1.2	-
Sediment source limit for A_1 and A_2		a_s	(g L^{-1})(mm d^{-1})$^{-0.4}$	3	0.8	5	0.5	0.63

[a] A_i is the area fraction for components of zones 1 (saturated area), 2 (degraded area), and 3 (infiltration area); S_{max} is the maximum water storage capacity; $t_{1/2}$ is the time in days required to reduce the volume of the baseflow reservoir by a factor of 2 under no-recharge conditions; BS_{max} is the maximum baseflow storage of the linear reservoir; τ^* is the duration of the period after a single rainstorm until interflow ceases; a_t is the calibrated sediment transport limiting parameter, and a_s is the sediment source limiting parameter for the saturated area (1) and degraded area (2).

by the river. The larger-than-expected τ* for the Enkulal watershed (table 1) is likely a consequence of missing peak flows, especially later in the rainy season, due to the sample collection timing. The half-life ($t_{1/2}$) for the aquifer system is generally small (table 1) and almost independent of watershed size, indicating that there is not a large aquifer. With the Nile flowing over bedrock, this should not be a surprise. Finally, the hydrology model could not be fitted very well to the Esopus Creek watershed discharge data because, in a temperate climate, snowmelt requires another subroutine and because of the large elevation differences in the watershed. The proportions of surface runoff zones and permeable hillslopes were derived statistically from the discharge data. The simple hydrology SEEModel was able to simulate the discharge pattern quite well in the watersheds with large relief and permeable soils usually over a hard pan at shallow to intermediate depths on the hillslopes.

The Nash-Sutcliffe efficiencies (NSE) and coefficients of determination (R^2) in table 2 for all watersheds are reasonably good. The NSE for validation of the daily discharge data in the Anjeni watershed was 0.80 (table 2). The NSE for the 7-day average discharge in Andit Tid was similar at 0.78, and the NSE for the 10-day average discharge in the entire Blue Nile basin was 0.92. The SEEModel was able to simulate the discharge pattern quite well in these watersheds. The predicted and observed discharges for the 1989 validation year for the Anjeni watershed and for the 1990 validation year for Andit Tid are shown in figures 3a and 3b, respectively. Supplementary calibration and validation data for all years are shown for Anjeni in figures A1 and A2 and for Andit Tid in figures A3 and A4 in Appendix A. In Anjeni, the peak daily flows were overestimated for 1988 and 1989, after the soil and water conservation practices had been implemented in 1986 (Tilahun et al., 2012), and underestimated after soils had filled up behind the bunds (1990 in fig. Ala, and 1991 to 1997 in fig. A1b). In all years, the peak flows were underestimated because the model had fixed saturated areas; in reality, the saturated area expands with large storms. The years 1995 and 1996 were not simulated because the data for these periods were incomplete. The fit for Andit Tid during calibration (fig. A3) was reasonable, as shown by the NSE in table 2. The year 1987 was not included in the simulation due to missing data.

Data for the Enkulal watershed were only collected in 2010, and the weekly running-average discharges for 2010 are compared in figure 3c. The fit is not great and is partly caused by the uncertainty of the peak flows at the end of the rainy season, which likely occurred at night when manual measurements were not possible. The validation for the Blue Nile basin for 2003 is shown in figure 3d, and the calibration and validation are shown in figures A5 and A6.

Table 2. Simulation efficiency as evaluated by statistical measures for the five watersheds.[a]

	Discharge		Sediment Concentration	
Watershed (and Time Step)	Calibration	Validation	Calibration	Validation
Anjeni (1 day)	1988 and 1990	1989, 1991-1993, and 1997	1990	1991-1993
Observed mean	2.06	1.88	0.72	0.67
Predicted mean	2.26	1.92	0.65	0.65
NSE	0.84	0.80	0.78	0.68
R^2	0.88	0.82	0.80	0.70
RMSE	1.28	1.19	1.5	1.2
Andit Tid (7 days)	1986 and 1988-1989	1990-1994	1986 and 1988	1989 and 1991-1993
Observed mean	2.41	2.27	0.76	0.65
Predicted mean	2.31	2.65	0.86	0.69
NSE	0.91	0.78	0.71	0.60
R^2	0.91	0.83	0.79	0.73
RMSE	1.09	2.32	0.82	0.95
Enkulal (7 days)	2010	-	2010	-
Observed mean	2.7	-	4.1	-
Predicted mean	2.9	-	3.5	-
NSE	0.77	-	0.76	-
R^2	0.8	-	0.77	-
RMSE	0.96	-	3.51	-
Blue Nile basin (10 days)	1993	2003-2004	1993	2003-2004
Observed mean	9.66	9.43	0.85	1.28
Predicted mean	9.53	9.20	1.26	0.92
NSE	0.93	0.92	0.84	0.86
R^2	0.97	0.93	0.87	0.87
RMSE	2.59	2.73	0.59	1.69
Esopus Creek (1 day)	-	-	2003-2004	2007-2008
Observed mean	-	-	0.018	0.02
Predicted rating curve	-	-	0.017	0.024
Predicted SEEModel	-	-	0.017	0.018
NSE rating curve	-	-	0.84	0.37
NSE SEEModel	-	-	0.63	0.56
R^2 rating curve	-	-	0.84	0.59
R^2 SEEModel	-	-	0.63	0.56
RMSE rating curve	-	-	0.008	0.0025
RMSE SEEModel	-	-	0.0013	0.0021

[a] Discharge is in mm d^{-1}, and sediment concentration is in g L^{-1}; NSE = Nash-Sutcliffe efficiency; RMSE = root mean square error and has the same units as discharge and sediment concentration.

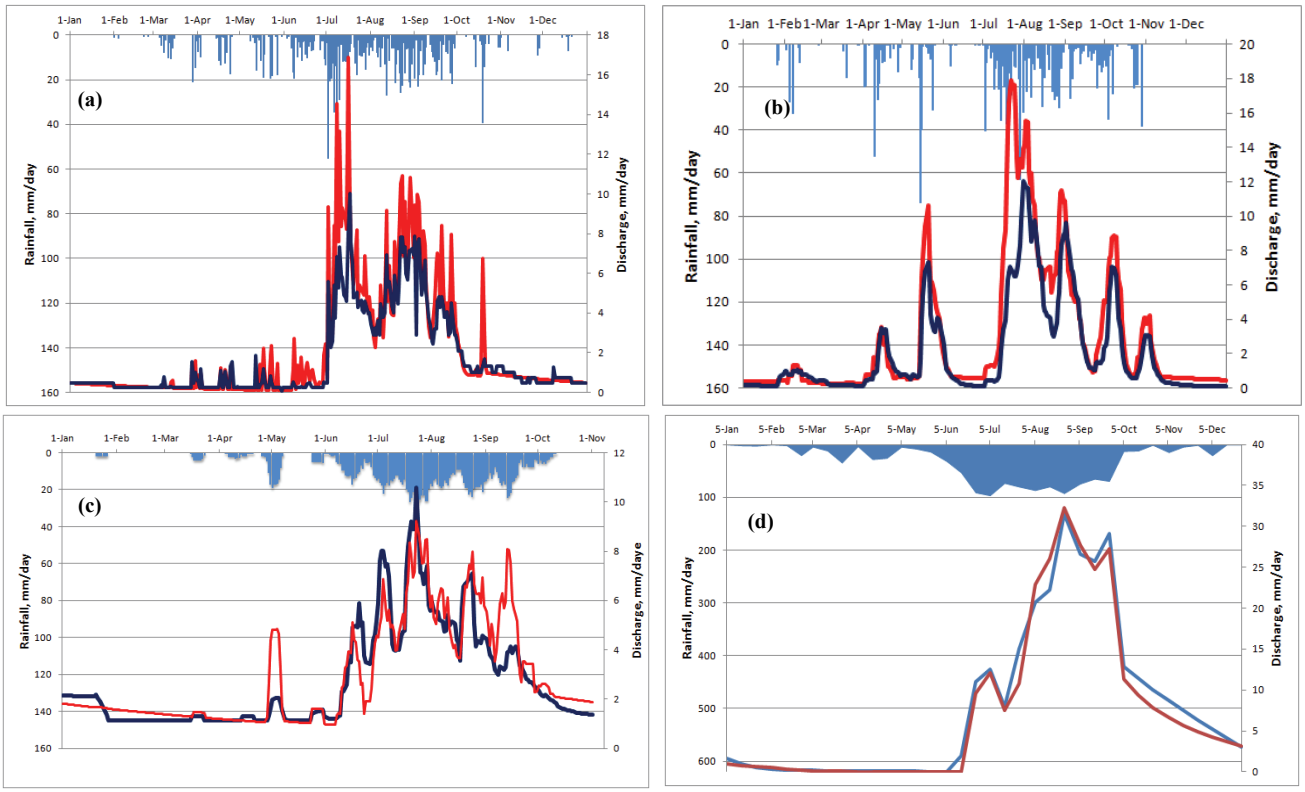

Figure 3. Predicted (red line) and observed (blue line) discharge data for (a) validation of Anjeni daily discharge in 1992, (b) validation of Andit Tid weekly average discharge in 1993, (c) calibration of Enkulal weekly running-average discharge in 2010, and (d) validation of Blue Nile discharge at the Ethiopia-Sudan border in 2003. Rainfall (mm d^{-1}) is shown by the blue chart at the top of each graph.

The NSE values for Anjeni were improved over the spreadsheet model of Collick et al. (2009), and the NSE values for the entire Ethiopian Blue Nile basin are comparable to the SWAT-WB model of Easton et al. (2010). The good fit of the hydrology model is a consequence of the model recognizing that the hydrological pathways need to become active (i.e., the runoff source areas are saturated and the permeable hillslopes are at or above field capacity) before the watershed discharge can respond to precipitation after the dry season. For degraded areas, this could occur early in the rainy season because the impermeable layer is close to the surface and little rain is needed for these soils to become saturated. The good fit also shows that the occasions when rainfall intensity exceeds the infiltration capacity are relatively minor.

Erosion Model

In simulating sediment losses, we first need to determine the fraction of plowed land with active rill formation to define the H value in equation 6. Tebebu et al. (2010) and Zegeye et al. (2010) found that erosion was greatest just after plowing and stopped after rills were formed in the field around 1 August. Cultivation begins after the first rainfall and then continues for approximately a three to four week period. Therefore, in the model, we assumed that the concentration from the runoff areas is at the transport limit (i.e., H = 1) for the first four weeks after the first rainfall event, and H then declines from one to zero over the next months. By 1 August, the sediment concentration from the runoff areas is at the source limit, except for the Esopus Creek watershed, where the sediment remains at its source limit due to the large proportion of forest and virtually no agricultural lands.

The sediment concentrations shown in figure 4 were calculated according to equation 6 by using the H values as specified above and the discharges predicted by the hydrology model. Coefficients a_t and a_s in table 2 were calibrated for the first year of data and then validated with the remaining years of data. The observed and predicted values for the four watersheds with multiple years of data fit the sediment concentrations very well (table 2, figs. 4a to 4d, and figs. B1 to B6). The sediment concentrations for the Enkulal watershed actually fit better than the discharge data (compare figs. 3c and 4c). The reason is that when measurements were taken in the morning after a nighttime storm, the peak flow had subsided but the sediment concentrations were still elevated. The modeling approach reported in this article gave a slightly better simulation result than our first attempt (Tilahun et al., 2012) using only transport limiting concentrations, as demonstrated by the improved NSE and R^2 values. The NSE for Anjeni did not improve during calibration but improved for validation from 0.64 to 0.68. In addition, the RMSE decreased from 1.66 to 1.5 g L^{-1} during calibration and from 1.32 to 1.2 g L^{-1} during validation. The NSE for the Blue Nile basin was previously 0.76 for both calibration and validation (Tilahun et al., 2012), and this improved to 0.84 for calibration and 0.86 for validation using both transport and source limiting factors. The error measured by RMSE decreased from 0.73 to 0.59 g L^{-1} during calibration and from 1.89 to 1.69 g L^{-1}

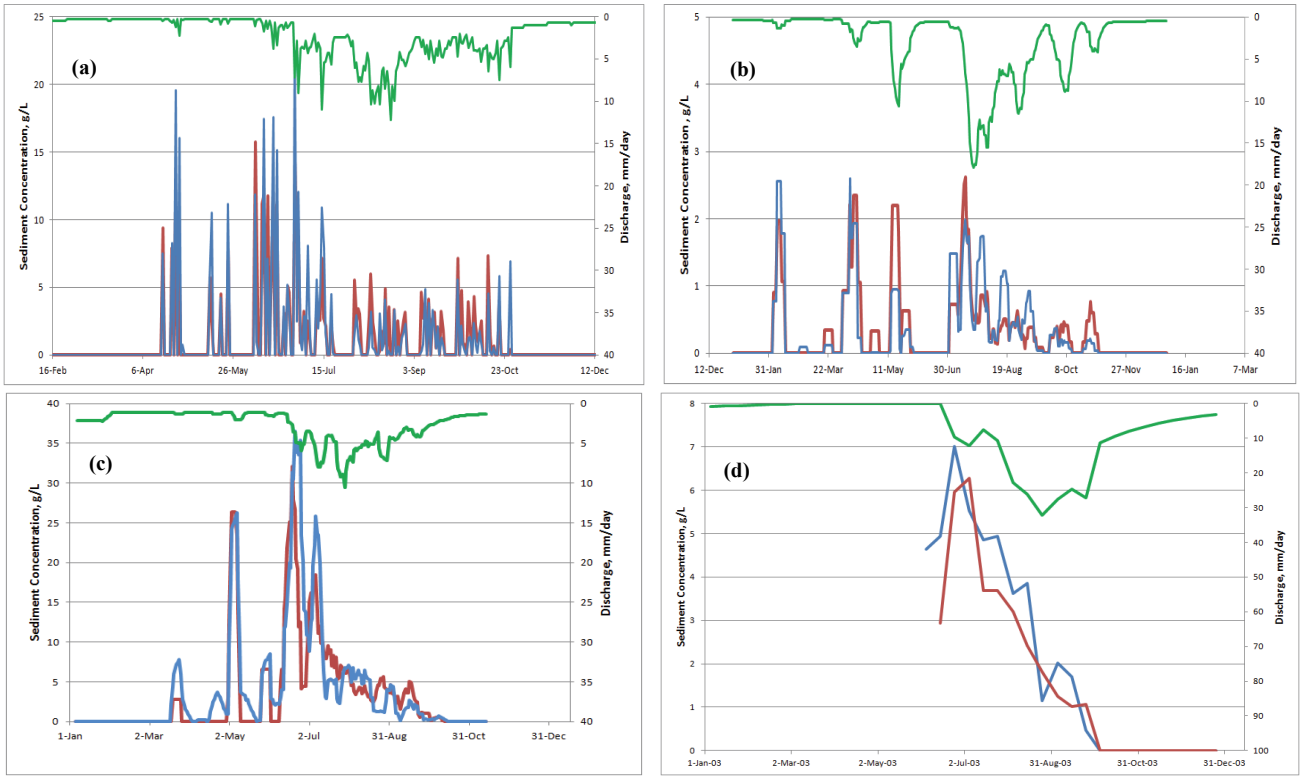

Figure 4. Predicted (red line) and observed (blue line) sediment concentration for (a) validation of Anjeni daily concentration in 1992, (b) validation of Andit Tid weekly concentration in 1993, (c) calibration of Enkulal weekly running-average concentration in 2010, and (d) validation of 10-day average for the Blue Nile at the Ethiopia-Sudan border in 2003. Discharge (mm d^{-1}) is shown by the green line at the top of each graph.

during validation. However, this improvement was achieved by doubling the number of parameters from two (a_{t1} and a_{t2}) in Tilahun et al. (2012) to four (a_{t1}, a_{s1}, a_{t2}, and a_{s2}) in the current modeling approach, as described by equation 6.

We could not use the model employed for Ethiopia for the Esopus Creek watershed because of the inability to simulate snowmelt accurately. Therefore, based on long-term statistical analysis, the average area contributing to baseflow and interflow (A_3 in eq. 6) was found to be 0.68, and the relative portion of both runoff source areas was 0.32. Since we could not distinguish between degraded hillslopes and near-stream areas, we assigned them all to area A_1. This does not cause a loss in accuracy, as the whole watershed is forested and the a values in equation 6 are therefore the same for both runoff source areas. There was no plowing in the Esopus Creek watershed, and therefore the H value was kept constant at 0. We left the exponential term n = 0.4 and calibrated the value of the source limiting capacity as 0.63 (fig. 5). This was much lower than in the Nile basin, likely because the Esopus Creek watershed was completely forested. The NSE was 0.63 for calibration (table 2). A simple power function rating curve (using two calibration parameters and data from the same period) had a better NSE of 0.84 (table 2). However, during the validation period, the one-parameter model (eq. 6) performed better (NSE = 0.56) than the rating curve (NSE = 0.37). Unlike the rating curve, the SEEModel was able to capture the variability in the stream discharge-turbidity relationship to a certain extent (fig. 5).

The transport limiting capacity (a_t) values for Andit Tid and the Blue Nile are surprisingly similar (table 1). The transport limiting capacity (a_t) values for Anjeni and Enkulal are greater than the other two, likely because both watersheds have more cultivated land and the soils in Enkulal watershed are sandier than in the remaining watersheds. The source limits for all four watersheds spanning a range of scales in Ethiopia varied between 0.5 and 5 (table 1).

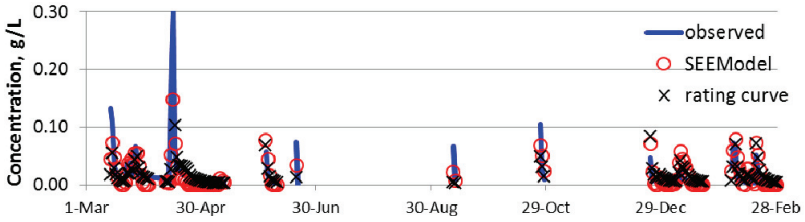

Figure 5. Validation of Esopus Creek watershed in 2007-2008.

CONCLUSIONS

Sediment concentrations in the streams of four watersheds in the Ethiopian highlands were predicted with the recently developed Saturation Excess Erosion Model (SEEModel). This model was developed by assuming that the sediment concentrations in the streams were at the transport limiting capacity at the time the fields were plowed and then became equal to the source limit once the rill networks in the fields were fully developed. The Nash-Sutcliffe efficiencies were remarkably good for such a simple model over such a wide range of scales and were better than most values reported in the literature for the Blue Nile basin. The results suggest that simulating the surface and subsurface flow within a watershed helps to improve the sediment concentration prediction for the watershed. Although the hydrology model could not be used in a temperate climate where runoff is produced by snowmelt, the sediment relationships seemed to apply there as well.

ACKNOWLEDGEMENTS

Funding was provided by the International Foundation for Science (IFS), Higher Education for Development (HED), and the USDA International Science and Education (ISE) program. The runoff and sediment data were made available by the Amhara Regional Agricultural Research Institute.

REFERENCES

Arnold, J. G., and P. M. Allen. 1999. Automated methods for estimating baseflow and groundwater recharge from streamflow. *J. American Water Resources Assoc.* 35(2): 411-424.

Bayabil, H. K., S. A. Tilahun, A. S. Collick, and T. S. Steenhuis. 2010. Are runoff processes ecologically or topographically driven in the Ethiopian highlands? The case of the Maybar watershed. *Ecohydrol.* 3(4): 457-466.

Bosshart, U. 1997. Catchment discharge and suspended sediment transport as indicators of physical soil and water conservation in the Minchet catchment, Anjeni research unit. Soil Conservation Research Report 40. Bern, Switzerland: University of Bern, Centre for Development and Environment.

Ciesiolka, C. A. A., K. J. Coughlan, C. W. Rose, M. C. Escalante, G. M. Hashim, E. P. Paningbatan Jr., and S. Sombatpanit. 1995. Methodology for a multi-country study of soil erosion management. *Soil Tech.* 8(3): 179-192.

Collick, A. S., Z. M. Easton, T. Ashagrie, B. Biruk, S. A. Tilahun, E. Adgo, S. B. Awulachew, G. Zeleke, and T. S. Steenhuis. 2009. A simple semidistributed water balance model for the Ethiopian highlands. *Hydrol. Proc.* 23(26): 3718-3727.

Demisse, B. A. 2011. Discharge and sediment yield modeling in Enkulal watershed, Lake Tana region, Ethiopia. MPS Project Paper in International Agriculture and Rural Development. Ithaca, N.Y.: Cornell University.

Easton, Z. M., D. R. Fuka, E. D. White, A. S. Collick, B. Biruk, B. Ashagre, M. McCartney, S. B. Awulachew, A. A. Ahmed, and T. S. Steenhuis. 2010. A multi-basin SWAT model analysis of runoff and sedimentation in the Blue Nile, Ethiopia. *Hydrol. Earth Syst. Sci.* 14(10): 1827-1841.

Engda, T. A., H. K. Bayabil, E. S. Legesse, E. K. Ayana, S. A. Tilahun, A. S. Collick, Z. M. Easton, A. Rimmer, S. B. Awulachew, and T. S. Steenhuis. 2011. Watershed hydrology of the (semi) humid Ethiopian highlands. In *Nile River: Hydrology, Climate, and Land Use*, 145-162. A. Melesse, ed. New York, N.Y.: Springer Science.

Guzman, C. D. 2011. Suspended sediment concentration and discharge relationships in the Ethiopian highlands. MS thesis. Ithaca, N.Y.: Cornell University, Department of Biological and Environmental Engineering.

Hairsine, P. B., and C. W. Rose. 1992. Modeling water erosion due to overland flow using physical principles: 2. Rill flow. *Water Resour. Res.* 28(1): 245-250.

Kandel, D., A. Western, R. Grayson, and H. Turral. 2001. Testing current generation soil erosion models at two minute and daily scales using plot-scale data from a mid-hill catchment of Nepal. In *Proc. Intl. Congress on Modelling and Simulation (MODSIM 2001), Volume 1: Natural Systems Modelling and Simulation*, 365-370. F. Ghassemi, D. Post, M. Sivapalan, and R. Vertessy, eds. Canberra, Australia: Australian National University, Center for Resource and Environmental Studies.

Liu, B. M., A. S. Collick, G. Zeleke, E. Adgo, Z. M. Easton, and T. S. Steenhuis. 2008. Rainfall-discharge relationships for a monsoonal climate in the Ethiopian highlands. *Hydrol. Proc.* 22(7): 1059-1067.

Rose, C. W. 2001. Soil erosion models and implications for conservation of sloping tropical lands. In *Sustaining the Global Farm: Selected papers from the 10th Intl. Soil Conservation Organization Meeting*, 852-859. D. E. Stott, R. H. Mohtar, and G. C. Steinardt, eds. West Lafayette, Ind.: International Soil Conservation Organization in cooperation with the USDA and Purdue University.

Rose, C. W., J. R. Williams, G. C. Sander, and D. A. Barry. 1983. A mathematical model of soil erosion and deposition processes: I. Theory for a plane land element. *SSSA J.* 47(5): 991-995.

Siepel, A. C., T. S. Steenhuis, C. W. Rose, J.-Y. Parlange, and G. F. McIsaac. 2002. A simplified hillslope erosion model with vegetation elements for practical applications. *J. Hydrol.* 258(1-4): 111-121.

Steenhuis, T. S., and W. H. van der Molen. 1986. The Thornthwaite-Mather procedure as a simple engineering method to predict recharge. *J. Hydrol.* 84(3-4): 221-229.

Steenhuis, T. S., A. S. Collick, Z. M. Easton, E. S. Leggesse, H. K. Bayabil, E. D. White, S. B. Awulachew, E. Adgo, and A. A. Ahmed. 2009. Predicting discharge and erosion for the Abay (Blue Nile) with a simple model. *Hydrol. Proc.* 23(26): 3728-3737.

Tebebu, T. Y., A. Z. Abiy, H. E. Dahlke, Z. M. Easton, A. D. Zegeye, S. A. Tilahun, A. S. Collick. S. Kidnau, S. Moges, F. Dadgari, and T. S. Steenhuis. 2010. Surface and subsurface flow effect on permanent gully formation and upland erosion near Lake Tana in the northern highlands of Ethiopia. *Hydrol. Earth Syst. Sci.* 14(11): 2207-2217.

Tesemma, Z. K., Y. A. Mohamed, and T. S. Steenhuis. 2010. Trends in rainfall and runoff in the Blue Nile basin: 1964-2003. *Hydrol. Proc.* 24(25): 3747-3758.

Tilahun, S. A., C. D. Guzman, A. D. Zegeye, T. A. Engda, A. S. Collick, A. Rimmer, and T. S. Steenhuis. 2012. An efficient semi-distributed hillslope erosion model for the sub-humid Ethiopian highlands. *Hydrol. Earth Syst. Sci.* 9(2): 2121-2155.

Vanmaercke, M., A. Zenebe, J. Poesen, J. Nyssen, G. Vertstraeten, and J. Deckers. 2010. Sediment dynamics and the role of flash floods in sediment export from medium-sized catchments: A case study from the semi-arid tropical highlands in northern Ethiopia. *J. Soils and Sediments* 10(4): 611-627.

Yu, B., C. W. Rose, B. C. Ciesiolka, K. J. Coughlan, and B. Fentie. 1997. Toward a framework for runoff and soil loss prediction using GUEST technology. *Australian J. Soil Res.* 35(5): 1191-1212.

Zegeye, A. D., T. S. Steenhuis, R. W. Blake, S. Kidnau, A. S. Collick, and F. Dadgari. 2010. Assessment of upland erosion processes and farmer perception of land conservation in Debre-Mewi watershed, near Lake Tana, Ethiopia. *Ecohydrol. Hydrobiol.* 10(2-4): 297-306.

APPENDIX A
STREAMFLOW TIME SERIES AND SCATTER PLOTS

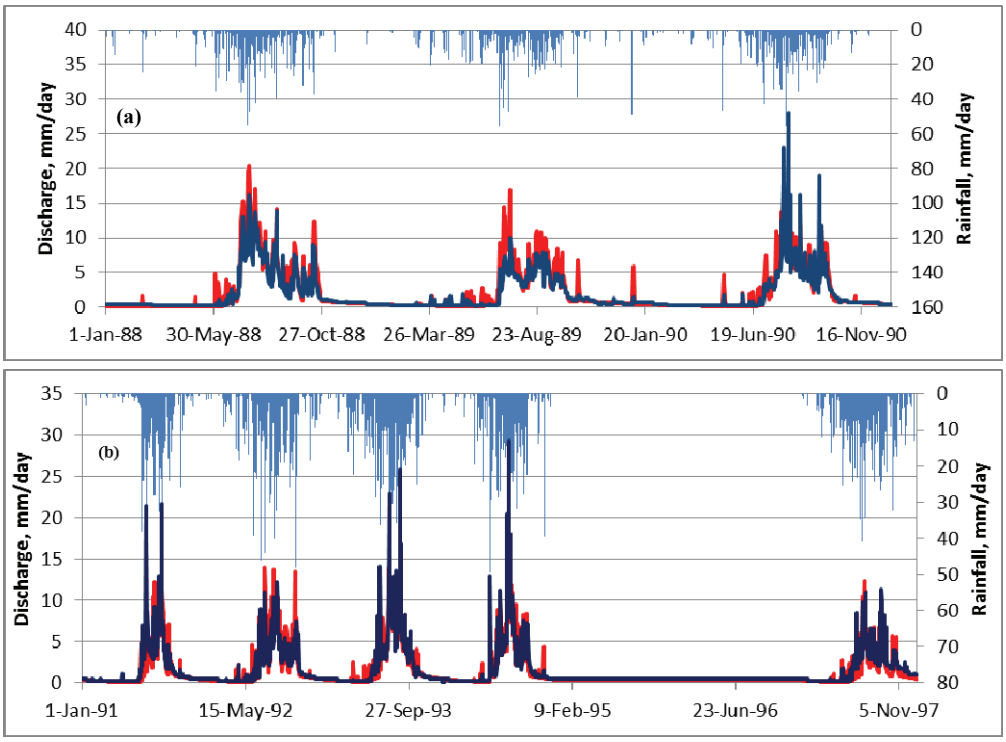

Figure A1. Predicted (red line) and observed (blue line) data for (a) calibration and (b) validation of Anjeni daily discharge. Rainfall (mm d^{-1}) is shown by the blue chart at the top of each graph.

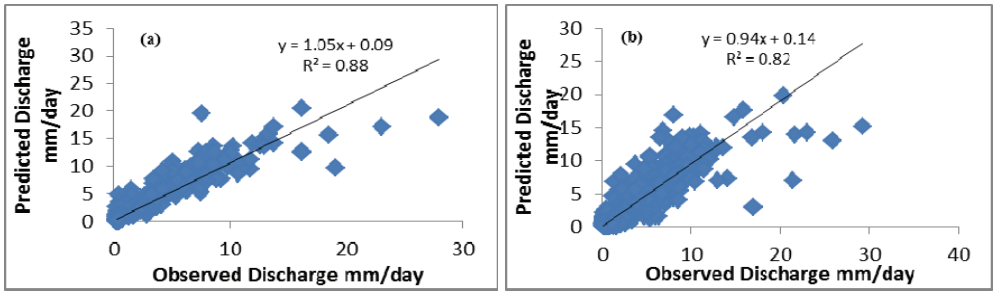

Figure A2. Scatter plots for (a) calibration and (b) validation of Anjeni daily discharge.

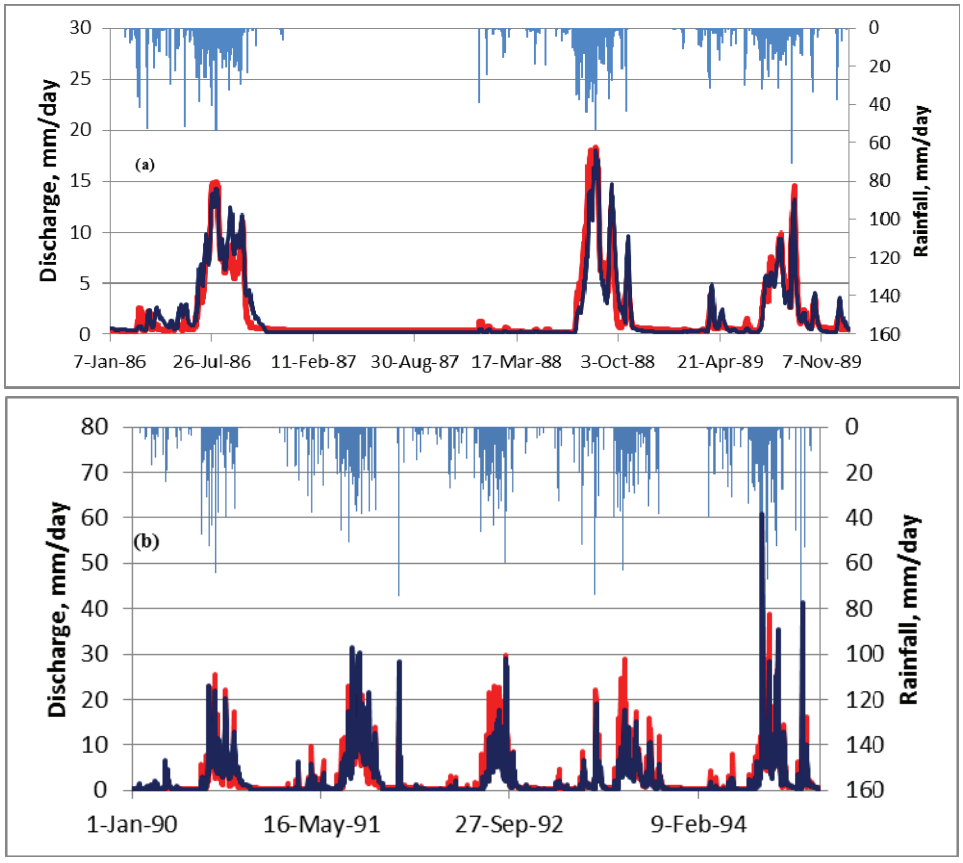

Figure A3. Predicted (red line) and observed (blue line) data for (a) calibration and (b) validation of Andit Tid weekly discharge. Rainfall (mm d^{-1}) is shown by the blue chart at the top of each graph.

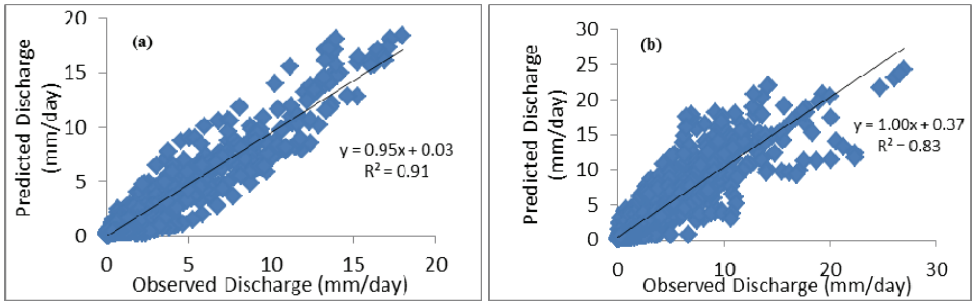

Figure A4. Scatter plots for (a) calibration and (b) validation of Andit Tid weekly discharge.

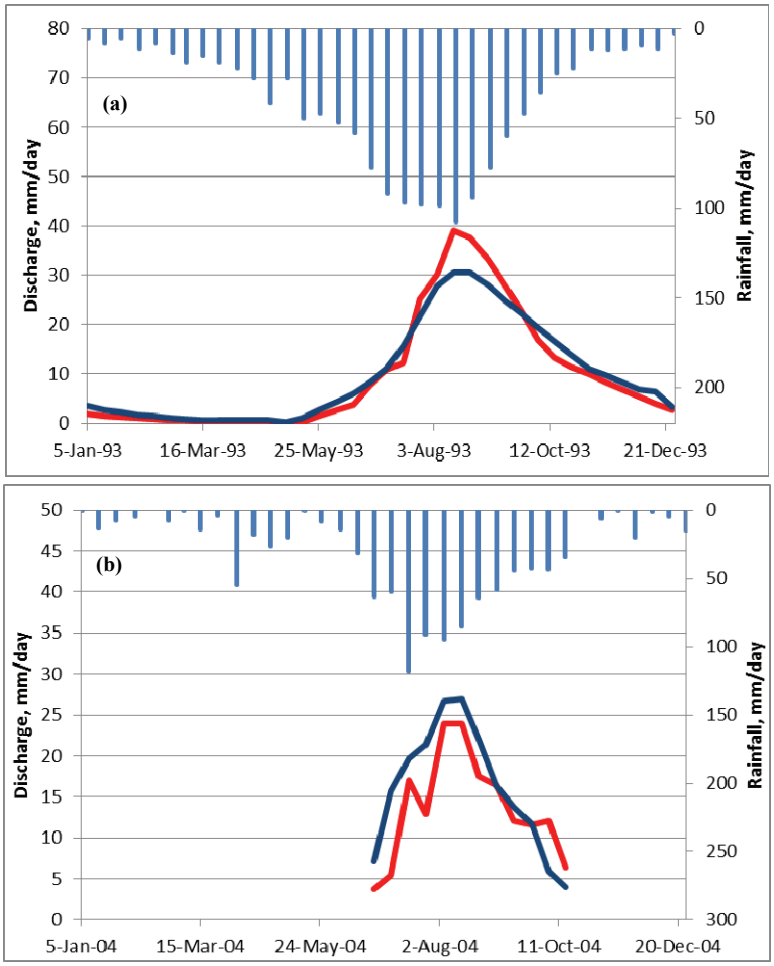

Figure A5. Predicted (red line) and observed (blue line) data for (a) calibration and (b) validation of Blue Nile basin 10-day average discharge. Rainfall (mm d^{-1}) is shown by the blue chart at the top of each graph.

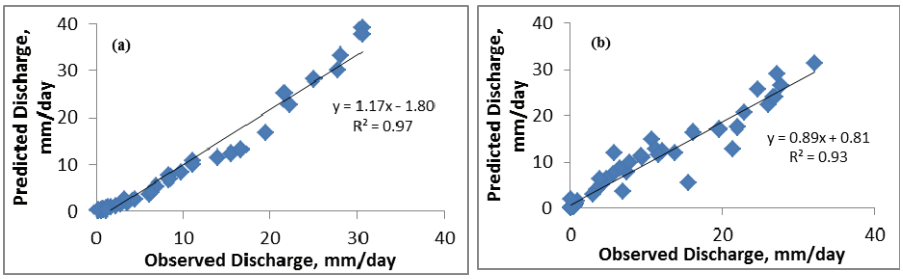

Figure A6. Scatter plots for (a) calibration and (b) validation of Blue Nile basin 10-day average discharge.

APPENDIX B
SEDIMENT TIME SERIES AND SCATTER PLOTS

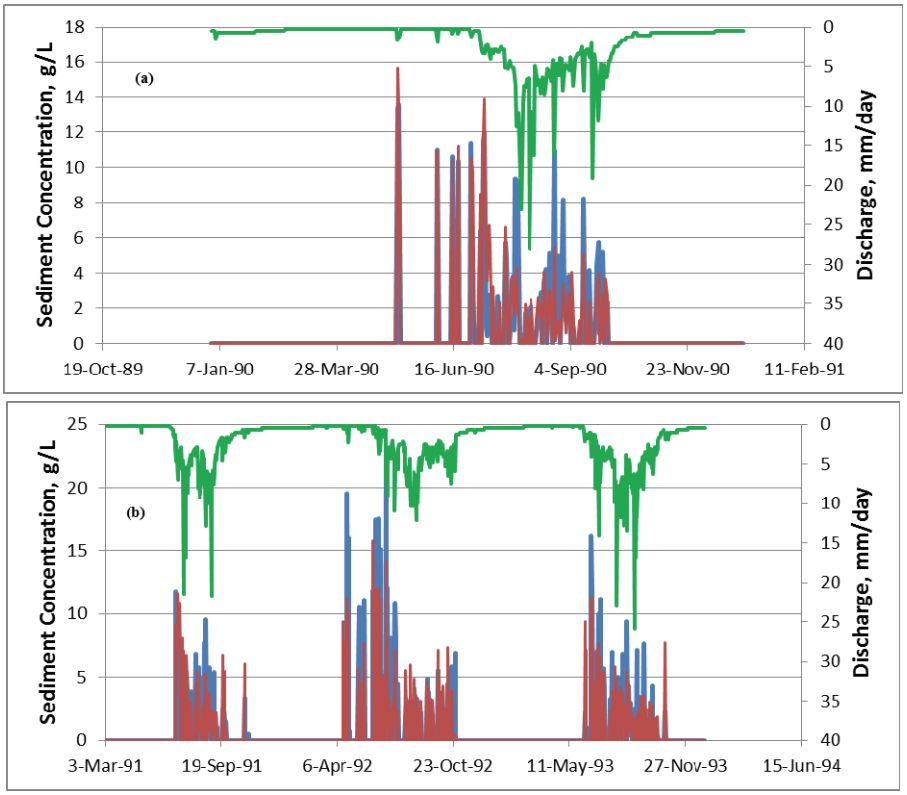

Figure B1. Predicted (red line) and observed (blue line) data for (a) calibration (b) validation of Anjeni daily sediment concentration. Discharge (mm d^{-1}) is shown by the green line at the top of each graph

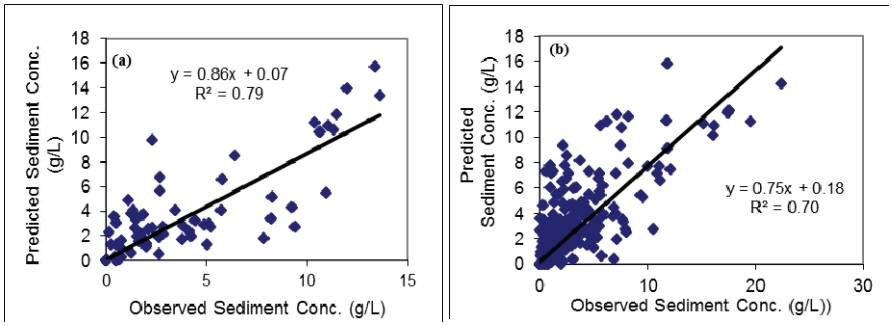

Figure B2. Scatter plots for (a) calibration (b) validation of Anjeni daily sediment concentration.

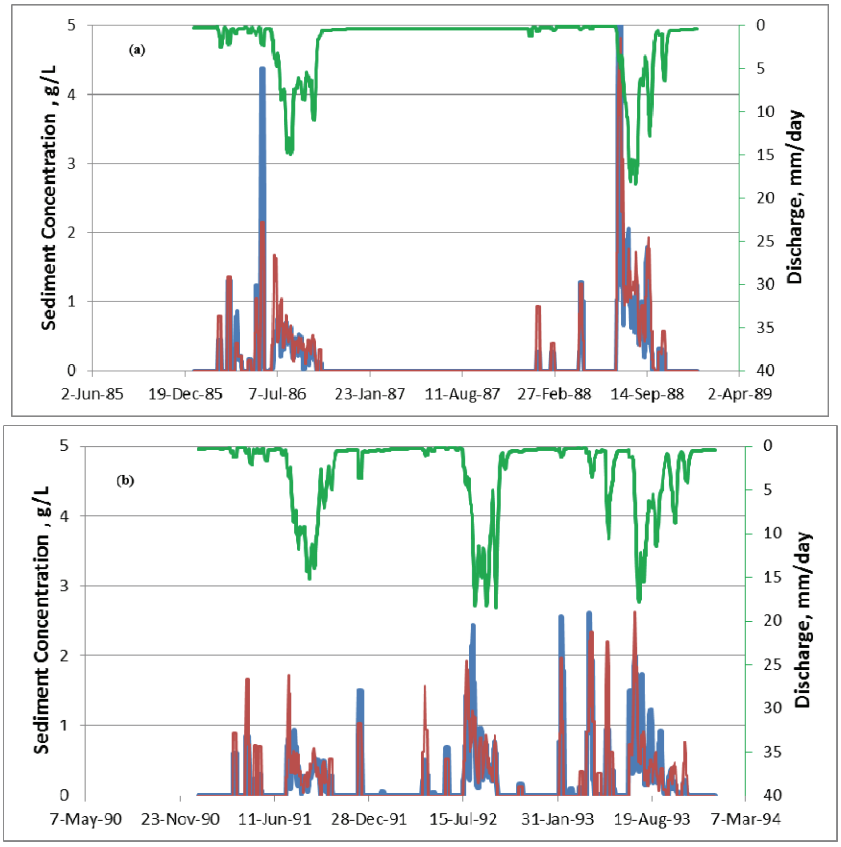

Figure B3. Predicted (red line) and observed (blue line) data for (a) calibration and (b) validation of Andit Tid weekly sediment concentration. Discharge (mm d^{-1}) is shown by the green line at the top of each graph.

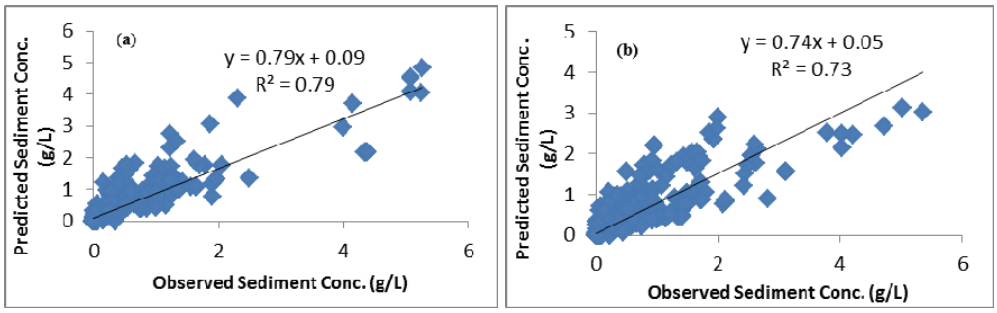

Figure B4. Scatter plots for (a) calibration and (b) validation of Andit Tid weekly sediment concentration.

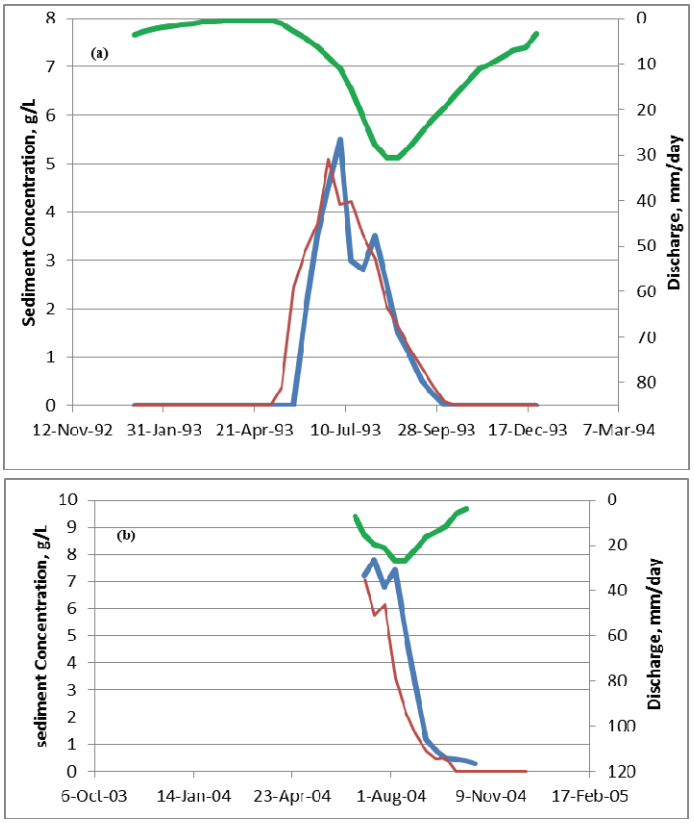

Figure B5. Predicted (red line) and observed (blue line) data for (a) calibration and (b) validation of Blue Nile basin 10-day average sediment concentration. Discharge (mm d^{-1}) is shown by the green line at the top of each graph.

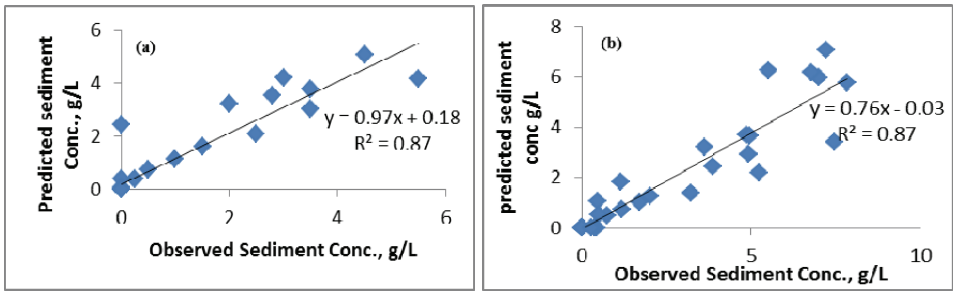

Figure B6. Scatter plots for (a) calibration and (b) validation of Blue Nile basin 10-day average sediment concentration.